TECHNISCHE UNIVERSITÄT MÜNCHEN

Lehrstuhl für Numerische Mechanik

Geometrically Exact Finite Element Formulations for Slender Beams and Their Contact Interaction

Christoph Anton Meier

Vollständiger Abdruck der von der Fakultät für Maschinenwesen der Technischen Universität München zur Erlangung des akademischen Grades eines

Doktor-Ingenieurs (Dr.-Ing.)

genehmigten Dissertation.

Vorsitzender:	Univ.-Prof. Dr. mont. habil. Dr. rer. nat. h. c. Ewald Werner
Prüfer der Dissertation:	
	1. Univ.-Prof. Dr.-Ing. Wolfgang A. Wall
	2. Prof. Ignacio Romero, Ph.D. Universidad Politécnica de Madrid, Madrid / Spanien

Die Dissertation wurde am 23. Mai 2016 bei der Technischen Universität München eingereicht und durch die Fakultät für Maschinenwesen am 07. Juli 2016 angenommen.

Abstract

Highly slender fiber- or rod-like components represent essential constituents of mechanical systems in countless fields of application and scientific disciplines such as mechanical engineering, biomedical engineering, material science as well as bio- or molecular physics. Examples are high-tensile industrial ropes and webbings, fiber-reinforced composite materials or synthetic polymer materials. On entirely different time and length scales, such slender components are relevant when analyzing the supercoiling process of DNA strands, the characteristics of carbon nanotubes or the Brownian dynamics within the cytoskeleton of biological cells, a biopolymer network of highly slender filaments that crucially influences biologically relevant processes such as cell division and cell migration. Often, these slender components can be modeled as 1D Cosserat continua based on a geometrically nonlinear beam theory. In all mentioned cases, mechanical contact interaction crucially influences the overall system behavior. In this thesis, mechanical models for very slender beams and their contact interaction are proposed on the basis of the geometrically exact Kirchhoff-Love beam theory. From these models, novel finite element formulations are derived that allow for an accurate, robust and efficient numerical simulation of complex mechanical systems composed of highly slender fibers with arbitrary orientation.

Compared to other classes of geometrically nonlinear beam elements, geometrically exact beam element formulations are characterized by a high degree of accuracy and computational efficiency. While the existing representatives are almost exclusively based on the Simo-Reissner theory of shear-deformable beams, the current thesis proposes novel finite element formulations based on the geometrically exact Kirchhoff-Love theory of thin beams. The proposed formulations are the first of this category that consider curved 3D beam geometries with anisotropic cross-section shapes and fulfill fundamental mechanical properties such as observer invariance. For finite elements derived from 3D Boltzmann continua such properties are standard. However, the non-additivity and non-commutativity of the configuration space underlying geometrically exact beams, which can be identified as a nonlinear manifold, requires special interpolation strategies. Thereto, novel orthonormal rotation interpolation schemes are proposed that eventually yield two alternative beam elements based on a strong and a weak enforcement of the Kirchhoff constraint, respectively. It is confirmed analytically and numerically that these finite element formulations offer considerable numerical advantages for the simulation of highly slender continua and yield an increased efficiency and robustness as compared to the existing counterparts of Simo-Reissner type. Additionally, a reduced torsion-free beam element formulation is derived from the general theory that results in considerably simplified and very efficient algorithms. The extent of validity of this reduced formulation is strictly analyzed and shown to be relevant for a variety of practical applications. The smooth geometry representation of the proposed formulations can be regarded as highly beneficial for the development of robust beam contact algorithms.

Existing beam contact formulations can be categorized in point-based contact models that consider discrete contact forces and line-based models that assume distributed contact forces. Line-based formulations applied to slender beams represent accurate models in the range of small contact angles, whereas the computational efficiency considerably decreases with increasing contact angles. On the other hand, point-based formulations are very efficient in the regime of large contact angles. However, based on an analytic criterion derived in this thesis, it is shown that these

models are inapplicable for a considerable range of small contact angles as consequence of non-unique closest point projections. In order to combine the advantages of these two basic models, a novel beam contact approach, denoted as all-angle beam contact (ABC) formulation, is proposed. It employs a point contact formulation in the range of large contact angles and a newly developed line contact formulation in the range of small contact angles. The latter is based on a consistently linearized integration interval segmentation that avoids numerical integration across strong discontinuities. This approach in combination with a smooth contact force law and the proposed C^1-continuous beam element formulations leads to a drastic reduction of the numerical integration error, which in many cases only enables optimal convergence behavior under uniform mesh refinement. The point and line contact model are smoothly connected by means of a variationally consistent model transition approach. Based on a sound mechanical derivation, two different transition laws are investigated and optimal algorithmic parameters are suggested. The proposed ABC formulation is supplemented by a step size control of the nonlinear solver allowing for displacement increments per time step that exceed the beam cross-section dimensions and an efficient two-stage contact search based on dynamically adapted search segments.

For both the proposed Kirchhoff beam elements and the beam contact formulation, fundamental properties such as objectivity, conservation of energy and momentum as well as consistent spatial convergence behavior are predicted theoretically and verified by means of suitable numerical test cases. The combination of all the individual methodological constituents proposed in this thesis results in accurate mechanical models for thin beams and their contact interaction. The interplay of the developed algorithmic building blocks yields a highly efficient and robust implicit simulation framework allowing for the analysis of physically relevant time scales in complex mechanical systems composed of highly slender fibers with arbitrary orientation.

Zusammenfassung

Hochschlanke faser- oder stabartige Komponenten sind essentielle Bestandteile mechanischer Systeme in zahllosen Anwendungsfeldern und wissenschaftlichen Disziplinen wie etwa in den Ingenieurwissenschaften, in der Medizintechnik, in den Materialwissenschaften oder in der Bio- und Molekularphysik. Beispiele sind hochfeste Seile und Gewebe, faserverstärkte Verbundwerkstoffe oder synthetische Polymerwerkstoffe. Auf gänzlich anderen Zeit- und Längenskalen sind solche Komponenten etwa relevant zur Analyse des Supercoiling-Prozesses von DNA-Strängen, der Eigenschaften von Carbon Nanotubes oder der Brownschen Teilchenbewegung im Cytoskelett biologischer Zellen. Letzteres stellt ein biopolymeres Netzwerk aus schlanken Filamenten dar, welches biologisch relevante Prozesse wie Zellteilung oder Zellmigration entscheidend beeinflusst. Oft können diese schlanken Komponenten als 1D-Cosserat-Kontinua basierend auf einer geometrisch nichtlinearen Balkentheorie modelliert werden. In allen genannten Fällen wird das globale Systemverhalten entscheidend durch mechanische Kontaktinteraktion beeinflusst. Ziel dieser Arbeit ist die Entwicklung mechanischer Modelle für sehr schlanke Balken und deren Kontaktinteraktion auf Basis der geometrisch exakten Kirchhoff-Love Balkentheorie. Ausgehend von diesen Modellen werden neuartige Finite Elemente Formulierungen abgeleitet, welche die Voraussetzungen schaffen für eine akkurate, robuste und effiziente numerische Simulation komplexer mechanischer Systeme aus hochschlanken Fasern beliebiger Orientierung.

Verglichen mit anderen Klassen geometrisch nichtlinearer Balkenelemente zeichnen sich geometrisch exakte Balkenelementformulierungen durch einen hohen Grad an Genauigkeit und Recheneffizienz aus. Während die bestehenden Repräsentanten beinahe ausschließlich auf der Simo-Reissner Theorie schubweicher Balken basieren, schlägt die vorliegende Arbeit neuartige Finite Elemente Formulierungen basierend auf der geometrisch exakten Kirchhoff-Love Theorie dünner Balken vor. Die entwickelten Formulierungen sind die ersten ihrer Art, welche für gekrümmte 3D-Balkengeometrien mit anisotropen Querschnitten geeignet sind und gleichzeitig grundlegende mechanische Prinzipien wie etwa Objektivität erfüllen. Vom 3D-Boltzmannkontinuum abgeleitete Finite Elemente erfüllen diese Eigenschaften oft standardmäßig. Die Nicht-Additivität und Nicht-Kommutativität des Konfigurationsraumes geometrisch exakter Balken, welcher als nichtlineare Mannigfaltigkeit identifiziert werden kann, erfordert hingegen spezielle Interpolationstechniken. Hierzu werden neuartige, orthonormale Rotationsinterpolationen vorgeschlagen, welche schließlich in zwei alternativen Balkenelementformulierungen, basierend auf einer starken beziehungsweise einer schwachen Erfüllung der Kirchhoff-Zwangsbedingung, resultieren. Es kann sowohl analytisch als auch numerisch nachgewiesen werden, dass diese Finite Elemente Formulierungen beträchtliche Vorteile in der Simulation hochschlanker Kontinua bieten und in einer höheren Recheneffizienz und Robustheit resultieren als existierende Varianten basierend auf der Simo-Reissner Theorie. Darüber hinaus wird eine reduzierte torsionsfreie Balkenelementformulierung von der allgemeinen Theorie abgeleitet, welche zu stark vereinfachten und sehr effizienten Algorithmen führt. Der Gültigkeitsbereich dieser reduzierten Formulierung wird stringent analysiert. Außerdem wird gezeigt, dass dieser für viele praktische Anwendungen relevant ist. Die glatte Geometriedarstellung der entwickelten Formulierungen erweist sich als äußerst vorteilhaft für die Entwicklung robuster Balkenkontaktalgorithmen.

Existierende Balkenkontaktformulierungen können in punktbasierte Kontaktmodelle, welche diskrete Kontaktkräfte annehmen, und linienbasierte Modelle, welche verteilte Kontaktkräfte annehmen, unterteilt werden. Linienbasierte Formulierungen angewendet auf schlanke Balken stellen präzise Modelle im Bereich kleiner Kontaktwinkel dar, während die resultierende Recheneffizienz mit zunehmenden Kontaktwinkeln erheblich abnimmt. Andererseits können punktbasierte Formulierungen als sehr effizient im Bereich großer Kontaktwinkel erachtet werden. Allerdings kann anhand eines in dieser Arbeit abgeleiteten analytischen Kriteriums gezeigt werden, dass diese Modelle aufgrund nicht eindeutiger Closest-Point-Projektionen innerhalb eines beträchtlichen Bereichs kleiner Kontaktwinkel nicht anwendbar sind. Um nun die Vorteile dieser beiden grundlegenden Modelle zu kombinieren, wird ein neuartiger Ansatz, bezeichnet als All-Angle Beam Contact (ABC) Formulierung, vorgeschlagen. Diese Formulierung wendet eine Punktkontaktformulierung im Bereich kleiner Kontaktwinkel sowie eine neu entwickelte Linienkontaktformulierung im Bereich großer Kontaktwinkel an. Letztere basiert auf einer konsistent linearisierten Integrationsintervall-Segmentierung, welche eine numerische Integration über starke Diskontinuitäten hinweg vermeidet. In Kombination mit einem glatten Kontaktkraftgesetz und den entwickelten C^1-stetigen Balkenelementformulierungen führt dieser Ansatz zu einer drastischen Reduzierung des numerischen Integrationsfehlers, wodurch in vielen Fällen erst ein optimales Konvergenzverhalten bei gleichmäßiger Netzverfeinerung ermöglicht wird. Der glatte Übergang zwischen Punkt- und Linienkontaktmodell wird auf variationell konsistente Weise gewährleistet. Basierend auf einer stringenten Herleitung werden zwei unterschiedliche Modellübergangsgesetze untersucht und optimale algorithmische Parameter vorgeschlagen. Die entwickelte ABC-Formulierung wird durch eine Schrittweitenregelung des nichtlinearen Lösers ergänzt, welche Verschiebungsinkremente pro Zeitschritt ermöglicht, die die Balkenquerschnittsdimensionenen überschreiten. Der Algorithmus wird schließlich durch eine effiziente, zweistufige Kontaktsuche basierend auf dynamisch angepassten Suchsegmenten komplettiert.

Sowohl für die vorgeschlagenen Kirchhoff-Balkenelemente als auch für die Balkenkontaktformulierung werden grundlegende Eigenschaften wie Objektivität, Energie- und Impulserhaltung, aber auch konsistentes räumliches Konvergenzverhalten theoretisch sowie durch numerische Tests verifiziert. Die Kombination all der einzelnen, in dieser Arbeit vorgeschlagenen methodischen Bestandteile führt zu einem präzisen mechanischem Modell für dünne Balken und deren Kontaktinteraktion. Das Zusammenspiel der entwickelten algorithmischen Komponenten liefert ein hocheffizientes und robustes implizites Simulationswerkzeug, welches die Untersuchung physikalisch relevanter Zeitskalen in komplexen mechanischen Systemen bestehend aus hochschlanken Fasern beliebiger Orientierung ermöglicht.

Contents

Nomenclature

Representation of scalars, tensors and other quantities

q, Q	Scalar quantity, Euclidean norm of corresponding vectors $\mathbf{q}, \mathbf{Q}$
$\mathbf{q}, \mathbf{Q}$	Tensor of order one or higher, matrix representation
$\boldsymbol{q}, \mathcal{Q}$	Tensor object of 3D continuum mechanics
q	Vector or matrix containing elementwise assembled discrete quantities
Q	Vector or matrix containing globally assembled discrete quantities
$\mathcal{Q}$	Function space

Operators and symbols

$\otimes$	Dyadic product
$\times$	Vector product
$\cdot$	Inner product
$(.)^T$	Transpose of a tensor
$(.)^{-1}$	Inverse of a tensor or mapping
$(.)^{-T}$	Transpose of the inverse of a tensor
$\det(.)$	Determinant
$\mathbf{I}_n$	Identity tensor of dimension $n \times n$
$\delta(.)$	Variation of a quantity (additive in all cases besides $\delta\boldsymbol{\theta}$ and $\delta\boldsymbol{\Theta}$)
$\delta_o(.)$	Objective part of the variation of a quantity
$\Delta(.)$	Finite increment of a quantity (additive in all cases besides $\Delta\boldsymbol{\theta}$ and $\Delta\boldsymbol{\Theta}$)
$\|\|(.)\|\|$	Euclidean norm
$\|\|(.)\|\|_\infty$	Infinity norm
$\mathrm{rv}(.)$	Extraction of rotation vector from rotation tensor
ϵ_{ijk}	Levi-Civita-Symbol
$\delta^{ij}, \delta_{ij}, \delta^i_j$	Kronecker delta symbol
$\mathrm{sr}(.)$	Smallest rotation mapping
$\mathrm{nl}(.)$	Arbitrary function that depends on its arguments in a nonlinear manner
$\bar{(.)}$	Quantities associated with reference triad of smallest rotation mapping
$(.)'$	Derivative with respect to arc-length parameter s
$\dot{(.)}$	Time derivative
$\mathbf{diag}\big[.\big]$	Diagonal matrix
$L(.)$	Linearization of a quantity

Superscripts and subscripts

$(.)_{\mathbf{E}_i}$	Matrix representation of a tensor given in the basis $\mathbf{E}_i$
$(.)_{\mathbf{g}_i}$	Matrix representation of a tensor given in the basis $\mathbf{g}_i$
$(.)_M$	Quantity associated with intermediate triad
$(.)_{M_\varphi}$	Quantity associated with intermediate triad of spatial SR mapping
$(.)_{M_{\hat{\varphi}}}$	Quantity associated with intermediate triad of temporal SR mapping
$(.)_{SR}$	Quantity associated with smallest rotation mapping
$(.)_{FS}$	Quantity associated with Frenet-Serret frame of a curve
$(.)_\parallel$	Vector component parallel to centerline tangent or line contact contribution
$(.)_\perp$	Vector component normal to centerline tangent or point contact contribution
$(.)_0$	Quantity of initial configuration
$(.)_u$	Quantity at Dirichlet boundary
$(.)_\sigma$	Quantity at Neumann boundary
$(.)_{int}$	Contribution of internal forces
$(.)_{ext}$	Contribution of external forces
$(.)_{kin}$	Contribution of kinetic forces
$(.)_{con}$	Contribution of contact forces
$(.)_{\lambda_\epsilon}$	Contribution due to inextensibility constraint
$(.)_h$	Spatially discretized quantity, domain or function space
$(.)^*$	Changed quantity as consequence of a rigid body motion
$(.)_{ref}$	Reference solution for a quantity of interest
$(.)_a$	Quantity associated with axial tension mode
$(.)_s$	Quantity associated with shear mode
$(.)_t$	Quantity associated with torsion mode
$(.)_b$	Quantity associated with bending mode
$(.)_{TAN}$	Quantity associated with triad parametrization via nodal tangents
$(.)_{ROT}$	Quantity associated with triad parametrization via nodal rotation vectors
$(.)_{bl}$	Contact quantity associated with a bilateral closest point projection
$(.)_{ul}$	Contact quantity associated with a unilateral closest point projection
$(.)_c$	Contact quantity that is evaluated at the bilateral or unilateral closest points

Representation of spatial and material quantities in associated frames

$\mathbf{q}$	Spatial tensor
$\mathbf{Q}$	Material tensor
q_i	Components of spatial tensor when expressed in the frame $\mathbf{e}_1, \mathbf{e}_2, \mathbf{e}_3$
Q_i	Components of material tensor when expressed in the frame $\mathbf{E}_1, \mathbf{E}_2, \mathbf{E}_3$
Q_i	Components of spatial tensor when expressed in the frame $\mathbf{g}_1, \mathbf{g}_2, \mathbf{g}_3$
q_{g_1}, q_n, q_b	Components of a spatial vector $\mathbf{q}$ expressed in the Frenet-Serret frame

3D continuum mechanics

$\mathcal{X}(\mathfrak{s})$	Initial position of cross-section point with convective coordinates $\mathfrak{s}$
$\boldsymbol{x}(\mathfrak{s})$	Current position of cross-section point with convective coordinates $\mathfrak{s}$
$\boldsymbol{x}_A$	Reference vector defining moment stress resultants
$\mathfrak{s}$	Collection of convective coordinates describing material cross-section point
s_1, s_2, s_3	Individual convective coordinates describing material cross-section point
$\mathcal{P}$	First Piola-Kirchhoff stress tensor
$\bar{S}$	Second Piola-Kirchhoff stress tensor
$\boldsymbol{\sigma}$	Cauchy stress tensor
$\boldsymbol{t}_1, \boldsymbol{t}_2, \boldsymbol{t}_3$	Piola surface stress vectors
$\mathcal{F}$	Deformation gradient
$\mathcal{E}$	Cauchy-Green deformation tensor
$\mathcal{C}$	Material constitutive tensor of Saint-Venant-Kirchhoff material
$\boldsymbol{g}_i, \mathcal{G}_i$	Spatial and material covariant base vectors for $i = 1, 2, 3$
$\boldsymbol{g}^i, \mathcal{G}^i$	Spatial and material contravariant base vectors for $i = 1, 2, 3$

Large rotations and 1D kinematics

$\mathbf{g}_1, \mathbf{g}_2, \mathbf{g}_3$	Base vectors spanning the beam cross-section, also denoted as material triad
$\mathbf{E}_1, \mathbf{E}_2, \mathbf{E}_3$	Material base vectors of Cartesian frame
$\mathbf{e}_1, \mathbf{e}_2, \mathbf{e}_3$	Spatial base vectors of Cartesian frame
$\boldsymbol{\Lambda}$	Rotation tensor, material triad with base vectors $\mathbf{g}_1, \mathbf{g}_2, \mathbf{g}_3$
$\tilde{\boldsymbol{\Lambda}}$	Relative rotation tensor between initial and current material triad
$SO(3)$	Special orthogonal group
$so(3)$	Set of skew symmetric tensors
$T_{\boldsymbol{\Lambda}}SO(3)$	Tangent space of $SO(3)$ at $\boldsymbol{\Lambda}$
$\mathbf{S}(\mathbf{a})$	Skew symmetric tensor with arbitrary axial vector $\mathbf{a} \in \Re^3$
$\exp(\mathbf{S}(\mathbf{a}))$	Representation of rotation tensor with rotation vector $\mathbf{a}$ via exponential map
$\mathbf{q}$	Arbitrary primary variable for rotation parametrization
$\boldsymbol{\psi}$	Spatial (total) rotation vector
ψ	Euclidean norm of rotation vector $\boldsymbol{\psi}$
$\mathbf{e}_{\boldsymbol{\psi}}$	Normalized rotation vector representing axis of rotation
$\boldsymbol{\Psi}$	Material (total) rotation vector
$\Delta\boldsymbol{\psi}, \Delta\boldsymbol{\Psi}$	Spatial and material additive (finite) rotation vector increment
$\Delta\boldsymbol{\theta}, \Delta\boldsymbol{\Theta}$	Spatial and material multiplicative (finite) rotation vector increment
$\delta\boldsymbol{\psi}, \delta\boldsymbol{\Psi}$	Spatial and material additive rotation vector variation
$\delta\boldsymbol{\theta}, \delta\boldsymbol{\Theta}$	Spatial and material multiplicative rotation vector variation
$\mathbf{k}, \mathbf{K}$	Spatial and material curvature vector
$\mathbf{w}, \mathbf{W}$	Spatial and material angular velocity vector
$\mathbf{a}, \mathbf{A}$	Spatial and material angular acceleration vector
$\mathbf{r}$	Beam centerline curve
$\mathbf{u}$	Displacement of beam centerline curve
$\boldsymbol{\kappa}$	Mechanically relevant Frenet-Serret curvature vector of a curve
τ	Mechanically relevant torsion of Frenet-Serret frame of a curve
$\bar{\boldsymbol{\kappa}}$	Geometrical Frenet-Serret curvature vector of a curve

$\bar{\tau}$	Geometrical torsion of Frenet-Serret frame of a curve
$\bar{r}$	Geometrical curvature radius of a curve
$\mathbf{n}_{FS}$	Normal vector of Frenet-Serret frame of a curve
$\mathbf{b}_{FS}$	Binormal vector of Frenet-Serret frame of a curve
$\mathbf{T}$	Transformation between additive and multiplicative variations $\delta\boldsymbol{\psi}$ and $\delta\boldsymbol{\theta}$
$\mathbf{t}$	Non-unit tangent vector aligned to beam centerline
t	Norm of non-unit tangent vector $\mathbf{t}$
$\tilde{\mathbf{t}}$	Non-unit tangent vector $\mathbf{t}$ normalized with t^2
φ	Relative angle between intermediate frame and material triad
$\bar{\boldsymbol{\Lambda}}$	Reference triad of smallest rotation mapping
$\boldsymbol{\Lambda}_M$	Intermediate triad
$\mathbf{T}_{\Theta_{M1}\mathbf{t}}$	Transformation matrix between the variations $\delta\Theta_{M1}$ and $\delta\mathbf{t}$
$\mathbf{T}_{\boldsymbol{\theta}\mathbf{t}}$	Transformation matrix between the variations $\delta\boldsymbol{\theta}$ and $\delta\mathbf{t}$
$\mathbf{T}_M$	Transformation matrix between the variations $(\delta\mathbf{t}, \delta\varphi)$ and $(\delta\boldsymbol{\theta}, \delta t)$
$\mathbf{T}_{\varphi\boldsymbol{\theta}}$	Transformation matrix between the variations $\delta\varphi$ and $\delta\boldsymbol{\theta}$
$\tilde{\mathbf{T}}$	Transformation matrix between the variations $(\delta\mathbf{t}, \delta\Theta_1)$ and $(\delta\boldsymbol{\theta}, \delta t)$
$\boldsymbol{\Lambda}_R$	Rigid body rotation
$\mathbf{r}_R$	Rigid body translation

1D stress resultants, constitutive laws and balance equations

s	Arc-length parameter on initial beam centerline
l	Beam length in initial configuration
Ω_l	Beam arc-length domain
$\tilde{s}$	Arc-length parameter on current beam centerline
$\tilde{l}$	Beam length in current configuration
t	Time
T	Total simulation time
Γ_σ	Neumann boundary of the beam
Γ_u	Dirichlet boundary of the beam
$C(\mathbf{r}, \mathbf{q})$	Configuration of the beam with primary variable fields $\mathbf{r}$ and $\mathbf{q}$
$\tilde{\mathbf{f}}, \tilde{\mathbf{m}}$	Distributed external forces and moments per unit length
$\mathbf{f}_\rho, \mathbf{m}_\rho$	Distributed inertia forces and moments per unit length
$\tilde{\mathbf{f}}_\rho$	Sum of distributed inertia and external forces per unit length
$\tilde{\mathbf{m}}_\rho$	Sum of distributed inertia and external moments per unit length
$\mathbf{f}_\sigma, \mathbf{m}_\sigma$	Forces and moments at the Neumann boundary Γ_σ
$\mathbf{f}, \mathbf{m}$	Spatial force and moment stress resultants
$\mathbf{F}, \mathbf{M}$	Material force and moment stress resultants
$G(\mathbf{r}, \mathbf{q})$	Weak form of the balance equations with primary variable fields $\mathbf{r}$ and $\mathbf{q}$
$\mathcal{L}(\mathbf{r}, \mathbf{q})$	Lagrangian of variational problem with primary variable fields $\mathbf{r}$ and $\mathbf{q}$
$\boldsymbol{\gamma}, \boldsymbol{\Gamma}$	Spatial and material deformation measures representing tension and shear
$\boldsymbol{\omega}, \boldsymbol{\Omega}$	Spatial and material deformation measures representing torsion and bending
ϵ	Axial tension

$\mathbf{H}$	Material strain vector
$\tilde{\Pi}_{int}, \Pi_{int}$	Length-specific and total hyperelastic stored energy function
$\tilde{\Pi}_{kin}, \Pi_{kin}$	Length-specific and total kinetic energy
$\mathbf{c}_m, \mathbf{C}_M$	Spatial and material rotational constitutive tensor
$\mathbf{c}_f, \mathbf{C}_F$	Spatial and material translational constitutive tensor
A	Beam cross-section area
R	Beam cross-section radius
ζ	Beam slenderness ratio
ζ_{ele}	Element slenderness ratio
$\bar{A}_2, \bar{A}_3$	Reduced cross-section areas
I_2, I_3	Principal moments of inertia
I	Principal moment of inertia for isotropic cross-sections
I_T	Torsional moment of inertia
I_P	Polar moment of inertia
E	Young's modulus
G	Shear modulus
ν	Poisson's ratio
$\mathbf{c}_\rho, \mathbf{C}_\rho$	Spatial and material inertia tensor
ρ	Mass density
$\tilde{\mathbf{l}}, \mathbf{l}$	Length-specific and total linear momentum
$\tilde{\mathbf{h}}, \mathbf{h}$	Length-specific and total angular momentum
$\mathbf{f}_{ext}, \mathbf{m}_{ext}$	Total external forces and moments
$\Pi_{\lambda_{\Gamma 23}}$	Lagrange multiplier potential for weak enforcement of Kirchhoff constraint
$\lambda_{\Gamma 2}, \lambda_{\Gamma 3}$	Lagrange multiplier fields for weak enforcement of Kirchhoff constraint
Π_{λ_ϵ}	Lagrange multiplier potential for inextensibility constraint
λ_ϵ	Lagrange multiplier fields for inextensibility constraint
c_ϵ	Scaling factor for augmented Lagrange type inextensibility constraint
c	Wave speed
ω	Eigenfrequency
$< M_t >$	Spatially averaged norm of torsional moment
$< M_b >$	Spatially averaged norm of bending moment
$\bar{M}_t$	Spatially and temporally averaged norm of torsional moment
$\bar{M}_b$	Spatially and temporally averaged norm of bending moment

Function spaces

$\mathcal{U}$	Trial space for translational and rotational primary variable fields
$\mathcal{V}$	Test space for translational and rotational primary variable fields
$\mathcal{U}_{\lambda_{\Gamma 23}}$	Lagrange multiplier trial space for weak enforcement of Kirchhoff constraint
$\mathcal{V}_{\lambda_{\Gamma 23}}$	Lagrange multiplier test space for weak enforcement of Kirchhoff constraint
$\mathcal{U}_{\lambda_\epsilon}$	Lagrange multiplier trial space for inextensibility constraint
$\mathcal{V}_{\lambda_\epsilon}$	Lagrange multiplier test space for inextensibility constraint
$\mathcal{U}_{\lambda_c}$	Lagrange multiplier trial space for line contact constraint
$\mathcal{V}_{\lambda_c}$	Lagrange multiplier test space for line contact constraint
$\mathcal{W}^{m,2}$	Sobolev space of functions with square integrable derivatives up to order m

Spatial discretization

m_r	Highest derivative of centerline curve in weak form
m_Λ	Highest derivative of triad field in weak form
n_{ele}	Number of elements
l_{ele}, h	Initial length of a finite element
$(.)^i, (.)^j$	Quantity associated with node i, j
$\hat{(.)}^i, \hat{(.)}^j$	Primary solution variable associated with node i, j
$(.)^{(e)}$	Quantity associated with element e
$(.)^k$	Quantity evaluated at Newton iteration k
ξ	Element parameter coordinate
$N_r(\xi)$	General shape functions associated with centerline interpolation
$L(\xi)$	Lagrange shape functions
$H_d(\xi)$	Hermite shape functions associated with nodal positions
$H_t(\xi)$	Hermite shape functions associated with nodal tangents
n_r	Number of element nodes associated with centerline interpolation
$n_{r,tot}$	Total number of nodes associated with centerline interpolation
$N_q(\xi)$	General shape functions associated with rotation interpolation
n_Λ	Number of element nodes associated with rotation interpolation
n_n	Number of element nodes in the case $n_\Lambda = n_r$
$n_{\Lambda,tot}$	Total number of nodes associated with rotation interpolation
$\hat{\mathbf{d}}^i$	Nodal position vector
$\hat{\mathbf{t}}^i$	Nodal tangent vector
$J(\xi)$	Element Jacobian
$\hat{\mathbf{x}}$	Vector containing all nodal primary variables of a finite element
$\mathbf{X}$	Vector containing all primary variables of the global problem
$\mathbf{D}$	Global vector of all primary variables relevant for centerline interpolation
n_X	Size of the vector $\mathbf{X}$
$\mathbf{r}$	Element residual vector
$\mathbf{R}$	Global residual vector
$\mathbf{k}$	Element tangent stiffness matrix
$\mathbf{K}$	Global tangent stiffness matrix
$\delta_\mathbf{X}, \delta_\mathbf{R}$	Tolerances to be fulfilled for Newton convergence
λ	Load factor
$n_{iter,n}$	Number of Newton iterations in time step n
$n_{iter,max}$	Maximal admissible number of Newton iterations per time step
$n_{iter,tot}$	Total number of Newton iterations during a simulation
$\mathbf{L}$	Elementwise matrix of Lagrange shape functions
$\mathbf{H}$	Elementwise matrix of Hermite shape functions
$\hat{\mathbf{d}}$	Elementwise vector of nodal primary variables of centerline interpolation
c	Constant of Hermite interpolation
c_{opt}	Optimal value for constant of Hermite interpolation
$\mathbf{\Lambda}^i_{M_{\hat{\varphi}},n}$	Nodal intermediate triad: SR mapping in time from $\mathbf{\Lambda}^i_{M_{\hat{\varphi}},n-1}$ to $\mathbf{\Lambda}^i_{M_{\hat{\varphi}},n}$
$\hat{\varphi}^i$	Nodal relative angle associated with nodal intermediate triads $\mathbf{\Lambda}^i_{M_{\hat{\varphi}},n}$

$\mathbf{\Lambda}_{M_\varphi,n}(\xi)$	Intermediate triad field: SR mapping in space from $\mathbf{\Lambda}_{M,n}(\xi^r)$ to $\mathbf{\Lambda}_{M_\varphi,n}(\xi)$
$\varphi_h(\xi)$	Relative angle field associated with intermediate triad field $\mathbf{\Lambda}_{M_\varphi,n}(\xi)$
$\mathbf{\Lambda}_r$	Reference triad for triad interpolation
$\mathbf{\Phi}_{lh}(\xi)$	Material relative rotation vector field employed for triad interpolation
$\mathbf{\Phi}^{IJ}$	Material relative rotation vector between nodes I and J
$\tilde{\mathbf{I}}^i(\xi)$	Shape function matrices of rotation vector-based triad interpolation
$\delta\hat{\boldsymbol{\theta}}$	Elementwise assembly of nodal spin vectors
$\mathbf{L}_\parallel$	Elementwise matrix of Lagrange shape functions for interpolation of $\delta\Theta_1$
$\delta\hat{\mathbf{\Theta}}$	Elementwise assembly of nodal spin vector components $\delta\hat{\Theta}_1^i$
$\Delta\hat{\mathbf{\Theta}}$	Elementwise assembly of the nodal multiplicative increments $\Delta\hat{\Theta}_1^i$
$\mathbf{v}_{...}$	Elementwise auxiliary vectors for representation of discrete variations
r	Constraint ratio
n_{eq}	Number of equations
$n_{eq,c}$	Number of constraint equations
n_{uk}	Number of unknowns
n_G	Number of Gauss integration points per element
n_{CP}	Number of collocation points
$\bar{(.)}(\xi)$	Re-interpolated field based on the values at discrete collocation points
$\|\|e\|\|^2_{rel}$	Relative L^2-error
$\|\|e\|\|_{e,rel}$	Relative energy error
u_{max}	Maximal displacement occurring in a simulation
k	Polynomial order of interpolation function
$\tilde{\mathbf{T}}_{\hat{\mathbf{x}}}$	Elementwise transformation matrix between element variants TAN and ROT
$\tilde{\mathbf{T}}_{\mathbf{X}}$	Global transformation matrix between element variants TAN and ROT

Temporal discretization

Δt	Time step size
Δt_0	Initial time step size of load step adaption scheme
N	Number of time steps
N_{min}	Minimal number of time steps required for convergence
N_0	Initial number of time steps of load step adaption scheme
n	Time step index
t_n	Time at time step n
$(.)_n$	Evaluation of a quantity at time t_n
$\tilde{\boldsymbol{\theta}}_{n+1}$	Spatial multiplicative rotation increment between time steps t_n and t_{n+1}
$\tilde{\mathbf{\Theta}}_{n+1}$	Material multiplicative rotation increment between time steps t_n and t_{n+1}
$\tilde{\mathbf{u}}_{n+1}$	Spatial (additive) displacement increment between time steps t_n and t_{n+1}
$\ddot{\mathbf{r}}_{mod}$	Modified translational acceleration of Lie-Group generalized-α scheme
$\mathbf{A}_{mod}$	Modified angular acceleration of Lie-Group generalized-α scheme
β, γ	Parameters of Newmark's method
α_f, α_m	Parameters of generalized-α method
ρ_∞	Spectral radius in the high-frequency limit

Beam contact

$(.)^{(c)}$	Quantity associated with contact element pair c
$(.)_1$	Quantity associated with element 1 of contact pair (=slave for line contact)
$(.)_2$	Quantity associated with element 2 of contact pair (=master for line contact)
ξ, η	Parameter coordinates of element 1 or element 2 of a contact element pair
$(.)'$	Parameter derivative of a quantity associated with element 1 or element 2
$d(\xi, \eta)$	Distance function
d_{bl}, g	Bilateral minimal distance value and gap
ξ_c, η_c	Bilateral closest point coordinates
$d_{ul}(\xi), g(\xi)$	Unilateral minimal distance value and gap at position ξ
$\eta_c(\xi)$	Unilateral closest point coordinate at position ξ
p_1, p_2	Orthogonality conditions to be solved for closet point projection
$\Pi_{c\varepsilon}$	Penalty potential
$\mathbf{f}_{c\varepsilon}$	Penalty contact force vector
$\mathbf{n}$	Contact normal vector
ε	Penalty parameter
$\Pi_{c\lambda}$	Lagrange multiplier potential for beam contact
λ_c	Lagrange multiplier representing contact force
$\mathbf{f}_{c\lambda}$	Lagrange multiplier-based contact force vector
α	Contact angle enclosed by tangent vectors at contact point
z	Cosine of contact angle defined by inner product of tangents
α_{min}	Lower bound for contact angle in order to guarantee for unique CPP
β_1, β_2	Angle enclosed by contact normal and Frenet normal vectors 1 and 2
$\hat{\mathbf{d}}_{12}$	Vector of all translational nodal primary variables of elements 1 and 2
μ_{max}	Maximal admissible ratio of cross-section to curvature radius
n_{II}	Number of contact integration intervals per slave beam element
n_{GR}	Number of integration points per integration interval
n_{GP}	Total number of integration points per slave element
J_{c1}	Total Jacobian required for integration of line contact forces
$\xi_{1,i}, \xi_{2,i}$	Element parameter coordinates confining the integration interval i
$\bar{\xi}_j$	Gauss point coordinate within a local integration interval
ξ_{ij}	Element parameter coordinate of integration point $\bar{\xi}_j$ in interval i
$(.)^{ij}$	General quantity associated with integration point $\bar{\xi}_j$ in interval i
w_j	Gauss weight associated with Gauss point coordinate $\bar{\xi}_j$
η_{EP}	Master beam element parameter coordinates of physical beam endpoints
ξ_B	Projection of η_{EP} on slave beam element
$N^j_{\lambda 1}(\xi)$	Shape functions of discretized Lagrange multiplier field $\lambda_{ch}(\xi)$
$\mathbf{N}_{\lambda 1}(\xi)$	Elementwise assembly of shape functions $N^j_{\lambda 1}(\xi)$
$\hat{\lambda}^j_1$	Nodal Lagrange multipliers
$\hat{\boldsymbol{\lambda}}_1$	Elementwise assembly of Lagrange multipliers $\hat{\lambda}^j_1$
n_λ	Number of nodes per slave element for Lagrange multiplier interpolation
$\hat{g}^j$	Averaged nodal gaps
$\hat{\lambda}^j_{\varepsilon 1}$	Averaged nodal penalty forces

g_n	Normalized gap
g_{min}	Prescribed minimal value of gap
$g_{n,min}$	Prescribed minimal value of normalized gap
$\Delta\tilde{s}_{GP}$	Arc-length distance between two successive Gauss points
$\Delta\tilde{s}_{GP,max}$	Maximal admissible distance between two successive Gauss points
$n_{GP,min}$	Minimal admissible number of Gauss points per slave element
$k_{...}$	Safety factor
α_1, α_2	Shifting angles defining transition angle range of ABC formulation
$\bar{\alpha}_{12}$	Mean shifting angle
$k(\alpha)$	Transition factor describing smooth model transition
$f_{c\varepsilon}$	Scalar contact force
$m_{c\varepsilon}$	Scalar contact moment
$\mathbf{v}_1, \mathbf{v}_2$	Auxiliary vectors for representation of discrete variations
r_s	Radius of spherical search boxes for first search stage
n_{seg}	Number of search segments per beam element
l_{seg}	Length of search segment
β_{max}	Prescribed maximal deviation between straight search segment and centerline
r_{cyl}	Radius of cylindrical search boxes for second search stage
γ	Intersection angle between two straight search segments
$\bar{g}$	Gap value at which contact force becomes active for regularized penalty law
$\tilde{\Pi}_{c\varepsilon}$	Penalty potential normalized by penalty parameter
W_{con}	Mechanical work contribution of contact forces
W_{tot}	Total mechanical work
E_{tot}	Total system energy
ΔD_{max}	Maximal displacement per time step

Abbreviations

ABC	All-angle Beam Contact
AMG	Algebraic MultiGrid method
ANS	Assumed Natural Strains
CG	Conjugate Gradient method
CJ	Reissner-type beam element formulation by Crisfield and Jelenić
CP	Collocation Point
CPP	Closest Point Projection
CS	Consistent Spin interpolation
DoF	Degree of Freedom
EMM	Energy-Momentum Method
FEM	Finite Element Method
FS	Frenet-Serret
$GEMM$	Generalized Energy-Momentum Method
$GMRES$	Generalized Minimal RESidual method
HSR	Hermitian Simo-Reissner element
IE	InExtensibility constraint
ILU	Incomplete Lower Upper triangular matrix

IP	Integration Point
IT	IsoTropic element formulation
LBB	Ladyshenskaya-Babuska-Brezzi condition
LU	Lower Upper triangular matrix
MCS	Minimally Constrained Strains
MWR	Method of Weighted Residuals
PDE	Partial Differential Equation
$PMTPE$	Principle of Minimum of Total Potential Energy
PVW	Principle of Virtual Work
RI	Reduced Integration
ROT	Triad parametrization via nodal ROTation vectors
SK	Strong enforcement of Kirchhoff constraint
$SPDE$	Stochastic Partial Differential Equation
SR	Smallest Rotation
SSC	Step Size Control of Newton-Raphson scheme
ST	Small Tension
SV	Reissner-type beam element formulation by Simo and Vu-Quoc
TAN	Triad parametrization via nodal TANgents
TF	Torsion-Free element formulation
WK	Weak enforcement of Kirchhoff constraint

1 Introduction

1.1 Motivation

In countless fields of application, mechanical systems are characterized by the prevalence of slender fiber- or rod-like components. Often, these components crucially determine the mechanical characteristics of the overall system such as anisotropic strength and stiffness properties or relevant mechanisms of load transfer. While the rather descriptive notions of ”fibers” and ”rods” might immediately be associated with slender or lengthy bodies featuring more or less transverse flexibility, the more concise description for the class of mechanical components considered in this thesis is given by the notion ”beams”. Mechanically, a beam is a structural model appropriate to describe the motion and deformation of bodies whose dimension in length direction is much larger than the dimensions in transverse directions. Consequently, the applicability of beam models can be evaluated by the ratio of length to lateral dimensions of a body, denoted as slenderness or slenderness ratio. In this context, the mechanical model of ”ropes” represents the extreme case of beams with negligible stiffness in transverse direction.

In classical engineering applications, such slender beam-like components arise for example in form of lightweight construction frames, gear shafts or wheel axles in vehicles, cables, oil pipelines or deep drilling rods. In contrast to these single-component systems, their is a variety of technically relevant multi-component systems that crucially rely on the composition out of a large number of slender components. Examples are classical ropes or textile webbings, high-tensile industrial ropes and webbings, fiber-reinforced composite materials but also cellulose fibers determining the characteristics of paper [67, 69, 135]. Typically, there are two distinctive differences between the aforementioned single- and multi-component systems: Firstly, the mentioned multi-component systems typically consist of individual fibers with very high slenderness ratio as compared to most of the single-component systems summarized above. Secondly, the overall mechanical properties and the global system response of these multi-component systems is essentially determined by fiber-to-fiber contact interaction and the resulting force transfer between individual fibers. Exactly these two aspects, the modeling of mechanical components with highest slenderness ratios and their contact interaction will lie in the focus of this thesis. Mechanical systems unifying these two aspects can be found in numerous modern fields of application and are in the focus of several scientific disciplines that range far beyond the classical engineering examples considered above: In the field of material science, slender components can for example be identified in form of interconnected macromolecules occurring in synthetic polymer materials, in novel fiber-based porous materials with tailored constitutive properties on the basis of optimized fiber sizes, orientations and densities but also in fiber-based, acoustic and thermal insulation materials [186, 240]. Arterial stents, tube-shaped devices on the basis of thin steel wire structures, are employed in biomedical engineering in order to keep passage ways open

in human blood vessels. They can be identified as further practical applications that crucially rely on highly slender mechanical components and their contact interaction [94, 192]. Slender constituents at entirely different length and time scales can be found in biological systems: As examples, the fibers in biological tissue, muscle fibers or the filaments in biopolymer networks have to be mentioned [61, 99, 198]. A representative of the latter kind is the cytoskeleton of biological cells, which influences biologically highly relevant phenomena such as cell-division, cell migration or intracellular transport and has led to considerable research effort in the field of biophysics in recent years. Also the supercoiling process of DNA strands is crucially determined by the mechanical behavior of slender structures and their mutual interaction [236], and has attracted the interest of countless scientists in the field of molecular physics. As last example, the development of novel nano-materials is considered. One of the arguable most prominent applications for beam models in this field and related disceplines such as electronics or optics are carbon nanotubes [223]. While slenderness ratios above 10^3 are very common among the examples mentioned so far, these carbon molecules yield slenderness ratios up to 10^9.

As compared to experimental investigations of such systems, the approach of mechanical modeling and numerical simulation offers a considerably increased degree of flexibility. For example, parameter studies can be realized in a very efficient and flexible manner. Moreover, numerical simulation schemes can be extended by additional functionalities allowing for example for system optimization or inverse analysis, i.e. for a determination of certain system properties that can not be measured otherwise on the basis of a known mechanical loading state and a measured system answer. Finally, investigations on micro- and nano-scales as prevalent in the examples of the last paragraph but also in vivo studies of biological systems are often very difficult, in many cases even impossible, to be conducted in an experimental manner. Besides experiment and numerical simulation, analytic approaches can be considered as third essential instrument of system characterization. However, given the complexity of the systems and microstructures considered so far, analytic investigations are typically limited to very simple geometries and load cases and are mostly based on considerably simplifying assumptions. Throughout this thesis, the focus will lie on the development of accurate mechanical models as well as efficient and robust numerical simulation tools. While the mechanical description of slender components and their contact interaction will be based on geometrically nonlinear 3D beam models, the Finite Element Method (FEM) will be employed in order to allow for a numerical solution of these problems. Approximately, since the last fifty years, the FEM has been in the focus of method developers and applicants and can meanwhile be regarded as the dominating numerical approximation scheme for the solution of partial differential equations (PDEs) of diverse origin, with its roots lying in the field of solid and structural mechanics. Among others, the FEM benefits from its sound mathematical foundation as well as the desirable properties of the resulting, discrete system matrices, paving the way for efficient numerical solution schemes. Compared to alternative discretization techniques such as finite difference schemes, the FEM offers a high degree of generality and geometrical flexibility, which can be regarded as very beneficial when complex structures have to be modeled or when a coupling with further physical fields such as fluid, thermal or electrical fields is required. Both aspects are relevant for many of the applications mentioned above. In the following two sections, the state-of-the-art of existing methods as well as the objective of the current thesis will be presented separately for the two core contents of this thesis, which are finite element models for slender beams and for their contact interaction.

1.2 Geometrically Exact Finite Element Formulations for Nonlinear Beam Problems

The focus of this section lies on geometrically nonlinear, 3D beam formulations appropriate for the modeling of complex systems of highly slender fibers. Especially, so-called geometrically exact formulations based on a numerical realization by means of the finite element method are considered. Moreover, the emphasis lies on formulations based on the so-called Kirchhoff-Love theory of thin rods, which seems to be most suitable for the intended fields of application.

1.2.1 Fundamental approaches

Basically, two essential motivations for applying a beam theory instead of a 3D continuum mechanics theory for the modeling of slender bodies can be identified: In the early days of beam theories, it was the accessibility of analytic solutions as for example "Euler's Elastica", even for large deformation problems, that motivated the development and application of one-dimensional theories. Nowadays, it is the knowledge that the modeling of highly slender bodies via beam theories yields considerably more efficient, but also more well-posed, numerical formulations as it would be the case for 3D continuum theories. So-called *induced* beam theories can be regarded as reduced 1D continuum theories consistently derived from the 3D theory of continuum mechanics under consideration of a basic kinematic constraint that reflects the deformation states expected for slender bodies in a reasonable manner. Such 1D beam theories typically allow to describe the motion and deformation of slender bodies in 3D space on the basis of proper kinematic, kinetic and constitutive resultant quantities. In the case of induced beam theories, these resultant quantities can for example be derived via integration of 3D stress measures over the beam cross-section. The 3D stress measures typically result from the constrained 3D displacement field as well as standard 3D strain measures and constitutive relations. In this context, the cross-section of a beam represents the collection of all material points sharing the same beam length coordinate in the stress-free configuration. On the contrary, so-called *intrinsic* beam theories directly postulate the 1D resultant quantities. These theories are internally consistent in the sense that the resultant quantities as well as the 1D relations connecting these quantities still fulfill essential mechanical principles such as equilibrium of forces and moments, conservation of energy or rather existence of work conjugated stress-strain pairs, observer invariance or path-independence of conservative problems. Nevertheless, intrinsic beam theories are decoupled from the 3D continuum mechanics theory. Typically, the postulated constitutive constants relating stress and strain measures are determined experimentally, while the constitutive constants of induced beam theories follow directly from the corresponding 3D constitutive laws. Such postulated constitutive laws based on experimentally determined constants are favorable for applications where no 3D continuum foundation exists: Considering the low number of discrete molecules distributed over the thickness of macromolecules as occurring for example in biopolymer networks, DNA strands or carbon nanotubes - to come back to the applications mentioned above - no 3D continuum theory can be applied in a reasonable manner. Nevertheless, it is well-established that these slender components can be described in good approximation by 1D continuum theories and associated experimentally determined constitutive constants [198]. Finally, a compromise between the induced and intrinsic theories considered so far are so-called

semi-induced beam theories, where only the constitutive law is postulated and all the remaining kinetic and kinematic relations are consistently derived from the 3D theory.

Based on the Bernoulli hypothesis of undeformed cross-sections and the work of Euler, the "Kirchhoff beam" [125], proposed by Kirchhoff zu Heidelberg in 1859, was the first formulation allowing for arbitrary initial curvatures and large three-dimensional deformations including the states of bending and torsion. In 1944, this theory was enhanced by Love [153] to also account for small axial tension. A comprehensive historic overview of these early developments is given in the work of Dill [64]. It was Reissner in 1972 for the two-dimensional case [183] and in 1981 for the general three-dimensional case [184], who completed the theory by two additional deformation measures representing the shear deformation of the beam. While the 3D problem statement of Reissner was still based on some additional approximations, Simo [204] extended the work of Reissner to yield a formulation that is truly consistent in the sense of a semi-induced beam theory. Thus, starting from a basic kinematic assumption, all kinetic and kinematic quantities and relations are consistently derived from the 3D continuum theory, while the constitutive law has been postulated. Originally, this theory has been denoted as geometrically exact beam theory. Nowadays, it is also referred to as Simo-Reissner beam theory. According to the definition of Simo [204], also in this thesis, a beam theory is denoted as geometrically exact, if "the relationships between the configuration and the strain measures are consistent with the virtual work principle and the equilibrium equations at a deformed state *regardless of the magnitude of displacements, rotations and strains*" ([58], p. 1126). For that reason, also the notation "finite-strain beams" has been applied in the original work [204]. However, as later argued by several authors (see e.g. [58]) and in accordance with corresponding derivations in the literature (see e.g. [2, 3, 153]), a consistency of the geometrically exact beam theory and the 3D theory of continuum mechanics in the sense of a (fully) induced beam theory can only be assumed as long as small strains are considered. The fulfillment of the basic kinematic assumption of rigid cross-sections underlying the geometrically exact beam theory requires pointwise six (translational and rotational) degrees of freedom in order to uniquely describe the (centroid) position and orientation of the cross-sections. Consequently, this beam theory can be identified as 1D Cosserat continuum [51], derived from a 3D Boltzmann continuum with pointwise three (translational) degrees of freedom. While there exists a variety of beam theories that also consider in-plane as well as out-of-plane cross-section distortion, the current thesis focuses on geometrically exact beam formulations on the basis of the rigid cross-section assumption as applied by Simo and Reissner. Furthermore, throughout this thesis, the notion Simo-Reissner theory will be preferred since the notion geometrically exact beam theory, when following the definition presented above, also applies to consistently derived shear-free formulations on the basis of the Kirchhoff-Love theory. In the remainder of this thesis, the notion "shear-free" represents the opposite of "shear-deformable" and thus is equivalent to "vanishing shear strains", but, of course, not to "vanishing shear stresses". Unfortunately, no absolute consensus concerning naming of the different beam models presented so far can be found in the literature. For that reason, the following nomenclature, trying to be consistent with the most important representatives in the literature, will be applied in this thesis: Geometrically nonlinear beam models capturing the modes of axial tension, torsion and bending and being appropriate for initially straight beams with isotropic cross-section shapes are denoted as nonlinear Euler-Bernoulli beams. The extension to arbitrary initial curvatures and anisotropic cross-section shapes is referred to as Kirchhoff-Love beam theory. Fi-

nally, the (geometrically exact) supplementation by shear deformation modes is covered by the Simo-Reissner theory. Euler-Bernoulli or Kirchhoff-Love formulations that neglect the mode of axial tension are denoted as inextensible Euler-Bernoulli or Kirchhoff-Love variants. Finally, the restriction of shear-free or shear-deformable theories to the geometrically linear regime yields the well-known linear Euler-Bernoulli and Timoshenko beam models [219].

By identifying the configuration space underlying the geometrically exact beam theory as nonlinear, differentiable manifold with Lie group structure and by pointing out important algorithmic consequences resulting from the non-additivity and non-commutativity of the associated group elements, the original work by Simo [204] and the subsequent work by Simo and Vu-Quoc [208] laid the foundation for abundant research work on this topic in the following years. The static beam theory [204, 208] has been extended to dynamics by Cardona and Geradin [43, 44] and by Simo and Vu-Quoc [209]. The contributions of Kondoh et al. [127], Dvorkin et al. [71] as well as Iura and Atluri [113] can be regarded as further pioneering works in this field. These contributions mark the starting point for the development of a large variety of geometrically exact beam element formulations [60, 106, 111, 115, 117, 172, 195, 211] which basically differ in the type of rotation interpolation (e.g. interpolation of incremental, iterative or total rotational vectors), the choice of nodal rotation parametrization (via rotation vectors, quaternions etc.), the type of iterative rotation updates (multiplicative or additive), or the time integration scheme applied to the rotational degrees of freedom (e.g. based on additive or multiplicative rotation increments). Also extensions of the geometrically exact beam theory to arbitrary cross-section shapes with shear centers differing from the cross-section centroid can be found [92]. An overview of the most important developments at that time is exemplarily given in the text books of Crisfield [56] as well as Geradin and Cardona [82]. An break in this development is given by the works of Crisfield and Jelenić [58, 116], who have shown that none of the rotation field discretizations of the formulations existent at that time could preserve both of the important properties objectivity and path-independence (see also [110] for a discussion of this topic). Furthermore, in [58] and [116], a new, objective and path-independent orthogonal interpolation scheme was proposed that directly acts on the rotation manifold and not on any of its rotation vector parametrizations as done in the works before. This formulation was the starting point for the development of many alternative rotation interpolation strategies for geometrically exact beams that also preserve these properties. Among others, orthogonal interpolations of relative rotation vectors (see e.g. [84, 194]) or quaternions (see e.g. [83, 187, 246]), non-orthogonal interpolation strategies in combination with modified beam models (see e.g. [27, 74, 190]) and non-orthogonal interpolation strategies with subsequent orthogonalization (see e.g. [187]) can be identified. As reported in the original work [58, 116], the rotation interpolation scheme proposed by Crisfield and Jelenić can exactly represent the state of constant curvature. Thus, it can be interpreted as geodesic, i.e. shortest, connection between two configurations on the rotation manifold. Consequently, these geodesic rotation interpolation schemes represent the counterpart to linear interpolations of translational quantities. The works [31, 32] as well as the recent contributions [194, 212, 213, 220] can be identified as further geometrically exact beam element formulations based on geodesic interpolations of the rotational (and translational) primary variable fields. A 2D extension of these so-called helicoidal interpolations to higher-order elements is given in [66]. A formulation with smooth centerline representation based on an isogeometric collocation scheme is proposed in [226]. Besides these purely displacement-based elements, also interpolation schemes directly acting at

the strain level combined with a subsequent derivation of the position and rotation field via integration (see e.g. [220, 244, 245]) as well as mixed formulations [197] have been proposed. Furthermore, a variety of contributions considering time integration of rotational variables can be found in this context [17, 26, 35, 62, 86, 109, 119, 144, 189, 210].

While all the formulations presented above have been based on the finite element method, also discrete representatives of Simo-Reissner beam formulations based on finite difference schemes can be found in the literature [118, 136, 137, 145]. These are often denoted as discrete elastic rods and based on the concept of discrete differential geometry (DDG). In the context of finite element formulations for geometrically nonlinear beam problems, again, a variety of alternatives to the geometrically exact formulations considered in the last two paragraphs can be found. The maybe most prominent representatives of these alternatives are the corotational method [55, 56, 59, 76, 81] as well as Absolute Nodal Coordinate (ANC) [200, 201] and solid beam element [14, 79] formulations. The corotational technique was initially introduced by Wempner [229] as well as Belytschko et al. [20, 21] and shows strong similarities to the "natural approach" of Argyris et al. [5]. The basic idea is to split the overall non-linear deformation into a contribution stemming from large rotations and a part stemming from local deformations expressed in a local, "corotated" frame. Often, the local deformation can be modeled on the basis of first- (or second-) order theories such that the entire degree of nonlinearity is represented by the rotation of the local frame. The basic idea of ANC beam element formulations is to employ standard shape functions as known from solid finite element formulations in order to interpolate the 3D displacement field within the beam. Instead of introducing a kinematic constraint and deriving a resultant 1D model, different polynomial degrees are typically applied for the interpolation in beam length direction and in transverse directions. Numerical comparisons as performed e.g. by Romero [187, 188] and Bauchau et al. [18] advocate geometrically exact beams in general, and orthogonal triad interpolation schemes (see e.g. [58]) in particular, with regard to computational accuracy and efficiency. All in all, it can be stated that finite element formulations based on the geometrically exact beam theory have become well-established in the meantime and can arguably be regarded as state-of-the-art methods for the computational treatment of geometrically nonlinear beam problems. Formulations of this category will be in the focus of this thesis.

In the context of the geometrically nonlinear Kirchhoff-Love beam theory, several discrete realizations based on finite difference schemes have recently been proposed [1, 24, 25, 88, 140]. In contrast to the Simo-Reissner theory, also several works based on an analytic treatment of Kirchhoff-Love beam problems exist in the modern literature [138, 202]. Interestingly, most approaches of these two categories can be found in the field of bio- or molecular physics. Although, the theoretical basis of shear-free Kirchhoff-Love beam formulations has a much longer tradition than the Simo-Reissner theory of shear-deformable beams, there are only a few geometrically nonlinear shear-free finite element representations, which have not reached the excellent properties of geometrically exact Simo-Reissner formulations so far. In his recent works [6] and [7], Armero and Valverde gave a historic overview of existing Kirchhoff finite elements and pointed out their drawbacks. Accordingly, the first Kirchhoff type element formulations have applied different interpolations (C^0-continuous Lagrange polynomials for the axial displacements and C^1-continuous Hermite polynomials for the transversal displacements) to the different displacement-components, which led to a loss of objectivity [6]. In later works, the

objectivity could be preserved by employing e.g. trigonometric shape functions, but the corresponding formulations were limited to the investigation of plane circular arches (see e.g. [10] or [11]). A different approach was the development of framework or corotational shear-free beams [57, 100–102, 141], a category of formulations, which naturally preserves the objectivity of the continuous problem. As pointed out in [6], these types of Kirchhoff type formulations often exhibit a comparatively poor accuracy; a fact, which can directly be traced back to the lack of an exact representation of the kinematic quantities. A further critical issue relevant in the context of thin Kirchhoff beams is membrane locking, a locking phenomenon given distinction to by Stolarski and Belytschko [215]. In general, membrane locking denotes the inability of curved structural elements, e.g. beams or shells, to represent the inextensibility constraint of vanishing membrane / axial strains. For thin Kirchhoff beams, [77] was one of the first contributions in which this effect was investigated by relating the beam slenderness ratio to the condition number of the stiffness matrix, but without explicitly using the term locking. Diverse methods have been proposed in the literature in order to avoid membrane locking of Kirchhoff rods. Amongst others, these are the approaches of reduced / selective integration (see e.g. [168, 176, 177]), assumed strains based on the Hu-Washizu functional (see e.g. [49, 121, 142]), assumed stresses based on the Hellinger-Reissner functional (see e.g. [42, 168]) or penalty relaxation / stabilization techniques in combination with membrane correction factors (see e.g. [154, 218]). Most of the works considered so far are limited to 2D beam problems. A historic overview concerning the development of Kirchhoff beam element formulations in general and the key issues of objectivity and membrane locking in particular is given in the recent works of Armero and Valverde [6, 7].

The shear-free beam elements presented by now are typically based on additional kinematic assumptions, thus not being consistent with the concept of geometrically exact beams. The number of existing *geometrically exact* finite element formulations on the basis of the Kirchhoff-Love theory is very limited. For example, the recent contribution of Sansour [196] proposes an energy-momentum method for 2D, initially straight geometrically exact elements based on the nonlinear Euler-Bernoulli theory. The first geometrically exact, 3D, large-deformation, shear-free beam elements fulfilling also the essential requirement of objectivity have been proposed by Boyer [36] and Weiss [227, 228]. In his recent work [37], Boyer extended the original formulation [36] for the modeling of undersea cables. However, these geometrically nonlinear Euler-Bernoulli formulations only treat the special case of beams with circular cross-sections and a straight initial configuration, i.e. the case of beams with rotationally symmetric reference geometry denoted as isotropic bending. This limitation simplifies the theory drastically, and already the modeling of simple piecewise straight frames is difficult since no variables are available that determine the cross-section orientation required for kinematic constraints at beam-to-beam joints. The more recent contributions [238, 239] allow for anisotropic cross-sections but still focus on initially straight beams. In addition to the restrictions mentioned so far, most of these geometrically exact 3D element formulations did not consider the issue of membrane locking. Besides the contributions considered by now, also *global* finite element and finite difference discretization approaches for Kirchhoff beams can be found in the literature [25, 75, 236]. These are typically based on a rotation or curvature interpolation strategy and a subsequent integration of the rotation field along the entire beam length in order to yield an explicit beam centerline representation. Unfortunately, these global approaches yield dense system matrices and not the desirable sparse system matrices with small bandwidths as typical for standard FEM approaches.

Due to these obvious limitations of existing shear-free finite element formulations, Armero and Valverde developed plane and three-dimensional Kirchhoff-Love beam elements for arbitrarily curved initial geometries that guarantee the fundamental properties of objectivity and geometrical exactness [6, 7]. However, these beam elements only cover the geometrically linear case of infinitesimal deformations. On the other hand, in the very recent works of Greco et al. [90, 91], some first steps towards geometrically nonlinear isogeometric Kirchhoff beam elements have been made. However, the proposed formulations have only been applied to geometrically linear examples. Bauer et al. [19] adapted the ideas of Greco and facilitated an application to geometrically nonlinear examples. Nevertheless, the important properties of objectivity and path-independence have not been considered in the works of Greco and Bauer. Thus, it can be concluded that none of the existing geometrically exact shear-free beam element formulations of Kirchhoff-Love type is comparable to the existing shear-deformable formulations of Simo-Reissner type in terms of generality and fulfillment of essential mechanical principles. Also detailed comparisons and evaluations of these two categories of geometrically exact beam element formulations when applied to general problems of slender beams are still missing.

1.2.2 Research objectives

The obvious backlog of existing shear-free beam elements as compared to existing geometrically exact Simo-Reissner element formulations with their excellent properties is the motivation for the development of geometrically exact, three-dimensional, large-deformation Kirchhoff-Love beam element formulations accounting for arbitrary initial geometries and anisotropic cross-section shapes and fulfilling essential mechanical principles such as objectivity and path-independence. Of course, the ultimate objective of this thesis is not only to develop Kirchhoff-Love beam element formulations that are comparable with the existing counterparts of Simo-Reissner type. Instead, novel element formulations are proposed being advantageous in the range of high slenderness ratios and for the modeling of beam contact interaction as compared to existing approaches. In the next two sections, the most important requirements and the novel scientific contributions related to the beam element formulations proposed in this thesis are presented.

1.2.2.1 Specification of requirements

The following requirements are regarded as essential for accurate, efficient and robust beam element formulations applicable to the range of applications mentioned in the beginning:

1) Representability of general geometries and loads: In this thesis, 3D, large-deformation, dynamic problems of thin beams with arbitrary initial geometries and anisotropic cross-section shapes loaded by arbitrary point-wise and distributed forces and moments will be considered. The proposed rotation interpolation schemes have to be capable of representing such general scenarios without exhibiting any singularities for practically relevant configurations.

2) Geometrical exactness: As already mentioned in Section 1.2.1, the proposed beam element formulations have to be geometrically exact in the sense that the derived deformation measures are consistent with the virtual work principle and the equilibrium equations at any deformed state independent of the magnitude of displacements, rotations and strains.

3) Fulfillment of essential mechanical principles: The essential mechanical principles of objectivity, i.e. observer or frame invariance, as well as path-independence have to be preserved by the employed discretization schemes. Further properties such as conservation of linear momentum, conservation of angular momentum and conservation of energy for arbitrarily rough spatial discretizations are very desirable for the proposed spatial interpolation schemes.

4) Fulfillment of general requirements on finite element discretizations: For all presented finite element formulations, accuracy will be verified on the basis of proper reference solutions. Expected optimal convergence rates will be investigated theoretically as well as numerically. Furthermore, effective methods for the avoidance of membrane locking are required such that no remaining locking-related deterioration of the spatial convergence behavior will be observed for the resulting finite element formulations, even in the range of very high slenderness ratios.

5) Energy-stable time integration: The focus of this thesis lies on the development of spatial finite element discretizations for geometrically nonlinear beam problems. The resulting finite element formulations are combined with a finite difference time integration scheme for large rotations recently proposed by Brüls and Cardona [40]. This implicit scheme allows for energy-stable, second-order accurate time integration on the basis of optimized numerical dissipation and can be identified as a Lie-group extension of the well-known generalized-α scheme.

6) Simple realization of essential boundary conditions and joints: Choices of nodal primary variables, especially with respect to the rotation parametrization, are demanded that enable the formulation of practically relevant Dirichlet boundary conditions but also of node-wise joints between several beams without the need of additional constraint equations. Such joints will for example be required for the modeling of complex microstructures. This is not standard for most of the existing geometrically exact shear-free beam element formulations.

7) Avoidance of Lagrange multipliers and saddle point systems: Also existing geometrically exact beam elements of Simo-Reissner type can be subjected to the Kirchhoff constraint by means of additional Lagrange multiplier fields. Such a procedure typically results in saddle point systems and the need of a special class of linear solvers or requires global condensation strategies. While for comparison reasons, the additional enforcement of inextensibility by means of Lagrange multipliers will be demonstrated, the standard (extensible) Kirchhoff-Love beam elements considered in this work should neither rely on Lagrange multipliers nor should they yield in saddle point systems. All required calculations have to be feasible in an element-local manner.

8) Suitability for high-performance computing: In the context of finite difference and finite element discretizations of the Kirchhoff-Love beam theory, several schemes have been proposed that rely on global strategies for the construction of the rotational field. Even though, these schemes show otherwise desirable properties, they typically suffer from two elementary drawbacks: Mostly, these schemes result in dense discrete system matrices and depend on a successive, i.e. serial, evaluation of the individual finite elements within a discretization. These two properties make such formulations virtually impossible for high-performance computing. From the finite element formulations proposed here, it is required to result in sparse system matrices with small bandwidths and to be suitable for parallel computing element evaluation routines.

While many of the (recently developed) beam element formulations of Simo-Reissner type are conform with the standards presented so far, most of the existing geometrically exact shear-free formulations fulfill only a few of these eight basic requirements. In the following, some potential benefits of the shear-free formulations proposed in this thesis as compared to existing Simo-Reissner type elements should be outlined. These advantages predominantly arise in the range of high beam slenderness ratios and in beam-to-beam contact problems, thus, exactly in scenarios prevalent in many of the practically relevant applications considered in Section 1.1.

1.2.2.2 Potential benefits of shear-free beam elements

1) Numerical benefits in the range of high slenderness ratios: The most essential difference between the proposed Kirchhoff-Love and existing Simo-Reissner beam element formulations lies in the neglect of shear deformation in the beam theory underlying the former category. This property is independent from the chosen discretization strategy. Consequently, if otherwise comparable interpolation strategies are applied, it can be assumed that the Kirchhoff type formulations require less degrees of freedom in order to yield the same polynomial approximation quality, and eventually the same discretization error level, since no additional primary variables are required in order to represent shear deformation. Furthermore, in the range of very high slenderness ratios, the influence of the shear modes on the overall beam deformation is not only negligible, it can also be very beneficial to abstain from these high stiffness contributions from a numerical point of view: Mechanical problems of slender beams typically lead to stiff differential equations and ill-conditioned numerical problems deteriorating for example the performance of time integration schemes, nonlinear solvers and linear solvers. The avoidance of the stiff shear mode contributions can considerably improve the situation. Concretely, detailed numerical investigations on several numerical test cases involving highly slender beams will be considered. These test cases will reveal a considerably improved performance of nonlinear solution schemes when Kirchhoff type instead of Reissner type discretizations are employed. Similar trends will be predicted - at least theoretically - for the behavior of linear solvers and time integration schemes.

2) Smooth geometry representation: The proposed finite element formulations for geometrically exact Kirchhoff beams will be based on C^1-continuous interpolations of the beam centerline. These interpolations will eventually result in smooth beam-to-beam contact kinematics, a property that is highly desirable in order to yield efficient and robust contact algorithms.

3) Derivation of reduced models: In addition to the full Kirchhoff model, also a special reduced model, denoted as torsion-free beam theory, will be derived in a consistent manner starting with the general theory. This torsion-free beam model will only be valid for special problem classes concerning the beam geometry and the external loads. Of course, the development of such a reduced formulation is not only warrantable from a theoretical point of view. Firstly, the geometries and external loads in fields of applications such as the ones considered in Section 1.1 often fulfill the requirements in order to apply these reduced models. Secondly, the finite elements resulting from such a reduced model typically feature a simplified numerical implementation and an increased computational efficiency. Concretely, the proposed torsion-free element formulation will completely abstain from rotational degrees of freedom, a characteristic that drastically simplifies many procedures within a finite element algorithm for geometrically exact beams.

1.2.2.3 Proposal for geometrically exact finite element formulations based on the Kirchhoff-Love theory of thin beams

In the development of geometrically exact Kirchhoff-Love beam elements fulfilling the requirements stated in the last subsections, considerable novel scientific contributions originated from the current thesis. The most important are summarized in the following (see also [156, 157]):

- Up to the best of the author's knowledge, the first Kirchhoff type beam element formulations have been developed that fulfill all the requirements of Section 1.2.2.2, especially the first formulations that fulfill the most essential requirements 1) - 4). Concretely, two different Kirchhoff beam element formulations are proposed: i) The first formulation is based on a strong enforcement of the Kirchhoff constraint. Employing the concept of intermediate triad fields, the space-continuous problem setting is consistently derived. For spatial discretization, a novel orthonormal interpolation scheme is proposed that fulfills the Kirchhoff constraint in a strong manner. ii) The space-continuous theory of the second variant is based on a weak enforcement of the Kirchhoff constraint. The discrete realization of the Kirchhoff constraint is based on a properly chosen collocation strategy. In combination with the employed smooth centerline interpolation this strategy allows for a complete avoidance of Lagrange multipliers. While this formulation in principle allows for arbitrary rotation interpolations, the numerical realization performed in this thesis relies on the well-known orthonormal, geodesic interpolation scheme proposed in [58]. The fulfillment of the essential properties 3) and 4) by these two finite element formulations are verified analytically as well as numerically. Furthermore, for each of these two element formulations, two different sets of nodal rotation parametrizations are proposed. One is based on nodal rotation vectors and one on nodal tangent vectors. While these different choices are shown to yield identical FEM solutions, they differ in the resulting performance of nonlinear solvers and the effort required for the modeling of essential boundary conditions and joints. The four finite element formulations resulting from a combination of the two interpolation schemes and the two choices of nodal primary variables are subject to detailed comparisons with respect to resulting discretization error levels and the performance of nonlinear solution schemes. The applied smooth centerline interpolation is based on Hermite polynomials. Detailed theoretical and numerical investigations are conducted on the optimal choice of the required Hermite constant in the context of geometrically exact beam formulations. Moreover, the concept of Minimally Constrained Strains (MCS) is proposed in order to avoid membrane locking effects. This concept, based on the method of assumed strains, is especially suited for smooth interpolation schemes with increased continuity, but still of a very general nature. This fact lays the foundation for a possible transfer of the method to other locking phenomena and to further structural members.

- A further original contribution of this thesis is the detailed and systematic numerical comparison performed between (the most general representatives of) geometrically exact Kirchhoff-Love and Simo-Reissner beam element formulations. Specifically, resulting spatial convergence rates, discretization error levels as well as the performance of nonlinear solution schemes are compared for different beam slenderness ratios. Also some first comparisons with inextensible Kirchhoff type formulations are considered.

- From the general Kirchhoff-Love theory, a reduced torsion-free theory as well as a corresponding beam element realization have been consistently derived that fulfill the same essential properties 2) - 4) as the general element formulations as long as some strictly specified limitations concerning external loads and initial geometry as compared to requirement 1) are fulfilled. A special focus lies in stringently defining the extent of validity of this torsion-free model and assessing possible model errors in a quantitative manner. For cases where the limitations with respect to external loads and initial geometry are fulfilled, it is shown theoretically and verified numerically that the derived torsion-free beam element formulation can be applied without deteriorating the overall approximation quality. Concretely, as compared to the general Kirchhoff-Love formulations, the torsion-free formulation yields i) correct results for static problems as well as ii) good approximations for typical, low-frequency-dominated dynamic problems with a resulting overall model error that decreases quadratically with increasing beam slenderness ratio.
- Up to the best of the author's knowledge, the current work represents the first application of a Lie group time integration scheme based on optimized numerical dissipation to geometrically exact Kirchhoff-Love beam elements, and one of the first applications of such a scheme to geometrically nonlinear beam element formulations at all.

1.3 Finite Element Formulations for Nonlinear Beam-to-Beam Contact Problems

The focus of this section lies on geometrically nonlinear, 3D finite element formulations for the mechanical modeling and numerical solution of beam-to-beam contact problems. Considering the potential practical applications presented in Section 1.1, especially the requirements on numerical algorithms that result from high beam slenderness ratios as well as complex contact configurations with arbitrary beam-to-beam orientations will be emphasized.

1.3.1 Fundamental approaches

Some recent contributions focusing on the analytical modeling of contact interaction between thin fibers are for example the investigation of ropes with single- and bi-helical fiber substructures [235], the theoretical treatment of knot-mechanics [114], or the analysis of optimal topologies and packing densities in filamentous materials based on an implicit consideration of contact [89]. While these analytic approaches enable a detailed analysis of special geometrical configurations, there is an inevitable need for robust and efficient numerical simulation tools in order to cover general cases of complex contact configurations relevant for many applications. Despite the large number of publications considering geometrically nonlinear beam element formulations and despite the obvious need for robust and accurate beam contact formulations in many fields of application, there exists only a comparatively limited amount of literature focusing on beam-to-beam contact interaction. On the contrary, intensive research work has been done in the solid contact modeling of 3D continua within the last two decades. Important aspects in this field of research are for example the investigation of different constraint enforcement strategies (Lagrange multiplier method, penalty method, augmented Lagrange method etc.), types of contact

discretization (node-to-segment/collocation-point-to-segment, Gauss-point-to-segment, mortar-like formulations), efficient contact search and active set strategies, procedures for Lagrange multiplier condensation, accurate integration schemes and surface smoothing strategies. Exemplarily, the reader is referred to the monographs [139, 233] and the review articles [173, 231].

In contrast to contact formulations for 3D continua, which are typically based on a 2D contact traction field acting on the contact surfaces, the arguably most popular beam contact formulation originally proposed by Wriggers and Zavarise [234] models mechanical beam-to-beam contact interaction by means of a discrete contact force acting at the closest point between the two space curves representing the contacting beams (with circular cross-sections). This model, in the following denoted as point-to-point contact formulation, results in an elegant and efficient numerical formulation, which subsequently has been extended to frictional problems considering friction forces [237] as well as friction torques [129], rectangular beam cross-section shapes [151, 152], smoothed centerline geometries [147], constraint enforcement via Lagrange multipliers [146] instead of penalty-based constraint enforcement and adhesion effects [135]. Quite recently, it has been applied to self-contact problems [162] and extended to contact interactions of beams with rigid surfaces [164, 165]. In [33, 34], the authors supplemented the point-to-point contact formulation by additional electromechanical and thermomechanical effects. In [185], first steps towards a large-penetration beam contact formulation have been considered. The recent contribution [122], suggests a modified penalty-type force law in order to implicitly take into account the cross-section deformation of the contacting beams. Very recently, a beam-to-beam contact formulation has been proposed that is suitable for superelliptical cross section shapes [163]. A detailed presentation of the general point-to-point contact model can also be found in the textbooks [148] and [233]. One of the limitations of these point-to-point contact formulations can be attributed to the question whether contact between beams enclosing small contact angles, i.e. nearly parallel or entangled beams, should rather be modeled by means of a distributed line force instead of a discrete point force from a mechanical point of view? This question has been addressed by the recent publications [149] and [150], which propose additional contact points located in the neighborhood of the closest point in order to somewhat distribute the contact force in such configurations. A similar approach, however based on integrated contact forces, has been proposed in [224, 225]. Unfortunately, these formulations still rely on the existence of a locally unique closest point projection between the contacting beams.

It is precisely this requirement that represents the second and essential limitation of point-based beam contact formulations. In very general scenarios, such as in the applications mentioned in the beginning, where arbitrary beam-to-beam orientations can occur, a unique closest point projection cannot be guaranteed for all potential contact regions. Consequently, some mechanically relevant contact points might be missed leading to large nonphysical penetrations or even to an entirely undetected crossing of the considered beams. In complex systems of arbitrarily oriented thin fibers, such undetected large penetrations do not only yield a nonphysical behavior, they can considerably deteriorate the performance of nonlinear solution schemes or prohibit convergence at all, even if such configurations only occur at individual spatial positions and single points in time. In Konjukhov et al. [128, 129], the solvability of the relevant closest point projection has already been investigated by means of geometrical criteria. Nevertheless, a mathematically concise and practically easily realizable criterion is still missing. There are only a few alterna-

tive beam-to-beam contact formulations available in the literature today that can overcome this limitation. The perhaps most popular alternative is the formulation developed by Durville [67–70, 221], which is based on a collocation-point-to-segment type formulation and the definition of proximity zones on an intermediate geometry. A second alternative proposed by Chamekh et al. [46, 47] is based on a Gauss-point-to-segment type formulation and has primarily been applied to self-contact problems. What these two formulations have in common is that the contact forces are assumed to be *distributed* along the two beams. Consequently, these types of formulations will be denoted as line-to-line contact formulations in the following. These formulations, especially the one proposed by Durville, have been proven to be very robust and applicable to complex systems of thin fibers. Nevertheless, as compared to the variety of elaborate contact discretization and constraint enforcement strategies available in the field of 3D solid contact mechanics, there still seems to be a considerable potential for improvements with respect to resulting contact discretization and integration errors or the fulfillment of smoothness conditions relevant for nonlinear solution and time integration schemes. Furthermore, even though, line contact approaches yield accurate contact models in the entire range of possible contact angles, their computational efficiency decreases considerably with increasing slenderness ratio. Especially in the range of large contact angles, the number of contact evaluation points required by these approaches and the resulting computational effort is prohibitively high as compared to point-based formulations.

1.3.2 Research objectives

The mentioned shortfalls of existing purely point-based and purely line-based beam-to-beam contact models is the motivation to further improve these two individual models and eventually to propose a novel unified beam-to-beam contact formulation that combines the desirable properties of the two basic formulations while abstaining from their drawbacks. In Section 1.3.2.1, the most important requirements for such a formulation are stated. Section 1.3.2.2 summarizes the novel and original scientific contributions resulting from the realization of this formulation.

1.3.2.1 Specification of requirements

The two central requirements on overall beam contact algorithms are efficiency and robustness: Especially when considering complex systems with a large number of contact interaction regions and when applying higher-order geometrically exact beam elements, which enable low discretization errors already for comparatively rough spatial discretizations, the overall computational effort is typically dominated by the beam contact algorithms. As argued above, for standard beam contact formulations this is especially true when high beam slenderness ratios and arbitrary beam-to-beam orientations are involved. Thus, efficiency of the contact formulation is a key factor. Furthermore, already the solution of nonlinear systems resulting from discretized problems involving very thin beams and highly nonlinear deformation states is numerically challenging. The consideration of an additional nonlinearity in form of contact interaction, a physically non-smooth phenomenon, further intensifies the situation. Eventually, the implicit treatment of complex, strongly interconnected systems of thin fibers, all of them mutually influencing each other, requires a nonlinear solution scheme that is highly robust but still efficient. Of course, the resulting formulations also have to provide a sufficient degree of accuracy required for the intended modeling purposes. These basic demands will be concretized in the following.

1) Representation of arbitrary contact configurations: Arbitrary configurations of highly slender beams spanning the entire range of possible contact angles and especially including configurations that involve endpoint-to-endpoint and endpoint-to-segment contacts have to be representable by the proposed formulations. The fulfillment of this requirement is particularly important in order to yield a robust behavior of the nonlinear solution scheme.

2) Accurate representation of small-angle regime: Especially in the range of small contact angles, an accurate representation of the distributed line contact forces resulting from the interaction of parallel or entangled beams is important. Simple point contact formulations will in general not yield such a model quality. Nevertheless, the required accuracy has to be achieved in an efficient manner allowing for sufficiently rough spatial contact discretizations.

3) Efficient representation of large-angle regime: In the range of large contact angles, an accurate resolution of contact force distributions is of secondary interest, since the latter can be modeled as point contact forces in good approximation. Consequently, this range should not be covered with computationally expensive line-contact formulations that typically require a very fine slenderness-dependent spatial contact discretization in the large-angle regime.

4) Smoothness: The proposed contact formulations have to guarantee that all spatial distributions and temporal evolutions of contact forces are sufficiently smooth. This smoothness requirement allows for a consistent linearization of all deformation-dependent quantities and for a robust behavior of tangent-based nonlinear solvers within an implicit time integration scheme. Further benefits occur in terms of increased energy stability of the applied time integration scheme and a higher approximation quality of the resulting contact force distributions.

5) Reasonable time step sizes: The physical time scales relevant for many applications lead to accumulated transverse displacements during a simulation that are typically by several orders of magnitude larger than the beam cross-section dimensions. The simulation of such problems is only feasible if the time step sizes can be chosen large enough such that the displacements per time step clearly exceed the dimensions of the beam cross-section. Many existent formulations, however, depend on displacements per time step that are smaller than the cross-section radius.

6) Efficient global contact search strategies: For systems involving a large number of beams, efficient global search strategies based on tight bounding boxes are indispensable in order to reduce the number of potential contact pairs where computationally expensive projections have to be performed. Especially for higher-order beam elements that might be subject to highly nonlinear element deformations, the creation of tight bounding boxes is a demanding task.

7) Application of only one global nonlinear solution scheme: All nonlinearities resulting from the beam element and from the beam contact formulation have to be captured within one global Newton scheme. Especially, no additional fixed-point iteration schemes should be required.

8) Fulfillment of essential properties: Besides the suitability for arbitrary cross-section shapes, all requirements of Section 1.2.2.2 have also to be fulfilled by the beam contact formulations.

1.3.2.2 Proposal for a unified beam-to-beam contact approach: The All-angle Beam Contact (*ABC*) formulation

In this thesis, a novel beam-to-beam contact formulation is proposed that fulfills the requirements stated in the last section. The most important original scientific contributions underlying this formulation are summarized in the following (see also [158, 159]):

- In this thesis, a mathematically concise and rigorous investigation of the existence of the closest-point-projection required for point-to-point contact is performed. Up to the best of the author's knowledge, these investigations yield the first closed-form and general analytic criterion that is valid for arbitrary contact configurations and that is based on proper and easy-to-determine control quantities. Based on this analytic criterion, it can be concluded that the standard point-to-point contact formulation is not applicable in a considerable range of practically relevant contact configurations.

- An improved line-to-line beam contact formulation is proposed which is inspired by some well-known and successful techniques from contact mechanics for 3D solids. The new beam contact formulation is based on a Gauss-point-to-segment type contact discretization and a penalty regularization of the contact constraint. Additionally, theoretical considerations concerning alternative constraint enforcement strategies by means of Lagrange multipliers and alternative contact discretizations based on mortar methods are made. However, detailed theoretical and numerical investigations of these different approaches suggest the penalty-based Gauss-point-to-segment formulation as the variant that is most suitable for beam-to-beam contact and as the method of choice for the applications considered in this thesis. In contrast to existing line-to-line beam contact formulations, the proposed approach is extended by a consistently linearized integration interval segmentation that avoids numerical integration across strong discontinuities. It is verified by means of suitable numerical examples that precisely this component in combination with a smoothed contact force law and the applied C^1-continuous beam element formulation leads to a drastic reduction of the numerical integration error. This, in turn, improves spatial convergence rates and in many cases only enables optimal convergence behavior under uniform mesh refinement. Furthermore, a criterion is derived for the minimally required number of Gauss points in dependence on the beam slenderness ratio and the contact angle.

- Based on these investigations on point and line contact models, it is concluded that, on the one hand, the point-to-point contact formulation serves as sensible mechanical model and very efficient numerical algorithm in the range of intermediate and large contact angles while it is not applicable for small contact angles. On the other hand, the line-to-line contact formulation provides a very accurate and robust mechanical model in the small-angle regime whereas the computational efficiency dramatically decreases with increasing contact angles. On the basis of these conclusions, a novel All-angle Beam Contact (*ABC*) formulation is proposed that combines the advantages of point and line contact models while abstaining from their disadvantages: The formulation is based on a standard point-to-point contact formulation applied in the range of large contact angles while the scope of small contact angles is covered by the newly developed line-to-line contact formulation. Two different variants of a smooth model-transition procedure between the regimes

of point and line contact are investigated, a variationally consistent transition on penalty potential level and a simpler variant on contact force level. Both variants lead to exact conservation of linear and angular momentum, while only the variationally consistent variant enables exact energy conservation. Based on analytic investigations, recommendations are made concerning the optimal ratio between the two penalty parameters of the point and the line contact, the required number of line contact Gauss points and the choice of the model transition angle interval. All configuration-dependent quantities are consistently linearized allowing for an application within implicit time integration schemes.

- The resulting formulation is supplemented by contact contributions of the beam endpoints, whereas all existing contact formulations, no matter if point- or line-based, typically search for minimal distance solutions only within the beams interior, but not for boundary minima. On the basis of a suitable numerical example, it is shown that in many applications these endpoint contact scenarios can appear with considerable frequency. Although, the influence of these endpoint forces on the overall solution might be of secondary interest, it is shown that neglecting these contributions will drastically reduce the robustness of the nonlinear solution scheme in many cases and may even prohibit convergence at all. In dynamic simulations, a neglect of these contributions can even prohibit energy stability.

- A step size control for the nonlinear solver is proposed, which allows for displacement increments per time step that exceed the order of magnitude of the cross-section radius, but still avoids the occurrence of undetected crossings of the contacting beams.

- Furthermore, a very efficient two-stage contact search algorithm based on dynamically adapted search segments for each finite element is proposed. This algorithm does not only result in a very tight set of potential contact pairs, but it also enables a subdivision into potential point-to-point and potential line-to-line contact pairs. The latter property is essential in order to fully exploit the efficiency potential of the proposed *ABC* formulation.

- Up to the best of the author's knowledge, the current thesis represents the first work that systematically investigates conservation properties, integration and discretization errors as well as spatial convergence rates for beam-to-beam contact theoretically and via numerical examples. Especially, a numerical test case suitable for line-to-line contact scenarios has been designed and an analytic solution based on the Kirchhoff-Love theory has been derived. This test case and the associated analytic solution can serve as valuable benchmark for the proposed formulation but also for future beam-to-beam contact approaches.

- All the presented algorithmic components are tailored for the most challenging, but also practically relevant, case of arbitrary discretization orders and lengths, which typically leads to high element slenderness ratios and deformations. The employed global search strategies are especially suited for higher-order geometrically exact finite elements, while beam-to-beam contact search schemes typically applied in the literature, at least implicitly, assume the simple case of straight beam elements. This high degree of generality is the key for a beam-to-beam contact formulation that is based on a truly C^1-continuous (and not subsequently smoothed), geometrically nonlinear beam centerline representation.

All in all, the interplay of these individual constituents will yield a novel beam-to-beam contact formulation that combines a significant degree of robustness and universality in the treatment of complex contact scenarios and arbitrary beam-to-beam orientations with high computational efficiency, especially in the limit of extreme beam and element slenderness ratios.

1.4 Outline

Reflecting the core objectives of this thesis, its content can be subdivided into two main constituents: The development of finite element formulations for the modeling of slender beams and for the modeling of beam-to-beam contact. While Chapters 2 and 3 consider the space- and time-continuous beam problem as well as its discrete counterpart, Chapter 4 focuses on the continuous and discrete representation of beam contact. The detailed structure is given in the following.

Chapter 2 begins with a brief introduction in the so-called $SO(3)$ group and supplies the reader with some mathematical tools required for the treatment of large rotations. Afterwards, the geometrically exact Simo-Reissner theory of shear-deformable beams is introduced. Having stated the basic kinematic assumptions, the focus lies on deriving the strong and weak form of the balance equations, 1D stress resultants, work-conjugated deformation measures and proper constitutive relations. After having presented the Simo-Reissner theory, the degree of generality of the considered beam models is reduced step by step throughout the chapter. Abstaining from the shear-deformation mode yields the Kirchhoff-Love beam theory, based on strong or weak constraint enforcement. Then, the possibility of abstaining from the axial tension mode on the basis of an inextensibility constraint is presented. Eventually, the chapter is completed by introducing two reduced beam models: The isotropic beam theory is applicable to initially straight beams with isotropic cross-sections. The torsion-free beam theory allows to additionally abstain from the torsion mode in case certain restrictions concerning the external loads are fulfilled.

In Chapter 3, finite difference schemes for temporal discretization as well as finite element schemes for spatial discretization are presented, with the focus lying on the latter. After briefly introducing the basic concept of finite elements, novel interpolation strategies for the translational and rotational primary variable fields underlying the considered beam theories are proposed. Moreover, the compliance of these interpolation schemes with fundamental mechanical principles such as objectivity and path-independence or conservation of energy and momentum is analyzed. Afterwards, from these interpolation strategies and the theory presented in the previous chapter, novel beam element formulations of different degree of generality are derived. Eventually, the fulfillment of fundamental mechanical properties is verified numerically. Moreover, the performance of the proposed element formulations compared to standard formulations known from the literature is evaluated on the basis of proper numerical test cases.

Chapter 4 is devoted to the development of beam contact formulations. In the beginning, the basics of standard point contact formulations are presented and their limitations are investigated. Thereupon, a novel line-to-line contact formulation is proposed. The benefits of this formulation are analyzed, possible alternatives are discussed and, finally, also general limitations of line-based models are highlighted. Based on the considered point and line contact model, a novel

All-angel Beam Contact (*ABC*) formulation is derived. After discussing different variants of this formulation and the optimal choice of the underlying parameters, the *ABC* formulation is supplemented by some important algorithmic components concerning contact search, nonlinear solution scheme, extended penalty force laws and the treatment of endpoint contact contributions. At the end of the chapter, basic properties of the developed line contact formulation and of the novel *ABC* formulation are verified numerically. Eventually, four practically relevant applications are considered in order to verify the overall robustness and efficiency of the proposed beam element and beam contact formulations and the interplay of the individual components.

Finally, Chapter 5 summarizes the most important results and accomplishments, but also gives a brief outlook on future extensions of the proposed finite element formulations for slender beams and their contact formulations. There, also potential future applications will be in the focus.

2 Geometrically Exact Beam Theory

In this chapter, the essential concepts of geometrically exact beam theories, required for the derivation of corresponding finite element formulations in the following chapter, will be derived. One distinctive property of geometrically exact beam formulations is the presence of large rotations within the associated configuration space. In order to provide the theoretical basis for subsequent derivations, in the following Section 2.1, the $SO(3)$ group of large rotations as well as possible parametrizations will be introduced. In Section 2.2, the most general type of geometrically exact beam formulations considered in this thesis, the Simo-Reissner theory of thick (shear-deformable) beams, will be presented. The underlying continuum theory will be identified as a 1D Cosserat continuum exhibiting pointwise six degrees of freedom, three translational and three rotational ones. Furthermore, also the relation between the 1D Cosserat continuum theory and the 3D Boltzmann continuum theory will be addressed at this point. Subsequently, in Section 2.3, the general theory will be restricted to the Kirchhoff-Love theory of thin (shear-free) beams. There, different methodologies of imposing the Kirchhoff constraint of vanishing shear strains in a strong or weak sense, but also the possibility of further restricting the theory by means of additional inextensibility constraints, will be investigated. Finally, in Section 2.4, reduced variants of the general Kirchhoff-Love theory will be presented which represent the basis for considerably simplified beam elements specified in the subsequent chapter. In this section, the main focus will lie on investigating the range of applicability of these reduced theories.

2.1 The Rotation Group SO(3)

The category of beam theories considered throughout this thesis assumes the beam cross-sections to be rigid. Consequently, the cross-section kinematics are point-wise uniquely defined by six degrees of freedom, three translational ones representing the position vector of the cross-section centroid and three rotational ones describing the cross-section orientation. Thereto, an orthonormal triad consisting of the base vectors $\mathbf{g}_1, \mathbf{g}_2, \mathbf{g}_3 \in \Re^3$ is attached on the beam cross-sections. Furthermore, a right-handed inertial Cartesian frame $\mathbf{E}_1, \mathbf{E}_2, \mathbf{E}_3 \in \Re^3$ associated with the material configuration and a corresponding right-handed inertial Cartesian frame $\mathbf{e}_1, \mathbf{e}_2, \mathbf{e}_3 \in \Re^3$ of the spatial configuration are introduced. Nevertheless, for simplicity, it is assumed that both frames coincide, thus $\mathbf{e}_i = \mathbf{E}_i$ for $i = 1, 2, 3$. Now, the rotation from the global frame $\mathbf{E}_i$ onto the local frame $\mathbf{g}_i$ is described via the orthogonal transformation $\mathbf{\Lambda} \in SO(3)$ as follows:

$$\mathbf{g}_i = \mathbf{\Lambda}\mathbf{E}_i \quad \text{with} \quad \mathbf{\Lambda} = \mathbf{g}_j \otimes \mathbf{E}_j = (\mathbf{g}_1, \mathbf{g}_2, \mathbf{g}_3)_{\mathbf{E}_j} \quad \text{for} \quad i, j = 1, 2, 3. \tag{2.1}$$

Throughout this thesis, the summation convention over repeated indices holds. Furthermore, no distinction is made between co- and contravariant bases and no index notation with sub- and superscripts for associated base vectors and components is applied as long as Cartesian systems are considered. According to (2.1), rotations are linear transformations in $\Re^3$, thus allowing for a

corresponding matrix representation. Moreover, the columns of the matrix representation when expressed with respect to the global (material) basis $\mathbf{E}_i$ are represented by the (spatial) base vectors $\mathbf{g}_i$. Here and in the following, the index near a matrix (for example the index $(.)_{\mathbf{E}_i}$ in equation (2.1)) denotes the basis in which the associated tensor is represented. Furthermore, from (2.1) it is obvious that $\mathbf{\Lambda}$ is a two-point tensor. In the context of geometrically exact beam theories, $\mathbf{\Lambda}$ acts as push-forward operator (see e.g. [155]) between material and spatial objects. From a rather mathematical point of view, the rotation tensor $\mathbf{\Lambda}$ can be identified as an element of the Special Orthogonal group $SO(3)$ of orthogonal transformations according to

$$SO(3) := \{\mathbf{\Lambda} \in \Re^{3\times3} | \mathbf{\Lambda}^T\mathbf{\Lambda} = \mathbf{I}_3, \det(\mathbf{\Lambda}) \ = \ 1\}, \tag{2.2}$$

under the action of non-commutative multiplication $SO(3)\times SO(3)\rightarrow SO(3)$, $\mathbf{\Lambda}_3 = \mathbf{\Lambda}_1\mathbf{\Lambda}_2 \neq \mathbf{\Lambda}_2\mathbf{\Lambda}_1$ with inverse element $\mathbf{\Lambda}^{-1} = \mathbf{\Lambda}^T$ and identity element $\mathbf{I}_3$. Here, $\det(.)$, $(.)^T$ and $(.)^{-1}$ are the determinant, transpose and inverse. $\mathbf{I}_3$ is a 3×3 identity matrix. The $SO(3)$ group forms a smooth differentiable manifold. Consequently, it can be classified as Lie group with tangent space

$$\delta\mathbf{\Lambda} \in T_{\mathbf{\Lambda}}SO(3) := \{\mathbf{S}(\mathbf{a})\mathbf{\Lambda} | \mathbf{S}(\mathbf{a}) \in so(3)\}. \tag{2.3}$$

Here, $so(3)$ denotes the set of skew symmetric tensors with $\mathbf{S}(\mathbf{a})\mathbf{b} = \mathbf{a}\times\mathbf{b}$ for $\mathbf{a}, \mathbf{b} \in \Re^3$. The isomorphism between $so(3)$ and $\Re^3$ enables a unique expression of $\mathbf{S}(\mathbf{a}) \in so(3)$ by the vector $\mathbf{a} \in \Re^3$ denoted as axial vector. By inserting the special choice $\mathbf{\Lambda} = \mathbf{I}_3$ into (2.3) it can easily be verified that $so(3)$ can be identified as the tangent space to $SO(3)$ at the identity:

$$so(3) := T_{\mathbf{I}}SO(3) = \{\mathbf{S}(\mathbf{a}) | \mathbf{S}(\mathbf{a}) = -\mathbf{S}(\mathbf{a})^T \, \forall \, \mathbf{a} \in \Re^3\}. \tag{2.4}$$

In the nomenclature of Lie groups, $so(3)$ is also denoted as Lie algebra of $SO(3)$. The Lie group $SO(3)$ and its Lie algebra $so(3)$ are related by the exponential map $\exp(.)$: $so(3) \rightarrow SO(3)$:

$$\exp(\mathbf{S}(\mathbf{a})) := \mathbf{I}_3 + \mathbf{S}(\mathbf{a}) + \frac{\mathbf{S}(\mathbf{a})^2}{2!} + \frac{\mathbf{S}(\mathbf{a})^3}{3!} + \dots \ . \tag{2.5}$$

So far, the rotation group $SO(3)$ has been introduced without stating a specific parametrization of the rotation tensor $\mathbf{\Lambda}$. In the following two sections, two possible parametrizations, which will be useful in the development of beam element formulations according to the Simo-Reissner and Kirchhoff-Love theory, are presented. Further mathematical details about Lie groups in general can e.g. be found in [30]. For fundamentals of the $SO(3)$ group and the treatment of large rotations, the interested reader is referred to [4] and [134] or also to [43, 111, 204, 208] for the treatment of large rotations in the context of geometrically exact beam element formulations.

2.1.1 SO(3) parametrization via rotation vectors

In (2.1), the rotation tensor $\mathbf{\Lambda} \in \Re^{3\times3}$ has been introduced without a specific parametrization. However, it can be shown that only three of the nine components of the rotation tensor are independent [4, 217], which is a direct consequence of the six orthonormality constraints present in the $SO(3)$. There exist various parametrizations of the rotation tensor such as rotation (pseudo-) vectors, Euler angles or Rodrigues parameters that are based on a minimal set of three parameters. Also four-parametric representations of the rotation tensor such as quaternions have proven

to be very useful for practical purposes. Within this thesis, two different parameterizations will be employed: The one presented in this section is based on rotation vectors $\boldsymbol{\psi} \in \Re^3$. In Section 2.1.2, an alternative parametrization especially suited for Kirchhoff formulations is presented. The rotation vector parametrization can explicitly be given via the well-known Rodrigues formula:

$$\boldsymbol{\Lambda}(\boldsymbol{\psi}) = \exp(\mathbf{S}(\boldsymbol{\psi})) = \left[\mathbf{I} + \sin\psi \mathbf{S}(\boldsymbol{e}_{\boldsymbol{\psi}}) + (1 - \cos\psi)\mathbf{S}(\boldsymbol{e}_{\boldsymbol{\psi}})\mathbf{S}(\boldsymbol{e}_{\boldsymbol{\psi}})\right]. \tag{2.6}$$

Here, $\psi = ||\boldsymbol{\psi}||$ represents the scalar rotation angle and $\mathbf{e}_{\boldsymbol{\psi}} = \boldsymbol{\psi}/||\boldsymbol{\psi}||$ the axis of rotation. Throughout this thesis, $||(.)||$ denotes the Euclidean norm in $\Re^3$. As indicated by the notation $\exp(\mathbf{S}(\boldsymbol{\psi}))$, equation (2.6) represents a closed-form representation of the exponential map initially introduced in (2.5) of the last section. The equivalence of both representations can easily be shown by making use of the series expansions of $\sin(.)$ and $\cos(.)$ (see e.g. [56]). The rotation vector of a given rotation tensor can for example be extracted by employing Spurrier's algorithm [214]. In order to simplify notation, throughout this thesis the following abbreviation $\mathrm{rv}(.) := (\mathbf{S}^{-1} \circ \exp^{-1})(.)$ is used whenever this extraction shall be formulated explicitly:

$$\boldsymbol{\psi} = \mathrm{rv}(\boldsymbol{\Lambda}) \quad \Leftrightarrow \quad \exp(\mathbf{S}(\boldsymbol{\psi})) = \boldsymbol{\Lambda}. \tag{2.7}$$

However, it has to be noted that a unique extraction of the rotation vector is only possible within the interval $\boldsymbol{\psi} \in]-\pi, \pi]$. If a subsequent rotation $\exp(\mathbf{S}(\Delta\boldsymbol{\theta}))$ by a finite angle $\Delta\boldsymbol{\theta} \in \Re^3$ is superimposed onto the given triad $\boldsymbol{\Lambda}$, the resulting triad $\boldsymbol{\Lambda}_n$ follows the relation:

$$\boldsymbol{\Lambda}_n = \exp(\mathbf{S}(\boldsymbol{\psi}_n)) = \exp(\mathbf{S}(\boldsymbol{\psi} + \Delta\boldsymbol{\psi})) = \exp(\mathbf{S}(\Delta\boldsymbol{\theta}))\exp(\mathbf{S}(\boldsymbol{\psi})) \neq \exp(\mathbf{S}(\boldsymbol{\psi} + \Delta\boldsymbol{\theta})). \tag{2.8}$$

It has to be emphasized, that the rotation vectors associated with two successive rotations are not additive, i.e. $\boldsymbol{\psi}_n \neq \boldsymbol{\psi} + \Delta\boldsymbol{\theta}$ (see e.g. [56] for the actual calculation of $\boldsymbol{\psi}_n$), consequently $\Delta\boldsymbol{\theta}$ is commonly referred to as multiplicative rotation increment. Besides this non-additivity, the nonlinear manifold $SO(3)$ is also non-commutative with respect to multiplication of its elements. In this context, one can formulate the counterpart to the left-translation update formula (2.8), which is based on right-multiplication with a multiplicative rotation increment $\Delta\boldsymbol{\Theta} \neq \Delta\boldsymbol{\theta}$:

$$\boldsymbol{\Lambda}_n = \exp(\mathbf{S}(\boldsymbol{\psi}_n)) = \boldsymbol{\Lambda}\exp(\mathbf{S}(\Delta\boldsymbol{\Theta})) = \exp(\mathbf{S}(\boldsymbol{\psi}))\exp(\mathbf{S}(\Delta\boldsymbol{\Theta})). \tag{2.9}$$

When applying the compound rotation $\boldsymbol{\Lambda}_n$ according to (2.9), $\Delta\boldsymbol{\Theta}$ directly acts on a non-rotated, material object, while $\Delta\boldsymbol{\theta}$ as appearing in (2.8) acts on a rotated, spatial object. Consequently, $\Delta\boldsymbol{\Theta}$ can be identified as the material counterpart of the spatial object $\Delta\boldsymbol{\theta}$. With the help of the transformation properties of the tensors $\mathbf{S}(.)$ and $\exp(\mathbf{S}(.))$ according to

$$\boldsymbol{\Lambda}\mathbf{S}(\tilde{\boldsymbol{\psi}})\boldsymbol{\Lambda}^T = \mathbf{S}(\boldsymbol{\Lambda}\tilde{\boldsymbol{\psi}}) \;\rightarrow\; \boldsymbol{\Lambda}\exp(\mathbf{S}(\tilde{\boldsymbol{\psi}}))\boldsymbol{\Lambda}^T = \exp(\mathbf{S}(\boldsymbol{\Lambda}\tilde{\boldsymbol{\psi}})) \;\forall\; \tilde{\boldsymbol{\psi}} \in \Re^3,\, \boldsymbol{\Lambda} \in SO(3) \tag{2.10}$$

the two multiplicative rotation increments can be related by the following rule

$$\boldsymbol{\Lambda}_n = \boldsymbol{\Lambda}\exp(\mathbf{S}(\Delta\boldsymbol{\Theta})) = \boldsymbol{\Lambda}\exp(\mathbf{S}(\Delta\boldsymbol{\Theta}))\boldsymbol{\Lambda}^T\boldsymbol{\Lambda} = \exp(\mathbf{S}(\boldsymbol{\Lambda}\Delta\boldsymbol{\Theta}))\boldsymbol{\Lambda} \;\rightarrow\; \Delta\boldsymbol{\theta} = \boldsymbol{\Lambda}\Delta\boldsymbol{\Theta}. \tag{2.11}$$

Thus, $\Delta\boldsymbol{\theta}$ and $\Delta\boldsymbol{\Theta}$ are related by the push-forward operator $\boldsymbol{\Lambda}$. Replacing the finite rotation $\Delta\boldsymbol{\theta}$ by the infinitesimal spatial quantity $\delta\boldsymbol{\theta}$, denoted as multiplicative rotation vector variation or spin vector, yields the following expression for the variation of the rotation tensor $\boldsymbol{\Lambda}$:

$$\delta\boldsymbol{\Lambda} := \frac{d}{d\epsilon}\Big|_{\epsilon=0} \exp\left(\epsilon\mathbf{S}(\delta\boldsymbol{\theta})\right)\boldsymbol{\Lambda} = \mathbf{S}(\delta\boldsymbol{\theta})\boldsymbol{\Lambda} \quad \text{or} \quad \delta\mathbf{g}_i = \delta\boldsymbol{\theta} \times \mathbf{g}_i. \tag{2.12}$$

Thus, as already introduced in (2.3), the skew-symmetric matrix $\mathbf{S}(\delta\boldsymbol{\theta}) \in so(3)$ of the spin vector describes infinitesimal variations $\delta\boldsymbol{\Lambda}$ of $\boldsymbol{\Lambda}$ within the tangent space $T_{\boldsymbol{\Lambda}}SO(3)$. Similarly to (2.12), the variation $\delta\boldsymbol{\Lambda}$ can be expressed by the material spin vector $\delta\boldsymbol{\Theta} = \boldsymbol{\Lambda}^T\delta\boldsymbol{\theta}$:

$$\delta\boldsymbol{\Lambda} := \frac{d}{d\epsilon}\Big|_{\epsilon=0} \boldsymbol{\Lambda}\exp\left(\epsilon\delta\boldsymbol{\Theta}\right) = \boldsymbol{\Lambda}\mathbf{S}(\delta\boldsymbol{\Theta}). \tag{2.13}$$

Expressing the spin vectors $\delta\boldsymbol{\Theta}$ and $\delta\boldsymbol{\theta}$ in the associated frames $\mathbf{E}_i$ and $\mathbf{g}_i$, respectively, yields:

$$\delta\boldsymbol{\Theta} = \delta\Theta_i\mathbf{E}_i, \quad \delta\boldsymbol{\theta} = \delta\Theta_i\mathbf{g}_i. \tag{2.14}$$

Thus, the components of the spatial spin vector expressed in the local basis $\mathbf{g}_i$ are identical to the components of the material spin vector expressed in the global basis $\mathbf{E}_i$. This relation also holds for all the other pairs of spatial / material quantities considered in this thesis (see e.g. [204]). Based on the defining equation (2.13) and the representation of skew-symmetric tensors by means of the Levi-Civita-Symbol ϵ_{ijk}, the components of $\mathbf{S}(\delta\boldsymbol{\Theta})$ can be determined:

$$\mathbf{S}(\delta\boldsymbol{\Theta}) = \boldsymbol{\Lambda}^T\delta\boldsymbol{\Lambda} = (\mathbf{E}_i\otimes\mathbf{g}_i)\cdot(\delta\mathbf{g}_j\otimes\mathbf{E}_j) = \underbrace{\mathbf{g}_i^T\delta\mathbf{g}_j}_{=:S_{ij}(\delta\boldsymbol{\Theta})}\mathbf{E}_i\otimes\mathbf{E}_j \quad \text{with} \quad S_{ij}(\delta\boldsymbol{\Theta}) = -\epsilon_{ijk}\delta\Theta_k. \tag{2.15}$$

For later use, the components $\delta\Theta_i$ shall be expressed by $\mathbf{g}_i$ and $\delta\mathbf{g}_i$. From (2.15), it follows:

$$\delta\Theta_1 = \mathbf{g}_3^T\delta\mathbf{g}_2 = -\mathbf{g}_2^T\delta\mathbf{g}_3, \quad \delta\Theta_2 = \mathbf{g}_1^T\delta\mathbf{g}_3 = -\mathbf{g}_3^T\delta\mathbf{g}_1, \quad \delta\Theta_3 = \mathbf{g}_2^T\delta\mathbf{g}_1 = -\mathbf{g}_1^T\delta\mathbf{g}_2. \tag{2.16}$$

It has already been stated, that the finite rotations occurring e.g. in (2.8) are not additive. However, this holds even for the infinitesimal rotations, i.e. $\delta\boldsymbol{\theta} \neq \delta\boldsymbol{\psi}$. A relation between infinitesimal additive and multiplicative increments is given by the tangent operator $\mathbf{T}$ according to

$$\delta\boldsymbol{\psi} =: \mathbf{T}\delta\boldsymbol{\theta}, \quad \mathbf{T} = \frac{1}{\psi^2}\mathbf{S}(\boldsymbol{\psi})\mathbf{S}(\boldsymbol{\psi})^T + \frac{\psi/2}{\tan\left(\psi/2\right)}\left(\mathbf{I} - \frac{1}{\psi^2}\mathbf{S}(\boldsymbol{\psi})\mathbf{S}(\boldsymbol{\psi})^T\right) - \frac{1}{2}\mathbf{S}(\boldsymbol{\psi}). \tag{2.17}$$

The inversion of (2.17), expressing multiplicative by means of additive increments, is given by:

$$\delta\boldsymbol{\theta} = \mathbf{T}^{-1}\delta\boldsymbol{\psi}, \ \mathbf{T}^{-1} = \frac{1}{\psi^2}\left(1 - \frac{\sin\left(\psi\right)}{\psi}\right)\mathbf{S}(\boldsymbol{\psi})\mathbf{S}(\boldsymbol{\psi})^T + \frac{\sin\left(\psi\right)}{\psi}\mathbf{I} + \frac{1-\cos\left(\psi\right)}{\psi^2}\mathbf{S}(\boldsymbol{\psi}). \tag{2.18}$$

For details on the derivation of the transformations $\mathbf{T}$ and $\mathbf{T}^{-1}$, the interested reader is e.g. referred to [43, 56, 111, 209]. While the rotation vector parametrization presented so far represents a well-known tool in the formulation of geometrically exact beam elements of Simo-Reissner type, in the following section, an alternative parametrization of large rotations will be proposed which offers some advantages in the description of Kirchhoff type beam element formulations.

Remark: Formally, one could also introduce the material rotation vector $\boldsymbol{\Psi} = \boldsymbol{\Lambda}^T\boldsymbol{\psi}$. However, since $\boldsymbol{\psi}$ is an eigenvector of $\boldsymbol{\Lambda} = \exp(\mathbf{S}(\boldsymbol{\psi}))$ (and also of $\boldsymbol{\Lambda}^T$) with eigenvalue one, both variants are identical, i.e. $\boldsymbol{\Psi} = \boldsymbol{\Lambda}^T\boldsymbol{\psi} = \boldsymbol{\psi}$, and will not be further distinguished.

2.1.2 SO(3) parametrization via "smallest rotation" triads

The alternative parametrization considered in this section consists of four degrees of freedom $(\mathbf{t}, \varphi)$ with $\mathbf{t} \in \Re^3$ and $\varphi \in \Re$. In the context of Kirchhoff beam element formulations presented later in this work, $\mathbf{t}$ will be the *non-unit* tangent vector aligned to the space curve representing the beam centerline. Due to the Kirchhoff constraint of vanishing shear strains, the first base vector $\mathbf{g_1}$ of the cross-section triad $\mathbf{\Lambda} = (\mathbf{g}_1, \mathbf{g}_2, \mathbf{g}_3)_{\mathbf{E}_i}$, can be expressed by this tangent vector:

$$\mathbf{g_1} = \frac{\mathbf{t}}{||\mathbf{t}||}. \tag{2.19}$$

Based on the tangent vector $\mathbf{t}$ and an arbitrary given triad $\bar{\mathbf{g}}_i$, one can determine a triad $\mathbf{g}_{Mi}$, in the following denoted as interMediate or Medium triad (index M), that results when the triad $\bar{\mathbf{g}}_i$ is rotated onto the tangent vector $\mathbf{t}$ via the "Smallest Rotation" (SR) as e.g. described in [56]. This mapping can be interpreted as the rotation of a given triad $\bar{\mathbf{g}}_i$ such that its first base vector $\bar{\mathbf{g}}_1$ is rotated onto the given vector $\mathbf{t}$ and the corresponding rotation angle is minimized. Since the associated rotation angle $\Delta\boldsymbol{\theta}_{SR}$ is perpendicular on the initial and on the resulting first base vector, i.e. $\Delta\boldsymbol{\theta}_{SR}^T \bar{\mathbf{g}}_1 = \Delta\boldsymbol{\theta}_{SR}^T \mathbf{g}_1 = 0$, the smallest rotation is commonly also denoted as "rotation without twist". The resulting base vectors can be represented by the following expressions:

$$\mathbf{g}_{M1} = \mathbf{g}_1 = \frac{\mathbf{t}}{||\mathbf{t}||}, \quad \mathbf{g}_{M2} = \bar{\mathbf{g}}_2 - \frac{\bar{\mathbf{g}}_2^T \mathbf{g}_1}{1 + \bar{\mathbf{g}}_1^T \mathbf{g}_1} (\mathbf{g}_1 + \bar{\mathbf{g}}_1), \quad \mathbf{g}_{M3} = \bar{\mathbf{g}}_3 - \frac{\bar{\mathbf{g}}_3^T \mathbf{g}_1}{1 + \bar{\mathbf{g}}_1^T \mathbf{g}_1} (\mathbf{g}_1 + \bar{\mathbf{g}}_1). \tag{2.20}$$

In order to shorten notation, the abbreviation $\mathrm{sr}(.)$ is introduced for the SR mapping of (2.20):

$$\mathbf{\Lambda}_M := (\mathbf{g}_{M1}, \mathbf{g}_{M2}, \mathbf{g}_{M3})_{\mathbf{E}_i} =: \mathrm{sr}(\bar{\mathbf{\Lambda}}, \mathbf{g}_1) \quad \text{with} \quad \bar{\mathbf{\Lambda}} := (\bar{\mathbf{g}}_1, \bar{\mathbf{g}}_2, \bar{\mathbf{g}}_3)_{\mathbf{E}_i}. \tag{2.21}$$

In principle, the triad $\bar{\mathbf{g}}_i$ can be chosen arbitrarily, for example according to $\bar{\mathbf{g}}_i = \mathbf{E}_i$. However, by having a closer look at the equations above, one realizes that a singularity occurs for $1 + \bar{\mathbf{g}}_1^T \mathbf{g}_1 = 0$, i.e. when the vectors $\mathbf{g}_1$ and $\bar{\mathbf{g}}_1$ are antiparallel. Of course, in practical simulations, the scenario $\mathbf{g}_1 = -\mathbf{E}_1$ can easily occur, resulting in a non-defined triad $\mathbf{\Lambda}_M$. Consequently, alternative choices for the triad $\bar{\mathbf{g}}_i$ are required where this singularity will not occur. In the context of a temporally discretized problem setting, the triad at a given time step t_n could for example be chosen as the intermediate triad at the subsequent time step, i.e. $\bar{\mathbf{g}}_i(t_n) = \mathbf{g}_{Mi}(t_{n-1})$, resulting in an Updated Lagrangian type of formulation. In this case, the singularity can only appear, if the rotation per time step exceeds $180°$. In general, reasonable time step sizes employed in practical simulations will not allow for such large rotations per time step, thus recommending this choice for $\bar{\mathbf{g}}_i$. In Appendix A.1, it is shown that each mapping that defines a triad based on a given tangent vector $\mathbf{t}$ contains a singularity. In this context, a singularity appearing at a rotation of $180°$ can be considered as an optimum since such a rotation already describes the maximal difference in orientation two given triads can have. Subsequently to the definition of an intermediate triad $\mathbf{\Lambda}_M$ according to (2.21), the cross-section triad $\mathbf{g}_i$ can be defined based on a relative rotation of the intermediate triad $\mathbf{\Lambda}_M$ with respect to the tangent $\mathbf{t}$ by an relative angle of φ:

$$\mathbf{\Lambda} = \exp(\mathbf{S}(\varphi \mathbf{g}_1)) \mathbf{\Lambda}_M. \tag{2.22}$$

Alternatively, this simple 2D rotation can also be noted for the individual base vectors:

$$\mathbf{g}_1 = \mathbf{g}_{M1}, \ \mathbf{g}_2 = \mathbf{g}_{M2} \cos\varphi + \mathbf{g}_{M3} \sin\varphi, \ \mathbf{g}_3 = \mathbf{g}_{M3} \cos\varphi - \mathbf{g}_{M2} \sin\varphi. \tag{2.23}$$

Thus, the fourth degree of freedom (DoF) φ introduced above is simply the relative angle that rotates the intermediate triad $\mathbf{\Lambda}_M$ onto the frame $\mathbf{\Lambda}$ by means of a rotation with respect to the tangent vector. Equations (2.20) and (2.22) uniquely define a triad $\mathbf{\Lambda}$ parametrized by the four degrees of freedom $(\mathbf{t}, \varphi)$. Evidently, one of these four degrees of freedom, namely the norm $||\mathbf{t}||$ of the tangent vector, will not influence the triad orientation. However, as it will turn out in the next sections, the non-unit tangent vector $\mathbf{t}$ is a quantity that directly results from the beam centerline description. Thus, the only additional degree of freedom introduced in order to describe the triad orientation is the relative angle φ and consequently, the proposed type of triad parametrization is not redundant. For later use, also the spatial spin vector $\delta\boldsymbol{\theta}$ shall be expressed by means of additive increments $(\delta\mathbf{t}, \delta\varphi)$ of the four parameters $(\mathbf{t}, \varphi)$. Therefore, this vector is split into a component $\delta\boldsymbol{\theta}_{\parallel}$ parallel to $\mathbf{g}_1$ and a component $\delta\boldsymbol{\theta}_{\perp}$ perpendicular to $\mathbf{g}_1$ as follows:

$$\delta\boldsymbol{\theta} = \delta\boldsymbol{\theta}_{\parallel} + \delta\boldsymbol{\theta}_{\perp} = \delta\Theta_1\mathbf{g}_1 + \delta\boldsymbol{\theta}_{\perp}. \tag{2.24}$$

Throughout this thesis, the indices $(.)_{\parallel}$ and $(.)_{\perp}$ of a vector will denote the components of the vector which are parallel or perpendicular to the vector $\mathbf{g}_1$, respectively. Taking advantage of (2.12), the following relation can be derived for the variation of the vector $\mathbf{g}_1$:

$$\delta\mathbf{g}_1 = \delta\boldsymbol{\theta} \times \mathbf{g}_1 = \delta\boldsymbol{\theta}_{\perp} \times \mathbf{g}_1. \tag{2.25}$$

Permutation of the orthogonal vectors occurring in (2.25) yields an explicit expression for $\delta\boldsymbol{\theta}_{\perp}$:

$$\delta\boldsymbol{\theta}_{\perp} = \mathbf{g}_1 \times \delta\mathbf{g}_1 = \frac{\mathbf{t}}{||\mathbf{t}||} \times \delta\left(\frac{\mathbf{t}}{||\mathbf{t}||}\right) = \frac{\mathbf{t} \times \delta\mathbf{t}}{||\mathbf{t}||^2} = \frac{\mathbf{g}_1 \times \delta\mathbf{t}}{||\mathbf{t}||} \quad \text{with} \quad \delta\mathbf{t} \in \Re^3. \tag{2.26}$$

In a next step, equations (2.16) and (2.23) can be exploited in order to formulate $\delta\Theta_1$:

$$\delta\Theta_1 = \mathbf{g}_3^T\delta\mathbf{g}_2 = \mathbf{g}_{M3}^T\delta\mathbf{g}_{M2} + \delta\varphi =: \delta\Theta_{M1} + \delta\varphi \tag{2.27}$$

By variation of the basis vector $\delta\mathbf{g}_{M2}$ defined in (2.20), the tangential component $\delta\Theta_{M1}$ of the spin vector associated with the smallest rotation intermediate triad can be determined to:

$$\delta\Theta_{M1} = \frac{(\mathbf{g}_1 \times \bar{\mathbf{g}}_1)^T}{1+\mathbf{g}_1^T\bar{\mathbf{g}}_1}\delta\mathbf{g}_1 = -\frac{\bar{\mathbf{g}}_1^T\mathbf{S}(\mathbf{g}_1)}{1+\mathbf{g}_1^T\bar{\mathbf{g}}_1}\frac{\delta\mathbf{t}}{||\mathbf{t}||} =: \mathbf{T}_{\Theta_{M1}\mathbf{t}}\delta\mathbf{t} \quad \rightarrow \quad \delta\Theta_1 = \mathbf{T}_{\Theta_{M1}\mathbf{t}}\delta\mathbf{t} + \delta\varphi. \tag{2.28}$$

In the derivation of (2.28), use had been made of the fact that the base vectors of the triad $\bar{\mathbf{\Lambda}}$ do not depend on the current configuration and the corresponding displacement state, i.e. $\delta\bar{\mathbf{g}}_i = \mathbf{0}$. Inserting (2.26)-(2.28) into (2.24) yields the following expression for the spatial spin vector:

$$\delta\boldsymbol{\theta} = \mathbf{g}_1\delta\varphi + \underbrace{\frac{1}{t}\left(\mathbf{I} - \frac{\mathbf{g}_1 \otimes \bar{\mathbf{g}}_1^T}{1+\mathbf{g}_1^T\bar{\mathbf{g}}_1}\right)\mathbf{S}(\mathbf{g}_1)\,\delta\mathbf{t}}_{=:\mathbf{T}_{\boldsymbol{\theta}\mathbf{t}}} \quad \text{with} \quad \mathbf{g}_1 = \frac{\mathbf{t}}{t}, \quad t := ||\mathbf{t}||. \tag{2.29}$$

So far, the four degrees of freedom $(\mathbf{t}, \varphi)$ have been applied in order to uniquely describe a tangent vector $\mathbf{t}$, defined by its orientation and its length, as well as the orientation of a triad $\mathbf{\Lambda} = (\mathbf{g}_1, \mathbf{g}_2, \mathbf{g}_3)$ aligned parallel to this tangent vector. In the following, these two geometric entities, the non-unit tangent vector $\mathbf{t}$ and the triad $\mathbf{\Lambda}$, shall be described by the alternative set of

four degrees of freedom $(\boldsymbol{\psi}, t)$. Here, $\boldsymbol{\psi}$ represents the rotation vector associated with the triad $\boldsymbol{\Lambda}$ via the Rodrigues formula (2.6) and $t := ||\mathbf{t}||$ is the norm of the tangent vector. It can easily be derived, that the following transformations hold between these two sets of degrees of freedom:

$$\boldsymbol{\Lambda} = \exp(\mathbf{S}(\boldsymbol{\psi})),\ \mathbf{g}_1 = \boldsymbol{\Lambda}\mathbf{E}_1,\ \mathbf{t} = t\mathbf{g}_1,\ \exp(\mathbf{S}(\varphi\mathbf{g}_1)) = \boldsymbol{\Lambda}\mathrm{sr}(\bar{\boldsymbol{\Lambda}}, \mathbf{g}_1)^{-1}. \tag{2.30}$$

Based on (2.30), the set $(\mathbf{t}, \varphi)$ can be calculated from $(\boldsymbol{\psi}, t)$ and the other way round. Next, also a transformation rule between the variations $(\delta\mathbf{t}, \delta\varphi)$ and the variations $(\delta\boldsymbol{\theta}, \delta t)$ associated with the set $(\boldsymbol{\psi}, t)$ shall be derived. The variation δt can directly be written in terms of $\delta\mathbf{t}$:

$$\delta t = \delta||\mathbf{t}|| = \frac{\mathbf{t}^T}{t}\delta\mathbf{t} = \mathbf{g}_1^T\delta\mathbf{t}. \tag{2.31}$$

Combining (2.29) and (2.31) yields a transformation between the sets $(\delta\boldsymbol{\theta}, \delta t)$ and $(\delta\mathbf{t}, \delta\varphi)$:

$$\begin{pmatrix} \delta\boldsymbol{\theta} \\ \delta t \end{pmatrix} = \underbrace{\begin{pmatrix} \mathbf{T}_{\boldsymbol{\theta}\mathbf{t}} & \mathbf{g}_1 \\ \mathbf{g}_1^T & 0 \end{pmatrix}}_{=:\mathbf{T}_M^{-1}} \begin{pmatrix} \delta\mathbf{t} \\ \delta\varphi \end{pmatrix}. \tag{2.32}$$

By using the auxiliary relations $\delta\mathbf{t} = \delta(t\mathbf{g}_1) = \delta t\mathbf{g}_1 + t\mathbf{S}(\delta\boldsymbol{\theta})\mathbf{g}_1 = \delta t\mathbf{g}_1 - t\mathbf{S}(\mathbf{g}_1)\delta\boldsymbol{\theta}$ as well as $\delta\varphi = \mathbf{g}_1^T\delta\boldsymbol{\theta} - \delta\Theta_{M1}$, the inverse transformation of (2.32) can be derived in an analogous manner:

$$\begin{pmatrix} \delta\mathbf{t} \\ \delta\varphi \end{pmatrix} = \underbrace{\begin{pmatrix} -t\mathbf{S}(\mathbf{g}_1) & \mathbf{g}_1 \\ \mathbf{T}_{\varphi\boldsymbol{\theta}} & 0 \end{pmatrix}}_{=:\mathbf{T}_M} \begin{pmatrix} \delta\boldsymbol{\theta} \\ \delta t \end{pmatrix} \quad \text{with} \quad \mathbf{T}_{\varphi\boldsymbol{\theta}} = \frac{(\mathbf{g}_1 + \bar{\mathbf{g}}_1)^T}{1 + \mathbf{g}_1^T\bar{\mathbf{g}}_1}. \tag{2.33}$$

Again, the mapping $\mathbf{T}_M$ and the inverse $\mathbf{T}_M^{-1}$ exist provided that $\mathbf{g}_1 \neq -\bar{\mathbf{g}}_1$, i.e. for rotations per time step which are smaller than $180°$. The mappings $\mathbf{T}_M$ and $\mathbf{T}_M^{-1}$ transform between multiplicative rotation increments and additive increments of the chosen parametrization. Thus, they represent the analogon to the transformations $\mathbf{T}$ and $\mathbf{T}^{-1}$ in case of a rotation vector parametrization (see Section 2.1.1). Since the Kirchhoff constraint of vanishing shear deformation solely influences the component $\delta\boldsymbol{\theta}_\perp$ of the spin vector, it will in the following sections often be useful to express only this component by additive increments $\delta\mathbf{t}$, while the tangential spin vector component $\delta\Theta_1$ instead of the additive increment $\delta\varphi$ is regarded as independent primary variable. In this case, relations (2.32) and (2.33) simplify and yield the map between $(\delta\boldsymbol{\theta}, \delta t)$ and $(\delta\mathbf{t}, \delta\Theta_1)$:

$$\begin{pmatrix} \delta\boldsymbol{\theta} \\ \delta t \end{pmatrix} = \underbrace{\begin{pmatrix} \frac{1}{t}\mathbf{S}(\mathbf{g}_1) & \mathbf{g}_1 \\ \mathbf{g}_1^T & 0 \end{pmatrix}}_{=:\tilde{\mathbf{T}}^{-1}} \begin{pmatrix} \delta\mathbf{t} \\ \delta\Theta_1 \end{pmatrix}, \quad \begin{pmatrix} \delta\mathbf{t} \\ \delta\Theta_1 \end{pmatrix} = \underbrace{\begin{pmatrix} -t\mathbf{S}(\mathbf{g}_1) & \mathbf{g}_1 \\ \mathbf{g}_1^T & 0 \end{pmatrix}}_{=:\tilde{\mathbf{T}}} \begin{pmatrix} \delta\boldsymbol{\theta} \\ \delta t \end{pmatrix}. \tag{2.34}$$

Again, $\tilde{\mathbf{T}}$ and $\tilde{\mathbf{T}}^{-1}$ represent the corresponding mappings. Since these mappings solely transform the component $\delta\boldsymbol{\theta}_\perp$, they are independent from the actual definition of the triad $\boldsymbol{\Lambda}_M$. Consequently, the index M has been omitted for the transformation matrices $\tilde{\mathbf{T}}$ and $\tilde{\mathbf{T}}^{-1}$.

2.2 Simo-Reissner Beam Theory

In this section, the fundamentals of the geometrically exact Simo-Reissner beam theory based on the work of Reissner [183, 184] as well as Simo and Vu-Quoc [204, 208] will be presented. The results of this section will provide an essential basis for the subsequent derivation of Kirchhoff type beam formulations. As already explained in the beginning of this thesis, beam models can be classified in intrinsic, induced and semi-induced beam theories. Based on this notion, the geometrically exact Simo-Reissner beam theory can be identified as a semi-induced beam theory: In [204], 1D representations of the strong and weak form of the balance equations based on internal, external and inertia forces as well as work-conjugated strain measures have been derived that are fully consistent with the 3D continuum theory. However, in contrary to a fully induced theory, the constitutive relations are directly postulated on the 1D level. As already argued in [58] and in accordance with derivations in [3], [153] or [172], a consistency of the geometrically exact beam theories and the corresponding three-dimensional theory of continuum mechanics in the sense of a fully induced beam theory can only be assumed as long as small local strains are considered. In order to confirm this statement, in Section 2.2.5, a derivation of the constitutive relations between 1D stress resultants and deformation measures from their 3D counterparts is given. First, the basics of the geometrically exact Simo-Reissner beam theory in terms of basic kinematic assumptions, strong and weak form of balance equations, stress resultants, work-conjugated deformation measures and constitutive relations are presented in Sections 2.2.1-2.2.4.

2.2.1 Basic kinematic assumptions

Throughout this work, prismatic beams with anisotropic cross-section shape are considered. In the initial (unstressed) configuration, the beam centerline, which is defined as the line connecting the cross-section centroids, is described by the space curve $s \rightarrow \mathbf{r}_0(s) \in \Re^3$. Here and in the following, the index 0 of a quantity refers to the unstressed, initial configuration. Furthermore, $s \in [0, l] =: \Omega_l \subset \Re$ is an arc-length parametrization of the curve and $l \in \Re$ the beam length in the initial configuration. The description of the initial configuration is completed by a field of right-handed orthonormal triads $s \rightarrow \mathbf{g}_{01}(s), \mathbf{g}_{02}(s), \mathbf{g}_{03}(s) \in \Re^3$ attached to the beam cross-sections, with $\mathbf{g}_{01}$ being the unit tangential vector to the initial centerline, i.e

$$\mathbf{g}_{01}(s) \equiv \mathbf{r}_0'(s), \tag{2.35}$$

and with the base vectors $\mathbf{g}_{02}(s)$ and $\mathbf{g}_{03}(s)$ coinciding with the principal axes of inertia of the cross-section at s. Throughout this work, the prime $(.)' = \frac{d}{ds}(.)$ denotes the derivative with respect to the arc-length parameter s. The rotation from the global frame $\mathbf{E}_i$ onto the local frame $\mathbf{g}_{0i}(s)$ is described via the orthogonal transformation $s \rightarrow \mathbf{\Lambda}_0(s) \in SO(3)$ as introduced in (2.1):

$$\mathbf{g}_{0i}(s) = \mathbf{\Lambda}_0(s)\mathbf{E}_i \quad \text{with} \quad \mathbf{\Lambda}_0(s) = \mathbf{g}_{0j}(s) \otimes \mathbf{E}_j \quad \text{for} \quad i, j = 1, 2, 3. \tag{2.36}$$

The basic kinematic assumption of the geometrically exact Simo-Reissner theory allows to describe the initial spatial position of an arbitrary material point according to

$$\mathcal{X}(\boldsymbol{\imath}) = \mathbf{r}_0(s) + s_2\mathbf{g}_{02}(s) + s_3\mathbf{g}_{03}(s) \quad \text{with} \quad \boldsymbol{\imath} = (s, s_2, s_3)^T = (s_1, s_2, s_3)^T. \tag{2.37}$$

where (s_2, s_3) represent convective coordinates describing the position of a material point within the cross-section. In order to simplify the notation for subsequent derivations, the convective coordinate vector $\boldsymbol{\imath} = (s_1, s_2, s_3)^T$ as well as the redundant name $s_1 := s$ for the arc-length s has been introduced. The initial configuration $s \to C_0 := (\mathbf{r}_0(s), \boldsymbol{\Lambda}_0(\boldsymbol{\psi}_0(s))) \in \Re^3 \times SO(3)$ of the beam is therefore uniquely defined by the initial position vector field $\mathbf{r}_0(s)$ of the cross-section centroids and the field $\boldsymbol{\Lambda}_0(s)$ describing the initial orientation of the beam cross-sections. Correspondingly, the deformed configuration of the beam centerline at time $t \in \Re$ is represented by the space curve $s, t \to \mathbf{r}(s,t) \in \Re^3$. However, as consequence of axial tension, s is not an arc-length parametrization of the current deformed centerline $\mathbf{r}(s,t)$ any longer, thus leading to

$$||\mathbf{r}_0'(s)|| \equiv 1 \quad \text{but} \quad ||\mathbf{r}'(s,t)|| \neq 1, \tag{2.38}$$

in general. The orientation of the beam cross-section in the deformed configuration is specified by the current orientation $s, t \to \mathbf{g}_1(s,t), \mathbf{g}_2(s,t), \mathbf{g}_3(s,t) \in \Re^3$ of the attached right-handed orthonormal triad. The base vectors $\mathbf{g}_2(s,t)$ and $\mathbf{g}_3(s,t)$ are oriented along the same material fibers, i.e. the principal axes of inertia of the cross-section, as the base vectors $\mathbf{g}_{02}(s)$ and $\mathbf{g}_{03}(s)$ in the initial configuration. For that reason, $\mathbf{g}_i(s,t)$ will also be denoted as material frame or material triad in the following. The base vector $\mathbf{g}_1(s,t) := \mathbf{g}_2(s,t) \times \mathbf{g}_3(s,t)$ completes the triad. The latter is perpendicular to the cross-section but in general not tangential to the deformed centerline due to shear deformation. The current frame $\mathbf{g}_i(s,t)$ is again characterized by

$$\mathbf{g}_i(s,t) = \boldsymbol{\Lambda}(s,t)\mathbf{E}_i \quad \text{with} \quad \boldsymbol{\Lambda}(s,t) = \mathbf{g}_j(s,t) \otimes \mathbf{E}_j \quad \text{for} \quad i,j = 1,2,3. \tag{2.39}$$

Based on the basic kinematic assumption, the current spatial position of a material point reads:

$$\boldsymbol{x}(\boldsymbol{\imath}, t) = \mathbf{r}(s,t) + s_2\mathbf{g}_2(s,t) + s_3\mathbf{g}_3(s,t). \tag{2.40}$$

Together, equations (2.40) and (2.37) represent the Bernoulli assumption of rigid cross-sections. The deformed configuration $s, t \to C := (\mathbf{r}(s,t), \boldsymbol{\Lambda}(\boldsymbol{\psi}(s,t))) \in \Re^3 \times SO(3)$ is uniquely defined by the current position vector field $\mathbf{r}(s,t)$ of the cross-section centroids and the field $\boldsymbol{\Lambda}(s,t)$ describing the current orientation of the beam cross-sections. According to Section 2.1, $\boldsymbol{\Lambda}(s,t)$ can be represented by three rotation parameters (e.g. by a rotation vector $\boldsymbol{\psi}(s,t)$), leading to pointwise six, three translational and three rotational, degrees of freedom. The kinematic quantities defining the initial and deformed configuration are illustrated in Figure 2.1.

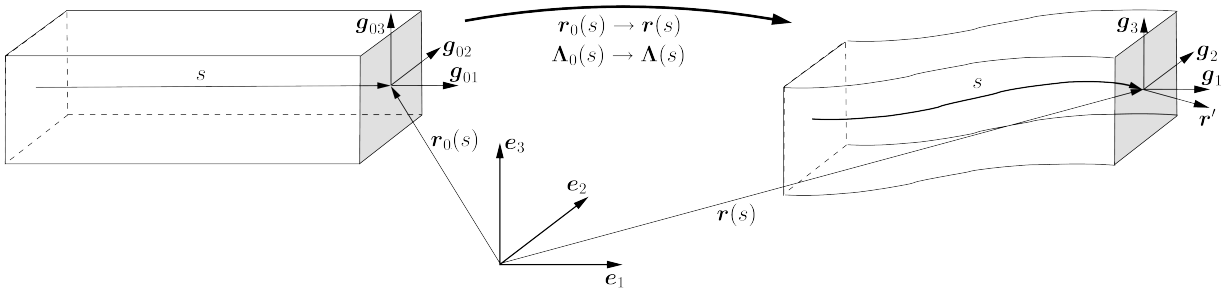

Figure 2.1: Kinematic quantities defining the initial and deformed configuration of the beam.

In order to simplify notation, the time argument t will be dropped in the following derivations. Later in this section, the arc-length derivative of the base vectors $\mathbf{g}_i(s)$ will be required in order to define deformation measures. Similar to (2.12), this derivative can be formulated as

$$\boldsymbol{\Lambda}'(s) = \mathbf{S}(\mathbf{k}(s))\boldsymbol{\Lambda}(s) \quad \text{or} \quad \mathbf{g}_i'(s) = \mathbf{k}(s) \times \mathbf{g}_i(s), \tag{2.41}$$

where $\mathbf{k}(s)$ is commonly referred to as spatial curvature vector. By means of the orthogonal transformation $\boldsymbol{\Lambda}(s)$, it is straightforward to employ the material curvature vector $\mathbf{K}(s) := \boldsymbol{\Lambda}^T(s)\mathbf{k}(s)$:

$$\boldsymbol{\Lambda}'(s) = \mathbf{S}(\mathbf{k}(s))\boldsymbol{\Lambda}(s) = \boldsymbol{\Lambda}(s)\boldsymbol{\Lambda}^T(s)\mathbf{S}(\mathbf{k}(s))\boldsymbol{\Lambda}(s) = \boldsymbol{\Lambda}(s)\mathbf{S}(\boldsymbol{\Lambda}^T(s)\mathbf{k}(s)) = \boldsymbol{\Lambda}(s)\mathbf{S}(\mathbf{K}(s)). \tag{2.42}$$

From equations (2.41) and (2.42), explicit calculation rules for the curvatures can be derived:

$$\mathbf{S}(\mathbf{k}(s)) = \boldsymbol{\Lambda}'(s)\boldsymbol{\Lambda}^T(s), \quad \mathbf{S}(\mathbf{K}(s)) = \boldsymbol{\Lambda}^T(s)\boldsymbol{\Lambda}'(s) \qquad \mathbf{K} = K_i\mathbf{E}_i,\ \mathbf{k} = K_i\mathbf{g}_i. \tag{2.43}$$

In a similar manner, the spatial and material angular velocity vectors $\mathbf{w}$ and $\mathbf{W}$ are defined:

$$\mathbf{S}(\mathbf{w}(s)) = \dot{\boldsymbol{\Lambda}}(s)\boldsymbol{\Lambda}^T(s), \quad \mathbf{S}(\mathbf{W}(s)) = \boldsymbol{\Lambda}^T(s)\dot{\boldsymbol{\Lambda}}(s) \qquad \mathbf{W} = W_i\mathbf{E}_i,\ \mathbf{w} = W_i\mathbf{g}_i. \tag{2.44}$$

For completeness, the spin vectors, which have been introduced in Section 2.1, are repeated here:

$$\mathbf{S}(\delta\boldsymbol{\theta}(s)) = \delta\boldsymbol{\Lambda}(s)\boldsymbol{\Lambda}^T(s), \quad \mathbf{S}(\delta\boldsymbol{\Theta}(s)) = \boldsymbol{\Lambda}^T(s)\delta\boldsymbol{\Lambda}(s) \qquad \delta\boldsymbol{\Theta} = \delta\Theta_i\mathbf{E}_i,\ \delta\boldsymbol{\theta} = \delta\Theta_i\mathbf{g}_i. \tag{2.45}$$

Throughout this thesis, the dot $\dot{(.)} = \frac{d}{dt}(.)$ denotes the derivative with respect to the time t. For later use, some important relations between these quantities will be derived. In order to shorten notation, the index s will often be omitted in the following. Applying the Young theorem $(\dot{\boldsymbol{\Lambda}}') = (\dot{\boldsymbol{\Lambda}})'$ and making use of the vector identity $\mathbf{S}(\mathbf{a})\mathbf{S}(\mathbf{b}) - \mathbf{S}(\mathbf{b})\mathbf{S}(\mathbf{a}) = \mathbf{S}(\mathbf{S}(\mathbf{a})\mathbf{b})$ yields:

$$\begin{aligned} &\frac{d}{dt}\big(\overbrace{\boldsymbol{\Lambda}\mathbf{S}(\mathbf{K})}^{\boldsymbol{\Lambda}'}\big) = \boldsymbol{\Lambda}\mathbf{S}(\mathbf{W})\mathbf{S}(\mathbf{K}) + \boldsymbol{\Lambda}\mathbf{S}(\dot{\mathbf{K}}) \doteq \frac{d}{ds}\big(\overbrace{\boldsymbol{\Lambda}\mathbf{S}(\mathbf{W})}^{\dot{\boldsymbol{\Lambda}}}\big) = \boldsymbol{\Lambda}\mathbf{S}(\mathbf{K})\mathbf{S}(\mathbf{W}) + \boldsymbol{\Lambda}\mathbf{S}(\mathbf{W}') \\ &\quad \rightarrow \mathbf{S}(\dot{\mathbf{K}}) = \mathbf{S}(\mathbf{W}') + \mathbf{S}(\mathbf{K})\mathbf{S}(\mathbf{W}) - \mathbf{S}(\mathbf{W})\mathbf{S}(\mathbf{K}) \ \rightarrow\ \dot{\mathbf{K}} = \mathbf{W}' - \mathbf{W}\times\mathbf{K}. \end{aligned} \tag{2.46}$$

In a similar manner, a relation between the spatial counterparts of $\mathbf{K}$ and $\mathbf{W}$ can be derived:

$$\begin{aligned} &\frac{d}{dt}\big(\overbrace{\mathbf{S}(\mathbf{k})\boldsymbol{\Lambda}}^{\boldsymbol{\Lambda}'}\big) = \mathbf{S}(\mathbf{k})\mathbf{S}(\mathbf{w})\boldsymbol{\Lambda} + \mathbf{S}(\dot{\mathbf{k}})\boldsymbol{\Lambda} \doteq \frac{d}{ds}\big(\overbrace{\mathbf{S}(\mathbf{w})\boldsymbol{\Lambda}}^{\dot{\boldsymbol{\Lambda}}}\big) = \mathbf{S}(\mathbf{w})\mathbf{S}(\mathbf{k})\boldsymbol{\Lambda} + \mathbf{S}(\mathbf{w}')\boldsymbol{\Lambda} \\ &\quad \rightarrow \mathbf{S}(\dot{\mathbf{k}}) = \mathbf{S}(\mathbf{w}') + \mathbf{S}(\mathbf{w})\mathbf{S}(\mathbf{k}) - \mathbf{S}(\mathbf{k})\mathbf{S}(\mathbf{w}) \ \rightarrow\ \dot{\mathbf{k}} = \mathbf{w}' + \mathbf{w}\times\mathbf{k}. \end{aligned} \tag{2.47}$$

It is emphasized that the final relations (2.46) and (2.47) only differ by a "-". Similar relations can be derived between (2.43) and (2.45) or between (2.44) and (2.45). The final results are:

$$\begin{aligned} \dot{\mathbf{k}} &= \mathbf{w}' + \mathbf{w}\times\mathbf{k}, & \delta\mathbf{k} &= \delta\boldsymbol{\theta}' + \delta\boldsymbol{\theta}\times\mathbf{k}, & \delta\mathbf{w} &= \delta\dot{\boldsymbol{\theta}} + \delta\boldsymbol{\theta}\times\mathbf{w}, \\ \dot{\mathbf{K}} &= \mathbf{W}' - \mathbf{W}\times\mathbf{K}, & \delta\mathbf{K} &= \delta\boldsymbol{\Theta}' - \delta\boldsymbol{\Theta}\times\mathbf{K}, & \delta\mathbf{W} &= \delta\dot{\boldsymbol{\Theta}} - \delta\boldsymbol{\Theta}\times\mathbf{W}. \end{aligned} \tag{2.48}$$

After having stated the basic kinematic assumptions of the geometrically exact beam theory, in the following section, stress resultants and the strong form of equilibrium will be presented.

2.2.2 Stress resultants and strong form of equilibrium

With $\tilde{\mathbf{f}}$ and $\tilde{\mathbf{m}}$ denoting distributed external forces and moments per unit length and $\mathbf{f}_\rho$ and $\mathbf{m}_\rho$ representing the force and moment contributions due to inertia effects, the strong form of the equilibrium equations for the considered beam problem reads (see e.g. [3, 184, 204]):

$$\begin{aligned} \mathbf{f}' + \tilde{\mathbf{f}} + \mathbf{f}_\rho &= \mathbf{0}, \\ \mathbf{m}' + \mathbf{r}' \times \mathbf{f} + \tilde{\mathbf{m}} + \mathbf{m}_\rho &= \mathbf{0}. \end{aligned} \tag{2.49}$$

In (2.49), $\mathbf{f}$ and $\mathbf{m}$ represent the force and moment vector resulting from the internal stresses acting on the beam cross-section area A. According to [204], these spatial objects are defined as:

$$\begin{aligned} \mathbf{f}(s) &:= \int_A \boldsymbol{\mathcal{P}}(s, s_2, s_3) \cdot \mathbf{E}_1 ds_2 ds_3 = \int_A \boldsymbol{t}_1(s, s_2, s_3) ds_2 ds_3, \\ \mathbf{m}(s) &:= \int_A \underbrace{(\boldsymbol{x}(s, s_2, s_3) - \mathbf{r}(s))}_{=:\boldsymbol{x}_A} \times \boldsymbol{t}_1(s, s_2, s_3) ds_2 ds_3. \end{aligned} \tag{2.50}$$

In the definition (2.50), the first Piola-Kirchhoff stress tensor $\boldsymbol{\mathcal{P}}$ has been introduced. Based on the Piola surface stress vectors $\boldsymbol{t}_1$, $\boldsymbol{t}_2$ and $\boldsymbol{t}_3$, this two-point tensor can be formulated as follows:

$$\boldsymbol{\mathcal{P}}(s, s_2, s_3) = \boldsymbol{t}_1(s, s_2, s_3) \otimes \mathbf{E}_1 + \boldsymbol{t}_2(s, s_2, s_3) \otimes \mathbf{E}_2 + \boldsymbol{t}_3(s, s_2, s_3) \otimes \mathbf{E}_3. \tag{2.51}$$

It should be noted that a detailed introduction into 3D continuum mechanics lies beyond the scope of the present work, which focuses on 1D continuum theories. For a thorough definition of the Piola-Kirchhoff stress tensor $\boldsymbol{\mathcal{P}}(s, s_2, s_3)$ and further objects defined in the field of 3D solid continuum mechanics required in the subsequent Section 2.2.5, the interested reader is exemplarily referred to the text books of Bonet and Wook [29], Gurtin [93], Holzapfel [98], Marsden and Hughes [155], Odgen [169] or Simo and Hughes [206]. Similar to 3D continuum mechanics, also a material form of the 1D equilibrium equations can be derived. This is achieved by inserting the material stress resultants $\mathbf{F} := \boldsymbol{\Lambda}^T \mathbf{f}$ and $\mathbf{M} := \boldsymbol{\Lambda}^T \mathbf{m}$ into the balance equations (2.49).

2.2.3 Weak form and objective deformation measures

In this section, the balance equations already given by the strong form (2.49) shall be transferred into the associated weak form. In the following, it is assumed that the reader is familiar with the *Method of Weighted Residuals* (MWR) and its mechanical interpretations as *Principle of Virtual Work* (PVW) or as *Principle of Minimum of Total Potential Energy* (PMTPE). Details on these principles can for example be found in the textbooks of Bathe [13], Hughes [103], Zienkiewicz and Taylor [242] and Zienkiewicz [243]. Following the PVW, the admissible variations, i.e. infinitesimal small and arbitrary (additive or multiplicative) changes of the current configuration $s \to \delta C := (\delta \mathbf{r}(s), \delta \boldsymbol{\theta}(s)) \in \Re^3 \times \Re^3$ that are compatible with the employed boundary conditions are introduced. Here, $\delta \boldsymbol{r}(s) \in \Re^3$ represents the vector of (additive) virtual displacements and $\delta \boldsymbol{\theta}(s) \in \Re^3$ the vector of (multiplicative) virtual rotations, also denoted as spin vector. By multiplication of (2.49) with $\delta \boldsymbol{r}$ and $\delta \boldsymbol{\theta}$ and integration by parts, the spatial weak form is derived:

$$G = \int_0^l \Big(\delta \boldsymbol{\theta}'^T \mathbf{m} + (\delta \mathbf{r}' - \delta \boldsymbol{\theta} \times \mathbf{r}')^T \mathbf{f} - \delta \boldsymbol{\theta}^T (\tilde{\mathbf{m}} + \mathbf{m}_\rho) - \delta \mathbf{r}^T (\tilde{\mathbf{f}} + \mathbf{f}_\rho) \Big) ds - \Big[\delta \mathbf{r}^T \mathbf{f}_\sigma \Big]_{\Gamma_\sigma} - \Big[\delta \boldsymbol{\theta}^T \mathbf{m}_\sigma \Big]_{\Gamma_\sigma} \doteq 0. \tag{2.52}$$

Here, $\mathbf{f}_\sigma$ and $\mathbf{m}_\sigma$ denote external forces and moments at the Neumann boundary Γ_σ of the considered beam. According to the principle of virtual work, the variations of the (so far unknown) deformation measures $\boldsymbol{\gamma}$ and $\boldsymbol{\omega}$ being work-conjugated to the spatial stress resultants $\mathbf{f}$ and $\mathbf{m}$ can be identified by means of work-pairing. If the spatial strong form (2.49) is chosen as basis for this procedure, the spatial deformation measures $\boldsymbol{\gamma}$ and $\boldsymbol{\omega}$ can be identified as

$$\delta_o\boldsymbol{\gamma} = \delta\mathbf{r}' - \delta\boldsymbol{\theta} \times \mathbf{r}', \quad \delta_o\boldsymbol{\omega} = \delta\boldsymbol{\theta}', \tag{2.53}$$

where the "objective variation" δ_o of an arbitrary vector $\mathbf{a} \in \Re^3$ is defined as the objective part $\delta_o\mathbf{a} := \delta\mathbf{a} - \delta\boldsymbol{\theta} \times \mathbf{a}$ (see e.g. [204]). The term $\delta\boldsymbol{\theta} \times \mathbf{a}$ represents the variation of the base vectors:

$$\delta\mathbf{a} = \delta a_i \mathbf{g}_i + a_i \delta\mathbf{g}_i = \underbrace{\delta a_i \mathbf{g}_i}_{\delta_o\mathbf{a}} + \underbrace{a_i \delta\boldsymbol{\theta} \times \mathbf{g}_i}_{\delta\boldsymbol{\theta}\times\mathbf{a}}. \tag{2.54}$$

If the material counterpart of equation (2.49) is chosen as starting point (see e.g [58]), the variation of the (so far unknown) material deformation measures $\boldsymbol{\Gamma}$ and $\boldsymbol{\Omega}$ being work-conjugated to the material stress resultants $\mathbf{F}$ and $\mathbf{M}$ can be determined in an analogous manner:

$$\delta\boldsymbol{\Gamma} = \boldsymbol{\Lambda}^T(\delta\mathbf{r}' + \mathbf{r}' \times \delta\boldsymbol{\theta}), \quad \delta\boldsymbol{\Omega} = \boldsymbol{\Lambda}^T\delta\boldsymbol{\theta}'. \tag{2.55}$$

Alternatively, the same results can be derived by starting with the spatial / material balance equations of the 3D-continuum instead of the spatial / material 1D-resultant equation (see [204]). It can be shown that the associated antiderivatives of the spatial differential quantities are:

$$\boldsymbol{\gamma} = \mathbf{r}' - \mathbf{g}_1, \;\; \mathbf{S}(\boldsymbol{\omega}) = \boldsymbol{\Lambda}'\boldsymbol{\Lambda}^T - \boldsymbol{\Lambda}\boldsymbol{\Lambda}_0^T\boldsymbol{\Lambda}_0'\boldsymbol{\Lambda}^T = \mathbf{S}(\boldsymbol{k}) - \mathbf{S}(\boldsymbol{\Lambda}\boldsymbol{\Lambda}_0^T\boldsymbol{k_0}) \;\rightarrow\; \boldsymbol{\omega} = \boldsymbol{k} - \boldsymbol{\Lambda}\boldsymbol{\Lambda}_0^T\boldsymbol{k_0}. \tag{2.56}$$

Similarly, the antiderivatives of the material differential quantities can be derived as:

$$\boldsymbol{\Gamma} = \boldsymbol{\Lambda}^T\mathbf{r}' - \mathbf{E}_1, \quad \mathbf{S}(\boldsymbol{\Omega}) = \boldsymbol{\Lambda}^T\boldsymbol{\Lambda}' - \boldsymbol{\Lambda}_0^T\boldsymbol{\Lambda}_0' = \mathbf{S}(\boldsymbol{K}) - \mathbf{S}(\boldsymbol{K_0}) \;\rightarrow\; \boldsymbol{\Omega} = \boldsymbol{K} - \boldsymbol{K}_0. \tag{2.57}$$

It is easy to verify that all of these deformation measures vanish for the stress-free initial configuration, i.e. when the relations $\boldsymbol{\Lambda} = \boldsymbol{\Lambda}_0$, $\mathbf{r}' = \mathbf{r}_0'$ and $\mathbf{g}_1 = \mathbf{g}_{01} = \mathbf{r}_0' = \boldsymbol{\Lambda}_0\mathbf{E}_1$ are valid. Mechanically, the components of $\boldsymbol{\Gamma}$ represent axial tension (first component) and shear deformation (second and third component). The components of $\boldsymbol{\Omega}$ represent torsion (first component) as well as bending (second and third component). While the current and initial material curvature vector can be subtracted directly in (2.57), a rotation of the initial spatial curvature vector $\boldsymbol{k_0}$ from the initial basis $\mathbf{g}_{0i}$ onto the current basis $\mathbf{g}_i$ is necessary in (2.56) in order to fulfill objectivity.

Remark: In [204], the orientation of the material frame $\mathbf{g}_i$ was described via a rotation $\tilde{\boldsymbol{\Lambda}}$ of the initial local frame $\mathbf{g}_{0i}$, thus $\tilde{\boldsymbol{\Lambda}} := \boldsymbol{\Lambda}\boldsymbol{\Lambda}_0^T = \mathbf{g}_i \otimes \mathbf{g}_{0i}$. The corresponding pull-back mapping via $\tilde{\boldsymbol{\Lambda}}$ is the one that naturally appears, e.g. in the initial spatial curvature vector of equation (2.56) or when the corresponding spatial / material quantities (e.g. spatial / material stress resultants) of the beam theory are deduced from their spatial / material counterparts of 3D continuum mechanics (e.g. Cauchy stresses / 2^{nd} Piola Kirchhoff stresses, see Section 2.2.5). In this case, the components of spatial quantities expressed in the current material frame $\mathbf{g}_i$ are identical to the components of their material counterparts expressed in the initial material frame $\mathbf{g}_{0i}$. This pull-back operation can be interpreted as a rotation of spatial quantities from the current, curved beam configuration onto the initial, curved beam configuration. By contrast, the pull-back operation via $\boldsymbol{\Lambda}$ as applied here, or e.g. in [58], can be interpreted as a rotation of spatial quantities from the current curved beam configuration onto a fictitious, in general not stress-free, straight beam configuration, in which the material frame $\mathbf{g}_i$ coincides with the global frame $\mathbf{E}_i$.

2.2.4 Constitutive relations

Finally, constitutive relations between the material stress resultants $\mathbf{M}$ and $\mathbf{F}$ and the deformation measures $\boldsymbol{\Omega}$ and $\boldsymbol{\Gamma}$ are required. The simplest constitutive law of this type and the one considered in this thesis is represented by a length-specific hyperelastic stored energy function according to:

$$\tilde{\Pi}_{int}(\boldsymbol{\Omega},\boldsymbol{\Gamma}) = \frac{1}{2}\boldsymbol{\Omega}^T\mathbf{C}_M\boldsymbol{\Omega} + \frac{1}{2}\boldsymbol{\Gamma}^T\mathbf{C}_F\boldsymbol{\Gamma}, \quad \mathbf{M} = \frac{\partial\tilde{\Pi}_{int}}{\partial\boldsymbol{\Omega}} = \mathbf{C}_M\cdot\boldsymbol{\Omega}, \quad \mathbf{F} = \frac{\partial\tilde{\Pi}_{int}}{\partial\boldsymbol{\Gamma}} = \mathbf{C}_F\cdot\boldsymbol{\Gamma}. \tag{2.58}$$

Here, the material constitutive tensors $\mathbf{C}_M$ and $\mathbf{C}_F$ have the following diagonal structure:

$$\mathbf{C}_M = \mathbf{diag}\big[C_{M1}, C_{M2}, C_{M3}\big]_{\mathbf{E}_i} \quad \text{and} \quad \mathbf{C}_F = \mathbf{diag}\big[C_{F1}, C_{F2}, C_{F3}\big]_{\mathbf{E}_i}. \tag{2.59}$$

In the following, $\mathbf{diag}\big[A,B,C\big]_{\mathbf{E}_i}$ represents a diagonal matrix with entries $A, B, C \in \Re$. Again, the index $\mathbf{E}_i$ denotes the basis in which the associated tensor is represented. The six constitutive constants $C_{Mi}, C_{Fi} \in \Re$ can either be determined experimentally or derived from the 3D continuum theory. If the latter approach is chosen (see e.g. Section 2.2.5), the constants can be expressed by quantities related to the beam geometry and the hyper-elastic material law of the 3D-continuum. The simplest section constitutive model of this kind yields the relations

$$C_{M1} = GI_T, \quad C_{M2} = EI_2, \quad C_{M3} = EI_3, \quad C_{F1} = EA, \quad C_{F2} = G\bar{A}_2, \quad C_{F3} = G\bar{A}_3. \tag{2.60}$$

Here, E and G are the Young's modulus and the shear modulus, A, $\bar{A}_2$ and $\bar{A}_3$ are the cross-section and the two reduced cross-sections, I_2 and I_3 are the two principal moments of inertia and I_T is the torsional moment of inertia. The push-forward of these material relations yields:

$$\begin{aligned} \mathbf{m} &= \mathbf{c}_m\cdot\boldsymbol{\omega} \qquad \text{and} \qquad \mathbf{f} = \mathbf{c}_f\cdot\boldsymbol{\gamma} \\ \mathbf{c}_m &= \mathbf{diag}\big[C_{M1}, C_{M2}, C_{M3}\big]_{\mathbf{g}_i} \quad \text{and} \quad \mathbf{c}_f = \mathbf{diag}\big[C_{F1}, C_{F2}, C_{F3}\big]_{\mathbf{g}_i}. \end{aligned} \tag{2.61}$$

Similarly to (2.58), the length-specific kinetic energy $\tilde{\Pi}_{kin}$ of the beam can be formulated:

$$\tilde{\Pi}_{kin}(\mathbf{w},\dot{\mathbf{r}}) = \frac{1}{2}\mathbf{w}^T\mathbf{c}_\rho\mathbf{w} + \frac{1}{2}\rho A\dot{\mathbf{r}}^T\dot{\mathbf{r}}, \quad \mathbf{c}_\rho = \boldsymbol{\Lambda}\mathbf{C}_\rho\boldsymbol{\Lambda}^T, \quad \mathbf{C}_\rho = \mathbf{diag}\big[\rho(\underbrace{I_2+I_3}_{=:I_P}), \rho I_2, \rho I_3\big]_{\mathbf{E}_i}. \tag{2.62}$$

Here, ρ is the mass density, $\mathbf{C}_\rho$ the material inertia tensor and $\mathbf{w}$ represents the spatial angular velocity vector, which has already been introduced in (2.44). From the kinetic energy (2.62), the spatial vectors of length-specific linear momentum $\tilde{\mathbf{l}}$ and angular momentum $\tilde{\mathbf{h}}$ can be derived:

$$\tilde{\mathbf{l}} := \frac{\partial\tilde{\Pi}_{kin}}{\partial\dot{\mathbf{r}}} = \rho A\dot{\mathbf{r}}, \quad \tilde{\mathbf{h}} := \frac{\partial\tilde{\Pi}_{kin}}{\partial\mathbf{w}} = \mathbf{c}_\rho\mathbf{w} = \boldsymbol{\Lambda}\mathbf{C}_\rho\boldsymbol{\Lambda}^T\mathbf{w} = \boldsymbol{\Lambda}\mathbf{C}_\rho\mathbf{W}. \tag{2.63}$$

Similar to the length-specific external forces $\tilde{\mathbf{f}}$ and $\tilde{\mathbf{m}}$, also the length-specific energies $\tilde{\Pi}_{int}$ and $\tilde{\Pi}_{kin}$ and the length-specific linear and angular momentum $\tilde{\mathbf{l}}$ and $\tilde{\mathbf{h}}$ have been furnished with the $\tilde{(.)}$-symbol. The total counterparts $\mathbf{f}_{ext}$, $\mathbf{m}_{ext}$, Π_{int}, Π_{kin}, $\mathbf{l}$ and $\mathbf{h}$ are obtained by integration:

$$\begin{aligned} \mathbf{f}_{ext} &:= \int_0^l \tilde{\mathbf{f}}\,ds + \Big[\mathbf{f}_\sigma\Big]_{\Gamma_\sigma}, \quad \mathbf{m}_{ext} := \int_0^l \Big(\mathbf{r}\times\tilde{\mathbf{f}} + \tilde{\mathbf{m}}\Big)\,ds + \Big[\mathbf{r}\times\mathbf{f}_\sigma + \mathbf{m}_\sigma\Big]_{\Gamma_\sigma}, \\ \Pi_{int} &:= \int_0^l \tilde{\Pi}_{int}\,ds, \quad \Pi_{kin} := \int_0^l \tilde{\Pi}_{kin}\,ds, \quad \mathbf{l} := \int_0^l \tilde{\mathbf{l}}\,ds, \quad \mathbf{h} := \int_0^l (\tilde{\mathbf{h}} + \mathbf{r}\times\tilde{\mathbf{l}})\,ds. \end{aligned} \tag{2.64}$$

The additional subscript $(.)_{ext}$ has been applied to the integrated external forces and moments in order to avoid a confusion with the stress resultants $\mathbf{f}$ and $\mathbf{m}$. Furthermore, the origin of the global coordinate frame has been chosen as reference point for the total external moment $\mathbf{m}_{ext}$ and angular momentum $\mathbf{h}$. These definitions will be required for subsequent derivations. Next, based on (2.63), the inertia forces $\mathbf{f}_\rho$ and the inertia moments $\mathbf{m}_\rho$ yield (see e.g. [204]):

$$-\mathbf{f}_\rho = \dot{\tilde{\mathbf{l}}} = \rho A \ddot{\mathbf{r}}, \quad -\mathbf{m}_\rho = \dot{\tilde{\mathbf{h}}} = \mathbf{\Lambda}\left[\mathbf{S}(\mathbf{W})\mathbf{C}_\rho \mathbf{W} + \mathbf{C}_\rho \mathbf{A}\right] = \mathbf{S}(\mathbf{w})\mathbf{c}_\rho \mathbf{w} + \mathbf{c}_\rho \mathbf{a}, \quad \mathbf{a} := \dot{\mathbf{w}}, \quad \mathbf{A} := \dot{\mathbf{W}}. \tag{2.65}$$

Similar to $\mathbf{w} = \mathbf{\Lambda}\mathbf{W}$, also the angular accelerations are related via the push-forward operator:

$$\mathbf{a} := \dot{\mathbf{w}} = \frac{d}{dt}\left(\mathbf{\Lambda}\mathbf{W}\right) = \mathbf{\Lambda}\mathbf{S}(\mathbf{W})\mathbf{W} + \mathbf{\Lambda}\dot{\mathbf{W}} = \mathbf{\Lambda}\dot{\mathbf{W}} =: \mathbf{\Lambda}\mathbf{A}, \quad \text{since} \quad \mathbf{S}(\mathbf{W})\mathbf{W} = \mathbf{0}. \tag{2.66}$$

When the considered beam problem has to be discretized in time (see Section 3.1 for details), the vectors $\mathbf{w}$ and $\mathbf{a}$ can either be directly employed in a time integration scheme [116, 209, 210] or, alternatively, they can be expressed via the (additive) rate of the primary variable $\boldsymbol{\psi}$ [43]. Similar to (2.17), one can formulate the following relations in order to express $\mathbf{w}$ and $\mathbf{a}$:

$$\mathbf{w} = \mathbf{T}^{-1}\dot{\boldsymbol{\psi}}, \quad \mathbf{a} = \dot{\mathbf{T}}^{-1}\dot{\boldsymbol{\psi}} + \mathbf{T}^{-1}\ddot{\boldsymbol{\psi}}. \tag{2.67}$$

Finally, the problem setup presented in Sections 2.2.1-2.2.4 has to be completed by boundary and initial conditions in order to end up with a well-defined initial boundary value problem:

$$\begin{aligned} &\mathbf{r} = \mathbf{r}_u,\ \boldsymbol{\psi} = \boldsymbol{\psi}_u \text{ on } \Gamma_u, \quad \mathbf{f} = \mathbf{f}_\sigma,\ \mathbf{m} = \mathbf{m}_\sigma \text{ on } \Gamma_\sigma, \quad \Gamma_\sigma \cap \Gamma_u = \varnothing,\ \Gamma_\sigma \cup \Gamma_u = \{0, L\} \\ &\qquad\qquad \mathbf{r} = \mathbf{r}_0,\ \dot{\mathbf{r}} = \mathbf{v}_0,\ \mathbf{\Lambda} = \mathbf{\Lambda}_0,\ \mathbf{w} = \mathbf{w}_0 \text{ at } t = 0. \end{aligned} \tag{2.68}$$

Based on a trial space $(\mathbf{r}(s,t), \mathbf{\Lambda}(\boldsymbol{\psi}(s,t))) \in \mathcal{U}$ of functions with square-integrable first derivatives satisfying (2.68) and an associated weighting space $(\delta\mathbf{r}(s), \delta\boldsymbol{\theta}(s)) \in \mathcal{V}$ of functions with square-integrable first derivatives satisfying $\delta\mathbf{r} = \mathbf{0},\ \delta\boldsymbol{\theta} = \mathbf{0}$ on Γ_u, the weak form (2.52) is equivalent to the strong form (2.49) supplemented by the boundary conditions (2.68).

Remark: Two possible time integration schemes can be derived from the variants of either employing $\mathbf{W}$ and $\mathbf{A}$ directly or expressing them via additive rates given by (2.67):

$$\begin{aligned} &1) \quad (\dot{\mathbf{r}}, \ddot{\mathbf{r}}, \mathbf{w}, \mathbf{a})_{n+1} = \mathbf{f}((\mathbf{r}, \mathbf{\Lambda})_{n+1}, (\mathbf{r}, \mathbf{\Lambda})_n, (\dot{\mathbf{r}}, \mathbf{w})_n, (\ddot{\mathbf{r}}, \mathbf{a})_n), \\ &2) \quad (\dot{\mathbf{r}}, \ddot{\mathbf{r}}, \dot{\boldsymbol{\psi}}, \ddot{\boldsymbol{\psi}})_{n+1} = \mathbf{f}((\mathbf{r}, \boldsymbol{\psi})_{n+1}, (\mathbf{r}, \boldsymbol{\psi})_n, (\dot{\mathbf{r}}, \dot{\boldsymbol{\psi}})_n, (\ddot{\mathbf{r}}, \ddot{\boldsymbol{\psi}})_n). \end{aligned} \tag{2.69}$$

Here, the indices $(.)_n$ and $(.)_{n+1}$ refer to two successive time steps of the time-discrete problem and $\mathbf{f}(.)$ represents a typical finite difference time integration scheme (e.g. a Newmark scheme). The first variant, i.e. time integration directly based on the angular velocities and accelerations (see Section 3.1.2) can be considered as being more flexible since it does not require any specific rotation parametrization. It can directly be applied to Reissner type beam formulations as well as to Kirchhoff type beam formulations with strong or weak Kirchhoff constraint enforcement without the need for further adaptions. Due to this flexibility and the very simple and compact time integrator resulting from this procedure, this will be the method of choice employed throughout this thesis.

Remark: Since the material triad field $\mathbf{\Lambda}(s)$ is fully defined via a rotation vector field parametrization $\boldsymbol{\psi}(s)$, the trial space can also be formulated as $(\mathbf{r}(s,t), \boldsymbol{\psi}(s,t)) \in \mathcal{U}$.

Remark: It is shown in Appendix A.2 how the strong and weak forms (2.49) and (2.52) can alternatively be derived by means of variational principles (viz. the Hamilton principle). The starting point for this procedure is the Lagrangian $\mathcal{L} = \int (\tilde{\Pi}_{kin} - \tilde{\Pi}_{int}) ds$ based on the kinetic and hyperelastic energy according to (2.62) and (2.58).

Remark: In principle, the geometrically exact beam theory is capable of describing the orientation of arbitrary cross-section shapes. Thus, it is not limited to the simple case of isotropic shapes (such as circular or quadratic cross-sections), often denoted as kinetic symmetry, as it is the case for many Kirchhoff type beam formulations that can be found in the literature (see e.g. [36], [227] or [228]). However, with the introduction of the specific section constitutive laws chosen in this section, the following considerations will from now on be confined to cross-section shapes whose center of shear coincides with the cross-section centroid (e.g. bi-symmetric cross-sections). While the beam theory presented in Sections 2.2.1-2.2.3 remains valid for arbitrary cross-sections, some adaptions of the constitutive law would be necessary if this confinement should be resigned.

2.2.5 Relation between 1D and 3D constitutive laws

The aim of the following considerations is to derive the constitutive laws (2.58)-(2.60) in a consistent manner from the 3D continuum theory. Thereto, the deformation gradient $\mathcal{F}$ of the 3D position field subject to the kinematic constraints (2.40) and (2.37) of the geometrically exact beam theory shall be derived. Subsequently, also the Cauchy-Green deformation tensor $\mathcal{E}$ is required. These two objects can be formulated based on the following definitions:

$$\mathcal{E} := \frac{1}{2}\big(\mathcal{F}^T\mathcal{F} - \mathbf{I}_3\big) \quad \text{with} \quad \mathcal{F} := \frac{\partial \boldsymbol{x}}{\partial \mathcal{X}} = \frac{\partial \boldsymbol{x}}{\partial \boldsymbol{\imath}}\frac{\partial \boldsymbol{\imath}}{\partial \mathcal{X}} = \boldsymbol{g}_i \otimes \mathcal{G}^i. \tag{2.70}$$

In order to evaluate the deformation gradient (2.70), (the non-orthonormal), covariant basis vectors $\boldsymbol{g}_i = \partial \boldsymbol{x}(\boldsymbol{\imath})/\partial s_i$ and $\mathcal{G}_i = \partial \mathcal{X}(\boldsymbol{\imath})/\partial s_i$ have to be determined from (2.40) and (2.37):

$$\begin{aligned} \boldsymbol{g}_1 &= \mathbf{r}' + \mathbf{k} \times (s_2\mathbf{g}_2 + s_3\mathbf{g}_3)\,,\ \boldsymbol{g}_2 = \mathbf{g}_2,\ \boldsymbol{g}_3 = \mathbf{g}_3, \\ \mathcal{G}_1 &= \mathbf{g}_{01} + \mathbf{k}_0 \times (s_2\mathbf{g}_{02} + s_3\mathbf{g}_{03})\,,\ \mathcal{G}_2 = \mathbf{g}_{02},\ \mathcal{G}_3 = \mathbf{g}_{03}. \end{aligned} \tag{2.71}$$

Furthermore, the associated contravariant base vectors $\mathcal{G}^i$ can be determined from the second line of (2.71) via the definition $\mathcal{G}_i^T\mathcal{G}^j = \delta_i{}^j$, which yields after some algebraic manipulations:

$$\mathcal{G}^1 = \frac{1}{C}\mathbf{g}_{01},\quad \mathcal{G}^2 = \mathbf{g}_{02} + \frac{K_{01}s_3}{C}\mathbf{g}_{01},\quad \mathcal{G}^3 = \mathbf{g}_{03} - \frac{K_{01}s_2}{C}\mathbf{g}_{01},\quad C := 1 - K_{03}s_2 + K_{02}s_3. \tag{2.72}$$

Making use of the relation $\mathbf{r}' = \mathbf{g}_1 + \boldsymbol{\gamma}$ according to (2.56) and inserting the first line of (2.71) as well as (2.72) into (2.70) yields the following expression for the deformation gradient:

$$\mathcal{F} = \frac{1}{C}\big[\mathbf{g}_1 + \boldsymbol{\gamma} + \mathbf{k} \times (s_2\mathbf{g}_2 + s_3\mathbf{g}_3)\big] \otimes \mathbf{g}_{01} + \mathbf{g}_2 \otimes \big[\mathbf{g}_{02} + \frac{K_{01}s_3}{C}\mathbf{g}_{01}\big] + \mathbf{g}_3 \otimes \big[\mathbf{g}_{03} - \frac{K_{01}s_2}{C}\mathbf{g}_{01}\big]. \tag{2.73}$$

Finally, by inserting (2.73) into (2.70), the individual components of the Cauchy-Green deformation tensor can be determined. However, in order to gain further insight into the underlying

structure of the deformation gradient, the procedure suggested by Geradin and Cardona [82] (for initially straight beams) as well as Linn et al. [145] (for initially curved beams) is employed by slightly reformulating the expression (2.73) on the basis of the relative rotation tensor $\tilde{\boldsymbol{\Lambda}} := \boldsymbol{\Lambda}\boldsymbol{\Lambda}_0^T$. By applying the auxiliary relation $1/C = 1+(1-C)/C$ to the pre-factor of $\mathbf{g}_1$ and solving all the products in (2.73), the deformation gradient can be reformulated according to:

$$\boldsymbol{\mathcal{F}} = \tilde{\boldsymbol{\Lambda}}\,(\mathbf{I}_3 + \boldsymbol{H}\otimes\mathbf{g}_{01}) \quad \text{with} \quad \boldsymbol{H} := H_i\mathbf{g}_{0i},\quad \mathbf{I}_3 = \mathbf{g}_{0i}\otimes\mathbf{g}_{0i},\quad \tilde{\boldsymbol{\Lambda}} = \mathbf{g}_i\otimes\mathbf{g}_{0i}. \tag{2.74}$$

The components of the vector $\boldsymbol{H}$, denoted as *material strain vector* in [82] and [145], read:

$$\begin{aligned} H_1 &= \frac{1}{C}\left[\Gamma_1 + (K_2 - K_{02})s_3 - (K_3 - K_{03})s_2\right], \\ H_2 &= \frac{1}{C}\left[\Gamma_2 - (K_1 - K_{01})s_3\right], \quad H_3 = \frac{1}{C}\left[\Gamma_3 - (K_1 - K_{01})s_2\right]. \end{aligned} \tag{2.75}$$

Based on the deformation gradient (2.74), the Cauchy-Green deformation tensor can be derived:

$$\boldsymbol{\mathcal{E}} = \frac{1}{2C}\left[\boldsymbol{H}\otimes\mathbf{g}_{01} + \mathbf{g}_{01}\otimes\boldsymbol{H}\right] + \frac{\boldsymbol{H}^T\boldsymbol{H}}{2C^2}\mathbf{g}_{01}\otimes\mathbf{g}_{01}. \tag{2.76}$$

The result (2.76) has been consistently derived from the basic kinematic assumptions (2.40) and (2.37) without any additional approximations. However, in order to finally end up with the simple constitutive laws of the geometrically exact beam theory which is based on the quadratic form (2.58), from now on, the following well-known assumption of small local strains is made:

$$\Gamma_i \ll 1 \quad \text{and} \quad R\cdot K_i \ll 1,\ R\cdot K_{0i} \ll 1 \text{ for } i = 1,2,3. \tag{2.77}$$

The assumptions (2.77) state that small local axial and shear strains are considered and that the radii of initial and deformed centerline curvature have to be small as compared to the cross-section radius R. In the following, a first-order approximation in these small quantities is considered by setting $C \approx 1$ and neglecting the last, quadratic term in (2.76). Based on these small-strain assumptions, the approximated Cauchy-Green deformation tensor reads

$$\boldsymbol{\mathcal{E}} \approx \bar{\boldsymbol{\mathcal{E}}} = \frac{1}{2}\left[\boldsymbol{H}\otimes\mathbf{g}_{01} + \mathbf{g}_{01}\otimes\boldsymbol{H}\right] =: \bar{\mathcal{E}}_{ij}\mathbf{g}_{0i}\otimes\mathbf{g}_{0j}. \tag{2.78}$$

The components $\bar{\mathcal{E}}_{ij}$ of the approximated Cauchy-Green deformation tensor $\bar{\boldsymbol{\mathcal{E}}}$ finally yield:

$$\begin{aligned} \bar{\mathcal{E}}_{11} &= \Gamma_1 + (K_2 - K_{02})s_3 - (K_3 - K_{03})s_2, \\ \bar{\mathcal{E}}_{12} &= \bar{\mathcal{E}}_{21} = \frac{1}{2}\left(\Gamma_2 - (K_1 - K_{01})s_3\right), \\ \bar{\mathcal{E}}_{13} &= \bar{\mathcal{E}}_{31} = \frac{1}{2}\left(\Gamma_3 + (K_1 - K_{01})s_2\right), \\ \bar{\mathcal{E}}_{22} &= \bar{\mathcal{E}}_{33} = \bar{\mathcal{E}}_{23} = \bar{\mathcal{E}}_{32} = 0. \end{aligned} \tag{2.79}$$

By applying a Saint-Venant-Kirchhoff material with corresponding material constitutive tensor $\mathcal{C} = \mathcal{C}^{ijkl}\mathbf{g}_{0i}\otimes\mathbf{g}_{0j}\otimes\mathbf{g}_{0k}\otimes\mathbf{g}_{0l}$, the 2. Piola-Kirchhoff stress tensor $\bar{\mathcal{S}} = \bar{\mathcal{S}}^{ij}\mathbf{g}_{0i}\otimes\mathbf{g}_{0j}$ can be

formulated component-wise based on the approximated Cauchy-Green deformation tensor $\bar{\mathfrak{E}}$:

$$\begin{aligned}
\bar{\mathcal{S}}^{11} &= \bar{E}(\Gamma_1 + (K_2 - K_{02})s_3 - (K_3 - K_{03})S_2), \\
\bar{\mathcal{S}}^{22} &= \bar{\mathcal{S}}^{33} = -\nu\mathcal{E}_{11}, \\
\bar{\mathcal{S}}^{12} &= \bar{\mathcal{S}}^{21} = G\left(\Gamma_2 - (K_1 - K_{01})s_3\right), \\
\bar{\mathcal{S}}^{13} &= \bar{\mathcal{S}}^{31} = G\left(\Gamma_3 + (K_1 - K_{01})s_2\right), \\
\bar{\mathcal{S}}^{23} &= \bar{\mathcal{S}}^{32} = 0.
\end{aligned} \tag{2.80}$$

The scaled Young's modulus $\bar{E}$ and the shear modulus G have been introduced according to

$$\bar{E} := \frac{(1-\nu)E}{(1+\nu)(1-2\nu)}, \quad G := \frac{E}{2(1+\nu)}, \tag{2.81}$$

where E is Young's modulus and ν is Poisson's ratio. From (2.80), it gets obvious that the standard relations known in the geometrically exact beam theory in terms of vanishing in-plane stress components $\bar{\mathcal{S}}^{22} = \bar{\mathcal{S}}^{33} = 0$ and of a constitutive parameter E in front of the normal stress $\bar{\mathcal{S}}^{11}$, only holds for the special case $\nu = 0$. This is a consequence of the kinematic assumption of rigid cross-sections, which requires the existence of in-plane reaction forces in general. In order to resolve these two putative contradictions for general cases $\nu \neq 0$, the constraint of rigid cross-sections can be weakened by allowing for a uniform lateral contraction of the cross-section with in-plane strain components $\bar{\mathfrak{E}}^{22} = \bar{\mathfrak{E}}^{33} = -\nu E_{11}$ and for a proper in-plane warping field (see [145] or [227] for further details). Alternatively, the approximation $\nu = 0$ can be employed in the first two lines of (2.80). In praxis, this slight inconsistency is often taken into account, which is not unusual in the field of structural theories (see e.g. [3] or [126]). In the last step required to identify the 1D section constitutive law, the material force resultants are determined by integration of the stress vector $\boldsymbol{t}_1 = \mathcal{S} \cdot \mathbf{g}_{01}$ acting on a cross-section defined by the material normal vector $\mathbf{g}_{01}$. This procedure is similar to that performed in the defining equations (2.50) of the stress resultants:

$$\begin{aligned}
\tilde{\mathbf{F}} := \int_A \boldsymbol{t}_1 dA &= \int_A \big[E(\Gamma_1 + (K_2 - K_{02})s_3 - (K_3 - K_{03})s_2)\mathbf{g}_{01} \\
&\quad + G\left(\Gamma_2 - (K_1 - K_{01})s_3\right)\mathbf{g}_{02} + G(\Gamma_3 + (K_1 - K_{01})s_2)\mathbf{g}_{03}\big] dA \\
&= \begin{bmatrix} EA & 0 & 0 \\ 0 & GA & \\ 0 & 0 & GA \end{bmatrix}_{\mathbf{g}_{0i}} \cdot \begin{bmatrix} \Gamma_1 \\ \Gamma_2 \\ \Gamma_3 \end{bmatrix}_{\mathbf{g}_{0i}} = \tilde{\mathbf{C}}_F \tilde{\mathbf{\Gamma}}.
\end{aligned} \tag{2.82}$$

$$\begin{aligned}
\tilde{\mathbf{M}} := \int_A \boldsymbol{x}_A \times \boldsymbol{t}_1 dA &= \int_A (s_2\mathbf{g}_{02} + s_3\mathbf{g}_{03}) \times \big[E(\Gamma_1 + (K_2 - K_{02})s_3 - (K_3 - K_{03})s_2)\mathbf{g}_{01} \\
&\quad + G\left(\Gamma_2 - (K_1 - K_{01})s_3\right)\mathbf{g}_{02} + G\left(\Gamma_3 + (K_1 - K_{01})s_2\right)\mathbf{g}_{03}\big] dA \\
&= \begin{bmatrix} GI_P & 0 & 0 \\ 0 & EI_2 & \\ 0 & 0 & EI_3 \end{bmatrix}_{\mathbf{g}_{0i}} \cdot \begin{bmatrix} K_1 - K_{01} \\ K_2 - K_{02} \\ K_3 - K_{03} \end{bmatrix}_{\mathbf{g}_{0i}} = \tilde{\mathbf{C}}_M \tilde{\mathbf{\Omega}}.
\end{aligned} \tag{2.83}$$

Here, the defintions of the moments of inertia of area $I_2 := \int_A s_3^2 dA$ and $I_3 := \int_A s_2^2 dA$ as well as $\int_A s_3 dA = \int_A s_2 dA = \int_A s_2 s_3 dA = 0$ have been applied. As expected, (2.82) and (2.83) yield

a constitutive law that is identical to the one postulated in (2.58). Comparable derivations based on similar small-strain assumptions can e.g. be found in the original works of Kirchhoff [125] and Love [153] in the context of shear-free beam formulations as well as in the current contributions [82, 120, 145] in the context of geometrically exact Simo-Reissner type formulations. As mentioned in the remark at the end of Section 2.2.3, the presented derivation yields alternative material objects $\tilde{\mathbf{F}}$, $\tilde{\mathbf{C}}_F$ and $\tilde{\mathbf{\Gamma}}$ as well as $\tilde{\mathbf{M}}$, $\tilde{\mathbf{C}}_M$ and $\tilde{\mathbf{\Omega}}$ that are pulled-back to the curved, initial reference configuration and not to the straight reference configuration as it was the case for the material objects considered so far. However, the components of the alternative material objects, e.g. $\tilde{\mathbf{F}} = F_i \mathbf{g}_{0i}$, when expressed with respect to the "curved", local basis $\mathbf{g}_{0i}$ are identical to the components of the original material objects, e.g. $\mathbf{F} = F_i \mathbf{E}_i$, when expressed with respect to the "straight", global basis $\mathbf{E}_i$. Accordingly, on the basis of the following push-forward operations, also the 1. Piola-Kirchhoff stress tensor $\mathcal{P}$ and the Cauchy stress tensor $\boldsymbol{\sigma}$ can be determined.

$$\mathcal{P} = \mathcal{F}\mathcal{S}, \quad \boldsymbol{\sigma} = \frac{1}{\det\mathcal{F}} \mathcal{F}\mathcal{S}\mathcal{F}^T. \tag{2.84}$$

Starting with the 1. Piola-Kirchhoff stress tensor or with the Cauchy stress tensor, the spatial stress resultants, e.g. $\mathbf{f} = F_i \mathbf{g}_i$, can be derived similarly to (2.82) and (2.83). Since again only first-order terms of the small strains (2.77) are relevant, it is sufficient to approximate the deformation gradient, required for the push-forward, by neglecting the linear terms in the small strains (2.77):

$$\mathcal{F} \approx \tilde{\mathbf{\Lambda}} = \mathbf{g}_i \otimes \mathbf{g}_{0i}, \quad \det\mathcal{F} \approx 1. \tag{2.85}$$

Consequently, as already postulated in the sections before, the relevant pull-back / push-forward operator is given by a rotation tensor $\tilde{\mathbf{\Lambda}}$. If for the derivations above a 3D continuum formulation with material strain and stress measures based on a straight reference configuration had been applied, the resulting 1D material objects would be based on the global basis $\mathbf{E}_i$ and the total rotation tensor $\mathbf{\Lambda}$ could be identified as the corresponding pull-back / push-forward operator.

Remark: As already mentioned above, in the derivations made in this section, the initial, curved configuration has been considered as material reference configuration. In order to remain consistent with the convention of representing spatial objects by small letters and material objects by capital letters, the alternative notation $\mathbf{G}_i = \mathbf{g}_{0i}$ for the cross-section triad in the reference configuration would have been appropriate. However, in order to avoid confusions due to double declarations, this slight inconsistency has been accepted.

2.3 Kirchhoff-Love Beam Theory

In order to describe the configuration space of Reissner type beams, pointwise six degrees of freedom are necessary, namely the three translational components of $\mathbf{r}(s)$ and three rotational degrees of freedom $\boldsymbol{\psi}(s)$, which parametrize the triad $\mathbf{\Lambda}(s)$. Now, in this chapter, the assumption of vanishing shear strains is made, which can be assumed as a sensible approximation in the range of highly slender beams (see e.g. [153]). Thus, the beam cross-sections spanned by the local base vectors $\mathbf{g}_2$ and $\mathbf{g}_3$ have to remain perpendicular to the tangent vector $\mathbf{t}(s) := \mathbf{r}'(s)$:

$$\mathbf{g}_2(s) \cdot \mathbf{t}(s) \equiv 0 \quad \text{and} \quad \mathbf{g}_3(s) \cdot \mathbf{t}(s) \equiv 0 \quad \text{or} \quad \mathbf{g}_1(s) \equiv \frac{\mathbf{t}(s)}{||\mathbf{t}(s)||}. \tag{2.86}$$

Principally, this so-called Kirchhoff constraint of vanishing shear deformations can be enforced in a strong or in a weak manner. If the same parametrization $(\mathbf{r}(s), \boldsymbol{\psi}(s))$ as in the Reissner case is chosen, additional fields of Lagrange multipliers $\lambda_2(s)$ and $\lambda_3(s)$ are necessary, in order to integrate (2.86) into a constrained variational problem in a weak sense (see Section 2.3.5). In the following sections, a parametrization consisting of 4 degrees of freedom $(\mathbf{r}(s), \varphi(s))$ is chosen, which fulfills the Kirchhoff constraint in a strong manner. As already introduced in Section 2.1.2, the scalar-valued quantity $\varphi(s)$ will describe the relative rotation between the material frame $\mathbf{g}_i(s)$ and an intermediate frame $\mathbf{g}_{Mi}(s)$ with respect to the tangent vector $\mathbf{t}(s)$ according to (2.22). By means of (2.20), one example for a suitable intermediate frame $\mathbf{g}_{Mi}(s)$ has already been given, the "Smallest Rotation" intermediate frame. Nevertheless, the following derivations are made in a rather general manner, which allows to insert arbitrary alternative intermediate frame definitions $\mathbf{g}_{Mi}(s)$. In such a general manner, kinematic relations, strong and weak form of the balance equations, deformation measures and stress resultants and finally also the constitutive laws are formulated for the Kirchhoff case, thus providing the basis for the corresponding Kirchhoff beam element formulation, which will be proposed in the subsequent chapter. In Section 2.3.4, a brief excurse on the analytic treatment of Kirchhoff beams is presented. There, one possible alternative intermediate frame, the Frenet-Serret frame, is employed. The resulting strong form of the balance equations based on this intermediate frame is ideal for the analytic treatment of Kirchhoff beam problems and will for example be exploited in order to derive analytic solutions for numerical examples presented in subsequent chapters. Finally, in Section 2.3.5, the alternative of imposing the Kirchhoff constraint in a weak sense will be presented, while Section 2.3.6 focuses on the weak enforcement of an inextensibility constraint.

2.3.1 Kinematics

Throughout the following sections, the Kirchhoff constraint (2.86) of vanishing shear strains is strongly enforced based on the following representation of the material base vectors (see (2.23))

$$\begin{aligned} &\mathbf{g}_1(s) = \mathbf{g}_{M1}(s) = \frac{\mathbf{t}(s)}{||\mathbf{t}(s)||} = \frac{\mathbf{r}'(s)}{||\mathbf{r}'(s)||} \quad \text{with} \quad \mathbf{t}(s) = \mathbf{r}'(s), \\ &\mathbf{g}_2(s) = \mathbf{g}_{M2}(s)\cos\varphi(s) + \mathbf{g}_{M3}(s)\sin\varphi(s), \;\; \mathbf{g}_3 = \mathbf{g}_{M3}(s)\cos\varphi(s) - \mathbf{g}_{M2}(s)\sin\varphi(s), \end{aligned} \tag{2.87}$$

where the centerline-aligned intermediate triad base vectors $\mathbf{g}_{Mi}(s) = \mathbf{g}_{Mi}(\mathbf{r}'(s))$ are completely defined by the centerline field $\mathbf{r}(s)$ but not further specified for now (a possible example is given by (2.20)). Now, the Kirchhoff constraint is incorporated by expressing the current configuration $s, t \rightarrow C := (\mathbf{r}(s,t), \boldsymbol{\Lambda}(\mathbf{r}(s,t), \varphi(s,t))) \in \Re^3 \times SO(3)$ via the new set of primary variables $(\mathbf{r}(s,t), \varphi(s,t))$. As a first step, the spatial and material curvature vector have to be expressed in dependence of the intermediate triad base vectors and the relative angle $\varphi(s)$. In analogy to equations (2.24)-(2.27) and by replacing the variation $\delta(.)$ by the arc-length derivative $(.)'$, the spatial curvature vector $\mathbf{k}$ as defined in equation (2.43) can be reformulated according to:

$$\mathbf{k} = \mathbf{k}_{\|} + \mathbf{k}_{\perp} = K_1 \mathbf{g}_1 + \mathbf{S}(\mathbf{g}_1)\mathbf{g}_1' = (K_{M1} + \varphi')\mathbf{g}_1 + \underbrace{\frac{\mathbf{S}(\mathbf{r}')\mathbf{r}''}{||\mathbf{r}'||^2}}_{=:\boldsymbol{\kappa}}. \tag{2.88}$$

The component K_1, representing the mechanical torsion, consists of two contributions: the derivative φ' of the relative angle and the torsion K_{M1} of the intermediate triad (see also (2.27)):

$$K_{M1} := \mathbf{g}_{M3}^T \mathbf{g}_{M2}' \tag{2.89}$$

Furthermore, the Frenet curvature vector $\boldsymbol{\kappa}$ represents the curvature of the beam centerline $\mathbf{r}(s)$. In components, the spatial as well as the material curvature vector read:

$$\boldsymbol{k} = \begin{pmatrix} K_{M1} + \varphi' \\ \mathbf{g}_2^T \boldsymbol{\kappa} \\ \mathbf{g}_3^T \boldsymbol{\kappa} \end{pmatrix}_{\mathbf{g}_i} \quad \text{and} \quad \boldsymbol{K} = \begin{pmatrix} K_{M1} + \varphi' \\ \mathbf{g}_2^T \boldsymbol{\kappa} \\ \mathbf{g}_3^T \boldsymbol{\kappa} \end{pmatrix}_{\mathbf{E}_i} . \tag{2.90}$$

The intermediate torsion K_{M1} is the only term in (2.90) that depends on the specific choice of the intermediate triad. In order to keep the formulation general, at the moment, this term is not further specified (by inserting concrete intermediate base vectors $\mathbf{g}_{M2}$ and $\mathbf{g}_{M3}$ into (2.89)). Besides the curvature vectors, also the spin vector $\delta\boldsymbol{\theta}$ has to be adapted to the Kirchhoff constraint. By means of (the first three rows of) (2.34), the spatial spin vector is already expressed for the case that the first base vector $\mathbf{g}_1$ of the material triad is described by a non-unit vector $\mathbf{t}$. In the case considered here, this vector $\mathbf{t}$ represents the tangent vector $\mathbf{r}'$ to the beam centerline. For completeness, the spatial spin vector with $\mathbf{t} = \mathbf{r}'$ and $t = ||\mathbf{r}'||$ is repeated here:

$$\delta\boldsymbol{\theta} = \delta\Theta_1 \mathbf{g}_1 + \delta\boldsymbol{\theta}_\perp = \delta\Theta_1 \mathbf{g}_1 + \frac{\mathbf{S}(\mathbf{r}')\delta\mathbf{r}'}{||\mathbf{r}'||^2} = (\delta\Theta_{M1} + \delta\varphi)\mathbf{g}_1 + \frac{\mathbf{S}(\mathbf{r}')\delta\mathbf{r}'}{||\mathbf{r}'||^2}. \tag{2.91}$$

In analogy to Reissner type beam formulations, the first component $\delta\Theta_1$ of the spin vector, representing a multiplicative increment, will subsequently directly be employed in the weak form and not further expressed via additive increments according to $\delta\Theta_1 = \delta\Theta_{M1} + \delta\varphi$. Consequently, the admissible variations are $s \rightarrow \delta C := (\delta\mathbf{r}(s), \delta\boldsymbol{\theta}(\delta\mathbf{r}(s), \delta\Theta_1(s), \mathbf{r}(s,t))) \in \Re^3 \times \Re^3$ with the new set of variational primary variables $(\delta\mathbf{r}(s), \delta\Theta_1(s))$ defining the Kirchhoff case. Later, a relation between the curvature and angular velocity components K_1 and W_1 will be required. Left-multiplication of the first relation in the second line of (2.48) with $\mathbf{E}_1^T = (\boldsymbol{\Lambda}^T \mathbf{g}_1)^T$ yields:

$$\dot{K}_1 = W_1' + \dot{\mathbf{g}}_1^T(\mathbf{g}_1 \times \mathbf{g}_1'), \quad \text{with } \mathbf{E}_1^T(\mathbf{K} \times \mathbf{W}) = \mathbf{g}_1^T(\mathbf{k} \times \mathbf{w}) = \mathbf{g}_1^T(\mathbf{k}_\perp \times \mathbf{w}_\perp) = \dot{\mathbf{g}}_1^T(\mathbf{g}_1 \times \mathbf{g}_1'). \tag{2.92}$$

In a similar manner, the following relations between K_1, W_1 and $\delta\Theta_1$ can be derived from (2.48):

$$\dot{K}_1 = W_1' + \dot{\mathbf{g}}_1^T(\mathbf{g}_1 \times \mathbf{g}_1'), \quad \delta K_1 = \delta\Theta_1' + \delta\mathbf{g}_1^T(\mathbf{g}_1 \times \mathbf{g}_1'), \quad \delta W_1 = \delta\dot{\Theta}_1 + \delta\mathbf{g}_1^T(\mathbf{g}_1 \times \dot{\mathbf{g}}_1). \tag{2.93}$$

Remark: From equations (2.88) and (2.91), the following similarities become obvious:

$$\delta\boldsymbol{\theta} = \begin{pmatrix} \frac{1}{||\mathbf{t}||}\mathbf{S}(\mathbf{g}_1) & \mathbf{g}_1 \end{pmatrix} \begin{pmatrix} \delta\mathbf{t} \\ \delta\Theta_1 \end{pmatrix}, \quad \mathbf{k} = \begin{pmatrix} \frac{1}{||\mathbf{t}||}\mathbf{S}(\mathbf{g}_1) & \mathbf{g}_1 \end{pmatrix} \begin{pmatrix} \mathbf{t}' \\ K_1 \end{pmatrix}. \tag{2.94}$$

An equivalent relation can also be formulated for the angular velocities (see (2.102)).

2.3.2 Deformation measures and stress resultants

Having defined kinematics that are compatible with the Kirchhoff constraint according to (2.86), the deformation measures, constitutive relations and stress resultants presented in Section 2.2

can be adapted to the shear-free case. Inserting the constrained curvature vectors from (2.90) into the deformation measures $\boldsymbol{\Omega}$ and $\boldsymbol{\omega}$ according to (2.56) and (2.57) yields

$$\boldsymbol{\Omega} = \begin{pmatrix} K_{M1}+\varphi'-K_{M01}-\varphi_0' \\ \mathbf{g}_2^T\boldsymbol{\kappa} - \mathbf{g}_{02}^T\boldsymbol{\kappa}_0 \\ \mathbf{g}_3^T\boldsymbol{\kappa} - \mathbf{g}_{03}^T\boldsymbol{\kappa}_0 \end{pmatrix}_{\mathbf{E}_i} \quad \text{and} \quad \boldsymbol{\omega} = \begin{pmatrix} K_{M1}+\varphi'-K_{M01}-\varphi_0' \\ \mathbf{g}_2^T\boldsymbol{\kappa} - \mathbf{g}_{02}^T\boldsymbol{\kappa}_0 \\ \mathbf{g}_3^T\boldsymbol{\kappa} - \mathbf{g}_{03}^T\boldsymbol{\kappa}_0 \end{pmatrix}_{\mathbf{g}_i}. \tag{2.95}$$

The objective variations of $\boldsymbol{\Omega}$ and $\boldsymbol{\omega}$ have a similar form as stated in (2.53) and (2.55), i.e.

$$\delta\boldsymbol{\Omega} = \boldsymbol{\Lambda}^T\delta\boldsymbol{\theta}', \quad \delta_o\boldsymbol{\omega} = \delta\boldsymbol{\theta}'. \tag{2.96}$$

However, in the Kirchhoff case the constrained spin vector (2.91) has to be employed. By construction, the shear components of $\boldsymbol{\Gamma}$ and $\boldsymbol{\gamma}$ in (2.56) and (2.57), vanish due to (2.86):

$$\boldsymbol{\Gamma} = \epsilon\mathbf{E}_1 \quad \text{and} \quad \boldsymbol{\gamma} = \epsilon\mathbf{g}_1 \quad \text{with} \quad \epsilon := ||\mathbf{r}'|| - 1. \tag{2.97}$$

Here, the abbreviation ϵ has been introduced for the remaining component representing the axial tension. In this case, also the corresponding objective variations of $\boldsymbol{\Gamma}$ and $\boldsymbol{\gamma}$ can be simplified:

$$\delta\boldsymbol{\Gamma} = \delta\epsilon\mathbf{E}_1, \quad \delta_o\boldsymbol{\gamma} = \boldsymbol{\Lambda}\delta\boldsymbol{\Gamma} = \delta\epsilon\mathbf{g}_1 \quad \text{with} \quad \delta\epsilon := \frac{\delta\mathbf{r}'^T\mathbf{r}'}{||\mathbf{r}'||} = \delta\mathbf{r}'^T\mathbf{g}_1. \tag{2.98}$$

While the constitutive matrices $\mathbf{C}_M$ and $\mathbf{c}_m$ from (2.59) and (2.61) and the relations $\mathbf{M} = \mathbf{C}_M\boldsymbol{\Omega}$ as well as $\mathbf{m} = \mathbf{c}_m\boldsymbol{\omega}$ remain unchanged, the constitutive matrices $\mathbf{C}_F$ and $\mathbf{c}_f$ as well as the deformation measures $\boldsymbol{\Gamma}$ and $\boldsymbol{\gamma}$ can be simplified to a scalar factor, since the transverse components $\mathbf{f}_\perp$ and $\mathbf{F}_\perp$ of the force stress resultants given by the following split relations

$$\mathbf{f} = \mathbf{f}_\parallel + \mathbf{f}_\perp = F_1\mathbf{g}_1 + \mathbf{f}_\perp \quad \text{and} \quad \mathbf{F} = \mathbf{F}_\parallel + \mathbf{F}_\perp = F_1\mathbf{E}_1 + \mathbf{F}_\perp \tag{2.99}$$

cannot be determined via a kinematic and constitutive relation anymore. In this case, the stored energy function of (2.58) and the corresponding constitutive relations simplify to:

$$\tilde{\Pi}_{int}(\boldsymbol{\Omega},\epsilon) = \frac{1}{2}\boldsymbol{\Omega}^T\mathbf{C}_M\boldsymbol{\Omega} + \frac{1}{2}EA\epsilon^2, \ \mathbf{M} = \frac{\partial\tilde{\Pi}_{int}}{\partial\boldsymbol{\Omega}} = \mathbf{C}_M\boldsymbol{\Omega} = \boldsymbol{\Lambda}^T\mathbf{m}, \ F_1 = \frac{\partial\tilde{\Pi}_{int}}{\partial\epsilon} = EA\epsilon. \tag{2.100}$$

The inertia forces $\mathbf{f}_\rho$ as well as the inertia moments $\mathbf{m}_\rho$ are identical to (2.65) and (2.66). Like in the Reissner case, the spatial or material angular velocities $\mathbf{w}$ and $\mathbf{W}$ as well as the spatial or material angular accelerations $\mathbf{a}$ and $\mathbf{A}$ can either be directly used in the employed time integration scheme or they can be expressed via the (additive) rate of the primary variables $(\mathbf{r}(s), \varphi(s))$. For the latter approach, transformation matrices depending on the definition of the employed intermediate triad (see e.g. $\mathbf{T}_M^{-1}$ in (2.32) in the case of the SR intermediate triad) as well as their time-derivatives are required in order to formulate relations similar to (2.67).

$$\mathbf{w} = \mathbf{T}_{\boldsymbol{\theta}\mathbf{t}}\dot{\mathbf{t}} + \dot{\varphi}\mathbf{g}_1, \quad \mathbf{a} = \dot{\mathbf{T}}_{\boldsymbol{\theta}\mathbf{t}}\dot{\mathbf{t}} + \mathbf{T}_{\boldsymbol{\theta}\mathbf{t}}\ddot{\mathbf{t}} + \dot{\varphi}\dot{\mathbf{g}}_1 + \ddot{\varphi}\mathbf{g}_1. \tag{2.101}$$

In the Kirchhoff case, a third variant can often be advantageous: Similar to the curvature vector $\mathbf{k}$ (see (2.88)) and the spin vector $\delta\boldsymbol{\theta}$ (see (2.91) or (2.34)), also the angular velocity $\mathbf{w}$ can be split into a component tangential and a component perpendicular to the beam centerline

$$\mathbf{w} = \mathbf{w}_\parallel + \mathbf{w}_\perp = W_1\mathbf{g}_1 + \mathbf{S}(\mathbf{g}_1)\dot{\mathbf{g}}_1 = W_1\mathbf{g}_1 + \frac{\mathbf{S}(\mathbf{r}')\dot{\mathbf{r}}'}{||\mathbf{r}'||^2}, \quad \mathbf{a} = \dot{W}_1\mathbf{g}_1 + W_1\dot{\mathbf{g}}_1 + \mathbf{S}(\mathbf{g}_1)\ddot{\mathbf{g}}_1. \tag{2.102}$$

While the component $\mathbf{w}_\perp$ is fully determined by the primary variable $\mathbf{r}(s)$, W_1 is not specified any further, i.e. it is not expressed via $\mathbf{r}(s)$ and $\varphi(s)$ and their time rates as done in (2.101).

Remark: Three possible time integration schemes result from the variants given above:

$$\begin{aligned}
&1) \quad (\dot{\mathbf{r}}, \ddot{\mathbf{r}}, \mathbf{w}, \mathbf{a})_{n+1} = \mathbf{f}((\mathbf{r}, \boldsymbol{\Lambda})_{n+1}, (\mathbf{r}, \boldsymbol{\Lambda})_n, (\dot{\mathbf{r}}, \mathbf{w})_n, (\ddot{\mathbf{r}}, \mathbf{a})_n), \\
&2) \quad (\dot{\mathbf{r}}, \ddot{\mathbf{r}}, \dot{\varphi}, \ddot{\varphi})_{n+1} = \mathbf{f}((\mathbf{r}, \varphi)_{n+1}, (\mathbf{r}, \varphi)_n, (\dot{\mathbf{r}}, \dot{\varphi})_n, (\ddot{\mathbf{r}}, \ddot{\varphi})_n), \\
&3) \quad (\dot{\mathbf{r}}, \ddot{\mathbf{r}}, W_1, \dot{W}_1)_{n+1} = \mathbf{f}((\mathbf{r}, \boldsymbol{\Lambda})_{n+1}, (\mathbf{r}, \boldsymbol{\Lambda})_n, (\dot{\mathbf{r}}, W_1)_n, (\ddot{\mathbf{r}}, \dot{W}_1)_n).
\end{aligned} \tag{2.103}$$

Here, the indices $(.)_n$ and $(.)_{n+1}$ refer to two successive time steps of the time-discrete problem and $\mathbf{f}(.)$ represents a typical finite difference time integration scheme (e.g. a Newmark scheme). The second variant according to (2.101) represents the most specific approach since the choice of a specific intermediate triad is needed for the matrix $\mathbf{T}_{\boldsymbol{\theta}\mathbf{t}}$. The third variant according to (2.102) requires no specific information concerning the employed intermediate triad field, but is still based on the assumption that the Kirchhoff constraint (2.86) is fulfilled in a strong manner. However, the first variant, i.e. time integration directly based on the angular velocities and accelerations (see Section 3.1.2) is the most flexible one and does not require any specific rotation parametrization. It can directly be applied to Reissner type beam formulations as well as to Kirchhoff type beam formulations with strong or weak Kirchhoff constraint enforcement without the need for further adaptions. Due to this flexibility and the simple and compact time integrator resulting from this procedure, this variant will be employed throughout this thesis.

2.3.3 Strong and weak form

In this section, the spatial representation of mechanical equilibrium will be considered. Analogous derivations can also be made starting with the material balance equations. In the following, the notation will be simplified by summarizing external forces and moments as well as inertia forces and moments according to $\tilde{\mathbf{f}}_\rho := \tilde{\mathbf{f}} + \mathbf{f}_\rho$ and $\tilde{\mathbf{m}}_\rho := \tilde{\mathbf{m}} + \mathbf{m}_\rho$. Now, the shear forces $\mathbf{f}_\perp$, which provide no work contribution in the Kirchhoff case of vanishing shear deformations, have to be eliminated. Thereto, (2.99) is exploited in order to split the vector valued moment equilibrium equations, i.e. the second line of (2.49), into a component parallel to the tangent vector, i.e.

$$\mathbf{g}_1^T \left(\mathbf{m}' + \tilde{\mathbf{m}}_\rho + \mathbf{r}' \times \mathbf{f}\right) = \mathbf{g}_1^T \left(\mathbf{m}' + \tilde{\mathbf{m}}_\rho\right) = 0, \tag{2.104}$$

and a component that is perpendicular to the centerline tangent vector $\mathbf{g}_1 = \mathbf{t}/||\mathbf{t}||$, i.e.

$$\left(\mathbf{m}' + \tilde{\mathbf{m}}_\rho + \mathbf{r}' \times \mathbf{f}\right) - \mathbf{g}_1^T \left(\mathbf{m}' + \tilde{\mathbf{m}}_\rho + \mathbf{r}' \times \mathbf{f}\right) \mathbf{t} = \left(\mathbf{m}' + \tilde{\mathbf{m}}_\rho\right)_\perp + \mathbf{r}' \times \mathbf{f}_\perp = \mathbf{0}. \tag{2.105}$$

In order to eliminate the shear forces, equation (2.105) is solved for the force component $\mathbf{f}_\perp$, viz.

$$\mathbf{f}_\perp = \frac{\mathbf{r}'}{||\mathbf{r}'||^2} \times \left(\mathbf{m}' + \tilde{\mathbf{m}}_\rho\right)_\perp = \frac{\mathbf{r}'}{||\mathbf{r}'||^2} \times \left(\mathbf{m}' + \tilde{\mathbf{m}}_\rho\right), \tag{2.106}$$

in order to insert this expression into the force equilibrium equations (first line of (2.49)). Together with equation (2.104), the following set of four differential equations can be formulated:

$$\begin{aligned} \mathbf{g}_1^T\left(\mathbf{m}' + \tilde{\mathbf{m}}_\rho\right) &= 0, \\ \mathbf{f}_\parallel' + \left[\frac{\mathbf{r}'}{||\mathbf{r}'||^2} \times \left(\mathbf{m}' + \tilde{\mathbf{m}}_\rho\right)\right]' + \tilde{\mathbf{f}}_\rho &= \mathbf{0}. \end{aligned} \tag{2.107}$$

The set (2.107) is sufficient in order to solve for the four primary variables $\mathbf{r}$ and φ as soon as the stress resultants $\mathbf{f}_\parallel$ and $\mathbf{m}$ are expressed by kinematic and constitutive relations from Section 2.3.2. Multiplying (2.107) with the admissible translational and rotational variations $\delta\mathbf{r}$ and $\delta\Theta_1$ and integrating along the beam gives the equivalent form of the equilibrium equations:

$$\int_0^l \left[\delta\mathbf{r}^T\left(\mathbf{f}_\parallel' + \left[\frac{\mathbf{r}'}{||\mathbf{r}'||^2} \times \left(\mathbf{m}' + \tilde{\mathbf{m}}_\rho\right)\right]' + \tilde{\mathbf{f}}_\rho\right) + \delta\Theta_1 \mathbf{g}_1^T\left(\mathbf{m}' + \tilde{\mathbf{m}}_\rho\right)\right] ds = 0. \tag{2.108}$$

A first integration by parts of the weighted residual (2.108) leads to the intermediate result:

$$\begin{aligned} &\int_0^l \left[\delta\mathbf{r}'^T\left(\mathbf{f}_\parallel + \frac{\mathbf{r}'}{||\mathbf{r}'||^2} \times \mathbf{m}'\right) + (\delta\Theta_1\mathbf{g}_1)'^T\mathbf{m} - \delta\mathbf{r}^T\tilde{\mathbf{f}}_\rho - \delta\Theta_1\mathbf{g}_1^T\tilde{\mathbf{m}}_\rho + \delta\mathbf{r}'^T\left(\frac{\mathbf{r}'}{||\mathbf{r}'||^2} \times \tilde{\mathbf{m}}_\rho\right)\right] ds \\ &- \left[\delta\mathbf{r}^T\mathbf{f}_\sigma + \delta\Theta_1\mathbf{g}_1^T\mathbf{m}_\sigma\right]_{\Gamma_\sigma} = 0. \end{aligned} \tag{2.109}$$

The boundary force $\mathbf{f}_\sigma$ has been derived by using (2.106). A second integration by parts yields

$$G = \int_0^l \Big[\underbrace{\delta\boldsymbol{\theta}'^T\mathbf{m}}_{\delta_o\boldsymbol{\omega}^T\mathbf{m}} + \underbrace{\delta\mathbf{r}'^T\mathbf{g}_1 F_1}_{\delta\epsilon F_1} - \delta\mathbf{r}^T\tilde{\mathbf{f}}_\rho - \delta\boldsymbol{\theta}^T\tilde{\mathbf{m}}_\rho\Big] ds - \Big[\delta\mathbf{r}^T\mathbf{f}_\sigma + \delta\boldsymbol{\theta}^T\mathbf{m}_\sigma\Big]_{\Gamma_\sigma} \doteq 0, \;\; \delta\boldsymbol{\theta} = \delta\Theta_1\mathbf{g}_1 + \frac{\mathbf{r}' \times \delta\mathbf{r}'}{||\mathbf{r}'||^2}. \tag{2.110}$$

In (2.110), the constrained spatial spin vector according to (2.91) has been identified and already substituted with the symbol $\delta\boldsymbol{\theta}$. As indicated by the curly brackets in (2.110), the pre-factors of the stress resultants $\mathbf{m}$ and F_1 are represented by the objective variations $\delta_o\boldsymbol{\omega}$ and $\delta\epsilon$ according to (2.96) and (2.98), underlining the geometrical exactness of the proposed Kirchhoff beam formulation. One can verify that the same result (2.110) would be obtained by simply inserting the constrained rotation vector variation of (2.91) into the weak form (2.52) of the Reissner beam. Thus, by restricting the arbitrary rotation vector variations to the admissible variations, which are kinematically consistent with the Kirchhoff constraint, the work contribution of the shear forces vanish, i.e. the shear force components are eliminated from the weak form. Finally, the problem setup has to be completed by proper boundary and initial conditions:

$$\begin{aligned} &\mathbf{r} = \mathbf{r}_u,\ \mathbf{g}_1 = \mathbf{g}_{1u},\ \varphi = \varphi_u \text{ on } \Gamma_u,\ \mathbf{f} = \mathbf{f}_\sigma,\ \mathbf{m} = \mathbf{m}_\sigma \text{ on } \Gamma_\sigma,\ \Gamma_\sigma \cap \Gamma_u = \varnothing,\ \Gamma_\sigma \cup \Gamma_u = \{0, l\} \\ &\mathbf{r} = \mathbf{r}_0,\ \dot{\mathbf{r}} = \mathbf{v}_0,\ \varphi = \varphi_0, \mathbf{w} = \mathbf{w}_0 \text{ at } t = 0. \end{aligned} \tag{2.111}$$

Here $\mathbf{g}_{1u}$ prescribes the orientation of the tangent vector and φ_u the orientation of the cross-section with respect to a rotation around the tangent vector. How these conditions can be modeled

Weak Form:

$$\int_0^l \Big[\delta\boldsymbol{\theta}'^T\mathbf{m}+\delta\epsilon F_1-\delta\mathbf{r}'^T\tilde{\mathbf{f}}_\rho-\delta\boldsymbol{\theta}^T\tilde{\mathbf{m}}_\rho\Big]\,ds-\Big[\delta\mathbf{r}^T\mathbf{f}_\sigma+\delta\boldsymbol{\theta}^T\mathbf{m}_\sigma\Big]_{\Gamma_\sigma}=0,\ \delta\boldsymbol{\theta}=\delta\theta_1\mathbf{g}_1+\frac{\mathbf{S}(\mathbf{r}')\delta\mathbf{r}'}{||\mathbf{r}'||^2},\ \delta\epsilon=\mathbf{r}'^T\mathbf{g}_1$$

Constitutive law:

$$\mathbf{m}=\mathbf{diag}\big[GI_T,EI_2,EI_3\big]_{\mathbf{g}_i}\cdot\boldsymbol{\omega},\quad F_1=EA\epsilon$$

Kinematic equations:

$$\boldsymbol{\omega}=\Big(K_{M1}+\varphi'-K_{M01}-\varphi_0',\ \mathbf{g}_2^T\boldsymbol{\kappa}-\mathbf{g}_{02}^T\boldsymbol{\kappa}_0,\ \mathbf{g}_3^T\boldsymbol{\kappa}-\mathbf{g}_{03}^T\boldsymbol{\kappa}_0\Big)^T_{\mathbf{g}_i},\ \ \epsilon=||\mathbf{r}'||-1,$$

$$\boldsymbol{\kappa}=\frac{\mathbf{S}(\mathbf{r}')\mathbf{r}''}{||\mathbf{r}'||^2},\ \ K_{M1}:=\mathbf{g}_{M3}^T\mathbf{g}_{M2}',$$

$$\mathbf{g}_1=\frac{\mathbf{r}'}{||\mathbf{r}'||},\ \ \mathbf{g_2}=\mathbf{g}_{M2}\cos\varphi+\mathbf{g}_{M3}\sin\varphi,\ \ \mathbf{g_3}=\mathbf{g}_{M3}\cos\varphi-\mathbf{g}_{M2}\sin\varphi$$

Inertia terms and external loads:

$$\tilde{\mathbf{f}}_\rho=\tilde{\mathbf{f}}+\mathbf{f}_\rho,\ \ \tilde{\mathbf{m}}_\rho=\tilde{\mathbf{m}}+\mathbf{m}_\rho,\ \ \mathbf{f}_\rho=-\rho A\ddot{\mathbf{r}},\ \ \mathbf{m}_\rho=-[\mathbf{S}(\mathbf{w})\mathbf{c}_\rho\mathbf{w}+\mathbf{c}_\rho\mathbf{a}]$$

Initial and boundary conditions:

$$\mathbf{r}=\mathbf{r}_u,\ \mathbf{g}_1=\mathbf{g}_{1u},\ \varphi=\varphi_u\ \text{on}\ \Gamma_u,\ \mathbf{f}=\mathbf{f}_\sigma,\ \mathbf{m}=\mathbf{m}_\sigma\ \text{on}\ \Gamma_\sigma,\ \ \Gamma_\sigma\cap\Gamma_u=\varnothing,\ \Gamma_\sigma\cup\Gamma_u=\{0,l\}$$
$$\mathbf{r}=\mathbf{r}_0,\ \dot{\mathbf{r}}=\mathbf{v}_0,\ \varphi=\varphi_0,\mathbf{w}=\mathbf{w}_0\ \text{at}\ t=0.$$

Table 2.1: Kirchhoff beam problem based on intermediate triads $\mathbf{g}_{M2}(\mathbf{r})$ and $\mathbf{g}_{M3}(\mathbf{r})$.

in practice is shown in Chapter 3. By introducing the trial space $(\mathbf{r},\boldsymbol{\Lambda}(\mathbf{r},\varphi))\in\mathcal{U}$ satisfying (2.111) and the weighting space $(\delta\mathbf{r},\delta\boldsymbol{\theta}(\delta\mathbf{r},\delta\Theta_1,\mathbf{r}))\in\mathcal{V}$, with $\delta\mathbf{r}=\mathbf{0},\ \delta\Theta_1=0$ on Γ_u, the beam problem is fully defined. For completeness, the spatial setting of the problem is summarized in Table 2.1. It should be emphasized that only the concrete analytic expressions for $\mathbf{g}_{M2}(\mathbf{r}(s))$ and $\mathbf{g}_{M3}(\mathbf{r}(s))$ depend on the specific choice of the intermediate triad definition.

Remark: According to (2.110), the spin vector $\delta\boldsymbol{\theta}$ represents the work-conjugated kinematic quantity associated with the vector of external moments. In order to impose the Kirchhoff constraint on the spin vector, it has been expressed by means of the four primary variables $(\mathbf{r},\varphi)$ and the admissible variations $(\delta\mathbf{r},\delta\Theta_1)$ (see (2.91)). Similar to the spin vector itself, also external moments can be split up into components parallel and perpendicular to the tangent vector according to $\mathbf{m}_\sigma=M_{\sigma1}\mathbf{g}_1+\mathbf{m}_{\sigma\perp}$. Thus, by multiplying the external moment $\mathbf{m}_\sigma$ with the constrained spin vector $\delta\boldsymbol{\theta}$ according to (2.91), the external moment is projected into the variational equations related to $\delta\Theta_1$ (the component $M_{\sigma1}$ parallel to the tangent induces twist modes) and into the variational equations related to $\delta\mathbf{r}'$ (the component $\mathbf{m}_{\sigma\perp}$ perpendicular to the tangent induces bending modes).

This projection is deformation-dependent and has to be considered in a consistent linearization. Due to the one-to-one mapping between the spin vector $\delta\boldsymbol{\theta}$, as used for Reissner beams, and the primary variables $\mathbf{r}, \varphi, \delta\mathbf{r}, \delta\Theta_1$ (see (2.34)) considered here, the external moment has the same physical meaning as for geometrically exact Reissner elements.

2.3.4 Intermediate triad based on the Frenet-Serret frame

While the construction of an intermediate triad field $\mathbf{g}_{Mi}(s)$ applicable for the proposed finite element formulations is presented in Section 3.2.3.4, in this section, an intermediate triad field is considered that is ideally suited for analytic purposes: The Frenet-Serret frame. The Frenet-Serret frame seems to be a natural choice in order to describe mechanical curvature measures of beams, since the Frenet-Serret frame itself is defined via the curvature of the space curve $\mathbf{r}(s)$. In particular, the normal vector $\mathbf{n}_{FS}(s)$ of the Frenet-Serret frame points towards the center of curvature of $\mathbf{r}(s)$ at position s. For two given vectors $\mathbf{g}_1(s) = \mathbf{r}'(s)/||\mathbf{r}'(s)||$ and $\mathbf{n}_{FS}(s)$, the binormal vector $\mathbf{b}_{FS}(s)$ completes the right-handed orthonormal triad at position s:

$$\mathbf{n}_{FS} := \frac{\mathbf{g}_1'}{||\mathbf{g}_1'||} \quad \text{and} \quad \mathbf{b}_{FS} := \mathbf{g}_1 \times \mathbf{n}_{FS} \quad \text{with} \quad \mathbf{g}_1 = \frac{\mathbf{r}'}{||\mathbf{r}'||}. \tag{2.112}$$

From these definitions, the following expressions for the intermediate triad $\mathbf{g}_{Mi}$ can be derived:

$$\mathbf{g}_{M2} = \mathbf{n}_{FS} = \frac{||\mathbf{r}'||}{||\mathbf{r}' \times \mathbf{r}''||}\left(\mathbf{r}'' - ||\mathbf{r}'||^2(\mathbf{r}'^T\mathbf{r}'')\mathbf{r}'\right) \quad \text{and} \quad \mathbf{g}_{M3} = \mathbf{b}_{FS} = \frac{\mathbf{r}' \times \mathbf{r}''}{||\mathbf{r}' \times \mathbf{r}''||}. \tag{2.113}$$

From (2.113), it becomes obvious that the binormal vector $\mathbf{b}_{FS}$ is parallel to the curvature vector

$$\boldsymbol{\kappa} = \kappa \mathbf{b}_{FS} = \kappa \mathbf{g}_{M3}, \tag{2.114}$$

with $\kappa = ||\boldsymbol{\kappa}||$. Using this relation, the deformation measures $\boldsymbol{\omega}$ and $\boldsymbol{\Omega}$ simplify slightly due to

$$\mathbf{g}_2^T\boldsymbol{\kappa} = \kappa \sin\varphi \quad \text{and} \quad \mathbf{g}_3^T\boldsymbol{\kappa} = \kappa\cos\varphi. \tag{2.115}$$

After calculating the derivative $\mathbf{g}_{M2}'$, the torsion $K_{M1} = \mathbf{g}_{M3}^T\mathbf{g}_{M2}'$ of this intermediate triad yields:

$$K_{M1} = \tau := \frac{\mathbf{r}'^T(\mathbf{r}'' \times \mathbf{r}''')\,||\mathbf{r}'||}{||\mathbf{r}' \times \mathbf{r}''||^2}. \tag{2.116}$$

Remark: The definitions of κ and τ applied here differ from the common definitions of the curvature $\bar{\kappa}$ and torsion $\bar{\tau}$ of parametrized curves by a factor of $||\mathbf{r}'|| = \epsilon + 1$. This is due to the fact that the mathematical curvature and torsion are defined as angle increments per arc-length increment of the considered curve. However, as consequence of axial tension, the centerline parameter s considered here is an arc-length parameter of the initial but not of the current centerline curve. The relation between an arbitrary parameter s and an arc-length parameter $\tilde{s}$ of parametrized curves is given by $d\tilde{s} = ||\mathbf{r}'||ds$. Using the common definitions of $\bar{\kappa}$ and $\bar{\tau}$ yields the following relations:

$$\bar{\kappa} := \left|\left|\frac{d\mathbf{g}_1}{d\tilde{s}}\right|\right| = \left|\left|\frac{d\mathbf{g}_1}{ds}\right|\right|\frac{ds}{d\tilde{s}} = \frac{\kappa}{||\mathbf{r}'||}, \quad \bar{\tau} := \left|\left|\frac{d\mathbf{b}_{FS}}{d\tilde{s}}\right|\right| = \left|\left|\frac{d\mathbf{b}_{FS}}{ds}\right|\right|\frac{ds}{d\tilde{s}} = \frac{\tau}{||\mathbf{r}'||}.$$

If axial tension is neglected ($||\mathbf{r}'|| \equiv 1$), both curvature and torsion measures are identical.

With (2.113) and (2.116), the problem description in Table 2.1 is completed. In the following, it will be shown that the Frenet-Serret intermediate frame can serve as an extremely useful tool for the analytic treatment of large-deformation Kirchhoff beam problems. However, from a numerical point of view, it has one considerable drawback, which makes it unfeasible for robust algorithms: From (2.113) it becomes obvious that these base vectors are not defined for straight curves, or more precisely, for curve segments with vanishing curvature, i.e. $\mathbf{r}'' = \mathbf{0}$. Furthermore, since the third derivative of the primary variable $\mathbf{r}$ appears in (2.116), at least a C^2-continuous discretization of $\mathbf{r}$ would be desirable when considering the weak form of Table 2.1 based on the Frenet-Serret intermediate triad. To overcome these drawbacks, alternative intermediate frames based on the "Smallest Rotation" mapping (Section 2.1.2) will be employed in Chapter 3.

Due to its natural curvature adaption, the Frenet-Serret frame seems to be an ideal tool for the analytic investigation of Kirchhoff beam problems. Later, this tool will be used in order to derive analytic reference solutions for numerical examples. For that purpose, the strong form of the balance equations (2.107), based on a Frenet-Serret intermediate triad field, will be considered. In the following, the components of this vector-valued strong form shall be formulated with respect to the Frenet-Serret frame. Thus, the moment stress resultant, the external force vector and the external moment vector have to be split into corresponding components:

$$\boldsymbol{m} =: m_{g_1}\mathbf{g}_1 + m_n\mathbf{n} + m_b\mathbf{b}, \quad \tilde{\boldsymbol{m}}_\rho =: \tilde{m}_{\rho g_1}\mathbf{g}_1 + \tilde{m}_{\rho n}\mathbf{n} + \tilde{m}_{\rho b}\mathbf{b}, \quad \tilde{\boldsymbol{f}}_\rho =: \tilde{f}_{\rho g_1}\mathbf{g}_1 + \tilde{f}_{\rho n}\mathbf{n} + \tilde{f}_{\rho b}\mathbf{b}. \tag{2.117}$$

Projecting the vector-valued equation of (2.107) into the directions $\mathbf{g}_1, \mathbf{n}$ and $\mathbf{b}$ and using the scalar equation of (2.107) directly yields the following set of four differential equations:

$$\begin{aligned}
f'_{g_1} + \frac{\kappa}{1+\epsilon}\left(\tau m_n + m'_b + \tilde{m}_{\rho b}\right) + \tilde{f}_{\rho g_1} &= 0, \\
-\left(\frac{\tau m_n + m'_b + \tilde{m}_{\rho b}}{1+\epsilon}\right)' - \frac{\tau}{1+\epsilon}\left(\kappa m_{g_1} + m'_n - \tau m_b + \tilde{m}_{\rho n}\right) + \kappa f_{g_1} + \tilde{f}_{\rho n} &= 0, \\
\left(\frac{-\tau m_b + m'_n + \kappa m_{g_1} + \tilde{m}_{\rho n}}{1+\epsilon}\right)' - \frac{\tau}{1+\epsilon}\left(\tau m_n + m'_b + \tilde{m}_{\rho b}\right) + \tilde{f}_{\rho b} &= 0, \\
m'_{g_1} - \kappa m_n + \tilde{m}_{\rho g_1} &= 0.
\end{aligned} \tag{2.118}$$

Furthermore, the following components of the stress resultants $f_{g_1}, m_{g_1}, m_n, m_b$ can be derived:

$$\begin{aligned}
f_{g_1} &= F_1 = EA\epsilon, \\
m_{g_1} &= GI_T\left(\tau + \varphi' - \tau_0 + \varphi'_0\right), \\
m_n &= EI_2\left(\kappa\sin\varphi - \kappa_0\sin\varphi_0\right)\cos\varphi - EI_3\left(\kappa\cos\varphi - \kappa_0\cos\varphi_0\right)\sin\varphi, \\
m_b &= EI_2\left(\kappa\sin\varphi - \kappa_0\sin\varphi_0\right)\sin\varphi + EI_3\left(\kappa\cos\varphi - \kappa_0\cos\varphi_0\right)\cos\varphi.
\end{aligned} \tag{2.119}$$

In the case of quasi-circular cross-sections, i.e. $EI_2 = EI_3 =: EI$, the initial material frame $\mathbf{g}_{0i}$ can be chosen as coinciding with the initial intermediate frame $\mathbf{g}_{M0i}$, thus $\varphi_0 \equiv 0$, which simplifies the bending moment components to $m_n = EI\kappa_0\sin\varphi$ and $m_b = EI\left(\kappa - \kappa_0\cos\varphi\right)$. Equations (2.119) inserted into equations (2.118) give a system of four differential equations, which determine the four unknowns ϵ, κ, τ and φ. With the definitions of ϵ, κ and τ as well as appropriate boundary conditions, the curve $\mathbf{r}$ can be determined afterwards. Analytical formulations comparable to (2.118) and (2.119) that can be found in the literature are mostly based on

the assumption of inextensible beam centerlines $\epsilon \equiv 0$ and / or quasi-circular cross-section shapes characterized by $EI_2 = EI_3 =: EI$. Under these circumstances, equations (2.118) and (2.119) coincide for example with the results derived by Drozdov et al. [65] for this specific case.

2.3.5 Weak enforcement of Kirchhoff constraint

In the last sections, the set of primary variable fields $(\mathbf{r}(s), \varphi(s))$ has been chosen in a way such that the Kirchhoff constraint (2.86) of vanishing shear strains is strongly fulfilled by construction. However, more flexibility in the subsequent discretization process (see Chapter 3) could be gained by formulating a Reissner type beam problem, which allows for two independent interpolations for the centerline field $\mathbf{r}(s)$ as well as the triad field $\mathbf{\Lambda}(s)$, and by weakly enforcing the Kirchhoff constraint of vanishing shear strains by means of additional constraint equations:

$$\Gamma_j(s) \equiv \mathbf{g}_j^T(s)\mathbf{r}'(s) \equiv 0 \quad \text{for} \quad j=2,3. \tag{2.120}$$

In order to integrate these constraint equations into the considered variational framework, the latter has to be supplemented by an additional Lagrange multiplier potential of the form:

$$\Pi_{\lambda_{\Gamma 23}} = \int_0^l (\lambda_{\Gamma 2}(s)\Gamma_2(s) + \lambda_{\Gamma 3}(s)\Gamma_3(s))ds. \tag{2.121}$$

The Lagrange multiplier fields $\lambda_{\Gamma 2}(s)$ and $\lambda_{\Gamma 3}(s)$ introduced in (2.121) can be interpreted as the shear force components $F_2(s)$ and $F_3(s)$, i.e. reaction forces which enforce the constraint of vanishing shear strains along the beam centerline. Variation of the Lagrange multiplier potential (2.121) leads to the contribution of the Kirchhoff constraint to the weak form:

$$\delta\Pi_{\lambda_{\Gamma 23}} = \int_0^l (\delta\lambda_{\Gamma 2}(s)\Gamma_2(s)+\delta\lambda_{\Gamma 3}(s)\Gamma_3(s))ds + \int_0^l (\lambda_{\Gamma 2}(s)\delta\Gamma_2(s)+\lambda_{\Gamma 3}(s)\delta\Gamma_3(s))ds. \tag{2.122}$$

The first term in (2.122) represents the weak statement of the Kirchhoff constraint (2.120) while the second term can be interpreted as the work contribution of the shear reaction forces. Similar to the displacement primary fields, a proper trial space $(\lambda_{\Gamma 2}, \lambda_{\Gamma 3}) \in \mathcal{U}_{\lambda_{\Gamma 23}}$ and a proper weighting space $(\delta\lambda_{\Gamma 2}, \delta\lambda_{\Gamma 3}) \in \mathcal{V}_{\lambda_{\Gamma 23}}$ have to be introduced which uniquely define the resulting mixed beam formulation. The discrete realization of the finite element formulation with weak enforcement of the Kirchhoff constraint will be presented in Section 3.5.

2.3.6 Kirchhoff theory of inextensible beams

As it will be further concretized in Section 3.3.4, the numerical advantages for subsequently derived finite element formulations (see Chapter 3) resulting from a neglect of shear deformation can be further increased by additionally abstaining from the axial tension terms, a deformation mode which is often of secondary interest in the range of high slenderness ratios. A neglect of axial tension means that the beam is subject to the following inextensibility constraint:

$$\epsilon(s) \equiv ||\mathbf{r}'(s)|| - 1 \equiv 0. \tag{2.123}$$

The Kirchhoff type beam formulation presented in the last sections was based on a set of primary variable fields that fulfilled the Kirchhoff constraint of vanishing shear strains by construction and without the need for additional constraint equations. In Section 3.6, it will be shown that in general it is difficult to find a set of primary variables that fulfills the constraint $\epsilon(s)$ of an inextensible beam centerline by construction. Therefore, in the following, it will be briefly described how the inextensibility constraint can be integrated into the considered variational problem in a weak sense. Similar to Section 2.3.5, the total potential associated with the Kirchhoff beam problem has to be extended by a corresponding Lagrange multiplier potential of the form:

$$\Pi_{\lambda_\epsilon} = \int_0^l \lambda_\epsilon(s)\epsilon(s)ds. \tag{2.124}$$

In this case, the Lagrange multiplier field $\lambda_\epsilon(s)$ represents the field of axial forces along the beam, which are now of reaction force type. Variation of (2.124) leads to the contribution of constraint (2.123) to the weak form of the Kirchhoff beam equilibrium equations:

$$\delta\Pi_{\lambda_\epsilon} = \int_0^l \delta\lambda_\epsilon(s)\epsilon(s)ds + \int_0^l \delta\epsilon(s)\lambda_\epsilon(s)ds. \tag{2.125}$$

The first term in (2.125) represents the weak statement of the inextensibility constraint (2.123) while the second term can be interpreted as the work contribution of the axial reaction forces. Since (2.125) enforces vanishing axial strains along the beam, the contribution of the axial strains to the weak form will not influence the final equilibrium configurations and can be neglected. However, in Section 3.6, it is shown that a consideration of these contributions leads to a more good-natured numerical problem resulting from spatial discretization. Thus, if both terms are considered simultaneously, the corresponding axial force contribution to the weak form reads:

$$\delta\Pi_{\lambda_\epsilon} = \int_0^l \delta\lambda_\epsilon(s)\epsilon(s)ds + \int_0^l \delta\epsilon(s)(\lambda_\epsilon(s) + EA\epsilon(s))ds. \tag{2.126}$$

As it will be illustrated in Section 3.3.4, a direct application of (2.126) would lead to the same undesirable stiffness terms EA as the extensible Kirchhoff formulation. Thus, the axial tension term, which does not influence the final solution, is scaled by an arbitrary constant factor c_ϵ:

$$\delta\Pi_{\lambda_\epsilon} = \int_0^l \delta\lambda_\epsilon(s)\epsilon(s)ds + \int_0^l \delta\epsilon(s)(\lambda_\epsilon(s) + c_\epsilon EA\epsilon(s))ds. \tag{2.127}$$

The factor c_ϵ can be chosen arbitrarily such that for example the performance of linear and nonlinear solvers is optimized without changing the final solution as compared to the pure Lagrange multiplier case. Thus, in the terminology of constraint enforcement, the regularized constraint equation (2.127) achieved by additionally considering the (scaled) axial tension terms can be interpreted as an Augmented Lagrange type scheme. The resulting mixed problem statement is completed as soon as a proper trial space $\lambda_\epsilon \in \mathcal{U}_{\lambda_\epsilon}$ and a proper weighting space $\delta\lambda_\epsilon \in \mathcal{V}_{\lambda_\epsilon}$ is defined. The discrete realization of the inextensibility constraint will be presented in Section 3.6.

2.4 Reduced Kirchhoff-Love Beam Theories

The Kirchhoff beam theory considered in Section 2.3 has been formulated as general as possible and accounts for beams with anisotropic cross-section shape and arbitrary initial curvatures in general 3D large deformation scenarios. In the following, some special cases concerning the beam geometry and the external loads are presented, which enable the application of simplified versions (denoted as reduced models) of the general theory presented in the last section. The motivation for the development of such reduced formulations is twofold: On the one hand, the numerical effort as well as the complexity of the formulation can be reduced drastically. As will be shown in the following, for none of these reduced models any intermediate or material triad has to be calculated. Consequently, the treatment of large rotations is not required anymore. On the other hand, the special cases presented below are of high practical relevance.

2.4.1 Isotropic Kirchhoff-Love beam theory

In this first subsection, the case of beams with quasi-circular cross-sections and vanishing initial curvature within a three-dimensional problem setting, in the following denoted as "isotropic bending"-case, will be treated. It is characterized by the following geometric specifications:

$$I_2 = I_3 =: I, \quad I_T = I_P = 2I \quad \text{and} \qquad \kappa_0 \equiv 0. \tag{2.128}$$

Based on (2.128), the moment stress resultants can be simplified. In the "isotropic bending"-case, the initial configuration of the beam is rotationally symmetric with respect to the centerline. Since any axis lying in the cross-section can be identified as principal axis of inertia, the initial triad $\mathbf{g}_{0i}(s)$ can be chosen arbitrarily. For simplicity, it will be chosen as constant field given by $\mathbf{g}_{0i}(s) \equiv \mathbf{g}_{0i} = \text{const.}$, which implies a vanishing initial torsion $K_{01} = K_{M01} + \varphi_0' \equiv 0$. Furthermore, the initial intermediate triad $\mathbf{g}_{M0i}$ is chosen to coincide with the initial material triad $\mathbf{g}_{0i}$. Under these circumstances, the following relations for the initial torsion and relative angle are valid:

$$K_{01} \equiv 0, \quad \varphi_0 \equiv 0. \tag{2.129}$$

Inserting (2.129) and (2.128) into (2.95) also yields simplified moment stress resultants:

$$\mathbf{m} = 2GI\big(\underbrace{K_{M1} + \varphi'}_{=K_1}\big)\mathbf{g}_1 + EI\boldsymbol{\kappa}. \tag{2.130}$$

Since the relative angle φ does not appear in the bending moment components anymore, the total torsion $K_1 = K_{M1} + \varphi'$, can be chosen as new primary variable instead of φ. For that reason, the quantity K_{M1} is not required and the resulting deformation measures do not depend on any intermediate triad anymore. Due to (2.128), also the inertia moments can be simplified:

$$-\mathbf{m}_\rho = \dot{\tilde{\mathbf{h}}} = \frac{d}{dt}\big(2\rho I W_1 \mathbf{g}_1 + \rho I \mathbf{w}_\perp\big) = \rho I\big(2\dot{W}_1\mathbf{g}_1 + 2W_1\dot{\mathbf{g}}_1 + \dot{\mathbf{w}}_\perp\big). \tag{2.131}$$

Inserting (2.131) into $\mathbf{g}_1^T\tilde{\mathbf{m}}_\rho = \mathbf{g}_1^T(\tilde{\mathbf{m}}+\mathbf{m}_\rho) = \tilde{M}_1 - 2\rho I\dot{W}_1$ and the result together with the intermediate result $\mathbf{g}_1^T\mathbf{m}' = 2GIK_1'$ into the strong form of the balance equations (2.107) yields:

$$\begin{aligned} 0 &= 2GIK_1' + \tilde{M}_1 - 2\rho I\dot{W}_1, \\ \mathbf{0} &= \mathbf{f}_\parallel' + \left[\frac{\mathbf{r}'}{||\mathbf{r}'||^2}\times\left(\mathbf{m}'+\tilde{\mathbf{m}}-\rho I\left(2W_1\dot{\mathbf{g}}_1+\underbrace{\dot{\mathbf{w}}_\perp}_{\approx 0}\right)\right)\right]' + \tilde{\mathbf{f}}_\rho, \\ &\text{with } \mathbf{m} = 2GIK_1\mathbf{g}_1 + EI\boldsymbol{\kappa},\ \ \mathbf{f}_\parallel = EA\epsilon\mathbf{g}_1,\ \ \tilde{\mathbf{f}}_\rho = \tilde{\mathbf{f}} - \rho A\ddot{\mathbf{r}}. \end{aligned} \tag{2.132}$$

Thus, due to (2.128), the perpendicular component $\rho I\mathbf{w}_\perp$ of the angular momentum $\tilde{\mathbf{h}}$ does only appear in the second (vector-valued) equation of (2.132). In the range of high beam slenderness ratios, these rotational inertia contributions can be assumed as small compared to the inertia forces $\mathbf{f}_\rho$ appearing in the same equation. Consequently, the inertia effects stemming from the perpendicular component of the angular momentum will be neglected (as indicated by the curly brackets in (2.132)) in this section as well as in Section 2.4.2. This assumption is typical for (isotropic) shear-free beam theories and distinguishes e.g. the Euler-Bernoulli from the Rayleigh beam model (see e.g. [36] for an application of both models in the geometrically nonlinear regime). Since the term $2\rho I\dot{W}_1$ represents the only inertia contribution to the first equation of (2.132), a simple cancelation of this term seems not to be justified (see also Section 2.4.2.2). In order to remain variationally consistent, also the term $2\rho I\dot{W}_1\mathbf{g}_1$ in the second equation of (2.132) is kept. Inserting these simplifications into the elastic (2.100) and kinetic (2.62) energy yields:

$$\tilde{\Pi}_{kin} = \frac{\rho A}{2}\dot{\mathbf{r}}^T\dot{\mathbf{r}} + \frac{\rho I_P}{2}W_1^2,\ \ \tilde{\Pi}_{int} = \frac{EA}{2}\epsilon^2 + \frac{EI}{2}\boldsymbol{\kappa}^T\boldsymbol{\kappa} + \frac{GI_T}{2}K_1^2. \tag{2.133}$$

Based on the energies (2.133), the weak form can be derived in a variational manner (see also Appendix A.2). Using the auxiliary relations $\delta K_1 = \delta\Theta_1' + \delta\mathbf{g}_1^T(\mathbf{g}_1\times\mathbf{g}_1') = \delta\Theta_1' + \delta\boldsymbol{\theta}_\perp^T\boldsymbol{\kappa}$ as well as $\delta W_1 = \delta\dot{\Theta}_1 + \delta\mathbf{g}_1^T(\mathbf{g}_1\times\dot{\mathbf{g}}_1) = \delta\dot{\Theta}_1 + \delta\boldsymbol{\theta}_\perp^T\dot{\mathbf{g}}_1$ according to (2.93), the weak form eventually yields:

$$\begin{aligned} G = &\int_0^l \left[\delta\epsilon EA\epsilon + \delta\boldsymbol{\kappa}EI\boldsymbol{\kappa} + \delta\Theta_1' 2GIK_1 + \delta\boldsymbol{\theta}_\perp^T 2GIK_1\boldsymbol{\kappa}\right] ds \\ &- \int_0^l \left[\delta\mathbf{r}^T\tilde{\mathbf{f}}_\rho + \delta\boldsymbol{\theta}_\perp^T(\tilde{\mathbf{m}}_\perp - 2\rho IW_1\dot{\mathbf{g}}_1) + \delta\Theta_1(\tilde{M}_1 - 2\rho I\dot{W}_1)\right] ds - \left[\delta\mathbf{r}^T\mathbf{f}_\sigma + \delta\boldsymbol{\theta}_\perp^T\mathbf{m}_{\sigma\perp} + \delta\Theta_1 M_{\sigma 1}\right]_{\Gamma_\sigma}. \end{aligned} \tag{2.134}$$

In (2.134), the external moments have been split, i.e. $\tilde{\mathbf{m}} = \tilde{M}_1\mathbf{g}_1 + \tilde{\mathbf{m}}_\perp$ and $\mathbf{m}_\sigma = M_{\sigma 1}\mathbf{g}_1 + \mathbf{m}_{\sigma\perp}$, and the spin vector $\delta\boldsymbol{\theta}$ is given according to (2.91). Furthermore, the variations $\delta\epsilon$ and $\delta\boldsymbol{\kappa}$ read:

$$\delta\epsilon = \frac{\delta\mathbf{r}'^T\mathbf{r}'}{||\mathbf{r}'||},\quad \delta\boldsymbol{\kappa} = \frac{||\mathbf{r}'||^2\left(\delta\mathbf{r}'\times\mathbf{r}'' + \mathbf{r}'\times\delta\mathbf{r}''\right) - 2\left(\delta\mathbf{r}'^T\mathbf{r}'\right)\left(\mathbf{r}'\times\mathbf{r}''\right)}{||\mathbf{r}'||^4},\quad \delta\boldsymbol{\theta}_\perp = \frac{\mathbf{r}'\times\delta\mathbf{r}'}{||\mathbf{r}'||^2}. \tag{2.135}$$

In deriving (2.134), use has been made of the relations $\delta_o\dot{\mathbf{r}}^T\dot{\mathbf{r}} = (\delta\dot{\mathbf{r}} - \delta\boldsymbol{\theta}\times\dot{\mathbf{r}})^T\dot{\mathbf{r}} = \delta\dot{\mathbf{r}}^T\dot{\mathbf{r}}$ and $\delta_o\boldsymbol{\kappa}^T\boldsymbol{\kappa} = (\delta\boldsymbol{\kappa} - \delta\boldsymbol{\theta}\times\boldsymbol{\kappa})^T\boldsymbol{\kappa} = \delta\boldsymbol{\kappa}^T\boldsymbol{\kappa}$ for the spatial vectors $\dot{\mathbf{r}}$ and $\boldsymbol{\kappa}$. Alternatively, the weak form can be derived by inserting the simplifications of this section into the weak form (2.110). This procedure is shown in Appendix A.3 (see equation (A.8)). It is easy to verify that (2.134) and (A.8) are

identical. According to (2.93), the angular velocity component W_1 cannot directly be expressed via the primary variable K_1, in particular $W_1' \neq \dot{K}_1$. In order to formulate W_1 and $\dot{W}_1$, one could for example employ (Lie-group) time integrators based on multiplicative rotation increments $\Delta\boldsymbol{\theta}$ as shown in Section 3.1.2 (see also [209]). However, this would (at least formally) require to determine material triads and associated rotation increments in every time step. Since such a procedure would almost negate the advantages of the isotropic theory as compared to the general Kirchhoff theory presented in Section 2.3, the former will solely be applied to static problems within this thesis. In this case, (2.134) is uniquely defined by the primary variables $(\mathbf{r}, K_1)$ and the variations $(\delta\mathbf{r}, \delta\Theta_1)$. Nevertheless, the dynamic isotropic case of this section will serve as an important intermediate step for the derivation of a torsion-free beam theory in the next section.

In the static case, the isotropic theory according to (2.134) *does not require any treatment of large rotations, in particular, no material or intermediate triads have to be determined*. Furthermore, it is emphasized that in the mentioned static case, the fields K_1, representing the torsional deformation, and $\mathbf{r}(s)$, representing the bending deformation, are only coupled by one term, namely $\delta\boldsymbol{\theta}_\perp^T 2GIK_1\boldsymbol{\kappa}$, which vanishes in the straight configuration. The static weak form (2.134) is identical to the weak form proposed in [36] for straight Kirchhoff beams with circular cross-sections. Thus, the beam element presented in [36] can be considered as special case that can be derived in a consistent manner from the general formulation given in Table 2.1.

2.4.2 Torsion-free Kirchhoff-Love beam theory

In a further step, the isotropic bending theory of Section 2.4.1 will be supplemented by the assumption that no torsional components of external moments are acting on the beam, viz.

$$\mathbf{g}_1(s,t)\cdot\tilde{\mathbf{m}}(s,t) = \tilde{M}_1(s,t) \equiv 0 \quad \text{and} \quad \Big[\mathbf{g}_1(t)\cdot\mathbf{m}_\sigma(t)\Big]_{\Gamma_\sigma} = \Big[M_{\sigma 1}(t)\Big]_{\Gamma_\sigma} = 0. \tag{2.136}$$

Furthermore, for dynamic problems it is assumed that the torsion K_1 as well as the tangential component W_1 of the angular velocity vector are zero in the initial configuration:

$$K_1(s, t=0) \equiv 0 \quad \text{and} \quad W_1(s, t=0) \equiv 0. \tag{2.137}$$

There are many fields of application where such restrictions are valid. As examples, the Brownian dynamics of filaments in biopolymer networks (see e.g. [61]), cables of high voltage lines (see e.g. [9]), fibers in biologial tisue or the fibers in industrial webbings or ropes (see e.g. [69]) can be mentioned. In Section 2.4.2.2, it will be proven that in (quasi-) static problems involving slender continua modeled by means of the general Kirchhoff beam theory of Section 2.3 the mechanical torsion K_1 will always exactly vanish as consequence of the restrictions (2.136) and (2.137) together with (2.128). This result remains valid for arbitrarily deformed beam centerlines and is independent from the resulting magnitude of displacements and rotations. Furthermore, it is shown that even in dynamics, at least for problems that are dominated by a low frequency response, the torsion K_1 (and also the angular velocity W_1) will be small with a magnitude decreasing quadratically with the beam slenderness ratio. In both cases, the torsion-free beam formulation presented in the next section can be applied. In the following, the term "torsion-free" is equivalent to "vanishing torsional moments" and simultaneously to "vanishing torsional deformation". This is in strong contrast to the notion "shear-free", which means

negligible shear deformation but non-vanishing shear forces. In the next section, the strong and weak form of the balance equations of such a torsion-free beam theory will be presented. In Section 2.4.2.2, the applicability of this theory to slender continua that can be modeled via the general Kirchhoff theory of Section 2.3 will be justified by showing that restrictions (2.136), (2.137) and (2.128) lead to a state of vanishing torsion in statics and to small torsion values in dynamics.

Remark: Alternatively, the torsion-free theory presented in the next section can of course also be applied to slender bodies without torsional stiffness $GI_T \approx 0$, i.e. slender "quasi-continua" which cannot produce torsional moments as consequence of their constitutive law. Examples are braided ropes with finite bending stiffness but negligible torsional resistance, filament species in bio-polymer networks (see e.g. [61], Section 4.2.) or chains. According to [191], the term "quasi-continua" is used for mechanical objects that are composed of a large number of primitive components (e.g. the links of a chain, or the individual monomers of a polymer macromolecule). The mechanical behavior of such objects can often be approximated by continuum theories with properly chosen constitutive constants, even though these objects are not continua in the classical sense. While for general slender continua with torsional stiffness the requirement (2.136) of vanishing external torsional moments has to be satisfied by the set of external loads in order to end up with a state of vanishing torsion, in the case of slender "quasi-continua" without torsional resistance, the deformed configurations will "automatically" arise in a way such that external moment loads will have no torsional component and obey the relations (2.136).

2.4.2.1 Strong and weak form of torsion-free beam theory

It is quite obvious that the first equation of (2.132) vanishes if the torsion-free beam theory according to $K_1 = W_1 = \dot{W}_1 = 0$ is applied, while the second set of equations simplifies to:

$$\mathbf{f}_{\parallel}' + \left[\frac{\mathbf{r}'}{||\mathbf{r}'||^2} \times (\mathbf{m}' + \tilde{\mathbf{m}}_{\perp}) \right]' + \tilde{\mathbf{f}} + \mathbf{f}_{\rho} = \mathbf{0} \;\text{ with }\; \mathbf{m} = EI\boldsymbol{\kappa},\;\; \mathbf{f}_{\parallel} = EA\epsilon\mathbf{g}_1,\;\; \mathbf{f}_{\rho} = -\rho A\ddot{\boldsymbol{r}}. \quad (2.138)$$

The weak form of a torsion-free beam theory as introduced in the last section results from (2.133) and (2.134) by setting $K_1 = W_1 = \dot{W}_1 = 0$ and removing the terms associated with $\delta\Theta_1$.

$$G = \int_0^l \left[\delta\epsilon EA\epsilon + \delta\boldsymbol{\kappa} EI\boldsymbol{\kappa} + \delta\mathbf{r}^T \rho A\ddot{\boldsymbol{r}} \right] ds - \int_0^l \left[\delta\mathbf{r}^T \tilde{\mathbf{f}} + \delta\boldsymbol{\theta}_{\perp}^{\boldsymbol{T}} \tilde{\mathbf{m}}_{\perp} \right] ds - \left[\delta\mathbf{r}^T \mathbf{f}_{\sigma} + \delta\boldsymbol{\theta}_{\perp}^{\boldsymbol{T}} \mathbf{m}_{\sigma\perp} \right]_{\Gamma_{\sigma}} \doteq 0. \quad (2.139)$$

The associated functions of kinetic and hyper-elastic stored energy yield in this case:

$$\tilde{\Pi}_{kin} = \frac{\rho A}{2} \dot{\mathbf{r}}^T \dot{\mathbf{r}},\;\; \tilde{\Pi}_{int} = \frac{EA}{2}\epsilon^2 + \frac{EI}{2}\boldsymbol{\kappa}^T\boldsymbol{\kappa}. \quad (2.140)$$

The formulation presented in this section is the shear-free counterpart to the torsion-free beam formulation presented in [191], which is based on the Simo-Reissner beam theory. Since the torsion term cancels out from the weak form, only the primary variable $\mathbf{r}$ and the variation $\delta\mathbf{r}$ have to be discretized. The corresponding finite element formulation is based on less degrees of freedom than the general formulation of Section 2.3 and is therefore numerically more efficient.

Furthermore, this formulation does not require any rotational degrees of freedom (or any other triad parametrization). This property dramatically simplifies standard procedures such as spatial discretization (in a manner that preserves objectivity of deformation measures), linearization, configuration updates, or time integration via finite differences in dynamics. These procedures are typically complicated by the presence of rotational degrees of freedom in common geometrically exact beam formulations. Furthermore, in contrast to standard geometrically exact beam formulations, (2.139) will result in a symmetric tangent stiffness matrix (as long as no external moment contributions are considered) and a symmetric and constant mass matrix. The torsion-free model also seems to provide an ideal tool for the mechanical investigation of cable-like structures. In pure cable formulations, artificial bending terms are often necessary in order to stabilize compressional modes (see e.g. [179]). On the contrary, the torsion-free formulation naturally provides such a stabilization in a mechanically consistent manner. In the next section, the applicability of this torsion-free beam theory is justified from a mechanical point of view.

2.4.2.2 Applicability of torsion-free beam theory

In the last section, the weak form of a torsion-free beam theory, i.e. a theory that neglects elastic and inertia contributions associated with twist degrees of freedom, has been derived. In this section, the theoretical justification for applying this torsion-free beam theory to practical problem classes characterized by the restrictions (2.128), (2.136) and (2.137) will be derived. Thereto, the first equation of (2.132), which is associated with the twist DoFs, is repeated here:

$$-GK_1' + \rho\dot{W}_1 = 0. \tag{2.141}$$

In the following, the partial differential equation (2.141) shall be solved. Actually, the second requirement in (2.136) would not allow for Dirichlet boundary conditions for the DoFs associated with twist since these type of boundary conditions could induce boundary torques $M_{\sigma 1}(t) \neq 0$ in general. However, in the next two sections, it will be shown that a beam with one clamped end will still exhibit a state of vanishing torsion while blocked twist DoFs at both ends of the beam can induce torsion even if the initial configuration is torsion-free. In order to investigate these scenarios, three types of boundary conditions for the twist DoFs will be considered:

$$\begin{aligned}
&\text{a) No twist DoFs blocked:} && K_1(s=0,t) = K_1(s=l,t) = 0. \\
&\text{b) Twist DoFs blocked at one end:} && K_1(s=0,t) = 0,\ W_1(s=l,t) = 0. \\
&\text{c) Twist DoFs blocked at both ends:} && W_1(s=0,t) = W_1(s=l,t) = 0.
\end{aligned} \tag{2.142}$$

In order to solve (2.141), the following relation between K_1 and W_1 (see (2.93)) will be used:

$$\dot{K}_1 = W_1' + F, \quad F := \mathbf{g}_1^T(\mathbf{k}\times\mathbf{w}) = \mathbf{g}_1^T(\mathbf{k}_\perp\times\mathbf{w}_\perp) = \dot{\mathbf{g}}_1^T(\mathbf{g}_1\times\mathbf{g}_1'). \tag{2.143}$$

Differentiation of (2.141) with respect to s, differentiation of (2.143) with respect to t and a subsequent insertion of $\dot{W}_1'$ from (2.143) into (2.141) yields the following PDE in $K_1(s,t)$:

$$-K_1'' + \frac{1}{c^2}\ddot{K}_1 = \frac{1}{c^2}\frac{d}{dt}F(s,t) =: \frac{1}{c^2}f(s,t) \ \text{ with } \ c^2 = \frac{G}{\rho}. \tag{2.144}$$

Here, the expression c can be identified as the wave speed of a linear torsional oscillator. Depending on the considered type of boundary conditions as listed in (2.142), it might be reasonable to

formulate the PDE (2.141) solely in terms of the tangential angular velocity component W_1. An analogous procedure than the one applied for the derivation of (2.144) yields:

$$-W_1'' + \frac{1}{c^2}\ddot{W}_1 = \frac{d}{ds}F(s,t) =: \tilde{f}(s,t) \;\text{ with }\; c^2 = \frac{G}{\rho}. \tag{2.145}$$

In a next step, the expression $F(s,t)$ will be further specified in order to simplify the subsequent derivation of inhomogeneous solutions for the PDEs (2.144) or (2.145). Thereto, the space curve $\mathbf{r}(s,t)$ with $s \in [0;l]$ and $t \in [0;T]$ is expanded as a two-dimensional Fourier-series:

$$\mathbf{r}(s,t) = \sum_{i=1}^{\infty}\sum_{j=1}^{\infty} \mathbf{r}_{ij} \sin\left(\frac{i\pi s}{l}\right) \sin\left(\frac{j\pi t}{T}\right). \tag{2.146}$$

Here, $\mathbf{r}_{ij}$ are the vector-valued coefficients of the Fourier-series. If the evolution of the curve $\mathbf{r}(s,t)$ can be assumed as sufficiently smooth, differentiation of (2.146) yields:

$$\mathbf{r}'(s,t) = \sum_{i=1}^{\infty}\sum_{j=1}^{\infty} \left(\frac{i\pi}{l}\right) \mathbf{r}_{ij} \cos\left(\frac{i\pi s}{l}\right) \sin\left(\frac{j\pi t}{T}\right). \tag{2.147}$$

In the range of high slenderness ratios, the axial strains are assumed to be small, i.e. $||\mathbf{r}'|| \approx 1$, and the base vector $\mathbf{g}_1$ can be expressed by the approximation $\mathbf{g}_1 \approx \mathbf{r}'$:

$$\mathbf{g}_1(s,t) \approx \mathbf{r}'(s,t) = \sum_{i=1}^{\infty}\sum_{j=1}^{\infty} \bar{\mathbf{r}}_{ij} \cos\left(\frac{i\pi s}{l}\right) \sin\left(\frac{j\pi t}{T}\right). \tag{2.148}$$

In (2.148), the term $i\pi/l$ has been included into the Fourier coefficient $\bar{\mathbf{r}}_{ij}$ in order to make the latter dimensionless. Further differentiation of (2.148) with respect to s and t results in:

$$\begin{aligned} \mathbf{g}_1'(s,t) &\approx \sum_{i=1}^{\infty}\sum_{j=1}^{\infty} -\left(\frac{i\pi}{l}\right) \bar{\mathbf{r}}_{ij} \sin\left(\frac{i\pi s}{l}\right) \sin\left(\frac{j\pi t}{T}\right), \\ \dot{\mathbf{g}}_1(s,t) &\approx \sum_{i=1}^{\infty}\sum_{j=1}^{\infty} \left(\frac{j\pi}{T}\right) \bar{\mathbf{r}}_{ij} \cos\left(\frac{i\pi s}{l}\right) \cos\left(\frac{j\pi t}{T}\right). \end{aligned} \tag{2.149}$$

With these approximations, the product $F(s,t) = \dot{\mathbf{g}}_1^T(\mathbf{g}_1 \times \mathbf{g}_1')$ in (2.144) and (2.145) yields:

$$F(s,t) = \sum_{i=1}^{\infty}\sum_{j=1}^{\infty} \frac{1}{l}\Omega_j \tilde{F}_{ij} \sin(\hat{\omega}_i s) \sin(\Omega_j t) \quad \text{with} \quad \hat{\omega}_i = \frac{i\pi}{l},\;\; \Omega_j = \frac{j\pi}{T}. \tag{2.150}$$

From (2.148) and (2.149) to (2.150), trigonometric relations have been used in order to end up with a Fourier series representation of $F(s,t)$ according to (2.150) within the finite interval $(s,t) \in [0;l] \times [0;T]$ with new (dimensionless) coefficients $\tilde{F}_{ij}$. For simplicity, also the term $i\pi$ has been included into the coefficients $\tilde{F}_{ij}$. Depending on the considered type of boundary conditions, it might be useful to use an equivalent cosine half range Fourier series instead of (2.150):

$$F(s,t) = \sum_{i=0}^{\infty}\sum_{j=1}^{\infty} \frac{1}{l}\Omega_j \bar{F}_{ij} \cos(\hat{\omega}_i s) \sin(\Omega_j t) \quad \text{with} \quad \hat{\omega}_i = \frac{i\pi}{l},\;\; \Omega_j = \frac{j\pi}{T}, \tag{2.151}$$

with coefficients $\bar{F}_{ij}$ differing from $\tilde{F}_{ij}$. In the following two sections, solutions for (2.144) and (2.145) will be derived for the (quasi-) static as well as for the dynamic case.

2.4.2.3 Verification of applicability in statics

In the (quasi-) static case, inertia terms can be neglected by setting $\rho = 0$ in (2.141), resulting in:

$$K_1' = 0. \tag{2.152}$$

Thus, a constant torsion $K_1 = \text{const.}$ and consequently a constant first component M_1 of the moment stress resultant $\mathbf{m}$ follow from (2.141). For the boundary condition types a) and b) the torsion K_1 vanishes at least at one end of the beam. Consequently, for these boundary conditions the constant value of M_1 equals zero, or in other words, the beam remains torsion-free. The treatment of the boundary condition c) is more intricate. In this case, it is sensible to re-express (2.152) via W_1. In the (quasi-) static case, the variant (2.145) simplifies to:

$$-W_1'' = \frac{d}{ds}F(s,t) =: \tilde{f}(s,t). \tag{2.153}$$

Based on (2.150), a twofold integration of (2.153) with respect to the coordinate s leads to:

$$W_1(s,t) = \sum_{i=1}^{\infty}\sum_{j=1}^{\infty} \frac{\Omega_j}{l\hat{\omega}_i}\tilde{F}_{ij}\cos(\hat{\omega}_i s)\sin(\Omega_j t) + c_1(t)s + c_2(t). \tag{2.154}$$

After evaluating the boundary conditions $W_1(s=0,t)=W_1(s=l,t)=0$, (2.154) becomes:

$$W_1(s,t) = \sum_{i=1}^{\infty}\sum_{j=1}^{\infty} \frac{\Omega_j}{l\hat{\omega}_i}\tilde{F}_{ij}\left[\cos(\hat{\omega}_i s) - \frac{(-1)^i - 1}{l}s - 1\right]\sin(\Omega_j t). \tag{2.155}$$

Relation (2.143) and the initial condition $K_1(s,t=0)=0$ enable the integration of $K_1(s,t)$:

$$K_1(s,t) = \sum_{i=1}^{\infty}\sum_{j=1}^{\infty} \frac{\tilde{F}_{ij}}{l}\frac{(-1)^i - 1}{i\pi}\cos(\Omega_j t) = -\sum_{j=1}^{\infty}\frac{\bar{F}_{0j}}{l}\big(\cos(\Omega_j t) - 1\big). \tag{2.156}$$

From the second to the third term in (2.156), the standard transformation rule between the coefficients of sine and cosine half range series has been applied. As expected, the resulting torsion $K_1(s,t)$ is constant along the beam and does not vanish in general 3D scenarios ($\bar{F}_{0j} \neq 0$). Thus, in case of boundary conditions of type c) (e.g. two clamped ends) the beam will not remain torsion-free in general. This is in contrast to the boundary conditions a) and b), where the torsion will always exactly vanish as long as (quasi-) static problems are considered. The variable t in (2.156) represents a pseudo time, describing the evolution of the quasi-static problem. These investigations will be extended to more general dynamic problems in the next section.

2.4.2.4 Verification of applicability in dynamics

In the dynamic case, the PDE (2.144) describing the dynamic evolution of the torsion $K_1(s,t)$ has to be solved. In a first step, boundary conditions of type a) shall be considered. Thereto, the homogeneous solution $K_{1h}(s,t)$ based on a Bernoulli separation approach according to $K_{1h}(s,t) = u(s)v(t)$ is determined such that the first line of (2.142) is fulfilled:

$$K_{1h}(s,t) = \sum_{i=1}^{\infty}\sin\left(\frac{\omega_i s}{c}\right)\left(A_i\cos(\omega_i t) + B_i\sin(\omega_i t)\right) \quad \text{with} \quad \omega_i = \frac{i\pi c}{l} = c\hat{\omega}_i. \tag{2.157}$$

As expected, the homogeneous solution is identical to that of a torsional oscillator of length l with free ends. For the derivation of an inhomogeneous solution, the time derivative, $f(s,t) = \dot{F}(s,t)$ is required. This time derivative follows through differentiation of the Fourier series (2.150):

$$f(s,t) = \sum_{i=1}^{\infty} \sum_{j=1}^{\infty} \frac{1}{l} \Omega_j^2 \tilde{F}_{ij} \sin\left(\frac{\omega_i s}{c}\right) \cos(\Omega_j t) \quad \text{with} \quad \omega_i = c\hat{\omega}_i. \tag{2.158}$$

In a next step, for the inhomogeneous solution $K_{1p}(s,t)$ of (2.144), an ansatz of the type

$$K_{1p}(s,t) = \sum_{i=1}^{\infty} \sum_{j=1}^{\infty} K_{ij} \sin\left(\frac{\omega_i s}{c}\right) \cos(\Omega_j t), \tag{2.159}$$

with unknown coefficients K_{ij} is made. Similar to the homogeneous solution, also (2.159) fulfills the boundary conditions of type a). In order to determine the coefficients K_{ij}, (2.158) and (2.159) are inserted into the PDE (2.144). A comparison of $\sin(\omega_i s/c)$- and $\cos(\Omega_j)$-coefficients yields:

$$K_{ij} = \frac{\eta_{ij}^2}{1-\eta_{ij}^2} \frac{\tilde{F}_{ij}}{l}, \qquad \text{with} \quad \eta_{ij} = \frac{\Omega_j}{\omega_i}. \tag{2.160}$$

Since (2.144) represents a linear PDE, the total solution for the torsion $K_1(s,t)$ follows from superposition of $K_{1h}(s,t)$ and $K_{1p}(s,t)$. The constants A_i and B_i can be determined from the initial conditions (2.137). From $K_1(s, t=0) = 0$, the constants A_i can be derived. It follows:

$$K_1(s,t) = \sum_{i=1}^{\infty} \sin\left(\frac{\omega_i s}{c}\right) \left[\sum_{j=1}^{\infty} \frac{\tilde{F}_{ij}}{l} \left(\frac{\eta_{ij}^2}{1-\eta_{ij}^2} [\cos(\Omega_j t) - \cos(\omega_i t)] \right) + B_i \sin(\omega_i t) \right]. \tag{2.161}$$

With $W_1' = \dot{K}_1 - F$ and the initial conditions $W_1(s, t=0) = W_1'(s, t=0) = 0$, the remaining constants B_i and the final solutions for $W_1(s,t)$ and $K_1(s,t)$ can be derived according to:

$$\begin{aligned} K_1(s,t) &= \sum_{i=1}^{\infty} \frac{1}{l} \sin\left(\frac{\omega_i s}{c}\right) \sum_{j=1}^{\infty} \tilde{F}_{ij} \left(\frac{\eta_{ij}^2}{1-\eta_{ij}^2} [\cos(\Omega_j t) - \cos(\omega_i t)] \right), \\ W_1(s,t) &= -\sum_{i=1}^{\infty} \frac{c}{l} \cos\left(\frac{\omega_i s}{c}\right) \sum_{j=1}^{\infty} \tilde{F}_{ij} \left(\frac{\eta_{ij}^2}{1-\eta_{ij}^2} [\sin(\omega_i t) - \eta_{ij} \sin(\Omega_j t)] - \eta_{ij} \sin(\Omega_j t) \right). \end{aligned} \tag{2.162}$$

Similarly, also the solutions $K_1(s,t)$ and $W_1(s,t)$ for the boundary conditions of type b) and c) can be derived (see Appendix A.4). In practical systems, the contributions stemming from the homogeneous solution are typically damped out after a certain time and the overall system dynamics are dominated by the external excitation represented by the inhomogeneous solution. Thus, only the inhomogeneous solutions for the boundary conditions a), b) and c) are compared:

$$\begin{aligned} a)\, K_{p1}(s,t) &= \sum_{i=1}^{\infty} \frac{1}{l} \sin\left(\frac{\omega_i s}{c}\right) \sum_{j=1}^{\infty} \tilde{F}_{ij} \frac{\eta_{ij}^2}{1-\eta_{ij}^2} \cos(\Omega_j t), \;\; \omega_i = \frac{i\pi c}{l}. \\ b)\, K_{p1}(s,t) &= \sum_{i=1}^{\infty} \frac{1}{l} \sin\left(\frac{\omega_i s}{c}\right) \sum_{j=1}^{\infty} \hat{F}_{ij} \frac{\eta_{ij}^2}{1-\eta_{ij}^2} \cos(\Omega_j t), \;\; \omega_i = \frac{(2i-1)\pi c}{2l}. \\ c)\, K_{p1}(s,t) &= \sum_{i=1}^{\infty} \frac{1}{l} \cos\left(\frac{\omega_i s}{c}\right) \sum_{j=1}^{\infty} \bar{F}_{ij} \frac{\eta_{ij}^2}{1-\eta_{ij}^2} \cos(\Omega_j t) - \sum_{j=1}^{\infty} \frac{\bar{F}_{0j}}{l} \big(\cos(\Omega_j t) - 1\big), \;\; \omega_i = \frac{i\pi c}{l}. \end{aligned} \tag{2.163}$$

In (2.163), the coefficients $\tilde{F}_{ij}$ and $\bar{F}_{ij}$ refer to the sine and cosine Fourier series (2.150) as well as (2.151) with $\hat{\omega}_i = i\pi/l$, while the coefficients $\hat{F}_{ij}$ stem from a sine Fourier series expansion of $F(s,t)$ with $\hat{\omega}_i = (2i-1)\pi/(2l)$ (see Appendix A.4.1). In the limit $\Omega_j \to 0$, i.e. $\eta_{ij} \to 0$, the results of these three cases are identical to the results already gained for the static case, i.e. the torsion vanishes for boundary conditions of type a) and b) while a constant torsion along the beam length results from type c). Consequently, the torsion resulting in dynamic problems from boundary conditions of type a) and b) remains small as long as the frequencies Ω_j describing the beam centerline dynamics are small as compared to the natural frequencies ω_i of the torsion modes. In the following considerations, it is assumed that the relevant frequencies Ω_j, with $j = 1, 2, ..., N_\Omega$, of a truncated version of the Fourier series expansion (2.146) at least lie within the same order of magnitude as the relevant eigenfrequencies of the linearized beam problem given in (3.120). For many practical applications, it can be assumed that the low eigenfrequencies and the associated deformation modes dominate the overall dynamic response while the amplitudes resulting from high modes can be assumed as being small or damped out by dissipative sources inherent to virtually all mechanical systems. In the range of high beam slenderness ratios, these most relevant low eigenfrequencies are associated with the bending modes (see (3.120)). With the assumption $\Omega_j \sim \omega_b$ for $j = 1, 2, ..., N_\Omega$, the following estimation can be made for η_{ij}:

$$\eta_{ij}^2 = \frac{\Omega_j^2}{\omega_i^2} \sim \left(\frac{1}{\zeta^2} \frac{E}{\rho l^2} \right) \Big/ \left(\frac{GI_T}{\rho I_P l^2} \right) \sim \frac{1}{\zeta^2}. \tag{2.164}$$

According to (2.163) and (2.164), the magnitude of the mechanical torsion, and consequently the magnitude of the error resulting from a neglect of torsion, decreases quadratically with increasing beam slenderness ratio $\zeta := l/R$ as long as the assumption $\Omega_j \sim \omega_b$ is justified. Thus, the torsion-free theory seems to be a reasonable specification of the general Kirchhoff beam theory, whose range of applicability also lies in the scope of high slenderness ratios as considered in this thesis.

2.4.2.5 Conclusion of static and dynamic analysis

In this section, a special torsion-free beam theory has been presented which exhibits the potential of resulting in considerably simplified finite element formulations (see Section 3.7) and numerical algorithms as compared to general, geometrically exact Reissner or Kirchhoff type beam formulations. Apart from the restrictions (2.128), (2.136) and (2.137) with respect to initial beam geometry and external (moment) loads (supplemented by proper twist Dirichlet boundary conditions given by the first two lines of (2.142)), this beam theory is able to model general 3D, large-deformation beam problems in statics and dynamics. For static problems fulfilling these restrictions, it has been shown in Section 2.4.2.3 that the solution of the torsion-free theory is identical to the solution of the general Kirchhoff theory. In the dynamic case, it has been shown in Section 2.4.2.4 that the error between the torsion-free and the general Kirchhoff beam theory decreases quadratically with increasing beam slenderness ratio as long as low-frequency dominated, i.e. bending dominated, mechanical problems are considered. Thus, the torsion-free theory can be regarded as a reasonable and promising specialization of the general Kirchhoff theory in the range of high beam slenderness ratios. Besides the investigated applicability to general, slender continua, the torsion-free beam theory represents an ideal model for quasi-continua without torsional resistance such as braided ropes, mechanical chains or polymer macro molecules.

3 Finite Element Formulations for Geometrically Exact Beams

In this chapter, the space-time-continuous beam problems presented in the last chapter will be discretized in order to allow for an approximate numerical solution. While spatial discretization is based on the finite element method (FEM), the generalized-α method, an implicit, one-step finite difference time integration scheme, is employed for temporal discretization. In the context of finite element methods for solid mechanics, it is often more convenient to perform time discretization on the semi-discrete problem setting resulting from spatial discretization. Here, just the opposite succession, i.e. the initial time discretization is followed by a subsequent spatial discretization, is chosen. This second variant is often applied in the development of geometrically exact beam finite element formulations and will lead to simpler discrete expressions. The differences arising from these two discretization successions will briefly be discussed in Appendix B.2. In Section 3.1.1, the basics of the standard generalized-α method as proposed by Chung and Hulbert [50] will be presented. In Section 3.1.2, a recently proposed extension of the generalized-α method from vector spaces to Lie groups [8, 40, 41], which is directly applicable to the beam element formulations proposed in this thesis, will be presented and compared to the standard generalized-α method. Afterwards, in Section 3.2, some basics of the FEM as well as different alternatives for the spatial discretization of the translational and rotational primary variable fields are presented. Based on these alternatives and the theory presented in Chapter 2, different beam element formulations will be proposed in Sections 3.3-3.7. There, the resulting element residual vectors will be derived. Since the linearization of the residuum by using either analytic techniques or automatic differentiation tools is rather straightforward, not for all considered element formulations this step is executed in detail. Finally, in Section 3.8, these concepts and the resulting element formulations will be verified by means of proper numerical test cases.

3.1 Temporal Discretization Methods for Primary Fields

Often, finite difference methods are applied in combination with the finite element method in order to discretize the problem of interest in time. A large variety of such finite difference schemes is available in the literature. Based on the introduction of a constant time step size Δt, the considered total time interval $t \in [0, T]$ is subdivided into equidistant subintervals $[t_n, t_{n+1}]$, where $n \in \mathbb{N}_0$ is the time step index. Consequently, the solution for the primary variable fields describing the current configuration $C(s,t) := (\mathbf{r}(s,t), \mathbf{\Lambda}(s,t))$ is computed at a series of discrete points in time with associated configurations $C(s,t_n) := (\mathbf{r}(s,t_n), \mathbf{\Lambda}(s,t_n)) =: (\mathbf{r}_n(s), \mathbf{\Lambda}_n(s))$.

One possible classification of time integration methods distinguishes between implicit and explicit schemes. For implicit schemes, the fully discretized problem are typically represented by a

system of equations that is nonlinear in the unknown discrete primary variables, which requires the application of a nonlinear solver, i.e. a Newton-Raphson scheme. On the contrary, explicit schemes allow for a direct extrapolation of the known configuration C_n to the unknown configuration C_{n+1}. The resulting system of equations is linear in the discrete unknowns such that only a linear solution step is required, which can often be further simplified by applying for example lumping techniques (see e.g. [73, 78, 97]. Within this thesis, solely implicit schemes will be considered. These are favorable for problems that are dominated by a low frequency response, while explicit schemes are rather suited to model high frequency responses and wave-like phenomena such as high velocity impacts. At least in the geometrically linear regime, implicit time integrators can be proven to be unconditionally stable, thus typically allowing for considerably larger time step sizes as compared to explicit schemes. Mechanical systems of slender beams typically result in a system of stiff differential equations as consequence of an increasingly large gap between the high-frequency and the low-frequency band with increasing beam slenderness ratio. Especially for such applications, implicit schemes are preferable. Nevertheless, implicit methods are arguably more challenging than their explicit counterparts, since typically a consistent linearization of all deformation-dependent quantities is required and the convergence of the nonlinear solution scheme has to be ensured. Particularly for highly complex configurations, which might for example occur when the contact interaction of many slender fibers shall be modeled (see Section 4.5.3.4), this is a demanding task. Further details concerning time integration in the context of nonlinear finite element methods can e.g. be found in [22]. In order to simplify notation required for subsequent derivations, the weak form G (see e.g. (2.52) or (2.110)) is split into the contributions G_{int} of internal forces, G_{kin} of kinetic forces and G_{ext} of external forces:

$$G = G_{int} + G_{kin} - G_{ext}. \tag{3.1}$$

Within this thesis, the standard generalized-α method will be applied in combination with the torsion-free beam element formulation proposed in Section 2.4.2.1, while a recently proposed extension of this method to Lie group time integration (see Section 3.1.2) will be used for temporal discretization of the general Reissner and Kirchhoff type beam elements considered herein. This distinction is made since the former finite element formulation is based on additive increments of primary variables formulated in a global vector space, which results in a constant and symmetric mass matrix. These properties are comparable with well-known nonlinear finite element formulations for solid mechanics and perfectly suited for the standard generalized-α method. On the contrary, the latter beam element variants will be formulated on the basis of multiplicative rotation increments defined on the tangent space of a nonlinear manifold. The resulting mass matrices are typically deformation-dependent and non-symmetric. Under such circumstances, a standard generalized-α scheme is not directly applicable and some modifications of the method are required in order to preserve the consistency of the finite difference scheme (see [8, 40]).

3.1.1 Generalized-α method for vector space time integration

The standard generalized-α method has been proposed by Chung and Hulbert [50] and represents a generalization of the well-known Newmark time integration scheme [166], the HHT-α method [96] and the WBZ-α method [232]. The generalized-α method applies a Newmark scheme in order to express the velocity $\dot{\mathbf{r}}_{n+1}(s)$ and acceleration field $\ddot{\mathbf{r}}_{n+1}(s)$ at the end of a

interval $[t_n, t_{n+1}]$ in terms of known quantities at time t_n and the unknown position field $\mathbf{r}_{n+1}(s)$:

$$\begin{aligned} \mathbf{r}_{n+1} &= \mathbf{r}_n + \Delta t \dot{\mathbf{r}}_n + \Delta t^2[(0.5-\beta)\ddot{\mathbf{r}}_n + \beta \ddot{\mathbf{r}}_{n+1}], \\ \dot{\mathbf{r}}_{n+1} &= \dot{\mathbf{r}}_n + \Delta t[(1-\gamma)\ddot{\mathbf{r}}_n + \gamma \ddot{\mathbf{r}}_{n+1}]. \end{aligned} \tag{3.2}$$

Solving this system of equations for the unknown velocities $\dot{\mathbf{r}}_{n+1}$ and accelerations $\ddot{\mathbf{r}}_{n+1}$ yields:

$$\begin{aligned} \dot{\mathbf{r}}_{n+1} &= \frac{\gamma}{\beta \Delta t}(\mathbf{r}_{n+1} - \mathbf{r}_n) - \frac{\gamma - \beta}{\beta}\dot{\mathbf{r}}_n - \frac{\gamma - 2\beta}{2\beta}\Delta t \ddot{\mathbf{r}}_n, \\ \ddot{\mathbf{r}}_{n+1} &= \frac{1}{\beta \Delta t^2}(\mathbf{r}_{n+1} - \mathbf{r}_n) - \frac{1}{\beta \Delta t}\dot{\mathbf{r}}_n - \frac{1 - 2\beta}{2\beta}\ddot{\mathbf{r}}_n. \end{aligned} \tag{3.3}$$

Here, $\beta \in]0, 0.5]$ and $\gamma \in [0, 1]$ are two parameters of the method determining the properties of the resulting time integration scheme. The basic idea of the generalized-α method lies in the introduction of generalized midpoints $t_{n+1-\alpha_m}, t_{n+1-\alpha_f} \in [t_n, t_{n+1}]$ at which the individual contributions to the weak form are evaluated. The following interpolations are commonly employed:

$$\begin{aligned} \mathbf{r}_{n+1-\alpha_f} &= (1-\alpha_f)\mathbf{r}_{n+1} + \alpha_f \mathbf{r}_n, \\ \dot{\mathbf{r}}_{n+1-\alpha_f} &= (1-\alpha_f)\dot{\mathbf{r}}_{n+1} + \alpha_f \dot{\mathbf{r}}_n, \\ \ddot{\mathbf{r}}_{n+1-\alpha_m} &= (1-\alpha_m)\ddot{\mathbf{r}}_{n+1} + \alpha_m \ddot{\mathbf{r}}_n, \\ G_{ext,n+1-\alpha_f} &= (1-\alpha_f)G_{ext,n+1} + \alpha_f G_{ext,n}, \\ G_{int,n+1-\alpha_f} &= (1-\alpha_f)G_{int}(\mathbf{r}_{n+1}, \delta\mathbf{r}) + \alpha_f G_{int}(\mathbf{r}_n, \delta\mathbf{r}). \end{aligned} \tag{3.4}$$

Here, the contributions of the external forces to the weak form at time t_n and t_{n+1} are given as:

$$\begin{aligned} G_{ext,n} &= G_{ext}(\mathbf{r}_n, \delta\mathbf{r}, \tilde{\mathbf{f}}_n, \tilde{\mathbf{m}}_n, \mathbf{f}_{\sigma,n}, \mathbf{m}_{\sigma,n}), \\ G_{ext,n+1} &= G_{ext}(\mathbf{r}_{n+1}, \delta\mathbf{r}, \tilde{\mathbf{f}}_{n+1}, \tilde{\mathbf{m}}_{n+1}, \mathbf{f}_{\sigma,n+1}, \mathbf{m}_{\sigma,n+1}). \end{aligned} \tag{3.5}$$

Remark: In this work, the contributions of the internal forces are considered by the trapezoidal rule. Alternatively, $G_{int,n+1-\alpha_f}$ could also be determined based on a midpoint rule:

$$G_{int,n+1-\alpha_f} = G_{int}(\mathbf{r}_{n+1-\alpha_f}, \delta\mathbf{r}).$$

Obviously, the two definitions coincide in the context of linear finite element problems.

Adding the weak form contributions of internal, kinetic and external forces yields the counterpart of equation (3.1), evaluated at the generalized midpoints $t_{n+1-\alpha_m}$ and $t_{n+1-\alpha_f}$:

$$G_{int,n+1-\alpha_f} + G_{kin}(\ddot{\mathbf{r}}_{n+1-\alpha_m}, \delta\mathbf{r}) - G_{ext,n+1-\alpha_f} \doteq 0. \tag{3.6}$$

The generalized-α method combines the properties of second-order accuracy, unconditional stability (within the linear regime), controllable damping of the high-frequency modes and minimized damping of the low-frequency modes. As soon as one of the four parameters β, γ, α_m and α_f is prescribed by the user in order to control the desired amount of high-frequency damping (third property), the remaining three parameters are fixed such that the first, second and fourth of the properties mentioned above are fulfilled. The degree of high-frequency damping is typically

prescribed by means of the spectral radius ρ_∞, which eventually plays the role of the only free parameter of the method. Depending on the choice of ρ_∞, the system parameters are given by:

$$\alpha_m = \frac{2\rho_\infty - 1}{\rho_\infty + 1}, \quad \alpha_f = \frac{\rho_\infty}{\rho_\infty + 1}, \quad \beta = \frac{(1 - \alpha_m + \alpha_f)^2}{4}, \quad \gamma = \frac{1}{2} - \alpha_m + \alpha_f. \tag{3.7}$$

The special choice $\rho_\infty = 0$ leads to an integration scheme which introduces no numerical dissipation into the system. Furthermore, the choice $\alpha_m = 0, \alpha_f = 0$ represents the Newmark method, the choice $\alpha_m = 0, \alpha_f \neq 0$ leads to the HHT-α scheme and the choice $\alpha_m \neq 0, \alpha_f = 0$ yields the WBZ-α method. Furthermore, it should be emphasized that the succession of spatial and temporal discretization makes no difference as long as the generalized-α method is combined with a spatial discretization scheme that depends linearly on nodal (discrete) degrees of freedom. This is the case for the torsion-free beam element formulation considered here (see also Section 3.7). For completeness, in Appendix B.1, the perhaps more common variant of applying temporal discretization to the already spatially discretized problem is shown. The variant presented here will enable detailed comparisons with the Lie group generalized-α scheme presented in the next section. There, the succession of spatial and temporal discretization indeed makes a difference.

Finally, a brief outlook shall be given concerning possible extensions of the employed time integration scheme. The arguably most important properties of a time integration scheme concern the stability as well as the accuracy of the method. In the geometrically linear regime, the focus often lies on the accuracy of the method since the requirement of unconditional stability is already satisfied by implicit schemes. However, when applied within the geometrically nonlinear regime of large displacements and rotations, these implicit schemes typically loose the property of unconditional stability. A sufficient condition for stability in nonlinear systems is given by the energy criterion which requires that the total system energy either is conserved or decreased within one time step, a property which is denoted as energy stability. Basically, three main categories of algorithms have been proposed in the literature in order to satisfy this energy criterion: methods which enforce conservation of energy by means of additional constraint equations, methods which satisfy algorithmic conservation of energy by construction as well as methods which employ numerical dissipation in order to fulfill the energy criterion (see also [131] for a detailed classification of these methods). Furthermore, besides accuracy and stability, also conservation of linear and angular momentum can be considered as desirable properties.

The first category of algorithms was established by Hughes et al. [105], who proposed the Constraint Energy Method. These algorithms enforce an additional constraint equation of constant system energy by means of Lagrange multipliers. However, it has been observed (see [132]) that these methods conserve the system energy perfectly in case an equilibrium solution can be found, but that these schemes often lead to non-convergent Newton-Raphson iterations which take place at configurations where algorithms without enforced energy conservation typically become unstable. A currently very popular category of time integration schemes which ensures exact conservation of energy, linear momentum as well as angular momentum by their algorithmic design are the so-called energy-momentum methods, which represent the second of the three categories mentioned above. The basic idea of these methods is to define the relation between the internal forces evaluated at a generalized midpoint within the interval $[t_n, t_{n+1}]$ and

the configurations at time t_n and t_{n+1} such that the resulting discrete values of energy and momentum are identical for two subsequent time steps. The first representative of this type, the energy-momentum method (EMM) proposed by Simo and Tarnow [207] was subsequently extended by Gonzalez [87] and supplemented by the possibility of including numerical dissipation, which yields the so-called generalized energy-momentum method (GEMM) [131, 133]. Finally, the generalized-α method is a representative of the third category. The basic idea of these well-known methods is to provide controllable high-frequency dissipation by the algorithmic design. The resulting schemes cannot guarantee for exact conservation of energy, linear and angular momentum. Also the parameter choice leading to stability in the linear regime does in general not guarantee for stability in the nonlinear regime. Nevertheless, the generalized-α method still combines the desirable properties of second-order accuracy and controllable dissipation of the high-frequency regime at minimal numerical dissipation of the lower modes. This behavior is not only favorable from a numerical point of view - since especially the high-frequency modes are affected by discretization errors - but also mimics, at least to some extent, the physical reality of low-frequency dominated mechanical systems. There, high-frequency contributions are often damped out by various physical sources of dissipation. Finally, the generalized-α method is simple to implement and very flexible: It can directly be applied to different types of element formulations, whereas e.g. energy-momentum methods would require specific adaptions. This holds especially for the beam element formulations presented in this thesis. Thereto, in the next section an extension of the standard generalized-α method will be presented that allows for time integration on Lie groups, as needed in the context of geometrically exact beam formulations. This integration scheme can directly be applied to the different variants of geometrically exact Simo-Reissner and Kirchhoff-Love beam elements without requiring further adaptions and thus allows for a straightforward comparison of different formulations. Of course, a future extension of the proposed beam elements to energy-momentum conserving algorithms is thinkable.

3.1.2 Generalized-α method for Lie group time integration

In this section, a Lie group extension of the standard generalized-α method originally proposed by [8, 40, 41] will be presented. This method will be applied for time discretization of the general Reissner and Kirchhoff type beam element formulations presented in subsequent sections, whose configuration space $C(s,t) = (\mathbf{r}(s,t), \mathbf{\Lambda}(s,t)) \in \Re^3 \times SO(3)$ is defined by the position field $\mathbf{r}(s,t)$ and the rotation field $\mathbf{\Lambda}(s,t)$. It is emphasized that the following procedure is independent from the rotation parametrization of $\mathbf{\Lambda}(s)$ employed to these different beam element formulations. The aim is again to express translational velocities and accelerations $\dot{\mathbf{r}}_{n+1}(s)$ and $\ddot{\mathbf{r}}_{n+1}(s)$ as well as angular velocities and accelerations $\mathbf{W}_{n+1}$ and $\mathbf{A}_{n+1}$ at the end of a time interval $[t_n, t_{n+1}]$ in terms of known quantities at time t_n and the unknown position field $\mathbf{r}_{n+1}(s)$ as well as the unknown rotation field $\mathbf{\Lambda}_{n+1}(s)$. Thereto, the vectors $\tilde{\boldsymbol{\theta}}_{n+1}$ and $\tilde{\mathbf{\Theta}}_{n+1}$, representing the multiplicative rotation increment between the time steps t_n and t_{n+1}, are introduced:

$$\exp(\mathbf{S}(\tilde{\mathbf{\Theta}}_{n+1})) = \mathbf{\Lambda}_n^T \mathbf{\Lambda}_{n+1}, \quad \tilde{\mathbf{\Theta}}_{n+1} = \mathbf{\Lambda}_n^T \tilde{\boldsymbol{\theta}}_{n+1} = \mathbf{\Lambda}_{n+1}^T \tilde{\boldsymbol{\theta}}_{n+1}. \tag{3.8}$$

Besides the distinctions already made for vector space time integrators in the last section (e.g. implicit or explicit scheme, one-step or multi-step scheme, employed methodology in order to guarantee stability and/or conservation properties) two further classifications can be made for

time integration schemes applied to rotational variables: First, depending on the type of spatial rotation interpolation employed for example in the context of geometrically exact beam finite elements, the succession of spatial and temporal discretization will in most cases influence the resulting discrete solution. Secondly, it can be distinguished between approaches that apply a time integration scheme directly to the vectors $(\tilde{\boldsymbol{\Theta}}, \mathbf{W}, \mathbf{A})$ and approaches that express angular velocities and accelerations by means of (additive) rates of the primary variables and apply a time integration scheme to these additive rates, e.g. to the vectors $(\boldsymbol{\psi}, \dot{\boldsymbol{\psi}}, \ddot{\boldsymbol{\psi}})$ in the case of a rotation vector parametrization (see also (2.67)). This distinction has already been indicated by equation (2.69) for the Reissner case and by equation (2.103) for the Kirchhoff case. Since, for example, the vectors $\dot{\boldsymbol{\psi}}$ and $\ddot{\boldsymbol{\psi}}$ simply represent additive changes of a vector $\boldsymbol{\psi}$ and all of these vectors are defined in the same global vector space, any standard vector space time integration scheme such as the well-known generalized-α method presented in the last section can be employed if such additive rates are considered. On the contrary, $\tilde{\boldsymbol{\Theta}}, \mathbf{W}$ and $\mathbf{A}$ are axial vectors associated with elements of the Lie algebra $so(3)$, which forms the tangent space of the Lie group $SO(3)$. Consequently, time integration schemes that are directly applied to the quantities $(\tilde{\boldsymbol{\Theta}}, \mathbf{W}, \mathbf{A})$ are commonly denoted as Lie group time integration schemes. In this context, it can be further distinguished between Lie group schemes that are based on the material vectors $(\tilde{\boldsymbol{\Theta}}, \mathbf{W}, \mathbf{A})$ and schemes that are based on their spatial counterparts $(\tilde{\boldsymbol{\theta}}, \mathbf{w}, \mathbf{a})$. However, following the results derived in [210], only the former variant will be applied within this thesis. Arguably, one of the first Lie group time integration schemes, at least in the context of geometrically exact beam formulations, has been proposed by Simo and Vu-Quoc [209] and represents the Lie group extension of the classical Newmark scheme. On the contrary, the scheme of [8, 40, 41], which will be presented in the following, is the Lie group extension of the standard generalized-α method. Similar to the last section, this scheme is based on the four parameters β, γ, α_m and α_f and simplifies to the variant of Simo and Vu-Quoc [209] for the special choice $\alpha_m = \alpha_f = 0$. A distinctive feature of the Lie group generalized-α scheme lies in the fact that all terms of the weak form are evaluated at the end point t_{n+1} of the considered time interval:

$$G_{n+1} = G(\mathbf{r}_{n+1}, \dot{\mathbf{r}}_{n+1}, \ddot{\mathbf{r}}_{n+1}, \boldsymbol{\Lambda}_{n+1}, \mathbf{W}_{n+1}, \mathbf{A}_{n+1}, \tilde{\mathbf{f}}_{n+1}, \tilde{\mathbf{m}}_{n+1}, \mathbf{f}_{\sigma,n+1}, \mathbf{m}_{\sigma,n+1}) \doteq 0. \tag{3.9}$$

The update formulas for translational quantities are given by a standard Newmark scheme

$$\begin{aligned} \tilde{\mathbf{u}}_{n+1} &:= \mathbf{r}_{n+1} - \mathbf{r}_n, \\ \tilde{\mathbf{u}}_{n+1} &= \Delta t \dot{\mathbf{r}}_n + + \Delta t^2 [(0.5 - \beta) \ddot{\mathbf{r}}_{mod,n} + \beta \ddot{\mathbf{r}}_{mod,n+1}], \\ \dot{\mathbf{r}}_{n+1} &= \dot{\mathbf{r}}_n + \Delta t [(1 - \gamma) \ddot{\mathbf{r}}_{mod,n} + \gamma \ddot{\mathbf{r}}_{mod,n+1}], \end{aligned} \tag{3.10}$$

which is slightly changed in form of a multiplicative configuration update for the rotations:

$$\begin{aligned} \exp(\mathbf{S}(\tilde{\boldsymbol{\Theta}}_{n+1})) &= \boldsymbol{\Lambda}_n^T \boldsymbol{\Lambda}_{n+1}, \\ \tilde{\boldsymbol{\Theta}}_{n+1} &= \Delta t \mathbf{W}_n + + \Delta t^2 [(0.5 - \beta) \mathbf{A}_{mod,n} + \beta \mathbf{A}_{mod,n+1}], \\ \mathbf{W}_{n+1} &= \mathbf{W}_n + \Delta t [(1 - \gamma) \mathbf{A}_{mod,n} + \gamma \mathbf{A}_{mod,n+1}]. \end{aligned} \tag{3.11}$$

The only difference between (3.10) and (3.2) lies in the definition of modified acceleration vectors $\ddot{\mathbf{r}}_{mod}$, which are related to the real / physical acceleration vectors $\ddot{\mathbf{r}}$ according to:

$$(1 - \alpha_m) \ddot{\mathbf{r}}_{mod,n+1} + \alpha_m \ddot{\mathbf{r}}_{mod,n} = (1 - \alpha_f) \ddot{\mathbf{r}}_{n+1} + \alpha_f \ddot{\mathbf{r}}_n \quad \text{with} \quad \ddot{\mathbf{r}}_{mod,0} = \ddot{\mathbf{r}}_0. \tag{3.12}$$

In a similar manner, the modified as well as the real/physical angular accelerations are related:

$$(1-\alpha_m)\mathbf{A}_{mod,n+1}+\alpha_m\mathbf{A}_{mod,n}=(1-\alpha_f)\mathbf{A}_{n+1}+\alpha_f\mathbf{A}_n \quad \text{with} \quad \mathbf{A}_{mod,0}=\mathbf{A}_0. \tag{3.13}$$

For later use, it is favorable to express $\dot{\mathbf{r}}_{n+1}$ and $\ddot{\mathbf{r}}_{n+1}$ in terms of the primary unknown $\mathbf{r}_{n+1}$:

$$\begin{aligned}
\dot{\mathbf{r}}_{n+1} &= \frac{\gamma}{\beta\Delta t}\tilde{\mathbf{u}}_{n+1}+\left(1-\frac{\gamma}{\beta}\right)\dot{\mathbf{r}}_n+\Delta t\left(1-\frac{\gamma}{2\beta}\right)\ddot{\mathbf{r}}_{mod,n},\\
\ddot{\mathbf{r}}_{n+1} &= \frac{1-\alpha_m}{\beta\Delta t^2(1-\alpha_f)}\tilde{\mathbf{u}}_{n+1}-\frac{1-\alpha_m}{\beta\Delta t(1-\alpha_f)}\dot{\mathbf{r}}_n\\
&\quad+\left[-\frac{(1-\alpha_m)(0.5-\beta)}{\beta(1-\alpha_f)}+\frac{\alpha_m}{1-\alpha_f}\right]\ddot{\mathbf{r}}_{mod,n}-\frac{\alpha_f}{1-\alpha_f}\ddot{\mathbf{r}}_n.
\end{aligned} \tag{3.14}$$

A similar relation can be formulated for the angular velocities $\mathbf{W}_{n+1}$ and accelerations $\mathbf{A}_{n+1}$:

$$\begin{aligned}
\mathbf{W}_{n+1} &= \frac{\gamma}{\beta\Delta t}\tilde{\boldsymbol{\Theta}}_{n+1}+\left(1-\frac{\gamma}{\beta}\right)\mathbf{W}_n+\Delta t\left(1-\frac{\gamma}{2\beta}\right)\mathbf{A}_{mod,n},\\
\mathbf{A}_{n+1} &= \frac{1-\alpha_m}{\beta\Delta t^2(1-\alpha_f)}\tilde{\boldsymbol{\Theta}}_{n+1}-\frac{1-\alpha_m}{\beta\Delta t(1-\alpha_f)}\mathbf{W}_n\\
&\quad+\left[-\frac{(1-\alpha_m)(0.5-\beta)}{\beta(1-\alpha_f)}+\frac{\alpha_m}{1-\alpha_f}\right]\mathbf{A}_{mod,n}-\frac{\alpha_f}{1-\alpha_f}\mathbf{A}_n.
\end{aligned} \tag{3.15}$$

In [40] and [41], it has been proven that the integration scheme given by equations (3.9)-(3.15) yields the same favorable properties as the standard generalized-α method, which are second-order accuracy, unconditional stability (within the linear regime), controllable damping of the high-frequency modes and minimized damping of the low-frequency modes. Remarkably, the parameter choice leading to this optimal behavior is identical to (3.7). Furthermore, it is shown that this scheme can consistently treat non-constant mass matrix contributions, such as the term $\boldsymbol{\Lambda}\mathbf{C}_\rho\mathbf{A}$ occurring in geometrically exact Reissner and Kirchhoff type beam formulations, as well as the presence of equality constraints (which might occur for Kirchhoff type element formulations where inextensibility is enforced by Lagrange multipliers). An extension of this scheme to inequality constraints (e.g. contact constraints which are enforced via Lagrange multipliers) is given in [48]. Similar to the last section, it has to be stated that also the extended generalized-α scheme cannot guarantee for exact conservation of energy, linear and angular momentum. Also in the field of Lie group time integration schemes, a large variety of methods aiming to guarantee these conservation properties has been proposed [17, 26, 35, 62, 86, 109, 119, 144, 189, 210]. However, the perhaps most essential advantage of the extended generalized-α scheme as compared to these alternatives lies again in its simplicity and flexibility. Independent of the beam theory (Reissner or Kirchhoff type), the employed spatial interpolation schemes as well as the chosen set of nodal primary variables (e.g. in terms of rotation parametrization), this time integration scheme can directly be applied without the need for any further adaptions.

3.2 Spatial Discretization Methods for Primary Fields

Spatial discretization is exclusively considered in the context of finite element methods within this thesis. It represents the core topic in the development of geometrically exact Kirchhoff beam

elements considered in this work. In the following Section 3.2.1, some basic concepts of the finite element method, already particularized to the 1D case of geometrically exact beams, are presented. However, this section solely intends to provide the most essential tools and concepts required for subsequent derivations. For a detailed introduction to the finite element method, the reader is referred to the literature, e.g. by Bathe [13], Belytschko et al. [22], Hughes [103], Reddy [182], Strang and Fix [216], Zienkiewicz and Taylor [242] and Zienkiewicz et al. [243]. Subsequently, in Sections 3.2.2 and 3.2.3, specific finite element interpolations employed to the translational and rotational primary variable fields considered in this thesis will be proposed. Finally, in Section 3.2.4, the most important requirements on the employed spatial discretizations and the resulting finite element formulations will be stated. In the subsequent sections, the fulfillment of these criteria will be verified for the finite element realizations presented there.

3.2.1 Basic concept of the finite element method

The starting point of the finite element discretization is given by the weak form of the balance equations (e.g. (2.52) for the Simo-Reissner beam theory, (2.110) for the general Kirchhoff-Love beam theory, (2.134) for the reduced isotropic beam theory or (2.139) for the reduced torsion-free beam theory) based on properly defined solution and weighting spaces $\mathcal{U}$ and $\mathcal{V}$:

$$\begin{aligned} \mathcal{U} &:= \left\{ \mathbf{r} \in \mathcal{W}^{m_r,2}(\Omega_l),\, \mathbf{\Lambda}(\mathbf{q}) \in \mathcal{W}^{m_\Lambda,2}(\Omega_l) | (\mathbf{r}, \mathbf{\Lambda}(\mathbf{q}))(s,t) = (\mathbf{r}_u, \mathbf{\Lambda}(\mathbf{q}_u)) \text{ on } \Gamma_u \right\}, \\ \mathcal{V} &:= \left\{ \delta\mathbf{r} \in \mathcal{W}^{m_r,2}(\Omega_l),\, \delta\mathbf{q} \in \mathcal{W}^{m_\Lambda,2}(\Omega_l) | (\delta\mathbf{r}, \delta\mathbf{q})(s) = \mathbf{0} \text{ on } \Gamma_u \right\}. \end{aligned} \tag{3.16}$$

Here, the notations $\mathbf{q}(s,t)$ and $\delta\mathbf{q}(s)$ have been employed as generalizations of the rotational primary variable field and its variation, which differ for the different beam theories considered in Chapter 2. Furthermore, $\mathcal{W}^{m,2}(\Omega_l)$ represents the Sobolev space of functions with square integrable derivatives of order i for $i = 0, ..., m$. Here and in the following, m_r and m_Λ denote the highest (arc-length) derivatives of the translational and rotational primary variable field occurring in the weak form, and consequently also in the associated hyper-elastic energy function. Throughout this thesis, the values $m_\Lambda = m_r = 1$ for Reissner type beam formulations and $m_\Lambda = 1, m_r = 2$ for Kirchhoff type beam formulations with corresponding Sobolev spaces $\mathcal{W}^{1,2}(\Omega_l)$ as well as $\mathcal{W}^{2,2}(\Omega_l)$ will be relevant. Now, the different weak forms derived in Chapter 2 can be summarized by the following general problem statement:

$$\text{Find } (\mathbf{r}, \mathbf{\Lambda}(\mathbf{q})) \in \mathcal{U} \text{ such that } G(\mathbf{r}, \mathbf{\Lambda}(\mathbf{q}), \delta\mathbf{r}, \delta\mathbf{q}) = 0 \;\forall\; (\delta\mathbf{r}, \delta\mathbf{q}) \in \mathcal{V}. \tag{3.17}$$

The basic concept of the finite element method relies on the Galerkin approach of approximating the analytic, space-continuous solution $(\mathbf{r}, \mathbf{\Lambda}(\mathbf{q}))$ by means of a discrete solution $(\mathbf{r}_h, \mathbf{\Lambda}_h(\mathbf{q}_h))$ represented by a weighted sum of shape functions out of a proper (square-integrable) function space $\mathcal{W}^{m,2}(\Omega_l)$. The finite element method particularizes the Galerkin approach to shape functions with local (element-wise) support, which offers several advantages with respect to the subsequent numerical solution process. Thus, the finite element discretization process simply represents a confinement of the trial and weighting space to finite-dimensional subspaces $\mathcal{U}_h \subset \mathcal{U}$ and $\mathcal{V}_h \subset \mathcal{V}$, yielding the following discrete equivalent to the weak form (3.17):

$$\text{Find } (\mathbf{r}_h, \mathbf{\Lambda}_h(\mathbf{q}_h)) \in \mathcal{U}_h \text{ such that } G(\mathbf{r}_h, \mathbf{\Lambda}_h(\mathbf{q}_h), \delta\mathbf{r}_h, \delta\mathbf{q}_h) = 0 \;\forall\; (\delta\mathbf{r}_h, \delta\mathbf{q}_h) \in \mathcal{V}_h. \tag{3.18}$$

Figuratively, in the FEM discretization process, the 1D beam domain described by the arc-length coordinate $s \in [0, l] = \Omega_l$ is subdivided into n_{ele} finite elements confined by $n_{ele}+1$ element boundary nodes with coordinates s^i and s^{i+1} for $i = 1, ..., n_{ele}$. The centerline curve $\mathbf{r}^{(e)}(s,t)$ on element e is approximated by local interpolation functions $N_r^{(e)i}(s)$ according to

$$\mathbf{r}^{(e)}(s,t) \approx \mathbf{r}_h^{(e)}(s,t) = \sum_{i=1}^{n_r} N_r^{(e)i}(s)\hat{\mathbf{d}}^i(t), \quad \mathbf{r}_0^{(e)}(s) \approx \mathbf{r}_{0h}^{(e)}(s) = \sum_{i=1}^{n_r} N_r^{(e)i}(s)\hat{\mathbf{d}}_0^i, \tag{3.19}$$

where the nodal vectors $\hat{\mathbf{d}}^i, \hat{\mathbf{d}}_0^i \in \Re^3$ represent e.g. nodal positions in case of Lagrange shape functions $N_r^{(e)i}(s) = L^{(e)i}(s)$ or nodal positions *and* tangents in case of Hermite shape functions $N_r^{(e)i}(s) = H^{(e)i}(s)$ and n_r denotes the number of nodes of one finite element (e) associated with the centerline interpolation (3.19). Here and in the following, the hat $\hat{(.)}$ refers to nodal primary variables. Moreover, throughout this thesis, the index $(.)_h$ refers to the discrete representation of a quantity and the superscript $(.)^{(e)}$ to a specific finite element. For simplicity, these indices will often be omitted in the following if there is no danger of confusion. In (3.19), the initial and current centerline interpolation, and consequently also the interpolation of the displacement field $\mathbf{u}_h(s,t) := \mathbf{r}_h(s,t) - \mathbf{r}_{0h}(s)$, are based on the same shape functions, an approach denoted as isoparametric concept. Typically, the arc-length space $s \in [s^{(e),1}, s^{(e),2}]$ underlying one finite element is mapped onto an elementwise parameter space $\xi \in [-1; 1]$. The element Jacobian $J(\xi) := ||\mathbf{r}_{0h,\xi}(\xi)||$ is defined by the interpolation of the initial beam centerline curve and describes the mapping between infinitesimal increments in the parameter space and the arc-length space according to $ds = J(\xi)d\xi$. Throughout this thesis, $(.)_{,\xi} = \frac{d}{d\xi}(.)$ represents the derivative with respect to the parameter coordinate ξ. The interpolation of the beam centerline variation $\delta\mathbf{r}(s)$ considered in this thesis is based on the Bubnov-Galerkin approach of applying identical shape functions as trial and test functions, yielding the following parameter-based descriptions:

$$\mathbf{r}_h^{(e)}(\xi,t) = \sum_{i=1}^{n_r} N_r^i(\xi)\hat{\mathbf{d}}^i(t), \quad \mathbf{r}_{0h}^{(e)}(\xi) = \sum_{i=1}^{n_r} N_r^i(\xi)\hat{\mathbf{d}}_0^i, \quad \delta\mathbf{r}_h^{(e)}(\xi) = \sum_{i=1}^{n_r} N_r^i(\xi)\delta\hat{\mathbf{d}}^i. \tag{3.20}$$

As a consequence of the parameter space representation, the shape functions $N_r^i(\xi)$ do not longer depend on the considered finite element (e) as it was the case for $N_r^{(e)i}(s)$. In contrary to (3.20), a Petrov-Galerkin approach would allow for different trial and test functions. Next, similarly to (3.20), also the rotational field $\mathbf{q}(s,t)$ and it variation $\delta\mathbf{q}(s)$ have to be approximated:

$$\begin{aligned} \mathbf{q}_h^{(e)}(\xi,t) &= \text{nl}(\hat{\mathbf{q}}^1(t), ..., \hat{\mathbf{q}}^{n_\Lambda}(t), \xi), \quad \mathbf{q}_{0h}^{(e)}(\xi) = \text{nl}(\hat{\mathbf{q}}_0^1, ..., \hat{\mathbf{q}}_0^{n_\Lambda}, \xi), \\ \delta\mathbf{q}_h^{(e)}(\xi,t) &= \sum_{i=1}^{n_\Lambda} \mathbf{N}_q^i(\xi,t)\delta\hat{\mathbf{q}}^i \quad \text{with} \quad \mathbf{N}_q^i(\xi,t) = \text{nl}(\hat{\mathbf{q}}^1(t), ..., \hat{\mathbf{q}}^{n_\Lambda}(t), \xi). \end{aligned} \tag{3.21}$$

Throughout this thesis, the operator $\text{nl}(.)$ represents a function that depends on its arguments in a nonlinear manner. In (3.21), the vectors $\hat{\mathbf{q}}^i, \hat{\mathbf{q}}_0^i$ and $\delta\hat{\mathbf{q}}^i$ represent the nodal values of the fields $\mathbf{q}_h(s,t), \mathbf{q}_{0h}(s)$ and $\delta\mathbf{q}_h(s,t)$ and n_Λ denotes the number of nodes of one finite element (e) associated with the rotation interpolation (3.21). According to (3.21), the interpolation schemes applied to the rotation fields will in general depend on the associated nodal values in a nonlinear manner. Furthermore, the weighting functions $\delta\mathbf{q}_h^{(e)}(\xi,t)$ are linear functions with respect to the

associated nodal variations. However, the employed generalized shape functions $\mathbf{N}_q^i(\xi,t)$ considered in this thesis will in general depend on the current deformation state, expressed by the nodal rotational degrees of freedom $\hat{\mathbf{q}}^i$. Furthermore, for the rotation field, also Petrov-Galerkin approaches, i.e. $\delta[\mathbf{q}_h] \neq \delta\mathbf{q}_h$, will be considered. In Figure 3.1, the employed element-local node numbering is visualized. Figure 3.1(a) represents the special case $n_r = n_\Lambda$. Within this thesis, a discretization with $n_r = 2$ and $n_\Lambda = 3$ as illustrated in Figure 3.1(b) will typically be applied to Kirchhoff type element formulations. Due to this numbering, the boundary nodes of the translational as well as the rotational interpolation scheme are addressed by the indices $i = 1, 2$.

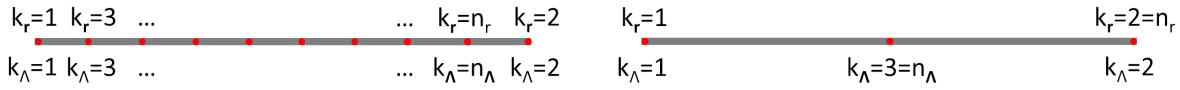

(a) Arbitrary node numbering with $n_r = n_\Lambda$.

(b) Node numbering applied to Kirchhoff elements.

Figure 3.1: Element-local node numbering of translational and rotational primary fields.

Throughout this thesis, the discrete nodal vectors $\hat{\mathbf{x}}^{(e)} := (\hat{\mathbf{d}}^{1T}, ..., \hat{\mathbf{d}}^{n_r T}, \hat{\mathbf{q}}^{1T}, ..., \hat{\mathbf{q}}^{n_\Lambda T})^T$ as well as $\delta\hat{\mathbf{x}}^{(e)} := (\delta\hat{\mathbf{d}}^{1T}, ..., \delta\hat{\mathbf{d}}^{n_r T}, \delta\hat{\mathbf{q}}^{1T}, ..., \delta\hat{\mathbf{q}}^{n_\Lambda T})^T$ collect all nodal primary variables and variations associated with one finite element. In a similar manner, the global vectors $\mathbf{X}$ and $\delta\mathbf{X}$ collecting the nodal primary variables of all finite elements as well as their variations can be defined. In order to simplify the notation for subsequent derivations, and since there is no danger of confusion, the $\hat{(.)}$ marking nodal primary variables, are omitted for assembled, global vectors such as $\mathbf{X}$. By making use of these abbreviations and inserting the discretizations (3.20) and (3.21) into one of the considered weak forms, the element residual vectors $\mathbf{r}$ (which should not be confused with the symbol $\mathbf{r}$ representing the beam centerline) and the global residual vector $\mathbf{R}$ can be identified:

$$G \approx G_h = \sum_{e=1}^{n_{ele}} \delta\hat{\mathbf{x}}^{(e)T} \int_{s^{(e),1}}^{s^{(e),2}} [.]\, ds =: \sum_{e=1}^{n_{ele}} \delta\hat{\mathbf{x}}^{(e)T} \mathbf{r}^{(e)} =: \delta\mathbf{X}^T \mathbf{R} \doteq 0 \quad \text{with} \quad \mathbf{r}^{(e)} := \int_{s^{(e),1}}^{s^{(e),2}} [.]\, ds. \tag{3.22}$$

Since the nodal variations occurring in $\delta\mathbf{X}$ are arbitrary, the discretized weak form (3.22) requires the global residual vector to vanish, i.e. $\mathbf{R} \doteq 0$. Furthermore, the global vectors and the element-wise counterparts employed in (3.22) are related by a proper assembly operator:

$$\mathbf{R} = \mathop{\mathsf{A}}_{e=1}^{n_{ele}} \mathbf{r}^{(e)}, \quad \mathbf{X} = \mathop{\mathsf{A}}_{e=1}^{n_{ele}} \hat{\mathbf{x}}^{(e)}, \quad \delta\mathbf{X} = \mathop{\mathsf{A}}_{e=1}^{n_{ele}} \delta\hat{\mathbf{x}}^{(e)}. \tag{3.23}$$

Similar to the splitting of the weak form according to (3.1), also the residual vectors can be split into contributions $(.)_{int}$ stemming form internal elastic forces, contributions $(.)_{ext}$ from external forces as well as contributions $(.)_{kin}$ from kinetic forces. In case a generalized-α time integration scheme according to Section 3.1.2 is applied for temporal discretization, all of these three contributions are evaluated at the current time step t_{n+1}, which eventually yields:

$$\mathbf{R}(\mathbf{X}_{n+1}) = \mathbf{R}_{int}(\mathbf{X}_{n+1}) + \mathbf{R}_{kin}(\mathbf{X}_{n+1}) - \mathbf{R}_{ext}(\mathbf{X}_{n+1}) \doteq 0. \tag{3.24}$$

The dependencies of the translational acceleration $\ddot{\mathbf{r}}$ as well as of the angular velocity $\mathbf{W}$ and acceleration $\mathbf{A}$ appearing in $\mathbf{R}_{kin}(\mathbf{X}_{n+1})$ on the nodal primary variables $\mathbf{X}_{n+1}$ is given by (3.14) and (3.15) together with the interpolation formulas (3.20) and (3.21). In order to solve the set of nonlinear algebraic equations (3.24) for the unknown primary variables $\mathbf{X}_{n+1}$, an iterative solution scheme is required. This question will be treated in the next sections.

Finally, a few comments concerning convergence of the finite element method shall be made. It is assumed that the space-time continuous problem setting defined by the weak form (3.17) exhibits a unique solution. For spatial convergence, basically the two requirements of *consistency* and *stability* have to be fulfilled by the employed FEM interpolation scheme. Consistency means that the applied trial functions of order p are expected to be complete, i.e. that they can exactly represent polynomials of order p, and that they fulfill proper continuity requirements at the element boundaries such that the highest (arc-length) derivative m occurring in the weak form still remains square-integrable and consequently that the associated energy functional remains bounded. The latter requirement is addressed by choosing the shape functions from proper Sobolev spaces $\mathcal{W}^{m,2}(\Omega_l)$ (see also (3.16)) and is typically fulfilled by C^{m-1}-continuous shape functions. Stability requires that the resulting discrete problem setting must satisfy certain well-posedness conditions which for example preclude the occurrence of non-physical zero-energy modes. In the context of geometrically exact beam element formulations this requirement also demands the function spaces employed for interpolation of the translational and rotational primary variable fields $\mathbf{r}$ and $\mathbf{\Lambda}(\mathbf{q})$ to be properly harmonised in order to avoid undesirable locking effects. For the beam element formulations considered within this work, these requirements as well as the expected convergence rates will be further specified in Section 3.2.4 and (at least heuristically) verified for the individual element types in Sections 3.3-3.5. For thorough mathematical derivations and proofs, the interested reader is exemplarily referred to the references mentioned above and to the textbooks of Brezzi and Fortin [39] as well as Reddy [181].

3.2.1.1 Linearization of residual vector

For the subsequently presented solution process by means of a Newton-Raphson scheme, the set of nonlinear algebraic equations (3.24) has to be linearized. Based on a truncated Taylor series expansion, the linearized variant of the residual equations given by equation (3.24) yields:

$$L\left(\mathbf{R}\right)\big|_{\mathbf{X}_{n+1}} := \mathbf{R}(\mathbf{X}_{n+1}) + \mathbf{K}(\mathbf{X}_{n+1})\Delta\mathbf{X}_{n+1} \doteq 0, \quad \mathbf{K}(\mathbf{X}_{n+1}) := \frac{d\mathbf{R}(\mathbf{X}_{n+1})}{d\mathbf{X}_{n+1}}. \tag{3.25}$$

The Jacobian $\mathbf{K}$ of $\mathbf{R}$ is commonly denoted as effective dynamic tangent stiffness matrix. Similarly to the residual, also the tangent stiffness matrix can be subdivided into element-wise, independently calculable element stiffness matrices $\mathbf{k}$ defined by the linearized variant of (3.22):

$$L\left(G_h\right) := \sum_{e=1}^{n_{ele}} \delta\hat{\mathbf{x}}^{(e)T} L(\mathbf{r}^{(e)}) =: \sum_{e=1}^{n_{ele}} \delta\hat{\mathbf{x}}^{(e)T}(\mathbf{r}^{(e)} + \mathbf{k}^{(e)}\Delta\hat{\mathbf{x}}^{(e)}) \doteq \delta\mathbf{X}^T(\mathbf{R} + \mathbf{K}\Delta\mathbf{X}). \tag{3.26}$$

Again, the global and element-wise matrices in (3.26) are related by a proper assembly operator:

$$\mathbf{K} = \bigA_{e=1}^{n_{ele}} \mathbf{k}^{(e)}, \quad \text{with} \quad \mathbf{k}(\hat{\mathbf{x}}_{n+1}) := \frac{d\mathbf{r}(\mathbf{x}_{n+1})}{d\hat{\mathbf{x}}_{n+1}}. \tag{3.27}$$

Similar to the residual, also the element stiffness matrix can be split into three contributions:

$$\mathbf{k} = \mathbf{k}_{int} + \mathbf{k}_{kin} - \mathbf{k}_{ext} := \frac{\partial \mathbf{r}_{int}(\hat{\mathbf{x}}_{n+1})}{\partial \hat{\mathbf{x}}_{n+1}} + \frac{\partial \mathbf{r}_{kin}(\hat{\mathbf{x}}_{n+1})}{\partial \hat{\mathbf{x}}_{n+1}} - \frac{\partial \mathbf{r}_{ext}(\hat{\mathbf{x}}_{n+1})}{\partial \hat{\mathbf{x}}_{n+1}}. \tag{3.28}$$

The first term represents the tangential stiffness matrix associated with the internal forces. As stated in [204] and elaborated earlier in [4, 5, 241], the loading by "moments with fixed axes", viz. $\tilde{\mathbf{m}}(s) \neq \mathbf{0}$ and $\mathbf{m}_\sigma \neq \mathbf{0}$ in the weak forms of the Reissner and Kirchhoff type beam formulations considered in Section 2, leads to non-conservative problems and consequently to non-symmetric (space-continuous) tangent operators. Furthermore, in [204], it has been shown that as consequence of the configuration space $C \in \Re^3 \times SO(3)$ represented by a nonlinear manifold, the tangent operator of geometrically exact beams (based on multiplicative rotation increments) is still non-symmetric for non-equilibrium configurations but symmetric for equilibrium configurations, as long as no external moments are considered. This property characterizes the space-continuous problem and is consequently also inherited by the finite element representation even if it is based on a Bubnov-Galerkin approach. The third term in (3.28) represents the stiffness contribution from external forces. In general, these contributions stem from deformation-dependent forces, e.g. follower loads, or deformation-dependent weighting functions. The latter case applies to geometrically exact beam formulations with strong enforcement of the Kirchhoff constraint in form of the constrained spin vector field $\delta\boldsymbol{\theta}(s)$ (if external moments are considered) and to the Bubnov-Galerkin (rotation interpolation) variants of the Reissner and Kirchhoff type beam element formulations presented in this thesis. As already stated earlier, the finite element formulation resulting from the torsion-free beam theory presented in Section 2.4.2 yields a vanishing contribution $\mathbf{k}_{ext} = \mathbf{0}$ and a tangent stiffness matrix $\mathbf{k}_{int} = \mathbf{k}_{int}^T$, which is symmetric even for non-equilibrium configurations as long as no external moment loads are employed. Finally, the second part in (3.28) represents the contribution to the effective dynamic stiffness matrix resulting from inertia forces. If the Lie-group scheme of Section 3.1.2 is employed, the stiffness contribution resulting from inertia forces has the following structure:

$$\begin{aligned} \mathbf{k}_{kin} := & \frac{1-\alpha_m}{\beta \Delta t^2 (1-\alpha_f)} \frac{\partial \mathbf{r}_{kin}(\hat{\mathbf{x}}_{n+1})}{\partial \ddot{\mathbf{r}}_{n+1}} \frac{\partial \mathbf{r}_{n+1}}{\partial \hat{\mathbf{x}}_{n+1}} \\ & + \frac{1-\alpha_m}{\beta \Delta t^2 (1-\alpha_f)} \frac{\partial \mathbf{r}_{kin}(\hat{\mathbf{x}}_{n+1})}{\partial \mathbf{A}_{n+1}} \frac{\partial \tilde{\boldsymbol{\Theta}}_{n+1}}{\partial \hat{\mathbf{x}}_{n+1}} + \frac{\gamma}{\beta \Delta t} \frac{\partial \mathbf{r}_{kin}(\hat{\mathbf{x}}_{n+1})}{\partial \mathbf{W}_{n+1}} \frac{\partial \tilde{\boldsymbol{\Theta}}_{n+1}}{\partial \hat{\mathbf{x}}_{n+1}} + \frac{\partial \mathbf{r}_{kin}(\hat{\mathbf{x}}_{n+1})}{\partial \hat{\mathbf{x}}_{n+1}}. \end{aligned} \tag{3.29}$$

While the first contribution, which stems from the translational primary variable field, represents a constant and symmetric contribution to the dynamic effective tangent stiffness matrix, the rotational contributions in the second line are in general deformation-dependent and non-symmetric. Again, for the torsion-free beam element formulation presented in Section 3.7, only the first term in (3.29) is required, thus yielding a standard constant and symmetric overall mass matrix.

3.2.1.2 Solution schemes for nonlinear systems of equations

In every time step t_{n+1}, the set of nonlinear equations (3.24) has to be solved for the nodal unknowns $\mathbf{X}_{n+1}$. For this purpose, the Newton-Raphson method, based on a repeated linearization of the residual (3.24), solution of the resulting set of linear algebraic equations and a subsequent incremental update of the nodal unknowns, is employed within this thesis. Within each iteration

k of the Newton-Raphson scheme, the linearized system (3.25) has to be evaluated for the current displacement state $\mathbf{X}_{n+1}^{k}$ and afterwards solved for the unknown increment $\Delta\mathbf{X}_{n+1}^{k+1}$:

$$\mathbf{K}(\mathbf{X}_{n+1}^{k})\Delta\mathbf{X}_{n+1}^{k+1} = -\mathbf{R}(\mathbf{X}_{n+1}^{k}). \tag{3.30}$$

If (3.25) has been formulated solely in terms of additive increments for all translational and rotation primary variables, the update procedure at the end of each iteration is given by

$$\mathbf{X}_{n+1}^{k+1} = \mathbf{X}_{n+1}^{k} + \Delta\mathbf{X}_{n+1}^{k+1}. \tag{3.31}$$

In case of a rotation vector-based triad parametrization, the linearization (3.25) can be formulated such that the increments $\Delta\hat{\mathbf{q}}$ of the rotation vectors represent either additive or multiplicative changes of the triad orientation. In the former case, (3.31) can directly be applied. In the latter case, translational and rotational unknowns have to be treated separately according to:

$$\begin{aligned} \hat{\mathbf{d}}_{n+1}^{i_r,k+1} &= \hat{\mathbf{d}}_{n+1}^{i_r,k} + \Delta\hat{\mathbf{d}}_{n+1}^{i_r,k+1} \qquad \text{with} \quad i_r = 1, ..., n_{r,tot}, \\ \mathbf{\Lambda}_{n+1}^{i_\Lambda,k+1} &= \exp\left(\mathbf{S}[\Delta\hat{\mathbf{q}}_{n+1}^{i_\Lambda,k+1}]\right)\mathbf{\Lambda}_{n+1}^{i_\Lambda,k} \quad \text{with} \quad i_\Lambda = 1, ..., n_{\Lambda,tot}. \end{aligned} \tag{3.32}$$

Here, $n_{r,tot}$ and $n_{\Lambda,tot}$ represent the total number of nodes associated with the centerline interpolation and with the rotation interpolation, respectively. The steps (3.30) together with either (3.31) or (3.32) are repeated until a certain user-defined convergence criterion is fulfilled. Within this thesis, the Euclidean norms of the displacement increment vector $\Delta\mathbf{X}_{n+1}^{k+1}$ and of the residual vector $\mathbf{R}(\mathbf{X}_{n+1}^{k+1})$ are checked. For convergence, these norms have to fall below prescribed tolerances $\delta_{\mathbf{R}}$ and $\delta_{\mathbf{X}}$, i.e. $||\mathbf{R}(\mathbf{X}_{n+1}^{k+1})|| < \delta_{\mathbf{R}}$ and $||\Delta\mathbf{X}_{n+1}^{k+1}|| < \delta_{\mathbf{X}}$. The perhaps most important advantage of the Newton-Raphson method as compared to alternative methods without tangent information, e.g. fixed-point iterations, lies in the quadratic convergence order of the iterative scheme (3.30)-(3.32), provided the initial estimate $\mathbf{X}_{n+1}^{0}$ lies within the convergence radius, i.e. it is sufficiently close to the (unknown) final solution $\mathbf{X}_{n+1}$. The simplest possible choice for the initial estimate is given by the solution of the previous time step, i.e. $\mathbf{X}_{n+1}^{0} = \mathbf{X}_{n}$. In all examples considered in this thesis, this simple "constant predictor" is employed. In dynamic examples, the initial estimates for translational and rotational velocities and accelerations are consistently derived from this choice based on the employed time integration scheme. Furthermore, within this thesis, solely exact Newton-Raphson methods based on a consistently determined tangent stiffness matrix as defined in (3.25) will be employed. An alternative is for example given by approximating the consistent tangent stiffness matrix with the initial tangent stiffness matrix of the first iteration. Such a procedure saves computation time in the iterative evaluation of (3.30), since $\mathbf{K}(\mathbf{X}_{n+1})$, the computationally most expensive part, only has to be calculated once in the beginning. On the other hand, the property of quadratic convergence does not hold for such a scheme anymore, which typically yields an increased number of iterations. Apart from these approximate schemes, there exists a large variety of extensions of the classical Newton-Raphson method aiming at an enhanced convergence radius and consequently at an increased overall efficiency and robustness. Well-known representatives are modified Newton methods such as line-search schemes (see e.g. [53, 85, 143]), which employ a scaled increment vector in the update formula (3.31), quasi-Newton methods such as pseudo-transient continuation schemes (see e.g. [45, 80, 124]), which employ modifications of the tangent stiffness matrix or Newton

schemes with step-size control based on algebraic constraint equations such as arc-length techniques (see e.g. [52, 54, 180]), which are typically applied to mechanically unstable systems. While for all examples of this chapter a classical Newton-Raphson scheme is employed, in the context of beam-to-beam contact as considered in Chapter 4, a modified Newton scheme with adapted update step (3.31) is proposed in order to guarantee for robust and reliable contact detection. For further details on nonlinear solution schemes, the reader is referred to the books of Ortega and Rheinboldt [170], Kelley [123], Nocedal and Wright [167] as well as Deuflhard [63].

3.2.1.3 Adaption of load step size

For conservative (quasi-)static problems, the final FEM solution (as well as the solution of the space-continuous problem) is independent from the loading path. Thus, in principle, it would be possible to apply the external loads "at once", i.e. within one load step. However, in order to ensure convergence of the Newton-Raphson scheme even for load cases inducing complex and highly nonlinear deformation states, the external load is typically applied "bit by bit" in form of an incremental procedure. For example, the external force $\mathbf{f}_{\sigma,n}$ at load step t_n is given by

$$\mathbf{f}_{\sigma,n} = \lambda_n \mathbf{f}_\sigma \quad \text{with} \quad \lambda_n = \frac{n\Delta t}{T} \quad \text{and} \quad n \in \{1, ..., N\}, \quad N = \frac{T}{\Delta t}, \tag{3.33}$$

in the simplest case (as considered here) that the load factor $\lambda_n \in [0; 1]$ is increased linearly in time. In (3.33), $\mathbf{f}_\sigma$ represents the final load for which an equilibrium configuration is searched, N denotes the number of load steps, Δt the load step size and T the pseudo-time representing the final state, which can typically be chosen as $T = 1$ in static simulations. In such an incremental procedure, the final solution of the last load step is chosen as initial guess for the Newton iteration of the current load step, i.e. $\mathbf{X}_{n+1}^0 = \mathbf{X}_n$. Consequently, the step size Δt has to be chosen small enough such that the initial guess lies within the convergence radius of the Newton-Raphson scheme. In highly nonlinear structural problems, such as the considered category of beam problems, the constant step size Δt is typically limited by only a few critical configurations occurring at certain load steps, while most of the remaining load steps would allow for a considerably increased step size. Consequently, an important gain in efficiency could be achieved by allowing for variable step sizes Δt during a simulation. For the static examples considered throughout this thesis, such a variable step sizes is achieved by the following simple procedure: Initially, a comparatively large step size $\Delta t_0 = 1/N_0$ (with $T = 1$) is chosen. If the Newton-Raphson scheme has not converged within a prescribed number of $n_{iter,max}$ iterations, the step size is halved and the load step is repeated. This procedure is repeated until convergence can be achieved. Then, after *four* converging load steps on the low step size level, the step size is doubled again. Also this procedure of successively doubling the step size after four converging load steps at the current step size level is repeated until the original step size Δt_0 is reached again.

This procedure will not only drastically increase the overall computational efficiency, it also allows for comparatively objective and fair comparisons of the performance of the Newton-Raphson scheme for different element formulations. In subsequent numerical examples, such

comparisons will be made on the basis of the accumulated number of Newton iterations

$$n_{iter,tot} := \sum_{n=1}^{N} n_{iter,n}, \tag{3.34}$$

required to solve the entire mechanical problem. Here, $n_{iter,n}$ is the number of iterations required for the step t_n. In the context of the "load step adaption scheme" mentioned above, non-converging steps are considered in the total number of iterations with $n_{iter,n} = n_{iter,max}$.

3.2.1.4 Solution schemes for systems of linear equations

As already stated above, in every Newton step i, a linear system of equations (3.30) needs to be solved. Equation (3.30) can be recast in the more general, and also more customary, form

$$\mathbf{AX} = \mathbf{B}, \tag{3.35}$$

with the so-called system matrix $\mathbf{A}$, the right-hand side vector $\mathbf{B}$ and the sought-after solution vector $\mathbf{X}$. Especially for large discrete system sizes, the linear solution process typically dominates the overall computational effort involved within one Newton step. In such cases, an efficient and robust linear solver is of highest importance. Even though the topic of linear solution schemes does not lie in the focus of this thesis, at least a few comments on this subject shall be given here for the following two reasons: On the one hand, the properties of the system matrix $\mathbf{A}$ are drastically influenced by the characteristics of the underlying physical problem, e.g. by the slenderness ratio of the considered beams. On the other hand, these properties of the system matrix typically have considerable influence on the performance of the employed linear solver. However, for details, the reader is exemplarily referred to the book of Quarteroni et al. [178].

In principle, linear solvers can be classified as direct and iterative schemes. Commonly, direct solvers lead to simpler algorithms and their performance is less sensitive with respect to the specific properties of the system matrix. Unfortunately, direct linear solvers, e.g. based on a LU-decomposition of the system matrix $\mathbf{A}$, typically become inefficient and too memory consuming for very large system sizes. The working principle of iterative linear solvers, such as the conjugate gradient method (CG, see e.g. [95]) or the generalized minimal residual method (GMRES, see e.g. [193]) relies on an iterative solution process applied to (3.35). The performance of iterative linear solvers is strongly influenced by the condition number of the system matrix $\mathbf{A}$, which can be approximated by the ratio of the largest and smallest eigenvalues of $\mathbf{A}$. Thereto, often a preconditioning step, i.e. an equivalence transformation of (3.35) based on proper scaling operators, is required in order to increase the efficiency or to enable the applicability of iterative solvers at all. Examples for commonly employed preconditioning schemes are Jacobi and Gauss-Seidel methods, incomplete factorization schemes (ILU) as well as algebraic multigrid methods (AMG). As indicated in Section 3.3.4, very high beam slenderness ratios will in general lead to system matrices with very high condition numbers. While moderate and high condition numbers might "only" require moderate extra effort in terms of a proper preconditioning scheme, very high beam slenderness ratios of $\zeta \approx 10000$ and above, as considered in this thesis and also prevalent in practical applications, eventually show the limits of such a procedure: In the

range of very high condition numbers, at some point, the round-off errors resulting from ill-conditioning might reach the limit of available computational accuracy (see e.g. Section 3.8.2). In such extreme cases, neither direct solvers nor properly preconditioned iterative solvers might be applicable at all or at least they would deliver results that are strongly affected by round-off errors. Consequently, in such scenarios, but also in general, it seems to be reasonable to directly address the mechanical model and to abstain for example from (physically less important) highly stiff deformation modes. Among others, this goal is addressed within this thesis by advancing the geometrically exact beam theory from Reissner type to Kirchhoff type element formulations.

3.2.2 Discretization of beam centerline

Next, the spatial discretization of the beam centerline curve $\mathbf{r}(s)$, generically given in (3.20), will be conducted. In the following two sections, an interpolation scheme based on Lagrange polynomials as well as an interpolation based on Hermite polynomials will be presented.

3.2.2.1 Discretization of beam centerline based on Lagrange polynomials

The highest derivative of the primary variable $\mathbf{r}(s)$ occurring in the weak form (2.52) of the Simo-Reissner beam theory is the first derivative $\mathbf{r}'(s)$ of the centerline curve. Consequently, a C^0-continuous interpolation of the beam centerline $\mathbf{r}(s)$ is sufficient in this case. Thus, for these formulations, the standard choice of trial functions for the interpolation of the initial and deformed centerline curve is based on Lagrange polynomials of order $n_r - 1$ according to:

$$\mathbf{r}_h(\xi) = \sum_{i=1}^{n_r} L^i(\xi)\hat{\mathbf{d}}^i =: \mathbf{L}\hat{\mathbf{d}} \quad \text{and} \quad \mathbf{r}_{0h}(\xi) = \sum_{i=1}^{n_r} L^i(\xi)\hat{\mathbf{d}}_0^i =: \mathbf{L}\hat{\mathbf{d}}_0. \tag{3.36}$$

In (3.36), the vectors $\hat{\mathbf{d}}^i, \hat{\mathbf{d}}_0^i \in \Re^3$ represent the current and initial nodal positions, whereas $L^i(\xi)$ are standard Lagrange polynomials satisfying the interpolation property $L^i(\xi^j) = \delta^{ij}$ at the element node coordinates ξ^j as well as proper completeness conditions. Here, δ^{ij} represents the Kronecker delta symbol. The matrix $\mathbf{L}$ and the vector $\hat{\mathbf{d}}$ represent proper element-wise assemblies of the shape functions L^i and the position vectors $\hat{\mathbf{d}}^i$ for $i = 1, ..., n_r$, which are given by $\mathbf{L} := (L^1(\xi)\mathbf{I}_3, ..., L^{n_r}(\xi)\mathbf{I}_3)$ as well as $\hat{\mathbf{d}} := (\hat{\mathbf{d}}^{1T}, ..., \hat{\mathbf{d}}^{n_r T})^T$. The element Jacobian yields:

$$ds = ||\mathbf{r}_{0h,\xi}(\xi)||d\xi =: J(\xi)d\xi \quad \text{with} \quad \mathbf{r}_{0h,\xi}(\xi) = \sum_{i=1}^{n_r} L^i_{,\xi}(\xi)\hat{\mathbf{d}}_0^i. \tag{3.37}$$

Following a Bubnov-Galerkin approach, the interpolation of the trial functions $\delta\mathbf{r}(s)$ reads:

$$\delta\mathbf{r}_h(\xi) = \sum_{i=1}^{n_r} L^i(\xi)\delta\hat{\mathbf{d}}^i =: \mathbf{L}\delta\hat{\mathbf{d}}. \tag{3.38}$$

In the next section, an alternative interpolation based on Hermite polynomials will be presented.

3.2.2.2 Discretization of beam centerline based on Hermite polynomials

The highest derivative of the primary variable $\mathbf{r}(s)$ occurring in the weak form (2.110) of the Kirchhoff-Love beam theory with strong constraint enforcement is the second derivative $\mathbf{r}''(s)$ of the centerline curve. Consequently, for the interpolation of the centerline $\mathbf{r}(s)$ shape functions are required that fulfill C^1-continuity at the element boundaries. Besides this requirement, a C^1-continuous centerline representation will be very beneficial for the numerical treatment of beam-to-beam contact interaction (see Chapter 4). In order to guarantee for C^1-continuity, Hermite shape functions are employed as trial functions for the interpolation of the centerline curve:

$$\mathbf{r}_h(\xi) = \sum_{i=1}^{2} H_d^i(\xi)\hat{\mathbf{d}}^i + \frac{c}{2}\sum_{i=1}^{2} H_t^i(\xi)\hat{\mathbf{t}}^i =: \mathbf{H}\hat{\mathbf{d}}, \;\; \mathbf{r}_{0h}(\xi) = \sum_{i=1}^{2} H_d^i(\xi)\hat{\mathbf{d}}_0^i + \frac{c}{2}\sum_{i=1}^{2} H_t^i(\xi)\hat{\mathbf{t}}_0^i =: \mathbf{H}\hat{\mathbf{d}}_0. \tag{3.39}$$

In (3.39), the vectors $\hat{\mathbf{d}}^i, \hat{\mathbf{d}}_0^i \in \Re^3$ and $\hat{\mathbf{t}}^i, \hat{\mathbf{t}}_0^i \in \Re^3$ represent nodal position and nodal tangent vectors at the two boundary nodes of the resulting finite elements. Again, the matrix $\mathbf{H}$ and the vector $\hat{\mathbf{d}}$ represent proper element-wise assemblies of the shape functions H_t^i and H_d^i as well as the nodal position and tangent vectors $\hat{\mathbf{d}}^i$ and $\hat{\mathbf{t}}^i$ for $i = 1, 2$. The explicit expressions are $\mathbf{H} := (H_d^1(\xi)\mathbf{I}_3, 0.5cH_t^1(\xi)\mathbf{I}_3, H_d^2(\xi)\mathbf{I}_3, 0.5cH_t^2(\xi)\mathbf{I}_3)$ as well as $\hat{\mathbf{d}} := (\hat{\mathbf{d}}^{1T}, \hat{\mathbf{t}}^{1T}, \hat{\mathbf{d}}^{2T}, \hat{\mathbf{t}}^{2T})^T$. Furthermore, $c > 0$ is a constant of the dimension length, which will be specified later. Finally, the Hermite shape functions employed in (3.39) obey the following polynomial representation:

$$\begin{aligned} H_d^1(\xi) &= \frac{1}{4}(2+\xi)(1-\xi)^2, \;\; H_d^2(\xi) = \frac{1}{4}(2-\xi)(1+\xi)^2, \\ H_t^1(\xi) &= \frac{1}{4}(1+\xi)(1-\xi)^2, \;\; H_t^2(\xi) = -\frac{1}{4}(1-\xi)(1+\xi)^2. \end{aligned} \tag{3.40}$$

It is straightforward to verify that these shape functions satisfy the interpolation properties

$$H_d^i(\xi^j) = \delta^{ij}, \quad H_{d,\xi}^i(\xi^j) = 0, \quad H_t^i(\xi^j) = 0, \quad H_{t,\xi}^i(\xi^j) = \delta^{ij} \quad \text{for} \quad i, j = 1, 2. \tag{3.41}$$

Moreover, the shape functions introduced in (3.40) fulfill the following completeness conditions

$$\begin{aligned} &\sum_{i=1}^{2} H_d^i(\xi) = 1, && \sum_{i=1}^{2} \left(\xi^i H_d^i(\xi) + H_t^i(\xi)\right) = \xi, \\ &\sum_{i=1}^{2} \left(\xi^{i2} H_d^i(\xi) + 2\xi^i H_t^i(\xi)\right) = \xi^2, && \sum_{i=1}^{2} \left(\xi^{i3} H_d^i(\xi) + 3\xi^{i2} H_t^i(\xi)\right) = \xi^3, \end{aligned} \tag{3.42}$$

and can consequently represent any polynomial of order three. For space curves, the Jacobian $J(\xi)$, which maps between infinitesimal arc-length and parameter coordinate increments, reads:

$$ds = ||\mathbf{r}_{0h,\xi}(\xi)||d\xi =: J(\xi)d\xi \quad \text{with} \quad \mathbf{r}_{0h,\xi}(\xi) = \sum_{i=1}^{2} H_{d,\xi}^i(\xi)\hat{\mathbf{d}}_0^i + \frac{c}{2}\sum_{i=1}^{2} H_{t,\xi}^i(\xi)\hat{\mathbf{t}}_0^i. \tag{3.43}$$

Based on (3.43), the first and second arc-length derivative of the centerline curve, which are needed for the Kirchhoff beam deformation measures defined in (2.95), yield:

$$\mathbf{r}_h'(\xi) = \frac{1}{J(\xi)}\mathbf{r}_{h,\xi}(\xi), \quad \mathbf{r}_h''(\xi) = \frac{1}{J(\xi)^2}\mathbf{r}_{h,\xi\xi}(\xi) - \frac{J_{,\xi}(\xi)}{J(\xi)^3}\mathbf{r}_{h,\xi}(\xi). \tag{3.44}$$

The derivative $J_{,\xi}(\xi)$ of the Jacobian follows directly from the defining equation (3.43):

$$J_{,\xi}(\xi) = \frac{d}{d\xi}||\mathbf{r}_{0h,\xi}|| = \frac{\mathbf{r}_{0h,\xi}^T \mathbf{r}_{0h,\xi\xi}}{||\mathbf{r}_{0h,\xi}||} \quad \text{with} \quad \mathbf{r}_{0h,\xi\xi}(\xi) = \sum_{i=1}^{2} H_{d,\xi\xi}^i(\xi)\hat{\mathbf{d}}_0^i + \frac{c}{2}\sum_{i=1}^{2} H_{t,\xi\xi}^i(\xi)\hat{\mathbf{t}}_0^i. \quad (3.45)$$

In the following, an initial geometry shall be discretized by means of n_{ele} elements, confined by $n_{ele}+1$ boundary nodes with arc-length coordinates s^i, $i = 1, 2, ..., n_{ele}+1$, on a given space curve $\mathbf{r}_0(s)$. It is assumed that either an analytical description of the curve $\mathbf{r}_0(s)$ exists, or at least the nodal positions $\mathbf{r}_0(s^i)$ and tangents $\mathbf{r}_0'(s^i)$ are known. Since s is chosen as arc-length parameter of the initial geometry and since the derivative of a parametrized curve with respect to an arc-length parameter always has a norm of one (see e.g. [23]), the initial tangent vectors have to be of unit length, i.e. $||\mathbf{r}_0'(s^i)|| = 1$. Now, the nodal positions and the nodal tangents are chosen according to $\hat{\mathbf{d}}_0^1 := \mathbf{r}_0(s^1)$, $\hat{\mathbf{d}}_0^2 := \mathbf{r}_0(s^2)$ and $\hat{\mathbf{t}}_0^1 := \mathbf{r}_0'(s^1)$, $\hat{\mathbf{t}}_0^2 := \mathbf{r}_0'(s^2)$ for each element. The interpolation property of this discretization with respect to nodal positions and tangents can be verified by making use of (3.39), (3.41) and (3.43) as well as the chain rule $\mathbf{r}_0' = \frac{\mathbf{r}_{0,\xi}}{J}$:

$$\mathbf{r}_{0,h}(\xi^1) = \hat{\mathbf{d}}_0^1, \quad \mathbf{r}_{0,h}(\xi^2) = \hat{\mathbf{d}}_0^2, \quad \mathbf{r}_{0,h}'(\xi^1) = \frac{c\hat{\mathbf{t}}_0^1}{||c\hat{\mathbf{t}}_0^1||} = \hat{\mathbf{t}}_0^1, \quad \mathbf{r}_{0,h}'(\xi^2) = \frac{c\hat{\mathbf{t}}_0^2}{||c\hat{\mathbf{t}}_0^2||} = \hat{\mathbf{t}}_0^2. \quad \square \quad (3.46)$$

Equivalent results can be obtained for the interpolation of the current centerline curve:

$$\mathbf{r}_h(\xi^1) = \hat{\mathbf{d}}^1, \quad \mathbf{r}_h(\xi^2) = \hat{\mathbf{d}}^2, \quad \mathbf{r}_h'(\xi^1) = \frac{c\hat{\mathbf{t}}^1}{||c\hat{\mathbf{t}}_0^1||} = \hat{\mathbf{t}}^1 \quad \text{and} \quad \mathbf{r}_h'(\xi^2) = \frac{c\hat{\mathbf{t}}^2}{||c\hat{\mathbf{t}}_0^2||} = \hat{\mathbf{t}}^2. \quad \square \quad (3.47)$$

Thus, due to $||\hat{\mathbf{t}}_0^1|| = ||\hat{\mathbf{t}}_0^2|| = 1$, the interpolation property for the nodal positions $\hat{\mathbf{d}}^i$, $\hat{\mathbf{d}}_0^i$ and tangents $\hat{\mathbf{t}}^i$, $\hat{\mathbf{t}}_0^i$ is fulfilled for any $c > 0$. This is in contrast to classical linear Euler-Bernoulli beam elements discretized by the Hermite shape functions (3.40). There, the constant c has to be chosen as the length of the (straight) element in order to fulfill the interpolation properties. Thus, the question arises how c has to be chosen in the considered context of geometrically exact beams. In the following, four different choices of the constant c shall be briefly discussed. In Appendix B.4, the influence of these different choices on the convergence behavior of the interpolation scheme (3.39) is investigated by means of proper Taylor expansions of $\mathbf{r}(s)$.

Variant 1: If an analytic representation $\mathbf{r}_0(\xi)$ of the initial geometry is available, the interpolation constant $c_1 = c_{opt}$ can be chosen as solution of an optimization problem given by:

$$\text{Find } c \in \Re^+ \text{ such that } \int_{-1}^{1} \left(\mathbf{r}_0(\xi) - \mathbf{r}_{0h}(\xi, c_1)\right)^2 d\xi \rightarrow \min. \quad (3.48)$$

For this variant, an analytic representation of the reference geometry is needed. The drawback of such an approach is the numerical effort of solving an additional optimization problem. However, the optimization problem has to be solved only once in the beginning of a simulation.

Variant 2: On the other hand, investigations on the approximation quality and the convergence behavior of the interpolation (3.39) (see Appendix B.3 and Appendix B.4) suggest a value $c_2 = l_{ele}$ in the range of the initial element length l_{ele} as a reasonable choice. Here l_{ele} denotes the

arc-length of an analytic curve segment defined by two successive nodes at s^i and s^{i+1}.

Variant 3: If no analytic representation of the initial geometry exists, the interpolated element length $c_3 = l_{ele,h}$ on the discretized geometry can be employed as alternative to the analytic segment length l_{ele}. The determination of c_3 requires the solution of the following equation:

$$c_3 = l_{ele,h} := \int_{-1}^{1} ||\mathbf{r}_{0h,\xi}(\xi, c_3)|| d\xi. \tag{3.49}$$

Since (3.49) represents a nonlinear function in c_3, it has to be solved iteratively (see also [6]).

Variant 4: Another, even simpler choice is to approximate the element length by the norm of the initial distance vector between the two element boundary nodes, i.e. $c_4 = ||\hat{\mathbf{d}}_0^2 - \hat{\mathbf{d}}_0^1||$.

In Appendix B.4, it is shown that in the limit of fine discretizations, i.e. $l_{ele} \to 0$, these four different choices for the constant c coincide, but only the first three of these choices guarantee the expected optimal convergence order of four in the centerline approximation, while the fourth variant leads to a decline in the convergence order to three. On the contrary, arbitrary choices of the constant c that drastically differ from the element length l_{ele} can further deteriorate convergence and can even lead to practically unfeasible discretizations. These considerations shall be further verified by means of a numerical example (see Figure 3.2 for illustration).

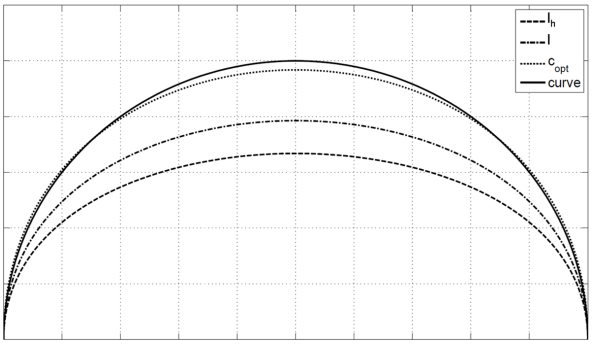

(a) 180^o-arc: $c = l_h$, $c = l$ and $c = c_{opt}$.

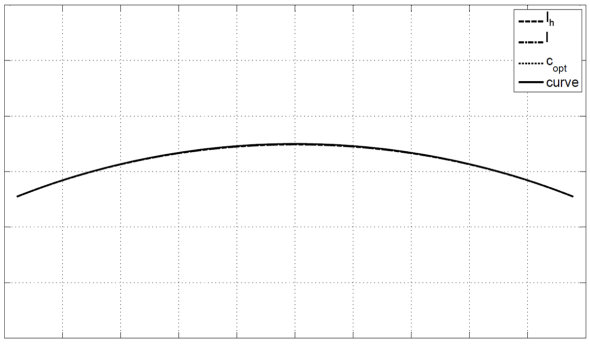

(b) 45^o-arc: $c = l_h$, $c = l$ and $c = c_{opt}$.

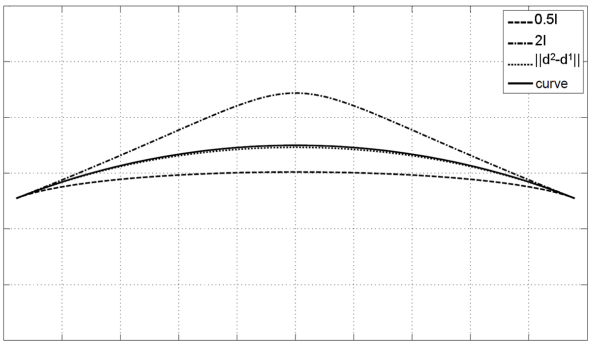

(c) 45^o-arc: $c = 0.5l$, $c = 2l$ and $c = ||\mathbf{d}^2 - \mathbf{d}^1||$.

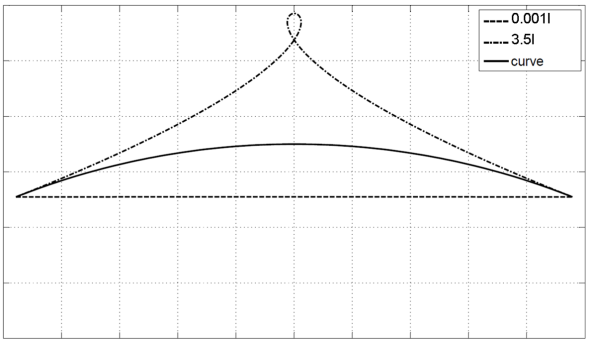

(d) 45^o-arc: $c = 0.001l$ and $c = 3.5l$.

Figure 3.2: Discretization of arc segments by one finite element with different choices for c.

Thereto, a single finite element ($l_{ele} = l$) with Hermite interpolation according to (3.39) is applied to discretize initial geometries in form of different arc segments. The results for different choices of the constant c are plotted in Figure 3.2. In Figure 3.2(a), a 180^o-arc has been discretized. By definition, the choice $c = c_{opt}$ delivers the best approximation of the arc, followed by the discretizations according to $c = l$ and $c = l_h$. Already for the discretization of an 45^o-arc (Figure 3.2(b)), there is no remaining visible difference between these three choices. In Figure 3.2(c), the roughest approximation for the element length, namely $c = ||\mathbf{d}^2 - \mathbf{d}^1||$, was applied to the 45^o-arc. Again, only marginal differences compared to the three choices of Figure 3.2(b) can be observed. However, a deviation from the element length by a factor 2 leads to a clearly visible decline in the approximation quality. Finally, in Figure 3.2(d), the deviation from the element length are extended to the higher factors 3.5 and 0.001, respectively. A factor 3.5 already leads to a loop in the discretized centerline curve, which makes the interpolation unfeasible for practical simulations. On the other hand, for the choice $c = 0.001l$, the influence of the nodal tangents is reduced to such an extent that the interpolation almost looks like a linear Lagrange interpolation of the two boundary nodes. Nevertheless, by zooming further into the plot, one would recognize that even in this case the interpolation property still holds for the nodal tangent vectors. Thus, as stated above, the interpolation property of (3.39) is independent of the constant c.

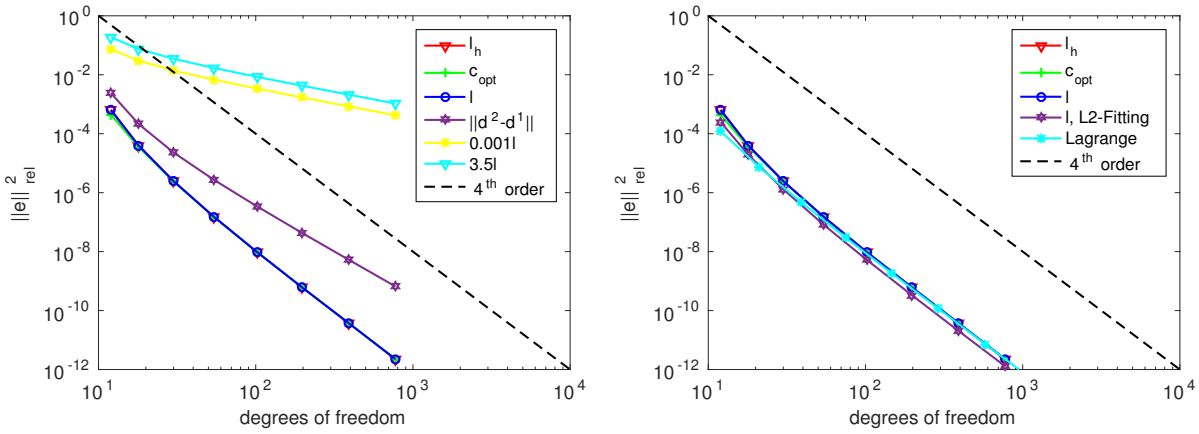

(a) Different choices for the constant c.

(b) Hermite and Lagrange shape functions.

Figure 3.3: L^2-errors for different discretizations applied to a 45^o-arc segment.

In Figure 3.3, the L^2-errors resulting from the discretization of an initial geometry in form of a 45^o-arc segment by different interpolation schemes is investigated. Figure 3.3(a) confirms the expected convergence rate of four for the variants 1-3 as well as the convergence rate of three for variant 4. Furthermore, it reveals that the extreme choices $c = 3.5l_{ele}$ and $c = 0.001l_{ele}$ still lead to convergence, but to a further reduced convergence rate of approximately 1. From Figure 3.3(b), it can be observed that the Hermite interpolation 3.39 based on the variants $c = c_{opt}$, $c = l_{ele}$ and $c = l_{ele,h}$ yields the same discretization error level per degree of freedom as the Lagrange interpolation 3.36. For all the interpolations considered so far, the nodal position vectors $\hat{\mathbf{d}}_0^i$ (and tangent vectors $\hat{\mathbf{t}}_0^i$) have been determined by the corresponding position vectors $\mathbf{r}_0(s^i)$ (and normalized tangent vectors $\mathbf{r}_0'(s^i)$) of the analytic initial geometry $\mathbf{r}_0(s)$. Of course, the approximation of the initial geometry could be further improved, if the initial nodal vectors $\hat{\mathbf{d}}_0^i$ (and $\hat{\mathbf{t}}_0^i$) are determined

via an optimization process that minimizes the resulting L^2-error. Also this variant, based on a L^2-fitting of the nodal vectors and the choice $c=l_{ele}$, has been plotted in Figure 3.3(b).

For all numerical examples presented in this thesis, the variant $c_3 = l_{ele,h}$ in combination with the initial nodal vectors $\hat{\mathbf{d}}_0^i = \mathbf{r}_0(s^i)$ and $\hat{\mathbf{t}}_0^i = \mathbf{r}_0'(s^i)$ is applied. Finally, also the variations $\delta\mathbf{r}(s)$ have to be discretized by properly chosen test functions. Following a Bubnov-Galerkin approach, also the interpolation of $\delta\mathbf{r}(s)$ is based on Hermite polynomials and given by the expression:

$$\delta\mathbf{r}_h(\xi) = \sum_{i=1}^{2} H_d^i(\xi)\delta\hat{\mathbf{d}}^i + \frac{c}{2}\sum_{i=1}^{2} H_t^i(\xi)\delta\hat{\mathbf{t}}^i =: \mathbf{H}\delta\hat{\mathbf{d}}. \tag{3.50}$$

The arc-length derivatives of (3.50) can be derived similarly to (3.44). In an analogous manner, the procedure presented here can also be extended to Hermite polynomials of higher order.

3.2.3 Discretization of rotation field

In Section 2.1.1, two parametrizations of rotation tensors have been investigated: a parametrization via rotation vectors $\boldsymbol{\psi}$ and a parametrization via the SR mapping on the basis of the set $(\mathbf{t}, \varphi)$. In the following two sections, these two variants will be employed in order to parametrize the rotation tensors $\boldsymbol{\Lambda}^i$ at the element nodes $i = 1, ..., n_\Lambda$. In the subsequent Sections 3.2.3.3 and 3.2.3.4, also two possible approaches for the interpolation of these nodal triads in the elements interior, one based on rotation vectors and one based on the SR mapping, will be presented.

3.2.3.1 Parametrization of nodal triads via rotation vectors

According to Section 2.1.1, rotation vectors $\hat{\boldsymbol{\psi}}_n^1, ..., \hat{\boldsymbol{\psi}}_n^{n_\Lambda}$ can be employed as primary variables in order to describe the nodal triads $\boldsymbol{\Lambda}_n^i = \boldsymbol{\Lambda}_n^i(\boldsymbol{\psi}_n^i),\ i = 1, 2, ..., n_\Lambda$, at time step t_n. For practical purposes, also the alternative of storing nodal orientations in terms of quaternions might be useful. However, the following considerations are only of an exemplary character and, thus, based on the simplest possible choice. As indicated in Section 3.2.1.2, the update of nodal orientations from iteration k to $k+1$ of a nonlinear solution scheme might either be based on additive rotation increments $\Delta\hat{\boldsymbol{\psi}}_n^{i,k+1}$ or on multiplicative rotation increments $\Delta\hat{\boldsymbol{\theta}}_n^{i,k+1}$ given by:

$$\begin{aligned} \boldsymbol{\Lambda}_n^{i,k+1}(\hat{\boldsymbol{\psi}}_n^{i,k+1}) &= \boldsymbol{\Lambda}_n^{i,k}(\hat{\boldsymbol{\psi}}_n^{i,k} + \Delta\hat{\boldsymbol{\psi}}_n^{i,k+1}) \\ \text{or } \boldsymbol{\Lambda}_n^{i,k+1}(\hat{\boldsymbol{\psi}}_n^{i,k+1}) &= \exp(\mathbf{S}[\Delta\hat{\boldsymbol{\theta}}_n^{i,k+1}])\boldsymbol{\Lambda}_n^{i,k}(\hat{\boldsymbol{\psi}}_n^{i,k}). \end{aligned} \tag{3.51}$$

Only for rotations with a magnitude smaller than 180° a unique rotation vector can be extracted from a given triad (by applying e.g. Spurrier's algorithm, see [214]). Within this work, rotation vectors are always extracted in a manner such that $\boldsymbol{\psi} \in]-\pi; \pi]$. Within this range, the transformation matrix $\mathbf{T}$ between additive and multiplicative rotation vector increments (see (2.17)) and its inverse, which do not exist at $\boldsymbol{\psi} = 2\pi$, are always well-defined.

3.2.3.2 Parametrization of nodal triads via smallest rotation mapping

Alternatively, the nodal triads can be defined via a relative rotation of nodal intermediate triads $\boldsymbol{\Lambda}_{M_{\hat{\varphi}}}^i$ by a nodal relative angle $\hat{\varphi}^i$ with respect to the tangent vector according to (2.22). The

nodal intermediate triads are defined by the smallest rotation mapping of the nodal intermediate triad $\bar{\mathbf{\Lambda}}^i_{M_{\hat{\varphi}},n} := \mathbf{\Lambda}^i_{M_{\hat{\varphi}},n-1}$ of the last time step onto the basis vector $\mathbf{g}^i_{1,n}$ of the current step t_n:

$$\mathbf{\Lambda}^i_n = \exp(\mathbf{S}[\hat{\varphi}^i_n \mathbf{g}^i_{1,n}])\mathbf{\Lambda}^i_{M_{\hat{\varphi}},n}, \quad \mathbf{\Lambda}^i_{M_{\hat{\varphi}},n} = \mathrm{sr}(\bar{\mathbf{\Lambda}}^i_{M_{\hat{\varphi}},n}, \mathbf{g}^i_{1,n}) \quad \text{with} \quad \bar{\mathbf{\Lambda}}^i_{M_{\hat{\varphi}},n} := \mathbf{\Lambda}^i_{M_{\hat{\varphi}},n-1}. \tag{3.52}$$

This variant will be used for Kirchhoff type beam element formulations in combination with the Hermite centerline interpolation (3.39), where the first base vector $\mathbf{g}^i_1$ is defined via the tangent vector to the beam centerline, i.e. $\mathbf{g}^i_1 = \mathbf{t}(\xi^i)/||\mathbf{t}(\xi^i)||$. All in all, the nodal triad is defined by the nodal relative angle $\hat{\varphi}^i$ and the tangent vector $\mathbf{t}(\xi^i)$ at the node i, i.e. $\mathbf{\Lambda}^i = \mathbf{\Lambda}^i(\varphi^i, \mathbf{t}(\xi^i))$. However, it has to be emphasized that in contrary to $\hat{\varphi}^i$, the vector $\mathbf{t}(\xi^i)$ does not necessarily have to be a nodal primary variable. If the considered node i coincides with one of the two element boundary nodes employed in the Hermite interpolation (3.39), this tangent vector indeed represents a nodal primary variable, i.e. $\mathbf{t}(\xi^i) = \hat{\mathbf{t}}^i$ for $i = 1, 2$, otherwise the tangent vector simply represents the interpolated centerline derivative at this position, i.e. $\mathbf{t}(\xi^i) = \mathbf{r}'(\xi^i)$. Based on (additive) increments $\Delta\hat{\varphi}^{i,k+1}_n$ of the nodal relative angles, the configuration update from iteration k to iteration $k+1$ of the Newton-Raphson scheme at time step t_n reads:

$$\mathbf{\Lambda}^{i,k+1}_n(\hat{\varphi}^{i,k+1}_n, \mathbf{g}^{i,k+1}_{1,n}) = \exp(\mathbf{S}[\hat{\varphi}^{i,k}_n + \Delta\hat{\varphi}^{i,k+1}_n, \mathbf{g}^{i,k+1}_{1,n}])\mathbf{\Lambda}^{i,k+1}_{M_{\hat{\varphi}},n}, \quad \mathbf{\Lambda}^{i,k+1}_{M_{\hat{\varphi}},n} = \mathrm{sr}(\bar{\mathbf{\Lambda}}^{i}_{M_{\hat{\varphi}},n}, \mathbf{g}^{i,k+1}_{1,n}). \tag{3.53}$$

The base vectors $\mathbf{g}^{i,k+1}_{1,n} = \mathbf{r}'^{k+1}_n(\xi^i)/||\mathbf{r}'^{k+1}_n(\xi^i)||$ are fully defined by the discrete centerline curve $\mathbf{r}'^{k+1}_n = \mathbf{r}'(\hat{\mathbf{d}}^{1,k+1}_n, \hat{\mathbf{d}}^{2,k+1}_n, \hat{\mathbf{t}}^{1,k+1}_n, \hat{\mathbf{t}}^{2,k+1}_n)$ based on an additive update of the degrees of freedom defining the beam centerline, i.e. $\hat{\mathbf{d}}^{i,k+1}_n = \hat{\mathbf{d}}^{i,k}_n + \Delta\hat{\mathbf{d}}^{i,k+1}_n$ as well as $\hat{\mathbf{t}}^{i,k+1}_n = \hat{\mathbf{t}}^{i,k}_n + \Delta\hat{\mathbf{t}}^{i,k+1}_n$.

Remark: Within this thesis, intermediate triads $\mathbf{\Lambda}_M$ based on the SR mapping are used for two different purposes: Firstly, they are used for the definition of nodal material triads $\mathbf{\Lambda}^i$ based on nodal relative angles $\hat{\varphi}^i$ and associated nodal intermediate triads $\mathbf{\Lambda}^i_{M_{\hat{\varphi}}}$ (SR mapping "in time" from $\bar{\mathbf{\Lambda}}^i_{M_{\hat{\varphi}},n} = \mathbf{\Lambda}^i_{M_{\hat{\varphi}},n-1}$ to $\mathbf{\Lambda}^i_{M_{\hat{\varphi}},n}$, see (3.52)). Secondly, they are used for the definition of an interpolated material triad field $\mathbf{\Lambda}(\xi)$ based on a relative angle field $\varphi(\xi)$ and an associated intermediate triad field $\mathbf{\Lambda}_{M_\varphi,n}(\xi)$ (SR mapping "in space" from a reference triad $\mathbf{\Lambda}_{r,n} = \mathbf{\Lambda}_n(\xi^r)$ to $\mathbf{\Lambda}_{M_\varphi,n}(\xi)$, see (3.63)). In order to distinguish these two applications, the additional index $\hat{\varphi}$ or φ of $\mathbf{\Lambda}_M$ refers to the associated relative angle.

3.2.3.3 Triad interpolation based on local rotation vectors

In this section, a triad interpolation is presentented that has originally been proposed by Shoemake [203] in the field of computer graphics and for the first time employed to geomerically exact beam element formulations by Crisfield and Jelenić [58, 116]. On each of the considered n_Λ nodes, a triad $\mathbf{\Lambda}^i$, with $i = 1, 2, ..., n_\Lambda$, is defined by primary degrees of freedom either according to Section 3.2.3.1 or to Section 3.2.3.2. The interpolation strategy presented in this section is independent from the specific choice of nodal primary variables. First, a reference triad $\mathbf{\Lambda}_r$ based on the triads at nodes I and J is defined according to the following averaging:

$$\mathbf{\Lambda}_r = \mathbf{\Lambda}^I \exp(\mathbf{S}(\mathbf{\Phi}^{IJ}/2)) \quad \text{with} \quad \exp(\mathbf{S}(\mathbf{\Phi}^{IJ})) = \mathbf{\Lambda}^{IT}\mathbf{\Lambda}^J. \tag{3.54}$$

The nodes I and J are chosen as the *two* middle triads for elements with an even number n_Λ of nodes and as the *one* middle triad (i.e. $I = J$) for elements with an odd number n_Λ of nodes (see

also equation (6.2) in [58], which is based on a sightly different node numbering). Based on the definition of the element reference triad $\mathbf{\Lambda}_r$, the interpolated triad field is defined as follows:

$$\mathbf{\Lambda}_h(\xi) = \mathbf{\Lambda}_r \exp(\mathbf{S}(\mathbf{\Phi}_{lh}(\xi))), \quad \mathbf{\Phi}_{lh}(\xi) = \sum_{i=1}^{n_\Lambda} L^i(\xi)\mathbf{\Phi}_l^i, \quad \exp(\mathbf{S}(\mathbf{\Phi}_l^i)) = \mathbf{\Lambda}_r^T \mathbf{\Lambda}^i. \tag{3.55}$$

Again, $L^i(\xi)$ represent the standard Lagrange polynomials of order $n_\Lambda - 1$ and $\mathbf{\Phi}_l^i$ the rotation vectors associated with the relative rotation between the triad $\mathbf{\Lambda}_i$ at node i and the reference triad $\mathbf{\Lambda}_r$. As indicated by the capital letter $\mathbf{\Phi}$, these vectors define the relative rotation via right-translation. The interpolation (3.55) represents an orthonormal interpolation scheme. Thus, the interpolated triad field is still an element of the rotation group, i.e. $\mathbf{\Lambda}_h(\xi) \in SO(3) \, \forall \, \xi \in [-1; 1]$. Furthermore, the interpolation scheme (3.55) preserves the objectivity of the space-continuous deformation measures (see [58]). The curvature vector (see (2.43)) resulting from (3.55) reads

$$\mathbf{K}_h(\xi) = \mathbf{T}^{-T}(\mathbf{\Phi}_{lh}(\xi))\mathbf{\Phi}'_{lh}(\xi), \tag{3.56}$$

and can exactly represent the state of constant curvature $\mathbf{K}_h = \text{const}$. Thus, the two-noded variant of (3.55) can be identified as a geodesic interpolation scheme, since it connects two points on the nonlinear manifold $SO(3)$ via the "shortest distance". Consequently, the two-noded variant of this interpolation represents the $SO(3)$-counterpart to the linear interpolation (3.36) of quantities in $\Re^3$. In contrast to the interpolations (3.36) and (3.39) of the beam centerline, the rotation interpolation (3.55) is nonlinear in the nodal degrees of freedom. Thus, if e.g. the field of rotation vectors $\boldsymbol{\psi}_h(\xi)$ with nodal values $\boldsymbol{\psi}_h(\xi^i) = \hat{\boldsymbol{\psi}}^i$ is employed for triad parametrization, the rotation vector interpolation resulting from (3.55) can be written in an abstract manner in the form $\boldsymbol{\psi}_h(\xi) = \text{nl}(\hat{\boldsymbol{\psi}}^1, ..., \hat{\boldsymbol{\psi}}^n_\Lambda, \xi)$ as already indicated in (3.21). While an explicit interpolation rule for the rotation vectors $\boldsymbol{\psi}_h(\xi)$ is not needed for practical purposes - the triad field is already given by (3.55) - the discrete version of the spin vector field $\delta\boldsymbol{\theta}_h(\xi)$ and the field of (multiplicative) rotation vector increments $\Delta\boldsymbol{\theta}_h(\xi)$ will be required in the next sections for the spatially discretized weak form of the balance equations and its linearization. In [58], these discretized fields have consistently been derived from the triad interpolation (3.55), leading to the following result:

$$\Delta\boldsymbol{\theta}_h(\xi) = \sum_{i=1}^{n_\Lambda} \tilde{\mathbf{I}}^i(\xi)\Delta\hat{\boldsymbol{\theta}}^i =: \tilde{\mathbf{I}}\Delta\hat{\boldsymbol{\theta}}, \quad \delta\boldsymbol{\theta}_h(\xi) = \sum_{i=1}^{n_\Lambda} \tilde{\mathbf{I}}^i(\xi)\delta\hat{\boldsymbol{\theta}}^i =: \tilde{\mathbf{I}}\delta\hat{\boldsymbol{\theta}}. \tag{3.57}$$

The arc-length derivatives of the interpolations (3.57) follow in a straightforward manner to:

$$\Delta\boldsymbol{\theta}'_h(\xi) = \sum_{i=1}^{n_\Lambda} \frac{1}{J(\xi)}\tilde{\mathbf{I}}^i_{,\xi}(\xi)\Delta\hat{\boldsymbol{\theta}}^i, \quad \delta\boldsymbol{\theta}'_h(\xi) = \sum_{i=1}^{n_\Lambda} \frac{1}{J(\xi)}\tilde{\mathbf{I}}^i_{,\xi}(\xi)\delta\hat{\boldsymbol{\theta}}^i. \tag{3.58}$$

The generalized shape function matrices $\tilde{\mathbf{I}}^i(\xi) \in \Re^3 \times \Re^3$ as well as their derivatives $\tilde{\mathbf{I}}^i_{,\xi}(\xi)$ have been derived in the original work [58] (see also Appendix B.5). Again, assembly matrices and vectors $\tilde{\mathbf{I}} := (\tilde{\mathbf{I}}^1, ..., \tilde{\mathbf{I}}^{n_\Lambda})$ as well as $\Delta\hat{\boldsymbol{\theta}} := (\Delta\hat{\boldsymbol{\theta}}^{1T}, ..., \Delta\hat{\boldsymbol{\theta}}^{n_\Lambda T})^T$ and $\delta\hat{\boldsymbol{\theta}} := (\delta\hat{\boldsymbol{\theta}}^{1T}, ..., \delta\hat{\boldsymbol{\theta}}^{n_\Lambda T})^T$ have been introduced. These shape functions depend on the rotational primary variables in a nonlinear manner, e.g. $\tilde{\mathbf{I}}^i(\xi) = \text{nl}(\hat{\boldsymbol{\psi}}^1, ..., \hat{\boldsymbol{\psi}}^n, \xi)$ if nodal rotation vectors according to Section 3.2.3.1 are employed. Consequently, they have to be re-calculated for every new configuration and this

dependency on the rotational primary variables would have to be considered within a consistent linearization procedure in case the spin vector interpolation $\delta\boldsymbol{\theta}_h(\xi)$ given in (3.57) is used in the weak form according to a Bubnov-Galerkin procedure. In order to avoid this additional linearization, it can be sensible to follow a Petrov-Galerkin approach based on an interpolation of $\delta\boldsymbol{\theta}_h(\xi)$ via Lagrange polynomials. This strategy is also applied within this work and leads to:

$$\delta\boldsymbol{\theta}_h(\xi) = \sum_{i=1}^{n_\Lambda} L^i(\xi)\delta\hat{\boldsymbol{\theta}}^i =: \mathbf{L}\delta\hat{\boldsymbol{\theta}}, \quad \delta\boldsymbol{\theta}'_h(\xi) = \sum_{i=1}^{n_\Lambda} \frac{1}{J(\xi)} L^i_{,\xi}(\xi)\delta\hat{\boldsymbol{\theta}}^i =: \mathbf{L}'\delta\hat{\boldsymbol{\theta}}. \tag{3.59}$$

Nevertheless, the interpolation $\Delta\boldsymbol{\theta}_h(\xi)$ is still based on (3.57) in order to end up with a consistent linearization of the rotation field. Finally, it has to be emphasized that the generalized shape functions fulfill the following interpolation and completeness properties

$$\tilde{\mathbf{I}}^i(\xi^j) = \delta^{ij}\mathbf{I}_3, \quad \sum_{i=1}^{n_\Lambda} \tilde{\mathbf{I}}^i(\xi) \equiv \mathbf{I}_3, \quad \sum_{i=1}^{n_\Lambda} \tilde{\mathbf{I}}^i_{,\xi}(\xi) \equiv \mathbf{0}, \tag{3.60}$$

i.e. these shape functions can exactly represent constant rotation vector increment fields. Since these properties are also fulfilled by the Lagrange polynomials, both the Bubnov-Galerkin interpolation (3.57) as well as the Petrov-Galerkin interpolation (3.59) of the spin vector field $\delta\boldsymbol{\theta}_h(\xi)$ can exactly represent a constant distribution $\delta\boldsymbol{\theta}_h(\xi) = \text{const.}$ in an element. This property is important with respect to conservation of angular momentum (see e.g. Sections 3.2.4.5 and 3.3.3).

3.2.3.4 Triad interpolation based on "Smallest Rotation" mapping

In this section, again, a triad interpolation with n_Λ nodes is considered. On each of these nodes, a triad $\boldsymbol{\Lambda}^i$, with $i = 1, 2, ..., n_\Lambda$, is defined by primary degrees of freedom either according to Section 3.2.3.1 or to Section 3.2.3.2. Similar to the last section, the interpolation strategy presented in the following is independent from the specific choice of nodal primary variables. Concretely, a novel interpolation scheme is proposed that defines an orthonormal triad field $\boldsymbol{\Lambda}_h(\xi) \in SO(3)\,\forall\,\xi \in [-1;1]$ based on a given tangent vector field $\mathbf{t}(\xi) = \mathbf{r}'(\xi)$ and nodal triads $\boldsymbol{\Lambda}^i = (\mathbf{g}^i_1, \mathbf{g}^i_2, \mathbf{g}^i_3)$ with $i = 1, 2, ..., n_\Lambda$. In the following, this tangent vector field is defined by a Hermite interpolation of the beam centerline according to (3.39) based on two nodes at the element boundary with six degrees of freedom $\hat{\mathbf{d}}^j, \hat{\mathbf{t}}^j$ and $j = 1, 2$, respectively. It has to be emphasized that the number of nodes of the triad interpolation can in general differ from the number of nodes of the Hermite centerline interpolation, i.e. $n_\Lambda \neq 2$ (see Figure 3.1(b)). The nodal triads are oriented tangential to the centerline. Thus, the first base vectors yield:

$$\mathbf{g}_1(\xi) = \frac{\mathbf{r}'(\xi)}{||\mathbf{r}'(\xi)||} \rightarrow \mathbf{g}^i_1 = \frac{\mathbf{r}'(\xi^i)}{||\mathbf{r}'(\xi^i)||}. \tag{3.61}$$

Similarly to Section 3.2.3.3, one nodal triad $\boldsymbol{\Lambda}^I$ initially has to be chosen as reference triad:

$$\boldsymbol{\Lambda}_r = \boldsymbol{\Lambda}^I \quad \text{with} \quad I \in \{1, 2, ..., n_\Lambda\}. \tag{3.62}$$

Based on the reference triad $\boldsymbol{\Lambda}_r$ and the nodal triads $\boldsymbol{\Lambda}^i$ the interpolation is defined according to:

$$\begin{aligned} &\boldsymbol{\Lambda}_h(\xi) = \exp(\mathbf{S}[\varphi_h(\xi)\mathbf{g}_1(\xi)])\,\boldsymbol{\Lambda}_{M_\varphi}(\xi), && \boldsymbol{\Lambda}_{M_\varphi}(\xi) = \text{sr}(\boldsymbol{\Lambda}_r, \mathbf{g}_1(\xi)), \\ &\varphi_h(\xi) = \sum_{i=1}^{n_\Lambda} L^i(\xi)\varphi^i, && \exp(\mathbf{S}[\varphi^i\mathbf{g}^i_1]) = \boldsymbol{\Lambda}^i\boldsymbol{\Lambda}^T_{M_\varphi}(\xi^i). \end{aligned} \tag{3.63}$$

The general curvature vector $\mathbf{K}_h(\xi)$ for interpolations that fulfill the Kirchhoff constraint in a strong manner is given by (2.90). The total torsion resulting from (3.63) can be derived as:

$$K_1 = K_{M_\varphi 1} + \varphi_h', \quad K_{M_\varphi 1} = \mathbf{g}_{M_\varphi 3}^T \mathbf{g}_{M_\varphi 2}' = -\frac{\boldsymbol{\kappa}^T \mathbf{g}_1^I}{1+\mathbf{g}_1^T \mathbf{g}_1^I}. \tag{3.64}$$

Remark: It is emphasized that the nodal relative angles $\varphi^i = \varphi_h(\xi^i)$ occurring in (3.63) are different from the nodal primary variables $\hat{\varphi}^i$ introduced in (3.52) of Section 3.2.3.2 for parametrization of nodal triads. For both quantities, the symbol φ has been chosen since in both cases the relative angle between the material triad $\boldsymbol{\Lambda}(\xi^i)$ and an intermediate triad $\boldsymbol{\Lambda}_{M_\varphi}(\xi^i)$ in case of φ^i (stemming from a SR mapping "in space") or an intermediate triad $\boldsymbol{\Lambda}_{M_{\hat{\varphi}}}^i$ in case of $\hat{\varphi}^i$ (stemming from a SR mapping "in time") is measured. The difference becomes clear by realizing that the intermediate triad $\boldsymbol{\Lambda}_{M_\varphi}(\xi^i)$ resulting from the smallest rotation of $\boldsymbol{\Lambda}_r$ onto $\mathbf{g}_1(\xi^i)$ (see (3.63)) will in general differ from the intermediate triad $\boldsymbol{\Lambda}_{M_{\hat{\varphi}}}^i$ resulting from the smallest rotation of $\bar{\boldsymbol{\Lambda}}_{M_{\hat{\varphi}}}^i$ onto $\mathbf{g}_1(\xi^i)$ (see (3.52)).

Remark: In the literature, the smallest rotation mapping defined in (2.20) of Section 2.1.2 is often alternatively denoted as "rotation without twist". Thus, sometimes it is mistakenly assumed that an intermediate triad field as employed in (3.63) would exhibit a vanishing torsion (see e.g. [90], where the slightly different interpolation scheme (3.78) has been employed). However, according to (3.64), the torsion of the intermediate triad field (3.63) constructed via the SR mapping does not vanish for general curved 3D configurations of the beam centerline. It can easily be shown that the torsion vanishes in the limit of very fine discretizations $l_{ele} := s^{(e),2} - s^{(e),1} \rightarrow 0$. In this limit, the intermediate triad field becomes identical to an elementwise Bishop frame [28] and the following relation holds:

$$\lim_{l_{ele}\rightarrow 0} K_{M_\varphi 1}(\xi) = -\lim_{\xi^I \rightarrow \xi} \frac{\boldsymbol{\kappa}^T \mathbf{g}_1^I}{1+\mathbf{g}_1^T \mathbf{g}_1^I} = -\lim_{\xi^I \rightarrow \xi} \frac{(\mathbf{g}_1(\xi) \times \mathbf{g}_1'(\xi))^T \mathbf{g}_1(\xi^I)}{1+\mathbf{g}_1^T(\xi)\mathbf{g}_1(\xi^I)} = 0. \tag{3.65}$$

However, as verified numerically in Section 3.8.6, a neglecting of $K_{M_\varphi 1}$ in the range of finite element lengths will in general lead to a decline in the spatial convergence rate.

Again, the discrete version of the spin vector field $\delta\boldsymbol{\theta}_h(\xi)$ has to be determined. Following a Petrov-Galerkin approach, the spin vector of (2.91) can be discretized as follows:

$$\delta\boldsymbol{\theta}_h(\xi) = \delta\Theta_{1h}(\xi)\mathbf{g}_1 + \frac{\mathbf{S}(\mathbf{r}')\delta\mathbf{r}'}{||\mathbf{r}'||^2} \quad \text{with} \quad \delta\Theta_{1h}(\xi) = \sum_{i=1}^{n_\Lambda} L^i(\xi)\delta\hat{\Theta}_1^i =: \mathbf{L}_\parallel \delta\hat{\boldsymbol{\Theta}}_1, \tag{3.66}$$

where the interpolation of $\mathbf{r}'$ and $\delta\mathbf{r}'$ follows (3.39) and (3.50). The matrix $\mathbf{L}_\parallel := (L^1, ..., L^{n_\Lambda})$ as well as the vector $\delta\hat{\boldsymbol{\Theta}}_1 := (\delta\hat{\Theta}_1^1, ..., \delta\hat{\Theta}_1^{n_\Lambda})^T$ represent proper assemblies of the Lagrange shape functions L^i and the nodal twist vector components $\delta\hat{\Theta}_1^i$. Alternatively, it can be discretized in a Bubnov-Galerkin manner based on the triad interpolation (3.63). In this case, it reads:

$$\delta\boldsymbol{\theta}_h(\xi) = \delta\Theta_{1h}(\xi)\mathbf{g}_1 + \frac{\mathbf{S}(\mathbf{r}')\delta\mathbf{r}'}{||\mathbf{r}'||^2}, \;\; \delta\Theta_{1h}(\xi) = \delta\Theta_{M_\varphi 1}(\xi) + \delta\varphi_h(\xi), \;\; \delta\varphi_h(\xi) = \sum_{i=1}^{n_\Lambda} L^i(\xi)\delta\varphi^i. \tag{3.67}$$

The spin vector $\delta\boldsymbol{\theta}_h(\xi)$ in (3.67) shall be completely expressed via nodal variations $\delta\hat{\boldsymbol{\Theta}}_1$ and $\delta\hat{\mathbf{d}}$, i.e. via assemblies of nodal primary variables. Thereto, $\delta\Theta_{M_\varphi 1}(\xi)$ and $\delta\varphi^i$ are expressed as

$$\begin{aligned}\delta\Theta_{M_\varphi 1}(\xi) &= \delta\Theta_1^I + \frac{\mathbf{g}_1^T(\mathbf{g}_1^I\times\delta\mathbf{g}_1^I) - \mathbf{g}_1^{IT}(\mathbf{g}_1\times\delta\mathbf{g}_1)}{1+\mathbf{g}_1^T\mathbf{g}_1^I},\\ \delta\varphi^i &= \delta\Theta_1^i - \delta\Theta_{M_\varphi 1}^i = \delta\Theta_1^i - \delta\Theta_1^I - \frac{\mathbf{g}_1^{iT}(\mathbf{g}_1^I\times\delta\mathbf{g}_1^I) - \mathbf{g}_1^{IT}(\mathbf{g}_1^i\times\delta\mathbf{g}_1^i)}{1+\mathbf{g}_1^{iT}\mathbf{g}_1^I},\end{aligned} \tag{3.68}$$

which directly follows from interpolation (3.63). Inserting the relations (3.68) into (3.67) yields:

$$\delta\Theta_{1h}(\xi) = \mathbf{L}_\parallel\delta\hat{\boldsymbol{\Theta}}_1 \underbrace{-\sum_{i=1}^{n_\Lambda} L^i \frac{\mathbf{g}_1^{iT}(\mathbf{g}_1^I\times\delta\mathbf{g}_1^I) - \mathbf{g}_1^{IT}(\mathbf{g}_1^i\times\delta\mathbf{g}_1^i)}{1+\mathbf{g}_1^{iT}\mathbf{g}_1^I} + \frac{\mathbf{g}_1^T(\mathbf{g}_1^I\times\delta\mathbf{g}_1^I) - \mathbf{g}_1^{IT}(\mathbf{g}_1\times\delta\mathbf{g}_1)}{1+\mathbf{g}_1^T\mathbf{g}_1^I}}_{=:\delta\Theta_{1,diff}(\xi)}. \tag{3.69}$$

In (3.69), the notion $\delta\Theta_{1,diff}(\xi)$ has been introduced for the term distinguishing the Petrov-Galerkin variant (3.66) and the Bubnov-Galerkin variant (3.67). In a next step, by making use of the abbreviations $\mathbf{x}_b = \mathbf{x}(\xi_b)$ as well as $\mathbf{x}_a = \mathbf{x}(\xi_a)$ and the following auxiliary relations

$$\mathbf{g}_{1a}^T(\mathbf{g}_{1b}\times\delta\mathbf{g}_{1b}) = \mathbf{g}_{1a}^T(\tilde{\mathbf{t}}_b\times\delta\mathbf{r}_b') = (\mathbf{g}_{1a}\times\tilde{\mathbf{t}}_b)^T\mathbf{H}'(\xi_b)\delta\hat{\mathbf{d}}, \quad \tilde{\mathbf{t}} := \frac{\mathbf{g}_1}{||\mathbf{r}'||} = \frac{\mathbf{r}'}{||\mathbf{r}'||^2}, \tag{3.70}$$

the Bubnov-Galerkin interpolation of the spin vector (3.67) can finally be formulated as:

$$\begin{aligned}\delta\boldsymbol{\theta}_h^T(\xi) &= \delta\hat{\boldsymbol{\Theta}}_1^T\mathbf{v}_{\theta_{\parallel\Theta}} + \delta\hat{\mathbf{d}}^T\mathbf{v}_{\theta_\perp} + \delta\hat{\mathbf{d}}^T\mathbf{v}_{\theta_{\parallel d}} \quad \mathbf{v}_{\theta_{\parallel\Theta}} = \mathbf{L}_\parallel^T\otimes\mathbf{g}_1^T, \;\; \mathbf{v}_{\theta_\perp} = -\mathbf{H}'^T\mathbf{S}(\tilde{\mathbf{t}}),\\ \mathbf{v}_{\theta_{\parallel d}} &= \left(\sum_{i=1}^{n_\Lambda} L^i\,\mathbf{v}_{1i} - \mathbf{v}_1\right)\otimes\mathbf{g}_1^T, \;\; \mathbf{v}_1 = \frac{\mathbf{H}'^T(\xi)(\mathbf{g}_1^I\times\tilde{\mathbf{t}}) - \mathbf{H}'^T(\xi_I)(\mathbf{g}_1\times\tilde{\mathbf{t}}^I)}{1+\mathbf{g}_1^T\mathbf{g}_1^I},\\ \mathbf{v}_{1i} &= \mathbf{v}_1(\xi_i) = \frac{\mathbf{H}'^T(\xi_i)(\mathbf{g}_1^I\times\tilde{\mathbf{t}}^i) - \mathbf{H}'^T(\xi_I)(\mathbf{g}_1^i\times\tilde{\mathbf{t}}^I)}{1+\mathbf{g}_1^{iT}\mathbf{g}_1^I}.\end{aligned} \tag{3.71}$$

Comparing equations (3.66) and (3.71) leads to the conclusion that the difference between the Bubnov-Galerkin and the Petrov-Galerkin variant is completely expressed by one additional term based on the vector $\mathbf{v}_{\theta_{\parallel d}}$. The arc-length derivative of the spin vector reads:

$$\begin{aligned}\delta\boldsymbol{\theta}_h'^T(\xi) &= \delta\hat{\boldsymbol{\Theta}}_1^T\mathbf{v}_{\theta_{\parallel\Theta}}' + \delta\hat{\mathbf{d}}^T\mathbf{v}_{\theta_\perp}' + \delta\hat{\mathbf{d}}^T\mathbf{v}_{\theta_{\parallel d}}',\\ \mathbf{v}_{\theta_{\parallel\Theta}}' &= \mathbf{L}_\parallel'^T\otimes\mathbf{g}_1^T + \mathbf{L}_\parallel^T\otimes\mathbf{g}_1'^T, \;\; \mathbf{v}_{\theta_\perp}' = -\mathbf{H}''^T\mathbf{S}(\tilde{\mathbf{t}}) - \mathbf{H}'^T\mathbf{S}(\tilde{\mathbf{t}}'), \;\; \tilde{\mathbf{t}}' = \frac{\mathbf{r}''}{||\mathbf{r}'||^2} - \frac{2(\mathbf{r}'^T\mathbf{r}'')\mathbf{r}'}{||\mathbf{r}'||^4}\\ \mathbf{v}_{\theta_{\parallel d}}' &= \Big(\sum_{i=1}^{n_\Lambda} L^{i\prime}\,\mathbf{v}_{1i} - \mathbf{v}_1'\Big)\otimes\mathbf{g}_1^T + \Big(\sum_{i=1}^{n_\Lambda} L^i\,\mathbf{v}_{1i} - \mathbf{v}_1\Big)\otimes\mathbf{g}_1'^T,\\ \mathbf{v}_1' &= \frac{\mathbf{H}'^T(\xi)(\mathbf{g}_1^I\times\tilde{\mathbf{t}}') + \mathbf{H}''^T(\xi)(\mathbf{g}_1^I\times\tilde{\mathbf{t}}) - \mathbf{H}'^T(\xi_I)(\mathbf{g}_1'\times\tilde{\mathbf{t}}^I)}{1+\mathbf{g}_1^T\mathbf{g}_1^I} - \frac{(\mathbf{g}_1'^T\mathbf{g}_1^I)\mathbf{v}_1}{1+\mathbf{g}_1^T\mathbf{g}_1^I}.\end{aligned} \tag{3.72}$$

Finally, it shall be investigated if the two variants (3.66) and (3.67) can represent a constant distribution $\delta\boldsymbol{\theta}_h^T(\xi) = \mathbf{w}_0 = \text{const.}$ and $\delta\boldsymbol{\theta}_h'^T(\xi) = \mathbf{0}$, as it is the case for their counterparts (3.57) and (3.59) of Section 3.2.3.3. Thereto, the nodal variations are chosen according to

$$\delta\hat{\mathbf{d}}^j = \mathbf{w}_0\times\hat{\mathbf{d}}^j, \quad \delta\hat{\mathbf{t}}^j = \mathbf{w}_0\times\hat{\mathbf{t}}^j, \quad \delta\hat{\Theta}_1^i = \mathbf{g}_1^T(\xi^i)\mathbf{w}_0 \;\text{ for }\; j=1,2; \quad i=1,...,n_\Lambda. \tag{3.73}$$

Inserting $\delta\hat{\mathbf{d}}^j$ and $\delta\hat{\mathbf{t}}^j$ according to (3.73) into (3.50) gives the desired result $\delta\mathbf{r}_h(\xi)=\mathbf{w}_0\times\mathbf{r}_h(\xi)$. With this result and by inserting (3.73) into the two different spin vector interpolations (3.66) and (3.67), which both fulfill the interpolation property for the tangential spin vector components $\delta\hat{\Theta}_1^i$, it can already be shown that $\mathbf{w}_0$ is at least represented correctly at the element nodes:

$$\delta\boldsymbol{\theta}_h(\xi^i)=(\mathbf{g}_1^T(\xi^i)\mathbf{w}_0)\mathbf{g}_1(\xi^i)+\frac{\mathbf{r}'(\xi^i)\times(\mathbf{w}_0\times\mathbf{r}'(\xi^i))}{||\mathbf{r}'(\xi^i)||^2}=\mathbf{w}_0 \quad \text{for } i=1,...,n_\Lambda. \tag{3.74}$$

Here, the Grassmann identity for double cross-products $\mathbf{a}\times(\mathbf{b}\times\mathbf{c})=(\mathbf{a}^T\mathbf{c})\mathbf{b}-(\mathbf{a}^T\mathbf{b})\mathbf{c}$ for arbitrary vectors $\mathbf{a},\mathbf{b},\mathbf{c}\in\Re^3$ as well as $\mathbf{g}_1=\mathbf{r}'/||\mathbf{r}'||$ have been employed. Next, it will be investigated for the two variants (3.66) and (3.67), if the choice (3.73) leads to a constant spin vector field along the entire beam element. Inserting (3.73) into (3.66) and using the Grassmann identity yields:

$$\begin{aligned}\delta\boldsymbol{\theta}_h(\xi)&=\left(\sum_{i=1}^{n_\Lambda}L^i(\xi)\mathbf{g}_1^T(\xi^i)\mathbf{w}_0\right)\mathbf{g}_1(\xi)+\frac{\mathbf{r}'(\xi)\times(\mathbf{w}_0\times\mathbf{r}'(\xi))}{||\mathbf{r}'(\xi)||^2}\\&=\Bigg[\mathbf{I}_3-\mathbf{g}_1(\xi)\otimes\underbrace{\left(\mathbf{g}_1^T(\xi)-\sum_{i=1}^{n_\Lambda}L^i(\xi)\mathbf{g}_1^T(\xi^i)\right)}_{\neq\mathbf{0}}\Bigg]\mathbf{w}_0\neq\mathbf{w}_0.\end{aligned} \tag{3.75}$$

Thus, the Petrov-Galerkin interpolation (3.66) cannot exactly represent a constant spin vector field. Since the interpolations (3.66) and (3.67) only differ in $\delta\Theta_{1,diff}(\xi)$ as introduced in (3.69), only this term will be investigated in the following. Inserting (3.73) into $\delta\Theta_{1,diff}(\xi)$ yields:

$$\begin{aligned}\delta\Theta_{1,diff}(\xi)&=-\sum_{i=1}^{n_\Lambda}L^i(\xi)(\mathbf{g}_1^T(\xi^i)\mathbf{w}_0)+\underbrace{\sum_{i=1}^{n_\Lambda}L^i(\xi)}_{=1}(\mathbf{g}_1^T(\xi^I)\mathbf{w}_0)+(\mathbf{g}_1^T(\xi)\mathbf{w}_0)-(\mathbf{g}_1^T(\xi^I)\mathbf{w}_0)\\&=\left(\mathbf{g}_1^T(\xi)-\sum_{i=1}^{n_\Lambda}L^i(\xi)\mathbf{g}_1^T(\xi^i)\right)\mathbf{w}_0.\end{aligned} \tag{3.76}$$

Thus, adding the term $\delta\Theta_{1,diff}(\xi)\mathbf{g}_1(\xi)$ to the Petrov-Galerkin variant (3.75) yields the desired result $\delta\boldsymbol{\theta}_h(\xi)=\mathbf{w}_0=$ const. for the Bubnov-Galerkin spin vector interpolation in case the nodal variations are given by (3.73). Alternatively, this result can be obtained by considering that (3.67) represents the consistent variation of the objective triad interpolation (3.63) (see also Section 3.2.4.2). Since this interpolation is objective, the variation of the discrete internal energy has to vanish for infinitesimal rigid body rotations. For an arbitrary stress resultant $\mathbf{m}$, this is only possible if $\delta\boldsymbol{\theta}_h'(\xi)\equiv\mathbf{0}$ and consequently $\delta\boldsymbol{\theta}_h(\xi)\equiv$ const. can be displayed exactly (see also the weak form (2.110)). Recapitulatory, the interpolation (3.67) can represent arbitrary constant spin vector distributions $\mathbf{w}_0$, while for the interpolation (3.66) this is only possible for 2D problems or in the special case $\mathbf{w}_0=\mathbf{0}$. This result will be important in order to investigate the conservation properties of the resulting finite element formulations (see e.g. Sections 3.2.4.5 and 3.4.4). Finally, the field of (multiplicative) rotation vector increments $\Delta\boldsymbol{\theta}_h(\xi)$ and the derivative $\Delta\boldsymbol{\theta}_h'(\xi)$, required for a consistent linearization of the discretized weak form, follow from equations (3.71) and (3.72) by simply replacing the variations $\delta(.)$ by increments $\Delta(.)$. The spin vector considered above is expressed via multiplicative nodal increments $\delta\hat{\Theta}_1^i$ as nodal primary variables. In

case a rotation parametrization of the nodal triads via nodal rotation vectors according to Section 3.2.3.1 is employed, the nodal vector of multiplicative iterative rotation increments given by $\Delta\hat{\boldsymbol{\Theta}}^i = (\Delta\hat{\Theta}^i_1, \Delta\hat{\Theta}^i_2, \Delta\hat{\Theta}^i_3)^T_{\mathbf{g}^i}$ can be directly used for triad update as shown in (3.51). However, if a rotation parametrization of the nodal triads via the SR mapping and nodal relative angles $\hat{\varphi}^i$ according to Section 3.2.3.2 is employed, the rotation vector increments shall be expressed by means of additive increments $\Delta\hat{\varphi}^i$ of the nodal primary variables $\hat{\varphi}^i$ as shown in (3.53). A relation between $\Delta\hat{\Theta}^i_1$ and $\Delta\hat{\varphi}^i$ can easily be derived on the basis of equations (2.27) and (2.28):

$$\Delta\hat{\Theta}^i_1 = \Delta\Theta^i_{M_{\hat{\varphi}}1} + \Delta\hat{\varphi}^i = -\frac{\bar{\mathbf{g}}_1^{iT}\mathbf{S}(\mathbf{g}^i_1)}{1+\mathbf{g}_1^{iT}\bar{\mathbf{g}}^i_1}\frac{\Delta\mathbf{t}^i}{||\mathbf{t}^i||} + \Delta\hat{\varphi}^i, \quad \Delta\mathbf{t}^i = \Delta\mathbf{r}'(\xi^i) = \mathbf{H}'(\xi^i)\Delta\hat{\mathbf{d}}. \tag{3.77}$$

Of course, at the two element boundary nodes, the last term in equation (3.77) can be simplified according to: $\Delta\mathbf{t}^j = \Delta\mathbf{r}'(\xi^j) = \mathbf{H}'(\xi^j)\Delta\hat{\mathbf{d}} = \Delta\hat{\mathbf{t}}^j$ if $j=1$ or $j=2$.

Remark: The triad interpolation scheme presented in this section is very similar to the approach presented by Meier et al. [156] (see Section 3.5.2). There, an intermediate triad field has been constructed in a manner similar to (3.63), but with the choice $\boldsymbol{\Lambda}_r = \boldsymbol{\Lambda}^1_{M_{\hat{\varphi}}}$. While the most essential properties of these two approaches are comparable, there are some slight advantages of the procedure presented here: Choosing a material triad $\boldsymbol{\Lambda}^i$ as reference triad $\boldsymbol{\Lambda}_r$ makes the interpolation scheme independent from the choice of the nodal primary variables (according to Section 3.2.3.1 or according to Section 3.2.3.2). Furthermore, locating the reference triad at the element middle node makes the element formulation symmetric and extends the maximal orientation difference of the material triads at the element boundary nodes that can be represented from $180°$ to $360°$. The latter property results from the maximal orientation difference of $180°$ allowed for two tangent vectors in order to yield a unique SR mapping (see also Section 2.1.2.)

Remark: In Meier et al. [156], also an alternative triad interpolation scheme (see Section 3.5.1 of [156]) has been investigated, which defines an intermediate triad field $\boldsymbol{\Lambda}_{M_\varphi}(\xi)$ directly via the smallest rotation mapping from the intermediate triad field $\bar{\boldsymbol{\Lambda}}_{M_\varphi}(\xi)$ of the last time step onto the current tangent vector field $\mathbf{g}_1(\xi)$ according to:

$$\begin{aligned} &\boldsymbol{\Lambda}_h(\xi) = \exp(\mathbf{S}[\varphi_h(\xi)\mathbf{g}_1(\xi)])\,\boldsymbol{\Lambda}_{M_\varphi}(\xi), && \boldsymbol{\Lambda}_{M_\varphi}(\xi) = \mathrm{sr}(\bar{\boldsymbol{\Lambda}}_{M_\varphi}(\xi), \mathbf{g}_1(\xi)), \\ &\varphi_h(\xi) = \sum_{i=1}^{n_\Lambda} L^i(\xi)\hat{\varphi}^i, && \bar{\boldsymbol{\Lambda}}_{M_\varphi,n+1}(\xi) = \boldsymbol{\Lambda}_{M_\varphi,n}(\xi). \end{aligned} \tag{3.78}$$

At first glance, this interpolation seems to be more straightforward than (3.63) since no nodal triads are required for constructing the intermediate triad field. However, as shown by Meier et al. [156], an interpolation of this kind is neither objective nor path-independent. For geometrically exact Kirchhoff beams, this triad interpolation has e.g. been employed in the recent contributions of Greco et al. [90] and Bauer et al. [19].

3.2.4 Requirements on spatial discretization methods

In this section, important requirements on the applied spatial discretizations of translational and rotational fields will be stated. In the subsequent sections, different beam element formulations will be presented. There, the fulfillment of these requirements will be investigated.

3.2.4.1 Differentiability of discrete fields

The first requirement for spatial discretization methods concerns differentiability. On the one hand, this requirement is related to the weak form of the balance equations: The highest arc-length derivative occurring in the weak form of the Simo-Reissner beam theory is of order one, leading to the requirement of at least C^0-continuous discrete centerline and triad fields. Such a continuity at the element boundaries is provided by the Lagrange centerline interpolation (3.36) as well as by the two discussed approaches of triad interpolation according to Sections 3.2.3.3 and 3.2.3.4. The second arc-length derivative of the beam centerline in the weak form of the balance equations is a distinctive property of the Kirchhoff-Love beam theory and requires the interpolation of the centerline to be at least C^1-continuous as guaranteed by (3.39). On the other hand, the beam-to-beam contact formulations presented in Chapter 4 require the existence of a well-defined tangent vector field along the entire beam centerline, which can conveniently be furnished by the Hermite interpolation (3.39). There exist well-known alternatives that enable the contact treatment based on C^0-continuous centerline representations and a modified/enhanced contact formulation. However, in Chapter 4, it will be shown that the employed Hermite interpolation does not only lead to a simpler finite element formulation - since no extra effort is necessary at locations without unique tangent vector - but that it also leads to advantages in terms of Newton convergence, energy stability as well as integration and discretization errors.

3.2.4.2 Objectivity and path-independence

The properties of objectivity and path-independence play a central role in the development of (geometrically exact) beam finite element formulations. The importance of these properties can be traced back to the nonlinear nature of the configuration space (resulting from the occurrence of large rotations) which complicates the interpolation of rotational quantities. Furthermore, it can be explained by the historic background that none of the early geometrically exact beam formulations fulfilled both of these properties (see [58]). As already explained in [58], the path-independence of the employed discretizations can directly be concluded from the fact that none of these interpolation schemes is based on any history values of interpolated quantities. Only the nodal primary variables depend on history values. However, the corresponding nodal displacements can always arise in a way such that the finite element solution is independent from the actual load path in case the considered physical problem is path-independent. In other words, the arising nodal displacements yield the path-independent solution to the discrete optimization problem (based on a Lagrangian as formulated in Appendix A.2) which is associated with the path-independent physical problem. In the numerical investigations performed at the end of this chapter, this property will be verified. However, throughout this section, the fundamental property of objectivity, i.e. the invariance of the applied deformation measures under rigid body motions, will be investigated. Thereto, a rigid body translation $\mathbf{r}_R$ and a rigid body rotation $\mathbf{\Lambda}_R$ are superimposed onto the beam centerline curve $\mathbf{r}(\xi)$ and the triad field $\mathbf{\Lambda}(\xi)$. A rigid body motion is characterized by constant fields $\mathbf{r}_R$ and $\mathbf{\Lambda}_R$ along the beam, thus $\mathbf{r}_R' \equiv \mathbf{0}$ and $\mathbf{\Lambda}_R' \equiv \mathbf{0}$. In the following, the subscript $(.)^*$ denotes quantities that result from the superimposed rigid body motion, thus $\mathbf{r}^*(\xi) = \mathbf{\Lambda}_R\,(\mathbf{r}(\xi)+\mathbf{r}_R)$ and $\mathbf{\Lambda}^*(\xi) = \mathbf{\Lambda}_R\mathbf{\Lambda}(\xi)$. A formulation is denoted as being objective if such a rigid body motion does not affect the material deformation measures $\mathbf{\Omega}$ and $\mathbf{\Gamma}$. It is straightforward to show that the space-continuous versions of the deformation measures

$\boldsymbol{\Omega}$ and $\boldsymbol{\Gamma}$ are objective, i.e. $\boldsymbol{\Omega}^* = \boldsymbol{\Omega}$ and $\boldsymbol{\Gamma}^* = \boldsymbol{\Gamma}$ (see e.g. [58]). The question of interest is if this objectivity is preserved by the employed spatial discretization schemes. In [58], it is shown that the fulfillment of the following requirement guarantees for the objectivity of a geometrically exact beam formulation based on the Simo-Reissner theory as introduced in Section 2.2:

$$\mathbf{r}_h^*(\xi) \doteq \boldsymbol{\Lambda}_R(\mathbf{r}_h(\xi)+\mathbf{r}_R)\,, \quad \boldsymbol{\Lambda}_h^*(\xi) \doteq \boldsymbol{\Lambda}_R\boldsymbol{\Lambda}_h(\xi) \;\rightarrow\; \boldsymbol{\Omega}_h^* = \boldsymbol{\Omega}_h, \quad \boldsymbol{\Gamma}_h^* = \boldsymbol{\Gamma}_h. \tag{3.79}$$

The following investigations will exclusively be applied to discretized quantities. However, in order to shorten notation, the subscript $(.)_h$ will be omitted throughout this section. First, it shall briefly be shown that the validity of (3.79) is also sufficient for the invariance of the deformation measures (2.95) and (2.97) of the Kirchhoff beam theory. If (3.79) is valid, it follows:

$$\mathbf{r}^{*\prime}(\xi) = \boldsymbol{\Lambda}_R\mathbf{r}'(\xi), \quad \mathbf{r}^{*\prime\prime}(\xi) = \boldsymbol{\Lambda}_R\mathbf{r}''(\xi), \quad \mathbf{g}_i^*(\xi) = \boldsymbol{\Lambda}_R\mathbf{g}_i(\xi), \quad \mathbf{g}_i^{*\prime}(\xi) = \boldsymbol{\Lambda}_R\mathbf{g}_i'(\xi). \tag{3.80}$$

Based on (3.80), the axial tension, the Frenet-Serret curvature vector and the total torsion read:

$$\begin{aligned}
||\mathbf{r}^{*\prime}|| &= \left(\mathbf{r}'^T\boldsymbol{\Lambda}_R^T\boldsymbol{\Lambda}_R\mathbf{r}'\right)^{0.5} = ||\mathbf{r}'|| \quad \rightarrow \quad \epsilon^* = ||\mathbf{r}^{*\prime}|| - 1 = ||\mathbf{r}'|| - 1 = \epsilon, \\
\boldsymbol{\kappa}^* &= \frac{\mathbf{r}^{*\prime}\times\mathbf{r}^{*\prime\prime}}{||\mathbf{r}^{*\prime}||^2} = \frac{\boldsymbol{\Lambda}_R(\mathbf{r}'\times\mathbf{r}'')}{||\mathbf{r}'||^2} = \boldsymbol{\Lambda}_R\boldsymbol{\kappa} \;\rightarrow\; \mathbf{g}_i^{*T}\boldsymbol{\kappa}^* = \mathbf{g}_i^T\boldsymbol{\Lambda}_R^T\boldsymbol{\Lambda}_R\boldsymbol{\kappa} = \mathbf{g}_i^T\boldsymbol{\kappa}, \\
K_1^* &= K_{M1}^* + \varphi^{*\prime} = \mathbf{g}_2^{*\prime T}\mathbf{g}_3^* = \mathbf{g}_2'^T\boldsymbol{\Lambda}_R^T\boldsymbol{\Lambda}_R\mathbf{g}_3 = \mathbf{g}_2'^T\mathbf{g}_3 = K_{M1} + \varphi' = K_1.
\end{aligned} \tag{3.81}$$

The identities $\boldsymbol{\Omega}^* = \boldsymbol{\Omega}$ and $\boldsymbol{\Gamma}^* = \boldsymbol{\Gamma}$ for the original and the rotated deformation measures of (2.95) and (2.97) are a direct consequence of (3.81). Thus, also for the Kirchhoff beam elements, the requirements (3.79) are sufficient in order to ensure objectivity. In the following, the validity of (3.79) will be investigated for the different interpolation strategies of Sections 3.2.2 and 3.2.3.

Objectivity of centerline interpolations: Due to the linear dependence of the interpolated centerline $\mathbf{r}(\xi)$ according to (3.36) or (3.39) on the nodal position (and tangent) vectors, the proof of the first part of (3.79) is trivial and independent from the intermediate triad field:

$$\mathbf{r}^*(\xi) = \boldsymbol{\Lambda}_R(\mathbf{r}(\xi)+\mathbf{r}_R) \quad \text{for} \quad \hat{\mathbf{d}}^{*i} = \boldsymbol{\Lambda}_R\left(\hat{\mathbf{d}}^i+\mathbf{r}_R\right) \quad \text{and} \quad \hat{\mathbf{t}}^{*i} = \boldsymbol{\Lambda}_R\hat{\mathbf{d}}^i. \;\square \tag{3.82}$$

Objectivity of triad interpolation based on local rotation vectors: The fulfillment of (3.79) and consequently of the objectivity requirement of the triad interpolation scheme (3.55) has already been shown in the original work [58]. The interested reader is referred to this reference.

Objectivity of triad interpolation based on "Smallest Rotation" mapping: Based on the relations (3.80)-(3.82) and the strong fulfillment of the Kirchhoff constraint, $\mathbf{g}_1^*(\xi)$ yields:

$$\mathbf{g}_1^*(\xi) = \frac{\mathbf{r}^{*\prime}(\xi)}{||\mathbf{r}^{*\prime}(\xi)||} = \frac{\boldsymbol{\Lambda}_R\mathbf{r}'(\xi)}{||\mathbf{r}'(\xi)||} = \boldsymbol{\Lambda}_R\mathbf{g}_1(\xi). \tag{3.83}$$

Next, the nodal primary variables are chosen such that the nodal triads are also rigidly rotated:

$$\boldsymbol{\Lambda}^{i*} = \boldsymbol{\Lambda}_R\boldsymbol{\Lambda}^i. \tag{3.84}$$

Using (3.83), (3.84) and the definition (2.20) of the smallest rotation mapping, the following relation between the base vectors $\mathbf{g}_{M_\varphi 2}(\xi)$ and $\mathbf{g}_{M_\varphi 3}(\xi)$ of the intermediate triad $\mathbf{\Lambda}_{M_\varphi}(\xi)$ (see (3.63)) and their counterparts $\mathbf{g}^*_{M_\varphi 2}(\xi)$ and $\mathbf{g}^*_{M_\varphi 3}(\xi)$ resulting from the rigid body motion can be derived:

$$\begin{aligned}\mathbf{g}^*_{M_\varphi i}(\xi) &= \mathbf{g}^*_{ri} - \frac{\mathbf{g}^{*T}_{ri}\mathbf{g}^*_1(\xi)}{1+\mathbf{g}^{*T}_{r1}\mathbf{g}^*_1(\xi)}\,(\mathbf{g}^*_1(\xi)+\mathbf{g}^*_{r1}) \\ &= \mathbf{\Lambda}_R\mathbf{g}_{ri} - \frac{\mathbf{g}^T_{ri}\mathbf{\Lambda}^T_R\mathbf{\Lambda}_R\mathbf{g}_1(\xi)}{1+\mathbf{g}^T_{r1}\mathbf{\Lambda}^T_R\mathbf{\Lambda}_R\mathbf{g}_1(\xi)}\,(\mathbf{\Lambda}_R\mathbf{g}_1(\xi)+\mathbf{\Lambda}_R\mathbf{g}_{r1}) = \mathbf{\Lambda}_R\mathbf{g}_{M_\varphi i}(\xi), \quad i=2,3.\end{aligned} \tag{3.85}$$

From (3.83) and (3.85), it can be concluded that the intermediate triad field is rigidly rotated:

$$\mathbf{\Lambda}^*_{M_\varphi}(\xi) = \mathbf{\Lambda}_R\mathbf{\Lambda}_{M_\varphi}(\xi). \tag{3.86}$$

If the transformation rule (2.10) together with (3.83), (3.84) as well as (3.86) are considered, the following result can be derived from the fourth equation of the triad interpolation scheme (3.63):

$$\begin{aligned}&\exp(\mathbf{S}[\varphi^{i*}\mathbf{g}^{i*}_1]) = \exp(\mathbf{S}[\varphi^{i*}\mathbf{\Lambda}_R\mathbf{g}^i_1]) \doteq \mathbf{\Lambda}^{i*}\mathbf{\Lambda}^{*T}_{M_\varphi}(\xi^i) = \\ &\mathbf{\Lambda}_R\mathbf{\Lambda}^i\mathbf{\Lambda}^T_{M_\varphi}(\xi^i)\mathbf{\Lambda}^T_R = \mathbf{\Lambda}_R\exp(\mathbf{S}[\varphi^i\mathbf{g}^i_1])\mathbf{\Lambda}^T_R = \exp(\mathbf{S}[\varphi^i\mathbf{\Lambda}_R\mathbf{g}^i_1]) \quad\rightarrow\quad \varphi^{i*} = \varphi^i.\end{aligned} \tag{3.87}$$

Thus, the interpolation $\varphi(\xi)$ in (3.63) is unchanged by the rigid body motion, i.e. $\varphi^*(\xi) = \varphi(\xi)$. Together with (3.83) and (3.86), the desired result for $\mathbf{\Lambda}^*(\xi)$ as stated in (3.79) can be derived:

$$\begin{aligned}&\mathbf{\Lambda}^*(\xi) = \exp(\mathbf{S}[\varphi^*(\xi)\mathbf{g}^*_1(\xi)])\,\mathbf{\Lambda}^*_{M_\varphi}(\xi) = \exp(\mathbf{S}[\varphi(\xi)\mathbf{\Lambda}_R\mathbf{g}_1(\xi)])\mathbf{\Lambda}_R\mathbf{\Lambda}_{M_\varphi}(\xi) \\ &= \mathbf{\Lambda}_R\exp(\mathbf{S}[\varphi(\xi)\mathbf{g}_1(\xi)])\mathbf{\Lambda}^T_R\mathbf{\Lambda}_R\mathbf{\Lambda}_{M_\varphi}(\xi) = \mathbf{\Lambda}_R\exp(\mathbf{S}[\varphi(\xi)\mathbf{g}_1(\xi)])\mathbf{\Lambda}_{M_\varphi}(\xi) = \mathbf{\Lambda}_R\mathbf{\Lambda}(\xi).\ \square\end{aligned} \tag{3.88}$$

In the reformulations made in (3.88), again use has been made of the auxiliary relation (2.10) and the definition (3.63) of the interpolation scheme. According to (3.88), the triad interpolation proposed in Section 3.2.3.4 fulfills the requirement of objectivity. As mentioned above and derived in the third line of (3.81), the fulfillment of (3.79) guarantees for objective deformation measures, provided that these are consistently derived from the triad interpolation. In order to verify this latter restriction, the two individual contributions K_{M1} and φ' appearing in the third line of (3.81) shall be subject to a closer investigation. Besides the relation $\varphi^*(\xi) = \varphi(\xi) \rightarrow \varphi^{*\prime}(\xi) = \varphi'(\xi)$, which has already been deduced above, also the torsion K^*_{M1} of the intermediate system can be calculated for the configuration resulting from the rigid body motion:

$$K^*_{M_\varphi 1} = -\frac{\boldsymbol{\kappa}^{*T}\mathbf{g}^{I*}_1}{1+\mathbf{g}^{*T}_1\mathbf{g}^{I*}_1} = -\frac{\boldsymbol{\kappa}^T\mathbf{\Lambda}^T_R\mathbf{\Lambda}_R\mathbf{g}^I_1}{1+\mathbf{g}^T_1\mathbf{\Lambda}^T_R\mathbf{\Lambda}_R\mathbf{g}^I_1} = -\frac{\boldsymbol{\kappa}^T\mathbf{g}^I_1}{1+\mathbf{g}^T_1\mathbf{g}^I_1} = K_{M_\varphi 1}.\ \square \tag{3.89}$$

As expected, $K_{M_\varphi 1}$ is not affected by the rigid body motion and, in turn, also the total torsion $K^*_1 = K^*_{M1} + \varphi^{*\prime} = K_{M1} + \varphi' = K_1$ remains unchanged. This result again underlines the objectivity of the proposed interpolation scheme and the consistency of the derived torsion measure.

3.2.4.3 Avoidance of locking effects

It is well-known that purely displacement-based finite elements are prone to locking. Locking effects particularly relevant for geometrically exact beam formulations are shear locking as well

as membrane locking. While shear locking can - by definition - only appear in beam formulations of Simo-Reissner type, membrane locking has already been observed for geometrically linear Kirchhoff beams (see e.g. [6] or [7]). In general, membrane locking refers to the inability of elements to exactly reproduce inextensibility, viz. a vanishing axial strain $\epsilon \equiv 0$, for curved structures such as shells or beams. This behavior can be traced back to a coupling between the kinematic quantities describing the axial tension mode and the curved geometry. While the focus of the subsequent investigations lies on membrane locking, some remarks on shear locking - which are relevant for the Kirchhoff elements of Section 3.5 - are made at the end of this section.

Characterization of locking: One possible definition of locking is the deterioration of the spatial convergence rate in dependence of a certain key parameter. Subsequent investigations will reveal that the element slenderness ratio $\zeta_{ele} := l_{ele}/R$ plays the role of such a key parameter associated with the membrane locking effect of slender beams. One question of interest is how the liability of a finite element formulation to locking can be assessed in a quantitative manner. From a mathematical point of view, this question can be answered by investigating the stability of the employed finite element formulation. For example, for mixed finite element formulations, a stability criterion is given by the well-known Ladyshenskaya-Babuska-Brezzi (LBB) condition, also denoted as inf-sup condition (see [38, 39]). Since a direct and general analysis of such conditions can often be intricate, also numerical inf-sup tests have been suggested in the literature (see e.g. [15, 112]). From a mechanical point of view, locking is typically explained by the occurrence of parasitic stresses, viz. the occurrence of modes in the discrete solution that are not part of the analytical solution. Consequently, the question if an element formulation is prone to locking or not can also be answered by investigating proper representative test cases for parasitic stresses. Besides these *mathematica*l and *mechanical* interpretations of locking, a third, namely a *numerical* perspective (see [130]) can often be helpful. From a numerical point of view, locking can be seen as the consequence of an over-constrained system of equations. As introduced in [103], the so-called constraint ratio allows for some, at least heuristic, evaluation of the locking behavior of a finite element formulation. The constraint ratio is defined as the ratio of the total number of equilibrium equations n_{eq} to the total number of constraint equations $n_{eq,c}$:

$$r := \frac{n_{eq}}{n_{eq,c}}. \tag{3.90}$$

In order to analyze the locking behavior, the constraint ratio r of the continuous problem and the constraint ratio r_h of the discretized problem evaluated for an infinite number of elements have to be compared. The underlying proposition is that elements with $r_h < r$ (especially $r_h < 1$, which means that more constraints than degrees of freedom are present) have a tendency to lock, whereas values $r_h > r$ of the constraint ratio indicate that not enough constraint equations are available in order to reproduce the constraint in an accurate manner. Following this hypothesis, the case $r_h = r$ has to be regarded as the optimal constraint ratio. Throughout this thesis, the relevant locking phenomena will be analyzed based on a mechanical as well as a numerical perspective. The corresponding concepts are applicable in a straightforward manner. In future work, the stability of the most promising element formulations also has to be investigated in a mathematically rigorous manner, either based on direct analysis or on numerical stability tests.

Membrane locking: In the case considered here, the discrete centerline curve $\mathbf{r}(\xi)$ represents the relevant kinematic quantity, which influences the axial tension $\epsilon(\xi) = ||\mathbf{r}'(\xi)|| - 1$ as well as the centerline curvature vector $\boldsymbol{\kappa}$ given in (2.88). In the following, the possibility of exactly representing a constant value $||\mathbf{r}'(\xi)|| \equiv 1$, which is equivalent to a vanishing axial tension, shall be investigated for the Hermite interpolation (3.39). Similar results can also be derived for the Lagrange interpolation (3.36). For simplicity, an initially straight beam element with length $l_{ele} = l$, thus leading to a constant Jacobian $||\mathbf{r}_{0,\xi}(\xi)|| \equiv l/2$, is considered. According to Section 3.2.2.2, the following expression can be stated for the norm of the centerline derivative:

$$||\mathbf{r}'|| = \frac{2}{l}\Big|\Big|\frac{1}{8}\underbrace{\left(-6\hat{\mathbf{d}}^1+6\hat{\mathbf{d}}^2-l\hat{\mathbf{t}}^1-l\hat{\mathbf{t}}^2\right)}_{||()||\doteq 4l}+\frac{\xi}{8}\underbrace{\left(-2l\hat{\mathbf{t}}^1+2l\hat{\mathbf{t}}^2\right)}_{\doteq\mathbf{0}}+\frac{\xi^2}{8}\underbrace{\left(6\hat{\mathbf{d}}^1-6\hat{\mathbf{d}}^2+3l\hat{\mathbf{t}}^1+3l\hat{\mathbf{t}}^2\right)}_{\doteq\mathbf{0}}\Big|\Big|. \quad (3.91)$$

The only solution that fulfills the requirements indicated by the curly brackets in order to exactly display the identity $||\mathbf{r}'(\xi)|| \equiv 1$ along the entire beam element is given by the nodal values

$$\hat{\mathbf{t}}^2 = \hat{\mathbf{t}}^1 =: \mathbf{t} \quad \text{and} \quad \hat{\mathbf{d}}^2 - \hat{\mathbf{d}}^1 = l\mathbf{t} \quad \text{with} \quad ||\mathbf{t}|| = 1. \quad (3.92)$$

The choice (3.92) leads to a constant derivative $\mathbf{r}'(\xi)$ of the centerline position vector field:

$$\mathbf{r}'(\xi) \equiv \mathbf{t} \quad \text{with} \quad ||\mathbf{t}|| = 1. \quad (3.93)$$

Thus, the only possible solution with $||\mathbf{r}'(\xi)|| \equiv 1$ is a straight line. In other words, inextensibility cannot exactly be reproduced for curved beam elements, which is precisely the definition of membrane locking. In order to further investigate the impact of membrane locking on the proposed Kirchhoff beam elements and to develop solution strategies, the following simple example will be investigated: An initially straight beam of length l with square cross-section of side length R ($A = R^2$ and $I_2 = I_3 = R^4/12$), clamped at its left end, loaded with a discrete end-moment at its right end and discretized by one finite element is considered. The external load is chosen as $M = EI_3\pi/(2l)$, which leads to an analytic beam centerline solution for the deformed configuration that is represented by a quarter circle (see Figure 3.4(a)).

In a next step, the energy contributions of the axial tension as well as the bending mode shall be examined. For simplicity, the nodal primary values are chosen such that the nodal position and tangent vectors resulting from the analytic centerline solution are exactly represented (being aware that the "best approximation" solution delivered by the FEM will differ from this choice):

$$\hat{\mathbf{d}}^1 = (0,0,0)^T, \quad \hat{\mathbf{d}}^2 = l\underbrace{(2/\pi,-2/\pi,0)^T}_{=:\tilde{\mathbf{d}}^2}, \quad \hat{\mathbf{t}}^1 = (1,0,0)^T, \quad \hat{\mathbf{t}}^2 = (0,1,0)^T. \quad (3.94)$$

Here, the dimensionless position vector $\tilde{\mathbf{d}}^2$ has been introduced. For the considered plane example of an initially straight beam, the length-specific hyper-elastic energy (2.100) simplifies:

$$\tilde{\Pi}_{int} = \tilde{\Pi}_{int,\epsilon} + \tilde{\Pi}_{int,\kappa} = \frac{1}{2}EA\epsilon^2 + \frac{1}{2}EI_3\kappa^2 \quad \text{with} \quad \kappa = ||\boldsymbol{\kappa}||. \quad (3.95)$$

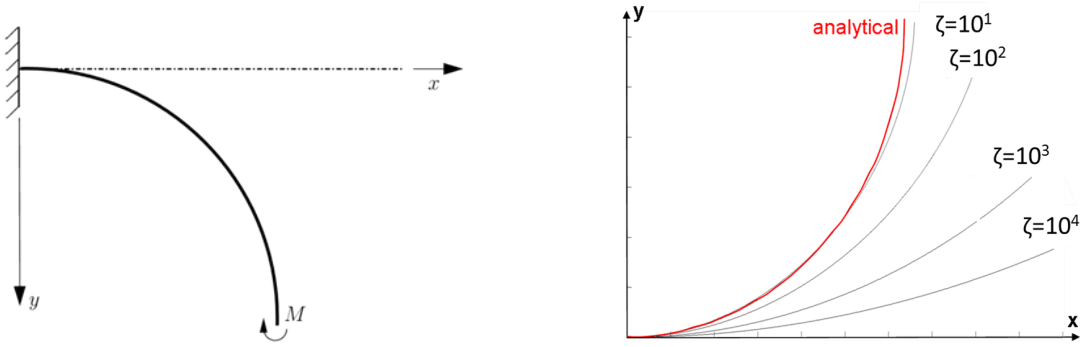

(a) Problem setup and analytic solution.

(b) Numerical solutions for different ζs.

Figure 3.4: Initially straight, clamped beam bent to a quarter circle by a discrete end-moment.

In (3.95), $\tilde{\Pi}_{int,\epsilon}$ and $\tilde{\Pi}_{int,\kappa}$ denote the discrete energy contributions of the axial tension and the bending deformation, respectively. Based on (3.91), the discretized axial tension yields:

$$\epsilon = \frac{1}{4}\left|\left|\left(6\tilde{\mathbf{d}}^2 - \hat{\mathbf{t}}^1 - \hat{\mathbf{t}}^2\right) + 2\xi\left(\hat{\mathbf{t}}^2 - \hat{\mathbf{t}}^1\right) + 3\xi^2\left(-2\tilde{\mathbf{d}}^2 + \hat{\mathbf{t}}^1 + \hat{\mathbf{t}}^2\right)\right|\right| - 1 =: \tilde{\epsilon}. \tag{3.96}$$

In order to simplify the analysis, the approximation $\boldsymbol{\kappa} = ||\mathbf{r}' \times \mathbf{r}''||/||\mathbf{r}'||^2 \approx ||\mathbf{r}' \times \mathbf{r}''||$ for the centerline curvature vector is employed. This approximation is based on the assumption of small axial tension being equivalent to $||(||\mathbf{r}'|| - 1)|| \ll 1$ and makes sense for the considered example whose analytic solution yields $\epsilon \equiv 0$. By inserting the discretization (3.39), $\kappa = ||\boldsymbol{\kappa}||$ yields:

$$\kappa \approx \frac{1}{2l}\underbrace{\left|\left|\left[3\tilde{\mathbf{d}}^2 \times (\hat{\mathbf{t}}^2 - \hat{\mathbf{t}}^1) - \hat{\mathbf{t}}^1 \times \hat{\mathbf{t}}^2\right] + \xi\left[6\tilde{\mathbf{d}}^2 \times (\hat{\mathbf{t}}^2 + \hat{\mathbf{t}}^1)\right] + \xi^2\left[3\tilde{\mathbf{d}}^2 \times (\hat{\mathbf{t}}^2 - \hat{\mathbf{t}}^1) - 3\hat{\mathbf{t}}^1 \times \hat{\mathbf{t}}^2\right]\right|\right|}_{=:2\tilde{\kappa}}. \tag{3.97}$$

In (3.96) and (3.97), the dimensionless quantities $\tilde{\epsilon}$ and $\tilde{\kappa}$ have been introduced. With these deformation measures, the proportion of axial tension energy to bending energy yields:

$$\frac{\tilde{\Pi}_{int,\epsilon}}{\tilde{\Pi}_{int,\kappa}} = 12\left(\frac{l}{R}\right)^2\left(\frac{\tilde{\epsilon}}{\tilde{\kappa}}\right)^2. \tag{3.98}$$

Since the dimensionless proportion $\tilde{\epsilon}/\tilde{\kappa}$ is independent of the problem scaling, the proportion of the parasitic axial strain energy to the bending strain energy scales quadratically with the element slenderness ratio $\zeta_{ele} = l_{ele}/R$. Thus, the key parameter for the considered locking phenomenon is the ratio of the element length $l_{ele} = l$ and the "effective cross-section radius" R. This result is in agreement with the investigations for geometrically linear Kirchhoff elements in [6].

The simulation results (based on the subsequently derived residual (3.122) of the SK-TAN element *without* re-interpolation of the axial strain) for the parameter choice $E = 1.0$, $l = 1000$ and the different slenderness ratios $\zeta = 10$, $\zeta = 100$, $\zeta = 1000$ and $\zeta = 10000$ are presented in Figure 3.4(b). The analytic solution is displayed in red color. Of course, for each slenderness ratio, the external moment has been adapted such that the respective analytic solution is given by a quarter circle. As expected, an increasing slenderness ratio aggravates the locking effect and

leads to a progressively stiff system answer. In Figure 3.5, the numerical results for $||\mathbf{r}'(\xi)||$ calculated via exact Gauss integration are plotted for simulations with different slenderness ratios. With increasing slenderness ratio, the ratio of axial stiffness to bending stiffness increases, which leads to a progressively strong penalization of the parasitic strains. Correspondingly, the FEM solutions show a decrease in the parasitic strains for increasing slenderness ratios. From Figure 3.5, it also gets obvious that the positions of the points fulfilling $||\mathbf{r}'(\xi)|| = 1$ are almost identical for the different slenderness ratios. Since $\mathbf{r}'(\xi)$ is a dimensionless quantity, the evolutions illustrated in Figure 3.5 are independent of the problem scaling and valid whenever a quarter circle is discretized by one finite element. However, with finer discretizations, the arc segment represented by one element shrinks. One can show that the fluctuation of $||\mathbf{r}'(\xi)||$ then decreases.

Remark: Actually, the residual vector stated in (3.122) consists of functional expressions that cannot be integrated exactly by Gauss integration. However, in numerical simulations, the deviations in the results for a number of Gauss points $n_G \geqslant 4$ turned out to be very small as compared to the discretization error. Therefore, the notion "exact integration" will be used whenever four or more Gauss points have been applied.

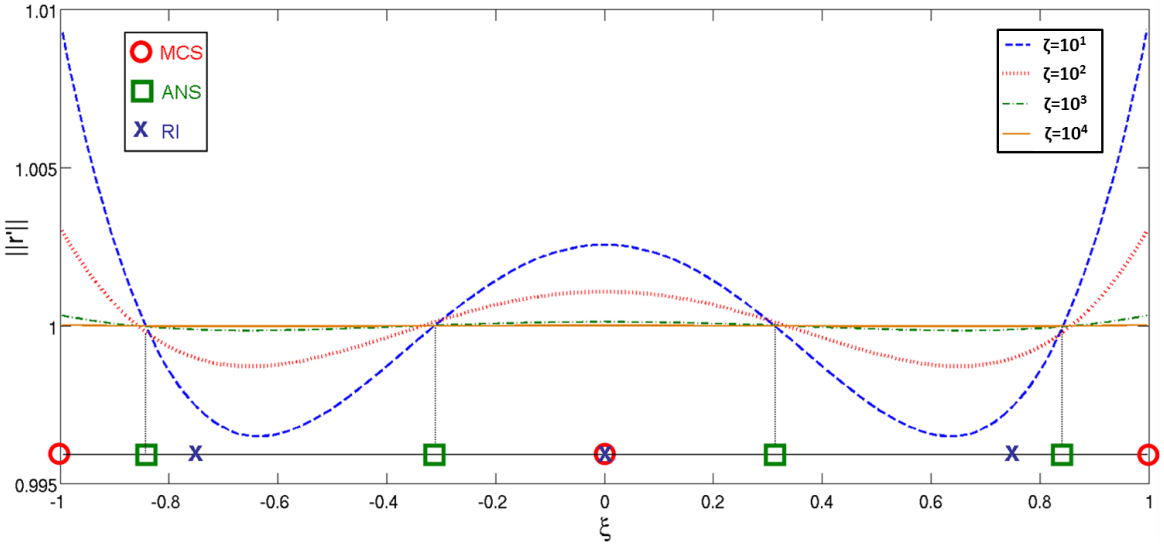

Figure 3.5: Straight beam bent to a quarter circle: Distribution of $||\mathbf{r}'(\xi)||$ within an element.

So far, the effect of membrane locking has been investigated from a mechanical point of view. The axial tension has been identified as the parasitic strain mode occurring in a pure bending test case. In a next, alternative step, this locking effect will be highlighted from a numerical perspective based on the concept of constraint ratios as introduced above. The 2D space-continuous problem of the considered Kirchhoff beam is described by two differential equations, which determine the two components of the centerline curve $\mathbf{r}(s)$, while one constraint equation has to be considered, namely $||\mathbf{r}(s)'|| \equiv 1$. Consequently, the constraint ratio yields $r = 2$ for the continuous problem. The nonlinear system of equations resulting from the spatially discretized 2D beam problem consists of $n_{eq} = 4n_{ele} + 1$ equations after proper Dirichlet conditions have been considered. For curved configurations, the identity $\epsilon \equiv 0$ cannot be represented exactly along the entire element. Thus, the number of constraint equations is given by the number of Gauss points,

at which the scalar constraint $\epsilon = 0$ has to be fulfilled. The choice $n_G = 4$, representing an exact integration (see also the remark above), yields a total of $n_{eq,c} = 4n_{ele}$ constraint equations. The resulting discrete constraint ratio r_h based on the limit $n_{ele} \to \infty$ follows as:

$$r_h = \lim_{n_{ele}\to\infty} \frac{4n_{ele}+1}{4n_{ele}} = 1 < r = 2. \tag{3.99}$$

According to the statements made above, a discrete constraint ratio that is smaller than the continuous one, i.e. $r_h < r$, indicates that the element formulation is prone to membrane locking.

Different solution strategies exist in order to get rid of these locking effects. In the following, the approach of Assumed Natural Strains (ANS, see e.g. [104]), Reduced Integration (RI, see e.g. [168]) and an alternative procedure recently proposed in Meier et al. [157], denoted as Minimally Constrained Strains (MCS), shall be compared. This new method can be characterized as an assumed strain/B-bar approach (see e.g. [205]) and can be derived in a variationally consistent manner. Concretely, the contribution G_ϵ of the axial tension to the weak form is replaced by $G_{\bar{\epsilon}}$:

$$\begin{aligned} G_\epsilon &= \underbrace{\delta \mathbf{r}'^T \mathbf{g}_1}_{\delta\epsilon} EA \underbrace{(||\mathbf{r}'|| - 1)}_{\epsilon} \quad \rightarrow \quad G_{\bar{\epsilon}} = \delta\bar{\epsilon} EA \bar{\epsilon}, \\ \bar{\epsilon}(\xi) &= \sum_{i=1}^{n_{CP}} L^i(\xi)\epsilon(\xi^i), \quad \delta\bar{\epsilon}(\xi) = \sum_{k=1}^{n_{CP}} L^i(\xi)\delta\epsilon(\xi^i), \quad \tilde{\Pi}_{int,\epsilon} = \frac{1}{2} EA \bar{\epsilon}^2. \end{aligned} \tag{3.100}$$

In (3.100), ξ^i denotes the parameter coordinate and n_{CP} the number of Collocation Points (CPs) where the "original" strains are evaluated. Moreover, $L^i(\xi)$ are Lagrange shape functions of polynomial order $n_{CP}-1$. By linearizing the residual (3.100) at the undeformed, straight configuration C_0, one can identify the B-bar structure typical for geometrically linear finite elements:

$$L(G_\epsilon)|_{C_0} := \delta\hat{\mathbf{d}}^T \underbrace{\mathbf{H}'^T \mathbf{t}_0}_{\mathbf{B}^T} K \underbrace{\mathbf{t}_0^T \mathbf{H}'}_{\mathbf{B}} \Delta\hat{\mathbf{d}}, \;\; L(G_{\bar{\epsilon}})|_{C_0} = \delta\hat{\mathbf{d}}^T \bar{\mathbf{B}}^T K \bar{\mathbf{B}} \Delta\hat{\mathbf{d}}, \;\; \bar{\mathbf{B}}(\xi) = \sum_{i=1}^{n_{CP}} L^i(\xi)\mathbf{B}(\xi^i). \tag{3.101}$$

Here, the abbreviation $K := EA$ has been introduced in order to shorten the notation.

> **Remark:** In the last section, it has been shown that the strain field $\epsilon(\xi)$ is objective and path-independent, meaning that the strain field does not change as a consequence of a rigid body motion and that its value at a certain configuration is independent from the deformation path leading to that configuration. Since the assumed strain field $\bar{\epsilon}(\xi)$ represents a pure re-interpolation of the original strain field $\epsilon(\xi^i)$ evaluated at fixed collocation points ξ^i, the former will also fulfill objectivity and path-independence.

Now, the essential question is how the number and locations of the CPs have to be chosen. As indicated by means of the green squares in Figure 3.5, the ANS approach is based on an interpolation of the axial tension values at the CPs with vanishing axial tension. Analogously, the blue crosses indicate the integration points (IPs) of a reduced Gauss integration scheme with three Gauss points. The MCS method, however, applies a third set of CPs, marked with red circles in Figure 3.5. In the following, the special choice of these collocation points will be motivated by the concept of constraint ratios and compared to other approaches. In case of a strain re-interpolation such as given by (3.100), it is sufficient that the constraint of vanishing axial strains

is fulfilled at the collocation points in order to end up with a vanishing axial strain energy. Since the Hermite interpolation (3.39) provides a C^1-continuous centerline curve, the first derivative $\mathbf{r}'$ and consequently also the axial tension ϵ is C^0-continuous at the element boundaries. Thus, exactly one constraint equation $||\mathbf{r}'(\xi^i)|| \doteq 1$ results from each (interior and element boundary) CP with coordinate ξ^i, thus leading to $n_{eq,c} = 2n_{ele}+1$. This, in turn, results in the desired optimal constraint ratio $r_h = \lim_{n_{ele}\to\infty}(4n_{ele}+1)/(2n_{ele}+1) = 2 = r = 2$ in the limit $n_{ele} \to \infty$.

Remark: The chosen CPs are motivated by the strain-continuity: If the axial strains were not C^0-continuous but exhibited jumps at the element boundaries, each element boundary node would provide two constraint equations, one for the previous element (e) and one for the subsequent element $(e+1)$ in the form $||\mathbf{r}'(\xi^{(e)} = 1)|| \doteq 1$ and $||\mathbf{r}'(\xi^{(e+1)} = -1)|| \doteq 1$.

In the following table, the constraint ratios resulting from the three methods ANS, RI and MCS are compared for different choices of the number and locations of the collocation or Gauss points:

-	MCS-3b	MCS-2b	MCS-3i	MCS-2i	ANS-4i	RI-3i	RI-2i
$n_{eq,c}$	$2n_{ele}+1$	$n_{ele}+1$	$3n_{ele}$	$2n_{ele}$	$4n_{ele}$	$3n_{ele}$	$2n_{ele}$
r_h/r	1	2	$2/3$	1	0.5	$2/3$	1

Table 3.1: Quantitative comparison of different "anti-locking" methods.

The index i in Table 3.1 indicates that all collocation or Gauss points lie in the elements interior while variants that are marked by an index b also employ the element boundary nodes $\xi = \pm 1$. According to the statements made above, the variants with $r_h/r = 1$ represent the constraints associated with the axial tension in an optimal manner, whereas variants with $r_h/r < 1$ have a tendency to lock. Consequently, at first glance, the variants MCS-3b, MCS-2i and RI-2i seem to be equally suitable. However, the (heuristic) criterion of constraint ratios is not the only aspect that has to be considered in this context. Additionally, it has to be ensured that the overall system of equations does not become singular as a consequence of too few constraint equations. Thus, the total number of (independent) equations $n_{eq,\kappa+\epsilon}$ resulting from the requirement of exactly displaying a state of constant axial tension (see (3.96)) and constant curvature (see (3.97)) must not be smaller than the total number of unknowns n_{uk}, i.e. $n_{eq,\kappa+\epsilon} \geq n_{uk}$. In this context, the case of a straight beam centerline, where axial tension and bending curvature are decoupled, represents the most critical configuration. In order to investigate this situation, again a discretization based on one finite element with the following nodal degrees of freedom

$$\hat{\mathbf{d}}^1 = \left(d_1^1, d_2^1, 0\right)^T, \quad \hat{\mathbf{d}}^2 = \left(d_1^2, d_2^2, 0\right)^T, \quad \hat{\mathbf{t}}^1 = \left(t_1^1, t_2^1, 0\right)^T, \quad \hat{\mathbf{t}}^2 = \left(t_1^2, t_2^2, 0\right)^T \tag{3.102}$$

shall be considered. Furthermore, the boundary conditions of a clamped end result in:

$$d_1^1 = d_2^1 = 0 \quad \text{and} \quad t_2^1 = 0. \tag{3.103}$$

By considering equation (3.97), it is easy to verify that the fulfillment of the two equations

$$d_2^2 \doteq 0 \quad \text{and} \quad t_2^2 \doteq 0 \tag{3.104}$$

is sufficient in order to reproduce a vanishing curvature along the entire beam element. Thus, in the straight configuration, besides the $n_{eq,dbc} = 3$ equations (3.103) representing the Dirichlet boundary conditions and the $n_{eq,\kappa} = 2$ equations (3.104) representing the state of vanishing

curvature, $n_{eq,c} := n_{eq,\epsilon} = 3$ additional equations stemming from the axial tension mode are necessary in order to ensure $n_{uk} = 8 \doteq n_{eq,\kappa+\epsilon} = n_{eq,dbc} + n_{eq,\kappa} + n_{eq,c}$. Analogously, one can easily show that a discretization with n_{ele} finite elements leads to $n_{eq,\kappa} = 2n_{ele}$ and to a required number of constraint equations according to $n_{eq,c} \doteq n_{uk} - n_{eq,dbc} - n_{eq,\kappa} = 4(n_{ele}+1) - 3 - 2n_{ele} = 2n_{ele}+1$. The variant MCS-3b exactly provides the minimal number $n_{eq,c} \doteq 2n_{ele}+1$ of required constraint equations. For that reason, this method has been denoted as method of Minimally Constrained Strains in Meier et al. [157]. On the contrary, the variants MCS-2i and RI-2i provide too few constraint equations $n_{eq,c} = 2n_{ele} < 2n_{ele}+1$, which leads to a singular tangent stiffness matrix, a result which can be traced back to the existence of a zero-energy mode in the straight configuration. In order to avoid zero-energy modes of this type and a corresponding rank deficient stiffness matrix, a strain re-interpolation based on the $n_{CP} = 3$ CPs with parameter coordinates $\xi^1 = -1$, $\xi^2 = 1$ and $\xi^3 = 0$ as illustrated in Figure 3.5 has to be applied. In a similar manner, an optimal constraint ratio of $r_h = r = 4$ and the avoidance of zero-energy modes can be verified for this choice of collocation points in the general 3D case. In this context, the higher constraint ratio of 3D problems suggests that membrane locking may play a *less* crucial role than in the 2D case. This prediction will be confirmed by subsequent numerical examples.

Remark: Of course, locking would be avoided if the beam element represented the internal energy (3.95) exactly for pure bending states, requiring $n_{uk} = n_{eq,\kappa+\epsilon}$. While for straight configurations, as shown above, this requirement holds, arbitrary curved configurations will yield a slightly over-constrained system of equations with $n_{uk} < n_{eq,\kappa+\epsilon}$ in general. Thus, the state of constant curvature and vanishing axial tension cannot be displayed exactly. However, as the subsequent numerical examples will show, membrane locking can still be avoided. This result is reasonable, since the variant MCS-3i still fulfills the optimal constraint ratio $r/r_h = 1$ for such arbitrarily curved configurations.

Remark: As an alternative to the variant MCS-3i, also a reduced Gauss-Lobatto integration scheme with integration points $\xi^1 = -1$, $\xi^2 = 1$ and $\xi^3 = 0$ could be applied to the axial tension term of the weak form, yielding the same number of constraint equations $n_{eq,c} = 2n_{ele} + 1$ as the MCS approach. However, within this thesis, the MCS method will be preferred due to its arguably more consistent variational basis and the uniform integration scheme resulting for the individual work contributions of the weak form.

All in all, it can be concluded that the choice of the element boundary nodes and the element midpoint as collocation points of the MCS method leads to the minimal possible number of constraint equations $n_{eq,c} = 2 \cdot n_{ele} + 1$ and to an optimal constraint ratio of $r_h = 2 = r$. Consequently, a successful avoidance of locking effects can be expected from this approach. A similar effectiveness can be expected from the application of a reduced Gauss-Lobatto integration scheme with integration points $\xi^1 = -1$, $\xi^2 = 1$ and $\xi^3 = 0$ to the axial tension terms of the weak form. On the contrary, the minimal number of three integration points possible for a reduced Gauss-Legendre integration scheme leads to an increased constraint ratio of $r_h = 3 > r$ and consequently to a suboptimal locking behavior expected for this standard approach. While the methodologies presented so far aim at a reduction of the number of constraint equations, the functional principle of the ANS approach is different: There, parameter coordinates have to be determined where the constraint is already correctly fulfilled by the original element formulation (when applying the latter to a representative test case). These parameter coordinates, indicated by means of green

squares in Figure 3.5, are chosen as CPs for the ANS approach. Such a procedure can avoid locking effects in a manner that is independent of the number of constraint equations. The drawback of the ANS method is that the positions of these points may change for general deformation states in the geometrically nonlinear regime, which might considerably deteriorate the effectiveness of this approach. All these theoretical considerations recommend the proposed MCS approach as method of choice in order to avoid locking effects for the Kirchhoff beam elements considered in this thesis. Subsequently presented numerical results will confirm this prediction.

Shear locking: The phenomenon of shear locking does not lie in the focus of the current work. Nevertheless, the cause for such locking effects shall at least be briefly compared with the situation already discussed for membrane locking. Shear locking denotes the inability of a finite element formulation to exactly represent the state of vanishing shear strains. This situation can again be illustrated by means of the pure bending example from above. It is assumed that the beam centerline is discretized either by Lagrange polynomials according to (3.36) or by Hermite polynomials according to (3.39) and that the triad interpolation is given by (3.55). It has already been stated that the triad interpolation (3.55) can exactly represent constant curvatures. On the other hand, it has been shown that the Hermite centerline representation (and also its counterpart based on Lagrange polynomials) cannot exactly display the state of constant curvature (based on the exact definition in (2.88)). This means, the state $\mathbf{r}'^T(\xi)\mathbf{g}_2(\xi) \equiv \mathbf{r}'^T(\xi)\mathbf{g}_3(\xi) \equiv 0$ cannot be displayed exactly in combination with a constant curvature. In other words, the interpolation spaces applied to the translation (i.e. to the beam centerline) and to the rotation field (i.e. to the triad field) do not optimally match in the sense that a state of constant curvature and vanishing shear deformation cannot be represented exactly. Similar to membrane locking, the ratio of the shear stiffness to the bending stiffness increases quadratically with the beam element slenderness ratio. Thus, again the element slenderness ratio represents the key parameter for this locking effect. Further 2D investigations on membrane and shear locking effects in geometrically linear and nonlinear shear-deformable beam element formulations can also be found in [108].

3.2.4.4 Optimal convergence orders

In order to compare the convergence behavior of different finite element formulations, a well-defined error measure is required. Thereto, the relative L^2-error $||e||^2_{rel}$ according to

$$||e||^2_{rel} = \frac{1}{u_{max}} \sqrt{\frac{1}{l} \int_0^l ||\mathbf{r}_h - \mathbf{r}_{ref}||^2 ds}, \tag{3.105}$$

will be considered in the numerical examples presented in Section 3.8. In the definition (3.105), $\mathbf{r}_h$ denotes the numerical solution of the beam centerline position for a certain discretization. For all examples without analytic solution, the standard choice for the reference solution $\mathbf{r}_{ref}$ is a numerical solution via the WK-TAN element (see Section 3.5.2) employing a spatial discretization that is by a factor of four finer than the finest discretization shown in the corresponding convergence plot. The normalization with the element length l makes the error independent of the length of the considered beam. The second normalization leads to a more convenient relative error measure, which relates the L^2-error to the maximal displacement u_{max} occurring for the

investigated load case. For some examples, also the relative energy error according to

$$||e||_{e,rel} = \frac{\Pi_{int,h} - \Pi_{int,ref}}{\Pi_{int,ref}}, \tag{3.106}$$

will be considered. Here, $\Pi_{int,h}$ and $\Pi_{int,ref}$ represent the (integrated) stored energy functions (see e.g. 2.100) associated with the investigated discretization and with the reference solution. Before the convergence plots of selected numerical examples will be discussed in Section 3.8, the optimal convergence rates in the error norms (3.105) and (3.106) expected for the different beam element formulations shall be briefly discussed. The convergence in the energy error (which is minimized by the finite element method) is dominated by the highest derivative m of the primary variable fields $\mathbf{r}(\xi)$ and $\mathbf{\Lambda}(\xi)$ occurring in the energy (see e.g. 2.100) and consequently in the weak form. Since the employed hyperelastic stored energy functions represent quadratic forms in the derivatives of these primary variable fields, the convergence rate in the energy error yields:

$$||e||_e = \mathcal{O}(h^{2(k-m+1)}). \tag{3.107}$$

Here, $h := l_{ele}$ denotes the element length and k the polynomial degree completely represented by the employed trial functions. In [216], it is shown that the expected convergence rate of the L^2-error for the Ritz solution to a variational problem of order m follows from (3.107) to:

$$||e||^2 = \mathcal{O}(h^{k+1} + h^{2(k-m+1)}). \tag{3.108}$$

The second term in (3.108) represents the dependence of the L^2-error convergence rate on the energy error convergence, reflecting the variational basis of the finite element method. The first term represents the pure polynomial approximation of the trial functions with respect to the considered primary variable field, e.g. $\mathbf{r}(\xi)$. In most cases, e.g. when displacement-based solid elements are considered, the first exponent is smaller than the second one and dominates the overall discretization error. For this reason, only the first term is considered by many authors. However, in the following, it will be shown that especially for Kirchhoff type beam element formulations also the second term of (3.108) is very important. Thereto, the expected convergence rates for Reissner and Kirchhoff type beam element formulations shall briefly be discussed.

Element formulations of Simo-Reissner type: The highest derivative of primary variable fields occurring in the weak form associated with the Simo-Reissner beam problem is $m = 1$. Thus, for the third-order ($k = 3$) Reissner beam elements considered in this work, a convergence rate of six is expected in the energy error (3.106), while the L^2-error is dominated by the first term of (3.108) leading to a corresponding optimal convergence rate of four.

Element formulations of Kirchhoff-Love type: The subsequently proposed Kirchhoff beam elements will lead to the values $k = 3$ for the polynomial degree of the triad functions and $m = 2$ for the highest arc-length derivative in the weak form. Consequently, the convergence of the energy error is of order four. Furthermore, the exponents of both terms in (3.108) take on a value of four, also leading to an expected convergence rate of four for the L^2-error. Thus, also the second, energy-related term has to be considered for Kirchhoff problems of this kind. For that reason, at least polynomials of order three should be chosen as trial functions for Kirchhoff beam elements:

Reducing the polynomial degree from $k=3$ to $k=2$ would lead to an undesirable decline in the L^2-convergence rate from four to two. Thus, the third-order Kirchhoff beam elements proposed in this thesis can be regarded as approximations of the lowest order that is reasonable from a numerical point of view. However, the fact that both exponents of (3.108) take on the same value for $k=3$ also means that in some cases, usually for examples involving complex deformation states and strain distributions, the second, energy-related term might determine the overall error-level. Thus, in order to fully exploit the approximation power of the employed discretization, it can often be sensible to apply trial functions of increased polynomial degree $k>3$. In this case, the first term of (3.108) will determine the overall error level for sufficiently fine discretizations (since the second term converges faster) and consequently the discretization error is exclusively limited by the approximation power of the applied polynomial order. The extension of the proposed Kirchhoff beam element formulations to Hermite interpolations of order $k>3$ is possible in a straightforward manner and will be treated in future research work. In the numerical example of Section 3.8.2, a first proof of concept will be given for such an extension.

Remark: Based on these considerations the question arises, which trial function orders k_{SR} and k_{KL} of element formulations based on the Simo-Reissner and the Kirchhoff-Love theory have to be chosen in subsequent numerical examples in order to perform a reasonable comparison of their convergence behavior. The answer to this question depends on the primary interest, which might either lie in the L^2-convergence or in the energy convergence. Within this thesis, the third-order Kirchhoff elements are compared to third-order Reissner elements, leading to equal L^2-error rates but to different energy error rates. Alternatively, one could also compare the third-order Kirchhoff elements with second-order Reissner elements, leading to equal energy error rates but to different L^2-error rates.

3.2.4.5 Conservation properties

Since the finite element solution converges towards the corresponding analytic solution in the limit of fine spatial discretizations, elementary properties of the analytic solution such as conservation of linear momentum (or rather equilibrium of forces in statics), conservation of angular momentum (or rather equilibrium of moments in statics) as well as conservation of energy (or rather balance of external and internal work for non-conservative problems) will also be fulfilled by the numerical solution for $l_{ele} \to 0$. However, often it is desirable to provide such properties already for arbitrarily rough spatial discretizations. The question, if these properties of the space-continuous problem are inherited by the spatially discretized problem, will later be investigated for the different beam element formulations proposed in subsequent sections. Thereto, use will be made of the fact that the discretized weak form of the balance equations is fulfilled for arbitrary values of the nodal primary variable variations. Choosing the nodal primary variable variations such that the associated virtual motion represents a rigid body translation given by

$$(\delta\mathbf{r}_h(\xi), \delta\boldsymbol{\theta}_h(\xi)) \equiv (\mathbf{u}_0, \mathbf{0}) \in \mathcal{V}_h \quad \text{with} \quad \mathbf{u}_0' = \mathbf{0}, \tag{3.109}$$

allows to investigate the conservation of linear momentum. The special choice (3.109) leads to $\delta\mathbf{r}_h'(\xi) \equiv \delta\boldsymbol{\theta}_h'(\xi) \equiv \mathbf{0}$ and consequently to vanishing contributions of the internal forces and moments in the discrete versions of the weak forms (2.52) and (2.110) associated with the Simo-

Reissner and the Kirchhoff-Love beam theory. Inserting (3.109) into these weak forms yields

$$\dot{\mathbf{l}} = \mathbf{f}_{ext} \quad \text{with} \quad \mathbf{l} := \int_0^l \tilde{\mathbf{l}} ds, \; \mathbf{f}_{ext} = \int_0^l \tilde{\mathbf{f}} ds + \Big[\mathbf{f}_\sigma\Big]_{\Gamma_\sigma}, \tag{3.110}$$

and consequently to exact conservation of linear momentum $\mathbf{l} = \text{const.}$ for the unloaded system, viz. if $\mathbf{f}_{ext} = \mathbf{0}$. Since possible reaction forces at Dirichlet supports are also included in $\mathbf{f}_{ext}$, (3.110) is equivalent to the equilibrium of forces in the static case, i.e. if $\mathbf{l} = \mathbf{0}$. Similarly, a choice of the nodal primary variable variations representing a rigid body rotation given by

$$(\delta\mathbf{r}_h(\xi), \delta\boldsymbol{\theta}_h(\xi)) \equiv (\mathbf{w}_0 \times \mathbf{r}_h(\xi), \mathbf{w}_0) \in \mathcal{V}_h \quad \text{with} \quad \mathbf{w}_0' = \mathbf{0}, \tag{3.111}$$

allows to investigate the angular momentum. Relation (3.111) leads to $\delta\mathbf{r}_h'(\xi) \equiv \mathbf{w}_0 \times \mathbf{r}_h'(\xi)$ as well as $\delta\boldsymbol{\theta}_h'(\xi) \equiv \mathbf{0}$ and consequently again to vanishing contributions of the internal forces and moments in the discrete versions of the weak forms (2.52) and (2.110) associated with the Simo-Reissner and the Kirchhoff-Love beam theory. Inserting (3.111) into these weak forms yields:

$$\dot{\mathbf{h}} = \mathbf{m}_{ext}, \quad \mathbf{h} := \int_0^l (\tilde{\mathbf{h}} + \mathbf{r} \times \tilde{\mathbf{l}}) ds, \; \mathbf{m}_{ext} = \int_0^l \left(\mathbf{r} \times \tilde{\mathbf{f}} + \tilde{\mathbf{m}}\right) ds + \Big[\mathbf{r} \times \mathbf{f}_\sigma + \mathbf{m}_\sigma\Big]_{\Gamma_\sigma}, \tag{3.112}$$

and consequently to exact conservation of angular momentum $\mathbf{h} = \text{const.}$ for the unloaded system, viz. if $\mathbf{m}_{ext} = \mathbf{0}$. Since possible reaction moments at Dirichlet supports are also included in $\mathbf{m}_{ext}$, relation (3.112) is equivalent to the equilibrium of moments in the static case, i.e. if $\mathbf{h} = \mathbf{0}$. Finally, a choice of the nodal primary variable variations according to

$$(\delta\mathbf{r}_h(\xi), \delta\boldsymbol{\theta}_h(\xi)) \equiv (\dot{\mathbf{r}}_h(\xi), \mathbf{w}_h(\xi)) \in \mathcal{V}_h, \tag{3.113}$$

allows to investigate the mechanical power balance. Inserting (3.113) into the discrete versions of the weak forms (2.52) and (2.110) associated with the Simo-Reissner and the Kirchhoff-Love theory, and making use of the relations $\dot{\tilde{\Pi}}_{int} = \mathbf{w}'^T\mathbf{m} + (\dot{\mathbf{r}}' - \mathbf{w} \times \mathbf{r}')^T\mathbf{f}$ and $\dot{\tilde{\Pi}}_{kin} = \mathbf{w}^T\mathbf{c}_\rho\mathbf{a}$ (see Appendix A.2) as well as $\mathbf{w}^T\mathbf{S}(\mathbf{w})\mathbf{c}_\rho\mathbf{w} = 0$, yields the following relation

$$\dot{\Pi}_{kin} + \dot{\Pi}_{int} = P_{ext} \quad \text{with} \quad P_{ext} = \int_0^l \left[\dot{\mathbf{r}}^T\tilde{\mathbf{f}} + \mathbf{w}^T\tilde{\mathbf{m}}\right] ds + \left[\dot{\mathbf{r}}^T\mathbf{f}_\sigma + \mathbf{w}^T\mathbf{m}_\sigma\right]_{\Gamma_\sigma}, \tag{3.114}$$

and consequently to exact energy conservation $\Pi_{kin} + \Pi_{int} = \text{const.}$ for the unloaded system, viz. if $P_{ext} = 0$. So far, it has been shown that exact conservation of linear momentum, angular momentum and energy (see equations (3.110), (3.112) and (3.114)) can be guaranteed for the spatially discretized (and time-continuous) problem, provided the special choices (3.109), (3.111) and (3.113) for the translational and rotational variation fields are contained in the discrete weighting space $\mathcal{V}_h$ of the considered finite element formulation. In the following sections, the question if (3.109), (3.111) and (3.113) can indeed be represented by the discrete weighting functions, will be investigated for the proposed beam element formulations. Of course, also the time integration scheme influences the conservation properties of the fully discrete system considerably. However, the investigation of this factor does not lie within the scope of this thesis.

3.3 Simo-Reissner Beam Element

Throughout this thesis, the Reissner type beam element formulation proposed by Crisfield and Jelenić [58, 116], in the following referred to as CJ element, will serve as reference formulation for numerical comparisons. In the next section, the main constituents required to derive the element residual vector will be presented. In the subsequent Sections 3.3.2 and 3.3.3, this element formulation will be investigated with respect to possible locking effects and the fulfillment of mechanical conservation properties as introduced in Sections 3.2.4.3 and 3.2.4.5.

3.3.1 Element residual vector

In this section, the element residual vector of the CJ element formulation will be derived from the general, space-continuous Simo-Reissner beam problem statement. First, all trial and weighting functions are replaced by their discrete counterparts taken from the finite-dimensional trial subspace $(\mathbf{r}_h, \boldsymbol{\Lambda}_h) \in \mathcal{U}_h \subset \mathcal{U}$ and the weighting subspace $(\delta\mathbf{r}_h, \delta\boldsymbol{\theta}_h) \in \mathcal{V}_h \subset \mathcal{V}$. In the following, n_n-noded elements with the nodal primary variables $\hat{\mathbf{x}}_{CJ} := (\hat{\mathbf{d}}^{1T}, \hat{\boldsymbol{\psi}}^{1T}, ..., \hat{\mathbf{d}}^{n_nT}, \hat{\boldsymbol{\psi}}^{n_nT})^T$ as well as $\delta\hat{\mathbf{x}}_{CJ} := (\delta\hat{\mathbf{d}}^{1T}, \delta\hat{\boldsymbol{\theta}}^{1T}, ..., \delta\hat{\mathbf{d}}^{n_nT}, \delta\hat{\boldsymbol{\theta}}^{n_nT})^T$ are considered. The centerline interpolation is based on Lagrange polynomials of order $n_n - 1$ according to Section (3.2.2.1), i.e. $n_r = n_n$. Furthermore, the rotation field interpolation follows equation (3.55) of Section 3.2.3.3 based on $n_\Lambda = n_n$ nodes, in combination with a Petrov-Galerkin approach for the spin vector discretization given by (3.59). In contrast to the original works [58, 116], here the modified generalized-α scheme of Section (3.1.2) is employed for time integration, thus defining the velocities and accelerations required for the inertia forces $\mathbf{f}_\rho$ and moments $\mathbf{m}_\rho$ as stated in (2.65). Inserting these interpolation schemes as presented in the previous sections into the weak form of the balance equations (2.52) yields the element residual vector contributions $\mathbf{r}_{CJ,\hat{\mathbf{d}}}$ and $\mathbf{r}_{CJ,\hat{\boldsymbol{\theta}}}$ according to

$$\begin{aligned}
\mathbf{r}_{CJ,\hat{\mathbf{d}}} &= \int_{-1}^{1} \left(\mathbf{L}'^T \mathbf{f} - \mathbf{L}^T \tilde{\mathbf{f}}_\rho \right) J(\xi) d\xi - \left[\mathbf{L}^T \mathbf{f}_\sigma \right]_{\Gamma_\sigma}, \\
\mathbf{r}_{CJ,\hat{\boldsymbol{\theta}}} &= \int_{-1}^{1} \left(\mathbf{L}'^T \mathbf{m} - \mathbf{L}^T \mathbf{S}(\mathbf{t}) \mathbf{f} - \mathbf{L}^T \tilde{\mathbf{m}}_\rho \right) J(\xi) d\xi - \left[\mathbf{L}^T \mathbf{m}_\sigma \right]_{\Gamma_\sigma} = \mathbf{0}.
\end{aligned} \tag{3.115}$$

The subscripts $(.)_{\hat{\mathbf{d}}}$ and $(.)_{\hat{\boldsymbol{\theta}}}$ distinguish the residual vector contributions associated with the variations $\delta\hat{\mathbf{d}}^i$ as well as $\delta\hat{\boldsymbol{\theta}}^i$. In contrary to the general form of the residual vector (3.22), the integration interval has already been shifted to the parameter space in (3.115). Within this thesis, a linearization $\Delta\mathbf{r}_{CJ} = \mathbf{k}_{CJ} \Delta\hat{\mathbf{x}}_{CJ}$ based on multiplicative rotation increments $\Delta\hat{\boldsymbol{\theta}}^i$ according to $\Delta\hat{\mathbf{x}}_{CJ} := (\Delta\hat{\mathbf{d}}^{1T}, \Delta\hat{\boldsymbol{\theta}}^{1T}, ..., \Delta\hat{\mathbf{d}}^{n_nT}, \Delta\hat{\boldsymbol{\theta}}^{n_nT})^T$ as given in [116] is employed. For dynamic problems, the element residual vector $\mathbf{r}_{CJ}$ and stiffness matrix $\mathbf{k}_{CJ}$ slightly differ from the original work [116] as consequence of the applied time integration scheme as introduced in Section 3.1.2.

Remark: Similar to the corresponding remark in Section 2.2.3, the discretized material triad field $\boldsymbol{\Lambda}_h(\xi)$ given by (3.55) is fully defined via the local rotation vector field $\boldsymbol{\Phi}_{lh}(\xi)$ (and $\boldsymbol{\Lambda}_r$). Thus, the discrete trial space can formally also be formulated as $(\mathbf{r}_h, \boldsymbol{\Phi}_{lh}) \in \mathcal{U}_h$.

3.3.2 Avoidance of locking effects

In [58] and [116], the authors proposed a reduced Gauss integration scheme in order to avoid shear locking and membrane locking in the range of high beam slenderness ratios. Thereto, n_n–1 integration points have been employed for the integration of the internal force contribution of a n_n-noded element. The effectiveness of this procedure will be verified in subsequent numerical examples and shall be briefly motivated by the following considerations: The 3D Simo-Reissner beam problem is based on $n_{eq}=6$ differential equations (2.49) describing the beam problem and pointwise $n_{eq,c}=3$ constraint equations in order to represent the state of vanishing axial strains $\mathbf{r}'^T\mathbf{g}_1 \equiv 1$ and vanishing shear strains $\mathbf{r}'^T\mathbf{g}_2 \equiv \mathbf{r}'^T\mathbf{g}_3 \equiv 1$ prevalent in a pure bending problem. Consequently, the constraint ratio of the space-continuous problem yields $r=n_{eq}/n_{eq,c}=2$. As consequence of the reduced integration, the discrete number of constraint equations takes on a value of $n_{eq,c}=3\cdot(n_n-1)\cdot n_{ele}$. Given the total number of equations $n_{eq}=6(n_n-1)\cdot n_{ele}$ after application of proper Dirichlet conditions, the constraint ratio of the discrete problem results in:

$$r_h = \lim_{n_{ele}\to\infty} \frac{3\cdot(n_n-1)\cdot n_{ele}}{6(n_n-1)\cdot n_{ele}} = 2 = r. \tag{3.116}$$

Relation (3.116) yields the optimal constraint ratio for this element formulation. Consequently, no locking effects are expected. The investigations made so far can be further refined by realizing that the CJ element can exactly represent the internal energy associated with a 3D pure bending state. In order to understand this statement, the internal energy is split into contributions stemming from torsion and bending and into contributions stemming from axial tension and shear deformation, i.e. $\Pi_{int,h}=\Pi_{int,\Omega,h}+\Pi_{int,\Gamma,h}$. For a pure bending state, the energy contribution $\Pi_{int,\Gamma,h}$ has to vanish, and thus the total internal energy of a pure bending state is given by $\Pi_{int,\Omega,h}$, which in turn is uniquely defined by the curvature vector field $\mathbf{K}_h(\xi)=$ const. In order to represent the desired (constant) distribution of the curvature vector field $\mathbf{K}_h(\xi)$, which is possible for the employed triad interpolation (3.55), only $(n_n-1)\cdot n_{ele}$ of the $(n_n-1)\cdot n_{ele}+1$ nodal rotation vectors have to arise properly, while the one remaining nodal rotation vector describes rotational rigid body modes of the beam. Since the curvature vector field is defined via the arc-length derivative of the rotation field, this one remaining nodal rotation vector can also be interpreted as integration constant resulting from an integration of the curvature field. Additionally, the nodal position vectors have to arise in a way such that $\Pi_{int,\Gamma,h}=0$. While the requirement $\mathbf{\Gamma}_h(\xi)\equiv\mathbf{0}$ cannot be fulfilled exactly for the employed triad trial function spaces, the reduced Gauss integration scheme applied for the CJ element yields a finite number of $3\cdot(n_n-1)\cdot n_{ele}$ constraint equations in order to satisfy $\Pi_{int,\Gamma,h}=0$. Thus, similar to the rotation field, only $(n_n-1)\cdot n_{ele}$ of the $(n_n-1)\cdot n_{ele}+1$ nodal position vectors have to arise properly in order to fulfill these constraint equations, while the one remaining nodal position vector describes translational rigid body modes of the beam. All in all, the $(n_n-1)\cdot n_{ele}+1$ nodal position and rotation vectors can always arise in a way such that a 3D pure bending case can be represented, which consists of a constant curvature vector field $\mathbf{K}_h(\xi)=$const., a vanishing (reduced integrated) energy contribution $\Pi_{int,\Gamma,h}$ of axial and shear strains as well as six superposed rigid body modes. Consequently, the torsion and bending modes represented by $\mathbf{\Omega}_h(\xi)$ as well as the axial tension and shear values at the Gauss points represented by $\mathbf{\Gamma}_h(\xi_{GP})$ are non-competing and no locking effects are expected. These considerations can easily be extended to arbitrary curvature fields $\mathbf{K}_h(\xi)$ that are representable by the employed triad interpolation and arbitrary fields $\mathbf{\Gamma}_h(\xi)$ for which the

term $\mathbf{\Gamma}_h^T \mathbf{\Gamma}_h$ as occurring in the energy integral can be integrated exactly by the reduced Gauss integration scheme. In Sections 3.8.2 and 3.8.3, the expected result that the discrete hyperelastic energies associated with pure bending states in 2D and in 3D can be represented exactly by this beam element formulation will be verified by means of corresponding numerical test cases.

3.3.3 Conservation properties

In the following, it will be investigated if the Simo-Reissner beam element formulation proposed by Crisfield and Jelenić and repeated in the section above can represent the variational fields (3.109), (3.111) and (3.113) required in order to guarantee conservation of linear momentum, conservation of angular momentum as well as conservation of energy. The representation of a rigid body translation (3.109) is trivial and given by the nodal primary variable variations

$$\delta\hat{\mathbf{d}}^i = \mathbf{u}_0, \quad \delta\hat{\boldsymbol{\theta}}^i = \mathbf{0} \;\text{ for }\; i = 1, ..., n_n. \tag{3.117}$$

Similarly, a rigid body rotation (3.111) can be displayed by the nodal primary variable variations

$$\delta\hat{\mathbf{d}}^i = \mathbf{w}_0 \times \hat{\mathbf{d}}^i, \quad \delta\hat{\boldsymbol{\theta}}^i = \mathbf{w}_0 \;\text{ for }\; i = 1, ..., n_n. \tag{3.118}$$

It follows from (3.117) and (3.118), that conservation of linear and angular momentum can be guaranteed. This statement holds for both spin-vector discretizations (3.57) and (3.59) and for the discretized centerline variation (3.38) since all of these variants fulfill proper completeness conditions and can exactly represent a constant vector field $\delta\boldsymbol{\theta} = \mathbf{w}_0$. If the nodal velocities and angular velocities of the time-continuous problem are chosen as primary variable variations

$$\delta\hat{\mathbf{d}}^i = \dot{\mathbf{d}}^i, \quad \delta\hat{\boldsymbol{\theta}}^i = \mathbf{w}^i \;\text{ for }\; i = 1, ..., n_n, \tag{3.119}$$

only the Bubnov-Galerkin variant (3.57) leads (per definition) to an exact representation of the rates of the spatially discretized hyperelastic and kinetic energy and consequently to exact energy conservation for the spatially discretized, time-continuous problem. On the contrary, the Petrov-Galerkin variant (3.59), which has been employed in (3.115), is not variationally consistent with the triad interpolation (3.55) occurring in the discrete internal and kinetic energies. Consequently, the weak form (3.115) does not represent exact energy rates of the spatially discretized problem and cannot guarantee for exact energy conservation.

3.3.4 Motivation for "shear-free" beam theories

Geometrically exact Simo-Reissner beam elements unify high computational efficiency and accuracy. In fields of application where thick beams are involved and the effect of shear deformation is important, they are favorable as compared to the Kirchhoff type counterparts. However, with increasing beam slenderness ratio $\zeta = l/R$, the shear contribution to the overall beam deformation decreases. Furthermore, it is exactly the avoidance of the high stiffness contributions of the shear modes which makes the Kirchhoff-Love theory of thin beams not only applicable, but also favorable in the range of high beam slenderness ratios. In Section 2.3.6, this concept was even pursued one step further by additionally applying inextensibility constraints which allow to also abstain from the high stiffness contributions of the axial tension mode. In this brief section,

possible benefits of applying (inextensible) Kirchhoff type beam elements in the range of high slenderness ratios will be illustrated and, at least approximately, quantified. In Section 3.8, most of these effects will also be investigated and verified by means of numerical examples.

In the following considerations, five sources for potential benefits of applying Kirchhoff type beam element formulations in the range of high beam slenderness ratios, classified with respect to the affected algorithmic building blocks within a finite element code, will be discussed. The first three sources of influence are related to the applied time integration schemes, nonlinear as well as linear solvers. The fourth source for potential benefits considers the possible reduction of discrete system sizes due to the application of Kirchhoff type element formulations. This effect will not only influence one specific, but several algorithmic building blocks. Finally, the fifth aspect concerns the torsion-free beam theory and resulting finite element realization, which can completely abstain from rotational DoFs. This property will again simplify several of the algorithmic building blocks as compared to standard geometrically exact beam element formulations.

1: Improved stability properties of time integration scheme: The dynamic equations of motion of highly slender beams typically result in very stiff Partial Differential Equations (PDEs). With increasing beam slenderness ratio, the ratio between high eigenfrequencies (associated with shear modes), intermediate eigenfrequencies (associated with axial tension and twisting modes) and low eigenfrequencies (associated with bending modes) increases considerably. As a consequence, the stability requirement of explicit time integration schemes leads to very small critical time step sizes as compared to the large oscillation periods of the bending modes. For many practical applications involving highly slender beams, such a fine temporal discretization means a wast of computational resources since often a temporal resolution of the slow bending modes would be sufficient. On the contrary, implicit time integration schemes can provide unconditional stability in the linear regime of small deformations. However, in the large deformation regime, also their performance is considerably deteriorated by such high-frequency contributions. Despite the stability aspect, high-frequent modes are strongly affected by the time discretization error and should be avoided as long as no high-frequency analysis is required by a specific application. In order to illustrate the relevant frequency spectrum, in the following, the proportionalities of the eigenfrequencies resulting from pure bending ω_b, pure torsion ω_t, pure axial tension ω_a and pure shearing ω_s are given for the linearized beam problem:

$$\omega_b \sim \sqrt{\frac{EI}{\rho A l^4}} \sim \frac{1}{\zeta}\sqrt{\frac{E}{\rho l^2}}, \quad \omega_t \sim \sqrt{\frac{GI_T}{\rho I_P l^2}} \sim \sqrt{\frac{E}{\rho l^2}}, \quad \omega_a \sim \sqrt{\frac{E}{\rho l^2}}, \quad \omega_s \sim \sqrt{\frac{GA}{\rho I}} \sim \zeta\sqrt{\frac{E}{\rho l^2}}. \tag{3.120}$$

According to the relations (3.120), the ratio of axial and torsional eigenfrequencies to bending eigenfrequencies increases linearly with increasing slenderness ratio. The ratio of shear eigenfrequencies to bending eigenfrequencies increases quadratically with increasing slenderness ratio. Thus, from a theoretical point of view, the avoidance of shear modes could already improve the numerical behavior considerably. On the other hand, an additional inextensibility constraint only seems to be promising for applications where no torsion is present. In Section 2.4.2, it has been investigated under which circumstances the influence of mechanical torsion on large-deformation beam problems can be neglected. In Section 3.7, a corresponding torsion-free beam element formulation is presented, which would, if combined with an inextensibility constraint,

completely abstain from both modes of the intermediate frequency regime. Of course, it would be desirable to verify these theoretical considerations numerically. Since the numerical examples of Section 3.8 mainly focus on static analysis and only present a brief outlook on possible dynamic investigations, such a numerical verification does not lie within the scope of this thesis.

However, numerical investigations of this question available in the literature confirm the predicted trend: Lang and Arnold [136] investigated the geometrically nonlinear oscillations of a slender beam, which has been modeled by means of the geometrically exact Simo-Reissner theory and discretized via finite differences (see also [137]). In order to measure the influence of high-frequency modes on time integration stability, the maximal possible time step sizes of the applied explicit time integration scheme have been determined for three different mechanical beam models: The full shear-deformable and extensible Simo-Reissner beam formulation, a beam formulation subject to the Kirchhoff constraint of vanishing shear deformation, and a beam formulation subject to the Kirchhoff constraint and an additional inextensibility constraint. For the roughest discretization considered in this numerical experiment and an investigated slenderness ratio of $\zeta = 100$, a rather moderate slenderness ratio as compared to the applications shown in Chapter 4, the time step size could be increased by a factor of ≈ 100 when abstaining from the shear mode and by a further factor of ≈ 5 when additionally abstaining from the axial tension mode. These results indicate the potential of the Kirchhoff type beam formulations. Furthermore, they suggest that the first step towards an extensible Kirchhoff beam formulation might already represent the essential one with respect to numerical savings.

2: Improved performance of (iterative) linear solvers: According to the previous argumentation, a high ratio of the highest to the lowest dynamical eigenfrequencies, measured by the dynamic spectral radius, deteriorates the performance of time integration schemes. In a similar manner, the performance of iterative linear solvers (see e.g. [178] and also Section 3.2.1.4) decreases with increasing ratio of the highest to the lowest eigenvalue of the tangent stiffness matrix, a measure for the condition number of this matrix. Furthermore, even if direct linear solvers are applied, very high condition numbers might considerably limit the achievable numerical accuracy. Especially in dynamics, where such round-off errors tend to accumulate, these effects are undesirable. In the following, the influence of the different deformation modes on the condition number is investigated. For simplicity, the physical units of the considered beam problem are chosen such that the element length lies in the range of $l_{ele} \approx 1$. Since the element length, or better the element Jacobian, typically enters the element formulation with different exponents occurring in different stiffness matrix entries, an element length of $l_{ele} \approx 1$ seems to be a reasonable choice with respect to conditioning. In this case, the resulting contributions to the element stiffness matrix of a Simo-Reissner beam element formulation that has been linearized with respect to the straight configuration, typically obeys the following proportionalities:

$$k_b \sim EI \sim ER^4, \;\; k_t \sim GI_T \sim ER^4, \;\; k_a \sim EA \sim ER^2, \;\; k_s \sim GA \sim ER^2. \tag{3.121}$$

Again, k_b, k_t, k_a and k_s denote stiffness contributions from bending, torsion, axial tension and shear modes. As long as $l_{ele} \approx 1$ holds and the discretization is kept fixed, the cross-section radius R decreases linearly with increasing slenderness ratio ζ. According to (3.121), it is expected that the ratio of high stiffness contributions (from shear and axial tension modes) to low stiffness contributions (from torsional and bending modes), and also the condition number, increases

quadratically with the beam slenderness ratio ζ. Furthermore, it is expected that a pure neglect of shear modes is not sufficient in order to improve conditioning. An additional inextensibility constraint seems to be required in order to get rid of the axial stiffness which scales quadratically with ζ just as the shear mode. In Section 3.8.2, this statement will be confirmed numerically.

3: Improved performance of nonlinear solvers: The relation between the performance of a nonlinear solver, e.g. of a Newton-Raphson scheme, and the conditioning of the considered problem, e.g. measured via the condition number of the tangent stiffness matrix, is not that clear as in the case of linear solvers. Nevertheless, typically, it is at least expected that the performance of tangent-based nonlinear solvers also deteriorates for ill-conditioned problems showing slope differences of the target function by several orders of magnitude when stepping in different directions (e.g. in directions that activate shear and axial tension modes or in directions that activate bending and torsional modes). Interestingly, all numerical examples investigated in this thesis will confirm the trend that the nonlinear solver performance of the considered Reissner type beam element formulations deteriorates drastically with increasing slenderness ratio, while the total number of Newton iterations required by the extensible Kirchhoff type formulations remains almost unchanged. A first numerical investigation performed on an inextensible Kirchhoff formulation suggests that this behavior is not noteworthy influenced, neither in a positive nor in a negative manner, by an additional inextensibility constraint. Thus, with respect to nonlinear solver performance, the avoidance of shear stiffness contributions seems to be the critical factor.

4: Reduced system size: Kirchhoff type beam element formulations do not require any degrees of freedom for representing the mode of shear deformation. It can be expected that, at least as long as no convergence deteriorating phenomena such as locking occur, the same polynomial approximation and the same discretization error level can be guaranteed with fewer degrees of freedom. This prediction will be confirmed by the numerical examples in Section 3.8.

5: Abstaining from algorithmic treatment of large rotations: In Section 3.7, the finite element realization of the torsion-free beam theory presented in Section 2.4.2 will be shown. The perhaps most considerable advantage of this torsion-free element formulation is that it is based on a pure centerline representation. Consequently, the treatment of large rotations and associated degrees of freedom can completely be avoided. Thus, many steps within a nonlinear finite element algorithm that are typically complicated by the presence of large rotations (e.g. spatial interpolation, time discretization, non-symmetric tangent stiffness matrix, non-constant and non-symmetric mass matrix, incremental and iterative configuration updates) are comparable to those of standard solid finite elements for the proposed torsion-free formulation.

These sources of potential benefits were the motivation for the development of shear-free beam element formulations based on the Kirchhoff-Love theory of thin beams. Different realizations of such element formulations, e.g. based on a weak or on a strong enforcement of the Kirchhoff constraint, will be presented in the next sections. The influence of the aforementioned aspects on the resulting numerical behavior will be verified in Section 3.8 by means of proper test cases.

3.4 Kirchhoff-Love Beam Element Based on Strong Constraint Enforcement

In this section, a finite element formulation based on a strong enforcement of the Kirchhoff constraint according to Section 2.3 is presented. In Section 3.4.1, a variant based on nodal triads parametrized via tangent vectors according to Section 3.2.3.2 is investigated. In Section 3.4.2, the transition to a rotation vector-based parametrization as in Section 3.2.3.1 is conducted.

Similar to the CJ element presented in the previous section, also for this element formulation, the avoidance of possible membrane locking effects as well as the fulfillment of mechanical conservation properties will be verified in Sections 3.4.3 and 3.4.4. Finally, Section 3.4.5 evaluates and compares the suitability of the tangent-based and rotation vector-based nodal triad parametrizations for the modeling of practically relevant Dirichlet boundary conditions and joints.

3.4.1 Residual vector of tangent-based parametrization

Similar to the Simo-Reissner case, the trial and weighting functions are replaced by their discrete counterparts taken from the finite-dimensional trial subspace $(\mathbf{r}_h, \varphi_h) \in \mathcal{U}_h \subset \mathcal{U}$ and the weighting subspace $(\delta\mathbf{r}_h, \delta\Theta_{1h}) \in \mathcal{V}_h \subset \mathcal{V}$. In the following, 3-noded elements with the nodal primary variables $\hat{\mathbf{x}}_{TAN} := (\hat{\mathbf{d}}^{1T}, \hat{\mathbf{t}}^{1T}, \hat{\varphi}^1, \hat{\mathbf{d}}^{2T}, \hat{\mathbf{t}}^{2T}, \hat{\varphi}^2, \hat{\varphi}^3)^T$ as well as the set of nodal primary variable variations $\delta\hat{\mathbf{x}}_{TAN} := (\delta\hat{\mathbf{d}}^{1T}, \delta\hat{\mathbf{t}}^{1T}, \delta\hat{\Theta}_1^1, \delta\hat{\mathbf{d}}^{2T}, \delta\hat{\mathbf{t}}^{2T}, \delta\hat{\Theta}_1^2, \delta\hat{\Theta}_1^3)^T$ are considered (see also Figure 3.1(b)). The centerline interpolation is based on Hermite polynomials according to Section 3.2.2.2 and completely defined by the two element boundary nodes. The rotation field interpolation follows equation (3.63). Concretely, a quadratic rotation interpolation based on three nodes, thus also involving the element center node, is considered. Since the orientation of the material triad field is determined by the relative angle $\varphi_h(\xi)$ as well as the tangent vector field $\mathbf{r}_h'(\xi)$, with the latter being a polynomial of order two, this second-order interpolation is sufficient for triad field discretization. In Meier et al. [156], it has been confirmed that a higher interpolation order $n_\Lambda > 3$ will not further improve the approximation quality while a lower interpolation order $n_\Lambda < 3$ will lead to a decline in the convergence rate. The time integration of Section 3.1 is employed, thus leading to the inertia forces $\mathbf{f}_\rho$ and moments $\mathbf{m}_\rho$ given in (2.65).

Inserting these discretizations into (2.110) in combination with the spin vector interpolation of (3.67) yields the residual vector of the Bubnov-Galerkin variant of this element formulation:

$$\begin{aligned}
\mathbf{r}_{SK-TAN+CS,\hat{\mathbf{d}}} = &\int_{-1}^{1} \Big(\Big[\mathbf{v}'_{\theta_\perp} + \mathbf{v}'_{\theta_{\parallel d}} \Big] \mathbf{m} + \mathbf{v}_\epsilon F_1 - \mathbf{H}^T \tilde{\mathbf{f}}_\rho - \Big[\mathbf{v}_{\theta_\perp} + \mathbf{v}_{\theta_{\parallel d}} \Big] \tilde{\mathbf{m}}_\rho \Big) J(\xi) d\xi \\
&- \left[\mathbf{H}^T \mathbf{f}_\sigma + \Big[\mathbf{v}_{\theta_\perp} + \mathbf{v}_{\theta_{\parallel d}} \Big] \mathbf{m}_\sigma \right]_{\Gamma_\sigma}, \qquad (3.122) \\
\mathbf{r}_{SK-TAN+CS,\hat{\boldsymbol{\Theta}}_1} = &\int_{-1}^{1} \Big(\mathbf{v}'_{\theta_{\parallel\Theta}} \mathbf{m} - \mathbf{v}_{\theta_{\parallel\Theta}} \tilde{\mathbf{m}}_\rho \Big) J(\xi) d\xi - \Big[\mathbf{v}_{\theta_{\parallel\Theta}} \mathbf{m}_\sigma \Big]_{\Gamma_\sigma} \quad \text{with} \quad \mathbf{v}_\epsilon = \frac{\mathbf{H}'^T \mathbf{t}}{||\mathbf{t}||}.
\end{aligned}$$

The Bubnov-Galerkin formulation (3.122) can be transformed into a Petrov-Galerkin variant based on the spin interpolation scheme (3.66) by simply omitting the terms $\mathbf{v}_{\theta_{\|d}}$, which yields:

$$\begin{aligned}
\mathbf{r}_{SK-TAN,\hat{\mathbf{d}}} &= \int_{-1}^{1} \left(\mathbf{v}'_{\theta_\perp} \mathbf{m} + \mathbf{v}_\epsilon F_1 - \mathbf{H}^T \tilde{\mathbf{f}}_\rho - \mathbf{v}_{\theta_\perp} \tilde{\mathbf{m}}_\rho \right) J(\xi) d\xi - \left[\mathbf{H}^T \mathbf{f}_\sigma + \mathbf{v}_{\theta_\perp} \mathbf{m}_\sigma \right]_{\Gamma_\sigma}, \\
\mathbf{r}_{SK-TAN,\hat{\boldsymbol{\Theta}}_1} &= \int_{-1}^{1} \left(\mathbf{v}'_{\theta_{\|\Theta}} \mathbf{m} - \mathbf{v}_{\theta_{\|\Theta}} \tilde{\mathbf{m}}_\rho \right) J(\xi) d\xi - \left[\mathbf{v}_{\theta_{\|\Theta}} \mathbf{m}_\sigma \right]_{\Gamma_\sigma} \quad \text{with} \quad \mathbf{v}_\epsilon = \frac{\mathbf{H}'^T \mathbf{t}}{||\mathbf{t}||}.
\end{aligned} \tag{3.123}$$

In Section 3.4.3, it will be shown that the element formulations based on (3.122) or (3.123) tend to membrane locking in the range of high element slenderness ratios and that these locking effects can be avoided by the following re-interpolation of the axial tension ϵ and its variation $\delta\epsilon$ based on the MCS procedure (3.100) and the nodal coordinates $\xi^1 = -1$, $\xi^2 = 1$ and $\xi^3 = 0$:

$$\begin{aligned}
&\bar{F}_1 = EA\bar{\epsilon},\ \bar{\epsilon}(\xi) = \sum_{i=1}^{3} L^i(\xi)\epsilon(\xi^i),\ \delta\bar{\epsilon}(\xi) = \sum_{i=1}^{3} L^i(\xi)\delta\epsilon(\xi^i), \\
&\epsilon(\xi^i) = (||\mathbf{r}'|| - 1)_{(\xi^i)},\ \delta\epsilon(\xi^i) = \left(\delta\mathbf{r}'^T \frac{\mathbf{r}'}{||\mathbf{r}'||} \right)_{(\xi^i)},\ \bar{\mathbf{v}}_\epsilon = \sum_{i=1}^{3} L^i(\xi)\mathbf{v}_\epsilon(\xi^i).
\end{aligned} \tag{3.124}$$

Thus, a locking-free element formulation can be obtained by simply replacing the axial force F_1 by $\bar{F}_1$ and the discrete axial tension variation operator $\mathbf{v}_\epsilon$ by $\bar{\mathbf{v}}_\epsilon$ in the discrete weak form (3.122). The discrete expression for the internal energy associated with the modified axial tension $\bar{\epsilon}$ reads:

$$\tilde{\Pi}_{int,\bar{\epsilon}} = \frac{1}{2} EA\bar{\epsilon}^2. \tag{3.125}$$

Throughout this thesis, the element formulation based on the degrees of freedom $\hat{\mathbf{x}}_{TAN}$ and $\delta\hat{\mathbf{x}}_{TAN}$, the residual (3.123) together with (3.124) will be denoted as SK-TAN element, which stands for "Strong Kirchhoff constraint enforcement combined with nodal triad parametrization via nodal TANgents". Correspondingly, the combination of the degrees of freedom $\hat{\mathbf{x}}_{TAN}$ and $\delta\hat{\mathbf{x}}_{TAN}$, the residual (3.122) together with (3.124) will be denoted as SK-TAN+CS element, referring to the Consistent Spin vector interpolation underlying the Bubnov-Galerkin variant. It has to be emphasized that the replacement of the original axial tension terms with the corresponding MCS terms according to (3.124) is standard for *all* Kirchhoff type beam element formulations considered in this thesis. Only in examples where for comparison reasons also variants without MCS method are considered, an additional abbreviation ...-MCS, e.g. SK-TAN-MCS, is employed. For the SK-TAN element, a linearization $\Delta\mathbf{r}_{SK-TAN} = \mathbf{k}_{SK-TAN}\Delta\hat{\mathbf{x}}_{TAN}$ based on the increment vector $\Delta\hat{\mathbf{x}}_{TAN} := (\Delta\hat{\mathbf{d}}^{1T}, \Delta\hat{\mathbf{t}}^{1T}, \Delta\hat{\varphi}^1, \Delta\hat{\mathbf{d}}^{2T}, \Delta\hat{\mathbf{t}}^{2T}, \Delta\hat{\varphi}^2, \Delta\hat{\varphi}^3)^T$ will be employed (see Appendix B.6). In contrary to the multiplicative rotation variations $\delta\hat{\Theta}_1^i$ occurring in $\delta\mathbf{r}_{SK-TAN}$, the quantities $\Delta\hat{\varphi}^i$ represent additive rotation increments of the nodal relative angles $\hat{\varphi}^i$.

3.4.2 Residual vector of rotation vector-based parametrization

In some scenarios, e.g. applications where complex rotational Dirichlet or coupling conditions should be prescribed at the element boundary, it can be beneficial to employ the alternative

parametrization of the triads $\boldsymbol{\Lambda}^1$ and $\boldsymbol{\Lambda}^2$ at the element boundary nodes via rotation vectors according to Section 3.2.3.1. In such a case, an alternative set of nodal primary variables given by $\hat{\mathbf{x}}_{ROT} := (\hat{\mathbf{d}}^{1T}, \hat{\boldsymbol{\psi}}^{1T}, \hat{t}^1, \hat{\mathbf{d}}^{2T}, \hat{\boldsymbol{\psi}}^{2T}, \hat{t}^2, \hat{\varphi}^3)^T$ and $\delta\hat{\mathbf{x}}_{ROT} := (\delta\hat{\mathbf{d}}^{1T}, \delta\hat{\boldsymbol{\theta}}^{1T}, \delta\hat{t}^1, \delta\hat{\mathbf{d}}^{2T}, \delta\hat{\boldsymbol{\theta}}^{2T}, \delta\hat{t}^2, \delta\hat{\Theta}_1^3)^T$ can be employed. Here, $\hat{\boldsymbol{\psi}}^1$ and $\hat{\boldsymbol{\psi}}^2$ represent the rotation vectors associated with these boundary triads, $\delta\hat{\boldsymbol{\theta}}^1$ and $\delta\hat{\boldsymbol{\theta}}^2$ are the corresponding spin vectors and $\hat{t}^1$ and $\hat{t}^2$ represent the magnitudes of the nodal tangents, i.e. $\hat{t}^1 := ||\mathbf{t}^1||$ and $\hat{t}^2 := ||\mathbf{t}^2||$, as introduced in Section 2.1.2. In this case, the nodal tangents of the Hermite interpolation (3.39) are no primary variables anymore, but have to be expressed by $\hat{\boldsymbol{\psi}}^1$ and $\hat{t}^1$ as well as $\hat{\boldsymbol{\psi}}^2$ and $\hat{t}^2$ (see also the transformation rule (2.30)):

$$\hat{\mathbf{t}}^i \rightarrow \mathbf{t}^i = \hat{t}^i \exp(\mathbf{S}(\hat{\boldsymbol{\psi}}^i))\mathbf{E}_1 \quad \text{for} \quad i = 1, 2. \tag{3.126}$$

The transformation between the variations $(\delta\hat{\boldsymbol{\theta}}^i, \delta\hat{t}^i)$ as well as $(\delta\hat{\mathbf{t}}^i, \delta\hat{\Theta}_1^i)$ for $i = 1, 2$ is given by the transformation matrices $\tilde{\mathbf{T}}$ and $\tilde{\mathbf{T}}^{-1}$ according to (2.30) and leads to the following relation:

$$\delta\hat{\mathbf{x}}_{TAN} = \tilde{\mathbf{T}}_{\hat{\mathbf{x}}}\delta\hat{\mathbf{x}}_{ROT} \quad \text{with} \quad \tilde{\mathbf{T}}_{\hat{\mathbf{x}}} = \begin{pmatrix} \mathbf{I}_3 & & & & & \\ & \tilde{\mathbf{T}}^1 & & & & \\ & & \mathbf{I}_3 & & & \\ & & & \tilde{\mathbf{T}}^2 & & \\ & & & & 1 & \end{pmatrix}, \tag{3.127}$$

where all blank entries are zero. The transformation matrices $\tilde{\mathbf{T}}^1$ and $\tilde{\mathbf{T}}^2$ follow from (2.30) as:

$$\tilde{\mathbf{T}}^1 = \begin{pmatrix} -\hat{t}^1\mathbf{S}(\mathbf{g}_1^1) & \mathbf{g}_1^1 \\ \mathbf{g}_1^{1T} & 0 \end{pmatrix}, \quad \tilde{\mathbf{T}}^2 = \begin{pmatrix} -\hat{t}^2\mathbf{S}(\mathbf{g}_1^2) & \mathbf{g}_1^2 \\ \mathbf{g}_1^{2T} & 0 \end{pmatrix} \quad \text{with} \quad \mathbf{g}_1^i = \exp(\mathbf{S}(\hat{\boldsymbol{\psi}}^i))\mathbf{E}_1. \tag{3.128}$$

In order to simplify the transformation between the two different sets of degrees of freedom considered in Sections 3.4.1 and 3.4.2, the residual contributions $\mathbf{r}_{TAN,\hat{\mathbf{d}}}$ and $\mathbf{r}_{TAN,\hat{\boldsymbol{\Theta}}_1}$ according to (3.122) are slightly reordered and the sought-after residual $\mathbf{r}_{ROT}$ is introduced:

$$\begin{aligned} \mathbf{r}_{TAN,\hat{\mathbf{d}}} &:= (\mathbf{r}_{TAN,\hat{\mathbf{d}}^1}^T, \mathbf{r}_{TAN,\hat{\mathbf{t}}^1}^T, \mathbf{r}_{TAN,\hat{\mathbf{d}}^2}^T, \mathbf{r}_{TAN,\hat{\mathbf{t}}^2}^T)^T, \\ \mathbf{r}_{TAN,\hat{\boldsymbol{\Theta}}_1} &:= (r_{TAN,\hat{\Theta}_1^1}, r_{TAN,\hat{\Theta}_1^2}, r_{TAN,\hat{\Theta}_1^3})^T, \\ \mathbf{r}_{TAN} &:= (\mathbf{r}_{TAN,\hat{\mathbf{d}}^1}^T, \mathbf{r}_{TAN,\hat{\mathbf{t}}^1}^T, r_{TAN,\hat{\Theta}_1^1}, \mathbf{r}_{TAN,\hat{\mathbf{d}}^2}^T, \mathbf{r}_{TAN,\hat{\mathbf{t}}^2}^T, r_{TAN,\hat{\Theta}_1^2}, r_{TAN,\hat{\Theta}_1^3})^T, \\ \mathbf{r}_{ROT} &:= (\mathbf{r}_{ROT,\hat{\mathbf{d}}^1}^T, \mathbf{r}_{ROT,\hat{\boldsymbol{\theta}}^1}^T, r_{ROT,\hat{t}^1}, \mathbf{r}_{ROT,\hat{\mathbf{d}}^2}^T, \mathbf{r}_{ROT,\hat{\boldsymbol{\theta}}^2}^T, r_{ROT,\hat{t}^2}, r_{ROT,\hat{\Theta}_1^3})^T. \end{aligned} \tag{3.129}$$

Inserting relation (3.127) into the virtual work contribution of one beam element yields:

$$\delta\hat{\mathbf{x}}_{TAN}^T\mathbf{r}_{TAN} = \delta\hat{\mathbf{x}}_{ROT}^T\tilde{\mathbf{T}}_{\hat{\mathbf{x}}}^T\mathbf{r}_{TAN} \doteq \delta\hat{\mathbf{x}}_{ROT}^T\mathbf{r}_{ROT} \quad \rightarrow \quad \mathbf{r}_{ROT} = \tilde{\mathbf{T}}_{\hat{\mathbf{x}}}^T\mathbf{r}_{TAN}. \tag{3.130}$$

According to (3.128) and (2.34), the matrix $\tilde{\mathbf{T}}$ and its inverse $\tilde{\mathbf{T}}^{-1}$ are well-defined as long as $\hat{t}^1 \neq 0$ and $\hat{t}^2 \neq 0$. The physical interpretation of $\hat{t}^i = 0$ is that an arc-segment on the beam centerline at the position of the node i with initial length ds would be compressed to a length of zero. Since such a scenario is impossible from a physical point of view, these requirements are assumed to be fulfilled. Consequently, the transformation from the residual vector $\mathbf{r}_{TAN}$ to the residual vector $\mathbf{r}_{ROT}$ is based on a non-singular matrix $\tilde{\mathbf{T}}_{\hat{\mathbf{x}}}$. The same statement holds for the

transformation of the global residual vectors $\mathbf{R}_{TAN}$ and $\mathbf{R}_{ROT}$ via the matrix $\tilde{\mathbf{T}}_{\mathbf{X}}$ which represents an assembly of the element matrices $\tilde{\mathbf{T}}_{\hat{\mathbf{x}}}$. Thus, the following relation can be established:

$$\mathbf{R}_{ROT} = \tilde{\mathbf{T}}_{\mathbf{X}}^{T} \mathbf{R}_{TAN}, \;\; \tilde{\mathbf{T}}_{\mathbf{X}} \in \Re^{n_X} \times \Re^{n_X}, \;\; \text{rank}(\tilde{\mathbf{T}}_{\mathbf{X}}) = n_X \quad \rightarrow \quad \mathbf{R}_{TAN} = \mathbf{0} \Leftrightarrow \mathbf{R}_{ROT} = \mathbf{0}. \tag{3.131}$$

As long as a unique solution of $\mathbf{R}_{TAN} = \mathbf{0}$ exists, the solution of $\mathbf{R}_{ROT} = \mathbf{0}$ will lead to the same mechanical equilibrium configuration. In other words, the pure re-parametrization performed from Section 3.4.1 to Section 3.4.2 will not change the results of the discretized beam problem. Nevertheless, the transformation matrix $\tilde{\mathbf{T}}_{\mathbf{X}}$ depends on the primary degrees of freedom in a non-linear manner and has to be considered within a consistent linearization procedure.

Throughout this thesis, the element formulation based on the degrees of freedom $\hat{\mathbf{x}}_{ROT}$ and $\delta\hat{\mathbf{x}}_{ROT}$, the residual (3.123) transformed via (3.130) together with the MCS approach (3.124) will be denoted as SK-ROT element, which stands for "Strong Kirchhoff constraint enforcement combined with nodal triad parametrization via nodal ROTation vectors". Correspondingly, the combination of the degrees of freedom $\hat{\mathbf{x}}_{ROT}$ and $\delta\hat{\mathbf{x}}_{ROT}$, the residual (3.123) transformed via (3.130) together with the MCS approach (3.124) will be denoted as SK-ROT+CS element. Since the SK-ROT and the SK-TAN element yield the same finite element solution (expressed via different nodal primary variables), the following theoretical investigations concerning locking behavior and conservation properties will only be performed for the SK-TAN element.

For the SK-ROT element, a linearization $\Delta\mathbf{r}_{SK-ROT} = \mathbf{k}_{SK-ROT}\Delta\hat{\mathbf{x}}_{ROT}$ based on the increment vector $\Delta\hat{\mathbf{x}}_{ROT} := (\Delta\hat{\mathbf{d}}^{1T}, \Delta\hat{\boldsymbol{\theta}}^{1T}, \Delta\hat{t}^{1}, \Delta\hat{\mathbf{d}}^{2T}, \Delta\hat{\boldsymbol{\theta}}^{2T}, \Delta\hat{t}^{2}, \Delta\hat{\varphi}^{3})^{T}$ will be employed (see Appendix B.8). Here, $\Delta\hat{\boldsymbol{\theta}}^{1}$ and $\Delta\hat{\boldsymbol{\theta}}^{2}$ are multiplicative increments and $\Delta\hat{\varphi}^{3}$ is an additive increment.

3.4.3 Avoidance of locking effects

In order to investigate the locking behavior of the SK-TAN element, the investigations already made in Section 3.2.4.3 only have to be extended from 2D to the general 3D case. In 3D, the Kirchhoff beam problem is described by $n_{eq} = 4$ differential equations (2.107) and constrained by $n_{eq,c} = 1$ constraint equation in case a pure bending state shall be represented. Thus, the constraint ratio of the space-continuous problem yields $r = n_{eq}/n_{eq,c} = 4$. Due to the employed MCS method, the discrete number of constraint equations takes on a value of $n_{eq,c} = 2n_{ele}+1$. Given the total number of equations $n_{eq} = 8n_{ele}+1$ after application of proper Dirichlet boundary conditions, the constraint ratio of the discrete problem resulting from the SK-TAN element yields:

$$r_h = \lim_{n_{ele}\rightarrow\infty} \frac{8n_{ele}+1}{2n_{ele}+1} = 4 = r. \tag{3.132}$$

Relation (3.132) yields the optimal constraint ratio for this element formulation. Consequently, no locking effects are expected. Furthermore, it has been shown in Section 3.2.4.3 that the requirement of representing a straight beam configuration with arbitrary distribution of $\bar{\epsilon}_h(\xi)$ yields a number of independent equations that equals the number of degrees of freedom. Consequently, such a state can be represented exactly and no zero-energy modes associated with this state have to be expected. The extension of this statement to 3D is straightforward and will not be further

investigated here. Moreover, it has also been shown in Section 3.2.4.3 that the discrete hyperelastic energy $\Pi_{int,h}$ associated with a pure 2D bending case, i.e. $\bar{\epsilon}_h(\xi) \equiv 0$ and $\kappa_h(\xi) \equiv const.$, cannot be displayed exactly by the SK-TAN element. Of course, this statement still holds in 3D. In Sections 3.8.2 and 3.8.3, the expected result that the discrete hyperelastic energies associated with pure bending states in 2D and in 3D cannot be represented in an exact manner by this beam element formulation will be verified by means of corresponding numerical test cases. There, it will also be shown that this property leads to a slightly increased discretization error level as compared to the subsequently derived WK-TAN element. However, this observation is independent from the element slenderness ratio and cannot be attributed to membrane locking.

3.4.4 Conservation properties

Also for the proposed SK-TAN beam element formulation with strong enforcement of the Kirchhoff constraint, it shall be investigated if the variational fields (3.109), (3.111) and (3.113) required for conservation of linear momentum, conservation of angular momentum and conservation of energy can be represented by the corresponding discrete weighting subspace $\mathcal{V}_h$. The representation of a rigid body translation (3.109) is given by the nodal primary variable variations

$$\delta\hat{\mathbf{d}}^j = \mathbf{u}_0, \quad \delta\hat{\mathbf{t}}^j = \mathbf{0}, \quad \delta\hat{\Theta}_1^i = 0 \;\text{ for }\; j = 1,2; \;\text{ and }\; i = 1,2,3. \tag{3.133}$$

This result can be verified by inserting the choices for $\delta\hat{\mathbf{d}}^j$ and $\delta\hat{\mathbf{t}}^j$ made in (3.133) into the Hermite interpolation (3.50) and making use of the first completeness condition in (3.42), which yields $\delta\mathbf{r}_h(\xi) = \mathbf{u}_0 = \text{const.}$ as well as $\delta\mathbf{r}_h'(\xi) = \delta\mathbf{g}_{1h}'(\xi) = \mathbf{0}$. Inserting these relations together with $\delta\hat{\Theta}_1^i = 0$ into either (3.66) or (3.67) results in the required vanishing of the discrete spin vector field. Thus, both the Petrov-Galerkin as well as the Bubnov-Galerkin variant for the spin vector interpolation lead to an exact conservation of the linear momentum. Next, a rigid body rotation (3.111) has to be displayed by the following nodal primary variable variations

$$\delta\hat{\mathbf{d}}^j = \mathbf{w}_0 \times \hat{\mathbf{d}}^j, \quad \delta\hat{\mathbf{t}}^j = \mathbf{w}_0 \times \hat{\mathbf{t}}^j, \quad \delta\hat{\Theta}_1^i = \mathbf{g}_1^T(\xi^i)\mathbf{w}_0 \;\text{ for }\; j = 1,2; \;\text{ and }\; i = 1,2,3. \tag{3.134}$$

Inserting $\delta\hat{\mathbf{d}}^j$ and $\delta\hat{\mathbf{t}}^j$ according to (3.118) into (3.50) gives the desired result $\delta\mathbf{r}_h(\xi) = \mathbf{w}_0 \times \mathbf{r}_h(\xi)$. In Section 3.2.3.4 (see (3.73)-(3.76)), it has already been shown that based on the nodal values (3.134) the Bubnov-Galerkin interpolation (3.67) can exactly represent such a "virtual" rigid body rotation, while the Petrov-Galerkin variant (3.66) cannot. Consequently, only the Bubnov-Galerkin interpolation can guarantee for exact conservation of angular momentum. This result will be confirmed by subsequent numerical examples. Finally, also the conservation of energy will be investigated for the Kirchhoff type element. If the nodal velocities and angular velocities of the time-continuous problem are chosen as nodal primary variable variations according to

$$\delta\hat{\mathbf{d}}^j = \dot{\mathbf{d}}^j, \quad \delta\hat{\mathbf{t}}^j = \dot{\mathbf{t}}^j, \quad \delta\hat{\Theta}_1^i = \mathbf{g}_1^T(\xi^i)\mathbf{w}^i \;\text{ for }\; j = 1,2; \;\text{ and }\; i = 1,2,3, \tag{3.135}$$

again, only the Bubnov-Galerkin variant (3.67) leads (per definition) to an exact representation of the rates of the discrete internal and kinetic energy and consequently to exact energy conservation for the spatially discretized, time-continuous problem. On the contrary, the Petrov-Galerkin variant (3.66) is not variationally consistent with the triad interpolation (3.63) occurring in the discrete energies and will not guarantee for energy conservation of the time-continuous problem.

3.4.5 Modeling of Dirichlet boundary conditions and joints

For many applications, the formulation of proper Dirichlet boundary conditions or kinematic joints between the nodes of different beam elements are of a high practical relevance. This section represents a brief interlude, where the possibility of formulating some basic constraint conditions of this type will be investigated for the SK-ROT and the SK-TAN element.

3.4.5.1 SK-ROT element

Since the SK-ROT element simplifies the formulation of Dirichlet boundary conditions and kinematic constraints in many practically relevant cases, it will be considered first.

Dirichlet boundary conditions: A simple support at element node a can be realized via

$$\hat{\mathbf{d}}^a = \hat{\mathbf{d}}^a_u = \hat{\mathbf{d}}^a_0 \rightarrow \Delta\hat{\mathbf{d}}^a = \mathbf{0}. \tag{3.136}$$

If a clamped end should be modeled, also the cross-section orientation has to be fixed, i.e.

$$\boldsymbol{\Lambda}^a = \boldsymbol{\Lambda}^a_u = \boldsymbol{\Lambda}^a_0, \quad \text{and} \quad \hat{\boldsymbol{\psi}}^a = \hat{\boldsymbol{\psi}}^a_0 \rightarrow \Delta\hat{\boldsymbol{\theta}}^a = \mathbf{0}. \tag{3.137}$$

Thus, the modeling of Dirichlet boundary conditions for the employed translational and rotational degrees of freedom is similar to the procedure of standard finite elements that are purely based on translational degrees of freedom. This procedure can also be extended to inhomogeneous Dirichlet conditions. However, the determination of $\Delta\hat{\boldsymbol{\theta}}^a$ requires special care in this case:

$$\begin{aligned} \hat{\mathbf{d}}^a &= \hat{\mathbf{d}}^a_u(t) \rightarrow \Delta\hat{\mathbf{d}}^a_{n+1} = \hat{\mathbf{d}}^a_{u,n+1} - \hat{\mathbf{d}}^a_{u,n}, \\ \boldsymbol{\Lambda}^a &= \boldsymbol{\Lambda}^a_u(t) \rightarrow \exp(\mathbf{S}(\Delta\hat{\boldsymbol{\theta}}^a_{n+1})) = \boldsymbol{\Lambda}^a_{u,n+1}\boldsymbol{\Lambda}^{aT}_{u,n}. \end{aligned} \tag{3.138}$$

The multiplicative procedure of the second line simplifies to the additive procedure according to the first line if the prescribed rotation is additive, which only holds for 2D rotations.

Connections: In order to realize a simple (moment-free) joint between the two nodes a and b of two connected beam elements, the following procedure is sufficient:

$$\hat{\mathbf{d}}^b = \hat{\mathbf{d}}^a, \quad \delta\hat{\mathbf{d}}^b = \delta\hat{\mathbf{d}}^a, \quad \Delta\hat{\mathbf{d}}^b = \Delta\hat{\mathbf{d}}^a. \tag{3.139}$$

Thus, the degrees of freedom $\hat{\mathbf{d}}^b$ can be eliminated from the global system of equations in a standard manner by simply assembling the corresponding lines and columns of the global residual vector and stiffness matrix properly. A rigid joint between two elements prescribed at the nodes a and b additionally requires to suppress any relative rotation between the associated nodal triads. It is assumed that the corresponding nodal triads differ by some fixed relative rotation $\boldsymbol{\Lambda}_0$:

$$\boldsymbol{\Lambda}^a = \boldsymbol{\Lambda}^b\boldsymbol{\Lambda}_0 \quad \text{or} \quad \exp(\mathbf{S}(\Delta\hat{\boldsymbol{\theta}}^a)) = \exp(\mathbf{S}(\Delta\hat{\boldsymbol{\theta}}^b))\boldsymbol{\Lambda}_0 \quad \rightarrow \quad \boldsymbol{\Lambda}_0 = \boldsymbol{\Lambda}^{bT}\boldsymbol{\Lambda}^a. \tag{3.140}$$

From (3.140), the following relations between the associated rotation increments can be derived:

$$\delta\boldsymbol{\Lambda}^a = \delta\boldsymbol{\Lambda}^b\boldsymbol{\Lambda}_0 \rightarrow \mathbf{S}(\delta\hat{\boldsymbol{\theta}}^a)\boldsymbol{\Lambda}^a = \mathbf{S}(\delta\hat{\boldsymbol{\theta}}^b)\boldsymbol{\Lambda}^b\boldsymbol{\Lambda}_0 \rightarrow \delta\hat{\boldsymbol{\theta}}^b = \delta\hat{\boldsymbol{\theta}}^a \rightarrow \Delta\hat{\boldsymbol{\theta}}^b = \Delta\hat{\boldsymbol{\theta}}^a. \tag{3.141}$$

Consequently, also the rotational degrees of freedom $\hat{\boldsymbol{\psi}}^b$ can be eliminated from the global system of equations in a standard manner by simply assembling the corresponding lines and columns of the global residual vector and of the global stiffness matrix properly.

Remark: It is emphasized that a rigid joint according to (3.140) is formulated via right-translation of the rotation tensor $\boldsymbol{\Lambda}_0$. This is mandatory since a rigid joint represents a fixed orientation difference between material quantities, i.e. a fixed relative rotation with respect to material axes. A left-translation of the rotation tensor $\boldsymbol{\Lambda}_0$ via

$$\boldsymbol{\Lambda}^a = \boldsymbol{\Lambda}_0 \boldsymbol{\Lambda}^b \quad \rightarrow \quad \boldsymbol{\Lambda}_0 = \boldsymbol{\Lambda}^a \boldsymbol{\Lambda}^{bT} \quad \rightarrow \quad \delta\hat{\boldsymbol{\theta}}^b = \boldsymbol{\Lambda}_0^T \delta\hat{\boldsymbol{\theta}}^a \neq \delta\hat{\boldsymbol{\theta}}^a, \tag{3.142}$$

i.e. a fixed relative rotation with respect to spatial axes, has a different physical meaning.

Remark: If additive increments $\Delta\hat{\boldsymbol{\psi}}^a$ and $\Delta\hat{\boldsymbol{\psi}}^b$ of the global rotation vectors $\hat{\boldsymbol{\psi}}^a$ and $\hat{\boldsymbol{\psi}}^b$ instead of the multiplicative increments $\Delta\hat{\boldsymbol{\theta}}^a$ and $\Delta\hat{\boldsymbol{\theta}}^b$ were applied in the linearization process, equation (3.141) would have to be replaced by the relations:

$$\Delta\hat{\boldsymbol{\theta}}^b = \Delta\hat{\boldsymbol{\theta}}^a \quad \rightarrow \quad \Delta\hat{\boldsymbol{\psi}}^b = \mathbf{T}(\hat{\boldsymbol{\psi}}^b)\mathbf{T}^{-1}(\hat{\boldsymbol{\psi}}^a)\Delta\hat{\boldsymbol{\psi}}^a \neq \Delta\hat{\boldsymbol{\psi}}^a. \tag{3.143}$$

If these additive increments are employed, a direct elimination of the degrees of freedom $\hat{\boldsymbol{\psi}}^b$ via a proper assembly of the global stiffness matrix is not possible. Instead, the corresponding columns have to be scaled with the transformation matrix $\mathbf{T}(\hat{\boldsymbol{\psi}}^b)\mathbf{T}^{-1}(\hat{\boldsymbol{\psi}}^a)$.

Remark: Physically reasonable boundary conditions can be completely defined by the cross-section orientation and centroid position. For all of the considered types of boundary conditions, the degrees of freedom $\hat{t}^a$ and $\hat{t}^b$, which are a measure for the axial force at the corresponding nodes, are part of the FEM solution and *must not be prescribed*.

3.4.5.2 SK-TAN element

The treatment of the translational degrees of freedom required for the subsequently considered boundary conditions is identical to the last section and will therefore be omitted here.

Dirichlet boundary conditions: The realization of a simple support at node a is identical to (3.136). In order to model a clamped end, the simplest case of a tangent vector that is parallel to a global base vector, e.g. $\hat{\mathbf{t}}^a \parallel \mathbf{e}_1$, is considered. In this case, (3.136) has to be supplemented by

$$\hat{\mathbf{t}}^{aT}\mathbf{e}_2 = \hat{\mathbf{t}}^{aT}\mathbf{e}_3 = 0 \rightarrow \Delta\hat{t}_2^a = \Delta\hat{t}_3^a = 0 \quad \text{and} \quad \hat{\varphi}^a = \hat{\varphi}_0^a \rightarrow \Delta\hat{\varphi}^a = 0. \tag{3.144}$$

Here, the representation $\hat{\mathbf{t}}^a = \hat{t}_i^a \mathbf{e}_i$ of the tangent vector in the global coordinate frame $\mathbf{e}_i$ has been exploited. In order to prescribe boundary conditions with arbitrary triad orientation, the tangent vector has to be expressed by means of the basis vectors of the prescribed material triad:

$$\boldsymbol{\Lambda}^a = \boldsymbol{\Lambda}_u^a = \boldsymbol{\Lambda}_0^a, \quad \hat{\mathbf{t}}^a = \hat{T}_i^a \mathbf{g}_i^a \rightarrow \hat{T}_2^a = \hat{T}_3^a = 0 \rightarrow \Delta\hat{T}_2^a = \Delta\hat{T}_3^a = 0, \quad \hat{\varphi}^a = \hat{\varphi}_0^a \rightarrow \Delta\hat{\varphi}^a = 0. \tag{3.145}$$

Consequently, in this case, the equations of the linearized residual vector that are associated with the degrees of freedom $\hat{\mathbf{t}}^a$ have to be transformed by the rotation tensor $\boldsymbol{\Lambda}_0^a$ and the Dirichlet conditions have to be formulated in this rotated coordinate system. Again, the first component $\hat{T}_1$

of the tangent vector, when expressed in the material frame, represents its magnitude and must not be prescribed. If the Dirichlet conditions are time-dependent, the prescribed evolution of the relative angle has to be adapted, since now the intermediate frame $\boldsymbol{\Lambda}^a_{M_{\hat{\varphi}}}$ might change in time:

$$\exp(\mathbf{S}[\hat{\varphi}^a_{n+1}\mathbf{g}^a_{1,n+1}]) = \boldsymbol{\Lambda}^a_{n+1}\boldsymbol{\Lambda}^{aT}_{M_{\hat{\varphi}},n+1} \quad \text{with} \quad \boldsymbol{\Lambda}^a_{M_{\hat{\varphi}},n+1} = \mathrm{sr}(\boldsymbol{\Lambda}^a_{M_{\hat{\varphi}},n}, \mathbf{g}^a_{1,n+1}). \tag{3.146}$$

Thus, the required value $\hat{\varphi}^a_{n+1}$ has to be determined in a recursive manner based on the prescribed current triad $\boldsymbol{\Lambda}^a_{n+1}$ and the intermediate triad $\boldsymbol{\Lambda}^a_{M_{\hat{\varphi}},n}$ of the last time step (see also Section 3.2.3.2 for more details). The remaining conditions remain unchanged as compared to (3.145).

Connections: Based on (3.140) and (3.141) and the transformation rules stated in (2.34), the following relations between the sets $(\hat{\mathbf{t}}^a, \hat{\varphi}^a)$ as well as $(\hat{\mathbf{t}}^b, \hat{\varphi}^b)$ can be stated:

$$\begin{aligned}
\delta\hat{\mathbf{t}}^b &= -t^b\mathbf{S}(\mathbf{g}^b_1)\underbrace{\delta\boldsymbol{\theta}^b}_{\doteq\delta\boldsymbol{\theta}^a} + \mathbf{g}^b_1\delta t^b = -t^b\mathbf{S}(\mathbf{g}^b_1)\left(\frac{1}{t^a}\mathbf{S}(\mathbf{g}^a_1)\delta\hat{\mathbf{t}}^a + \mathbf{g}^a_1\delta\hat{\Theta}^a_1\right) + \mathbf{g}^b_1\delta\hat{t}^b, \\
\delta\hat{\Theta}^b_1 &= \mathbf{g}^{bT}_1\underbrace{\delta\boldsymbol{\theta}^b}_{\doteq\delta\boldsymbol{\theta}^a} = \mathbf{g}^{bT}_1\left(\frac{1}{t^a}\mathbf{S}(\mathbf{g}^a_1)\delta\hat{\mathbf{t}}^a + \mathbf{g}^a_1\delta\hat{\Theta}^a_1\right).
\end{aligned} \tag{3.147}$$

Combining these two relations eventually yields the following total transformation matrix:

$$\begin{pmatrix} \delta\hat{\mathbf{t}}^b \\ \delta\hat{\Theta}^b_1 \end{pmatrix} = \underbrace{\begin{pmatrix} -t^b\mathbf{S}(\mathbf{g}^b_1)\frac{1}{t^a}\mathbf{S}(\mathbf{g}^a_1) & -t^b\mathbf{S}(\mathbf{g}^b_1)\mathbf{g}^a_1 & \mathbf{g}^b_1 \\ \mathbf{g}^{bT}_1\frac{1}{t^a}\mathbf{S}(\mathbf{g}^a_1) & \mathbf{g}^{bT}_1\mathbf{g}^a_1 & 0 \end{pmatrix}}_{=:\mathbf{T}_{RC}} \begin{pmatrix} \delta\hat{\mathbf{t}}^a \\ \delta\hat{\Theta}^a_1 \\ \delta\hat{t}^b \end{pmatrix}. \tag{3.148}$$

A similar relation can be formulated for the iterative increments. Since the rotation increments $\Delta\Theta_1 = \mathbf{T}_{\Theta_{M1}\mathbf{t}}\Delta\mathbf{t} + \Delta\varphi$ (see (2.28)) have to be expressed by additive increments $\Delta\mathbf{t}$ and $\Delta\varphi$ for the chosen linearization scheme, an additional transformation is required as compared to (3.148):

$$\begin{pmatrix} \Delta\hat{\mathbf{t}}^b \\ \Delta\hat{\varphi}^b \end{pmatrix} = \tilde{\mathbf{T}}_{RC1}\mathbf{T}_{RC}\tilde{\mathbf{T}}_{RC2}\begin{pmatrix} \Delta\hat{\mathbf{t}}^a \\ \Delta\hat{\varphi}^a_1 \\ \Delta\hat{t}^b \end{pmatrix}, \quad \tilde{\mathbf{T}}_{RC1} := \begin{pmatrix} \mathbf{I}_3 & \mathbf{0} \\ -\mathbf{T}_{\Theta_{M1}\mathbf{t}} & 1 \end{pmatrix}, \quad \tilde{\mathbf{T}}_{RC2} := \begin{pmatrix} \mathbf{I}_3 & \mathbf{0} & \mathbf{0} \\ \mathbf{T}_{\Theta_{M1}\mathbf{t}} & 1 & 0 \\ \mathbf{0}^T & 0 & 1 \end{pmatrix} \tag{3.149}$$

Equations (3.148) and (3.149) allow to transform the corresponding lines and columns of the global residual vector and stiffness matrix properly and to eliminate the degrees of freedom $(\hat{\mathbf{t}}^b, \hat{\varphi}^b)$ from the global system of equations. Again, the magnitude of the tangent vector $\hat{t}^b$ is not influenced by the rigid joint and enters the system of equations as new degree of freedom. While in the last section, the motion of the rigid joint was completely determined by the set $(\hat{\mathbf{d}}^a, \hat{\boldsymbol{\psi}}^a, \hat{t}^a, \hat{t}^b)$, in this section the alternative set $(\hat{\mathbf{d}}^a, \hat{\mathbf{t}}^a, \hat{\varphi}^a, \hat{t}^b)$ is employed.

All in all, it can be concluded that the realization of clamped ends with arbitrary orientation or of rigid joints between beams is simpler for the SK-ROT formulation based on nodal rotation vectors. While for these elements such conditions can directly be formulated in the global coordinate system, the tangent vector-based SK-TAN formulation requires an additional transformation of the corresponding lines and columns of the global residual vector and stiffness matrix. In Section 3.8, some properties of the tangent vector-based variant will become apparent

which make this type of formulation favorable for many applications. If certain element nodes require Dirichlet conditions of the type considered here, it is still possible to apply a hybrid approach, and to replace the nodal tangents by nodal rotation vectors as primary variables only at the specific nodes where such conditions are required. All the results derived so far apply in a similar manner to the WK-TAN and WK-ROT elements that will be derived in the next section.

3.5 Kirchhoff-Love Beam Element Based on Weak Constraint Enforcement

As alternative to the formulation presented in the last section, a beam element will now be presented that is based on the weak fulfillment of the Kirchhoff constraint. Thus, the basis for the intended element formulation is provided by the Simo-Reissner beam theory. In a first step, a finite element formulation of Simo-Reissner type with a C^1-continuous centerline representation will be derived in Section 3.5.1. Afterwards, the Kirchhoff constraint of vanishing shear strains will be enforced in order to end up with a finite element formulation of Kirchhoff type. Following the derivations in Section 2.3.5, the weak statement of the Kirchhoff constraint (2.122) can be realized by introducing spatial interpolations for the Lagrange multipliers and their variations, i.e. by choosing a proper discrete trial space $(\lambda_{\Gamma,2,h}, \lambda_{\Gamma,3,h}) \in \mathcal{U}_{\lambda_{\Gamma 23},h} \in \mathcal{U}_{\lambda_{\Gamma 23}}$ and a proper discrete weighting space $(\delta\lambda_{\Gamma,2,h}, \delta\lambda_{\Gamma,3,h}) \in \mathcal{V}_{\lambda_{\Gamma 23},h} \in \mathcal{V}_{\lambda_{\Gamma 23}}$. The resulting nonlinear system of discrete equilibrium equations will contain discrete Lagrange multipliers as additional nodal primary variables and exhibit a saddle point type structure. In order to avoid the additional effort of solving a large system of equations with saddle point structure, a slightly different approach is chosen here. In the next section, a modified Reissner type beam element formulation will be presented, which is based on a smooth Hermite centerline interpolation and a MCS type strain re-interpolation not only of the axial strain $\epsilon_h(\xi)$ but also of the shear strains $\Gamma_{2,h}(\xi)$ and $\Gamma_{3,h}(\xi)$. Applying the constraint of vanishing shear strains in a consistent manner directly on the re-interpolated strain fields $\bar{\Gamma}_{2,h}(\xi)$ and $\bar{\Gamma}_{3,h}(\xi)$ yields a collocation point type approach of constraint enforcement which does not require additional Lagrange multipliers (see Section 3.5.2). Throughout this thesis, this variant will be preferred since it does neither yield additional Lagrange multiplier degrees of freedom nor a saddle point type system of equations. Also for this element formulation, the two variants concerning nodal rotation parametrization according to Sections 3.2.3.1 and 3.2.3.2 will be presented in the following Sections 3.5.2 and 3.5.3.

3.5.1 Basic formulation: Hermitian Simo-Reissner element

The Reissner type beam element formulated in this section represents an intermediate step in the derivation of a corresponding Kirchhoff type beam element formulation in the next section. The discrete beam centerline representation is given by the Hermite interpolation (3.39) based on the position and tangent vectors $\hat{\mathbf{d}}^i$ and $\hat{\mathbf{t}}^i$ at the two element boundary nodes. Furthermore, the rotation interpolation is given by a three-noded representation of (3.55) with nodal triads $\mathbf{\Lambda}^1$, $\mathbf{\Lambda}^2$ and $\mathbf{\Lambda}^3$. Again, a finite element formulation will be considered on the basis of a strain re-interpolation similar to the MCS method (3.124). While in the Kirchhoff case (3.124), only the axial strain has been treated, now the entire deformation measure $\mathbf{\Gamma}$, consisting of axial and

shear strains, will be re-interpolated in order to avoid membrane as well as shear locking:

$$\bar{\mathbf{\Gamma}}(\xi) = \sum_{i=1}^{3} L^i(\xi)\mathbf{\Gamma}(\xi^i), \quad \delta\bar{\mathbf{\Gamma}}(\xi) = \sum_{i=1}^{3} L^i(\xi)\delta\mathbf{\Gamma}(\xi^i) \quad \xi^1 = -1, \xi^2 = 1, \xi^3 = 0. \tag{3.150}$$

On the basis of (3.150), also the hyper-elastic stored energy function $\tilde{\Pi}_{int}(\mathbf{\Omega}, \mathbf{\Gamma})$ given in (2.58) has to be replaced by $\tilde{\Pi}_{int}(\mathbf{\Omega}, \bar{\mathbf{\Gamma}})$. Now, one can introduce the following set of degrees of freedom $\hat{\mathbf{x}}_{HSR} := (\hat{\mathbf{d}}^{1T}, \hat{\mathbf{t}}^{1T}, \hat{\boldsymbol{\psi}}^{1T}, \hat{\mathbf{d}}^{2T}, \hat{\mathbf{t}}^{2T}, \hat{\boldsymbol{\psi}}^{2T}, \hat{\boldsymbol{\psi}}^{3T})^T$ as well as the associated variation vector $\delta\hat{\mathbf{x}}_{HSR} := (\delta\hat{\mathbf{d}}^{1T}, \delta\hat{\mathbf{t}}^{1T}, \delta\hat{\boldsymbol{\theta}}^{1T}, \delta\hat{\mathbf{d}}^{2T}, \delta\hat{\mathbf{t}}^{2T}, \delta\hat{\boldsymbol{\theta}}^{2T}, \delta\hat{\boldsymbol{\theta}}^{3T})^T$. Based on the weak form (2.52), (3.150), the definitions (2.55) and (2.57), (3.39) and (3.55), the element residual vector can be derived as:

$$\begin{aligned}
\mathbf{r}_{HSR,\hat{\mathbf{d}}} &= \int_{-1}^{1} \left(\mathbf{v}_{\mathbf{\Gamma}_1} \bar{\mathbf{F}} - \mathbf{L}^T \tilde{\mathbf{f}}_\rho \right) J(\xi) d\xi - \left[\mathbf{L}^T \mathbf{f}_\sigma \right]_{\Gamma_\sigma} \\
\mathbf{r}_{HSR,\hat{\boldsymbol{\theta}}} &= \int_{-1}^{1} \left(\mathbf{L}'^T \mathbf{m} + \mathbf{v}_{\mathbf{\Gamma}_2} \bar{\mathbf{F}} - \mathbf{L}^T \tilde{\mathbf{m}}_\rho \right) J(\xi) d\xi - \left[\mathbf{L}^T \mathbf{m}_\sigma \right]_{\Gamma_\sigma} = \mathbf{0}, \\
\bar{\mathbf{F}} &= \mathbf{C}_F \bar{\mathbf{\Gamma}}, \quad \mathbf{v}_{\mathbf{\Gamma}_1} = \sum_{i=1}^{3} L^i(\xi) \left(\mathbf{H}'^T \mathbf{\Lambda} \right)_{(\xi^i)}, \quad \mathbf{v}_{\mathbf{\Gamma}_2} = \sum_{i=1}^{3} L^i(\xi) \left(\mathbf{L}^T \mathbf{S}(\mathbf{t}) \mathbf{\Lambda} \right)_{(\xi^i)}.
\end{aligned} \tag{3.151}$$

This element formulation could e.g. be applied to problems of thick beams with higher continuity requirements (e.g. beam-to-beam contact). However, within this thesis, the formulation (3.151) solely represents an intermediate step in the derivation of Kirchhoff beam elements with weak enforcement of the Kirchhoff constraint as performed in the next two sections.

3.5.2 Residual vector of tangent-based parametrization

Due to (3.150), the general weak constraint enforcement of Section (2.3.5) can be simplified:

$$\bar{\Gamma}_2(\xi) \equiv \bar{\Gamma}_3(\xi) \equiv 0 \;\rightarrow\; \mathbf{r}'^T(\xi^i)\mathbf{g_2}(\xi^i) \doteq \mathbf{r}'^T(\xi^i)\mathbf{g_3}(\xi^i) \doteq 0 \quad \text{for} \quad i = 1, 2, 3. \tag{3.152}$$

According to (3.152), the Kirchhoff constraint is exactly fulfilled at the three collocation points. In the following, a parametrization is chosen that directly fulfills these constraints without the need for additional Lagrange multipliers. Thereto, the same set of nodal degrees of freedom $\hat{\mathbf{x}}_{TAN} = (\hat{\mathbf{d}}^{1T}, \hat{\mathbf{t}}^{1T}, \hat{\varphi}^1, \hat{\mathbf{d}}^{2T}, \hat{\mathbf{t}}^{2T}, \hat{\varphi}^2, \hat{\varphi}^3)^T$ as well as the set of nodal primary variable variations $\delta\hat{\mathbf{x}}_{TAN} = (\delta\hat{\mathbf{d}}^{1T}, \delta\hat{\mathbf{t}}^{1T}, \delta\hat{\Theta}_1^1, \delta\hat{\mathbf{d}}^{2T}, \delta\hat{\mathbf{t}}^{2T}, \delta\hat{\Theta}_1^2, \delta\hat{\Theta}_1^3)^T$ as in Section 3.4.1 are chosen. In case of a Bubnov-Galerkin approach, the following discrete spin vector field results from the triad interpolation (3.55) in combination with the Kirchhoff constraint (3.152) (see also (3.57)):

$$\delta\boldsymbol{\theta}_h(\xi) = \sum_{i=1}^{3} \tilde{\mathbf{I}}^i(\xi)\delta\boldsymbol{\theta}^i \quad \text{with} \quad \delta\boldsymbol{\theta}^i = \left(\delta\hat{\Theta}_1^i \mathbf{g}_1(\xi^i) + \frac{\mathbf{S}[\mathbf{r}'(\xi^i)]\delta\mathbf{r}'(\xi^i)}{||\mathbf{r}'(\xi^i)||^2} \right). \tag{3.153}$$

Since the Kirchhoff constraint is exactly fulfilled at the three element nodes, the constrained variant (2.91) of the nodal spin vectors $\delta\boldsymbol{\theta}^i$ has been combined with (3.57). Based on the Petrov-Galerkin approach (3.59), the Kirchhoff constraint (3.152) yields for the spin vector field:

$$\delta\boldsymbol{\theta}_h(\xi) = \sum_{i=1}^{3} L^i(\xi)\delta\boldsymbol{\theta}^i \quad \text{with} \quad \delta\boldsymbol{\theta}^i = \left(\delta\hat{\Theta}_1^i \mathbf{g}_1(\xi^i) + \frac{\mathbf{S}[\mathbf{r}'(\xi^i)]\delta\mathbf{r}'(\xi^i)}{||\mathbf{r}'(\xi^i)||^2} \right). \tag{3.154}$$

Similar to the CJ element, only the latter version (3.154) will be employed throughout this thesis. The final element residual vector resulting from these discretized fields reads:

$$\begin{aligned}
\mathbf{r}_{WK-TAN,\hat{\mathbf{d}}} &= \int_{-1}^{1} \left(\bar{\mathbf{v}}'_{\theta_\perp} \mathbf{m} + \bar{\mathbf{v}}_\epsilon \bar{F}_1 - \mathbf{H}^T \tilde{\mathbf{f}}_\rho - \bar{\mathbf{v}}_{\theta_\perp} \tilde{\mathbf{m}}_\rho \right) J(\xi) d\xi - \left[\mathbf{H}^T \mathbf{f}_\sigma \right]_{\Gamma_\sigma} - \left[\bar{\mathbf{v}}_{\theta_\perp} \mathbf{m}_\sigma \right]_{\Gamma_\sigma}, \\
\mathbf{r}_{WK-TAN,\hat{\boldsymbol{\Theta}}_1} &= \int_{-1}^{1} \left(\bar{\mathbf{v}}'_{\theta_\parallel \Theta} \mathbf{m} - \bar{\mathbf{v}}_{\theta_\parallel \Theta} \tilde{\mathbf{m}}_\rho \right) J(\xi) d\xi - \left[\bar{\mathbf{v}}_{\theta_\parallel \Theta} \mathbf{m}_\sigma \right]_{\Gamma_\sigma}, \\
\bar{\mathbf{v}}_{\theta_\perp} &= -\sum_{i=1}^{3} L^i(\xi) \mathbf{v}_{\theta_\perp}(\xi^i), \quad \bar{\mathbf{v}}_\epsilon = \sum_{i=1}^{3} L^i(\xi) \mathbf{v}_\epsilon(\xi^i), \\
\bar{\mathbf{v}}_{\theta_\parallel \Theta} &= \sum_{i=1}^{3} L^i(\xi) \mathbf{v}_{\theta_\parallel \Theta}(\xi^i) \quad \text{with} \quad \bar{\mathbf{v}}'_{...} = \sum_{i=1}^{3} \frac{L^i_{,\xi}(\xi)}{J(\xi)} \mathbf{v}_{...}(\xi^i).
\end{aligned} \tag{3.155}$$

In the following, the formulation based on the degrees of freedom $\hat{\mathbf{x}}_{TAN}$ and $\delta\hat{\mathbf{x}}_{TAN}$ and on the residual (3.155) will be denoted as WK-TAN element, which stands for "Weak Kirchhoff constraint enforcement combined with nodal triad parametrization via nodal TANgents". For the WK-TAN element, a linearization $\Delta\mathbf{r}_{WK-TAN} = \mathbf{k}_{WK-TAN} \Delta\hat{\mathbf{x}}_{TAN}$ based on the increment vector $\Delta\hat{\mathbf{x}}_{TAN} := (\Delta\hat{\mathbf{d}}^{1T}, \Delta\hat{\mathbf{t}}^{1T}, \Delta\hat{\varphi}^1, \Delta\hat{\mathbf{d}}^{2T}, \Delta\hat{\mathbf{t}}^{2T}, \Delta\hat{\varphi}^2, \Delta\hat{\varphi}^3)^T$ is employed (see Appendix B.7).

Remark: Actually, a collocation type approach has been applied in order to enforce the Kirchhoff constraint. Nevertheless, the notion "weak constraint enforcement" is kept throughout this thesis since such a procedure still represents the basis of the space-continuous formulation. Moreover, the difference to the formulation based on "strong constraint enforcement" of Section 3.4 shall be emphasized by this naming.

3.5.3 Residual vector of rotation vector-based parametrization

Also for the element formulation of Section 3.5.2 based on weak Kirchhoff constraint enforcement, a coordinate transformation from $\hat{\mathbf{x}}_{TAN}$ and $\delta\hat{\mathbf{x}}_{TAN}$ to the alternative primary variables $\hat{\mathbf{x}}_{ROT} := (\hat{\mathbf{d}}^{1T}, \hat{\boldsymbol{\psi}}^{1T}, \hat{t}^1, \hat{\mathbf{d}}^{2T}, \hat{\boldsymbol{\psi}}^{2T}, \hat{t}^2, \hat{\varphi}^3)^T$ and $\delta\hat{\mathbf{x}}_{ROT} := (\delta\hat{\mathbf{d}}^{1T}, \delta\hat{\boldsymbol{\theta}}^{1T}, \delta\hat{t}^1, \delta\hat{\mathbf{d}}^{2T}, \delta\hat{\boldsymbol{\theta}}^{2T}, \delta\hat{t}_1, \delta\hat{\Theta}_1^3)^T$ can be performed. The transformation rule for the residual vector $\mathbf{r}_{ROT} = \tilde{\mathbf{T}}_{\hat{\mathbf{x}}}^T \mathbf{r}_{TAN}$ is identical to (3.130) in Section 3.4.2. Throughout this thesis, the element formulation based on the degrees of freedom $\hat{\mathbf{x}}_{ROT}$ and $\delta\hat{\mathbf{x}}_{ROT}$ and on the element residual vector (3.155) transformed via (3.130) will be denoted as WK-ROT element, which stands for "Weak Kirchhoff constraint enforcement combined with nodal triad parametrization via nodal ROTation vectors". For the WK-ROT element, a linearization $\Delta\mathbf{r}_{WK-ROT} = \mathbf{k}_{WK-ROT} \Delta\hat{\mathbf{x}}_{ROT}$ based on the increment vector $\Delta\hat{\mathbf{x}}_{ROT} := (\Delta\hat{\mathbf{d}}^{1T}, \Delta\hat{\boldsymbol{\theta}}^{1T}, \Delta\hat{t}^1, \Delta\hat{\mathbf{d}}^{2T}, \Delta\hat{\boldsymbol{\theta}}^{2T}, \Delta\hat{t}_1, \Delta\hat{\varphi}^3)^T$ will be employed (see Appendix B.8).

3.5.4 Avoidance of locking effects

In the investigation of the locking behavior of the proposed WK-TAN element, many results already derived in Section 3.3.2 and 3.4.3 can be re-used. Since the numbers n_{eq} and $n_{eq,c}$ for the space-continuous as well as for the discrete problem are identical to the SK-TAN element, it can

readily be concluded that also the WK-TAN element formulation shows an optimal constraint ratio of $r = r_h = 4$ and that no membrane locking effects are expected for this element.

Similar to Section 3.3.2, it shall be shown that also the WK-TAN/-ROT elements can exactly represent the internal energy associated with a 3D pure bending state. This time, the internal energy is split into contributions stemming from torsion and bending and into contributions stemming from axial tension, i.e. $\Pi_{int,h} = \Pi_{int,\Omega,h} + \Pi_{int,\epsilon,h}$. For a pure bending state, the energy contribution $\Pi_{int,\epsilon,h}$ has to vanish, and thus the total internal energy of a pure bending state is given by $\Pi_{int,\Omega,h}$, which is uniquely defined by the curvature vector field $\mathbf{K}_h(\xi) = \text{const}$. In order to represent the desired (constant) distribution of the curvature vector field $\mathbf{K}_h(\xi)$, which is possible for the employed triad interpolation (3.55), only $2n_{ele}$ of the $2n_{ele}+1$ nodal triads have to arise properly, while the one remaining nodal triad describes rotational rigid body modes of the beam.

Although the nodal triads are not necessarily parametrized by nodal rotation vectors, still three conditions result from each of these $2n_{ele}$ nodal triads, thus resulting in a total of $n_{eq,\Omega} = 6n_{ele}$ conditions. Additionally, the axial strains at the collocation points have to vanish in order to yield a vanishing contribution $\Pi_{int,\epsilon,h} = 0$. This requirement results in $n_{eq,\epsilon} = 2n_{ele}+1$ additional conditions that have to be fulfilled at the collocation points. If again six further conditions are considered in order to superpose arbitrary rigid body modes (representing the minimally required number of Dirichlet boundary conditions in static problems), the total number of $n_{eq} = 8n_{ele}+7$ equations equals the total number of $n_{uk} = 7(n_{ele}+1)+n_{ele}$ unknowns contained in the global vector $\mathbf{X}$ for the considered WK-TAN/ROT elements. Thus, in case a unique FEM solution is existent, a 3D pure bending case can be represented exactly. Similar to the CJ element, the torsion and bending modes represented by $\boldsymbol{\Omega}_h(\xi)$ as well as the axial tension values at the collocation points represented by $\epsilon(\xi_{CP})$ are non-competing and no locking effects are expected.

Again, these considerations can easily be extended to arbitrary curvature fields $\mathbf{K}_h(\xi)$ that are representable by the employed triad interpolation and arbitrary second-order polynomials $\bar{\epsilon}(\xi)$ according to (3.124). In Sections 3.8.2 and 3.8.3, the expected result that the discrete hyperelastic energies associated with pure bending states in 2D and in 3D can exactly be represented by the WK-TAN/ROT elements will be verified by means of corresponding numerical test cases.

3.5.5 Conservation properties

Since the WK-TAN beam element formulation proposed above basically combines the triad interpolation and the spin vector interpolation $\delta\boldsymbol{\theta}_h(\xi)$ of the CJ element (see Section 3.3) with the centerline interpolation and its variation $\delta\mathbf{r}'_h(\xi)$ already applied to the SK-TAN element of Section 3.4, the corresponding conservation properties can directly be concluded from the investigations made in Sections 3.3.3 and 3.4.4. Consequently, this element formulation will exactly fulfill conservation of linear and angular momentum. Conservation of energy can only be guaranteed for the spatially discretized, time-continuous problem in case the Petrov-Galerkin spin vector interpolation (3.154) is replaced by its Bubnov-Galerkin counterpart (3.153).

3.6 Realization of Inextensibility Constraint

The different Kirchhoff type element formulations can additionally be complemented by an inextensibility constraint in order to get rid of the high stiffness contributions of the axial tension mode. Unfortunately, in contrast to the Kirchhoff constraint, there is no straightforward way to enforce the inextensibility constraint directly through a special choice of the primary variables or by a collocation approach that would allow for Lagrange multiplier elimination on element level, as long as the interpolation property $\mathbf{r}(x^i) = \hat{\mathbf{d}}^i$ with $i = 1, 2$ has to be fulfilled for the position vector field $\mathbf{r}(s)$ at the element boundary nodes. This statement can easily be illustrated by considering a straight beam element of arbitrary order. In order to avoid zero-energy modes, inextensibility means in such a case that the solution for the nodal position vectors at the two boundary nodes cannot arise independently, but have to fulfill a constraint (e.g. $||\hat{\mathbf{d}}^{\mathbf{1}} - \hat{\mathbf{d}}^{\mathbf{2}}|| \doteq l_{ele}$).

Since the primary field $\mathbf{r}(s)$ has to be at least C^0-continuous (for all beam element formulations considered in this thesis), the position vector at an element boundary node will always influence the displacement field of both adjacent finite elements, and thus the constraint cannot be formulated by means of a local Lagrange multiplier that can be eliminated on element level. Since this interpolation property, provided e.g. by Lagrange or Hermite shape functions, is very beneficial for example for the realization of Dirichlet boundary conditions, it should be kept for the formulations considered in this thesis. Thus, in contrast to the Kirchhoff constraint, the Lagrange multipliers resulting from the inextensibility constraint cannot be eliminated on element level. Following the derivations in Section 2.3.6, the weak statement of the inextensibility constraint (2.122) can be realized by introducing spatial interpolations for the Lagrange multipliers and their variations, i.e. by choosing discrete trial and weighting spaces $\lambda_{\epsilon,h} \in \mathcal{U}_{\lambda_\epsilon,h} \in \mathcal{U}_{\lambda_\epsilon}$ and $\delta\lambda_{\epsilon,h} \in \mathcal{V}_{\lambda_\epsilon,h} \in \mathcal{V}_{\lambda_\epsilon}$. However, similar to the enforcement of the Kirchhoff constraint in the last section, the alternative approach of enforcing inextensibility on the re-interpolated strain field $\bar{\epsilon}(\xi)$ rather than on the original strain field will be applied in the following:

$$\bar{\epsilon}(\xi) \equiv 0 \;\rightarrow\; \epsilon(\xi^i) = ||\mathbf{r}'(\xi^i)|| - 1 \doteq 0 \quad \text{for} \quad i = 1, 2, 3. \tag{3.156}$$

The result is again a collocation point type of constraint enforcement, where the norm of the centerline tangent vector has to be enforced to unity at the three collocation points $\xi^1 = -1$, $\xi^2 = 1$ and $\xi^3 = 0$. By applying a similar procedure as in Section 2.3.6 at the three collocation points and by additionally considering the (scaled) contributions from the tension field $\bar{\epsilon}(\xi)$ of the extensible case, the following element contribution to the discrete weak form can be derived:

$$\begin{aligned} \delta\Pi_{\lambda_\epsilon}^{(e)} &= \sum_{i=1}^{3} \delta\lambda_\epsilon^i \epsilon(\xi^i) + \sum_{i=1}^{3} \delta\epsilon(\xi^i)\lambda_\epsilon^i + c_\epsilon \int_{-1}^{1} \delta\bar{\epsilon}(\xi) EA \bar{\epsilon}(\xi) J(\xi) d\xi \\ &= \sum_{i=1}^{3} \delta\lambda_\epsilon^i \epsilon(\xi^i) + \sum_{i=1}^{3} \delta\epsilon(\xi^i) \left[\lambda_\epsilon^i + c_\epsilon EA \int_{-1}^{1} L^i(\xi) \bar{\epsilon}(\xi) J(\xi) d\xi \right]. \end{aligned} \tag{3.157}$$

Thus, the contributions of the inextensibility constraint to the element residual vector read:

$$\begin{aligned} \mathbf{r}_{\lambda_\epsilon,\hat{\mathbf{d}}} &= \sum_{i=1}^{3} \mathbf{v}_\epsilon(\xi^i) \left[\lambda_\epsilon^i + c_\epsilon EA \int_{-1}^{1} L^i(\xi)\bar{\epsilon}(\xi) J(\xi) d\xi \right], \\ \mathbf{r}_{\lambda_\epsilon,\boldsymbol{\lambda}} &= (\epsilon(\xi^1), \epsilon(\xi^2), \epsilon(\xi^3))^T. \end{aligned} \tag{3.158}$$

Since also for the variant (3.158), the Lagrange multipliers cannot be eliminated at element level (as discussed above), a weak constraint enforcement based on discrete Lagrange multiplier fields chosen from trial and weighting spaces $\mathcal{U}_{\lambda_\epsilon,h}$ and $\mathcal{V}_{\lambda_\epsilon,h}$ would not mean much extra effort. There are two slight advantages of the collocation type approach (3.158), for which reason this variant has been applied in this thesis. Firstly, it seams to be more consistent with the collocation point type enforcement of the Kirchhoff constraint of the WK-TAN/ROT element formulations. Secondly, for the SK/WK-ROT element formulations, i.e. the Kirchhoff formulations with rotation vector triad parametrization at the boundary nodes, the norm of the tangent vectors $\hat{t}^1$ and $\hat{t}^2$ at the boundary nodes are primary variables of the finite elements. For these variants, the primary variables can directly be set to $\hat{t}^1 = \hat{t}^2 = 1$ such that only one Lagrange multiplier per finite element is necessary in order to enforce the constraint $||\mathbf{r}'(\xi = 0)|| = 1$. Consequently, for these variants, the formulation of the inextensibility constraint via (3.158) does not require more degrees of freedom than the original variant, since only one additional Lagrange multiplier per element is required and (approximately) one degree of freedom per element can be saved due to the a priori knowledge $\hat{t}^1 = \hat{t}^2 = 1$. Nevertheless, the resulting system is a saddle point system.

Finally, the application of such an inextensibility constraint shall briefly be motivated by means of a numerical investigation: An initially straight beam with length $l = 1.0$, $E = 2G = 1.0$ is discretized by one third-order beam element. The resulting condition number of the tangent stiffness matrix shall be investigated for two different slenderness ratios $\zeta_1 = 10^2$ ($R = 10^{-2}$) and $\zeta_2 = 10^4$ ($R = 10^{-4}$). Thereto, the tangent stiffness matrices of the CJ element and the WK-TAN element are evaluated for the straight undeformed configuration of the beam. In order to yield a non-singular stiffness matrix, the Dirichlet boundary condition of a clamped end has been considered. For simplicity, the problem has been restricted to 2D by proper additional Dirichlet boundary conditions. For this configuration and the two investigated slenderness ratios, the tangent stiffness matrix of the Reissner type CJ element yields condition numbers of $5 \cdot 10^6$ and $2 \cdot 10^{11}$, respectively. These values have been approximated by the ratio of the highest and lowest eigenvalue of the tangent stiffness matrix. In a similar manner, the corresponding condition numbers for the WK-TAN element result in $2 \cdot 10^5$ and $2 \cdot 10^9$, respectively. As expected, the condition numbers of the Reissner and Kirchhoff type element formulations are (approximately) in the same order of magnitude. Furthermore, the condition number increases almost quadratically with the beam slenderness ratio. Condition numbers in the range of 10^{11} as observed for the CJ element formulation and a slenderness ratio of $\zeta_2 = 10^4$ can be regarded as drastic challenge for iterative linear solvers and as a severe limitation of the achievable computational accuracy. Moreover, finer spatial discretizations will yield even higher condition numbers. Now, the situation shall be improved by combining the WK-TAN element with an additional inextensibility

constraint. Applying the constraint (3.158) leads to an element stiffness matrix of the form:

$$\mathbf{k}_{ele,tot} = \begin{pmatrix} \mathbf{k}_{ele} & \mathbf{k}_{\lambda_\epsilon}^T \\ \mathbf{k}_{\lambda_\epsilon} & \mathbf{0} \end{pmatrix}. \tag{3.159}$$

Here, the block $\mathbf{k}_{\lambda_\epsilon} = d\mathbf{r}_{\lambda_\epsilon}/d\hat{\mathbf{x}}$ represents the linearization of the inextensibility constraint equation and $\mathbf{k}_{ele}$ is the counterpart to the stiffness matrix of the element formulation without inextensibility constraint. In the straight, undeformed configuration (with $\lambda_\epsilon^i = 0$ for $i = 1, 2, 3$), the submatrix $\mathbf{k}_{ele}$ is identical to the element stiffness matrix of the corresponding Kirchhoff beam element formulation without inextensibility constraint. Now, the condition number of the submatrix $\mathbf{k}_{ele}$ can be improved by choosing proper scaling factors $c_\epsilon < 1$. For the investigated example, the scaling factor $c_\epsilon = (\zeta_1/\zeta_2)^2 = 10^{-4}$ reduces the condition number of $\mathbf{k}_{ele}$ resulting from the slenderness ratio $\zeta_2 = 10^4$ from its initial value $2{\cdot}10^{11}$ to the value $5{\cdot}10^6$ associated with the slenderness ratio ζ_1 without changing the final FEM solution. A scaling factor of $c_\epsilon = 10^{-8}$ even yields a condition number of $2 \cdot 10^1$. While the condition number increases quadratically with the beam slenderness ratio, it increases (approximately) linearly with the scaling factor c_ϵ. Reduced condition numbers is only one possible benefit of inextensible Kirchhoff type beam element formulations. Further advantages can for example arise in terms of improved stability properties of the employed time integration scheme (see also Section 3.3.4).

Remark: Since the scaling factor c_ϵ is directly applied to the residual vector, it influences not only the linear solver but also the performance of the nonlinear solver. Consequently, for an optimal choice of the scaling factor c_ϵ, both aspects have to be considered and harmonized (see also Section 3.8.2.2 for a corresponding numerical test case).

Remark: Obviously, the inextensibility constraints (3.156) yield a linearized residual with saddle point structure, which requires the application of a special class of iterative linear solvers that are suitable for saddle point problems. However, in many cases, a saddle-point system with good-natured submatrix $\mathbf{k}_{ele}$ might be preferable to a non-saddle point system with strongly ill-conditioned matrix $\mathbf{k}_{ele}$. Nevertheless, the collocation point approach (3.156) can be regarded as one possible and very simple variant of enforcing inextensibility. Within this thesis, this approach has been chosen in order to demonstrate basic relationships and perform a first proof of principle. Future research work might for example focus on the development of tailored Lagrange multiplier interpolations $\lambda_{\epsilon,h}(\xi)$ that allow for a computationally cheap, global condensation of the Lagrange multipliers in order to avoid the saddle point structure of the global system of equations. Such constraint localization approaches based on dual Lagrange multiplier spaces are e.g. employed in the context of computational contact mechanics (see e.g. [173, 175, 231]).

3.7 Kirchhoff-Love Beam Elements Based on Reduced Beam Theories

3.7.1 Residual vector of torsion-free element formulation

In this section, also the finite element realization of the torsion-free theory of Section 2.4.2, in the following denoted as TF element, will be derived. It is completely defined by the beam

centerline curve with the set of nodal degrees of freedom $\hat{\mathbf{x}}_{TF} = (\hat{\mathbf{d}}^{1T}, \hat{\mathbf{t}}^{1T}, \hat{\mathbf{d}}^{2T}, \hat{\mathbf{t}}^{2T})^T$ as well as the set of nodal primary variable variations $\delta\hat{\mathbf{x}}_{TF} = (\delta\hat{\mathbf{d}}^{1T}, \delta\hat{\mathbf{t}}^{1T}, \delta\hat{\mathbf{d}}^{2T}, \delta\hat{\mathbf{t}}^{2T})^T$. Applying the Hermite centerline interpolation (3.39) to the weak form (2.139) yields:

$$\begin{aligned}
\mathbf{r}_{TF,\hat{\mathbf{d}}} &= \int_{-1}^{1} \left[\bar{\mathbf{v}}_\epsilon \bar{F}_1 + \mathbf{v}_\kappa \mathbf{m} + \mathbf{H}^T \mathbf{f}_\rho \right] \frac{l_{ele}}{2} d\xi - \int_{-1}^{1} \left[\mathbf{H}^T \tilde{\mathbf{f}} + \mathbf{v}_{\boldsymbol{\theta}_\perp} \tilde{\mathbf{m}}_\perp \right] \frac{l_{ele}}{2} d\xi - \left[\mathbf{H}^T \mathbf{f}_\sigma + \mathbf{v}_{\boldsymbol{\theta}_\perp} \mathbf{m}_{\sigma\perp} \right]_{\Gamma_\sigma} \doteq 0, \\
\mathbf{m} &= EI\boldsymbol{\kappa}, \quad \mathbf{v}_\kappa = \frac{||\mathbf{r}'||^2 \left[\mathbf{H}'^T \mathbf{S}(\mathbf{r}'') - \mathbf{H}''^T \mathbf{S}(\mathbf{r}') \right] - 2(\mathbf{H}'^T \mathbf{r}') \otimes (\mathbf{r}' \times \mathbf{r}'')^T}{||\mathbf{r}'||^4}.
\end{aligned} \tag{3.160}$$

In the element residual vector (3.160), the MCS method has been applied for axial strain re-interpolation with $\bar{\mathrm{v}}_\epsilon$ and $\bar{F}_1$ being given by (3.124). Moreover, the vector $\mathbf{v}_{\boldsymbol{\theta}_\perp}$ is given in (3.71). As already mentioned, in contrast to standard geometrically exact beam formulations, (3.160) will result in a symmetric tangent stiffness matrix (as long as no external moment contributions are considered) and, moreover, a symmetric and constant mass matrix. Furthermore, it can completely abstain from rotational degrees of freedom, which leads to considerable simplifications in the overall numerical algorithm (see also Section 2.4.2 for further details).

For the TF element, a linearization $\Delta\mathbf{r}_{TF} = \mathbf{k}_{TF} \Delta\hat{\mathbf{x}}_{TF}$ based on the purely additive increment vector $\Delta\hat{\mathbf{x}}_{TF} := (\Delta\hat{\mathbf{d}}^{1T}, \Delta\hat{\mathbf{t}}^{1T}, \Delta\hat{\mathbf{d}}^{2T}, \Delta\hat{\mathbf{t}}^{2T})^T$ will be employed (see Appendix B.9). Based on the definitions of $\boldsymbol{\kappa} = \mathbf{g}_1 \times \mathbf{g}_1'$ and $\delta\boldsymbol{\theta} = \mathbf{g}_1 \times \delta\mathbf{g}_1$, the identity $\delta\boldsymbol{\kappa}^T \boldsymbol{\kappa} = \delta\boldsymbol{\theta}' \boldsymbol{\kappa}$ can easily be shown. This allows to replace the variation $\delta\boldsymbol{\kappa}$ by $\delta\boldsymbol{\theta}'$ in the weak form (2.139). In this case, the vector $\mathbf{v}_\kappa$ has to be replaced with $\mathbf{v}'_{\theta\perp}$ in (3.160). Although, both variants yield identical residual vectors and stiffness matrices, the latter allows to formulate the stiffness matrix in a more compact form.

Remark: In Meier et al. [157], it has been shown how the IT element formulation can be considerably simplified on the basis of proper approximations assuming small axial strains $\epsilon \ll 1$. For comparison reasons, also this formulation, in the following denoted as TF+ST (Torsion-Free + Small Tension), will be considered in the numerical example of Section 3.8.5. For details, the interested reader is referred to the original work [157].

3.7.2 Locking and conservation properties of torsion-free element

Since the TF element represents a special case of the SK-TAN element, the locking behavior and the resulting conservation properties are similar. Thus, also for the TF element, an optimal constraint ratio can be derived, and no membrane locking effects are expected. Furthermore, the only difference between the Petrov-Galerkin variant SK-TAN and the Bubnov-Galerkin counterpart SK-TAN+CS lies in the interpolation of the twist component of the spin vector field, which results in exact conservation of linear momentum, angular momentum and energy for the latter formulation but not for the former. Since this twist component is not present for the TF element, it inherits these desirable three conservation properties from the SK-TAN+CS element.

3.7.3 Residual vector of isotropic element formulation

Throughout this thesis, the static isotropic beam element formulation according to (2.134), denoted as IT element, will play a less important role as the TF element. Nevertheless, for comparison reasons, it will also be applied to two of the following numerical examples and the residual vector shall be briefly stated here. However, as already argued in Section 2.4.1, only the static variant of this formulation will be considered here. The following set of nodal degrees of freedom $\hat{\mathbf{x}}_{TF} = (\hat{\mathbf{d}}^{1T}, \hat{\mathbf{t}}^{1T}, \hat{K}_1^1, \hat{\mathbf{d}}^{2T}, \hat{\mathbf{t}}^{2T}, \hat{K}_1^2)^T$ as well as the set of nodal primary variable variations $\delta\hat{\mathbf{x}}_{TF} = (\delta\hat{\mathbf{d}}^{1T}, \delta\hat{\mathbf{t}}^{1T}, \delta\hat{\Theta}_1^1, \delta\hat{\mathbf{d}}^{2T}, \delta\hat{\mathbf{t}}^{2T}, \delta\hat{\Theta}_1^2)^T$ will be employed for this element. Based on the Hermite centerline interpolation (3.39) and by introducing the additional linear interpolations

$$K_{1h}(\xi) = \sum_{i=1}^{2} L^i(\xi)\hat{K}_1^i \quad \text{and} \quad \delta\hat{\Theta}_{1h}(\xi) = \sum_{i=1}^{2} L^i(\xi)\delta\hat{\Theta}_1^i, \tag{3.161}$$

and neglecting all inertia terms, the corresponding element residual vector can be derived in a very similar manner as for the SK-TAN element or for the TF element presented above.

3.8 Numerical Examples

In this section, the previously proposed beam element formulations will be investigated numerically by means of proper test cases. All simulations results presented in this thesis rely on a software implementation of the proposed finite element formulations and numerical algorithms within the in-house finite element research code BACI (cf. Wall and Gee [222]), developed jointly at the Institute for Computational Mechanics at the Technical University of Munich. While most of the numerical examples (see Sections 3.8.1-3.8.8) are considered as quasi-static problems, eventually, in Sections 3.8.9 and 3.8.10, also two dynamic test cases are investigated. In a first step, these numerical examples aim to verify the principle applicability and accuracy of the proposed general and reduced Kirchhoff-Love beam element formulations in the range of different beam slenderness ratios. This verification process crucially relies on detailed comparisons with analytic reference solutions, benchmark tests known form the literature as well as numerical reference solutions generated by means of well-established geometrically exact beam element formulations of Simo-Reissner type. More specifically, also the essential requirements formulated in Section 1.2.2.2 such as objectivity and path-independence, avoidance of locking effects, consistent spatial convergence behavior as well as the fulfillment of conservation properties will be verified for the different beam element formulations presented in Sections 3.3-3.7. Finally, based on the arguments given in Section 3.3.4, the focus will also lie on detailed comparisons of Reissner and Kirchhoff type beam element formulations for example with respect to the resulting discretization error level or the performance of the Newton-Raphson scheme.

Since the Kirchhoff type beam element formulations based on a tangent-based triad parametrization and the formulations based on a rotation vector-based triad parametrization (compare e.g. Sections 3.4.1 and 3.4.2 or Sections 3.5.2 and 3.5.3) have been shown to yield identical FEM solutions, only the former category will be investigated with respect to spatial discretization errors. Furthermore, for all examples without analytic solution, the standard choice for the reference

solution $\mathbf{r}_{ref}$ (see also (3.105) of Section 3.2.4.4) is a numerical solution via the WK-TAN element (see Section 3.5.2) employing a spatial discretization that is by a factor of four finer than the finest discretization shown in the corresponding convergence plot. In order to achieve a good comparability among the different geometries and load cases, a standard set of geometrical and constitutive parameters has been applied in all simulations unless stated otherwise. This standard set consists of a beam with initial length $l = 1000$ and square cross-section with side length R. These parameters lead to a cross-section area of $A = R^2$ and to moments of inertia of area of $I_2 = I_3 =: I = R^4/12$ and $I_T = R^4/6$. Different beam slenderness ratios $\zeta := l/R$ are generated by varying the value $R = 0.1, 1.0, 10, 100$ of the cross-section side length. The standard choice for the constitutive parameters is $E = 1.0$ and $G = 0.5$, thus leading to $EI = GI_P = R^4/12$. For all numerical examples considered in the following sections, a Newton-Raphson scheme based on consistent linearization has been applied in order to solve the set of nonlinear equations resulting from the temporally and spatially discretized weak form of the balance equations (see Section 3.2.1 for further details). As indicated in Section 3.2.1.2, for convergence, both of the two criteria $||\mathbf{R}(\mathbf{X}_{n+1}^{k+1})|| < \delta_{\mathbf{R}}$ and $||\Delta\mathbf{X}_{n+1}^{k+1}|| < \delta_{\mathbf{X}}$ have to be fulfilled. Typical convergence tolerances chosen for the subsequent examples are in the range of $\delta_{\mathbf{X}} = 10^{-8}$ as well as $\delta_{\mathbf{R}} = 10^{-7}, 10^{-9}, 10^{-11}, 10^{-13}$ for the slenderness ratios $\zeta = 10, 100, 1000, 10000$.

3.8.1 Example 1: Verification of objectivity

The objectivity of the Kirchhoff beam element formulations proposed in Sections 3.4 and 3.5 has already been proven theoretically. In order to verify these results numerically, the following test case will be investigated (see Figure 3.6(a)): At the clamped end of an initially curved beam with slenderness ratio $\zeta = 10$, whose stress-free centerline configuration equals a quarter circle, a Dirichlet rotation with respect to the global x-axis is imposed. For the presented quasi-static example, a total rotation angle of 20π, increasing linearly over 100 load steps, is prescribed. In order to investigate objectivity, the normalized internal (hyperelastic) energy is plotted over the total number of rotations (see Figure 3.6(b)) for the WK-TAN and SK-TAN element as well as for the Bubnov-Galerkin variant of the SK-TAN element formulation with Consistent Spin (SK-TAN+CS) vector interpolation according to (3.122). For comparison reasons, also the non-objective SR Kirchhoff beam element formulation investigated in Meier et al. [156] will be considered (see also the last but one remark at the end of Section 3.2.3.4). For clearness, the internal energy Π_{int} is normalized by the factor $\Pi_{int,r} = 0.5EI\pi^2/(4l)$, which is equal to the amount of mechanical work that is required to bend the initially stress-free quarter circle into a straight beam by means of a discrete, external end-moment. Of course, the internal energy should vanish for a beam that is merely rotated out of its stress-free initial configuration.

From Figure 3.6(b), it becomes obvious, however, that the internal energy of the SR formulation increases over the number of rotations, which is a clear indication for the already theoretically predicted non-objectivity. Within 10 rotations, the normalized energy reaches a value of almost $\Pi_{int,r}/4$, which results in a clearly visible deformation of the initial quarter circle. On the contrary, the internal energy of all the other investigated element formulations results in a value that is zero up to machine precision. Finite element formulations based on such interpolation schemes as the investigated SR element might show reasonable results for static test cases (see e.g. [156]). However, especially in dynamic problems involving considerable rigid body motions,

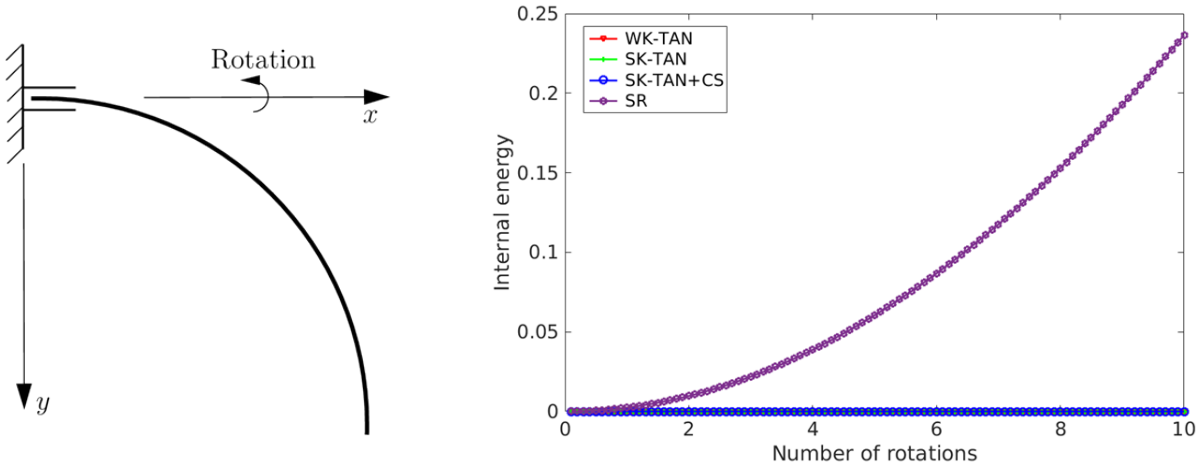

(a) Problem setup.

(b) Internal energy due to imposed rigid body rotation.

Figure 3.6: Objectivity test: Rigid body rotation of an initially stress-free quarter circle.

non-physical results as well as a drastic deterioration of the conservation properties investigated in Section 3.2.4.5 can follow from the application of such element formulations.

3.8.2 Example 2: Pure bending in 2D

The examples shown in this section exclusively focus on 2D geometries and load cases. The section is sub-divided into two subsections: In Section 3.8.2.1, two load cases, a pure pending case as well as a combined moment-and-force load case, yielding geometrically nonlinear, but still moderate centerline deformations, are considered. This section aims at the investigation of membrane locking effects and at the comparison of different anti-locking tools, especially of the MCS method proposed in Section 3.2.4.3. In Section 3.8.2.2, again a pure bending and a combined moment-and-force load case will be considered. However, due to higher load factors, the resulting degree of deformation is further increased as compared to the examples of Section 3.8.2.1. This higher degree of deformation reveals clear differences in the approximation quality of the WK and SK Kirchhoff beam element variants. Besides the comparison of these two variants, also a first proof of concept for the development of higher-order Hermitian Kirchhoff elements and inextensible Kirchhoff beam elements is given in this section.

3.8.2.1 Comparison of different anti-locking methods

An initially straight beam is clamped at one end. Two different load cases will be analyzed: The first load case M is identical to the example analyzed in Section 3.2.4.3 and solely consists of a discrete end-moment $\mathbf{M} = (0, 0, M)^T$ applied in one load step. The moment $M = EI\pi/(2l)$ exactly bends the beam into a quarter-circle shaped arc. In the second load case M+F, the end-moment and an additional tip force $\mathbf{F} = (0, F, 0)^T$ in global y-direction are applied in one load step. The initial and deformed geometries for these two load cases are illustrated in Figure 3.7.

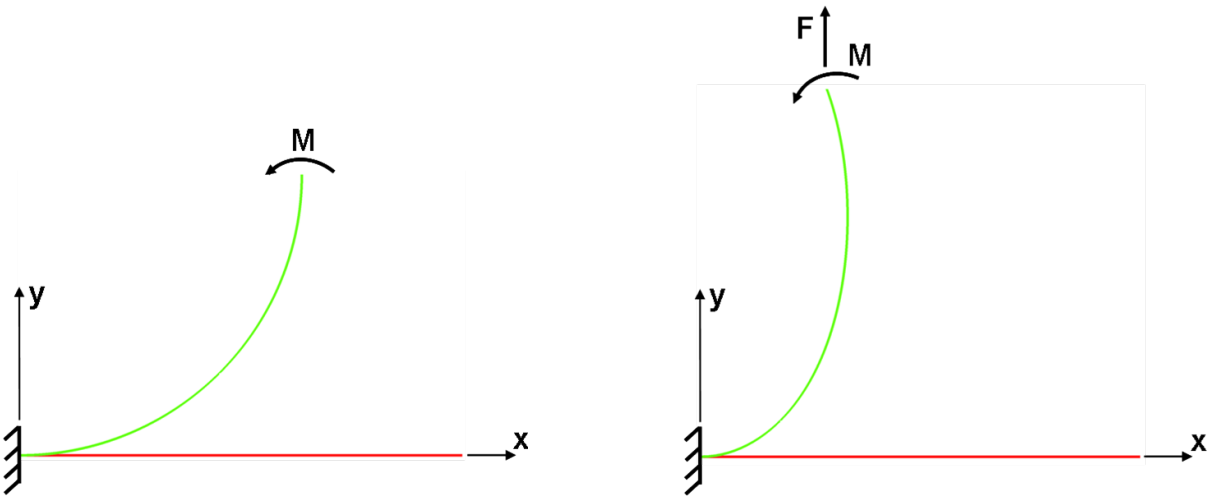

(a) Straight beam bent by end-moment. (b) Straight beam bent by end-moment and -force.

Figure 3.7: Initial and deformed configuration of an initially straight beam for two load cases.

While the standard parameters and the slenderness ratios $\zeta = 10, 100, 1000, 10000$ have been chosen for the load case M, only the highest and therefore most critical slenderness ratio $\zeta = 10000$ in combination with an external force of $F = 1.0 \cdot 10^{-10} \approx 10M/l$ has been investigated for the load case M+F. In a first step, the SK-TAN element formulation according to (3.123) is applied in combination with a full Gauss-Legendre integration ("SK-TAN-FI") with $n_G = 4$, a reduced Gauss-Legendre integration ("SK-TAN-RI") with $n_G = 3$, a classical assumed natural strain approach ("SK-TAN-ANS") as well as the MCS method according to (3.124) based on $n_G = 4$ integration points ("SK-TAN-MCS") (see Section 3.2.4.3 for further details on these variants).

In Figure 3.8(a), the relative L^2-error of the load case M and different slenderness ratios is plotted with respect to an analytic reference solution. For spatial discretization, the variant SK-TAN-FI based on meshes with $1, 2, 4, 8, 16, 32$ and 64 elements has been applied. As already indicated by the deformed shapes illustrated in Figure 3.4(b) of Section 3.2.4.3, the convergence is slowed down dramatically with increasing slenderness ratio. If the beam is e.g. discretized by one finite element ($l_{ele} = 1000$), the relative error increases almost by two orders of magnitude when enhancing the slenderness ratio from $\zeta = 10$ to $\zeta = 10000$. However, Figure 3.8(a) also reveals that this effect decreases with decreasing element sizes and almost completely disappears for discretizations with more than 32 elements. The reason for this behavior lies in the fact that the element slenderness ratio $\zeta_{ele} = l_{ele}/R$ is the key-parameter for the observed locking effect and that the latter also decreases with decreasing element sizes. However, for typical engineering applications with relative error bounds in the range of 1%, the effect is by no means negligible. For sufficiently fine discretizations the expected convergence order of four is reached.

In Figure 3.8(b), the relative L^2-error is plotted for the same slenderness ratios as before, but for the variant SK-TAN-MCS, which is supplemented by the MCS method according to (3.124). As expected, the locking effect completely disappears for all investigated slenderness ratios. However, as shown in Figure 3.8(c), for the load case M and the highest investigated slenderness ratio

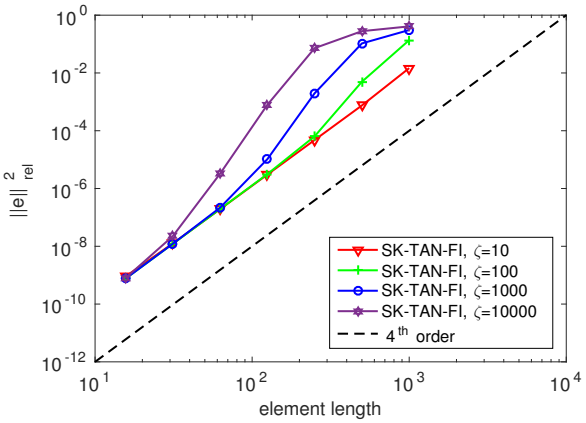

(a) Reference: Analytic, different slenderness ratios.

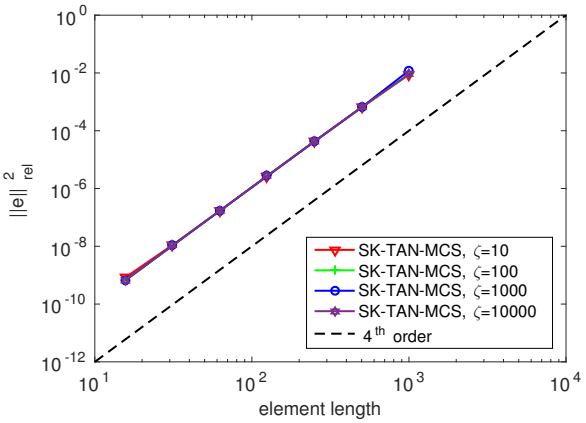

(b) Reference: Analytic, different slenderness ratios.

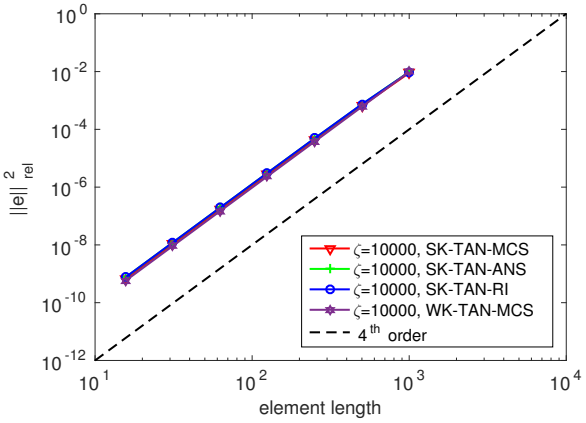

(c) Reference: Analytic, $\zeta = 10000$.

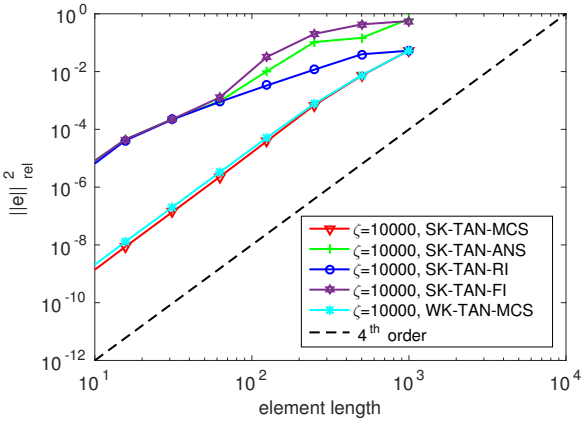

(d) Reference: WK-TAN-MCS, $\zeta = 10000$.

Figure 3.8: Straight beam subject to the load cases M and M+F: Relative L^2-error.

of $\zeta = 10000$, the same effect can alternatively be achieved by applying a simple reduced integration procedure (variant SK-TAN-RI) or a classical ANS approach (variant SK-TAN-ANS). On the contrary to load case M, Figure 3.8(d) reveals that no distinctive improvement of the locking behavior can be obtained by these alternative methods for the load case M+F: Both the ANS approach as well as the reduced integration scheme can only slightly alleviate the locking effect in the range of rather coarse discretizations as compared to the variant SK-TAN-FI. The MCS approach, however, completely eliminates the error offset due to membrane locking also for this load case. The explanation for this observation is obvious and in agreement with the statements of Section 3.2.4.3: Similar to the working principle of the MCS method, the reduced integration scheme can alleviate locking effects by reducing the number of constraint equations.

Yet, as shown in Section 3.2.4.3, the MCS method leads to a lower number of constraint equations as compared to the simple reduced integration scheme, which makes the latter method less effective. While the reduced integration scheme seems to be sufficient for the load case M, a special case yielding symmetric curvature distributions within the elements, the more general deformed configurations resulting from the load case F+M already demonstrate the limits of this

simple method. On the other hand, the working principle of the standard ANS method does not aim at a reduction of the number of constraint equations, but rather at an evaluation of the critical axial tension term at selected collocation points with vanishing parasitic strains. In the geometrically nonlinear regime of large deformations, the parameter space positions of these optimal collocation points are deformation-dependent. Obviously, the load case M+F already leads to a change in these positions up to an extent that almost completely destroys the working principle and impact of the ANS method. Summing up, it is to say that based on these two examples the proposed MCS method seems to be superior to standard methods such as reduced integration or ANS in terms of locking avoidance when combined with the considered geometrically exact Kirchhoff beam elements. In example 8 of Section 3.8.8, a further comparison of these different anti-locking methodologies on the basis of a very general problem setting involving 3D deformation states and an initially curved geometry will be presented, which will confirm this result. For completeness, in Figures 3.8(c) and 3.8(d), also the L^2-error of the WK-TAN-MCS element based on a weak enforcement of the Kirchhoff constraint according to (3.155) has been plotted. For the load cases M and M+F, this formulation yields a comparable convergence behavior and discretization error level as the SK-TAN-MCS element. Next, it will be shown that this behavior will change with increasing deformation. Throughout this thesis, the MCS method will be employed per default and the abbreviation ...-...-MCS in the element name will be omitted.

3.8.2.2 Comparison of different element formulations

In the convergence plots investigated for the two load cases M and M+F, no noteworthy differences between the SK and WK element could be observed. In order to investigate the difference in the two general approaches of enforcing the Kirchhoff constraint in a strong or in a weak manner further in detail and to perform first comparisons with geometrically exact beam element formulations of Simo-Reissner type, two additional load cases will be considered (see Figure 3.9): The first load case considered in this section, in the following denoted as $\tilde{M}$, simply increases the magnitude of the external moment by a factor of eight as compared to the previous load case M, i.e. $\tilde{M} = 8M$, thus leading to a deformed geometry that is represented by a double circle (see Figure 3.9(a)). Since the contribution of Simo and Vu-Quoc [208], this load case has been established as a standard test case for geometrically exact beam element formulations. Finally, in a fourth load case, denoted as $\tilde{M}$+$\tilde{F}$, the end-moment $\tilde{M} = 8M$ is supplemented by a tip force $\mathbf{F} = (0, \tilde{F}, 0)^T$ in global $y-$direction, whose magnitude is this time exactly chosen as $\tilde{F} = 10\tilde{M}/l = 0.08M$. The final configuration of this last load case is illustrated in Figure 3.9(b).

In Figure 3.10(a), the L^2-error resulting from the load case $\tilde{M}$ has been plotted for the WK-TAN and the SK-TAN element as well as for the Reissner type CJ beam element formulation proposed by Crisfield and Jelinic [58, 116] and presented in Section 3.3. Here, discretizations with $8, 16, 32, 64, 128$ and 256 elements have been employed. These discretizations are comparable to the load case M since similarly to that example, also here, the roughest discretization is based on *one* finite element per $90°$-arc segment of the analytic solution. In order to enable a reasonable comparison of different element formulations, here and in the following, the discretization error will be plotted over the total number of degrees of freedom resulting from the respective finite element discretization. Since no shear deformation is present for this example, the Reissner and Kirchhoff type elements converge towards the same analytic solution. All element formulations

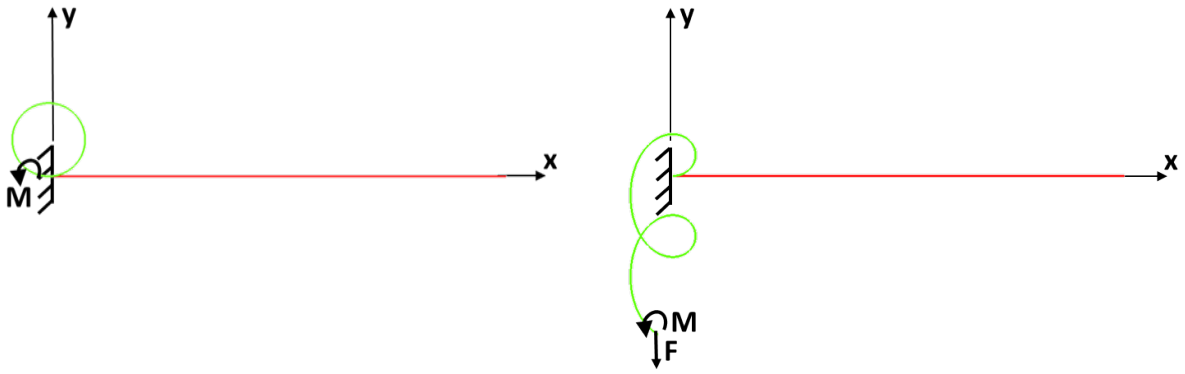

(a) Straight beam bent by end-moment. (b) Straight beam bent by end-moment and -force.

Figure 3.9: Initial and deformed configuration of an initially straight beam for two load cases.

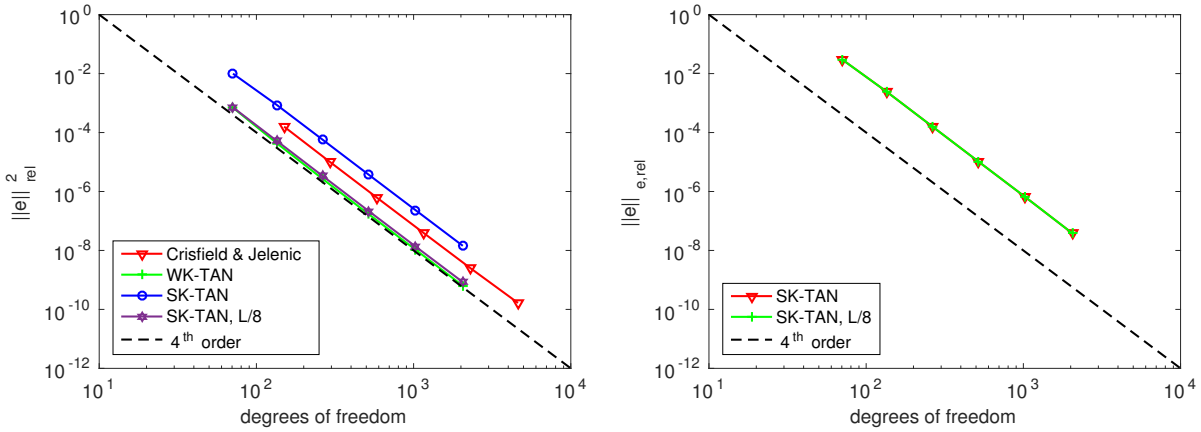

(a) Reference: Analytic, L^2-error. (b) Reference: Analytic, energy error.

Figure 3.10: Straight beam and load case $\tilde{M}$: convergence of L^2- and energy error.

exhibit the expected optimal convergence order of four, indicated by the black dashed line. The WK-TAN element shows the expected result that Kirchhoff element formulations can represent the same discretization error level with less degrees of freedom as compared to the Reissner type element formulation (see Section 3.3.4). Furthermore, for this example, it can even be shown that the lines representing the discretization error of the WK-TAN element and of the CJ element formulation would be almost identical if the discretization error was plotted solely over the degrees of freedom associated with the centerline interpolation. Thus, the observable difference in Figure 3.10(a) is a pure result of the additional rotational degrees of freedom required for Reissner type element formulations in order to represent shear deformation. Such a behavior is expected for this pure bending example since the two considered element formulations can exactly represent the internal energy associated with a pure bending state (see Sections 3.3.2 and 3.5.4). Consequently, the discretization error contribution stemming from the second term in (3.108) vanishes, the finite element problem degenerates to a pure problem of polynomial curve approximation represented by the first term in (3.108) and, thus, the discretization error plotted over

the number of centerline DoFs yields similar results for the Lagrange centerline interpolation of the Reissner type element and the Hermite centerline interpolation of the Kirchhoff type element.

The situation is completely different for the SK-TAN element, which cannot exactly represent the internal energy associated with a pure bending state. A closer investigation would confirm the expected result that the SK-TAN element exhibits a remaining error in the length-specific hyperelastic stored energy (2.100), which is more or less constant along the beam length. Based on this finding, it can easily be answered why the discretization error level of the SK-TAN element applied to the load case $\tilde{M}$ is considerably increased as compared to the first load case M (while an identical level of the length-specific L^2-error has been observed for the WK-TAN and the CJ element): By the FEM, solely the distribution of the second centerline derivative $\mathbf{r}''$ is optimized in order to yield a minimal energy error within the beam domain Ω_l, while the centerline field $\mathbf{r}$ itself is only constrained at the clamped end of the beam. Thus, with increasing distance from the clamped end, the discretization error in the centerline field $\mathbf{r}$, resulting from a two-fold integration of the (more or less) constant error in the second derivative $\mathbf{r}''$ along an increasing arc-length segment, also increases. Consequently, by assuming comparable errors in the length-specific energy for comparable discretizations (i.e. the same number of finite elements representing the same angle segment of the analytic solution), a higher length-specific discretization error is expected for the load case $\tilde{M}$ as compared to the load case M. Figure 3.10(b) confirms the expected result that the energy error of the SK-TAN element does not vanish for this example and exhibits a convergence order of four. Furthermore, it is shown that the length-specific energy error "averaged" along the entire beam length is identical to the length-specific energy error "averaged" only along the first eighth of the beam (representing a quarter circle). As consequence of the error accumulation described above, the length-specific L^2-error is lower (and similar to load case M) if it is only "averaged" along the first eighth of the beam (see Figure 3.10(a)).

From a rather mathematical point of view, the increased discretization error level of the SK-TAN element can be explained by a high level of the second, energy-related term in (3.108) that dominates the overall discretization error. This behavior, in turn, is a pure consequence of the fact that the two exponents $k+1$ and $2(k-m+1)$ in (3.108) are identical for trial functions of polynomial degree $k=3$. However, for polynomial degrees $k>3$, the second term in (3.108) is expected to converge with a higher rate and consequently, for sufficiently fine discretizations, the first term reflecting the pure polynomial approximation power will determine the overall discretization error level. In this range, a lower discretization error per DoF can be expected for the Kirchhoff type beam element formulations independently of the beam length, the complexity of the deformation state or the type of boundary conditions. For a first proof of principle, in Figure 3.11(b), the L^2-error resulting from the CJ element with fifth-order Lagrange interpolation as well as from the SK-TAN element based on a fifth-order Hermite interpolation are depicted: While for very rough discretizations, the energy-related error contribution with higher convergence rate still seems to dominated the overall discretization error of the SK-TAN element, the expected optimal gap between the Reissner discretization error (higher level) and the Kirchhoff discretization error (lower level) can be observed. For comparison reasons, in Figure 3.11(a), the results of the corresponding third-order variants of Figure 3.10(a) are repeated. Since this thesis focuses on the development of third-order Kirchhoff beam elements, no further details on the construction of higher-order Hermite polynomials (either by introducing additional nodes or by

considering higher-order derivatives) will be given at this point. However, it is expected that a comparable behavior as illustrated in Figure 3.11(b), can also be achieved for the other test cases considered throughout this thesis, if fifth-order SK and WK elements are employed. A detailed investigation of general geometrically exact beam element formulations of Kirchhoff-Love type with polynomial degree $k>3$ will be considered in future research work.

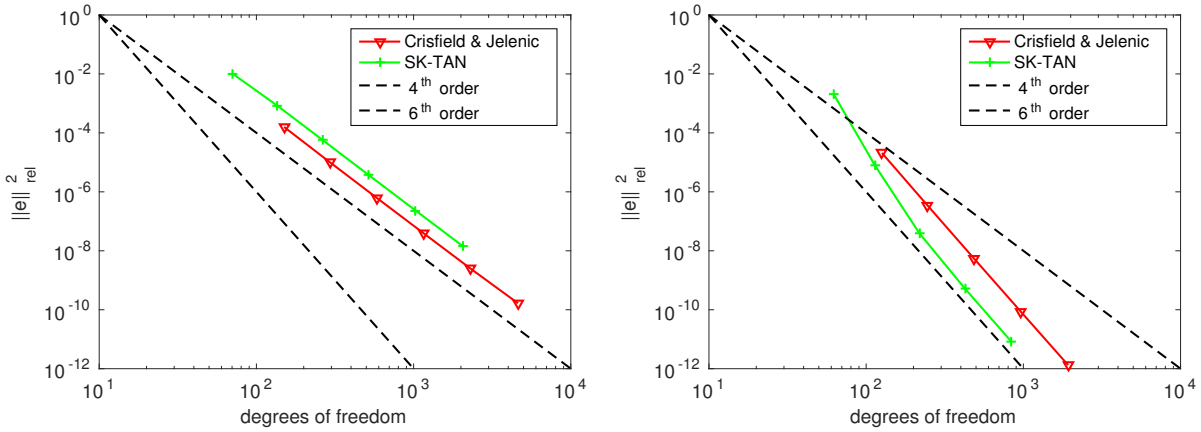

(a) Reference: Analytic, third-order elements.

(b) Reference: Analytic, fifth-order elements.

Figure 3.11: Straight beam and load case $\tilde{M}$: convergence of third- and fifth-order elements.

Eventually, also the convergence behavior of the fourth load case shall be investigated. In Figures 3.12(a) and 3.12(b) the L^2-error of the CJ, the WK-TAN and the SK-TAN element is plotted for the two beam slenderness ratios $\zeta = 100$ and $\zeta = 10000$. Since no closed-form analytic solution has been available for this example, a numerical reference solution based on the element formulation of Crisfield and Jelenić has been employed. As a consequence of shear deformation induced by the tip force $\tilde{F}$, the result derived from the Reissner and Kirchhoff type beam element formulations will differ in the limit of very fine discretizations $h \to 0$. This "model error" of the shear-free Kirchhoff elements becomes visible in form of a kink in the convergence diagram and a certain cutoff error level that remains constant even for arbitrarily fine discretizations. As expected, the model difference between the Simo-Reissner and the Kirchhoff-Love beam theory decreases with increasing beam slenderness ratio, a property that is reflected by a lower cutoff error level for the higher slenderness ratio $\zeta = 10000$. For the lower slenderness ratio $\zeta = 100$, the relative error distinguishing the Kirchhoff from the Reissner solution lies below 10^{-3}, which can be assumed as reasonable approximation for many engineering applications. For the high slenderness ratio $\zeta = 10000$, the relative error between these two models is smaller than 10^{-7}. For the investigated cases of $\zeta = 100$ and $\zeta = 10000$, the cutoff error scales almost quadratically with the slenderness ratio, which would be the expected result for the displacement solution of the geometrically linear theory. This result is quite remarkable for this highly nonlinear example.

Despite the fact that the Simo-Reissner formulations yield the more general solutions, which also contain the effects of shear deformation, the Kirchhoff type WK-TAN element formulation will be considered as numerical reference solution throughout this thesis (see Figures 3.12(c)

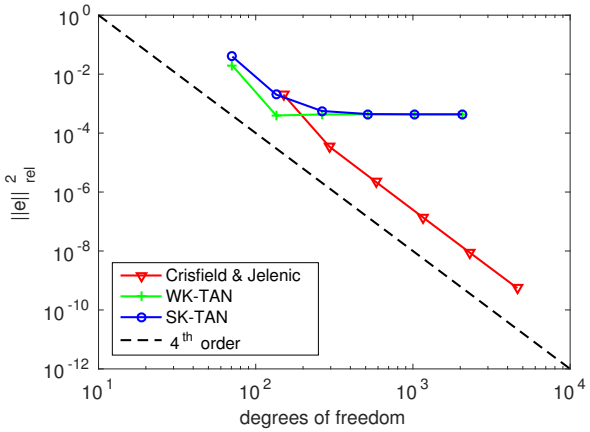

(a) Reference: Crisfield & Jelenić, $\zeta = 100$.

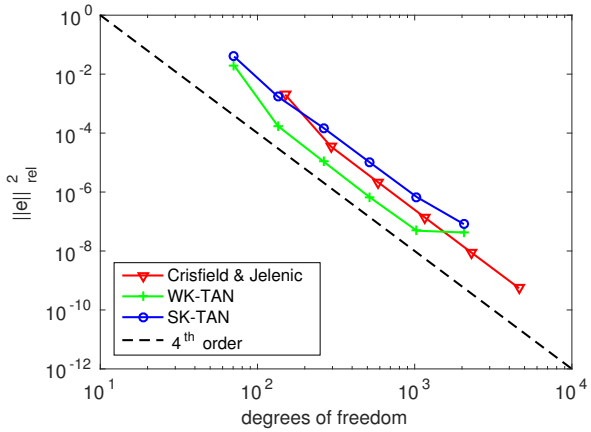

(b) Reference: Crisfield & Jelenić, $\zeta = 10000$.

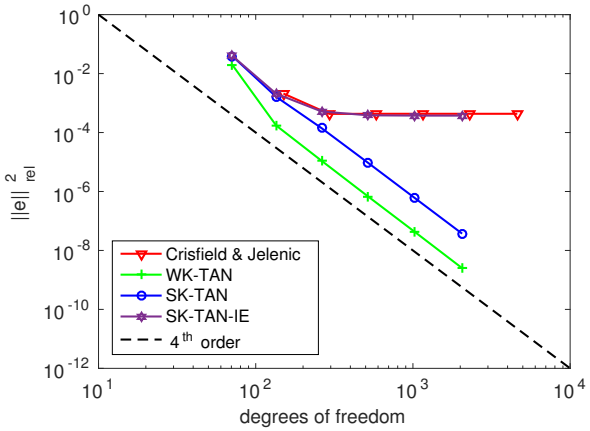

(c) Reference: WK-TAN, $\zeta = 100$.

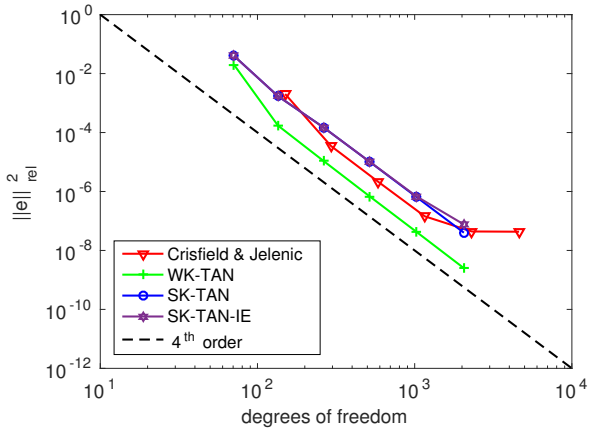

(d) Reference: WK-TAN, $\zeta = 10000$.

Figure 3.12: Load case $\tilde{M}$+$\tilde{F}$: L^2-error for different element formulations.

and 3.12(d) for illustration). Such a procedure seems to be sensible, since within this thesis, the convergence behavior of the Kirchhoff type elements and not of the Reissner type elements shall be studied. Nevertheless, the model error of the Kirchhoff type beam elements is still observable, but this time in form of a kink and a remaining cutoff error level in the convergence plots of the Reissner type formulation. From Figures 3.12(c) and 3.12(d), it can again be observed that all element formulations exhibit the expected convergence rate of four, that the error level of the SK-TAN element lies slightly above and that the error level of the WK-TAN element lies below the error level of the CJ element. Furthermore, also the variant SK-TAN-IE of the SK-TAN element that has been supplemented by an additional inextensibility constraint according to Section 3.6, has been considered in these plots. Within its range of applicability, this element yields similar results as the original SK-TAN element and a cutoff error as compared to the extensible Kirchhoff variants which lies in the same range as the cutoff error between Kirchhoff and Reissner formulations. Thus, it represents a reasonable next step of model reduction aiming at improved numerical properties. As mentioned in Section 3.6, the inextensibility constraint can be combined with all element formulations considered in this thesis. Here, only a first proof of

principle should be given. Further investigations on the construction of inextensible Kirchhoff beam elements and their numerical properties will be addressed in future research work.

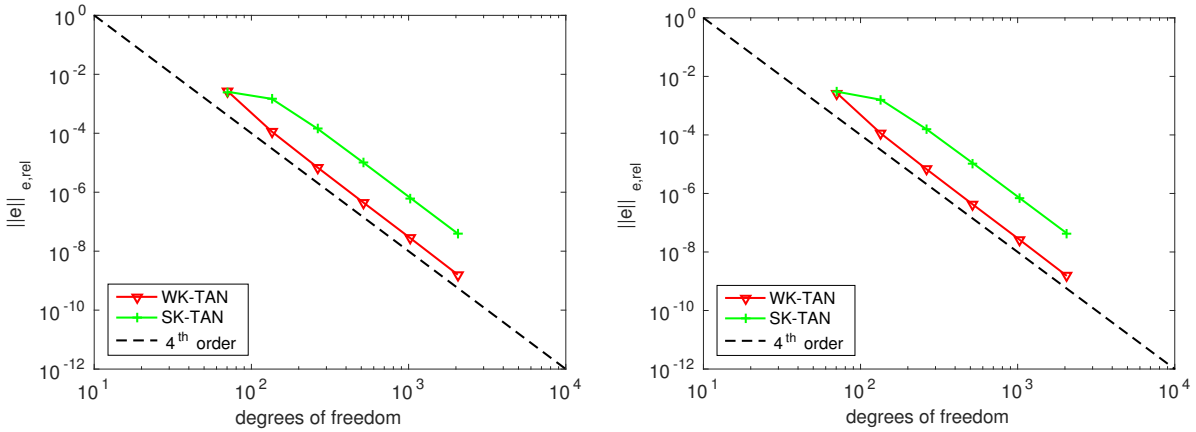

(a) Reference: WK-TAN, $\zeta = 100$.

(b) Reference: WK-TAN, $\zeta = 10000$.

Figure 3.13: Load case $\tilde{M}$+$\tilde{F}$: Energy-error for different element formulations.

While the WK-TAN element was able to exactly represent the internal energy of the load case $\tilde{M}$, now, for the load case $\tilde{M}$+$\tilde{F}$, the energy convergence of the formulations WK-TAN and SK-TAN can be compared (see Figures 3.13(a) and 3.13(b) for the two slenderness ratios $\zeta = 100$ and $\zeta = 10000$). Both element formulations exhibit the expected convergence order of four, and similar to the load case $\tilde{M}$, the WK-TAN element yields a better approximation of the internal energy than the SK-TAN element. This is observable in form of a lower energy error level in Figures 3.13(a) and 3.13(b) and the reason for the lower L^2-error level visible in Figures 3.12(c) and 3.12(d). A possible explanation for the better performance of the WK-TAN element may be found by considering the interaction of the employed translational and rotational interpolation schemes: As shown in Section 3.5.4, the number of unknowns equals the number of equations required for the WK-TAN element to (energetically) represent a pure bending state. This means that an exact representation of the internal energy associated with states of constant axial tension, bending curvature and torsion is possible. This property does not hold for the SK-TAN element (see e.g. Section 3.4.3), where the corresponding system of equations that has to be fulfilled for representing a pure bending state is slightly over-constrained. While the difference between the WK and the SK elements in the L^2-error level is expected to vanish with higher-order trial functions, such an effect can in general not be predicted for the energy error. Eventually, it has to be mentioned that for both the L^2-error as well as the energy error plots of the load case $\tilde{M}$+$\tilde{F}$, no difference between the slenderness ratios $\zeta = 100$ and $\zeta = 10000$ is evident, which again underlines the successful avoidance of membrane locking and the effectiveness of the MCS method. Finally, also the performance of the Newton-Raphson scheme shall be investigated and compared between Kirchhoff and Reissner type element formulations (see Figure 3.14). Since the computationally expensive steps of solving a nonlinear system of equations and evaluating the tangent stiffness matrix have to be conducted in every Newton iteration, a reduction in the total number of Newton iterations $n_{iter,tot}$ as defined in (3.34) would considerably increase the

overall efficiency of the numerical algorithm. In Figures 3.14(a) and 3.14(b), the total number of Newton iterations $n_{iter,tot}$ of the load case $\tilde{M}$+$\tilde{F}$ in combination with slenderness ratios of $\zeta = 100$ and $\zeta = 10000$ has been plotted for the element formulations CJ, WK-TAN, SK-TAN, WK-ROT and SK-ROT and different spatial discretizations. While the final FEM solutions have been shown to be independent from the choice of nodal rotation parametrization, the number of Newton iterations required for the SK/WK-ROT and SK/WK-TAN variants might differ considerably. Therefore, also the Newton performance of these variants has been investigated. For solving the highly nonlinear beam problem, the load step adaption scheme presented in Section 3.2.1.3 based on an initial number of $N_0 = 2$ load steps has been employed.

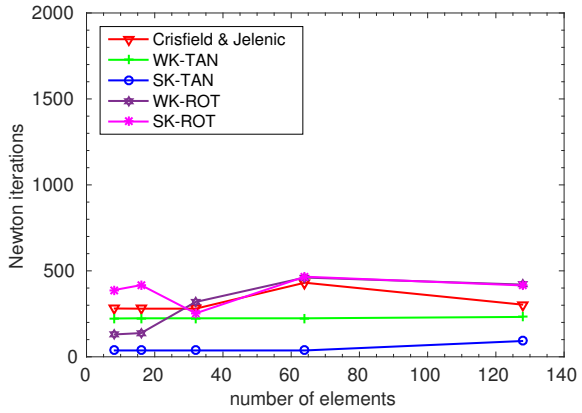

(a) Moderate slenderness ratio: $\zeta = 100$.

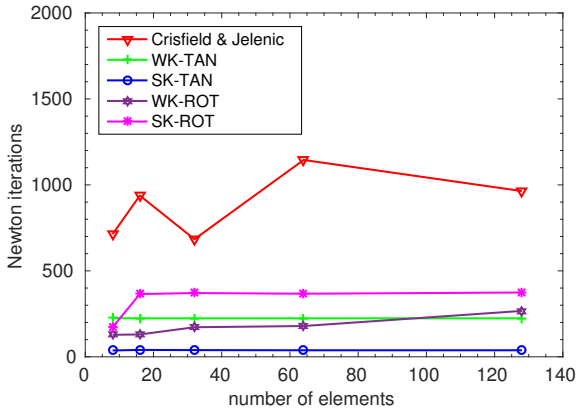

(b) High slenderness ratio: $\zeta = 10000$.

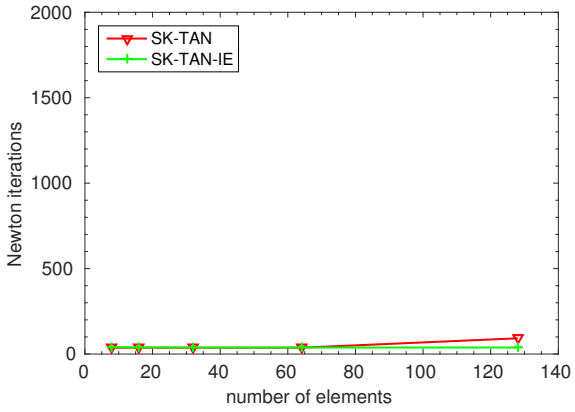

(c) Moderate slenderness ratio: $\zeta = 100$.

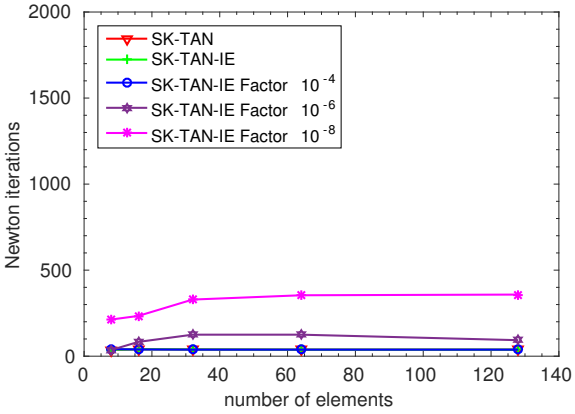

(d) High slenderness ratio: $\zeta = 10000$.

Figure 3.14: Load case $\tilde{M}$+$\tilde{F}$: Total number of Newton iterations.

By comparing Figures 3.14(a) and 3.14(b), one realizes that the Newton performance of the Kirchhoff type element formulations is rarely influenced by the considered slenderness ratio, while the number of Newton iterations required by the Reissner element increases drastically with increasing slenderness ratio. Furthermore, it seems that the SK/WK-TAN variants require fewer Newton iterations than the SK/WK-ROT variants. These trends will be confirmed, and

even more pronounced, in more general 3D examples presented in subsequent sections. Furthermore, in Figures 3.14(c) and 3.14(d), the element SK-TAN is compared with its counterpart SK-TAN-IE supplemented by an additional inextensibility constraint according to Section 3.6. Accordingly, the pure consideration of an additional inextensibility constraint does not seem to lead to a noteworthy change in the Newton performance within the considered range of slenderness ratios. As mentioned in Section 3.6, in order to take advantage of the inextensible formulation in terms of conditioning, it is recommended to scale the axial tension residual terms by means of a proper factor c_ϵ. In Figure 3.14(d), the required number of Newton iterations resulting from scaling factors $c_\epsilon = 10^{-4}$, $c_\epsilon = 10^{-6}$ and $c_\epsilon = 10^{-8}$ is plotted: A factor of $c_\epsilon = 10^{-4}$ leads to no noteworthy change in the Newton performance, a factor of $c_\epsilon = 10^{-6}$ to a visible increase of $n_{iter,tot}$ and a factor of $c_\epsilon = 10^{-8}$ to a drastic increase of $n_{iter,tot}$. This behavior seems to be reasonable since a too "soft" stiffness contribution stemming from the axial tension terms might be contradictory to the inextensibility constraint, which can be interpreted as an infinitely stiff contribution. Nevertheless, scaling factors up to $c_\epsilon = 10^{-4}$ seem to be sensible, since the Newton performance is not influenced in this range, and the condition number of the submatrix $\mathbf{k}_{ele}$ in (3.159) can already be decreased considerably (namely by a factor of c_ϵ). Of course, a further improvement of the condition number could be achieved by applying proper preconditioning operations, which only influence the linear but not the nonlinear solver. As already mentioned above, this 2D example only represents a first proof of concept for inextensible, geometrically exact Kirchhoff beam elements. Further research work on this topic is intended.

In summary, the following conclusions can be drawn from the 2D examples considered in this section: 1) The proposed Kirchhoff elements yield accurate results with acceptable model errors for slenderness ratios of $\zeta \geq 100$ and a model error that decreases quadratically with increasing beam slenderness ratio. 2) The expected convergence orders of four in the L^2- as well as in the energy error could be confirmed for all investigated Kirchhoff elements. 3) In combination with the MCS method, none of the considered element formulations exhibited an influence of the element slenderness ratio on the resulting discretization error. This result confirms the effectiveness of the MCS method in the avoidance of membrane locking. 4) The discretization error level of the WK-TAN element lies below the error level of the Reissner type element and also below the error level of the SK-TAN element above. The increased error level of the SK-TAN element has been shown to vanish with higher polynomial degree $k > 3$ of the trial functions. 5) While the total number of Newton iterations required by the Reissner type element formulations considerably increases with increasing beam slenderness ratio, the number of iterations remains more or less constant for the Kirchhoff type formulations. These conclusions drawn from the considered 2D tests will be confirmed by the more general examples investigated in the following sections.

3.8.3 Example 3: Pure bending in 3D

In this section, the 3D extension of the pure bending examples (load cases M and $\tilde{M}$) investigated in the last section will be considered. Again, the focus lies on an initially straight, clamped beam of standard length $l = 1000$ investigated for the two different slenderness ratios $\zeta = 100$ and $\zeta = 10000$. However, this time, the beam is loaded by a 3D end-moment $\mathbf{M}_1 := (M, 0, M)^T$, with $M = 10$ for $\zeta = 100$ as well as $M = 10^{-7}$ for $\zeta = 10000$, which contains an additional moment component in beam length direction inducing torsional deformation. For this load case,

an analytic solution can be derived by means of the differential equations given in Section 2.3.4. The initial and deformed configuration of this problem setting are illustrated in Figure 3.15(a).

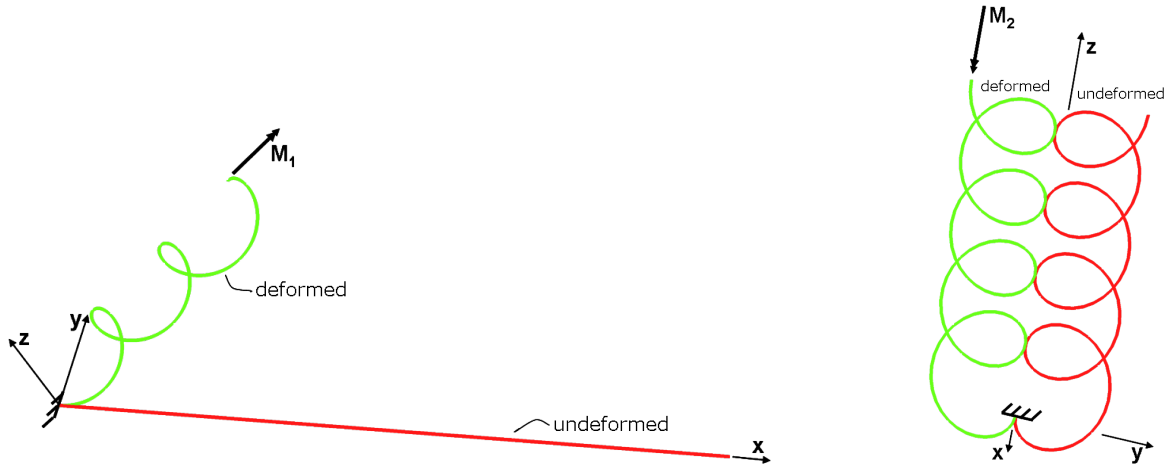

(a) Straight beam loaded with a 3-dimensional discrete end-moment. (b) Helix-shaped beam.

Figure 3.15: Straight beam bent to a helix and helix-shaped beam bent to an inverse helix.

It can easily be verify that the differential equations (2.118) and (2.119) presented in Section 2.3.4 as well as the Dirichlet- and Neumann boundary conditions of this example are fulfilled by an analytic solution which is characterized by the following representation:

$$\mathbf{r}(s) = R_0 \begin{pmatrix} \frac{1}{\sqrt{2}}\left(\sin\beta + \beta\right) \\ \left(1 - \cos\beta\right) \\ \frac{1}{\sqrt{2}}\left(\beta - \sin\beta\right) \end{pmatrix} \quad \text{with} \quad R_0 = \frac{EI}{2M} \quad \text{and} \quad \beta = \frac{s}{\sqrt{2}R_0}. \tag{3.162}$$

This solution represents a helix whose mid-axis points into the $(1,0,1)^T$-direction, viz. in the direction of the applied external moment. The special parameter choice of this example leads to a radius R_0 of the enveloping cylinder that is identical to the slope of the helix. In Figures 3.16, the deformed centerlines are illustrated for $\zeta = 100$ and different magnitudes of the external moment.

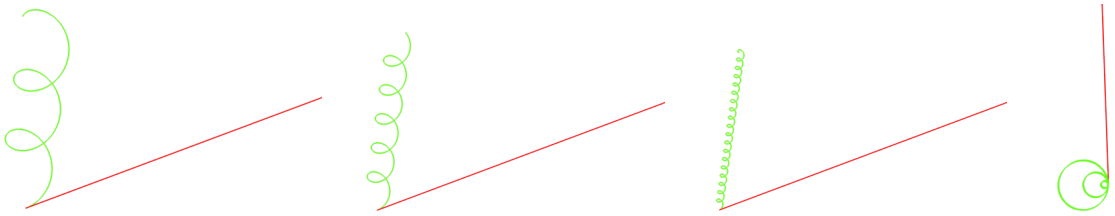

(a) External moment M=10. (b) External moment M=20. (c) External moment M=70. (d) Top view.

Figure 3.16: Deformed shapes for different magnitudes of the applied 3-dimensional moment.

In Figure 3.17(a), the relative L^2-error resulting from the two investigated slenderness ratios is plotted for the element formulations CJ, WK-TAN and SK-TAN as well as spatial discretizations based on $8, 16, 32, 64, 128$ and 256 elements. Again, all element formulations exhibit the

expected convergence order of four and the discretization error level of the WK-TAN element is lower, whereas the discretization error of the SK-TAN element is slightly higher than for the CJ element. Furthermore, no visible difference can be observed between the discretization error levels associated with the two different slenderness ratios. Due to the choice $GI_T = EI_2 = EI_3$, it can easily be verified that this example results in an analytic solution exhibiting vanishing axial tension and shear deformation as well as a constant spatial and material curvature vector along the entire beam pointing into the direction of the external moment vector, i.e. $\mathbf{k} = \mathbf{K} = M/(EI)(1,0,1)^T = \text{const}$. Thus, already the roughest discretizations of the CJ and WK-TAN elements can exactly represent the hyperelastic stored energy function for this pure bending case, which can be interpreted as a simple 3D patch test for geometrically exact beams.

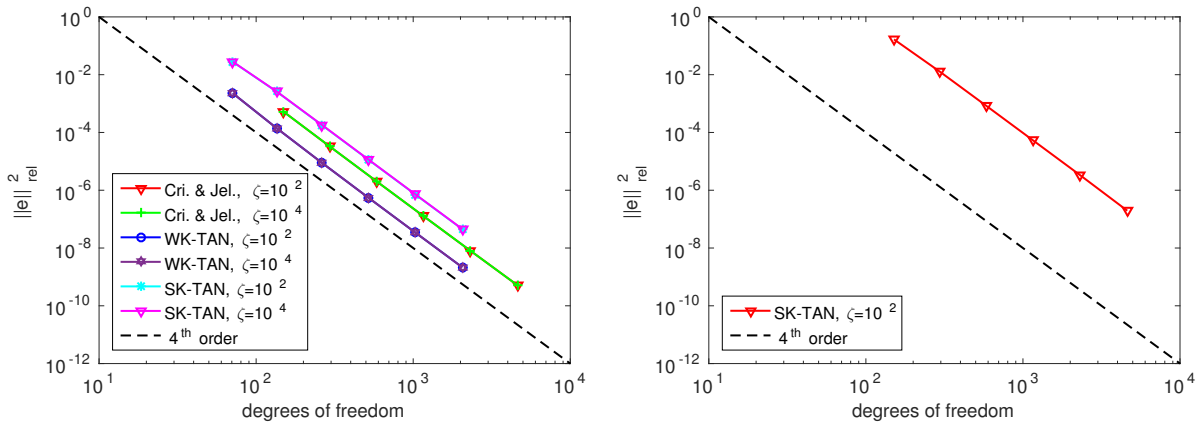

(a) "Straight to helix", reference: analytic.

(b) "Inversion of helix", reference: analytic.

Figure 3.17: Convergence plot of load cases "straight to helix" and "inversion of helix".

Finally, also the number of Newton iterations shall be investigated (see Figure 3.18). In order to enable more general conclusions, this time, a second Reissner type beam element formulation, which is based on a completely different triad interpolation scheme, has additionally been included in the comparison. Concretely, this element represents an "interpretation" formulated by Crisfield [56] (see Chapter 17.2) of the original variant proposed by Simo and Vu-Quoc [208], in the following denoted as SV element. This time, the load step adaption scheme presented in Section 3.2.1.3 based on an initial number of $N_0 = 10$ load steps has been employed.

Similarly to the 2D case considered in the last section, the Newton performance of the Reissner type element formulations drastically deteriorates with increasing slenderness ratio whereas the performance of the Kirchhoff type elements remains unchanged (or is even slightly improved in case of the WK/SK-TAN variants). Concretely, for the slenderness ratio $\zeta = 10000$, all investigated discretizations of the WK/SK-TAN elements exhibit a remarkably constant number of $n_{iter,tot} = 140 \pm 4$ iterations, while the total number of iterations required by the WK/SK-ROT elements increases from $n_{iter,tot} \approx 500$ to $n_{iter,tot} \approx 2000$ with increasing number of elements and the total number of iterations required by the Reissner type formulations is almost by two orders of magnitude higher than for the WK/SK-TAN elements and lies constantly above a value of $n_{iter,tot} > 12000$. Seemingly, the considerable difference between the WK/SK-TAN elements

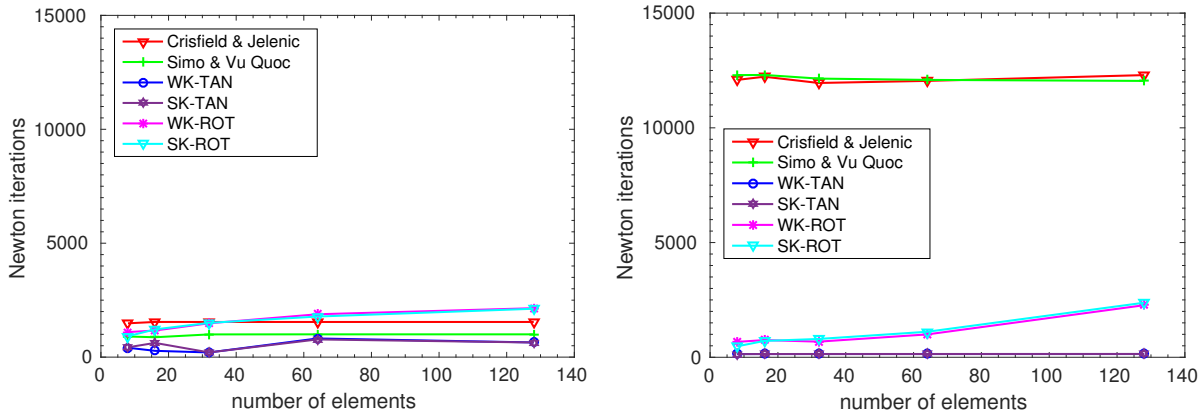

(a) Moderate slenderness ratio: $\zeta = 100$.

(b) High slenderness ratio: $\zeta = 10000$.

Figure 3.18: Load case "straight to helix": Total number of Newton iterations.

and the Reissner type element formulations can be attributed to two different effects: Firstly, the parametrization of nodal triads via tangent vectors seems to be more good-natured than the parametrization based on nodal rotation vectors. This effect already gets visible as difference between the WK/SK-TAN and the WK/SK-ROT variants and seems to be more or less independent from the beam slenderness ratio. Secondly, the high stiffness contributions resulting from the shear mode seem to considerably deteriorate the Newton convergence in the range of high slenderness ratios: This effect becomes obvious as difference between the WK/SK-ROT elements and the Reissner type elements. The linearizations of all of these four elements are based on multiplicative updates of nodal rotation vectors. This observation is emphasized by the two elements types WK-ROT and CJ, which additionally exhibit the same triad interpolation. These two elements only differ in the centerline interpolation (based on Lagrange or Hermite polynomials), which is not expected to influence the Newton convergence in such a drastic manner, and the fact that the WK-ROT element additionally enforces the constraint of vanishing shear strains. Consequently, the avoidance of shear modes seems to be the main reason for the considerably improved performance of the Kirchhoff type element formulations. Finally, the observation that the total number of Newton iterations required by the WK/SK-ROT variants increases with increasing number of elements is only of secondary practical interest since the discretizations relevant for practical applications are located in the range of small element numbers (on the left of Figure 3.18(b)). The observations made in Figures 3.18(a) and 3.18(b) and discussed so far, will be confirmed by further 3D examples presented in subsequent sections.

This section shall be concluded by an extension of the example presented so far: Thereto, the inverse problem as shown in Figure 3.15(b) will be considered. For the inverse problem, the initial geometry is already a helix according to (3.162). However, for the inverse problem, a slightly different radius $\tilde{R}_0 = l/(9\sqrt{2}\pi) < R_0$ has been chosen. Since the length of the beam still has the standard value of $l = 1000$, a higher number of 4.5 loops along the helix results from this choice. Again, one can verify by means of the differential equations (2.118) and (2.119) that the external moment $\mathbf{M}_2 := (-M_2, 0, -M_2)^T$ with $M_2 = EI/(2\tilde{R}_0)$ exactly bends the helix into a straight

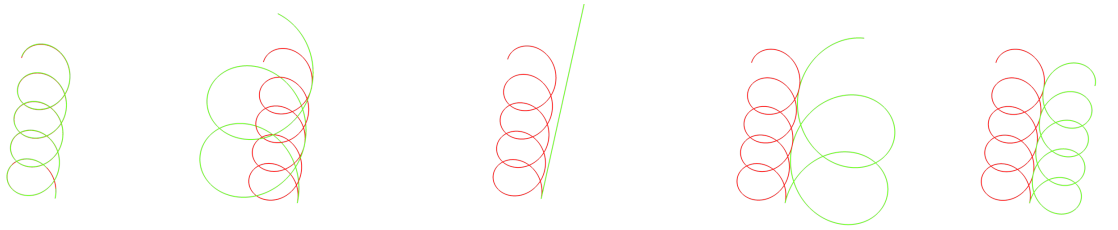

(a) Step t=0.0. (b) Step t=0.25. (c) Step t=0.50. (d) Step t=0.75. (e) Step t=1.0.

Figure 3.19: Inversion of a helix by an end-moment: Deformed shape at different load steps.

line (see Figure 3.19(c)). By doubling the magnitude of the external moment to $M_2 = EI/\tilde{R}_0$, the helix is exactly inverted, i.e. the analytic solution for the deformed geometry has the same form as for the initial geometry according to (3.162) (with $\tilde{R}_0$ instead of R_0), but with opposite sign in the second vector component. Different deformation states for the latter case are illustrated in Figure 3.19. The L^2-error resulting for this example from the SK-TAN element has been plotted in Figure 3.17(b), which yields the expected convergence order of four.

The examples considered in this section also clarify the relevance of the Frenet Serret intermediate triad field for analytical purposes (see Section 2.3.4), e.g. for the derivation of analytical solutions via (2.118) and (2.119). Firstly, helical curves represent a distinguished class of solutions for beams loaded with moments (see e.g. [3]). Secondly, this kind of solutions can easily be represented with respect to the Frenet-Serret intermediate triad, since the centerline curvature $\kappa_{helix} = \text{const.}$ and the torsion $\tau_{helix} = \text{const.}$ of the intermediate triad field are constant.

Remark: For some of the discretizations investigated in Figure 3.18, solutions of the SK-TAN element could already be found in one load step. However, since in these cases no convergence could be achieved for simulations based on two or three load steps, the solution of the problem by means of one load step can rather be regarded as a "lucky shot" than as a representative convergence behavior. In order to avoid a biased comparison resulting from such effects, the initial number of load steps has been increased to $N_0 = 10$. By this means and the load step adaption scheme of Section 3.2.1.3, an evaluation and comparison process is intended that is as fair and objective as possible. Nevertheless, this example shows that an absolute statement concerning the robustness of the nonlinear solution scheme based on a single example / discretization and a deliberately chosen "good-natured" step size, as sometimes done in the literature, is questionable. Here, the degree of arbitrariness is intended to be minimized by employing an automated scheme for determining the optimal load step size, by comparing the results of different test cases, different discretizations, different element types (here Reissner and Kirchhoff type beam elements) as well as different representatives for each element type. Furthermore, in order to avoid biased results as consequence of incorrect linearizations, the results of the Reissner type element formulations derived on the basis of an analytic representation of the consistent tangent stiffness matrix have been verified by simulations on the basis of a consistent tangent stiffness matrix derived via an automatic differentiation tool.

3.8.4 Example 4: Verification of path-independence

In Section 3.2.4.2, the fundamental property of objectivity has already been verified for the proposed Kirchhoff beam elements. In this section, it will be shown that these element formulations are also path-independent, i.e. for beam problems whose analytic solution is independent from a specific loading path, these beam element formulations also yield a discrete solution that is independent from a specific loading path. As numerical test case for path independence, an initially straight clamped beam with initial length $l = 1000$ and slenderness ratio $\zeta = 100$ (thus $R = 10$) is considered that is loaded by an end-moment $\mathbf{M} = (0, 0, M)^T$, with the moment $M = 4EI\pi/l \approx 10.47$ being defined such that it exactly bends the beam into a "double-circle", and an additional end-force $\mathbf{F} = (0, 0, F)^T$, with $F = 0.01 \approx M/l$. Again, for comparison reasons, also the case of an increased slenderness ratio $\zeta = 10000$ with correspondingly adapted loads $M = 4EI\pi/l \approx 1.047 \cdot 10^{-7}$ and $F = 10^{-10} \approx M/l$ will be investigated. The problem setup as well as the deformed configuration for this example are shown in Figure 3.20. In the following, two different possibilities how to apply these tip loads are investigated: In a first load case, the moment and the force are applied simultaneously (load case "sim"), while, in a second load case, the moment and the force are applied successively (load case "suc"). In the latter case, the external moment is increased linearly from zero to M in the pseudo-time interval $t \in [0; 0.5]$, whereas the external force is increased linearly from zero to F within $t \in [0.5; 1.0]$.

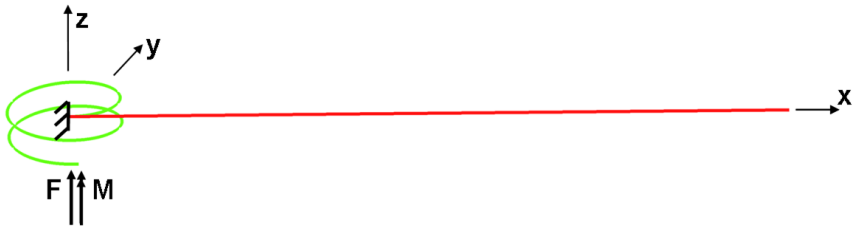

Figure 3.20: Problem setup: Initially straight beam bent by a discrete end-moment and -force.

The deformed shapes of both load cases have been plotted for the pseudo-time steps $t = 0.25$, $t = 0.5$, $t = 0.75$ and $t = 1.0$ in Figure 3.21. Apparently, the two load cases lead to different deformation paths, but to an identical final configuration. It contradicts intuition that this final deformed configuration lies completely in the half space with $z \leq 0$, although the tip force points into the positive z-direction. For the case of small forces F, this observation can easily be verified by deriving an analytical solution based on a linearization of equations (2.118) and (2.119) with respect to the double-circle configuration resulting from the end-moment M. Furthermore, this observation is in agreement with the results obtained in [107] and [16], where a similar example based on a slightly modified parameter choice has been analyzed.

In order to investigate possible path dependence effects also in a quantitative manner, the relative L^2-error has been calculated between the solution $\mathbf{r}_{h,suc}$ of the load case "suc" for a certain discretization and the solution $\mathbf{r}_{h,sim}$ of the load case "sim" for the same centerline discretization. Thus, basically the relative L^2-error definition of equation (3.105) has been applied, with $\mathbf{r}_h = \mathbf{r}_{h,suc}$ and $\mathbf{r}_{ref} = \mathbf{r}_{h,sim}$. The results obtained for the two different slenderness ratios and the investigated element formulations CJ, SK-TAN and WK-TAN are illustrated in Figure 3.22.

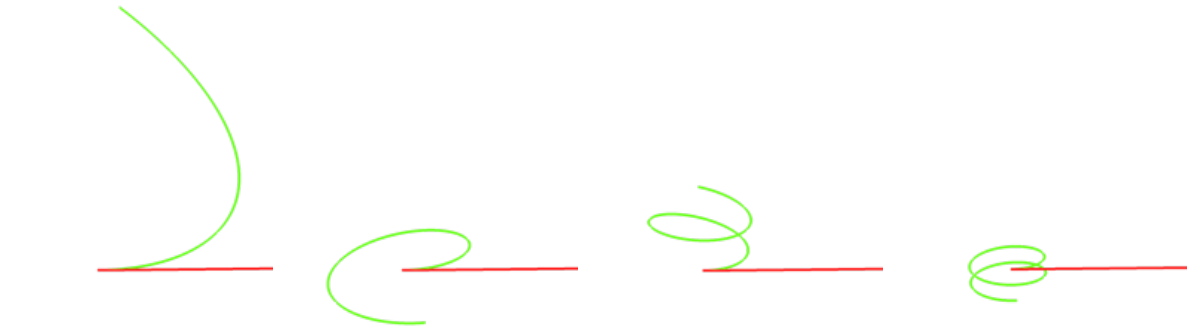

(a) Step t=0.25 (sim). (b) Step t=0.50 (sim). (c) Step t=0.75 (sim). (d) Step t=1.0 (sim).

(e) Step t=0.25 (suc). (f) Step t=0.50 (suc). (g) Step t=0.75 (suc). (h) Step t=1.0 (suc).

Figure 3.21: Deformed configurations for simultaneous (sim) and successive (suc) loading of an initially straight beam with a moment M and a force F at different load steps.

Accordingly, for all investigated element types, discretizations and slenderness ratios, this error vanishes up to machine precision, which verifies the path independence of these formulations.

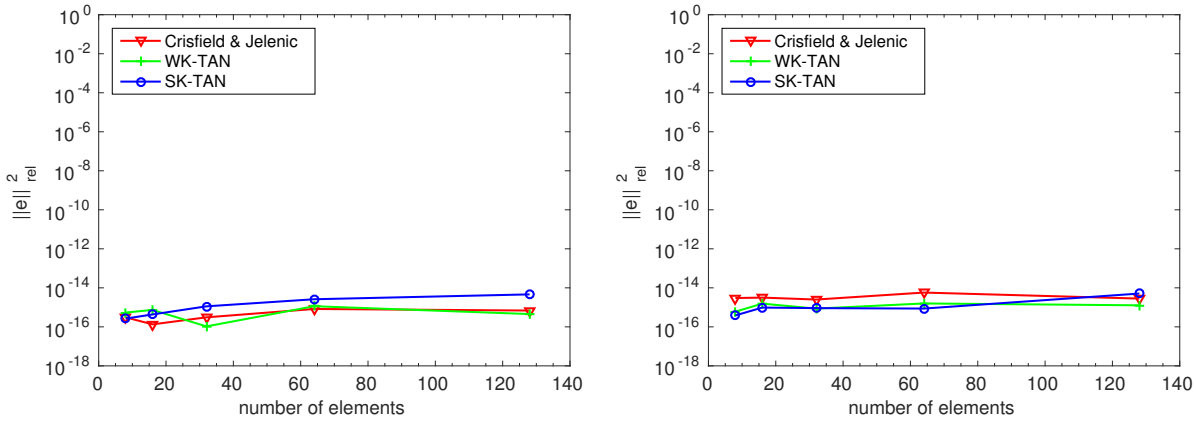

(a) Moderate slenderness ratio: $\zeta = 100$. (b) High slenderness ratio: $\zeta = 10000$.

Figure 3.22: L^2-error between the load cases "Simultaneously" and "Successively".

For completeness, Figure 3.23 represents the discretization error resulting from the CJ, SK-TAN and WK-TAN elements for the considered slenderness ratios of $\zeta = 100$ and $\zeta = 10000$. There, the observations already made in earlier examples with respect to convergence rate, discretization error level and cutoff error between Kirchhoff and Reissner type element formulations are confirmed. Similar to these earlier examples, also this test case involves an isotropic beam (i.e

no initial curvature, quasi-circular cross-section shape with $I_2 = I_3 =: I$) and a 3D deformation state with non-vanishing torsion and can consequently serve as test case for the isotropic Kirchhoff theory presented in Section 2.4.1 (see equation (2.134) for the corresponding weak form). As expected, the resulting isotropic beam element formulation can represent this test case correctly and shows a convergence rate of four and a similar discretization error level as the variant SK-TAN. The only reason why the discretization error level is slightly lower for the isotropic than for the SK-TAN element lies in the twist interpolation, which only requires two DoFs for the isotropic element but three DoFs for the SK-TAN element. In Section 3.2.3.4, the importance of a consistent torsion (3.64) of the intermediate triad field has been emphasized. Now, in Figure 3.23(b), the discretization error for a variant (SK-TAN no K_{M1}) has been plotted, where exactly this torsion term has been neglected. Surprisingly, the resulting discretization error level is identical to the "correct" SK-TAN element formulation. How can this contradiction be explained? In order to answer this question, it has to be realized that the actual triad orientation is not important for isotropic examples in order to yield a consistent centerline convergence. It can easily be verified that only the mechanical torsion has to be represented correctly, which is also the functional principle of the isotropic beam element. If the torsion of the intermediate triad field is neglected, the total torsion is solely represented by the derivative of the relative angle field $\varphi(\xi)$. Consequently, the relative angle arises in a way such that the total torsion is represented exactly, which in turn results in an inconsistent triad orientation. However, since for isotropic beams, only the torsion, but not the triad orientation, enters the weak form, the final result for the beam centerline is correct. Later in Section 3.8.6, it will be shown that the situation changes for anisotropic beams, i.e. beams with initial curvature or with anisotropic cross-section shapes. There, the neglect of the intermediate triad torsion will indeed lead to an inconsistent centerline solution resulting in a decreased spatial convergence rate. Furthermore, this investigation explains why certain Kirchhoff element formulations available in the literature, which accidentally neglect this torsion term, nevertheless produce correct results and consistent convergence rates for the centerline solution as long as isotropic beam problems are considered.

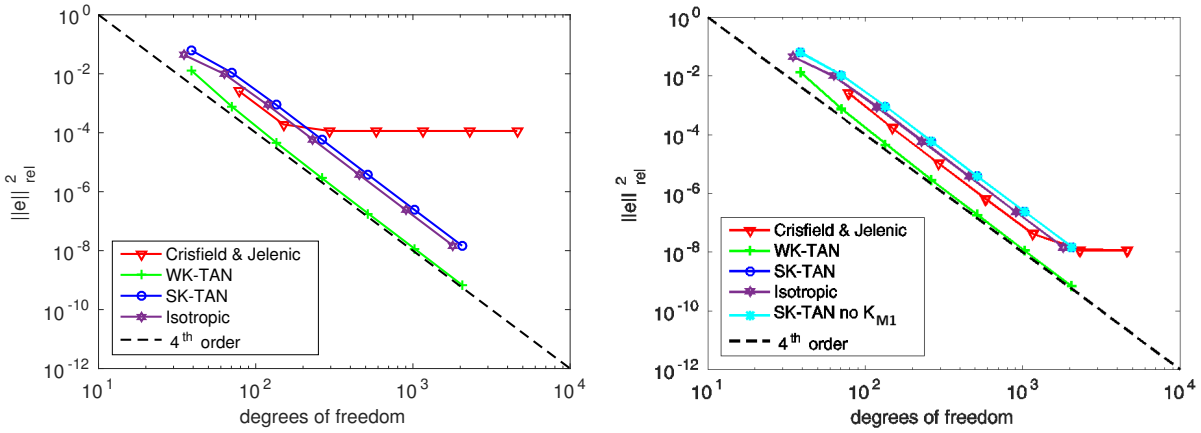

(a) Reference: WK-TAN, $\zeta = 100$.

(b) Reference: WK-TAN, $\zeta = 10000$.

Figure 3.23: Path independence: L^2-error for different element formulations.

Finally, in Figure 3.24, again, the total number of Newton iterations required by the different element formulations is plotted for the load case "sim" and the two investigated slenderness ratios. Here, the load step adaption scheme presented in Section 3.2.1.3 based on an initial number of $N_0 = 10$ load steps has been employed. The obtained results are very similar to the last section: The Newton performance of the Reissner type element formulations drastically deteriorates with increasing slenderness ratio whereas the performance of the Kirchhoff type elements remains unchanged. For the slenderness ratio $\zeta = 10000$, all investigated discretizations of the WK/SK-TAN elements exhibit a remarkably constant number of $n_{iter,tot} = 107 \pm 1$ iterations, while the total number of iterations required by the WK/SK-ROT elements increases from $n_{iter,tot} \approx 800$ to $n_{iter,tot} \approx 2500$ with increasing number of elements. Again, the total number of iterations required by the Reissner type beam element formulations is almost by two orders of magnitude higher than for the WK/SK-TAN elements and lies constantly above a value of $n_{iter,tot} > 6000$ for the CJ element formulation and $n_{iter,tot} > 7000$ for the SV element formulation.

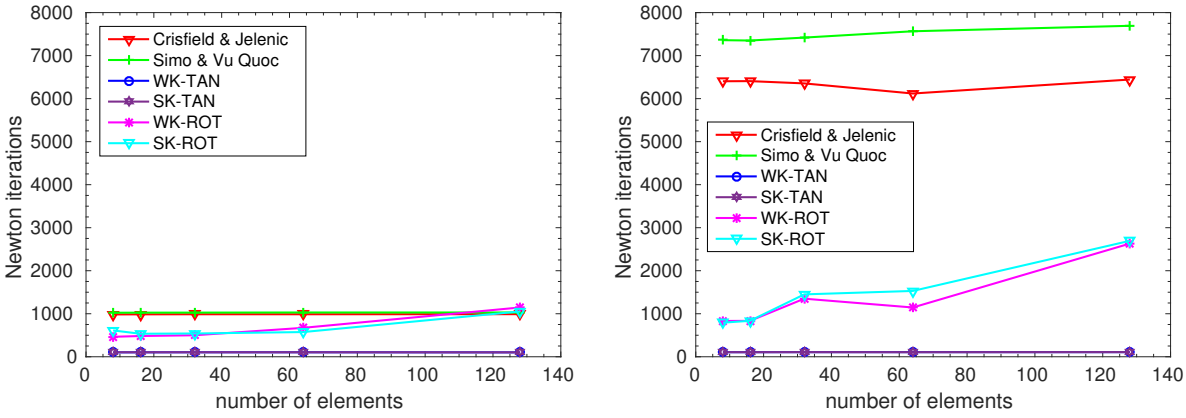

(a) Moderate slenderness ratio: $\zeta = 100$.

(b) High slenderness ratio: $\zeta = 10000$.

Figure 3.24: Load case "Simultaneously": Total number of Newton iterations.

3.8.5 Example 5: Beam with sinusoidal line load

In this section, an initially straight beam of length $l = 1000$ and slenderness ratio $\zeta = 10000$ with support and loading conditions as illustrated in Figure 3.25(a) is considered. While the left end of the beam is clamped, the right end only has two remaining degrees of freedom: the displacement u_x in x-direction and the rotation α with respect to the $x-$axis. The beam is loaded with a constant axial line load as well as a "rotating" transverse line load given by $\tilde{\mathbf{f}}(s) = (\tilde{f}_x, \tilde{f}_y, \tilde{f}_z)^T = (\tilde{f}_x, \tilde{f}_\perp \sin\phi, \tilde{f}_\perp \cos\phi)^T$, with $\tilde{f}_x / EI = \tilde{f}_\perp / (2EI) = 3.6 \cdot 10^{-8}$ and $\phi = 2\pi s/l$. The motivation for the investigation of this example is twofold: On the one hand, this is an example that fulfills the restrictions of both reduced beam theories presented in Section 2.4 (isotropic geometry and no external twisting moments). On the other hand, the resulting 3D and geometrically nonlinear deformation state, the external loading by means of distributed line loads as well as Dirichlet boundary conditions at both ends will yield very general beam configurations for which the isotropic theory of Section 2.4.1 and especially the torsion-free beam theory of

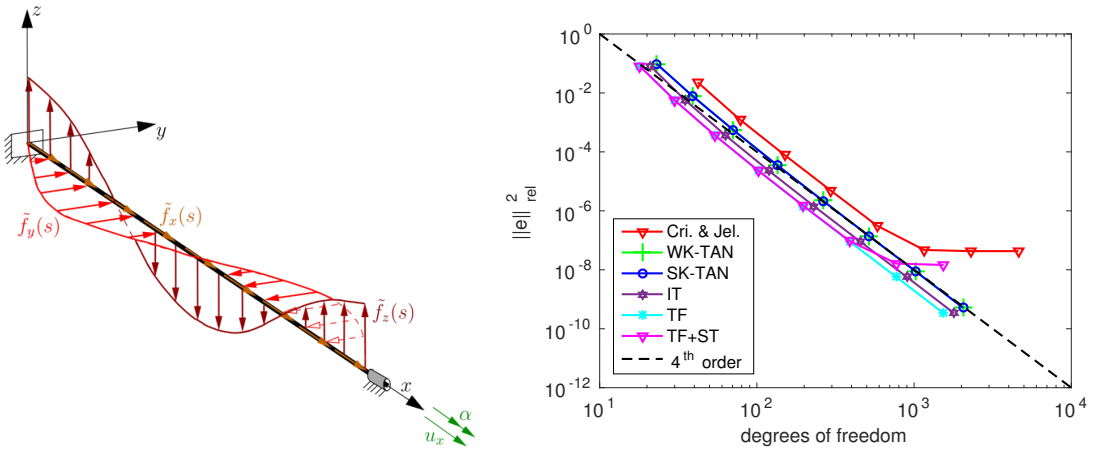

(a) Beam geometry and external loads.

(b) L^2-error, reference: WK-TAN, $\zeta = 10000$.

Figure 3.25: Initially straight, slender beam loaded with a "rotating" distributed lineload.

Section 2.4.2 can be verified. Therefore, this example represents an ideal test case for these formulations. The deformed configurations at different load steps are illustrated in Figure 3.26.

In Figure 3.25(b), the relative L^2-error of the CJ, SK-TAN and WK-TAN elements are plotted for discretizations with $1, 2, 4, 8, 16, 32, 64$ and 128 elements. All elements exhibit the expected convergence order of four. The relative cutoff error between Reissner and Kirchhoff formulations again lies in the range of 10^{-7}. According to Figure 3.25(b), the discretization error levels of the SK-TAN and the WK-TAN elements show no visible differences. The improved performance of the SK-TAN element as compared to the last examples might be attributed to the employment of Dirichlet conditions at both ends of the beam and to the fact that this example does not yield deformed configurations exhibiting multiple loops of the beam centerline. Moreover, the general SK-TAN element is compared with the reduced IsoTropic (IT) and the Torsion-Free (TF) element formulation of Section 3.7. Additionally, also an approximation of the torsion-free element based on the assumption of Small Tension (TF+ST) as derived in Meier et al. [157] (see also the remark in Section 3.7) has been plotted. As expected, the variants IT and TF converge to the correct solution since all of the requirements (2.128) and (2.136) are fulfilled for this example. The slightly decreased discretization error is a direct consequence of the fact that these elements require less (in case of the IT variant) or no (in case of the TF variant) degrees of freedom in order to represent the twist field. Apparently, the variant TF+ST based on the "small tension" assumption cannot go below a relative error level of $1.0 \cdot 10^{-8}$ for this example. This is exactly the expected result: While the reduced models IT and TF are exact formulations which can represent the correct analytic solution in case the corresponding restrictions concerning beam geometry and external loads are fulfilled, the "small tension" assumption of the variant TF+ST is based on an approximation and consequently yields an approximate solution. However, the resulting cutoff error lies below the model error between the Reissner and Kirchhoff formulations. Thus, this approximation seems to be justified resulting in a very simple and efficient element.

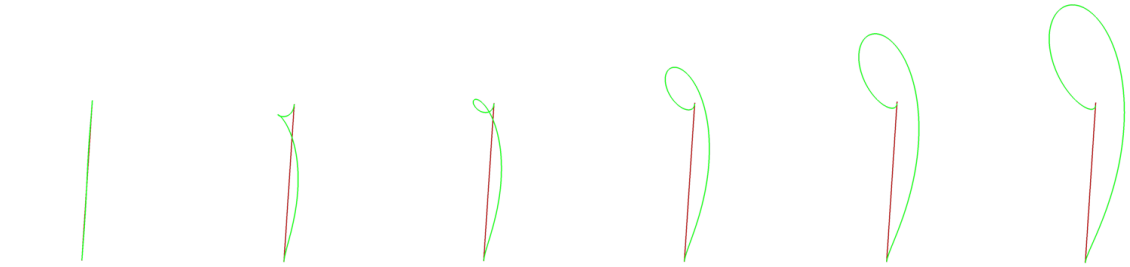

(a) Step t=0.0. (b) Step t=0.2. (c) Step t=0.4. (d) Step t=0.6. (e) Step t=0.8. (f) Step t=1.0.

Figure 3.26: Beam with a "rotating" lineload: Deformed configurations at different load steps.

This example also gives some interesting insight into the "one-way" coupling between bending and torsional moments in the geometrically nonlinear regime of isotropic beams: Despite the non-constant bending moment vector $\mathbf{m} = EI\boldsymbol{\kappa}(s)$ resulting from the three-dimensional deformed geometry of this example, the torsional moment vanishes at any position s along the entire beam. Thus, the bending moment field does not influence the distribution of the torsional moment. On the other hand, one can show that an additional external twist moment in global x-direction applied at the beams right end would lead to a constant torsional moment along the entire beam and to a change in the deformed centerline curve. This means that the torsional moment indeed influences the distribution of the bending moment. The term $\delta\boldsymbol{\theta}_{\perp}^{T} 2GIK_1\boldsymbol{\kappa}$ of the isotropic weak form (2.134) can be identified as the corresponding coupling term.

Finally, some comments concerning the applied twist boundary conditions shall be made. For the static problem considered here, only the boundary conditions of type b) and type c) in (2.142) can be employed. For the investigations made above, the twist boundary condition of type b) has been applied, which was predicted to yield a state of vanishing torsion. This prediction has been confirmed by observing that the torsion-free beam element formulation yields identical results as the general Kirchhoff beam element formulations. On the other hand, twist boundary conditions of type c), i.e. clamped twist DoFs at both ends of the beam, are expected to result in a state of non-vanishing torsion. In order to verify this statement, the ratio $<M_t>/<M_b>$ of the average torsion moment $<M_t>$ to the average bending moment $<M_b>$ based on the definitions

$$<M_t> := \sqrt{\frac{1}{l}\int_0^l M_t^2 ds}, \quad <M_b> := \sqrt{\frac{1}{l}\int_0^l M_b^2 ds}, \tag{3.163}$$

has been determined numerically for both types of boundary conditions. Thereto, a very fine finite element discretization with 512 CJ elements has been employed. This discretization is fine enough to yield a ratio $<M_t>/<M_b> \approx 0$ that vanishes up to machine precision for the twist boundary conditions of type b). On the contrary, the twist boundary conditions of type c) result in a ratio $<M_t>/<M_b> \approx 0.05$, and consequently in an average torsional moment that is only by one order of magnitude smaller than the average bending moment resulting from this load case. These numerical results confirm the theoretical predictions made in Section 2.4.2.

3.8.6 Example 6: Arc-segment with out-of-plane load

Besides the objectivity test in Section 3.8.1, all examples investigated in the previous sections were based on isotropic geometries, i.e. straight beams with quasi-circular cross-sections $EI_2 = EI_3$. Now, an initially curved beam will be considered. The initial geometry is represented by a $45°$-degree circular arc-segment with curvature radius $r_0 = 100$ that lies completely in the global x-y-plane and that is clamped at one end. The section constitutive parameters of the beam result from a quadratic cross-section shape with side length $R = 1$ and a Young's modulus of $E = 10^7$ as well as a shear modulus of $G = 0.5 \cdot 10^7$. This initial geometry is loaded by an out-of-plane force $\mathbf{f} = (0, 0, f_z)^T$ in global z-direction with magnitude $f_z = 600$. This example has initially been proposed by Bathe and Bolourchi [14] and can meanwhile be considered as standard benchmark test for geometrically exact beam element formulations that has been investigated by many authors (see e.g. [12, 43, 55, 60, 71, 74, 106, 116, 187, 188, 199, 208]). While the original definition of the slenderness ratio yields a value of $\zeta = l/R = 100\pi/4$ for this example, a slightly modified definition of the slenderness ratio according to $\tilde{\zeta} = r_0/R = 100$ is employed in the following. For comparison reasons, also a second variant of this example with increased slenderness ratio $\tilde{\zeta} = r_0/R = 10000$, i.e. $R = 0.01$, and adapted force $f_z = 6 \cdot 10^{-6}$ will be investigated. The initial and deformed geometry of the problem are illustrated in Figure 3.27.

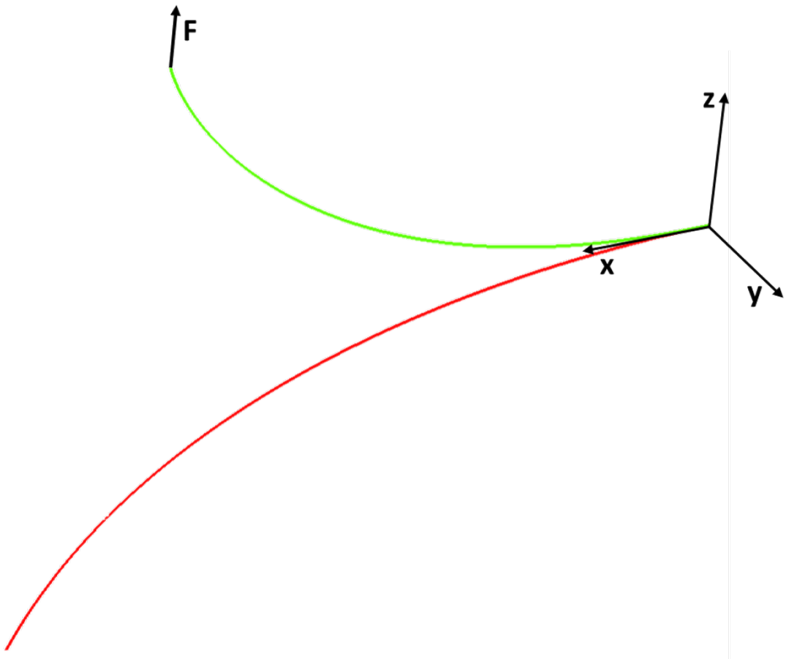

Figure 3.27: Arc-segment with out-of-plane force: Initial (red) and final (green) configuration.

In Tables 3.2 and 3.3, the tip displacements resulting from the two slenderness ratios and different discretizations with WK-TAN and SK-TAN Kirchhoff type elements as well as with Reissner type elements of Crisfield and Jelenić and Simo and Vu-Quoc are plotted. Due to rough spatial discretizations, and in some cases also due to additional model simplifications, the corresponding values derived in the literature for the case $\tilde{\zeta} = 100$ show a comparatively large variation.

Formulation	# Elements	$u_x(l)$	$u_y(l)$	$u_z(l)$
Crisfield & Jelenić	32	47.15044	15.68480	53.47486
Crisfield & Jelenić	8	47.15044	15.68480	53.47486
Simo & Vu-Quoc	8	47.14634	15.69146	53.47362
WK-TAN	32	47.15215	15.68535	53.47176
WK-TAN	8	47.15178	15.68510	53.47225
SK-TAN	8	47.15201	15.68557	53.47216

Table 3.2: Case $\tilde{\zeta} = 100$: tip displacement and relative error for different formulations.

Formulation	# Elements	$u_x(l)$	$u_y(l)$	$u_z(l)$
Crisfield & Jelenić	32	47.15129	15.68508	53.46860
Crisfield & Jelenić	8	47.15129	15.68508	53.46860
Simo & Vu-Quoc.	8	47.14719	15.69174	53.46736
WK-TAN	32	47.15129	15.68508	53.46860
WK-TAN	8	47.15093	15.68482	53.46908
SK-TAN	8	47.15115	15.68530	53.46900

Table 3.3: Case $\tilde{\zeta} = 10000$: tip displacement and relative error for different formulations.

On the contrary, the deviation in the results displayed in Table 3.2 is smaller than 0.1% for all investigated formulations. The fact that these results have been derived by representatives of different beam theories, i.e. of the Simo-Reissner and of the Kirchhoff-Love theory, indicates their correctness. While the Reissner and Kirchhoff values resulting from a discretization with 32 elements coincide up to the fourth significant digit for the case $\tilde{\zeta} = 100$, the corresponding values are identical in all seven significant digits displayed for the case $\tilde{\zeta} = 10000$.

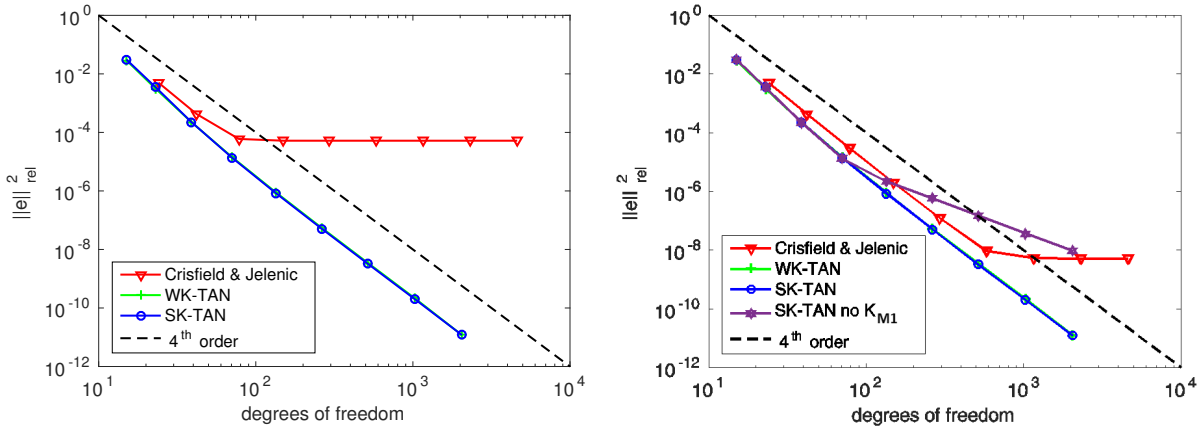

(a) Reference: WK-TAN, $\tilde{\zeta} = 100$.

(b) Reference: WK-TAN, $\tilde{\zeta} = 10000$.

Figure 3.28: Arc-segment with out-of-plane force: L^2-error for different formulations.

The observations described above are also confirmed by the convergence plots in Figure 3.28. All formulations yield the expected convergence orders, and, similar to the last example, the SK-TAN element exhibits an identical discretization error level as the WK-TAN element, since again no multiple centerline loops are involved for this example. Furthermore, similar to the example of Section 3.8.3, also a variant (SK-TAN no K_{M1}) has been investigated where the torsion of the intermediate triad field has been omitted. While the omission of this term did not influence the convergence order observed in Section 3.8.3, this inconsistency yields a decline in the convergence rate from four to two for the anisotropic example considered here. This underlines the importance of consistently considering this term (see also Section 3.8.3 for further explanation).

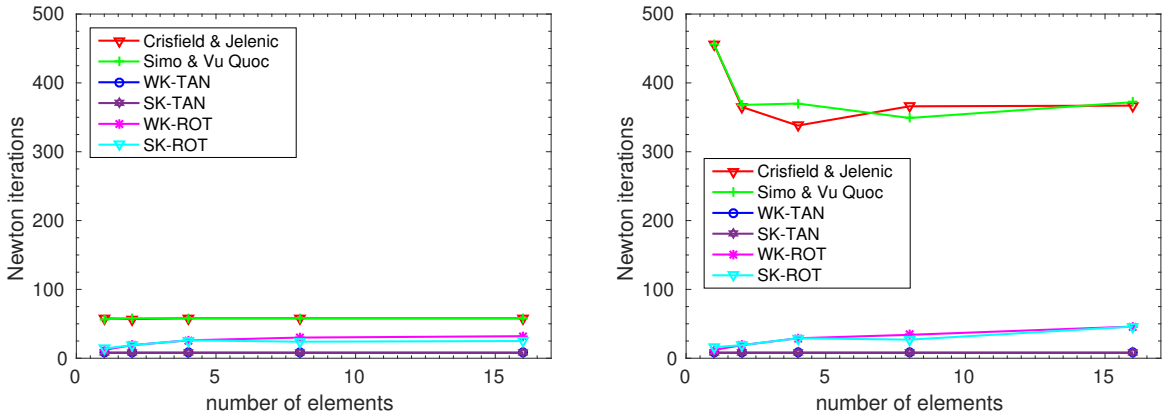

(a) Number of Newton iterations for $\tilde{\zeta} = 100$.

(b) Number of Newton iterations for $\tilde{\zeta} = 10000$.

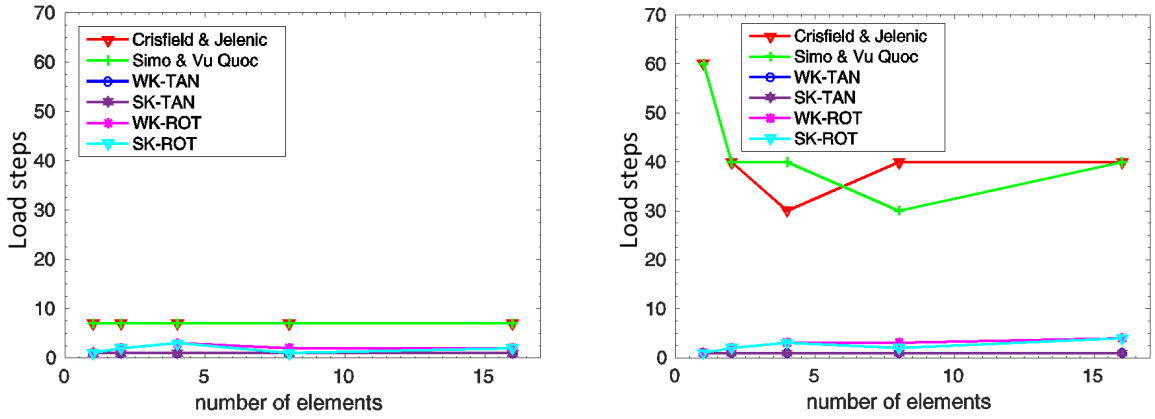

(c) Number of load steps for $\tilde{\zeta} = 100$.

(d) Number of load steps for $\tilde{\zeta} = 10000$.

Figure 3.29: Arc-segment with out-of-plane force: Number of Newton iterations and load steps.

Also for this example, the performance of the Newton-Raphson scheme will be evaluated. However, in order to enable a comparison with the values available in the literature, this time, not the load step adaption scheme of Section 3.2.1.3 is employed, but the following alternative procedure in order to determine the maximal constant load step size $\Delta t = \text{const.}$: Starting with a scheme based on one load step $N_0 = 1$, the number of load steps is increased by one, i.e. $N_{new} = N_{old} + 1$,

in the range $N = 1, ..., 10$ and increased by increments of 10, i.e. $N_{new} = N_{old} + 10$, in the range $N > 10$, until Newton convergence is achieved for all load steps. In order to avoid "lucky shots" (see the remark at the end of this section and also the remark in Section 3.8.3), a maximal load step size and an associated minimal number of load steps N_{min} is accepted only if also the next incrementation step of the load step size according to the procedure described above leads to Newton convergence for all load steps. In Figure 3.29, the total number of Newton iterations as well as the minimal number of load steps N_{min} resulting from the maximal constant load step size are plotted for the two different slenderness ratios. The results are similar to the observations made in previous sections, however, with a smaller difference between the SK/WK-TAN elements and the SK/WK-ROT elements. Concretely, the beam problem with slenderness ratio $\tilde{\zeta} = 100$ is solved in 1 load step and a total of 8 iterations for the SK/WK-TAN discretizations, in 1-3 load steps and a total of 10-40 iterations for the SK/WK-ROT discretizations and in 7 load steps and a total of 57-58 iterations for the discretizations based on Reissner type elements.

For the increased slenderness ratio $\tilde{\zeta} = 10000$, the problem is again solved in 1 load step and a total of 8 iterations for the SK/WK-TAN discretizations, in 1-4 load steps an a total of 10-50 iterations for the SK/WK-ROT discretizations and in 30-60 load steps and a total of 350-450 iterations for the Reissner discretizations. In Table 3.4, the corresponding values reported in the literature for the slenderness ratio $\tilde{\zeta} = 100$ are summarized. As already mentioned earlier, a direct comparison of these results is difficult since it is not clear which procedure has been applied by the different authors in order to determine the minimal number of Newton iterations (e.g. if it was required that also "subsequent refinement steps" have to be convergent or if, on the contrary, also singular occurrences of convergence for special, good-natured loading paths were accepted).

Nevertheless, the numbers summarized in Table 3.4 should at least give a first impression on the behavior of the Newton-Raphon scheme resulting from different finite element formulations. Accordingly, only a few formulations can solve the problem in less than 20 iterations. Furthermore, for the case $\tilde{\zeta} = 100$, only the Reissner type formulation proposed in [117] and investigated in [116] yields a lower number of Newton iterations than the SK/WK-TAN elements. However, as shown in [116], this beam element formulation is non-objective and path-dependent. Moreover, for all examples investigated so far, the real advantage of the Kirchhoff type formulations occurred especially for the high slenderness ratio $\tilde{\zeta} = 10000$, which has not been investigated in the literature. For the range of moderate and high slenderness ratios, it can be concluded that the proposed Kirchhoff beam elements can be considered as very robust and efficient formulations as compared to many (Reissner type) alternatives from the literature.

Remark: Maybe the reader is wondering why the SV element, which is an interpretation of the element proposed in [208], based on an identical discretization with eight first-order elements as investigated in [208], required more Newton iterations than reported in that reference. Actually, also in the numerical tests performed here, the nonlinear problem resulting from a discretization with eight first-order SV elements could be solved in three load steps. However, since a subsequent simulation based on four load steps was not convergent, the procedure for the avoidance of "lucky shots" as explained above has been applied, thus leading to minimal values of 7 load steps and 52 Newton iterations.

Reference	Elements	N_{min}	$n_{iter,tot}$	Remark
[60]	8 first-order	6	-	Number of iterations has not been reported.
[208]	8 first-order	3	27	-
[43]	8 first-order	6	47	-
[199]	8 first-order	3	30	Application of a standard Newton scheme.
[199]	8 first-order	2	11	Application of an accelerated Newton scheme.
[14]	8 first-order	60	-	Number of iterations has not been reported.
[55]	8 first-order	3	16	-
[116]	8 first-order	1	4	Non-objective variant proposed in [117].
CJ	8 first-order	7	59	Objective variant proposed in [116].
CJ	8 third-order	7	58	Objective variant proposed in [116].
SV	8 first-order	7	52	Interpretation of the formulation of [208].
SV	8 third-order	7	58	Interpretation of the formulation of [208].
SK-TAN	8 third-order	1	8	Kirchhoff type beam element formulation.
WK-TAN	8 third-order	1	8	Kirchhoff type beam element formulation.
SK-ROT	8 third-order	1	24	Kirchhoff type beam element formulation.
WK-ROT	8 third-order	2	30	Kirchhoff type beam element formulation.

Table 3.4: Low slenderness ratio $\tilde{\zeta} = 100$: Number of load steps as well as number of Newton iterations reported in the literature (top) and determined in this thesis (bottom).

3.8.7 Example 7: Instability of a circular ring

In this section, again a beam with 2D curved initial geometry, but this time in form of a closed circular ring is considered. This test case has e.g. been investigated in [187] and [211] and initially been proposed in [171]. An initially stress-free, closed circular ring with radius R_0 is exposed to prescribed rotation angles $\boldsymbol{\theta}_1 = (-\theta, 0, 0)^T$ at the material point with initial coordinate $(R_0, 0, 0)^T$ and $\boldsymbol{\theta}_2 = (\theta, 0, 0)^T$ at the material point with initial coordinate $(-R_0, 0, 0)^T$ (see Figure 3.30(a)). The rotation angle θ is increased linearly from zero to $\theta = 180°$ within 180 load steps. In order to allow for comparability, identical geometrical and constitutive parameters have been chosen as in [187] and [211]. Concretely, the elastic ring is characterized by a radius of $R_0 = 20$, a rectangular cross-section with width $b = 1/3$ and height $h = 1$ ($I_2 \approx 3.086 \cdot 10^{-3}$ and $I_3 \approx 2.778 \cdot 10^{-2}$) and a considered torsional moment of inertia of $I_T = 9.753 \cdot 10^{-3}$. As material parameters, a Young's modulus of $E = 21 \cdot 10^6$ and a Poisson's ratio of $\nu = 0.3$ has been chosen. In the following, this test case will exemplarily be simulated by means of the SK-TAN element.

It is shown in [171] that the analytic solution for this problem is a plane circular ring with radius $R_0/3$ as illustrated in Figure 3.30(a). The deformed configurations at different load steps are shown in Figure 3.30(b). In Figure 3.31(a), the analytical solution as well as the numerical results for the reaction moment M that is necessary to prescribe the rotation θ is plotted over the devolution of θ. The numerical and analytical results are in excellent agreement. Additionally, in Figures 3.31(b)-3.31(d), the numerical results for the displacement components of the material point P with initial coordinate $(0, R_0, 0)^T$ are shown (see also [187]). All numerical results have been determined for two different discretizations with 16 and 32 SK-TAN elements, respectively.

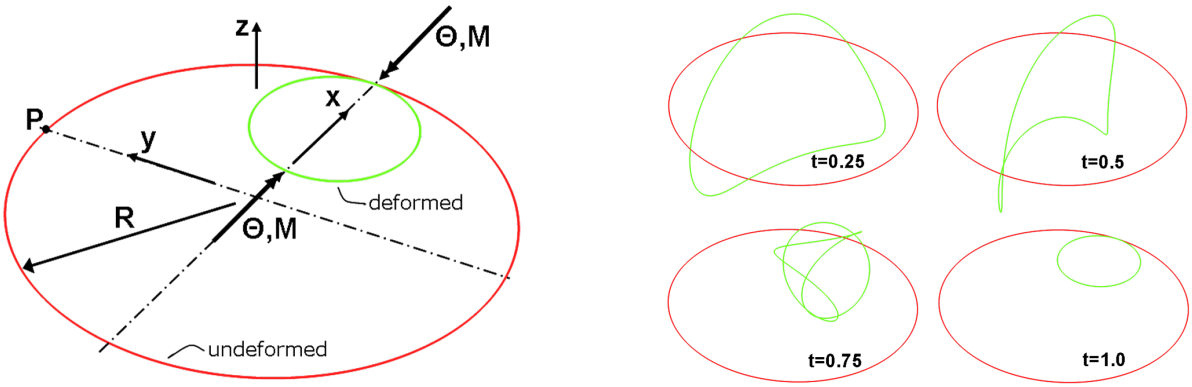

(a) Instability of a circular ring: Problem setup.

(b) Configurations at different load steps.

Figure 3.30: Deformation of an elastic ring: Problem setup and deformed configurations.

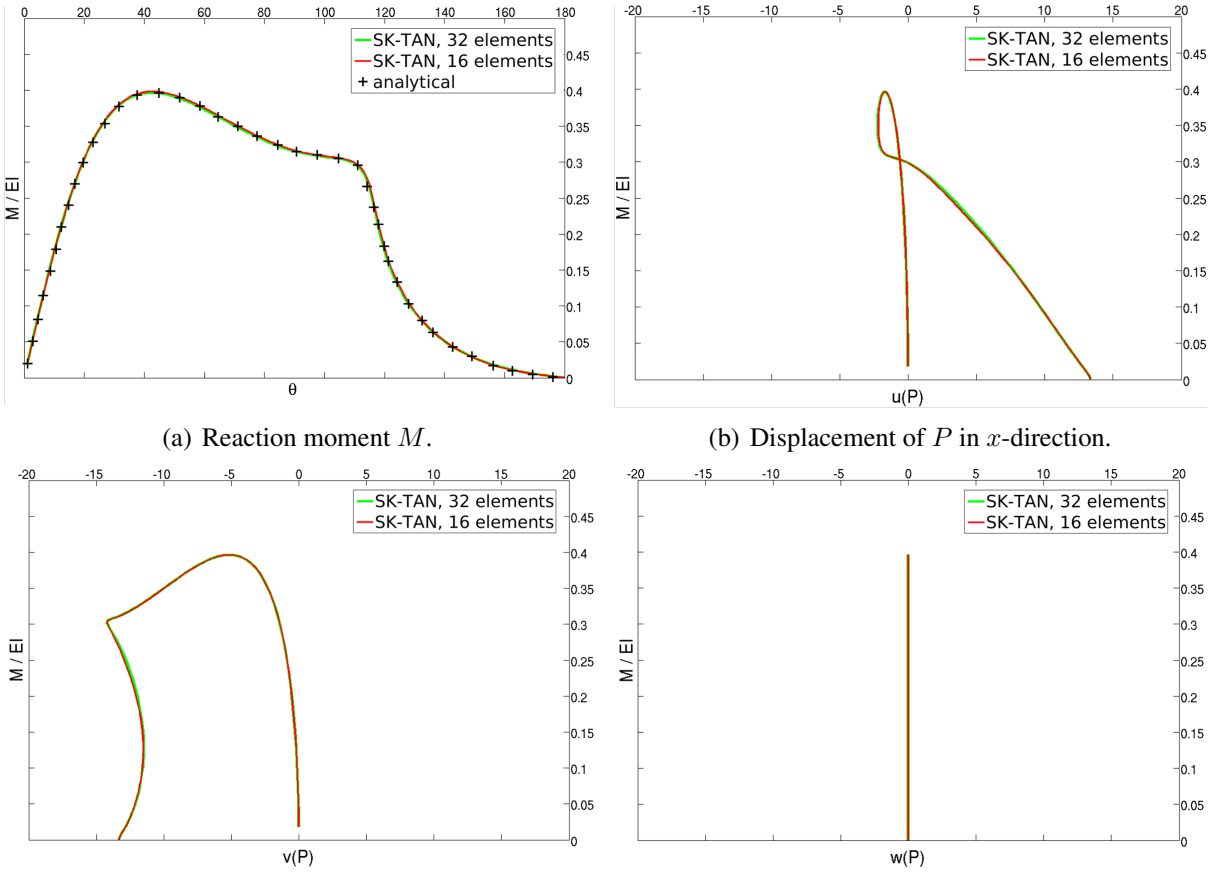

(a) Reaction moment M.

(b) Displacement of P in x-direction.

(c) Displacement of P in y-direction.

(d) Displacement of P in z-direction.

Figure 3.31: Load-rotation-curve of reaction moment M and displacement of material point P.

The results of both discretizations show only minor differences for all plots. The critical point in Figure 3.31(a), characterized by a horizontal tangent in the load-displacement curve, indicates a mechanical instability, thus, yielding a challenging test case for the employed element.

3.8.8 Example 8: Helix loaded with axial force

In the last static example considered in this chapter, the generality of the initial geometry shall be further increased: A helix with linearly increasing slope, clamped at one of its ends, is loaded with a discrete end-force $\mathbf{F} = (0, 0, F)^T$ (see Figure 3.32 for illustration).

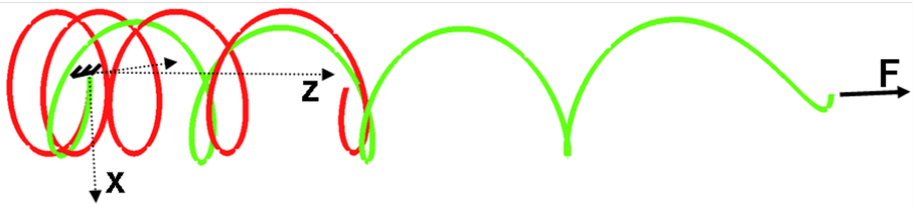

Figure 3.32: Helix with varying slope loaded with discrete force: Problem setup.

The initial geometry of the helix can be described via the following analytic representation:

$$\mathbf{r}_0(\beta) = R_0 \begin{pmatrix} \sin\beta \\ \cos\beta - 1 \\ \frac{6}{81\pi^2}\beta^2 \end{pmatrix}, \quad R_0 = \frac{l}{6\sqrt{\left(\frac{3\pi}{4}\right)^2 + 1} + \frac{27\pi^2}{8} \ln\left(\frac{4}{3\pi} + \sqrt{1 + \left(\frac{4}{3\pi}\right)^2}\right)} \approx 34.36. \quad (3.164)$$

The radius R_0 of the enveloping cylinder of the helix is chosen such that the helix exactly consists of 4.5 loops, i.e. $\beta \in [0; 9\pi]$, along the standard length of $l = 1000$. Also this example is investigated for two different slenderness ratios $\zeta = 100$ and $\zeta = 10000$ with associated axial forces $F = 2{\cdot}10^{-1}$ as well as $F = 2{\cdot}10^{-9}$. The ratio of these forces is chosen identical to the ratio of the bending stiffnesses of the cases $\zeta_1 = 100$ and $\zeta_2 = 10000$ leading to the comparable values $u_{z,max,1} \approx 267$ and $u_{z,max,2} \approx 266$ for the maximal tip-displacement in z-direction.

In Figure 3.33, the resulting relative L^2-error of the CJ, SK-TAN and WK-TAN element is plotted for discretizations with $16, 32, 64, 128, 256$ and 512 elements. All element formulations show the expected convergence rate of four, the discretization error level of the WK-TAN element is slightly lower than the discretization error level of the SK-TAN element. However, both discretization error levels lie below the error level of the Reissner type CJ element.

In Figure 3.34, the different anti-locking approaches already investigated for the 2D case in Section 3.8.2.1 are compared for the 3D helix example. For the low slenderness ratio $\zeta = 100$ depicted in Figure 3.34(a), no noteworthy locking effects can be observed. In case the high slenderness ratio $\zeta = 10000$ is considered, locking effects are visible, but as already predicted in Section 3.2.4.3, to a lower extent as in the 2D case. Again, with the MCS method, the occurrence of such effects can completely be avoided, while neither a standard reduced integration scheme nor a standard ANS approach can improve the situation. In conclusion, it can be stated that the proposed beam elements in combination with the MCS approach completely remedies unphysical locking effects even for extreme slenderness ratios and demanding geometries.

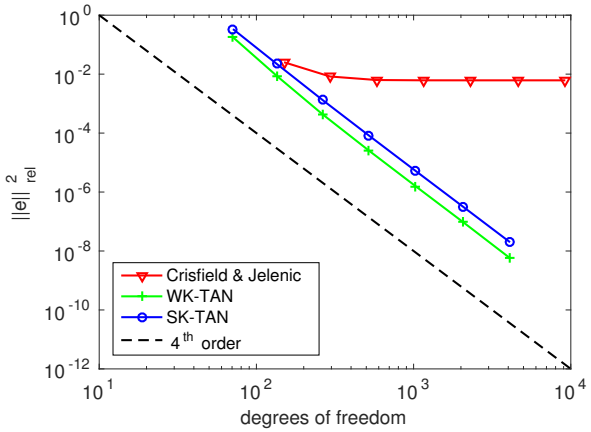

(a) Reference: WK-TAN, $\zeta = 100$.

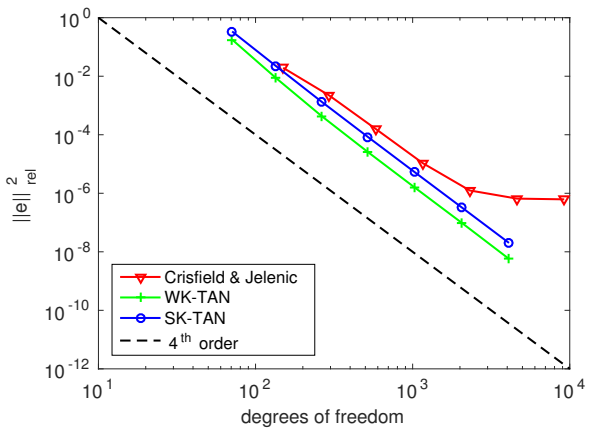

(b) Reference: WK-TAN, $\zeta = 10000$.

Figure 3.33: Helix loaded with axial force: L^2-error for different formulations.

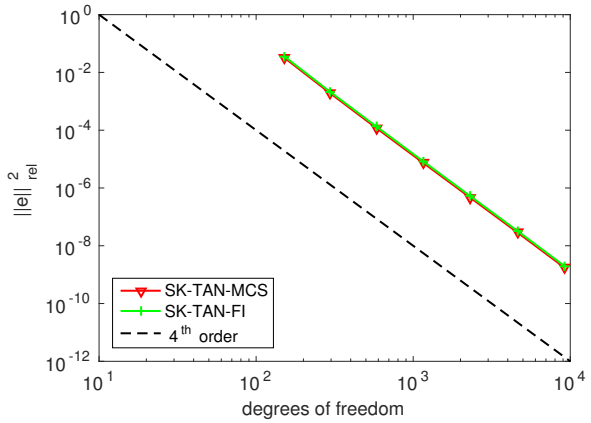

(a) Reference: SK-TAN, $\zeta = 100$.

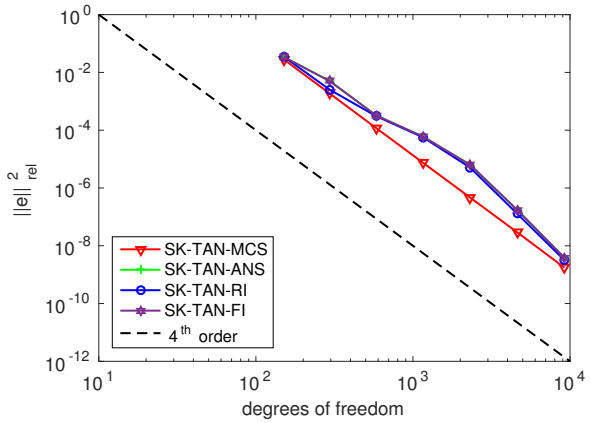

(b) Reference: SK-TAN, $\zeta = 10000$.

Figure 3.34: Helix loaded with axial force: Investigation of locking effects.

Finally, the helix problem shall be even more generalized by not only accounting for 3D initial curvatures but also for anisotropic cross-section shapes with initial twist as illustrated in Figure 3.35. Again, the two slenderness ratios $\zeta = 100$ and $\zeta = 10000$ have been investigated. The square cross-section of the last example is extended to a rectangular cross-section shape with dimensions $b = 10$ and $h = 5$ and an assumed torsional moment of inertia $I_T \approx 3.2875 \cdot 10^{-2}$ for the case $\zeta = 100$. The case $\zeta = 10000$ is defined by $b = 0.1$ and $h = 0.05$ and an assumed torsional moment of inertia $I_T \approx 3.2875 \cdot 10^{-6}$. The external forces have been chosen as $F = 5 \cdot 10^{-2}$ for $\zeta = 100$ and $F = 5 \cdot 10^{-10}$ for $\zeta = 10000$ and the initial twist as one twist rotation per helix loop. The resulting L^2-error plotted in Figure 3.36 again shows a consistent convergence behavior similar to Figure 3.33. Additionally, in Figure 3.35, also the Bubnov-Galerkin variant (SK-TAN+CS) of the SK-TAN element with consistent spin vector interpolation has been plotted. Accordingly, no visible difference compared to the Petrov-Galerkin (SK-TAN) variant can be observed.

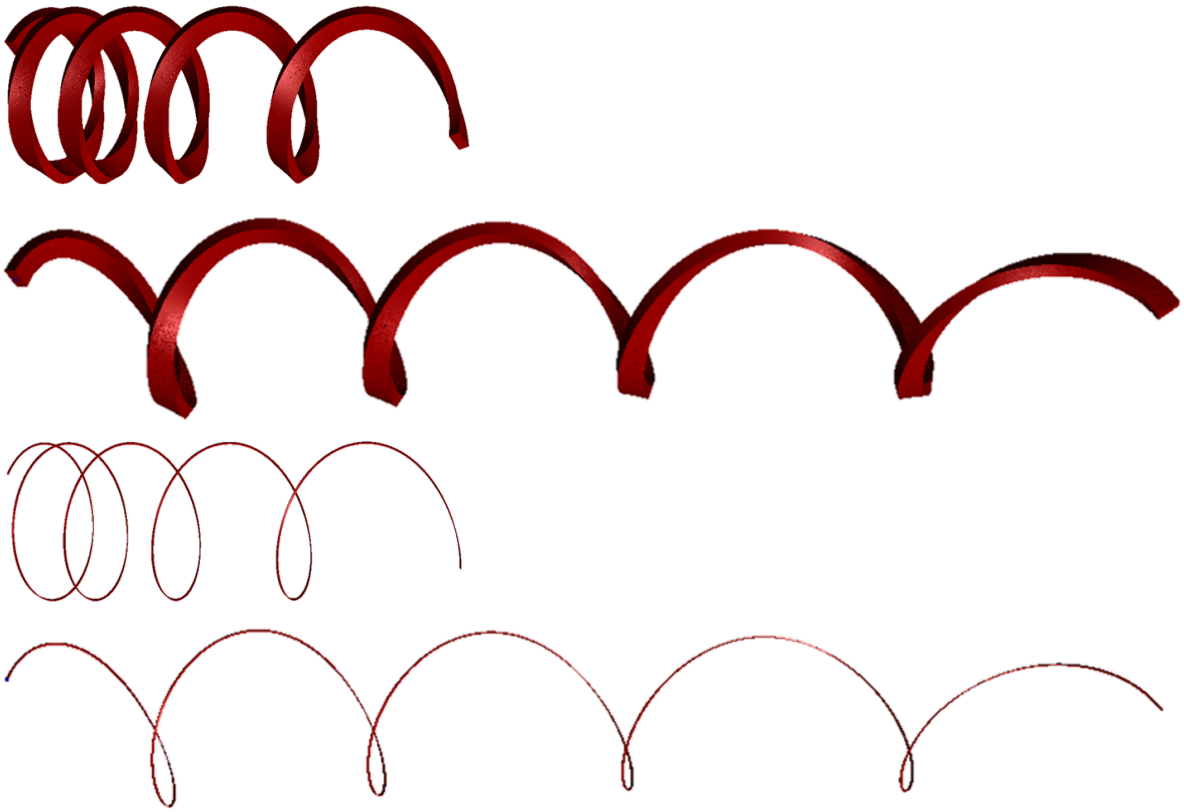

Figure 3.35: Twisted helix with axial force: Initial and final shape for $\zeta = 100$ and $\zeta = 1000$. For better visibility, the variant $\zeta = 1000$ has been plotted instead of $\zeta = 10000$.

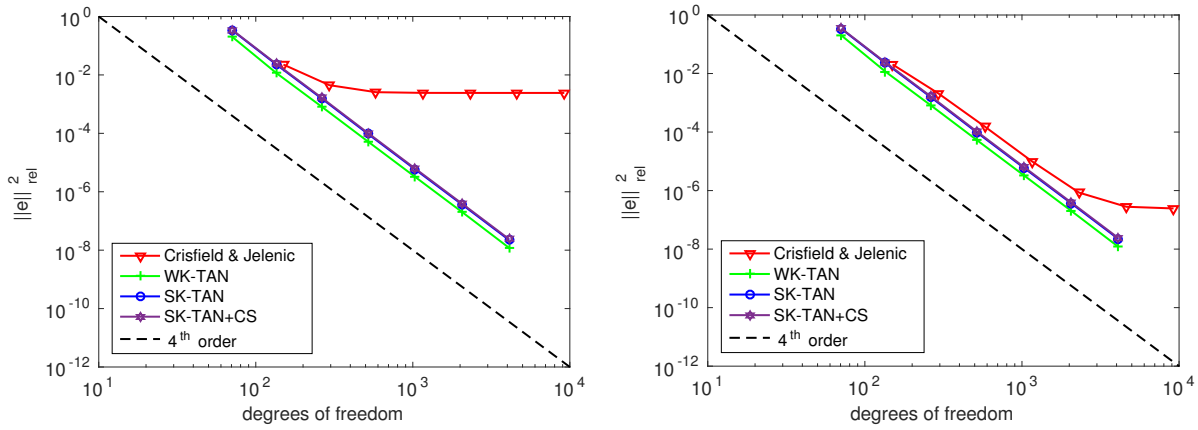

(a) Reference: WK-TAN, $\zeta = 100$.

(b) Reference: WK-TAN, $\zeta = 10000$.

Figure 3.36: Twisted helix loaded with axial force: L^2-error for different formulations.

In a last step, also the balances of forces and moments are investigated for this most general example of Figure 3.35. In Table 3.5, the reaction forces and moments at the clamped end of the helix at $s = 0$ and the force and moment contributions (with respect to the point $s = 0$) resulting

from the external load applied at $s = l$ are plotted for discretizations with eight elements. It can easily be verified that the balance of forces and moments is exactly fulfilled by the variants CJ, WK-TAN and SK-TAN+CS, while the Petrov-Galerkin variant SK-TAN only fulfills the balance of forces but not the balances of moments. This confirms the prediction made in Section 3.4.4.

	Cri. & Jel.	WK-TAN	SK-TAN	SK-TAN+CS
$F_1(0)$	0.0	0.0	0.0	0.0
$F_1(l)$	0.0	0.0	0.0	0.0
$F_2(0)$	0.0	0.0	0.0	0.0
$F_2(l)$	0.0	0.0	0.0	0.0
$F_3(0)$	5.00000000E-6	5.00000000E-6	5.00000000E-6	5.00000000E-6
$F_3(l)$	5.00000000E-6	5.00000000E-6	5.00000000E-6	5.00000000E-6
$M_1(0)$	-1.64350142E-4	-1.54617971E-4	-1.51929992E-4	-1.65509346E-4
$M_1(l)$	-1.64350142E-4	-1.54617971E-4	-1.52158798E-4	-1.65509346E-4
$M_2(0)$	-4.41005618E-5	-8.55776851E-6	-1.13519642E-5	-5.43051999E-6
$M_2(l)$	-4.41005617E-5	-8.55776851E-6	-2.30787384E-5	-5.43051999E-6
$M_3(0)$	0.0	0.0	0.0	0.0
$M_3(l)$	0.0	0.0	0.0	0.0

Table 3.5: Slenderness $\zeta = 10000$: Reaction forces and moments for different formulations.

3.8.9 Example 9: Oscillations of a beam with sinusoidal line load

In the next-to-last example of this chapter, a first dynamic test case will be considered. The general problem setup is identical to the example of Section 3.8.5 (see Figure 3.25(a)): An initially straight beam of length $l = 1000$ and slenderness ratio $\zeta = 10000$ (i.e. $R = 0.1$) is supported at both of its ends. The left end of the beam is clamped, and the right end has two remaining degrees of freedom, which are the displacement u_x in x-direction and the rotation α with respect to the x-axis. The distributed line load exciting the beam has been chosen as $\tilde{\mathbf{f}}(s,t) = \hat{f}(t)(\tilde{f}_x, \tilde{f}_y, \tilde{f}_z)^T = \hat{f}(t)(\tilde{f}_x, \tilde{f}_\perp \sin\phi, \tilde{f}_\perp \cos\phi)^T$, with $\tilde{f}_x = 6.0 \cdot 10^{-6}$, $\tilde{f}_\perp = 3.0 \cdot 10^{-7}$ and $\phi = 2\pi s/l$. The time-dependent function $\hat{f}(t)$ is linearly increased from $\hat{f} = 0$ at $t = 0$ to $\hat{f} = 1.0$ at $t = 0.5$ and then linearly decreased to $\hat{f} = 0$ at $t = 1$, while the overall simulation time as well as the time step size have been chosen as $T = 10$ and $\Delta t = 0.01$. Thus, the test case consists of two phases: An excited oscillation phase for $t \in [0, 1]$ and a free oscillation phase for $t \in [1, 10]$. Furthermore, the constitutive parameters as well as the density have been chosen as $E = 2G = 10^7$ and $\rho = 10^{-7}$. This combination of material parameters and external loads will again yield very general 3D geometrically nonlinear deformation states. All resulting section constitutive parameters, with $I_T/2 = I_2 = I_3 =: I$, as well as the oscillation periods T_b and T_t calculated for the lowest bending and torsion mode of the linearized problem, are presented in the first line of Table 3.6. Accordingly, the oscillation period associated with the lowest (bending) eigenfrequency resulting from this parameter choice takes on a value of $T_b \approx 1$, leading to approximately ten oscillations during the considered time interval $T = 10$. Furthermore, the time step size $\Delta t = 0.01$ should guarantee for a proper temporal resolution of the low bending modes. Similar to the last sections, also this example will be investigated for a second slenderness ratio

$\zeta = 100$. In order to yield a comparable test case, the amplitude and the excitation frequency of the line load as well as the time step size Δt and the time interval T would have to be adapted to the increased bending stiffnesses and eigenfrequencies resulting from this lower slenderness ratio. In order to simplify the following comparisons and to keep $\tilde{\mathbf{f}}(s,t)$, Δt and T unchanged, the constitutive parameters and the density are adapted to $E = 2G = 10^{-1}$ and $\rho = 10^{-11}$ such that the resulting bending stiffnesses and eigenfrequencies remain unchanged. All the material and geometrical parameters resulting from this choice are illustrated in the second line of Table 3.6. Accordingly, the axial stiffness EA is decreased, the rotational inertia terms ρI are increased and the translational inertia terms ρA remain constant due to the transition from $\zeta = 10000$ to $\zeta = 100$. Moreover, as expected, the lowest torsional eigenfrequency is decreased with decreasing slenderness ratio as compared to the lowest bending eigenfrequency (which remains unchanged).

ζ	R	A	I	E	ρ	EI	EA	ρI	ρA	T_b	T_t
10^4	10^{-1}	10^{-2}	$10^{-4}/12$	10^7	10^{-7}	$10^3/12$	10^5	$10^{-11}/12$	10^{-9}	≈ 1.0	$\approx 6{\cdot}10^{-4}$
10^2	10^1	10^2	$10^4/12$	10^{-1}	10^{-11}	$10^3/12$	10^1	$10^{-7}/12$	10^{-9}	≈ 1.0	$\approx 6{\cdot}10^{-2}$

Table 3.6: Material and geometrical parameters for the variants $\zeta = 100$ and $\zeta = 10000$.

Apart from (2.128) and (2.136), this time also the restrictions (2.137) for the initial conditions are fulfilled, thus again allowing for an approximation of the general Kirchhoff-Love theory by means of the torsion-free beam theory presented in Section 2.4.2. In the following, the results derived by means of the general Reissner and Kirchhoff type beam element formulations CJ, SK-TAN and WK-TAN will be compared with the results derived by the torsion-free element formulation according to (3.160). Time integration is based on the Lie group generalized$-\alpha$ scheme of Section 3.1.2 for the former three element formulations, while a standard (vector space) generalized$-\alpha$ scheme according to Section 3.1.1 is combined with the torsion-free element formulation. In both cases, a spectral radius of $\rho_\infty = 0.95$ has been employed. In Figures 3.37 and 3.38, the discretization errors resulting from twist boundary conditions of type b) (case illustrated in Figure 3.25(a)) and twist boundary conditions of type c) (additional clamping of the twist angle at the position $s = l$) are displayed for the different element formulations. In all cases, the expected spatial convergence rates of four can be observed. Figure 3.37 reveals similar discretization error levels for the SK-TAN and WK-TAN elements, which both lie below the error level of the Reissner type element CJ. Again, the even lower error level of the torsion-free element formulation results from the fact that no twist DoFs are required for this formulation. In contrary to the static example of Section 3.8.5, here, the discretization error plot of the torsion-free element formulation exhibits a kink and a remaining cutoff error level with respect to the WK-TAN reference solution. However, the amount of this remaining cutoff error level decreases with increasing slenderness ratio. This observation underlines the conclusions of Section 2.4.2.2 that the torsion-free theory yields exact solutions in statics, but only approximations to the general Kirchhoff theory in dynamics. Similar to the model error between the general Kirchhoff theory and the Reissner theory, also this model error decreases quadratically with increasing slenderness ratio. Consequently, the torsion-free beam theory, applied to dynamic problems, seems to be a sensible and consistent extension of the model reduction already initialized by deriving the shear-free Kirchhoff theory from the Reissner beam theory.

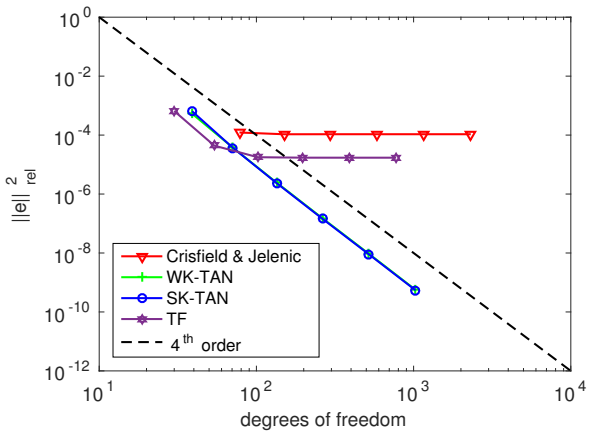

(a) Reference: WK-TAN, $\zeta = 100$.

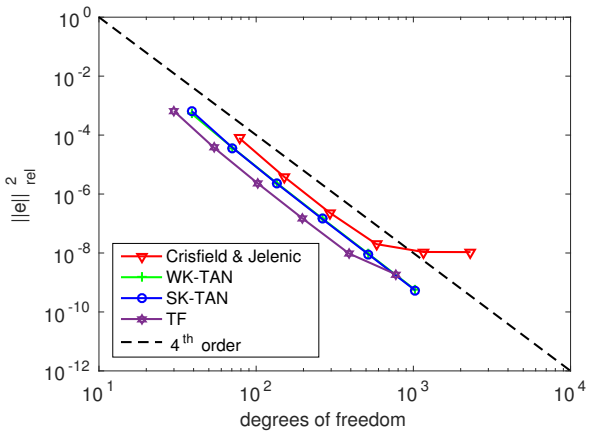

(b) Reference: WK-TAN, $\zeta = 10000$.

Figure 3.37: Beam with boundary conditions of type b): L^2-error for different formulations.

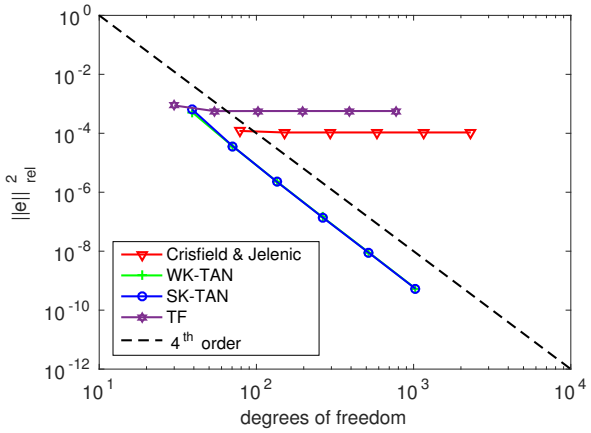

(a) Reference: WK-TAN, $\zeta = 100$.

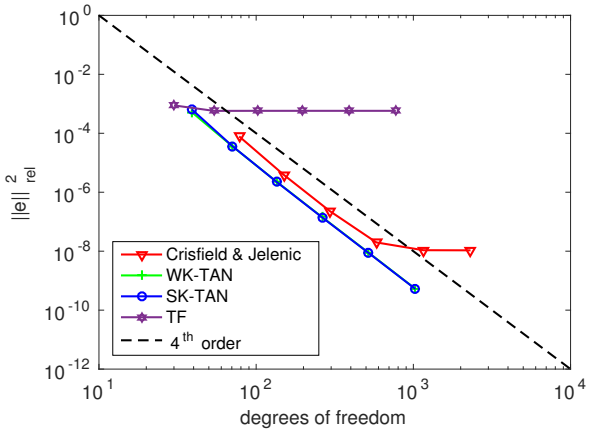

(b) Reference: WK-TAN, $\zeta = 10000$.

Figure 3.38: Beam with boundary conditions of type c): L^2-error for different formulations.

For comparison reasons, in Figure 3.38, the same investigations have also been conducted for the case of twist boundary conditions of type c). As expected, in this case, the torsion-free formulation yields a considerable model error which does not decrease with increasing beam slenderness ratio. It has already been shown in the static examples of Section 3.8.5 that boundary conditions of this type will not yield configurations with vanishing torsion for general 3D scenarios.

In order to further strengthen the theoretical statements of Section 2.4.2.2 and the numerical results derived so far, the ratio $\bar{M}_t/\bar{M}_b$ of the average torsional moment $\bar{M}_t$ and the average bending moment $\bar{M}_b$ shall be considered. As compared to Section 3.8.5, this time the moment components are not only "averaged in space", but also "averaged in time" according to

$$\bar{M}_t := \sum_{i=1}^{N} \frac{< M_t > (t_i)}{N}, \quad \bar{M}_b := \sum_{i=1}^{N} \frac{< M_b > (t_i)}{N}, \tag{3.165}$$

where $< M_t >$ and $< M_b >$ represent the corresponding spatially averaged quantities given in (3.163) and N is the number of time steps. In Table 3.7, the ratio $\bar{M}_t/\bar{M}_b$ according to (3.165) and (3.163) is shown for all three possible types of twist boundary conditions and the two investigated slenderness ratios $\zeta = 100$ and $\zeta = 10000$. Again, for the boundary conditions of type a) and b), a quadratic decrease of the average torsion with increasing beam slenderness ratio can be observed in good approximation, while the boundary conditions of type c) yield a considerably higher average torsion value that is independent of the slenderness ratio.

a) - $\zeta = 10^2$	a) - $\zeta = 10^4$	b) - $\zeta = 10^2$	b) - $\zeta = 10^4$	c) - $\zeta = 10^2$	c) - $\zeta = 10^4$
1.9E-4	1.8E-8	8.2E-4	6.2E-8	1.4E-2	1.4E-2

Table 3.7: Ratio $\bar{M}_t/\bar{M}_b$ of average torsional to average bending moment.

Finally, in Figure 3.39, the internal and kinetic system energies as well as their sum have been plotted for discretizations consisting of 256 Reissner type CJ elements and Kirchhoff type torsion-free elements, respectively. For both slenderness ratios $\zeta = 100$ and $\zeta = 10000$, the total system energy is preserved very well and no visible differences can be observed between the CJ and the torsion-free elements. In other words, the torsion-free formulation seems to provide a very good approximation to the analytic solution of this example already for the lower slenderness ratio $\zeta = 100$. Furthermore, in Figure 3.40, the internal and kinetic energies resulting from a discretization with 256 CJ elements is split into the individual contributions stemming from torsion modes (subscript $(.)_{M_t}$) and bending modes (subscript $(.)_{M_b}$) as well as the contributions stemming from axial tension and shear modes (subscript $(.)_F$). For both slenderness ratios, it can be observed that the overall dynamic system answer is dominated by the bending energy contributions and by the translational inertia forces. This effect gets more and more emphasized with increasing slenderness ratio. For the high slenderness ratio $\zeta = 10000$, the internal energy contributions of the "stiff" axial tension and shear modes are approximately by six orders of magnitude smaller than the energy contributions of the "soft" bending mode. Due to the fulfillment of requirements (2.128), (2.136) and (2.137), the internal energy contributions of the torsion mode, which can be identified as a "soft" mode with stiffness similar to the bending stiffness, are approximately by further eight orders of magnitude lower than the shear mode contributions. Furthermore, the rotational inertia contributions seem to be negligible for this high slenderness ratio, with twist contributions (subscript $(.)_{M_t}$) that are smaller than the rotation contributions associated with the component $\mathbf{w}_\perp$ (subscript $(.)_{M_t}$) of the angular velocity vector.

Of course, further numerical investigations of the torsion-free beam theory, especially when applied to dynamic problems, are intended for the future research work. Nevertheless, the numerical verifications performed in this section already confirm the theoretical statements made in Section 2.4.2. Accordingly, the torsion-free beam theory results in efficient and considerably simplified finite element formulations and numerical algorithms, which yield very accurate approximations to the dynamic solutions of the general Kirchhoff theory, and which consequently can be considered as a reasonable and consistent further step of model reduction.

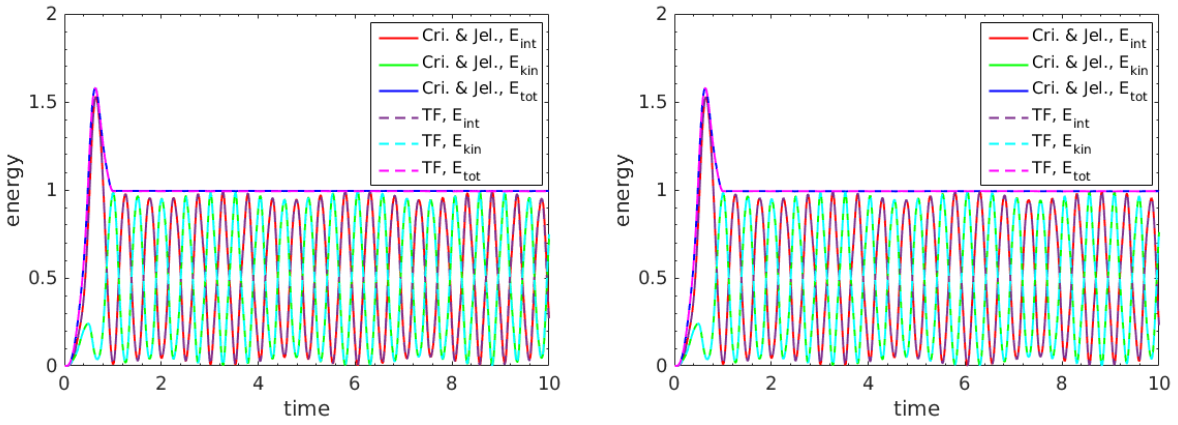

(a) Moderate slenderness ratio: $\zeta = 100$. (b) High slenderness ratio: $\zeta = 10000$.

Figure 3.39: Beam with boundary conditions of type b): Energy conservation.

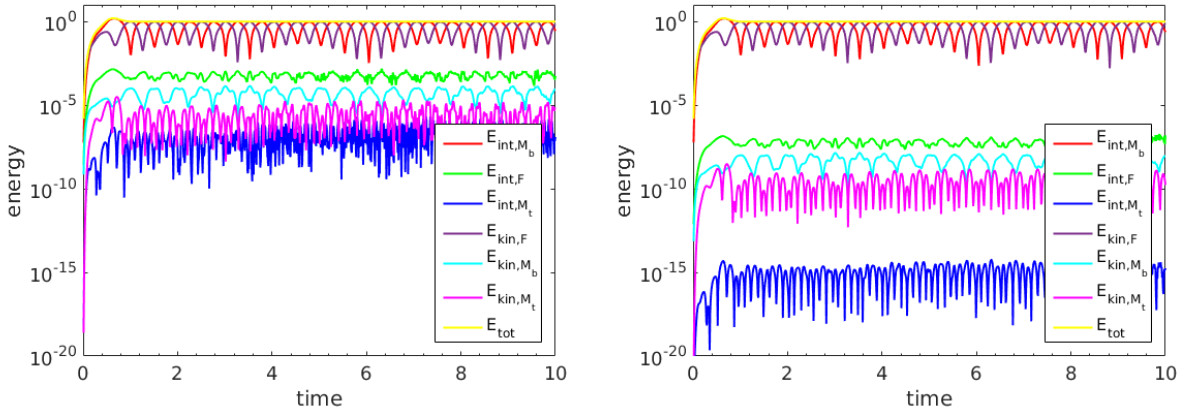

(a) Moderate slenderness ratio: $\zeta = 100$. (b) High slenderness ratio: $\zeta = 10000$.

Figure 3.40: Beam with boundary conditions of type b): Individual energy contributions.

3.8.10 Example 10: Free oscillations of an elbow cantilever

The final numerical example represents a more general dynamic test case as compared to the last section. The example has initially been investigated in [209] and subsequently been considered in several contributions in the field of geometrically nonlinear beam element formulations (see e.g. [116] and [41]). A right-angle elbow cantilever beam consists of two straight beam segments of length $l = 10$ being rigidly connected at one of their ends. In the initial configuration, the first segment points into global y-direction and the second segment into global x-direction.

The first segment of the cantilever is clamped at the position $s = 0$. In the original work, the cross-section of the beam is described by the section parameters $EA = GA_2 = GA_3 = 10^6$, $GI_T = EI_2 = EI_3 = 10^3$ as well as $\rho A = 1$ and $\rho I_P/2 = \rho I_2 = \rho I_3 = 10$. It can easily be verified that these section parameters can for example be represented by a quadratic cross-section with radius $R \approx 0.1$, thus resulting in a slenderness ratio of $\zeta \approx 100$ for each of the two segments, for

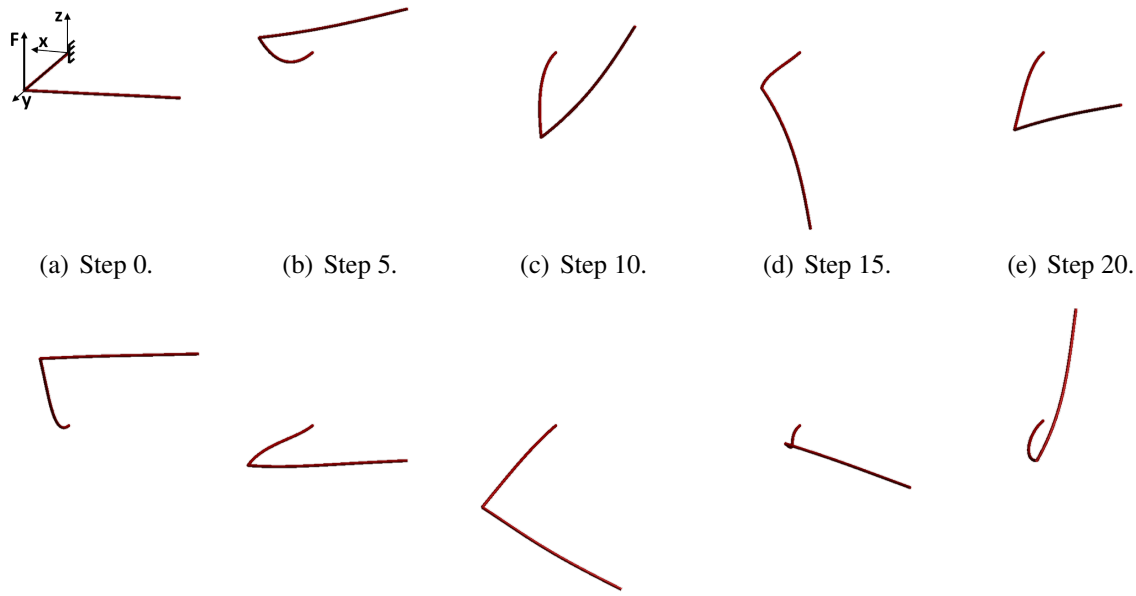

(a) Step 0. (b) Step 5. (c) Step 10. (d) Step 15. (e) Step 20.

(f) Step 25. (g) Step 30. (h) Step 35. (i) Step 40. (j) Step 45.

Figure 3.41: Free oscillations of an elbow cantilever: Initial and deformed configurations.

which the rotational inertia contributions are additionally scaled by a factor of 10^4. This artificial scaling has been applied in order to emphasize (and properly verify) the rotational inertia contributions, which would otherwise be comparatively small for the chosen slenderness ratio. This cantilever beam is loaded by a discrete force $\mathbf{F} = (0, 0, F_z)^T$ pointing in global z-direction and acting at the rigid corner of the elbow. The magnitude of the force is linearly increased from $F_z = 0$ at $t = 0$ to $F_z = 50$ at $t = 1$ and then linearly decreased to $F_z = 0$ at $t = 2$. In the remaining simulation time until $T = 50$, the cantilever executes geometrically nonlinear free oscillations in 3D space with amplitudes being in the range of the segment lengths. The initial and deformed configurations at different time steps are illustrated in Figure 3.41. For time integration, the modified generalized-α scheme of Section 3.1.2 with $\rho_\infty = 0.95$ has been employed. As spatial discretizations, the CJ element, the WK-ROT element as well as the Petrov-Galerkin variant SK-ROT and the Bubnov-Galerkin variant SK-ROT+CS with consistent spin vector interpolation according to (3.122) have been applied. This example yields a further complexity that has not been present in the previous test cases: The modeling of a rigid beam connection occurring at the corner of the elbow. As already mentioned in earlier sections, the modeling of such kinks in the beam centerline is easier to be realized by the SK/WK-ROT variants. Nevertheless, the resulting solutions are identical as for the SK/WK-TAN variants.

In Figure 3.42, the internal, kinetic and total system energy is plotted for different time step sizes and spatial discretizations. For discretizations with 8 WK-ROT and SK-ROT elements per elbow segment and a time step size of $\Delta t = 0.01$ as illustrated in Figures 3.42(a) and 3.42(b), no visible oscillations in the total system energy and no visible differences in the energy contributions of the Reissner and Kirchhoff type elements can be observed. In Figures 3.42(c)- 3.42(f), the energy

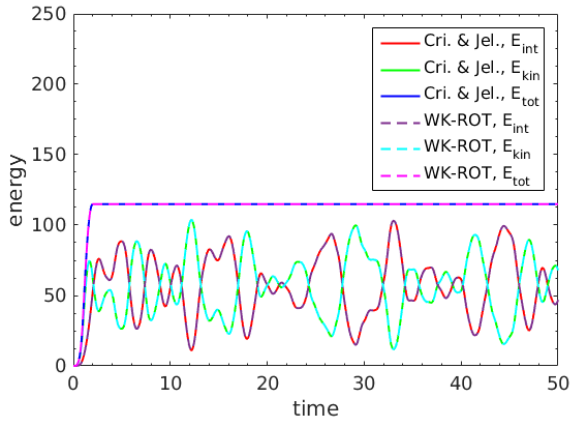

(a) WK-ROT, 16 elements, $\Delta t = 0.01$.

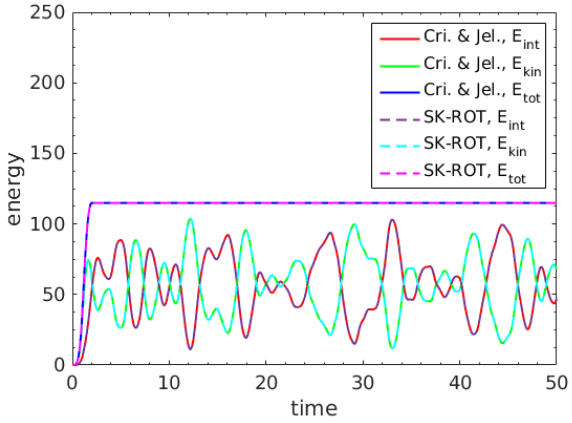

(b) SK-ROT, 16 elements, $\Delta t = 0.01$.

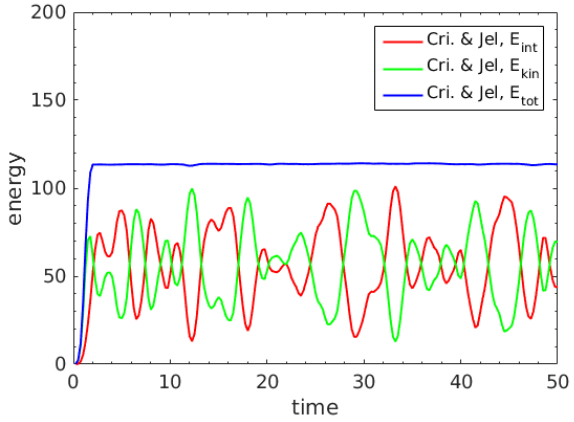

(c) Cri. & Jel., 2 elements, $\Delta t = 0.25$.

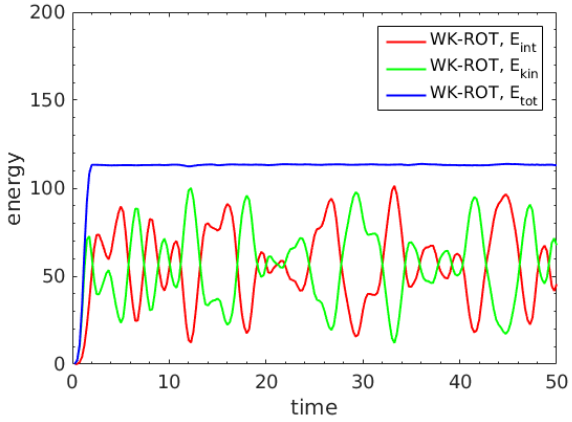

(d) WK-ROT, 2 elements, $\Delta t = 0.25$.

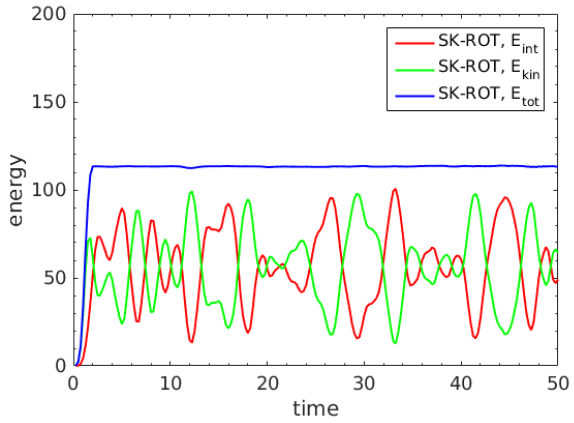

(e) SK-ROT, 2 elements, $\Delta t = 0.25$.

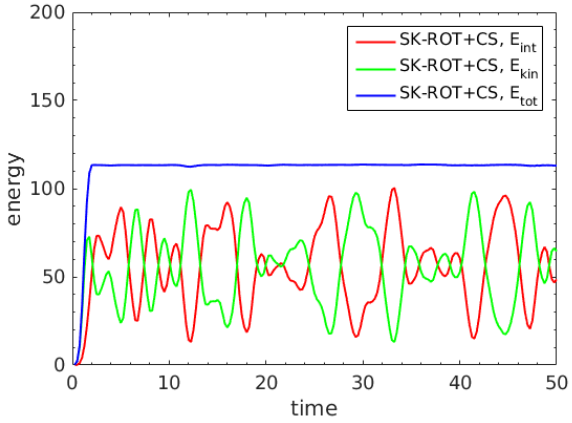

(f) SK-ROT+CS, 2 elements, $\Delta t = 0.25$.

Figure 3.42: Free oscillations of an elbow cantilever: Energy conservation.

contributions resulting from a larger time step size of $\Delta t = 0.25$ and a rougher spatial discretization based on one beam element per elbow segment has been plotted. Accordingly, also for these rough discretizations, the overall system energy is preserved very well. The fact that the to-

tal system energy approximation resulting from the (energetically consistent) Bubnov-Galerkin discretization SK-ROT+CS is rarely improved as compared to the Petrov-Galerkin variants CJ, WK-ROT and SK-ROT indicates that for the chosen spatial and temporal discretizations, the influence of the temporal discretization error might dominate the error in the total system energy. As compared to reference [116], where an identical time step size of $\Delta t = 0.25$ and a comparable spatial discretization consisting of one second-order CJ element per elbow segment has been applied, the oscillations of the total system energy could be considerably decreased and the instability observed there at the end of the considered time interval could be completely avoided. This improvement can be attributed to the applied Lie group extension of the generalized-α scheme according to Section 3.1.2, whereas in reference [116] the Lie group extension of a Newmark time integration scheme as proposed in [208] has been considered. Based on (simplified) Reissner type beam element formulation (see [144]), similar observations have already been made in reference [41], where the Lie group extension of the generalized-α scheme has been proposed.

Again, further numerical investigations on the combination of the generalized-α scheme according to Section 3.1.2 and the proposed Kirchhoff beam element formulations applied to dynamic problems might be desirable and are intended for future research work. However, these first numerical investigations suggest that the desirable properties of the Kirchhoff beam element formulations observed in static test cases might also be transferred to the dynamic regime. Especially, the C^1-continuous centerline interpolation and the excellent Newton convergence behavior in the range of high slenderness ratios qualify the proposed Kirchhoff beam element formulations for a combination with the beam-to-beam contact algorithm presented in the next chapter. In very complex contact scenarios as e.g. considered in Section 4.5.3.4 of the next chapter, the robustness and efficiency of the resulting implicit schemes, properties that are not least inherited from the underlying beam element formulations, will be of highest practical relevance.

4 Beam-to-Beam Contact

In this chapter, the geometrically exact beam models as well as their finite element realizations derived in Chapters 2 and 3 will be supplemented by beam-to-beam contact formulations and algorithms that allow for the numerical treatment of the contact interaction of highly slender beams in complex 3D configurations involving arbitrary beam-to-beam orientations. Existing beam contact formulations can be categorized in point-to-point contact models, which consider a discrete contact force at the closest point of the beams, and line-to-line contact models that assume distributed contact forces. In Section 4.1, the basics of standard point contact models, which represent sufficiently accurate and very efficient contact models in the regime of large contact angles, are presented. However, there it is shown in a mathematically concise manner that these contact models fail to describe a considerable range of small contact angles, i.e. configurations that are likely to occur in practical applications. In Section 4.2, an alternative formulation is proposed that models beam-to-beam contact by means of distributed line forces, a procedure that is shown to be applicable for arbitrary geometrical configurations. The proposed formulation is enhanced by a consistently linearized integration interval segmentation avoiding numerical integration of the distributed line forces across strong discontinuities. In combination with a smoothed contact force law and the employed C^1-continuous beam elements, this procedure drastically reduces the numerical integration error, an essential prerequisite for optimal spatial convergence rates. While the proposed line-to-line contact model applied to slender beams yields very accurate and robust numerical formulations in the range of small contact angles, it is shown that the computational efficiency of general line contact formulations considerably decreases with increasing contact angles. In order to combine the advantages of these basic formulations, a novel all-angle beam contact (*ABC*) formulation is developed in Section 4.3 that applies a point contact formulation in the range of large contact angles and a recently developed line contact formulation in the range of small contact angles, the two being smoothly connected by means of a variationally consistent model transition. Based on a stringent analysis, two different transition laws are investigated, optimal algorithmic parameters are suggested and conservation of linear momentum, angular momentum and total energy is shown. All configuration-dependent quantities within the point-, the line- and the transition-contact regime are consistently linearized, thus allowing for their application within implicit time integration schemes. Subsequently, in Section 4.4, additional algorithmic constituents will be proposed, which can be considered as important prerequisites for efficient and robust overall contact algorithms. Concretely, these algorithmic constituents consist of a novel two-stage contact search algorithm, a modified Newton-Raphson scheme with contact-specific step size control, a computational scheme for consistent consideration of beam end point contact contributions, as well as alternative, numerically good-natured penalty force laws. Finally, a series of numerical test cases is considered in Section 4.5. Specifically, in Sections 4.5.1 and 4.5.2 small (academic) test cases, partly based on analytic solutions, are analyzed in order to investigate properties such as overall accuracy and consistency of the proposed formulations regarding integration error, spatial convergence behavior, resulting

contact force distributions and mechanical conservation properties. Eventually, in Section 4.5.3, four practically relevant applications involving complex systems of slender fibers are considered in order to verify the overall robustness of the proposed algorithms but also for quantifying the efficiency gains as compared to standard beam contact formulations.

In the following sections, the contact contributions to the discrete problem setting shall be determined. Due to the consideration of contact, the global residual vector (3.24) has to be extended:

$$\mathbf{R}(\mathbf{X}_{n+1}) = \mathbf{R}_{int}(\mathbf{X}_{n+1}) + \mathbf{R}_{kin}(\mathbf{X}_{n+1}) + \mathbf{R}_{con}(\mathbf{X}_{n+1}) - \mathbf{R}_{ext}(\mathbf{X}_{n+1}) \doteq 0. \tag{4.1}$$

where $\mathbf{R}_{con}(\mathbf{X}_{n+1})$ represents the global residual contribution of the contact forces, which results from a proper assembly of the local element-pair-wise residual vectors denoted as

$$\mathbf{r}^{(c)}_{con,1}(\hat{\mathbf{x}}^{(c)}_{1,n+1}, \hat{\mathbf{x}}^{(c)}_{2,n+1}) \quad \text{and} \quad \mathbf{r}^{(c)}_{con,2}(\hat{\mathbf{x}}^{(c)}_{1,n+1}, \hat{\mathbf{x}}^{(c)}_{2,n+1}) \tag{4.2}$$

and associated with the elements 1 and 2 of the contact element pair (c). In the following sections, these local residual vectors will be derived for the different beam-to-beam contact formulations described above. All contact models considered in this chapter are based on the assumptions of circular beam cross-sections, neglect of shear deformation with respect to the resulting contact geometries as well as friction-less contact interaction. As direct result of these assumptions, the contact interaction can completely be described by the current centerline configurations of the contacting beams. An extension to frictional beam-to-beam contact interaction will be addressed in future research work (see also Section 5 for a brief outlook to this topic). Large parts of the following sections have been taken from the author's previous contributions [158, 159].

4.1 Point-to-Point Contact Formulation and Limitations

Within this section, the main constituents of a standard point-to-point beam contact formulation as introduced in [234] will be presented. Thereto, two arbitrarily curved beams with cross-section radii R_1 and R_2 are considered. Here and in the following, the subscripts $(.)_1$ and $(.)_2$ refer to these two beams. The beam centerlines are represented by two parametrized curves $\mathbf{r}_1(\xi)$ and $\mathbf{r}_2(\eta)$ with curve parameters ξ and η. In contrast to the beam theory presented in the last two chapters, where derivatives with respect to the (initial) arc-length parameter s were required, the space-continuous beam-to-beam contact problem is based on two arbitrary curve parametrizations ξ and η. Later, when the beam contact problem is discretized in space, these to parameters will be directly identified as element parameter coordinates as introduced in Chapter 3. Based on the two beam centerline curves introduced above, the non-unit tangent vectors $\mathbf{r}_{1,\xi}(\xi) = \mathbf{r}_1'(\xi)$ and $\mathbf{r}_{2,\eta}(\eta) = \mathbf{r}_2'(\eta)$ can be defined in a standard manner. In what follows, it is assumed that the considered space curves are at least C^1-continuous, thus providing a unique tangent vector at every position ξ and η. The kinematic quantities introduced above are illustrated in Figure 4.1.

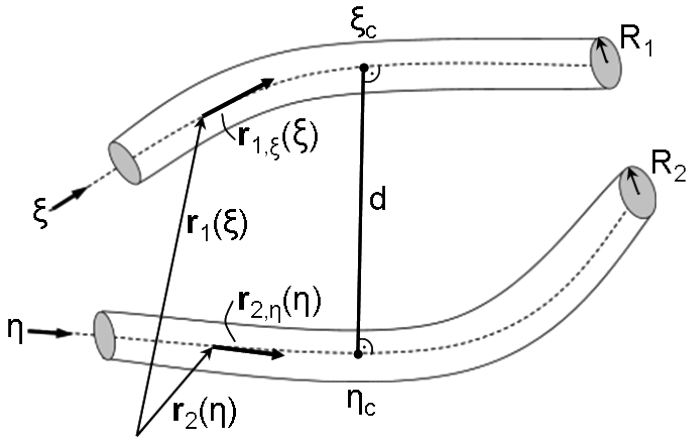

Figure 4.1: Kinematic quantities defining the point-to-point contact problem of two beams.

Remark: In contrast to the arc-length derivative $(.)'$, the derivative with respect to an arbitrary curve parameter ξ or η is denoted as $(.)^{\mathrm{I}}$. Thus, the following relations are valid:

$$(.)' := (.)_{,s} = \frac{\partial}{\partial s}(.) \quad \text{and} \quad (.)^{\mathrm{I}} := (.)_{,\xi} = \frac{\partial}{\partial \xi}(.) \quad \text{with} \quad (.)_{,s} = \frac{(.)_{,\xi}}{||\mathbf{r}_{0,\xi}||}. \tag{4.3}$$

Similar relations can be formulated for the curve parameter η describing the second beam.

4.1.1 Contact formulation and contribution to weak form

The point-to-point beam contact formulation enforces the contact constraint by prohibiting penetration of the two beams at the closest point positions ξ_c and η_c. Here and in the following, the subscript c indicates that a quantity is evaluated at the closest point coordinates ξ_c or η_c, respectively. These closest point coordinates are determined as solution of the bilateral ("bl") minimal distance problem, also denoted as bilateral closest point projection (CPP), with

$$d_{bl} := \min_{\xi,\eta} d(\xi,\eta) = d(\xi_c,\eta_c) \quad \text{with} \quad d(\xi,\eta) = ||\mathbf{r}_1(\xi) - \mathbf{r}_2(\eta)||. \tag{4.4}$$

This leads to two orthogonality conditions that have to be solved for the unknowns ξ_c and η_c:

$$\begin{aligned} p_1(\xi,\eta) &= \mathbf{r}_{1,\xi}^T(\xi)\,(\mathbf{r}_1(\xi) - \mathbf{r}_2(\eta)) \quad \rightarrow\ p_1(\xi_c,\eta_c) \doteq 0, \\ p_2(\xi,\eta) &= \mathbf{r}_{2,\eta}^T(\eta)\,(\mathbf{r}_1(\xi) - \mathbf{r}_2(\eta)) \quad \rightarrow\ p_2(\xi_c,\eta_c) \doteq 0. \end{aligned} \tag{4.5}$$

The contact condition of non-penetration is formulated by means of the inequality constraint

$$g \geq 0 \quad \text{with} \quad g := d_{bl} - R_1 - R_2, \tag{4.6}$$

where g is the gap function defined at the closest points ξ_c and η_c. This inequality constraint can be included into the considered variational problem setting via a penalty potential

$$\Pi_{c\varepsilon} = \frac{1}{2}\varepsilon\langle g\rangle^2 \quad \text{and} \quad \langle x\rangle = \begin{cases} x, & x \leq 0 \\ 0, & x > 0 \end{cases} \tag{4.7}$$

or alternatively via a contact contribution in terms of a Lagrange multiplier potential

$$\Pi_{c\lambda} = \lambda_c g \quad \text{and} \quad \lambda_c \geq 0, \;\; g \geq 0, \;\; \lambda_c g = 0. \tag{4.8}$$

Throughout this work, constraint enforcement via penalty regularization according to (4.7) (see also the remarks in Section 4.2.3.3) is considered exclusively. The constant ε in (4.7) is referred to as penalty parameter (not to be confused with the axial tension ϵ introduced in Chapter 2). Variation of (4.7) leads to the contribution of one contact point to the weak form:

$$\delta\Pi_{c\varepsilon} = \varepsilon\langle g\rangle \delta g = \varepsilon\langle g\rangle \left(\delta\mathbf{r}_{1c} - \delta\mathbf{r}_{2c}\right)^T \mathbf{n}. \tag{4.9}$$

In (4.9), the contact force vector $\mathbf{f}_{c\varepsilon}$ as well as the contact normal vector $\mathbf{n}$ can be identified:

$$\mathbf{f}_{c\varepsilon} = \underbrace{-\varepsilon\langle g\rangle}_{=:f_{c\varepsilon}} \mathbf{n}, \quad \mathbf{n} := \frac{\mathbf{r}_1(\xi_c) - \mathbf{r}_2(\eta_c)}{||\mathbf{r}_1(\xi_c) - \mathbf{r}_2(\eta_c)||}. \tag{4.10}$$

According to (4.10), the point-to-point beam contact formulation models the contact force $\mathbf{f}_{c\varepsilon}$ that is transferred between the two beams as a discrete point force acting at the closest points.

Remark: Since the values of the parameter coordinates ξ_c and η_c describing the location of the current contact point are deformation-dependent, the total variation or linearization of a quantity $X(\xi,\eta)$ can be split up into the following three contributions:

$$\delta\left(X(\xi,\eta)\right) = X_{,\xi}\delta\xi + X_{,\eta}\delta\eta + \delta X \quad \text{and} \quad \Delta\left(X(\xi,\eta)\right) = X_{,\xi}\Delta\xi + X_{,\eta}\Delta\eta + \Delta X.$$

Here, the first two contributions denote the change in $X(\xi,\eta)$ due to a change in the parameter coordinates ξ and η, whereas the contributions $\delta X/\Delta X$ represent the variation/linearization of $X(\xi,\eta)$ at fixed parameter coordinates. As derived in the original work by Wriggers and Zavarise [234], the total variation of the gap simplifies due to

$$\delta g = \mathbf{n}^T(\delta\left(\mathbf{r}_{1c}\right) - \delta\left(\mathbf{r}_{2c}\right)) = \mathbf{n}^T(\delta\mathbf{r}_{1c} + \mathbf{r}_{1c}'\delta\xi - \delta\mathbf{r}_{2c} - \mathbf{r}_{2c}'\delta\eta) = \mathbf{n}^T(\delta\mathbf{r}_{1c} - \delta\mathbf{r}_{2c})$$
$$\text{since } \mathbf{n}^T\mathbf{r}_{1c}' = \mathbf{n}^T\mathbf{r}_{2c}' = 0,$$

which is a consequence of the orthogonality conditions (4.5) at the closest points ξ_c and η_c.

For later use, also the contact angle between the tangents at the contact points shall be defined:

$$\alpha = \arccos\left(z\right) \quad \text{with} \quad z = \frac{||\mathbf{r}_1'^T(\xi_c)\mathbf{r}_2'(\eta_c)||}{||\mathbf{r}_1'(\xi_c)|| \cdot ||\mathbf{r}_2'(\eta_c)||}, \quad \alpha \in [0; 90^\circ]. \tag{4.11}$$

In a next step, spatial discretization has to be performed. Since, for simplicity, only the contact contribution of one contact point will be considered in the following, the indices 1 and 2 are directly transferred to the two finite elements where the point contact takes place. The beam-to-beam contact formulations considered in this thesis are completely defined by the beam centerline configuration. In what follows, it is assumed that the (C^1-continuous) interpolation of the beam centerline is given by (3.39) as well as (3.50). Inserting (3.39) into the orthogonality conditions (4.5) allows to solve the latter for the unknown closest point parameter coordinates

ξ_c and η_c. Since the system of equations provided by (4.5) is in general nonlinear in ξ and η, a local Newton-Raphson scheme is applied for its solution. The linearizations of (4.5) can e.g. be found in [234] and in Appendix C.1. Inserting equations (3.39) into equation (4.9) leads to the following contact residual contributions $\mathbf{r}_{con,1}$ and $\mathbf{r}_{con,2}$ of the two considered elements:

$$\delta\Pi_{c\varepsilon h} = \delta\hat{\mathbf{d}}_1^T \underbrace{\varepsilon\langle g\rangle \mathbf{H}_1^T(\xi_c)\mathbf{n}}_{=:\mathbf{r}_{con,1}} - \delta\hat{\mathbf{d}}_2^T \underbrace{\varepsilon\langle g\rangle \mathbf{H}_2^T(\eta_c)\mathbf{n}}_{=:\mathbf{r}_{con,2}}. \tag{4.12}$$

Finally, the linearization of the residual vector (4.12) is based on the following general form:

$$\mathbf{k}_{con,l} = \frac{d\mathbf{r}_{con,l}}{d\hat{\mathbf{d}}_{12}} = \frac{\partial\mathbf{r}_{con,l}}{\partial\hat{\mathbf{d}}_{12}} + \frac{\partial\mathbf{r}_{con,l}}{\partial\xi_c}\frac{d\xi_c}{d\hat{\mathbf{d}}_{12}} + \frac{\partial\mathbf{r}_{con,l}}{\partial\eta_c}\frac{d\eta_c}{d\hat{\mathbf{d}}_{12}} \quad \text{for} \quad l = 1, 2. \tag{4.13}$$

Here, the vector $\hat{\mathbf{d}}_{12} := (\hat{\mathbf{d}}_1^T, \hat{\mathbf{d}}_2^T)^T$ collecting the nodal degrees of freedom associated with the centerline interpolation of element 1 and element 2 has been introduced. The individual beam contact contributions to the element stiffness matrix are detailed in Appendix C.1.

Remark: The C^1-continuous Hermite shape functions guarantee for the existence of a unique tangent vector field. Nevertheless, the beam contact formulations presented in the following are general enough to be combined with any type of beam element formulation and shape function set. However, if such alternative shape functions do not satisfy the smoothness requirement, additional means are necessary in order to detect and evaluate mechanical contact at positions with non-unique tangent vectors.

Remark: So far, it has been assumed that the beam centerline discretization given by the Hermite interpolation (3.39) is completely described by the nodal degrees of freedom $\hat{\mathbf{d}}_{12} := (\hat{\mathbf{d}}_1^{1T}, \hat{\mathbf{t}}_1^{1T}, \hat{\mathbf{d}}_1^{2T}, \hat{\mathbf{t}}_1^{2T}, \hat{\mathbf{d}}_2^{1T}, \hat{\mathbf{t}}_2^{1T}, \hat{\mathbf{d}}_2^{2T}, \hat{\mathbf{t}}_2^{2T})^T$. However, strictly speaking, this is only true for the SK/WK-TAN and the TF elements, but not for the SK/WK-ROT elements, which rely on a rotation vector-based parametrization of the triads at the element boundary nodes. In the latter case, the element contact residuals derived in this and the following sections have to be transformed by the rule (3.130). Also in this case, the beam problem is still completely defined by the beam centerline curves, however, for the SK/WK-ROT elements these centerline curves also depend on nodal rotation vectors.

4.1.2 Limitations of point-to-point contact formulation

The point-to-point contact formulation provides an elegant and efficient contact model as long as sufficiently large contact angles are considered. However, its limitation lies in the requirement of a unique closest point solution according to (4.5), which cannot be guaranteed for arbitrary geometrical configurations. In [129], the authors have already treated the question of uniqueness and existence of the closest point projection by means of geometrical criteria based on so-called projection domains. Within this section, this question will be analyzed from a different perspective: This procedure will allow to define easy-to-evaluate control quantities and to derive proper upper and lower bounds of these control quantities, within which a unique closest point solution can be guaranteed in a mathematically rigorous manner. In the following, it will be derived that

the contact angle α defined in (4.11), the closest point distance d_{bl} and the geometrical curvature $\bar{\kappa}$ of the beam centerline, which is closely related to the mechanical curvature κ (2.88) via

$$\bar{\kappa} := \frac{\kappa}{||\mathbf{r}'||} = \frac{||\mathbf{r}' \times \mathbf{r}''||}{||\mathbf{r}'||^3} = ||\mathbf{r}_{,\tilde{s}\tilde{s}}|| \quad \text{since} \quad ||\mathbf{r}_{,\tilde{s}}|| = 1, \tag{4.14}$$

are such suitable control quantities. In (4.14), the parameter coordinate $\tilde{s} \in [0; \tilde{l}]$ represents the arc-length of the *current, deformed* beam centerline and $\tilde{l}$ denotes the corresponding *current* centerline length. For the following analytic derivations, which are based on the space-continuous problem setting, the current arc-length parameters $\tilde{s}_1$ and $\tilde{s}_2$ instead of the initial arc-length parameters s_1 and s_2 (required for the space-continuous problem setting of the beam formulations) or the normalized element parameters ξ and η (required for the spatially discretized problem setting) are employed. This choice simplifies many steps due to the essential property $||\mathbf{r}_{1,\tilde{s}_1}|| = ||\mathbf{r}_{2,\tilde{s}_2}|| = 1$. Next, the maximal cross-section to curvature radius ratio is defined as

$$\mu_{max} := \frac{R}{min\,(\bar{r})} \ll 1 \quad \text{with} \quad \bar{r} = \frac{1}{\bar{\kappa}} \approx \frac{1}{\kappa}, \tag{4.15}$$

i.e. as the quotient of the cross-section radius R and the minimal radius of curvature $\bar{r}$ occurring in the deformed geometry. As derived in Section 2.2.5, the application of the considered category of geometrically exact beam theories (and also of the majority of alternative geometrically nonlinear beam theories) is only justified for problems exhibiting small values of this ratio, i.e. $\mu_{max} \ll 1$. This property will be useful later on in this section. In order to simplify the following derivations, the definition of the unilateral ("ul") distance function field $d_{ul}(\tilde{s}_1)$, which assigns a closest partner point $\tilde{s}_{2c}$ of the second beam (in this context also denoted as master beam) for every given point $\tilde{s}_1$ on the first beam (in this context also denoted as slave beam), will be anticipated here and thoroughly derived in Section 4.2. The unilateral distance function field is defined via the following unilateral closest point projection (see Figure 4.3(a) for illustration):

$$d_{ul}(\tilde{s}_1) = \min_{\tilde{s}_2} d(\tilde{s}_1, \tilde{s}_2) = d(\tilde{s}_1, \tilde{s}_{2c}) \quad \text{with} \quad d(\tilde{s}_1, \tilde{s}_2) = ||\mathbf{r}_1(\tilde{s}_1) - \mathbf{r}_2(\tilde{s}_2)||. \tag{4.16}$$

Next, one has to realize that the bilateral closest point projection (4.4) represents a special case of the unilateral closest point projection (4.16). Concretely, the closest point coordinates (4.4) are found through minimization of the minimal distance function $d_{ul}(\tilde{s}_1)$ according to (4.16) with respect to the slave beam parameter $\tilde{s}_1$, represented by the following minimization problem:

$$d_{bl} = \min_{\tilde{s}_1} d_{ul}(\tilde{s}_1) = d_{ul}(\tilde{s}_{1c}). \tag{4.17}$$

Now, in a first step, the requirements for the existence of a unique solution of the unilateral closest point projection will be examined. As soon as a unique distance function $d_{ul}(\tilde{s}_1)$ can be guaranteed, the investigation of the existence and uniqueness of the bilateral closest point projection simplifies from the analysis of a function with 2D support occurring in (4.4) to the analysis of a function with 1D support according to (4.17). For a given point with coordinate vector $\mathbf{r}_1(\tilde{s}_1)$, the unilateral closest point projection according to (4.16) searches for the corresponding closest point coordinate $\tilde{s}_{2c}$ on the space curve $\mathbf{r}_2(\tilde{s}_2)$. The applied Hermite shape functions provide a C^1-continuous centerline curve and guarantee for a uniquely defined tangent vector field. In this

case, a necessary condition for the existence of the minimal distance solution (4.16) is satisfied if the requirement of a vanishing first derivative is fulfilled, i.e.

$$d_{,\tilde{s}_2}(\tilde{s}_1,\tilde{s}_{2c}) = -\frac{\mathbf{r}_{2,\tilde{s}_2}^T(\tilde{s}_{2c})\left(\mathbf{r}_1(\tilde{s}_1)-\mathbf{r}_2(\tilde{s}_{2c})\right)}{||\mathbf{r}_1(\tilde{s}_1)-\mathbf{r}_2(\tilde{s}_{2c})||}\dot{=}0 \;\rightarrow\; \mathbf{r}_{2,\tilde{s}_2}^T(\tilde{s}_{2c})\left(\mathbf{r}_1(\tilde{s}_1)-\mathbf{r}_2(\tilde{s}_{2c})\right)\dot{=}0. \quad (4.18)$$

This, in turn, is guaranteed by the second equation of (4.5). A sufficient condition for the existence of a locally unique closest point solution is given by (4.18) together with the requirement of a positive second derivative of the distance function field between the contacting beams:

$$\begin{aligned} d_{,\tilde{s}_2\tilde{s}_2}(\tilde{s}_1,\tilde{s}_{2c}) = &-\frac{\mathbf{r}_{2,\tilde{s}_2\tilde{s}_{2c}}^T(\tilde{s}_{2c})\left(\mathbf{r}_1(\tilde{s}_1)-\mathbf{r}_2(\tilde{s}_{2c})\right)-\mathbf{r}_{2,\tilde{s}_2}^T(\tilde{s}_{2c})\mathbf{r}_{2,\tilde{s}_2}(\tilde{s}_{2c})}{||\mathbf{r}_1(\tilde{s}_1)-\mathbf{r}_2(\tilde{s}_{2c})||} \\ &-\underbrace{\mathbf{r}_{2,\tilde{s}_2}^T(\tilde{s}_{2c})\left(\mathbf{r}_1(\tilde{s}_1)-\mathbf{r}_2(\tilde{s}_{2c})\right)}_{=0}\cdot(...)\dot{>}0. \end{aligned} \quad (4.19)$$

Together with the auxiliary relation $\mathbf{r}_{2,\tilde{s}_2}^T(\tilde{s}_{2c})\mathbf{r}_{2,\tilde{s}_2}(\tilde{s}_{2c})=1$, (4.19) leads to the requirement:

$$\rightarrow \quad \underbrace{\mathbf{r}_{2,\tilde{s}_2\tilde{s}_2}^T(\tilde{s}_{2c})}_{\bar{\kappa}_2(\tilde{s}_{2c})\mathbf{n}_{FS2}(\tilde{s}_{2c})}\underbrace{\left(\mathbf{r}_1(\tilde{s}_1)-\mathbf{r}_2(\tilde{s}_{2c})\right)}_{d_{ul}(\tilde{s}_1)\mathbf{n}(\tilde{s}_1)}-1\dot{<}0. \quad (4.20)$$

Making use of the definition of the geometrical curvature according to (4.14) and the definitions

$$\begin{aligned} \mathbf{n}_{FS2}(\tilde{s}_{2c}) &:= \frac{\mathbf{r}_{2,\tilde{s}_2\tilde{s}_2}(\tilde{s}_{2c})}{||\mathbf{r}_{2,\tilde{s}_2\tilde{s}_2}(\tilde{s}_{2c})||}, \\ \mathbf{n}(\tilde{s}_1) &:= \frac{\mathbf{r}_1(\tilde{s}_1)-\mathbf{r}_2(\tilde{s}_{2c})}{||\mathbf{r}_1(\tilde{s}_1)-\mathbf{r}_2(\tilde{s}_{2c})||}, \\ \beta_2(\tilde{s}_1) &:= \arccos\left(\mathbf{n}^T(\tilde{s}_1)\mathbf{n}_{FS2}(\tilde{s}_{2c})\right) \end{aligned} \quad (4.21)$$

of the Frenet-Serret unit normal vector $\mathbf{n}_{FS2}(\tilde{s}_{2c})$ (see also Section 2.3.4) aligned to the curve representing the master beam as well as the angle $\beta_2(\tilde{s}_1)$ between this vector and the contact normal vector $\mathbf{n}(\tilde{s}_1)$ (which is defined similarly to (4.10)), (4.20) can be reformulated as:

$$\bar{\kappa}_2(\tilde{s}_{2c})d_{ul}(\tilde{s}_1)\cos(\beta_2(\tilde{s}_1))\dot{<}1. \quad (4.22)$$

If the two beams are close enough so that the sought-after closest point $\tilde{s}_{2c}$ is relevant in terms of active contact forces ($g(\tilde{s}_1)=0 \rightarrow d_{ul}(\tilde{s}_1)=2R$) and under consideration of the worst case $\cos(\beta_2)(\tilde{s}_1)=1$, the following final requirement for a unique solution of (4.16) is obtained:

$$2\frac{R}{\bar{r}_2(\tilde{s}_{2c})} \leq 2\mu_{max}\dot{<}1 \quad \square \quad (4.23)$$

As a consequence of the maximal cross-section to curvature radius ratio $\mu_{max} \ll 1$, a uniquely defined unilateral distance function $d_{ul}(\tilde{s}_1)$ can be guaranteed as long as the beams are sufficiently close. A corresponding criterion for arbitrary distances defined via $d_{ul}(\tilde{s}_1) =: k \cdot R$ can be derived by replacing the factor 2 by k in (4.23). In a second step, also the requirements for

a unique bilateral closest point solution (4.17), based on a uniquely defined distance function $d_{ul}(\tilde{s}_1)$ (which is provided as consequence of (4.23)) are investigated. Again, the first derivative

$$\begin{aligned}\frac{d\,d_{ul}(\tilde{s}_1)}{d\tilde{s}_1} = \frac{d\,d(\tilde{s}_1,\tilde{s}_{2c}(\tilde{s}_1))}{d\tilde{s}_1} = \frac{\partial d}{\partial \tilde{s}_1} + \underbrace{\frac{\partial d}{\partial \tilde{s}_{2c}}}_{\equiv 0}\frac{\partial \tilde{s}_{2c}}{\partial \tilde{s}_1} = \frac{\mathbf{r}_{1,\tilde{s}_1}^T(\tilde{s}_1)\,(\mathbf{r}_1(\tilde{s}_1)-\mathbf{r}_2(\tilde{s}_{2c}))}{||\mathbf{r}_1(\tilde{s}_1)-\mathbf{r}_2(\tilde{s}_{2c})||} \\ \rightarrow\ \mathbf{r}_{1,\tilde{s}_1}^T(\tilde{s}_{1c})\,(\mathbf{r}_1(\tilde{s}_{1c})-\mathbf{r}_2(\tilde{s}_{2c})) \doteq 0,\end{aligned} \tag{4.24}$$

has to vanish. This is satisfied at the closest point $\tilde{s}_{1c}$ by the first line of (4.5). Furthermore, the additional identity $\partial d/\partial \tilde{s}_{2c} \equiv 0\,\forall\,\tilde{s}_1 \in [0;\tilde{l}_1]$ is fulfilled as consequence of the second line of (4.5). Again, a locally unique solution of the minimal distance problem (4.17) additionally requires a positive second derivative. Differentiation of the relation (4.24) yields:

$$\left.\frac{d^2\,d_{ul}(\tilde{s}_1)}{d\tilde{s}_1^2}\right|_{(\tilde{s}_{1c},\tilde{s}_{2c})} = \left.\frac{d^2\,d(\tilde{s}_1,\tilde{s}_{2c}(\tilde{s}_1))}{d\tilde{s}_1^2}\right|_{(\tilde{s}_{1c},\tilde{s}_{2c})} = \left.\left(\frac{\partial^2 d}{\partial \tilde{s}_1^2} + \frac{\partial^2 d}{\partial \tilde{s}_1\,\partial \tilde{s}_{2c}}\frac{\partial \tilde{s}_{2c}}{\partial \tilde{s}_1}\right)\right|_{(\tilde{s}_{1c},\tilde{s}_{2c})} \dot{>} 0. \tag{4.25}$$

The derivative $\partial \tilde{s}_{2c}/\partial \tilde{s}_1$ in (4.25) can be derived by consistently linearizing condition (4.18):

$$\left[\mathbf{r}_{2,\tilde{s}_2\tilde{s}_2}^T(\mathbf{r}_1-\mathbf{r}_2)-\mathbf{r}_{2,\tilde{s}_2}^T\mathbf{r}_{2,\tilde{s}_2}\right]\delta\tilde{s}_{2c}+\mathbf{r}_{2,\tilde{s}_2}^T\mathbf{r}_{1,\tilde{s}_1}\,\delta\tilde{s}_1 = 0 \rightarrow \frac{\partial \tilde{s}_{2c}}{\partial \tilde{s}_1} = \frac{\mathbf{r}_{2,\tilde{s}_2}^T\mathbf{r}_{1,\tilde{s}_1}}{\mathbf{r}_{2,\tilde{s}_2}^T\mathbf{r}_{2,\tilde{s}_2}-\mathbf{r}_{2,\tilde{s}_2\tilde{s}_2}^T(\mathbf{r}_1-\mathbf{r}_2)}. \tag{4.26}$$

After making use of this result and calculating the derivatives of (4.24) with respect to the current arc-length coordinates $\tilde{s}_1$ as well as $\tilde{s}_{2c}$, the requirement (4.25) finally yields:

$$\left.\frac{\mathbf{r}_{1,\tilde{s}_1\tilde{s}_1}^T(\mathbf{r}_1-\mathbf{r}_2)+\mathbf{r}_{1,\tilde{s}_1}^T\mathbf{r}_{1,\tilde{s}_1}-\mathbf{r}_{1,\tilde{s}_1}^T\mathbf{r}_{2,\tilde{s}_2}\cdot\frac{\mathbf{r}_{2,\tilde{s}_2}^T\mathbf{r}_{1,\tilde{s}_1}}{\mathbf{r}_{2,\tilde{s}_2}^T\mathbf{r}_{2,\tilde{s}_2}-\mathbf{r}_{2,\tilde{s}_2\tilde{s}_2}^T(\mathbf{r}_1-\mathbf{r}_2)}}{||\mathbf{r}_1-\mathbf{r}_2||}\right|_{(\tilde{s}_{1c},\tilde{s}_{2c})} \dot{>} 0. \tag{4.27}$$

Using the quantities defined in (4.21), the contact angle α according to (4.11) and the definitions

$$\mathbf{n}_{FS1}(\tilde{s}_{1c}) := \frac{\mathbf{r}_{1,\tilde{s}_1\tilde{s}_1}(\tilde{s}_{1c})}{||\mathbf{r}_{1,\tilde{s}_1\tilde{s}_1}(\tilde{s}_{1c})||}, \quad \beta_1(\tilde{s}_{1c}) := \arccos\left(\mathbf{n}^T(\tilde{s}_{1c})\mathbf{n}_{FS1}(\tilde{s}_{1c})\right), \tag{4.28}$$

condition (4.27) can be reformulated. Due to the strictly positive denominator observed in the inequality condition (4.27), only the numerator has to be considered in the following:

$$1+\bar{\kappa}_1 d_{bl}\cos(\beta_1)-\frac{\cos(\alpha)^2}{1-\bar{\kappa}_2 d_{bl}\cos(\beta_2)} \dot{>} 0 \Leftrightarrow \underbrace{\left(1+\overbrace{\bar{\kappa}_1 d_{bl}}^{\in[0;1[}\cos(\beta_1)\right)}_{>0}\underbrace{\left(1-\overbrace{\bar{\kappa}_2 d_{bl}}^{\in[0;1[}\cos(\beta_2)\right)}_{>0} \dot{>} \cos(\alpha)^2. \tag{4.29}$$

Here the (relevant) case of sufficiently close beams $d_{bl}=k\cdot R$, satisfying $\bar{\kappa}_1 d_{bl}<1$ and $\bar{\kappa}_2 d_{bl}<1$ as consequence of (4.15), is assumed. If the two beams are close enough such that the sought-after closest points $(\tilde{s}_{1c},\tilde{s}_{2c})$ are relevant in terms of active contacts ($g=0 \rightarrow d_{bl}=2R$), the inequality (4.29) can be reformulated by means of the following worst case estimates:

$$(1+2\bar{\kappa}_1 R\cos(\beta_1))(1-2\bar{\kappa}_2 R\cos(\beta_2)) \geq (1-2\bar{\kappa}_1 R)(1-2\bar{\kappa}_2 R) \geq (1-2\mu_{max})^2 \dot{>} \cos(\alpha)^2. \tag{4.30}$$

Since only positive angles $\alpha \in [0; 90°]$ are relevant, only the positive branch of the quadratic inequality (4.30) has to be considered, yielding the following lower bound for the contact angle:

$$\alpha \dot{>} \alpha_{min} = \arccos\left(1 - 2\mu_{max}\right). \tag{4.31}$$

The importance of the final requirement in (4.31) is quite obvious: As long as an upper bound μ_{max} for the admissible ratio of cross-section to curvature radius can be provided, (4.31) yields a lower bound for the admissible contact angles above which the closest point solution is unique. Again, condition (4.31) can be expanded to general, but still sufficiently small ($\bar{\kappa} d_{bl} < 1$!), distances $d_{bl} = k \cdot R$ by replacing the factor 2 by k. The three examples illustrated in Figure 4.2 shall

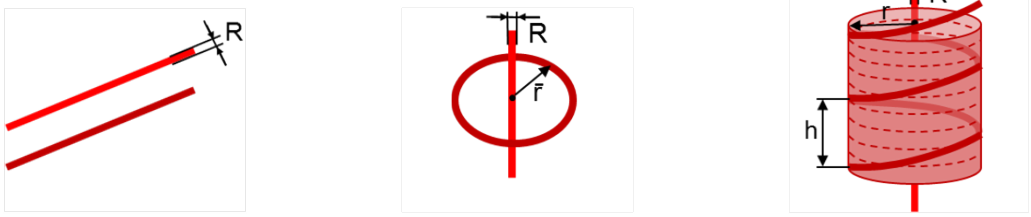

(a) Straight + Straight. (b) Straight + Circular. (c) Straight + Helical.

Figure 4.2: Contact interaction of two beams: Non-unique geometrical configurations.

visualize the important result in (4.31): If only straight rigid beams are considered ($\mu_{max} = 0$, see Figure 4.2(a)), the trivial requirement $\alpha > 0$ is obtained, which reflects the well-known singularity of the closest point projection for parallel beams. If a straight and a circular beam are considered, both being oriented in a centrical manner as depicted in Figure 4.2(b), a constant gap $g(\tilde{s}_1)$ =const. between both beams can be observed, thus leading to a non-unique bilateral closest point solution, but this time at a contact angle of $\alpha = 90°$. However, this case is not practically relevant, since contact in such a scenario can only occur if $\bar{r} \approx 2R$, therefore leading to a cross-section to curvature radius ratio $\mu \approx 0.5$, which is not supported by the considered beam theory, anyway. The third situation (Figure 4.2(c)) is similar to the example that will later be numerically investigated in Section 4.5.1.2. The contact interaction between a straight beam and a helical beam again leads to a constant gap function $g(\tilde{s}_1) =$ const. and consequently to a non-unique bilateral closest point solution. With decreasing slope h, the ratio of cross-section to curvature radius as well as the contact angle at which this non-unique solution appears increases. This is in perfect agreement with (4.31). In this context, the helix represents an intermediate configuration between the case of two straight parallel beams according to Figure 4.2(a) (slope $h \to \infty$) and the case of a straight and a circular beam according to Figure 4.2(b) (slope $h = 0$). In the numerical example of Section 4.5.1.2, it will be shown that for such geometries a comparatively large scope of contact angles $\alpha \in [0°; \alpha_{min}]$ cannot be modeled by means of the standard point-to-point contact formulation. In practical simulations, the lower bound (4.31) has to be supplemented by a proper safety factor in order to guarantee for a unique closest point solution not only when contact actually occurs ($g = 0$) but already for a sufficient range of small positive gaps $g > 0$. Furthermore, too small angles α marginally above the lower bound (4.31) might lead to an ill-conditioned system of equations in (4.5) even if a unique analytic solution exists. Thus, the important result of this section is that the standard point-to-point contact formulation is

not only unfeasible for examples including strictly parallel beams, but rather for a considerable range of small contact angles, since no locally unique closest point solution is existent in this range. According to (4.31), the size of this range depends on the ratio of the maximal bending curvature amplitude expected for the considered problem and the cross-section radius.

So far, only mathematical arguments have been used to show why the point-to-point beam contact formulation cannot be applied in the range of small contact angles. However, it is also questionable from a physical or mechanical point of view if the model of "point-to-point contact" itself is suitable to describe the contact interaction of beams enclosing very small angles. On the one hand, it is clear that configurations providing a strictly constant distance function, i.e. $d_{ul,\tilde{s}_1}(\tilde{s}_1) \equiv 0$, are best modeled by a line-to-line and not by a point-to-point contact formulation. On the other hand, if an exact constraint enforcement of beams with rigid cross-sections is assumed, a pure point-to-point contact situation would already occur for non-constant distance functions with very small slopes, i.e. $0 < ||d_{ul,\tilde{s}_1}(\tilde{s}_1)|| \ll 1$. However, this is a pure consequence of the rigid cross-section assumption inherent to the employed beam model, while a $3D$ continuum approach would naturally lead to *distributed* contact tractions. Consequently, also in the context of $1D$ continuum theories, such scenarios should better be modeled by a line rather than a point contact formulation. In the next section, a novel line contact formulation, which is capable of modeling arbitrary beam contact angles $\alpha \in [0°; 90°]$ and which is particularly beneficial for small contact angles and nearly constant distance functions $d_{ul}(\tilde{s}_1)$, will be proposed.

Remark: Criterion (4.31) does not automatically exclude the point-to-point contact model from applications where small contact angles $\alpha < \alpha_{min}$ might occur. In general, it is possible to apply the point-to-point contact formulation in the range of large contact angles and to switch to an alternative formulation for configurations where no unique bilateral closest point solution exists. Such an alternative formulation will typically be based on multiple contact evaluation points introduced at prescribed locations (e.g. Gauss points or collocation points) and will consequently be categorized as line-to-line type contact formulation by the notion applied here. However, the procedure of switching from one contact formulation to another is not trivial from an algorithmic point of view. It is desirable that the transition between two different contact formulations fulfills certain requirements such as smoothness or variational consistence. The former requirement can be necessary in order to preserve the convergence properties of tangent-based nonlinear solvers, the latter to enable energy conservation in dynamic problems. The formulation of smooth, variationally consistent transition laws between point- and line-based contact models will be considered in the subsequent Section 4.3 of this thesis.

Remark: By abstaining from the worst case estimates in (4.30), an alternative criterion for a unique solution of the bilateral closest point projection (4.4) can be derived:

$$\alpha \dot{>} \alpha_{min} = \sqrt{(1 + 2\bar{\kappa}_1 R\cos(\beta_1))\,(1 - 2\bar{\kappa}_2 R\cos(\beta_2))} \quad .$$

This criterion contains specific information of the considered contact pair such as the current curvature magnitudes $\bar{\kappa}_1$ and $\bar{\kappa}_2$ of the two contacting beams at the contact points as well as the angles β_1 and β_2 between the contact normal vector and the respective Frenet-Serret normal vectors of the two contacting beams at the contact points.

These angles describe the orientation of the respective centerline curvature vector with respect to the contact normal vector. Consequently, for an individual contact pair, this criterion provides a "better" lower bound α_{min} than the more conservative estimate (4.31). However, (4.31) is a global criterion that does not require the investigation of individual contact pairs as long as a global upper bound μ_{max} representing the maximal admissible curvature is provided by the applied beam theory. Such an upper bound can typically be formulated a priori and does not have to be evaluated during the actual simulation as it is the case for the quantities $\bar{\kappa}_1$, $\bar{\kappa}_2$, β_1 and β_2 appearing in the alternative criterion.

4.2 Line-to-Line Contact Formulation

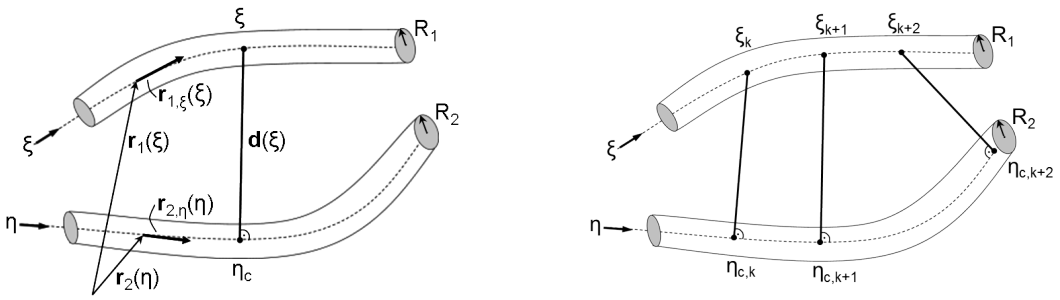

(a) Space-continuous problem setting.

(b) Discretized problem setting.

Figure 4.3: Kinematic quantities defining the line-to-line contact problem of two close beams.

In the following, a novel line-to-line contact formulation is proposed that does not formulate the contact condition in form of a point-constraint at the closest points anymore, but rather as a line constraint enforced along the entire beam length. Consequently, it is not searched for one closest pair of points, but rather for a closest point field $\eta_c(\xi)$ on the second beam (master) assigned to the parameter coordinate field ξ on the first beam (slave). The relevant kinematic quantities of this approach are illustrated in Figure 4.3(a). The closest master point η_c to a given slave point ξ is determined as solution of the following unilateral ("ul") minimal distance problem:

$$d_{ul}(\xi) := \min_{\eta} d(\xi,\eta) = d(\xi,\eta_c) \quad \text{with} \quad d(\xi,\eta) = ||\mathbf{r}_1(\xi) - \mathbf{r}_2(\eta)||. \tag{4.32}$$

It has already been shown in Section 4.1.2 (see (4.23)) that a unique unilateral closest point solution according to (4.32) can be guaranteed for arbitrary beam-to-beam orientations if the two beams are close enough so that contact can occur ($d_{ul}(\xi) \approx 2R$). Condition (4.32) leads to one orthogonality condition that has to be solved for the unknown parameter coordinate η_c:

$$p_2(\xi,\eta) = \mathbf{r}_{2,\eta}^T(\eta)\,(\mathbf{r}_1(\xi) - \mathbf{r}_2(\eta)) \quad \rightarrow\ p_2(\xi,\eta_c)\doteq 0 \tag{4.33}$$

Thus, on the contrary to the procedure of the last section, the normal vector is still perpendicular to the second beam but not to the first beam anymore. Furthermore, in the context of line contact, the subscript c indicates that a quantity is evaluated at the closest master point $\eta_c = \eta_c(\xi)$ associated with a given slave point ξ. In a next step, the contact condition of non-penetration

$$g(\xi) \geq 0 \,\forall\, \xi \quad \text{with} \quad g(\xi) := d_{ul}(\xi) - R_1 - R_2 \tag{4.34}$$

is formulated by an inequality-constraint for the gap function field $g(\xi)$ along the slave beam.

4.2.1 Constraint enforcement and contact residual contribution

Throughout this thesis, constraint enforcement based on the space-continuous penalty potential

$$\Pi_{c\varepsilon} = \frac{1}{2}\varepsilon \int_0^{l_1} \langle g(\xi) \rangle^2 ds_1 \tag{4.35}$$

is considered. In Section 4.2.3, it will be shown that this strategy is preferable in beam contact applications as compared to alternative methods known from contact modeling of $3D$ continua. The space-continuous penalty potential in (4.35) does not only serve as purely mathematical tool for constraint enforcement, but also has a physical interpretation: It can be regarded as a mechanical model for the flexibility of the surfaces and/or cross-sections of the contacting beams. While (4.35) represents the simplest possible potential of this kind, an extension to more elaborate penalty potentials taking into account the cross-section and surface constitutive behavior can be reasonable and is possible for the beam contact approaches presented here. Variation of the penalty potential (4.35) leads to the following contact contribution to the weak form:

$$\delta\Pi_{c\varepsilon} = \varepsilon \int_0^{l_1} \langle g(\xi) \rangle \delta g(\xi) ds_1 \quad \text{and} \quad \delta g(\xi) = (\delta \mathbf{r}_1(\xi) - \delta \mathbf{r}_2(\xi))^T \mathbf{n}(\xi). \tag{4.36}$$

In the virtual work expression (4.36), the contact force $\mathbf{f}_{c\varepsilon}(\xi)$ and normal vector $\mathbf{n}(\xi)$, given by

$$\mathbf{f}_{c\varepsilon}(\xi) = \underbrace{-\varepsilon \langle g(\xi) \rangle}_{=: f_{c\varepsilon}(\xi)} \mathbf{n}(\xi), \quad \mathbf{n}(\xi) := \frac{\mathbf{r}_1(\xi) - \mathbf{r}_2(\eta_c)}{||\mathbf{r}_1(\xi) - \mathbf{r}_2(\eta_c)||}, \tag{4.37}$$

can be identified. According to (4.37), the line-to-line beam contact formulation models the contact force $\mathbf{f}_{c\varepsilon}(\xi)$, which is transferred between the two contacting beams, as a distributed line force. For later use, again the contact angle field is defined according to:

$$\alpha(\xi) = \arccos\left(z(\xi)\right) \quad \text{with} \quad z(\xi) = \frac{||\mathbf{r}_1'^T(\xi)\mathbf{r}_2'(\eta_c)||}{||\mathbf{r}_1'(\xi)|| \cdot ||\mathbf{r}_2'(\eta_c)||}, \quad \alpha \in [0; 90^\circ]. \tag{4.38}$$

Next, spatial discretization has to be performed. For simplicity, only the contact contribution stemming from one finite element on the slave beam and one finite element on the master beam being, assigned to the former via projection (4.33), is considered in the following. Therefore, the indices 1 of the slave beam and 2 of the master beam will also be used in order to denote the two considered finite elements lying on these beams. Inserting the Hermite centerline interpolation (3.39) into the orthogonality condition (4.33) allows to solve the latter for the unknown closest point parameter coordinate $\eta_c(\xi)$ for any given slave coordinate ξ. The linearizations of (4.33) required for an iterative solution procedure can be found in Appendix C.2. Inserting the discretization (3.39) into equation (4.36) and replacing the analytic integral by a Gauss quadra-

ture finally leads to the following contributions of element 1 and 2 to the discretized weak form:

$$\begin{aligned}\delta\Pi_{c\varepsilon h}^{(1,2)} = \delta\hat{\mathbf{d}}_1^T \underbrace{\sum_{k=1}^{n_{GP}} w_k J_{c1}(\xi_k)\varepsilon\langle g(\xi_k)\rangle \mathbf{H}_1^T(\xi_k)\mathbf{n}(\xi_k)}_{=:\mathbf{r}_{con,1}} \\ - \delta\hat{\mathbf{d}}_2^T \underbrace{\sum_{k=1}^{n_{GP}} w_k J_{c1}(\xi_k)\varepsilon\langle g(\xi_k)\rangle \mathbf{H}_2^T(\eta_c(\xi_k))\mathbf{n}(\xi_k)}_{=:\mathbf{r}_{con,2}} .\end{aligned} \tag{4.39}$$

Here, n_{GP} is the number of Gauss points per slave element, w_k are the corresponding Gauss weights, ξ_k are the Gauss point coordinates in the parameter space $\xi \in [-1;1]$ and finally $\eta_{c,k}$ is the closest master point coordinate assigned to the Gauss point coordinate ξ_k on the slave beam (see also Figure 4.3(b)). The Jacobian $J_{c1}(\xi_k)$ maps between the slave beam arc-length increment ds_1 and an increment in the parameter space used for numerical integration (see Section 4.2.2), and $\mathbf{r}_{con,1}$ and $\mathbf{r}_{con,2}$ are the residual contributions of the slave (1) and master (2) element.

Remark: In (4.36), the same gap variation has been derived as for the point contact case. This time, the variation $\delta\xi$ is zero since ξ remains fixed, while the contribution from the variation of η vanishes due to the orthogonality condition on the slave side:

$$\begin{aligned}\delta g(\xi) &= \mathbf{n}^T(\xi)\left(\delta(\mathbf{r}_1(\xi)) - \delta(\mathbf{r}_2(\eta_c))\right) = \mathbf{n}^T(\xi)\left(\delta\mathbf{r}_1(\xi) - \delta\mathbf{r}_2(\eta_c) - \mathbf{r}_{2,\eta}(\eta_c)\delta\eta\right) \\ &= \mathbf{n}^T(\xi)\left(\delta\mathbf{r}_1(\xi) - \delta\mathbf{r}_2(\eta_c)\right) \quad \text{since} \quad \mathbf{n}^T(\xi)\mathbf{r}_{2,\eta}(\eta_c) = 0.\end{aligned}$$

Remark: The gap function in (4.34) describes the exact value of the minimal surface-to-surface distance between the two contacting beams at a given coordinate ξ only if the contact normal vector is perpendicular to both beam centerlines:

$$\mathbf{r}_{1,\xi}^T(\xi)\mathbf{n}(\xi) = 0 \quad \text{and} \quad \mathbf{r}_{2,\eta}^T(\eta_c)\mathbf{n}(\xi) = 0. \tag{4.40}$$

While both conditions in (4.40) are exactly satisfied at the closest point of the point-to-point contact formulation per definition, only the second condition is fulfilled for an arbitrary contact point ξ within an active line-to-line contact segment. However, on the one hand, when considering non-constant distributions of the centerline distance field along the beams, i.e. $d_{ul}(\xi) \neq$ const., the region of active line-to-line contact contributions characterized by $g(\xi) < 0$, decreases with increasing penalty parameter. In the limit $\varepsilon \to \infty$, the line-to-line contact formulation converges towards the point-to-point contact formulation, where both conditions (4.40) are fulfilled exactly. Thus, for a sensibly chosen penalty parameter, the gap function definition (4.34) provides also a good approximation for the line-to-line contact formulation. On the other hand, in configurations with constant centerline distance field $d_{ul}(\xi) =$ const., i.e. a range where no unique bilateral closest point solution exists and the point-to-point contact formulation cannot be applied, the two orthogonality conditions (4.40) are exactly fulfilled for the entire beam anyway.

4.2.2 Integration segments

From a pratical point of view, it is desirable to decouple the beam discretization and the contact discretization. This can be achieved by allowing for $n_{II} \geq 1$ contact integration intervals per slave beam element with n_{GR} integration points defining a Gauss rule of order $p = 2n_{GR} - 1$ on each of these integration intervals, thus leading to $n_{GP} = n_{II} \cdot n_{GR}$ integration points per slave element. In order to realize such a numerical integration procedure, one has to introduce n_{II} further parameter spaces $\bar{\xi}_i \in [-1; 1]$ with $i = 1, ..., n_{II}$ on each slave element:

$$\xi(\bar{\xi}_i) = \frac{1.0 - \bar{\xi}_i}{2}\xi_{1,i} + \frac{1.0 + \bar{\xi}_i}{2}\xi_{2,i} \quad \text{with} \quad i = 1, ..., n_{II}. \tag{4.41}$$

In the simplest case, the parameter coordinates $\xi_{1,i}$ and $\xi_{2,i}$ confining the i^{th} integration interval are chosen equidistantly within the slave element. Further information on the general determination of $\xi_{1,i}$ and $\xi_{2,i}$ is provided later on in this section. The total Jacobian $J_{c1}(\xi(\bar{\xi}_i)) = ds_1/d\bar{\xi}_i$ as employed in the contact residual contributions (4.39), follows directly from (4.41) and reads

$$J_{c1}(\xi(\bar{\xi}_i)) = \frac{ds_1}{d\bar{\xi}_i} = \frac{\partial s_1}{\partial \xi} \cdot \frac{\partial \xi}{\partial \bar{\xi}_i} = J_1(\xi(\bar{\xi}_i)) \cdot \frac{\xi_{2,i} - \xi_{1,i}}{2} \quad \text{with} \quad i = 1, ..., n_{II}, \tag{4.42}$$

where the mapping $J_1(\xi(\bar{\xi}_i))$ from the arc-length space s_1 to the element parameter space ξ on the slave beam results from the applied beam centerline interpolation (3.39) (see also (3.43)). Additionally, the sum over the number of Gauss points appearing in (4.39) has to be split:

$$\begin{aligned}
\mathbf{r}_{con,1} &= \sum_{i=1}^{n_{II}} \sum_{j=1}^{n_{GR}} \underbrace{w_j J_{c1}(\xi_{ij}, \xi_{1,i}, \xi_{2,i}) \varepsilon \langle g(\xi_{ij}) \rangle \mathbf{H}_1^T(\xi_{ij}) \mathbf{n}(\xi_{ij})}_{\mathbf{r}_{con,1}^{ij}}, \\
\mathbf{r}_{con,2} &= \sum_{i=1}^{n_{II}} \sum_{j=1}^{n_{GR}} \underbrace{-w_j J_{c1}(\xi_{ij}, \xi_{1,i}, \xi_{2,i}) \varepsilon \langle g(\xi_{ij}) \rangle \mathbf{H}_2^T(\eta_c(\xi_{ij})) \mathbf{n}(\xi_{ij})}_{\mathbf{r}_{con,2}^{ij}}.
\end{aligned} \tag{4.43}$$

Here, the terms $\mathbf{r}_{con,1}^{ij}$ and $\mathbf{r}_{con,2}^{ij}$ denote the residual contributions resulting from one individual Gauss point j lying in the integration interval i. Moreover, the element parameter coordinates ξ_{ij} are evaluated according to the rule (4.41) at the Gauss point coordinates $\bar{\xi}_j$:

$$\xi_{ij} = \frac{1.0 - \bar{\xi}_j}{2}\xi_{1,i} + \frac{1.0 + \bar{\xi}_j}{2}\xi_{2,i} \quad \text{for} \quad i = 1, ..., n_{II}, \;\; j = 1, ..., n_{GR}. \tag{4.44}$$

Similar to the Gauss weights w_j, these Gauss point coordinates $\bar{\xi}_j$ are constant, i.e. they are not deformation-dependent, and identical for all integration intervals in case the same Gauss rule is applied in each of these intervals. The Gauss quadrature applied for integration of (4.43) guarantees an exact integration of polynomials up to order $p = 2n_{GR} - 1$ when using an integration rule with n_{GR} quadrature points per integration interval. However, by simply integrating across the element boundaries of two successive master elements associated with the considered integration interval via the closest point projection (4.33), the integrand would not have a closed-form polynomial representation anymore and the mentioned polynomial order of exact integration cannot be guaranteed. On the one hand, the integrands in (4.43) are not of purely polynomial nature,

a fact, that precludes exact integration anyway. On the other hand, strong discontinuities in the integrand, such as jumps in the contact force from a finite value to zero at the master beam endpoints, might increase the integration error drastically. Thus, a compromise between integration accuracy and computational efficiency is aimed at. Thereto, the integration intervals introduced above are subdivided into sub-segments only when the projections of master beam endpoints lie within the considered integration interval. With this segmentation strategy, an integration across strong discontinuities at the master beam endpoints can be avoided (see Figure 4.4(b)).

(a) Segments at all master element boundaries. (b) Segments only at master beam endpoints.

Figure 4.4: Creation of integration sub-segments on the slave beam.

However, integration segments are *not* created at all master element boundaries, where weak discontinuities in the integrand might occur (see Figure 4.4(a)). A further example for locations showing weak discontinuities in the integrand are the boundaries of active contact zones, i.e. locations where the contact line force decreases from a positive value to zero. As will become clear later, the integration across this kind of discontinuities is rather unproblematic due to the applied beam formulation being C^1-continuous at the element boundaries (see Chapter 3) and an applied quadratic penalty law regularization (see Section 4.4.3) that leads to a smoother transition between contact and non-contact zones along the beam length. In order to find the boundary coordinate ξ_B of an integration sub-segment created at a given master beam endpoint η_{EP}, the latter has to be projected onto the slave beam according to the rule (with p_2 according to (4.33)):

$$p_2(\xi_B, \eta_{EP}) \doteq 0, \tag{4.45}$$

where the given parameter coordinate η_{EP} can take on the values -1.0 and 1.0 and ξ_B is in general found via an iterative solution of (4.45). The derivative $p_{2,\xi}$ needed for such an iterative solution procedure can be found in Appendix C.2. In the worst, yet very unlikely, case that two master beam endpoints have valid projections according to (4.45) within one integration interval, this interval has to be subdivided into three sub-segments. In this case, for one of these three sub-segments, both boundary coordinates $\xi_{1,i}$ and $\xi_{2,i}$ are determined via (4.45) and are deformation-dependent. Thus, in general, the coordinates $\xi_{1,i}$ and $\xi_{2,i}$ in (4.41) are given by:

$$\begin{aligned} \xi_{1,i} &= \begin{cases} -1+(i-1)\cdot\frac{2}{n_{II}} & \text{if no valid master beam endpoint projection exists} \\ \xi_{B1}(\eta_{EP}, \hat{\mathbf{d}}_{12}) & \text{if a valid master beam endpoint projection exists} \end{cases} \\ \xi_{2,i} &= \begin{cases} -1+i\cdot\frac{2}{n_{II}} & \text{if no valid master beam endpoint projection exists} \\ \xi_{B2}(\eta_{EP}, \hat{\mathbf{d}}_{12}) & \text{if a valid master beam endpoint projection exists} \end{cases} \end{aligned} \tag{4.46}$$

for $i = 1, ..., n_{II}$. Thus, in the standard case, these boundary coordinates are equidistantly distributed and constant. If a valid projection of a master beam endpoint onto an integration interval exists, $\xi_{B1}(\eta_{EP}, \hat{\mathbf{d}}_{12})$ denotes the resulting deformation-dependent lower boundary of a created

sub-segment, whereas $\xi_{B2}(\eta_{EP}, \hat{\mathbf{d}}_{12})$ denotes the upper boundary. Equation (4.46) together with (4.44) and (4.42) provide all necessary information in order to evaluate the element residual vectors according to (4.43). The linearization of the contributions $\mathbf{r}^{ij}_{con,1}$ and $\mathbf{r}^{ij}_{con,2}$ of one individual Gauss point on element 1 can be formulated by means of the following total differential:

$$\begin{aligned}
\mathbf{k}^{ij}_{con,l} = \frac{d\mathbf{r}^{ij}_{con,l}}{d\hat{\mathbf{d}}_{12}} &= \frac{\partial \mathbf{r}^{ij}_{con,l}}{\partial \hat{\mathbf{d}}_{12}} + \frac{\partial \mathbf{r}^{ij}_{con,l}}{\partial \xi_{ij}} \frac{d\xi_{ij}}{d\hat{\mathbf{d}}_{12}} + \frac{\partial \mathbf{r}^{ij}_{con,l}}{\partial \eta_c} \frac{d\eta_c}{d\hat{\mathbf{d}}_{12}} + \frac{\partial \mathbf{r}^{ij}_{con,l}}{\partial \xi_{1,i}} \frac{d\xi_{1,i}}{d\hat{\mathbf{d}}_{12}} + \frac{\partial \mathbf{r}^{ij}_{con,l}}{\partial \xi_{2,i}} \frac{d\xi_{2,i}}{d\hat{\mathbf{d}}_{12}}, \\
\text{with} \quad \frac{d\xi_{ij}}{d\hat{\mathbf{d}}_{12}} &= \frac{\partial \xi_{ij}}{\partial \xi_{1,i}} \frac{d\xi_{1,i}}{d\hat{\mathbf{d}}_{12}} + \frac{\partial \xi_{ij}}{\partial \xi_{2,i}} \frac{d\xi_{2,i}}{d\hat{\mathbf{d}}_{12}} \\
\text{and} \quad \frac{d\eta_c}{d\hat{\mathbf{d}}_{12}} &= \frac{\partial \eta_c}{\partial \xi_{ij}} \frac{d\xi_{ij}}{d\hat{\mathbf{d}}_{12}} + \frac{\partial \eta_c}{\partial \hat{\mathbf{d}}_{12}} \quad \text{for} \qquad l = 1, 2.
\end{aligned} \tag{4.47}$$

It is emphasized that *no* summation convention applies to the repeated indices in (4.47). Again, all basic linearizations of (4.47) are summarized in Appendix C.2. The linearization in (4.47) represents the most general case where the upper and lower boundary of an integration interval are deformation-dependent. However, this is only the case for slave elements with valid master beam endpoint projections according to (4.45) with $\xi_B \in [-1; 1]$. In practical simulations, this is not the case for the vast majority of contact element pairs, i.e. $d\xi_{1,i}/d\hat{\mathbf{d}}_{12} = \mathbf{0}$ and $d\xi_{2,i}/d\hat{\mathbf{d}}_{12} = \mathbf{0}$, thus leading to the following remaining linearization contributions of an individual Gauss point:

$$\mathbf{k}^{ij}_{con,l} = \frac{d\mathbf{r}^{ij}_{con,l}}{d\hat{\mathbf{d}}_{12}} = \frac{\partial \mathbf{r}^{ij}_{con,l}}{\partial \hat{\mathbf{d}}_{12}} + \frac{\partial \mathbf{r}^{ij}_{con,l}}{\partial \eta_c} \frac{\partial \eta_c}{\partial \hat{\mathbf{d}}_{12}}, \quad l = 1, 2. \tag{4.48}$$

The combination of a line-to-line type contact model with a consistently linearized integration interval segmentation at the beam end points as presented in this section, a quadratically regularized smooth penalty law and a C^1-continuous smooth beam centerline representation is a distinctive feature of the proposed contact formulation. The benefits of these means are a drastical reduction of the integration error enabling a consistent spatial convergence behavior for a low number of Gauss points (see Section 4.5.1 for verification), an increase of the algorithmic robustness and a reduction of possible contact force/energy jumps. The selective segmentation strategy provides these benefits without significantly increasing the computational effort.

4.2.3 Alternative constraint enforcement strategies

Similar to point-to-point contact formulations, the constraint equation resulting from the line-to-line contact formulation can be considered within a variational framework by means of a Lagrange multiplier potential or by means of a penalty potential. In contrast to the point-to-point case, however, the constraint in (4.34) is not only defined at a single point but rather on a parameter interval $\xi \in [\xi_a, \xi_b]$. According to Section 4.2.1, the penalty method, which introduces no additional degrees of freedom, can be directly applied in terms of a space-continuous penalty potential, see (4.35). This potential can alternatively be interpreted as a simple hyper-elastic stored-energy function representing the accumulated cross-section stiffness of the contacting beams. The final contact formulation resulting from such a procedure after spatial discretization and numerical integration is often denoted as Gauss-point-to-segment type formulation.

On the contrary, the Lagrange multiplier method applied to the constraint in (4.34) introduces an additional primary variable field $\lambda(\xi)$, which is typically discretized in a manner consistent to the spatial discretization of the displacement variables (discrete inf-sup stable pairing). Eventually, the nodal primary variables resulting from the discretization of the Lagrange multiplier field can be considered as additional unknowns or be eliminated by means of a penalty regularization (applied to a spatially discretized version of (4.34)). Both variants are typically denoted as mortar-type formulations (see e.g. [174, 175]). In Section 4.2.3.1, the main steps of applying a mortar formulation to beam contact problems, thus representing an alternative to the formulation of Section 4.2.1, are provided. Finally, in Sections 4.2.3.2 and 4.2.3.3, a detailed comparison and evaluation of the variants "Gauss-point-to-segment" versus "mortar" and "penalty method" versus "Lagrange multiplier method" is performed in the context of beam contact.

4.2.3.1 Constraint enforcement based on Lagrange multiplier discretization

Alternatively to Section 4.2.1, constraint enforcement via a Lagrange multiplier potential

$$\Pi_{c\lambda} = \int_0^{l_1} \lambda_c(\xi) g(\xi) ds_1 \quad \text{with} \quad \lambda_c(\xi) \geq 0, \;\; g(\xi) \geq 0, \;\; \lambda_c(\xi) g(\xi) = 0 \tag{4.49}$$

is intended in this section. Variation of the Lagrange multiplier potential according to (4.49) leads to the following contact contribution to the weak form of the balance equations:

$$\delta\Pi_{c\lambda} = \int_0^{l_1} \left[\lambda_c(\xi)\delta g(\xi) + \delta\lambda_c(\xi) g(\xi)\right] ds_1 \quad \text{and} \quad \delta g(\xi) = \left[\delta\mathbf{r}_1(\xi) - \delta\mathbf{r}_2(\xi)\right]^T \mathbf{n}(\xi). \tag{4.50}$$

In (4.50), the contact force $\mathbf{f}_{c\lambda}(\xi) = -\lambda_c(\xi)\mathbf{n}(\xi) =: f_{c\lambda}(\xi)\mathbf{n}(\xi)$ transferred between the two beams can again be interpreted as a distributed line force. This time, the Lagrange multiplier field represents the magnitude of this line force. Next, spatial discretization has to be performed. Again, the contribution of one slave beam element 1 and one master beam element 2 is considered. In addition to the spatial discretization (3.39), a trial space $\lambda_c \approx \lambda_{ch} \in \mathcal{U}_{\lambda_c h} \subset \mathcal{U}_{\lambda_c} \subset \Re$ and a weighting space $\delta\lambda_c \approx \delta\lambda_{ch} \in \mathcal{V}_{\lambda_c h} \subset \mathcal{V}_{\lambda_c} \subset \Re$ have to be defined for the Lagrange multipliers:

$$\begin{aligned} \lambda_c(\xi) \approx \lambda_{ch}(\xi) &= \sum_{j=1}^{n_\lambda} N_{\lambda 1}^j(\xi)\hat{\lambda}_1^j =: \mathbf{N}_{\lambda 1}(\xi)\hat{\boldsymbol{\lambda}}_1, \\ \delta\lambda_c(\xi) \approx \delta\lambda_{ch}(\xi) &= \sum_{j=1}^{n_\lambda} N_{\lambda 1}^j(\xi)\delta\hat{\lambda}_1^j =: \mathbf{N}_{\lambda 1}(\xi)\delta\hat{\boldsymbol{\lambda}}_1. \end{aligned} \tag{4.51}$$

Here, n_λ represents the number of nodes of the Lagrange multiplier discretization per slave element, the vector $\mathbf{N}_{\lambda 1}(\xi)$ collects the corresponding test and trial functions with support on slave beam 1, and $\hat{\boldsymbol{\lambda}}_1$ as well as $\delta\hat{\boldsymbol{\lambda}}_1$ contain the corresponding discrete nodal Lagrange multipliers and their variations, respectively (see e.g. [230] concerning the choice of the spaces $\mathcal{U}_{\lambda_c h}$ and $\mathcal{V}_{\lambda_c h}$). Inserting (3.39) and (4.51) into (4.50) and replacing the analytic integral by a Gauss quadrature

finally leads to the following contribution of elements 1 and 2 to the discretized weak form:

$$\begin{aligned}\delta\Pi_{c\lambda h}^{(1,2)} =& \delta\hat{\mathbf{d}}_1^T \underbrace{\sum_{k=1}^{n_{GP}} w_k J_{c1}(\xi_k)\lambda_c(\xi_k)\mathbf{H}_1^T(\xi_k)\mathbf{n}(\xi_k)}_{=\mathbf{r}_{con,1}} - \delta\hat{\mathbf{d}}_2^T \underbrace{\sum_{k=1}^{n_{GP}} w_k J_{c1}(\xi_k)\lambda_c(\xi_k)\mathbf{H}_2^T(\eta_{c,k})\mathbf{n}(\xi_k)}_{=\mathbf{r}_{con,2}} \\ &+ \delta\hat{\boldsymbol{\lambda}}_1^T \underbrace{\sum_{k=1}^{n_{GP}} w_k J_{c1}(\xi_k)\mathbf{N}_{\lambda 1}^T(\xi_k) g(\xi_k)}_{=\mathbf{r}_{\lambda,1,2}} .\end{aligned} \tag{4.52}$$

Again, $\mathbf{r}_{con,1}$ and $\mathbf{r}_{con,2}$ represent the contact force residual contributions of slave element 1 and master element 2, whereas $\mathbf{r}_{\lambda,1,2}$ denotes the corresponding residual contribution resulting from constraint equation (4.34). Based on (4.52), different strategies of constraint enforcement are possible: Considering the nodal Lagrange multipliers $\hat{\boldsymbol{\lambda}}_1$ as additional unknowns would lead to an exact satisfaction of the discrete version of the constraints (4.34). Alternatively, these discrete constraint equations can be regularized by means of a penalty approach. Let $n_{ele,s}$ denote the total number of slave elements. Then, one typically defines averaged nodal gaps $\hat{g}^j$ according to

$$\hat{g}^j := \sum_{e=1}^{n_{ele,s}} \sum_{k=1}^{n_{GP}} w_k J_{c1}(\xi_k) N_{\lambda 1}^j(\xi_k) g(\xi_k) \quad \text{for} \quad j = 1, ..., n_\lambda. \tag{4.53}$$

In (4.53), a summation over all slave elements with support of the shape function $N_{\lambda 1}^j(\xi)$ assigned to the nodal gap $\hat{g}_j$ is sufficient. Consequently, each nodal gap according to (4.53) represents one line of the total contact residual contribution resulting from constraint equation (4.34). Now, one can replace the nodal Lagrange multipliers by averaged nodal penalty forces:

$$\hat{\lambda}_{\varepsilon 1}^j = \varepsilon \langle \hat{g}^j \rangle \quad \text{for} \quad j = 1, ..., n_\lambda. \tag{4.54}$$

Inserting the nodal penalty forces instead of the nodal Lagrange multipliers into (4.52) yields:

$$\begin{aligned}\delta\Pi_{c\lambda_\varepsilon h}^{(1,2)} =& \delta\hat{\mathbf{d}}_1^T \underbrace{\sum_{k=1}^{n_{GP}} w_k J_{c1}(\xi_k)\lambda_{c\varepsilon}(\xi_k)\mathbf{H}_1^T(\xi_k)\mathbf{n}(\xi_k)}_{=\mathbf{r}_{con,1}} \\ &- \delta\hat{\mathbf{d}}_2^T \underbrace{\sum_{k=1}^{n_{GP}} w_k J_{c1}(\xi_k)\lambda_{c\varepsilon}(\xi_k)\mathbf{H}_2^T(\eta_{c,k})\mathbf{n}(\xi_k)}_{=\mathbf{r}_{con,2}} \quad \text{with} \quad \lambda_{c\varepsilon}(\xi) = \sum_{j=1}^{n_\lambda} N_{\lambda 1}^j(\xi)\hat{\lambda}_{\varepsilon 1}^j.\end{aligned} \tag{4.55}$$

This procedure eliminates the additional nodal unknowns $\hat{\boldsymbol{\lambda}}$. However, the constraint of vanishing nodal gaps $\hat{g}^j$ will not be exactly fulfilled anymore. The only difference of the discretized weak form (4.39), i.e. the one resulting from a space-continuous penalty potential, and (4.55), i.e. the one resulting from a discretized Lagrange multiplier potential and a subsequent penalty regularization, lies in the definition of the scalar contact forces $\lambda_{c\varepsilon}(\xi)$ and $\varepsilon\langle g(\xi)\rangle$, respectively.

4.2.3.2 Comparison of the two penalty approaches

The main advantage of the formulation presented in Section 4.2.3.1 is that it results from a consistent Lagrange multiplier discretization. As long as the trial and weighting spaces $\mathcal{U}_h, \mathcal{V}_h, \mathcal{U}_{\lambda_c h}$ and $\mathcal{V}_{\lambda_c h}$ are chosen such that a proper discrete inf-sup-stability condition is satisfied, no contact-related locking effects have to be expected, even for large values of the penalty parameter. This does in general not hold for the formulation presented in Section 4.2.1, where contact-related locking might occur for very high penalty parameters. When considering highly slender beams, moderate values of the penalty parameter are often sufficient in order to satisfy the contact constraint with the desired accuracy. In Section 4.5.1, it will be verified numerically that within this range of penalty parameters the spatial convergence behavior is not deteriorated by contact-related locking effects when applying the contact formulation according to Section 4.2.1. A crucial advantage of the latter formulation lies in its efficiency and its straight-forward implementation. On the one hand, the numerical implementation of the variant presented in Section 4.2.3.1 requires an additional element evaluation loop in order to determine the nodal gaps according to (4.53) or, in other words, the penalty-based elimination of the Lagrange multipliers cannot exclusively be conducted on element level. On the other hand, in combination with the standard gap function definition according to (4.34), this variant requires a very fine finite element discretization when applied to contact problems involving highly slender beams. This fact will be

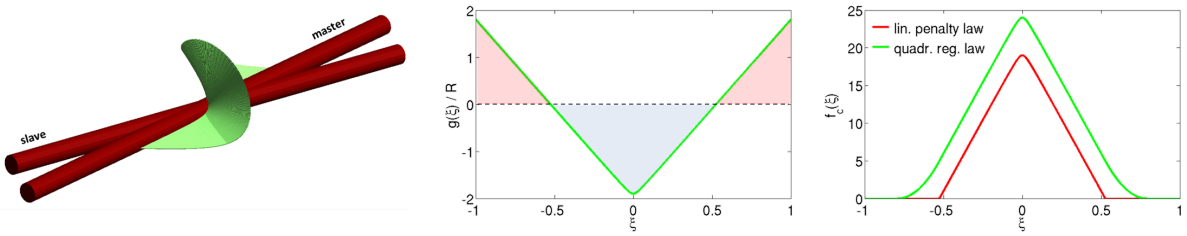

(a) Problem setup and geometry. (b) Evolution of gap function. (c) Evolution of contact force.

Figure 4.5: Two straight beam elements with large penetration and small contact angle.

illustrated in the following by means of Figures 4.5 and 4.6. In Figure 4.5(a), two straight beam elements with cross-section radii $R_1 = R_2 = R$ characterized by a comparatively small contact angle and a large penetration of almost $g(\xi_c) \approx 2R$ are depicted. The resulting contact line force vector field according to (4.37) is illustrated in green color. Furthermore, in Figure 4.5(b), the evolution of the gap function is plotted over the length of the slave beam element. With increasing penalty parameter, the formulation according to Section 4.2.3.1 forces the nodal gaps in (4.53) to vanish. Roughly speaking, this means that the areas enclosed by positive gaps and the areas enclosed by negative gaps, as indicated with red and blue color in Figure 4.5(b), must balance each other. For small contact angles and reasonable spatial discretizations, this is possible. However, when looking at the gap-function evolution resulting from two almost perpendicular beams as illustrated in Figure 4.6(b), such a balancing can only be achieved if the beam element length is reduced drastically. This need for a sufficiently fine spatial discretization increases the numerical effort of this method. Alternatively, one might modify the definition of the gap function $g(\xi)$, such that negative/positive gap contributions are weighted stronger/weaker. Since such an extra effort is not necessary for the procedure of Section 4.2.1, this variant will be preferred.

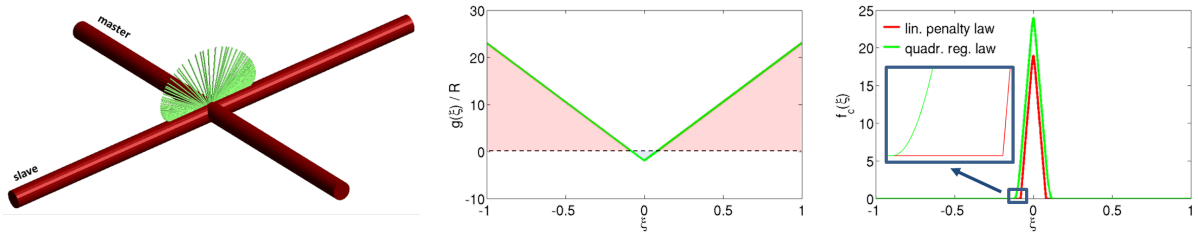

(a) Problem setup and geometry. (b) Evolution of gap function. (c) Evolution of contact force.

Figure 4.6: Two straight beam elements with large penetration and large contact angle.

4.2.3.3 Penalty method vs. Lagrange multiplier method

Constraint enforcement by means of Lagrange multipliers is common practice in the field of computational contact mechanics for solids, especially in combination with mortar methods (see Section 4.2.3.1), due to some advantageous properties, for example concerning the accuracy of contact resolution. Even though the application of the Lagrange multiplier method for constraint enforcement in beam-to-beam contact scenarios has already been investigated in [146], the vast majority of publications in this field is based on regularized constraint enforcement via the penalty method. This fact can be justified by a couple of reasons: When considering discretizations based on structural models the ratio of surface degrees of freedom to all degrees of freedom (=1 for beams) is much larger than for solid discretizations based on a 3D continuum theory. Consequently, also the ratio of additional Lagrange multiplier degrees of freedom to displacement degrees of freedom would be comparatively high when enforcing e.g. beam-to-beam line contact constraints (see Section 4.2.3.1) by means of Lagrange multipliers. Furthermore, when modeling slender structures by means of mechanical beam models, which are often based on the assumption of rigid cross-sections, computational efficiency is one of the key aspects whereas the resolution of exact contact pressure distributions and other mechanical effects on the length scale of the cross-section, which is typically by orders of magnitude smaller than the length dimension of the beam, is not of primary interest. If one is primarily interested in the global system behavior, even penetrations on the order of magnitude of the cross-section radius are often tolerable. Typically, penalty parameters required to limit the penetrations to such values decrease with the beam thickness. Often, the required values are proportional to the beam bending stiffness and therefore the penalty contributions do not significantly deteriorate the conditioning of the system matrix which is usually dominated by high axial and shear stiffness terms.

Besides the arguments above, there is one further crucial point, which makes the penalty method not only preferable to constraint enforcement via Lagrange multipliers, but which even prohibits the use of the latter method. Many of the perhaps most efficient and elegant beam models available in the literature (see e.g. the comparison of ANS beams and geometrically exact beams in [188]), are based on the assumption of rigid cross-sections. Especially when considering very thin beams, this assumption is well-justified and the properties of the resulting beam formulations are desirable from a numerical point of view. However, combining the assumption of rigid cross-sections and contact constraint enforcement via Lagrange multipliers leads to the following dilemma when considering e.g. the dynamic collision of two beams: In the range of large

contact angles, the initial kinetic energy will be transformed into elastic bending energy and back to kinetic energy during the impact. However, with decreasing contact angle the elastic bending deformation decreases and in the limit of two matching, exactly parallel beams the amount of elastic deformation during the collision drops to zero, since the cross-sections are rigid. The accelerations and contact forces resulting from such a scenario are unbounded and the resulting numerical problem becomes singular. Thus, undoubtedly, a certain amount of cross-section flexibility is indispensable when modeling such a scenario. This cross-section flexibility can be provided by a penalty force law such as the one in Section 4.2.1, which already has the structure of a typical hyper-elastic strain energy function and models the accumulated stiffness of the cross-sections of the two contacting beams. Of course, this idea can be refined by deriving more sophisticated penalty laws in form of reduced models based on a continuum mechanical analysis of the cross-section deformation and stiffness (see also [122]). However, since the primary intention is the regularization of parallel-impact scenarios and not the resolution of local deformations on the cross-section scale, the simple and convenient force law (4.88) will be kept. Nevertheless, the adaption of the presented theory to more general penalty laws is straightforward. Finally, with these considerations in mind, the penalty parameter in the context of rigid-cross-section beam contact is no longer a pure mathematical tool of constraint enforcement, but it rather has a physical meaning: it serves as mechanical model of the beam cross-section stiffness. This interpretation simplifies the determination of a proper penalty parameter.

4.2.4 Limitations of line-to-line contact formulation

According to Section 4.1.2, the unilateral closest point solution (4.33) required for the line-to-line contact formulation is unique in the range of admissible beam curvatures and for a sufficiently small distance between the contacting beams. However, the practical limitation of the line-to-line contact formulation is of a different nature and appears in terms of computational effort. In order to explain this statement, the top-view of two contacting straight beams with given contact angle α is illustrated in Figure 4.7. The crucial question is which distance $\Delta\tilde{s}_{GP}$ between two successive Gauss points (red circles) is admissible such that the normalized gap

$$g_n := g/R = (d_{bl} - 2R)/R \tag{4.56}$$

at the bilateral closest points (visualized by means of green circles) does not exceed a prescribed minimal value. From simple geometrical considerations, the following relation between the unilateral distance function d_{ul} associated with the Gauss point and its projection onto the master beam (visualized by blue circles), the bilateral distance function d_{bl} at the closest point pair $\tilde{s}_{1c}, \tilde{s}_{2c}$ (perpendicular to the slide plane) and the contact angle α can be derived:

$$d_{ul}^2 = d_{bl}^2 + \left(\frac{\Delta\tilde{s}_{GP}\sin(\alpha)}{2}\right)^2. \tag{4.57}$$

It is assumed that the penalty parameter ε of the line contact formulation is high enough such that $d_{ul} \approx 2R$ in case of an active/contacting Gauss point. Using this estimation together with equation (4.56), the relation (4.57) is exploited in order to derive the maximal admissible Gauss point

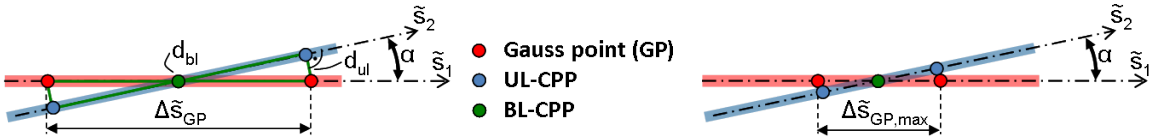

Figure 4.7: Contact interaction of two straight beams enclosing a given contact angle α.

distance $\Delta\tilde{s}_{GP,max}$ such that a prescribed minimal normalized gap $g_{n,min}$ will not be exceeded:

$$\Delta\tilde{s}_{GP,max} = \sqrt{1 - \left(\frac{g_{n,min}}{2} + 1\right)^2}\,\frac{4R}{\sin(\alpha)}. \tag{4.58}$$

From (4.58), two extreme cases can be deduced: Requiring (theoretically) a vanishing gap at the bilateral closest point $g_{n,min} = 0$ means that the distance between the Gauss points also would have to vanish. However, in order to simply prevent the beams from an undetected crossing ($g_{n,min} = 2$ represents the minimal possible gap occurring in case of crossing centerlines), a maximal distance of $4R/\sin(\alpha)$ (see Figure 4.7) must not be exceeded. From (4.58), the minimal number of (evenly distributed) Gauss points $n_{GP,min}$ required for a slave beam of length l_1 and an expected maximal contact angle α_{max} in order to limit the normalized gap to $g_{n,min}$ yields

$$n_{GP,min} = k_{GP}\left[1 - \left(\frac{g_{n,min}}{2} + 1\right)^2\right]^{-0.5}\frac{\sin(\alpha_{max})}{4}\zeta_1 \quad \text{with} \quad \zeta_1 = \frac{l_1}{R}, \tag{4.59}$$

where ζ_1 denotes the slenderness ratio of the slave beam. Here, k_{GP} represents a safety factor, which takes into account that the Gauss points are actually not evenly distributed, that in fact some small penetration at the Gauss points (and not exactly $d_{ul} = 2R$) appear and finally that in practical simulations one often requires a certain number of intermediate Gauss points for reasons of integration accuracy. Nevertheless, the required minimal number of Gauss points increases linearly with the slenderness ratio of the beams. Practical simulations of slender filaments confirm the prediction in (4.59), i.e. that the computational effort increases with the slenderness ratio of the beams and that the overall computational cost is dominated by the numerical evaluation of Gauss point quantities. The second interesting information provided by equation (4.59) is that the minimally required number of Gauss points $n_{GP,min}$ increases with the expected contact angle. Thus, the computational effort could be reduced dramatically if the expensive line-to-line contact formulation were only applied in the range of small contact angles.

Again, it is not only the numerical point of view that suggests a confinement of the line-to-line contact formulation to the range of small contact angles: With increasing contact angle and increasing penalty parameter, the force evolution resulting from the line contact model degenerates more and more to a Dirac-delta distribution, thus advocating the point contact model as mechanical model of choice to be applied in the range of large contact angles. In the following section, the findings of Section 4.1 and 4.2 will be combined in order to derive a novel all-angle beam contact formulation that is suitable for arbitrary beam-to-beam orientations.

4.3 All-angle Beam Contact (*ABC*) Formulation

The quintessence of the last two sections is rather straightforward: The point-to-point contact formulation serves as a sensible mechanical model and very efficient numerical algorithm in the range of intermediate and large contact angles, while it represents an insufficient mechanical model in the range of small contact angles and is even inapplicable for contact angles below the lower bound provided by (4.31). On the other hand, the line-to-line contact formulation provides a very accurate mechanical model and a robust and rather efficient numerical algorithm in the range of small contact angles, whereas the model quality and especially the computational efficiency dramatically decrease with increasing contact angles. According to (4.59), this situation aggravates with increasing beam slenderness ratio. The novel approach presented in the following is based on the simple idea of combining the advantages of these two types of formulations, while abstaining from their disadvantages. Thus, a point contact formulation is applied in the range of large contact angles, while the range of small contact angles is covered by a line contact formulation. The smooth model transition between these regimes within a prescribed interval

$$[\alpha_1;\alpha_2] \quad \text{with} \quad \alpha_1,\alpha_2 \in [0°;90°], \quad \alpha_1 < \alpha_2, \tag{4.60}$$

is realized in a variationally consistent manner without loosing essential properties such as conservation of linear momentum, angular momentum and energy. Furthermore, all configuration-dependent quantities describing the point, line and transition contact range are consistently linearized, thus allowing for their application within an implicit time integration scheme.

4.3.1 Derivation of *ABC* formulation

In the next sections, two different possibilities of carrying out the model transition will be investigated, the first one on penalty force level and the second one on penalty potential level.

4.3.1.1 Force-based model transition

The first variant proposes a beam contact model transition that is performed on the contact force level. Thereto, the overall contact contribution to the weak form is defined as follows:

$$\delta\Pi_{c\varepsilon} = \underbrace{[1-k(z_c)]\,\varepsilon_\perp\langle g\rangle}_{=:-f_{c\varepsilon\perp}}\delta g + \int_0^{l_1} \underbrace{k(z(\xi))\varepsilon_\parallel\langle g(\xi)\rangle}_{=:-f_{c\varepsilon\parallel}(\xi)}\delta g(\xi)ds_1. \tag{4.61}$$

Here and in the following, the indices $\perp$ and $\parallel$ of a quantity refer to the point contact or the line contact formulation, respectively. Additionally, the following notations $z_c := z(\xi_c,\eta_c)$ as well as $z(\xi) = z(\xi,\eta_c(\xi))$ are employed for the cosine of the contact angle (field). The angle-dependent transition factor $k(z)$ occurring in (4.61) is represented by the following analytic expression:

$$k(z) = \begin{cases} 1, & \alpha < \alpha_1 \\ 0.5\left(1-\cos\left(\pi\frac{z-z_2}{z_1-z_2}\right)\right), & \alpha_2 \geq \alpha \geq \alpha_1 \\ 0, & \alpha > \alpha_2 \end{cases}, \quad z = \cos(\alpha) = \frac{||\mathbf{r}_{1,\xi}^T\mathbf{r}_{2,\eta}||}{||\mathbf{r}_{1,\xi}||\,||\mathbf{r}_{2,\eta}||}. \tag{4.62}$$

Thus, (4.61) represents a pure point-contact formulation for large angles $\alpha > \alpha_2$, a pure line-contact formulation for small angles $\alpha < \alpha_1$ and a weighted sum of these two basic formulations for angles within the transition interval $\alpha \in n[\alpha_1; \alpha_2]$. Furthermore, the transition factor $k(z)$ according to (4.62) provides a C^1-continuous transition law for the corresponding contact force contributions. It would be an obvious choice to take the contact angle α as argument of the transition function k. However, in (4.62), $z = \cos(\alpha)$ has been employed, which represents the scalar product of the two unit tangent vectors (see also (4.11) or (4.38)) at the contact point instead of the contact angle α itself as argument of the transition function. Firstly, $\cos(\alpha)$ is a smooth and monotonic function for $\alpha \in [0; 90°]$ and $k(\cos(\alpha))$ can therefore model the transition in a similar manner as $k(\alpha)$. Secondly, this way, additional nonlinearities and singularities resulting from the $\arccos$ function, which is necessary in order to express α in terms of primary variables, can be avoided. Mechanically, the products $(1 - k(z_c(\alpha_c))\varepsilon_\perp \langle g \rangle$ and $k(z(\alpha(\xi))\varepsilon_\parallel \langle g(\xi) \rangle$ of the scaling factor, the penalty parameter and the gap occurring in (4.61) can be interpreted as angle-dependent penalty force laws $f(g, \alpha)$. Unfortunately, it can easily be shown that no potential $\Pi(g, \alpha)$ exists for such a force law: If a potential existed, the integrability condition

$$f_{g,\alpha} = -f_{\alpha,g} \quad \text{with} \quad f_g = \frac{\partial \Pi(g,\alpha)}{\partial g}, \quad f_\alpha = \frac{\partial \Pi(g,\alpha)}{\partial \alpha} \tag{4.63}$$

would have to be fulfilled by the force law. Since (4.61) only provides a force component $f_g = f_{c\varepsilon}$, but no force component that is work-conjugated with $\delta\alpha$ ($f_\alpha \equiv 0$), the integrability condition (4.63) cannot be fulfilled leading to a non-conservative force law. In contrast to mechanically motivated non-conservative force laws (e.g. friction forces), the non-conservative nature of (4.61) has a pure algorithmic reason. Thus, even for a conservative mechanical system, exact energy conservation cannot be achieved if the force law (4.61) employed. For that reason, an alternative, potential-based contact model transition will be proposed in the next section.

4.3.1.2 Potential-based model transition

In order to preserve energy conservation, again, a transition rule similar to (4.62) will be applied, but this time directly on the penalty potential level according to:

$$\Pi_{c\varepsilon} = \frac{1}{2}\varepsilon_\perp (1 - k(z_c)^2)\langle g \rangle^2 + \frac{1}{2}\varepsilon_\parallel \int_0^{l_1} k^2(z(\xi))\langle g(\xi) \rangle^2 ds_1. \tag{4.64}$$

Variation of the combined potential (4.64) yields the contact contribution to the weak form:

$$\begin{aligned} \delta\Pi_{c\varepsilon} = & \underbrace{\varepsilon_\perp \left(1 - k(z_c)^2\right) \langle g \rangle}_{=-f_{c\varepsilon\perp}} \; \delta g \quad \underbrace{- \varepsilon_\perp \langle g \rangle^2 k(z_c) \frac{\partial k(z_c)}{\partial \alpha}}_{=-m_{c\varepsilon\perp}} \; \delta\alpha \\ & + \int_0^{l_1} \Big[\underbrace{\varepsilon_\parallel k^2(z(\xi))\langle g(\xi) \rangle}_{=-f_{c\varepsilon\parallel}} \; \delta g(\xi) + \underbrace{\varepsilon_\parallel \langle g(\xi) \rangle^2 k(z(\xi)) \frac{\partial k(z(\xi))}{\partial \alpha}}_{=-m_{c\varepsilon\parallel}} \; \delta\alpha(\xi) \Big] ds_1 \; . \end{aligned} \tag{4.65}$$

While the terms on the left represent contact force contributions similar to the ones occurring in (4.61), the terms on the right can be identified as contact moment contributions that are work-conjugated to the variation of the contact angle α. These contact moments play the role of the additional contact contributions $f_\alpha = -m_{c\varepsilon}$ necessary in order to fulfill the integrability condition (4.63) and eventually make the force law conservative. The only reason why a quadratic transition factor $k(z)^2$ has been applied in (4.64) instead of a linear one is the derivative $\partial k/\partial\alpha$ occurring in (4.65). By this choice, also the transition in the contact moment contributions becomes C^1-continuous. For conservative problems where exact energy conservation is important, the weak form (4.65) has to be preferred. However, for non-conservative problems and/or problems where exact energy conservation is only of secondary interest, also the simpler variant according to (4.62) can be applied. This statement can be supported by the following three arguments: Firstly, for a sensible choice of the penalty parameter, the total energy contribution of the penalty forces is often small as compared to the internal elastic or kinetic energy. Secondly, the ratio of the contact moments $m_{c\varepsilon}$ to the moment contribution of the contact forces, which are typically in the order of magnitude of $f_{c\varepsilon} \cdot l$, can be formulated by means of the proportionality

$$\frac{m_{c\varepsilon}}{f_{c\varepsilon} \cdot l} \sim \frac{g}{l} \tag{4.66}$$

and is therefore expected to be small, since $g \ll l$ holds for a sensible choice of the penalty parameter. Thirdly, for reasonably balanced penalty parameters $\varepsilon_\perp$ and $\varepsilon_\parallel$ (see Section 4.3.3), the contact moments stemming from a decreasing/increasing point-contact potential and the ones stemming from an increasing/decreasing line-contact potential will mutually erase each other up to a certain degree. As a result, the total moment contribution of point-to-point and line-to-line contact together is smaller than the individual contributions. For all these reasons, the simpler force-based formulation (4.61) will be preferred for the applications in Section 4.5.3. Nevertheless, for comparison purposes, also the potential-based model will be consulted.

Remark: The contact moments occurring in (4.65) are not mechanically motivated. They are rather necessary from a mathematical point of view in order to enable exact energy conservation within the shifting interval. However, in Section 4.5.2.1, it will be shown that in general the pure line-to-line contact formulation already generates (mechanically motivated) accumulated contact moments with respect to the normal vector $\mathbf{n}$ at the (bilateral) closest point. There, it will be observed that for a sensibly chosen ratio of $\varepsilon_\perp$ and $\varepsilon_\parallel$ (see Section 4.3.3), the model error between the *ABC* formulation and the standard line-to-line contact formulation will not be increased in a noticeable manner by these algorithmic contact moments. Furthermore, as already mentioned above, the ratio of these contact moment contributions to moment contributions stemming from contact forces or external forces decreases with increasing penalty parameter. Nevertheless, an exact energy conservation can only be guaranteed if these terms are considered.

In a next step, spatial discretization is performed. The final discrete version of (4.65) (or 4.61) basically consists of the standard contributions of point contact (see Section 4.1) and line contact (see Section 4.2) as well as the transition factor defined in (4.62) and discretized by (3.39). The last missing term that has to be formulated in case of a potential-based transition is the variation $\delta k = (\partial k(z)/\partial\alpha) \cdot \delta\alpha$. In (4.65), the terms on the right have been formulated as variations with respect to α in order to illustrate the moment-character of these contributions. However, it is

sensible to slightly reformulate these terms, since the transition factor has been formulated as function of $z = \cos\alpha$ and the dependence on the contact angle α is only of implicit nature:

$$\delta k(z) = \frac{\partial k(z)}{\partial \alpha}\delta\alpha = \frac{\partial k(z)}{\partial z}\delta z, \quad \frac{\partial k(z)}{\partial z} = \begin{cases} 0, & \alpha < \alpha_1 \\ \frac{\pi}{2(z_1-z_2)} \sin\left(\pi \frac{z-z_2}{z_1-z_2}\right), & \alpha_2 \geq \alpha \geq \alpha_1 \\ 0, & \alpha > \alpha_2 \end{cases} \tag{4.67}$$

Variation of the term $z(\mathbf{r}_1(\xi), \mathbf{r}_2(\eta))$ according to (4.62) leads to the following expression:

$$\begin{aligned} \delta z &= \left[\mathbf{v}_1^T \left(\frac{d\mathbf{r}_1^{\shortmid}}{d\hat{\mathbf{d}}_{12}}\right) + \mathbf{v}_2^T \left(\frac{d\mathbf{r}_2^{\shortmid}}{d\hat{\mathbf{d}}_{12}}\right)\right] \delta\hat{\mathbf{d}}_{12} \\ \mathbf{v}_1^T &= \frac{\mathbf{g}_{1,2}^T}{||\mathbf{r}_1^{\shortmid}||}\left[\mathbf{I}_{3\times 3} - \mathbf{g}_{1,1} \otimes \mathbf{g}_{1,1}^T\right], \quad \mathbf{v}_2^T = \frac{\mathbf{g}_{1,1}^T}{||\mathbf{r}_2^{\shortmid}||}\left[\mathbf{I}_{3\times 3} - \mathbf{g}_{1,2} \otimes \mathbf{g}_{1,2}^T\right], \\ \mathbf{g}_{1,1} &= \frac{\mathbf{r}_1^{\shortmid}}{||\mathbf{r}_1^{\shortmid}||}, \quad \mathbf{g}_{1,2} = \frac{\mathbf{r}_2^{\shortmid}}{||\mathbf{r}_2^{\shortmid}||} \\ \frac{d\mathbf{r}_1^{\shortmid}}{d\hat{\mathbf{d}}_{12}} &= \frac{\partial \mathbf{r}_1^{\shortmid}}{\partial \hat{\mathbf{d}}_{12}} + \frac{\partial \mathbf{r}_1^{\shortmid}}{\partial \xi}\frac{d\xi}{d\hat{\mathbf{d}}_{12}} = \left[\left(\mathbf{H}_1^{\shortmid}, \mathbf{0}\right) + \mathbf{r}_1^{\shortparallel}\frac{d\xi}{d\hat{\mathbf{d}}_{12}}\right], \\ \frac{d\mathbf{r}_2^{\shortmid}}{d\hat{\mathbf{d}}_{12}} &= \frac{\partial \mathbf{r}_1^{\shortmid}}{\partial \hat{\mathbf{d}}_{12}} + \frac{\partial \mathbf{r}_2^{\shortmid}}{\partial \eta}\frac{d\eta}{d\hat{\mathbf{d}}_{12}} = \left[\left(\mathbf{0}, \mathbf{H}_2^{\shortmid}\right) + \mathbf{r}_2^{\shortparallel}\frac{d\eta}{d\hat{\mathbf{d}}_{12}}\right]. \end{aligned} \tag{4.68}$$

In the derivation of (4.68), the discretization according to (3.39) has already been inserted and, again, only the contribution of two beam elements with nodal degrees of freedom $\hat{\mathbf{d}}_{12}$ have been considered. The definition of the transition factor according to (4.62) and its variation according to (4.67) and (4.68) is valid for the point contact and for the line contact contribution. However, in the point-contact contribution, all terms have to be evaluated at the closest point pair ξ_c and η_c, while in the line contact contribution all terms have to be evaluated at the Gauss points ξ_{ij} (see also Section 4.2) and the corresponding closest master points $\eta_c(\xi_{ij})$. In contrast to the gap function variation δg, the derivation of δz also requires the variations of the contact point coordinates ξ and η for a variationally consistent formulation of the weak form. The corresponding derivatives $d\xi/d\hat{\mathbf{d}}_{12}$ and $d\eta/d\hat{\mathbf{d}}_{12}$ of these coordinates for the cases of point-to-point and line-to-line contact are summarized in Appendix C.1 and Appendix C.2. The basic steps in order to derive the final residual and stiffness contributions of the force-based as well as of the potential-based all-angle beam contact formulation are summarized in Appendix C.3.

4.3.2 Choice of shifting angles

A sensible choice of the shifting angles α_1 and α_2 is crucial for a robust and efficient contact algorithm based on the presented *ABC* formulation. For a given upper bound μ_{max} describing the maximal curvature admissible or expected for the considered example, (4.31) yields a lower bound for the shifting angle α_1 above which a unique bilateral closest point solution necessary for the point-to-point contact formulation can be guaranteed. Thus, α_1 is determined as

$$\alpha_1 = k_{\alpha_1} \arccos\left(1 - 2\mu_{max}\right). \tag{4.69}$$

Here, $k_{\alpha_1} > 1$ represents an additional safety factor. Next, the second shifting angle α_2 has to be chosen. For efficiency reasons, this angle should be as small as possible. However, the shifting interval should be large enough in order to ensure a model transition that is sufficiently smooth from a mechanical as well as from a numerical point of view. Since the point-to-point contact and the line-to-line contact model approach each other with increasing penalty parameters, also the shifting interval can be chosen tighter with increasing penalty parameters. In the numerical simulations presented in Section 4.5.3, typical shifting intervals will lie in the angle range of $\alpha_2 - \alpha_1 \approx 1° ... 5°$. Having prescribed α_2, also the lower bound for the required number of Gauss points of the line contact formulation can be determined by inserting $\alpha_{max} = \alpha_2$ into (4.59).

4.3.3 Adjustment of point and line penalty parameters

So far, $\varepsilon_\perp$ and $\varepsilon_\parallel$ represent two independent system parameters. In this section, an optimal ratio of these two parameters will be derived, such that only one penalty parameter has to be user-defined while the second one can be determined automatically. The criterion for this optimal choice is the minimization of the work contribution of the algorithmic contact moment contributions $m_{c\varepsilon\perp}$ and $m_{c\varepsilon\parallel}$. This approach is not only advantageous for the potential-based *ABC* formulation. As a consequence of this choice, the difference between the work contributions of the force-based and the potential-based formulation, which represents the non-conservative work contributions of the force-based formulation, will be minimized. In the following, it is not searched for the exact solution of the corresponding minimization problem, but rather for an approximate solution based on some simplifying assumptions. Thereto, the curves $\mathbf{r}_1(\xi)$ and $\mathbf{r}_2(\eta)$ are expressed as linear Taylor expansions with respect to the closest point (ξ_c, η_c), thus leading to a constant contact angle within the line-to-line contact region. In this case, the $m_{c\varepsilon\parallel}$-term can be simplified:

$$\begin{aligned} \varepsilon_\parallel \int_0^{l_1} \langle g(\xi) \rangle^2 k(z(\xi)) \frac{\partial k(z(\xi))}{\partial \alpha} \delta\alpha(\xi) ds_1 &= \varepsilon_\parallel \int_{s_{1,c}-\Delta s_\parallel}^{s_{1,c}+\Delta s_\parallel} g(\xi)^2 k(z(\xi)) \frac{\partial k(z(\xi))}{\partial \alpha} \delta\alpha(\xi) ds_1 \\ &\approx \varepsilon_\parallel \int_{s_{1,c}-\Delta s_\parallel}^{s_{1,c}+\Delta s_\parallel} g_l(\xi)^2 ds_1 \cdot k(z_c) \frac{\partial k(z_c)}{\partial \alpha} \delta\alpha_c. \end{aligned} \tag{4.70}$$

Here, $g_l(\xi)$ denotes the gap function based on linearly approximated beam geometries. This approximation is valid, since for a sensible choice of the penalty parameter and the shifting interval (see Section 4.3.2) the length $2\Delta s_\parallel$ of the domain with active contact forces ($g < 0$) is small compared to the beam length. Furthermore, this length decreases with increasing penalty parameter. Next, it is required that the contact moment work contributions balance each other:

$$\varepsilon_\parallel \int_{s_{1,c}-\Delta s_\parallel}^{s_{1,c}+\Delta s_\parallel} g_l(\xi)^2 ds_1 \cdot k(z_c) \frac{\partial k(z_c)}{\partial \alpha} \delta\alpha_c = \varepsilon_\perp g^2 k(z_c) \frac{\partial k(z_c)}{\partial \alpha} \delta\alpha_c \;\rightarrow\; \varepsilon_\perp = \frac{\varepsilon_\parallel}{g^2} \int_{s_{1,c}-\Delta s_\parallel}^{s_{1,c}+\Delta s_\parallel} g_l(\xi)^2 ds_1. \tag{4.71}$$

In general, equation (4.71) based on a linearly approximated geometry cannot be fulfilled for arbitrary contact angles and gaps by one constant penalty parameter $\varepsilon_\perp$. Therefore, only the

weaker requirement that (4.71) is exactly fulfilled for the minimal admissible gap g_{min} (going along with maximal contact work) and at the mean shifting angle $\bar{\alpha}_{12} := (\alpha_1 + \alpha_2)/2$ is stated:

$$\frac{\varepsilon_\perp}{\varepsilon_\parallel} = \frac{1}{g_{min}^2} \int\limits_{s_{1,c}-\Delta s_\parallel}^{s_{1,c}+\Delta s_\parallel} g_l(g_{min}, \bar{\alpha}_{12}, \xi)^2 ds_1 = \frac{\tilde{\Pi}_{c\varepsilon\parallel}(g_{min}, \bar{\alpha}_{12})}{\tilde{\Pi}_{c\varepsilon\perp}(g_{min})}. \tag{4.72}$$

Since an exact solution of (4.71) is not intended, but rather an approximation providing at least a sensible order of magnitude, a comparatively rough bound for the minimal gap g_{min} is sufficient. If the specific application prescribes some tolerable bound g_{min}, this value can be taken. With an implementation of the proposed *ABC* formulation at hand, it is a simple task to perform a pre-processing step, where the normalized penalty potential $\tilde{\Pi}_{c\varepsilon\perp}(g_{min})$ of the point-contact and $\tilde{\Pi}_{c\varepsilon\parallel}(g_{min}, \bar{\alpha}_{12})$ of the line-contact (see Section 4.4.3 for the definition of normalized penalty potentials and different penalty force laws) resulting from the contact interaction of two straight beams characterized by an enclosed angle $\bar{\alpha}_{12}$ and a gap g_{min} are calculated. With these energies and a given penalty parameter $\varepsilon_\parallel$, the corresponding value of $\varepsilon_\perp$ can be calculated according to (4.72). This procedure is valid for arbitrary penalty force or potential laws that depend linearly on the penalty parameter, such as for example the laws (4.87) and (4.88) (see Section 4.4.3). In case of a linear penalty law according to (4.87), the integral appearing in (4.72) can also be approximated analytically. Assuming the most conservative estimation for the minimal gap according to $g_{min} = -2R$ (intersection of the beam centerlines), and approximating the distribution of $g_l(\xi)$ as piecewise linear function in ξ yields the following relation:

$$\frac{\varepsilon_\perp}{\varepsilon_\parallel} \approx \frac{2}{g_{min}^2} \int\limits_{s_{1,c}}^{s_{1,c}+\Delta s_\parallel} \left[-g_{min} \left(1 - \frac{s_1 - s_{1,c}}{\Delta s_\parallel} \right) \right]^2 ds_1 = \frac{2\Delta s_\parallel}{3}. \tag{4.73}$$

By using (4.58) in case of intersecting beam centerlines ($g_{min} = -2R \rightarrow g_{n,min} = -2$) in order to determine the integration length as $2\Delta s_\parallel = 4R/\sin(\bar{\alpha}_{12})$, a simple relation can be stated:

$$\frac{\varepsilon_\perp}{\varepsilon_\parallel} \approx \frac{4R}{3\sin(\bar{\alpha}_{12})}. \tag{4.74}$$

A similar analytic approximation could also be derived for the quadratically regularized penalty force law introduced in Section 4.4.3. However, since in practical simulations the relation $\bar{g} \ll R$ often holds (see again Section 4.4.3 for the definition of $\bar{g}$), (4.74) can also be applied as approximation for this force law. In Section 4.5, it will be shown that in many cases a choice of $\varepsilon_\perp$ according to (4.74) is sufficient in order to reduce the non-conservative work contribution of the force-based formulation down to a practically tolerable level. Nevertheless, this behavior can be further improved by determining $\varepsilon_\perp$ via numerical integration of (4.72) based on the actually applied penalty law and a better estimation for the minimal gap g_{min}. With this suggestion at hand, only the line-to-line penalty parameter $\varepsilon_\parallel$ has to be prescribed independently. For the determination of $\varepsilon_\parallel$, the value of the cross section stiffness can serve as a starting point.

Remark: In (4.61), it seemed to be natural to introduce a scaling factor $[1-k(z)]$ for the point penalty parameter that is complementary to the scaling factor $k(z)$ of the line penalty parameter. With the knowledge of the last sections, one could imagine an alternative description of the angle-dependent evolution of the point penalty parameter. Thereto, one could apply the force-based *ABC* formulation, yet, not based on the applied $[1-k(z)]$-transition law in combination with a constant penalty parameter, but rather based on an individual point-to-point penalty parameter $\varepsilon_{\perp,i}$ at every contact point as additional unknown. In order to determine this additional unknown, one could formulate conditions similar to (4.71) for each individual contact point, such that the resulting evolution of $\varepsilon_{\perp,i}$ allows for exact energy conservation without the need for algorithmic contact moments as appearing in the potential-based *ABC* formulation. However, in Section 4.5.2 it will be verified numerically that the error in the energy conservation of the simple force-based *ABC* formulation in combination with a sensible, constant choice of $\varepsilon_{\perp}$ (see e.g. (4.72)) is in many cases negligible from a practical point of view. Thus, the numerical effort resulting from a formulation with additional unknowns $\varepsilon_{\perp,i}$ does not seem to be justified.

4.3.4 Conservation properties

In Section 3.2.4.5, the conservation of linear and angular momentum as well as the conservation of energy has already been formulated in a general manner for the proposed beam element formulations. Concretely, it has been shown that the conservation statements (3.110), (3.112) and (3.114) can directly be deduced in case the "virtual motions" (3.109), (3.111) and (3.113) can be represented by the chosen weighting spaces $\mathcal{V}_h$. Since the proposed beam-to-beam contact formulations are completely defined by the beam centerline field $\mathbf{r}(s)$ (and its variation $\delta\mathbf{r}(s)$), only the first of the two respective variational fields in (3.109), (3.111) and (3.113) that is related to the centerline variation $\delta\mathbf{r}_h$ is relevant in the following. In contrast to the discrete spin vector fields, it has already been shown that the discrete centerline variation fields given in (3.109), (3.111) and (3.113) can be exactly represented by all of the presented beam element formulations. Thus, the only remaining step is to investigate if these virtual centerline motions also result in a conservation of linear momentum, angular momentum and energy for the considered beam contact formulations. Concretely, the proposed *ABC* formulation in combination with a potential-based model transition given in (4.65) will be investigated, since it contains the variants "force-based transition" (neglect of contact moment contributions and replacement of $k(z)$ by $k^2(z)$), "pure point contact" ($k(z)\equiv 0$) and "pure line contact" ($k(z)\equiv 1$) as special cases.

Starting with the investigation of conservation of linear momentum, the specific test functions $\delta\mathbf{r}_{1h}(\xi) = \delta\mathbf{r}_{2h}(\eta) = \mathbf{u}_0 = \text{const.}$ are employed. In the following, it will be shown that inserting these test functions into (4.65) yields a vanishing overall contact contribution to the weak form:

$$\delta\Pi_{c\varepsilon}(\delta\mathbf{r}_{1h} = \delta\mathbf{r}_{2h} = \mathbf{u}_0) = 0. \tag{4.75}$$

In other words, the discrete contact forces at the contact interface exactly balance each other and global conservation of linear momentum according to (3.110) is still preserved. In order to prove this statement, one has to realize from (4.9) and (4.36) that $\delta g(\delta\mathbf{r}_{1h} = \delta\mathbf{r}_{2h} = \mathbf{u}_0) = 0$, which already yields vanishing contact force terms (terms on the left) in (4.65). Furthermore, inserting (3.109) into the expressions for $d\xi/d\hat{\mathbf{d}}_{12}$ and $d\eta/d\hat{\mathbf{d}}_{12}$ given in Appendix C.1 and C.2 delivers

the trivial result that the closest point projections are not influenced by a rigid body translation of the entire system, i.e. $d\xi(\delta\mathbf{r}_{1h}=\delta\mathbf{r}_{2h}=\mathbf{u}_0)/d\hat{\mathbf{d}}_{12} = d\eta(\delta\mathbf{r}_{1h}=\delta\mathbf{r}_{2h}=\mathbf{u}_0)/d\hat{\mathbf{d}}_{12}=\mathbf{0}$. Inserting this result together with $\mathbf{H}_1'\delta\hat{\mathbf{d}}_1(\mathbf{u}_0) = \mathbf{H}_2'\delta\hat{\mathbf{d}}_2(\mathbf{u}_0) = \mathbf{0}$ into (4.68) leads to $\delta z = \delta\alpha = 0$, and therefore also to vanishing contact moment contributions in (4.65). This concludes the proof of (4.75).

In order to investigate conservation of angular momentum, the test functions $\delta\mathbf{r}_{1h}=\mathbf{w}_0\times\mathbf{r}_1$ and $\delta\mathbf{r}_{2h}=\mathbf{w}_0\times\mathbf{r}_2$ based on a spatially constant vector $\mathbf{w}_0$=const. are considered. It will be shown that inserting these test functions into (4.65) again yields a vanishing contact contribution:

$$\delta\Pi_{c\varepsilon}(\delta\mathbf{r}_{ih}=\mathbf{w}_0\times\mathbf{r}_{ih}) = 0 \quad \text{for} \quad i=1,2. \tag{4.76}$$

In other words, the contact moments at the contact interface exactly balance each other and conservation of angular momentum according to (3.112) is preserved. In order to prove this statement, this specific choice of test functions is first inserted into (4.9) and (4.36):

$$\delta g(\delta\mathbf{r}_{ih}=\mathbf{w}_0\times\mathbf{r}_{ih}) = \left(\mathbf{w}_0\times\mathbf{r}_{1h}-\mathbf{w}_0\times\mathbf{r}_{2h}\right)^T\mathbf{n} = \mathbf{w}_0^T\left[(\mathbf{r}_{1h}-\mathbf{r}_{2h})\times\mathbf{n}\right] = 0. \tag{4.77}$$

Again, inserting this choice of test functions into the expressions for $d\xi/d\hat{\mathbf{d}}_{12}$ and $d\eta/d\hat{\mathbf{d}}_{12}$ presented in Appendix C.1 and C.2 yields the trivial result that the closest point projections are not influenced by a rigid body rotation, i.e. $d\xi(\delta\mathbf{r}_{ih}=\mathbf{w}_0\times\mathbf{r}_{ih})/d\hat{\mathbf{d}}_{12} = d\eta(\delta\mathbf{r}_{ih}=\mathbf{w}_0\times\mathbf{r}_{ih})/d\hat{\mathbf{d}}_{12}=\mathbf{0}$. An evaluation of the remaining terms in equation (4.68) finally results in

$$\delta z = \mathbf{v}_1^T\left(\mathbf{w}_0\times\mathbf{r}_{1h}'\right) + \mathbf{v}_2^T\left(\mathbf{w}_0\times\mathbf{r}_{2h}'\right) = \frac{\mathbf{r}_2'^T\left(\mathbf{w}_0\times\mathbf{r}_{1h}'\right)}{||\mathbf{r}_1'||\,||\mathbf{r}_2'||} + \frac{\mathbf{r}_1'^T\left(\mathbf{w}_0\times\mathbf{r}_{2h}'\right)}{||\mathbf{r}_1'||\,||\mathbf{r}_2'||} = 0, \tag{4.78}$$

where $(\mathbf{w}_0\times\mathbf{r}_{ih})' = \mathbf{w}_0\times\mathbf{r}_{ih}'$ was used. The results (4.77) and (4.78) complete the proof of (4.76).

In a last step, also the conservation of energy has to be verified. Thereto, the test functions $\delta\mathbf{r}_{1h} = \dot{\mathbf{r}}_{1h}$ as well as $\delta\mathbf{r}_{2h} = \dot{\mathbf{r}}_{2h}$ are considered. The contact contributions (4.65) have been derived from the potential (4.64) in a Bubnov-Galerkin manner under consistent consideration of the spatial discretization given by the Hermite centerline interpolation (3.39), i.e.

$$\begin{aligned}
\delta\Pi_{c\varepsilon} &= \sum_{i=1}^{2}\left(\frac{\partial\Pi_{c\varepsilon}}{\partial\mathbf{r}_i}\frac{d\mathbf{r}_i}{d\hat{\mathbf{d}}_{12}}\delta\hat{\mathbf{d}}_{12} + \frac{\partial\Pi_{c\varepsilon}}{\partial\mathbf{r}_i'}\frac{d\mathbf{r}_i'}{d\hat{\mathbf{d}}_{12}}\delta\hat{\mathbf{d}}_{12}\right), \\
\frac{d\mathbf{r}_1}{d\hat{\mathbf{d}}_{12}} &= \left[(\mathbf{H}_1,\mathbf{0}) + \mathbf{r}_h'\frac{d\xi}{d\hat{\mathbf{d}}_{12}}\right], \frac{d\mathbf{r}_1'}{d\hat{\mathbf{d}}_{12}} = \left[\left(\mathbf{H}_1',\mathbf{0}\right) + \mathbf{r}_1''\frac{d\xi}{d\hat{\mathbf{d}}_{12}}\right], \\
\frac{d\mathbf{r}_2}{d\hat{\mathbf{d}}_{12}} &= \left[(\mathbf{H}_2,\mathbf{0}) + \mathbf{r}_2'\frac{d\xi}{d\hat{\mathbf{d}}_{12}}\right], \frac{d\mathbf{r}_2'}{d\hat{\mathbf{d}}_{12}} = \left[\left(\mathbf{H}_2',\mathbf{0}\right) + \mathbf{r}_2''\frac{d\xi}{d\hat{\mathbf{d}}_{12}}\right].
\end{aligned} \tag{4.79}$$

Therefore, by replacing the variations $\delta(.)$ with time derivatives $\dot{(.)}$, the correspondingly discretized contact contributions (4.65) per definition represent the rate $\dot{\Pi}_{c\varepsilon}$ of the discrete penalty potential. Adding the contact terms to the internal, kinetic and external terms in (3.114) yields

$$\dot{\Pi}_{kin} + \dot{\Pi}_{int} + \dot{\Pi}_{c\varepsilon} = P_{ext}, \tag{4.80}$$

which again implies conservation of the sum of kinetic, internal and penalty energy in the absence of external forces, i.e. if $P_{ext} = 0$. In case of the non-conservative "force-based transition"

between the point and line contact regime, no potential of the contact forces exists and the term $\dot{\Pi}_{\varepsilon}$ in (4.80) has to be replaced by the negative power of the contact forces $-P_{c\varepsilon}$, viz.

$$P_{c\varepsilon} = \left(\dot{\mathbf{r}}_1 - \dot{\mathbf{r}}_2\right)^T \mathbf{f}_{c\varepsilon\perp} + \int_0^{l_1} \left[\left(\dot{\mathbf{r}}_1 - \dot{\mathbf{r}}_2\right)^T \mathbf{f}_{c\varepsilon\|} \right] ds_1, \quad \mathbf{f}_{c\varepsilon\perp} = f_{c\epsilon\perp}\mathbf{n}, \quad \mathbf{f}_{c\varepsilon\|} = f_{c\varepsilon\|}\mathbf{n}. \tag{4.81}$$

In summary, it can be stated that the properties of conservation of linear momentum, angular momentum and energy are preserved by the spatially discretized version of the proposed beam-to-beam contact formulations in combination with the geometrically exact beam element formulations proposed in Chapter 3. In Section 4.5.2.2, this statement will also be verified numerically. The question of preservation of these properties in the temporally discretized problem setting depends on the applied time integration scheme and is not content of this work.

4.4 Algorithmic Aspects

In the following Sections 4.4.1 and 4.4.2, further information concerning the employed contact search algorithm and a step size control applied to the iterative displacement increments within the Newton-Raphson scheme will be given. The latter method enables displacements per time step that are larger than the beam cross section radius, which is the typical time step size limitation of standard beam contact algorithms. In Section 4.4.3, different penalty force laws are presented before the contact contributions of the beam endpoints are considered in Section 4.4.4.

4.4.1 Contact search algorithm

The contact search algorithm combined with the proposed *ABC* formulation consists of two search steps. The first step is an element-based octree search and yields pairs of close-by finite elements (located on two different or for self-contact also on the same physical beam) that might potentially come into contact. The octree search assumes that (the 2D projection of) the maximal deformation of an initially straight beam segment discretized by one third-order finite element based on (3.39) does not exceed a half-circular shape. Having this restriction in mind, the octree search is based on an intersection of spherical bounding boxes defined by

$$\mathbf{r}_m = \frac{\hat{\mathbf{d}}^1 + \hat{\mathbf{d}}^2}{2}, \quad r_s = (1 + k_{r_s})\frac{||\hat{\mathbf{d}}^2 - \hat{\mathbf{d}}^1||}{2} \tag{4.82}$$

and illustrated in two dimensions in Figure 4.8. Here, the introduced parameter k_{r_s} represents an additional safety factor. While the spherical search box appears as a comparatively loose hull for straight beam elements (see Figure 4.8(a)) its application seems to be justified when considering strongly deformed beam elements as illustrated in Figure 4.8(b). In order to further limit the size and number of beam segments where (a large number of) unilateral closest-point projections have to be evaluated, a second search step is applied. Thereto, each beam element of the pairs found in the first step is subdivided into n_{seg} equidistant sub-segments as illustrated in Figure 4.8(c). Thereby, the number n_{seg} of sub-segments is doubled until the angles β_{jl} and β_{jr}

between the real geometry and the straight search segment at the left and right end of the search segments are smaller than a prescribed value β_{max}, i.e. $\beta_{jl}, \beta_{jr} < \beta_{max}$ for $j \in \{1, n_{seg}\}$. To fulfill this criterion for arbitrary configurations, n_{seg} is adapted dynamically in every Newton step.

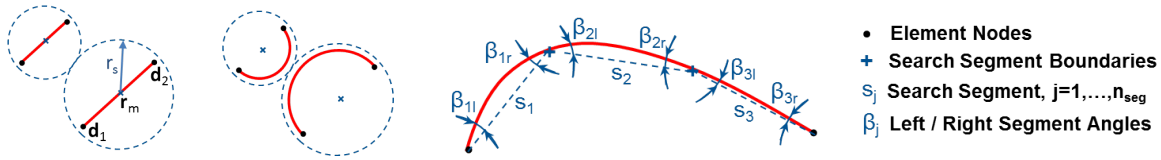

(a) Straight. (b) Curved. (c) Subdivision of each finite element into n_{seg} search segments.

Figure 4.8: Two-step search algorithm: 1) Element-wise octree search based on spherical search boxes (4.8(a) and 4.8(b)). 2) Dynamic subdivision into search segments (4.8(c)).

Next, it is assumed that for the search segments built by this procedure, the actual centerline geometry is completely enwrapped by a double cone with cone angle $2\beta_{max}$ (see Figure 4.9(a)). It seems to be rather intuitive when looking at Figure 4.9(a) that for the applied third-order Hermite polynomials this assumption is justified. For the examples of Section 4.5, this statement has also been verified numerically. Since the direct intersection of these double-cones is geometrically quite involved, they are replaced by enwrapping cylinders (see Figure 4.9(b)) with radius

$$r_{cyl} = k_{cyl} \cdot \tan(\beta_{max}) \cdot \frac{l_{seg}}{2} \quad \text{with} \quad l_{seg} = \frac{l_{ele}}{n_{seg}}. \tag{4.83}$$

Here, l_{ele} is the initial element length and k_{cyl} a safety factor. After the geometrically close-by segment pairs have been determined via intersection of these cylindrical bounding boxes (which can be done very efficiently by an analytic CPP between the straight cylinder axes and a subsequent check of the segment endpoints), the intersection angle γ can be determined. This enables an estimation of the potential contact angles possible for this segment pair, i.e. $\alpha \in [\gamma - 2\beta_{max}; \gamma + 2\beta_{max}]$. Consequently, from the set of close segment pairs found in the second search step, a subset of potential point contact segment pairs can be created for all pairs satisfying $\gamma > \alpha_1 - 2\beta_{max}$ and a subset of potential line contact segments for all pairs satisfying $\gamma < \alpha_2 + 2\beta_{max}$. Considerable advantages result from this second search step: First, compared to the element-wise spherical bounding boxes, the tighter segment-wise cylindrical bounding boxes deliver a smaller set of potential contact pairs for which the closest point projections have to be solved iteratively. Second, the subdivision into potential point and line contact pairs again reduces the number of (expensive) unilateral closest point projections necessary at the slave beam Gauss points for the line contact formulation. This means that the computational savings of the *ABC* formulation are twofold: On the one hand, the required Gauss point density can be reduced as compared to the pure line contact formulation. On the other hand, the number of beam segments evaluated by the (unilateral CPP of the) line formulation is reduced to those enclosing small contact angles, while segments with larger contact angles are evaluated by the (bilateral CPP of the) cheaper point contact formulation. The third advantage resulting from the proposed two-stage contact search is related to the iterative solution of the nonlinear orthogonality conditions (4.5) for the closest points ξ_c and η_c. Since the solution points ξ_c and η_c are necessary in order to determine the contact status (active or inactive) of a close-by segment pair, a robust

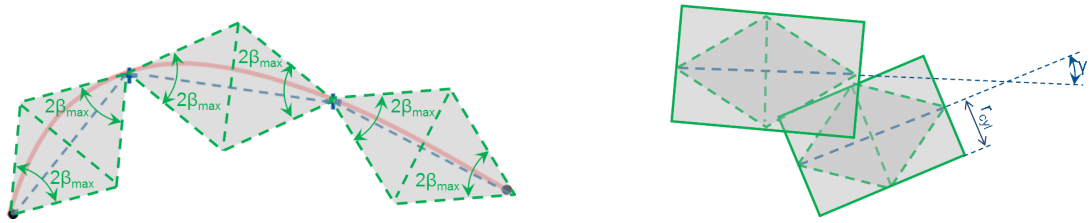

(a) Creation of conical search boxes.

(b) Intersection of cylindrical boxes.

Figure 4.9: Creation of segment-wise search boxes, intersection and determination of angle γ.

and reliable solution scheme is mandatory, but not trivial to provide when considering beam elements of arbitrary interpolation order. The choice of the shifting angle α_1 according to (4.69) guarantees that a unique closest point solution exists for the segment pairs relevant for point-to-point contact, i.e. for pairs with $\alpha > \alpha_1$. On the one hand, the contact search also delivers a certain amount of potential point contact pairs for which the actual contact angle at the (a priori unknown) closest point is smaller than α_1 and, consequently, for which no unique closest point solution can be guaranteed. On the other hand, the number of such segment pairs with $\alpha < \alpha_1$ is reduced drastically since the potential point contact segment pairs are already filtered on the basis of $\gamma > \alpha_1 - 2\beta_{max}$. By this means and as consequence of the good starting points (the search segment midpoints), the number of unconverged local Newton loops could be reduced drastically. Exemplarily, the example of Section 4.5.3.1, which leads to very complex beam-to-beam contact interaction scenarios with more than 100 independent point contact regions per time step, leads to less than one unconverged local Newton loop per 10 time steps.

In a second step, it has to be checked that these potential contact pairs with unconverged bilateral closest point solution are indeed not relevant in terms of active contact force contributions. With the proposed *ABC* formulation such a check basically comes at zero extra effort. Since the closest point projections of potential contact pairs lying in the transition range, i.e. $\gamma \in [\alpha_1 - 2\beta_{max}; \alpha_2 + 2\beta_{max}]$, are performed by both the point-to-point and the line-to-line contact formulation, one can use the results of the unilateral closest point projection associated with the line contact formulation in order to estimate the closest points ξ_c and η_c as well as the gap g and the contact angle α_c at this location for pairs with unconverged bilateral closest point projection of the point contact formulation. In the cases $g > 0$ or $\alpha < \alpha_1$, the corresponding unconverged pair is not relevant for point contact and the simulation can proceed. This procedure has been sufficient for convergence of all *relevant* bilateral closest point projections of the numerical examples that will be considered in Section 4.5. However, if a relevant bilateral closest point projection is not convergent, one could alternatively apply the estimation of the closest points ξ_c and η_c based on the unilateral closest point projection instead of the exact bilateral CPP solution. The strategies described above rely on convergent unilateral closest point projections. In Section 4.1.2, it has been shown that the solvability of this projection can be guaranteed for the entire range of possible contact angles. This prediction could be confirmed numerically: In combination with the applied two-stage contact search algorithm, all unilateral closest point projections carried out within the scope of examples considered in Section 4.5 have been convergent.

4.4.2 Step size control

In Section 4.2.4, it has been shown that an increasing beam slenderness ratio requires an increasingly fine spatial "contact discretization" in the sense of a higher Gauss point density necessary for the line contact formulation. Here, it will be shown that for standard beam-to-beam contact formulations also the maximal permissible time step size Δt decreases with increasing beam slenderness ratio. For illustration, two perpendicular beams are considered (see Figure 4.10).

Figure 4.10: Undetected crossing of two beams due to too large displacement increments.

If the norm of the iterative displacement increments $\Delta\hat{\mathbf{d}}_1^k$ of beam 1 and $\Delta\hat{\mathbf{d}}_2^k$ of beam 2 within the k^{th} Newton iteration of a time step is larger than the cross section diameter $2R$, the beams can cross completely without remaining penetration and therefore without contact being detected (see Figure 4.10 for illustration). Already for displacement norms in the range of the cross section radius R, the beam centerlines can cross, which results in a change of direction of the contact forces and, in turn, in an undetected crossing of the beams. To avoid such undesirable scenarios, the inf-norm of the global iterative displacement increment vector $\Delta\mathbf{D}^k$ is scaled if necessary:

$$\text{while } (\,||\Delta\mathbf{D}^k||_\infty > R\,)\ \{\,\Delta\mathbf{D}^k = 0.5\cdot\Delta\mathbf{D}^k\,\}. \tag{4.84}$$

Similar to the notation applied in Appendix B.1, the vector $\mathbf{D}$ represents a global assembly of all the (translational) degrees of freedom associated with the beam centerline interpolation. Thus, it differs from the global vector $\mathbf{X}$ by the rotational degrees of freedom. Furthermore, the notation $||(.)||_\infty$ represents the inf-norm of a vector. The modified Newton scheme resulting from this algorithm (see also Section 3.2.1.2) does not only prevent undetected beam crossing, but it also enhances the robustness of the nonlinear solution process in general. This does especially apply to examples with strongly fluctuating external loads and high peak forces (see Section 4.5.3.1) or abruptly opening contacts (e.g. when a beam slides across the end of a second beam; see also the example of Section 4.5.3.4). In addition to algorithm (4.84), the following criterion is checked in every iteration in order to control the maximal penetration of the contacting beams:

$$g > -k\cdot R \quad \text{with} \quad k\in[0;1]. \tag{4.85}$$

In combination, criteria (4.84) and (4.85) ensure that two beams cannot cross each other without contact detection. The standard alternative to the procedure proposed in this section is to simply choose the time step size small enough, such that the inf-norm of the displacement increment per time step Δt is smaller than the cross section radius of the contacting beams, i.e.

$$||\mathbf{D}(t_{n+1}) - \mathbf{D}(t_n)||_\infty < R. \tag{4.86}$$

In general, such a procedure leads to a higher number of total Newton iterations, because convergence is required for every displacement step of size R corresponding to one time step, while

in case of algorithm (4.84) some successive Newton iterations with (confined) displacement step size R can take place before the converged solution of the considered time step is found. In Section 4.5.3.1, this statement and the resulting efficiency gains will be confirmed.

4.4.3 Penalty laws

So far, the linear penalty law introduced in (4.37) (see Figure 4.11(a)) has been considered:

$$f_{c\varepsilon}(g) = \begin{cases} -\varepsilon g, \\ 0, \end{cases} \quad \text{and} \quad \Pi_{c\varepsilon}(g) = \begin{cases} \frac{\varepsilon}{2} g^2, & g \leq 0 \\ 0, & g > 0 \end{cases} . \tag{4.87}$$

In practical simulations, one often applies regularized penalty laws that allow for a smooth contact force transition as illustrated in Figure 4.11(b). This second variant is favorable from a numerical point of view: First of all, it may improve the performance of tangent-based iterative solution schemes applied to the nonlinear system of equations stemming from the considered discretized problem, since a unique tangent exists at the transition point $\bar{g}$ between the states of "contact" and "non-contact". Secondly, the time integration scheme applied in dynamic simulations benefits from such a smooth contact force law. Thirdly, also numerical integration of line contact forces (see Section 4.2.2) becomes more accurate for smooth force laws given by:

$$f_{c\varepsilon}(g) = \begin{cases} \bar{f} - \varepsilon g, \\ \frac{\varepsilon\bar{g} - \bar{f}}{\bar{g}^2} g^2 - \varepsilon g + \bar{f}, \\ 0, \end{cases} \quad \Pi_{c\varepsilon}(g) = \begin{cases} \frac{\varepsilon}{2} g^2 - \bar{f} g + \frac{\varepsilon \bar{g}^2}{6.0}, & g \leq 0 \\ -\frac{\varepsilon\bar{g} - \bar{f}}{3\bar{g}^2} g^3 + \frac{\varepsilon}{2} g^2 - \bar{f} g + \frac{\varepsilon \bar{g}^2}{6.0}, & 0 < g \leq \bar{g} \\ 0, & g > \bar{g} \end{cases} \quad \bar{f} = \frac{\varepsilon \bar{g}}{2} \tag{4.88}$$

For each force law an appropriate potential defined by $f_{c\varepsilon} = -\partial \Pi_{c\varepsilon} / \partial g$ and $\Pi_{c\varepsilon}(g = \bar{g}) = 0$ (with $\bar{g} = 0$ for the linear force law (4.87)) as well as a normalized potential $\tilde{\Pi}_{c\varepsilon} = \Pi_{c\varepsilon} / \varepsilon$ (see also Section 4.3.3) can be derived. For simplicity, all derivations in the previous sections are based on a linear penalty law according to (4.87). However, a more general form of these equations that is valid for arbitrary penalty laws can easily be derived by simply replacing all linear force-like expressions of the form $-\varepsilon \langle g \rangle$ by $f_{c\varepsilon}(g)$ and all quadratic potential-like expressions of the form $0.5 \varepsilon \langle g \rangle^2$ by $\Pi_{c\varepsilon}(g)$. For most simulations of this thesis, the regularized law (4.88) is applied.

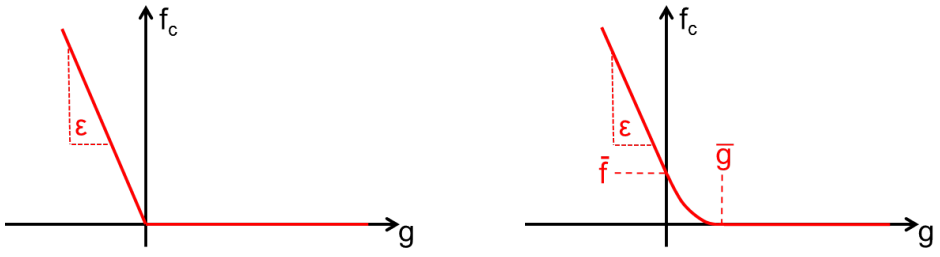

(a) Standard linear penalty law. (b) Quadratically regularized penalty law.

Figure 4.11: Graphical visualization of standard and quadratically regularized penalty law.

4.4.4 Endpoint-to-line and endpoint-to-endpoint contacts

The contact formulations presented so far have only considered solutions of the minimal distance problem within the element parameter domain $\xi, \eta \in [-1; 1]$ as represented by the blue area in Figure 4.12(a). Due to the C^1-continuity of the discrete centerline, also solutions coinciding with the element nodes are found by this procedure. However, a minimal distance solution can also occur in form of a boundary minimum at the physical endpoints of the beams. The boundary solutions indicated by the four red lines in Figure 4.12(a) represent solutions with one parameter taking on the value -1 or 1 and the other parameter being arbitary. Mechanically, these solutions can be interpreted as the minimal distance appearing between a physical beam endpoint and an arbitrary beam segment as indicated in Figure 4.12(b). Additionally, a minimum can also occur in form of the distance between the physical endpoints of both beams (see Figure 4.12(c)), which corresponds to the four green corner points in Figure 4.12(a). Neglecting these boundary minima can lead to impermissibly large penetrations and even to an undetected crossing of beams.

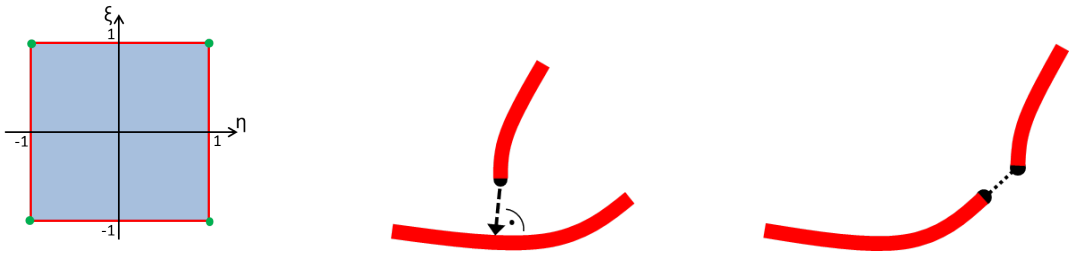

(a) Parameter space. (b) Endpoint-to-line. (c) Endpoint-to-endpoint.

Figure 4.12: Possible contact configurations involving the interior and endpoints of the beams.

At first glance, these contact configurations seem to be comparatively rare for thin beams and the mechanical influence of these contact contributions seems to be limited. However, practical simulations have shown that neglecting these contributions does not only lead to a slight inconsistency of the mechanical model itself but also to a drastically reduced robustness of the nonlinear solution scheme, since initially undetected large penetrations can lead to considerable jumps in the contact forces during the iterations of a nonlinear solution scheme. While for the endpoint-to-endpoint case, the contact point coordinates are already given, the endpoint-to-line case requires a unilateral closest-point-projection similar to the one in (4.32). Depending on which beam endpoint is given, this unilateral closest-point-projection either searches for the closest point η_c to a given point $\xi \in \{-1, 1\}$ or for the closest point ξ_c to a given point $\eta \in \{-1, 1\}$. As soon as the contact point coordinates are known, one can directly apply the residual contribution of the point-to-point contact formulation according to (4.12). From a geometrical point of view, applying this model means that the beam endpoints are approximated by hemispherical surfaces. Again, it is justified to only consider the variation contribution with fixed ξ and fixed η for δg according to (4.9), since either the considered parameter coordinate is indeed fixed (if representing a physical endpoint) or the corresponding tangent vector is perpendicular to the contact normal (if representing the projection onto a segment). Nevertheless, one has to distinguish between the cases endpoint-to-endpoint and endpoint-to-line contact in order to correctly include the increments $\Delta\xi$ and $\Delta\eta$ in the linearizations of the contact residuals (see Appendix C.1).

4.5 Numerical Examples

In this section, the theory presented so far will be verified by means of chosen numerical test cases. Specifically, in Sections 4.5.1 and 4.5.2, small (academic) test cases, partly based on analytic solutions, will be analyzed in order to investigate properties such as overall accuracy and consistency of the proposed formulations regarding integration error, spatial convergence behavior, resulting contact force distributions and mechanical conservation properties. Subsequently, in Section 4.5.3, four practically relevant applications involving complex systems of slender fibers will be considered in order to verify the overall robustness of the proposed algorithms but also for quantifying the efficiency gains as compared to standard beam contact formulations. For the numerical test cases of this section, the Newton-Raphson scheme with tolerances similar to Section 3.8 in combination with the step size control of Section 4.4.2 will be employed. Since the focus of the following examples lies on the investigation of the proposed contact formulations, the simplest possible beam element formulation, which means the torsion-free TF element, has been chosen as standard choice if not stated otherwise. The examples are chosen in a manner such that the requirements (2.128), (2.136) and (2.137) are fulfilled and that, consequently, the TF element yields exact solutions, i.e. solutions that would identically be obtained by the general Kirchhoff theory, for the considered static examples and good approximations for the dynamic examples (see also Section 2.4.2). Furthermore, as emphasized in Section 3.7, the spatial discretization underlying the TF element exactly preserves linear and angular momentum as well as energy. Nevertheless, in Section 4.5.3.2, also an application involving initially curved beam segments as well as non-trival coupling conditions between these segments will be considered. For this example, the WK-ROT element derived in Section 3.5.3 will be applied.

4.5.1 Test cases for line-to-line contact formulation

4.5.1.1 Example 1: Patch test

The first example is a simple static patch test that should verify the effectiveness of the integration interval segmentation introduced in Section 4.2.2. As illustrated in Figure 4.13, the example consists of one completely fixed, rigid beam discretized with three beam elements (different element lengths) and a second, deformable beam discretized by two beam elements with cross-section radii $R_1 = R_2 = 0.005$, Youngs moduli $E_1 = E_2 = 1.0 \cdot 10^9$, length of the first beam $l_1 = 2.0$ and length of the second beam $l_2 = 0.8$. The second beam is loaded by a constant transverse line load $p = 1.0$ and its left endpoint is exposed to a Dirichlet-displacement of $\Delta u = 1.001$ within 100 equidistant load steps. Furthermore, contact interaction between the two beams is modeled by the linear penalty law according to (4.87) with a penalty parameter $\varepsilon = 500$. As a consequence of the constant transverse line load and the chosen penalty parameter, there exists a trivial analytical

Figure 4.13: Static patch pest: Initial configuration.

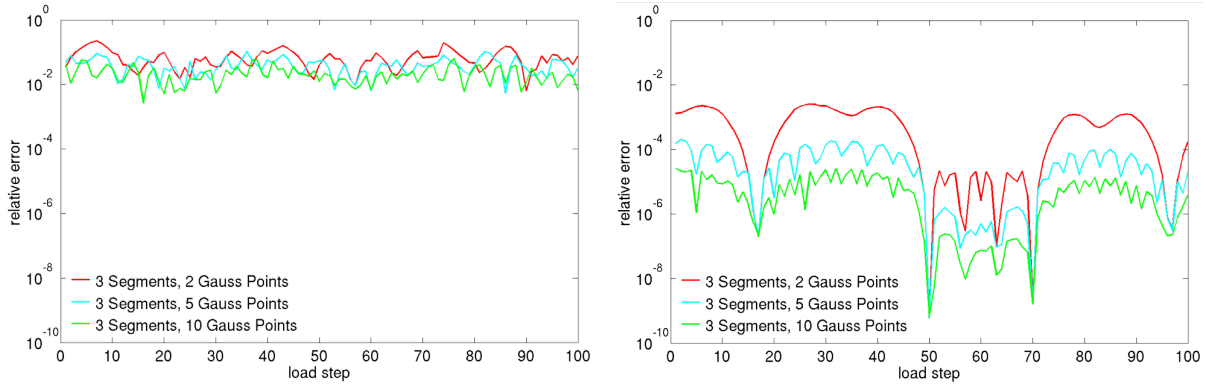

(a) Integration without segmentation at the endpoints.

(b) Integration with segmentation at the endpoints.

Figure 4.14: Average error of the gap at the Gauss points for different Gauss rules.

solution with a constant gap $g_{ref} = -p/\varepsilon = -0.002$ along the entire upper beam. In order to verify the working principle of the integration interval segmentation in the presence of strong discontinuities, the first (rigid) beam is chosen as slave. In Figure 4.14, the average relative error

$$e_{rel} = \sum_{i=1}^{n_{GP,tot}} \frac{g_i - g_{ref}}{n_{GP,tot} \cdot g_{ref}} \tag{4.89}$$

of the gaps g_i at the active Gauss points is plotted over the number of load steps for the formulations with and without integration interval segmentation at the beam endpoints in combination with different numbers of Gauss points $n_{GP,tot}$. In all cases, three integration intervals per slave element have been applied. From Figure 4.14(a), one observes that the strong discontinuity of the contact force $\varepsilon\langle g(\xi_{ij})\rangle$ occurring in the integrand of (4.43) leads to a considerable integration error that only gradually decreases when increasing the number of Gauss points. As expected, the formulation with integration interval segmentation (see Figure 4.14(b)) yields a significantly lower integration error level and a faster decline in the error with increasing number of Gauss points. Yet, even this formulation does not allow for an exact integration, in general, since the weighting functions $\mathbf{H}_1$ and $\mathbf{H}_2$ in (4.43) have no closed-form polynomial representation across the element boundaries. However, it will be shown in the next examples that the corresponding integration error is typically lower than the overall discretization error and therefore of no practical relevance. Furthermore, compared to a formulation with integration interval segmentation at all master beam element nodes, which would then allow for exact numerical integration, the proposed segmentation strategy is considerably less computationally expensive.

4.5.1.2 Example 2: Twisting of two beams

The second example aims at verifying the accuracy and consistency of the line contact formulation based on the spatial convergence behavior. Thereto, two initially straight and parallel beams are investigated with circular cross-sections and radii $R_1 = R_2 = R = 0.01$, initial lengths $l_1 = l_2 = l = 5$ and Young's moduli $E_1 = E_2 = E = 1.0 \cdot 10^9$ as illustrated in Figure 4.15(a). The

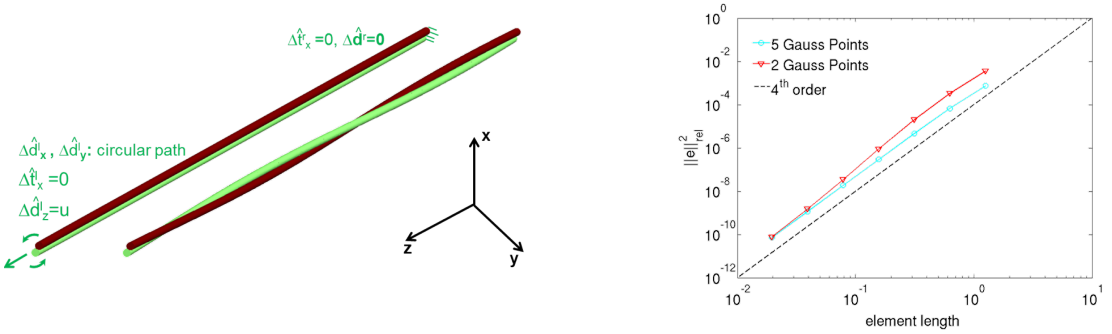

(a) Initial and deformed configurations.

(b) Relative L^2-error over element length.

Figure 4.15: Dirichlet-controlled twisting of two straight beams into a double-helical shape.

initial geometries of the two beams $k=1,2$ are given by the analytic expression:

$$\mathbf{r}_{0k}(s) = \begin{pmatrix} (-1)^{k-1}r \\ 0 \\ s \end{pmatrix}, \quad s \in [0;l], \quad r = R - \frac{|g_0|}{2}, \quad k = 1,2. \tag{4.90}$$

The distance between the beams is chosen such that they exhibit an initial gap of $g_0 = -0.1R$. The beams are clamped at one end and their cross-sections at the other end are moved in a Dirichlet-controlled manner such that the corresponding cross-section center points describe a circular path. By this procedure, the two beams get twisted into a double-helical shape as illustrated in Figure 4.15(a). The system parameters are chosen in a way such that the analytic solution for the deformed beams is exactly represented by a helix with constant slope given by

$$\begin{aligned} \mathbf{r}_k(\varphi) &= \begin{pmatrix} r\cos\left[\varphi + (k-1)\pi\right] \\ r\sin\left[\varphi + (k-1)\pi\right] \\ h\varphi \end{pmatrix}, \quad \varphi \in [0;2\pi], \quad r = R - \frac{|g_0|}{2}, \\ h &= \sqrt{\left(\left(\frac{(1.0+\epsilon)l}{2\pi}\right)^2 - r^2\right)}, \quad \epsilon = 0.01, \quad k = 1,2. \end{aligned} \tag{4.91}$$

In the following, the required parameters are directly presented. The derivation based on the ODEs (2.118) and (2.119) is summarized in Appendix C.4. Before the actual twisting process starts, the beams are pre-stressed by an axial displacement at the left endpoints (superscript "l")

$$\Delta\hat{d}^l_{1,z} = \Delta\hat{d}^l_{2,z} = u = 2\pi h - l \approx 4.9647 \cdot 10^{-2} \tag{4.92}$$

within one load step. Then, these points are moved on a circular path with radius $r = R - |g_0|/2$

$$\begin{aligned} \Delta\hat{d}^l_{1,x} &= -r\left[1 - \cos\left(\frac{k2\pi}{N}\right)\right], \quad \Delta\hat{d}^l_{1,y} = r\sin\left(\frac{k2\pi}{N}\right), \\ \Delta\hat{d}^l_{2,x} &= r\left[1 - \cos\left(\frac{k2\pi}{N}\right)\right], \quad \Delta\hat{d}^l_{2,y} = -r\sin\left(\frac{k2\pi}{N}\right), \quad k = 1, ..., N, \end{aligned} \tag{4.93}$$

within $N = 8$ further load steps in order to end up with one full twist rotation. The translational displacements at the right endpoints of the right beams (superscript "r") are set to zero, i.e.

$$\Delta\hat{d}^r_{1,x} = \Delta\hat{d}^r_{2,x} = \Delta\hat{d}^r_{1,y} = \Delta\hat{d}^r_{2,y} = \Delta\hat{d}^r_{1,z} = \Delta\hat{d}^r_{2,z} = 0. \tag{4.94}$$

Furthermore, the x-components of all tangential degrees of freedom are set to zero, i.e.

$$\Delta\hat{t}^l_{1,x} = \Delta\hat{t}^l_{2,x} = \Delta\hat{t}^r_{1,x} = \Delta\hat{t}^r_{2,x} = 0, \tag{4.95}$$

whereas the y- and z-components of the nodal tangents are not prescribed but part of the numerical solution. As shown in Appendix C.4, these boundary conditions for the tangential degrees of freedom are sufficient in order to impose the required boundary moments at the beam endpoints. If eventually the penalty parameter (see again Appendix C.4) is chosen as

$$\varepsilon = -\frac{(1+\epsilon)r}{(r^2+h^2)g_0}\left(EA\epsilon + \frac{EI(1+\epsilon)h^2}{(r^2+h^2)^2}\right), \tag{4.96}$$

the resulting analytic solution finally obeys the analytic representation of (4.91), thus showing a gap of g_0 between the two beams that is constant along the beam lengths. As already mentioned earlier, the penalty parameter and the resulting gap between the two beams occurring in the analytic solution (4.91) can be interpreted as a mechanical model for the contact-surface/cross-section flexibility of the considered beams. Furthermore, the derived analytic solution corresponds to a mechanical state consisting of constant axial tension ϵ, constant bending curvature $\kappa = \frac{(1+\epsilon)r}{r^2+h^2}$ and vanishing torsion along both beams. In Figure 4.15(b), the relative L^2-error (3.105) of the FE solution for beam 1 is plotted with respect to the analytic solution over the element length for discretizations with $4, 8, 16, 32, 64, 128$ and 256 elements per beam.

In order to investigate the influence of the applied Gauss integration rule, the cases of a 5-point and a 2-point Gauss rule with one integration interval per element in both cases are considered. According to Figure 4.15(b), the 5-point-variant converges towards the analytic solution up to machine precision with the optimal order $\mathcal{O}(h^4)$ as expected for the applied third-order beam elements. Throughout this work, this 5-point-rule will be the default value if nothing is mentioned to the contrary. Reducing the number of Gauss integration points to a value of 2 leads to a slight increase of the L^2-error in the range of comparatively rough spatial discretizations. However, for finer discretizations the 2-point curve converges towards the 5-point curve. When looking at the upper right data point in Figure 4.15(b), one observes the remarkable result that a total of 8 contact evaluation points per beam (4 elements per beam with 2 Gauss points per element) is sufficient in order to end up with a relative error that is far below 1%.

In Section 4.1.2, a lower bound α_{min} for the contact angle has bee derived, above which a unique bilateral closest point projection exists. Next, the corresponding result (4.31) shall briefly be verified by means of a slightly modified version of the considered twisting example. Thereto, it is assumed that the maximal admissible ratio of cross-section to curvature radius supported by the beam theory is 1%, i.e. $\mu_{max} = 0.01$. For simplicity, the helix radius given in (4.91) is approximated by the cross-section radius, i.e. $r = R$, thus $g_0 = 0$. With $\mu_{max} = 0.01$, the minimal admissible slope for a helix with constant slope similar to (4.91) can be calculated as:

$$\mu_{max} = \bar{\kappa}R = \frac{R^2}{R^2 + h^2_{min}} = 0.01 \quad \rightarrow \quad h^2_{min} = 99R^2. \tag{4.97}$$

Furthermore, after some geometrical considerations, one can calculate the actual (constant) contact angle enclosed by two corresponding tangents for the case $h = h_{min}$:

$$\alpha = \arccos\left(\frac{\mathbf{r}_{1,\varphi}^T(\varphi)\mathbf{r}_{2,\varphi}(\varphi)}{||\mathbf{r}_{1,\varphi}(\varphi)||||\mathbf{r}_{2,\varphi}(\varphi)||}\right) = \arccos\left(\frac{h_{min}^2 - R^2}{h_{min}^2 + R^2}\right) = \arccos(0.98) \approx 11.5°. \quad (4.98)$$

This is exactly the same result that would be obtained for the lower bound α_{min} by inserting $\mu_{max} = 0.01$ into (4.31). This means that the helix geometry according to example 2 represents an extreme case, where all worst-case assumptions made in the derivation (4.30) become true and where, for a given admissible radius ratio $\mu_{max} = 0.01$, a non-unique closest point solution appears exactly at the contact angle α_{min} predicted as lower bound by equation (4.31). On the other hand, this example shows that (4.31) provides the best possible lower bound, since it actually occurs in a practical example. It can be concluded that for this example, leading to a constant gap along the beams, no unique closest point solution exists and consequently standard point-to-point contact formulations cannot directly be applied.

4.5.1.3 Example 3: General contact of two beams

So far, only scenarios with a constant gap function along the beam have been considered. Based on the following examples, the more general case of non-constant gaps, and especially the case of a change in sign in the gap evolution along the beam, will be investigated. At positions with a change in sign in the gap function, the contact force according to the standard law in (4.87) drops to zero. As illustrated in Figure 4.5(c), this leads to a kink in the force evolution at this point, which becomes more and more pronounced with increasing contact angle (see Figure 4.6(c)).

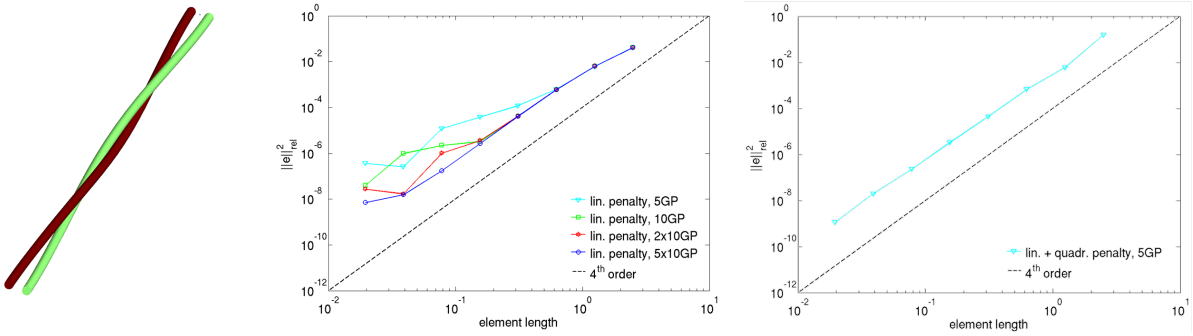

(a) Final geometry. (b) L^2-error for linear penalty law. (c) L^2-error for regularized penalty law.

Figure 4.16: Two initially straight and parallel beams with larger initial distance.

This weak discontinuity in the integrand may in general increase the numerical integration error and can be avoided by replacing the standard linear force law by the smoothed law (4.88) (see again Figures 4.5(c) and 4.6(c)). The influence of these two different force laws on the integration error and eventually on the spatial convergence behavior will be investigated by means of the following example: Beam geometries and material parameters identical to the last example are considered. The penalty parameter is decreased to $\varepsilon = 1000$. Also, the initial configuration is similar to the one illustrated in Figure 4.15(a) of the last example. However, this time, the initial

distance between the beams is increased to a value of $2r = 4R = 0.04$. The Dirichlet boundary conditions of the tangential degrees of freedom are slightly changed in order to completely avoid any cross-section rotation at the boundaries. Correspondingly, the following relations hold:

$$\Delta\hat{t}^l_{1,x} = \Delta\hat{t}^l_{2,x} = \Delta\hat{t}^r_{1,x} = \Delta\hat{t}^r_{2,x} = \Delta\hat{t}^l_{1,y} = \Delta\hat{t}^l_{2,y} = \Delta\hat{t}^r_{1,y} = \Delta\hat{t}^r_{2,y} = 0. \tag{4.99}$$

Thus, the tangents are completely clamped at both ends. Moreover, no pre-stressing is applied:

$$\Delta\hat{d}^l_{1,z} = \Delta\hat{d}^l_{2,z} = 0. \tag{4.100}$$

The remaining Dirichlet conditions are similar to the last example, see (4.93) and (4.94). The resulting deformed configuration is illustrated in Figure 4.16(a). Due to the larger separation of the beams, the gap function increases from negative values to positive values when approaching the beam endpoints. The corresponding contact force evolutions resulting from different spatial discretizations are illustrated in Figure 4.17(a). In Figures 4.16(b) and 4.16(c), the relative L^2-error with respect to a numerical reference solution is plotted for the formulation based on a linear penalty law and the formulation based on the quadratically regularized force law (regularization parameter $\bar{g} = 0.1R = 0.001$). In case of the simple linear penalty law, the number of Gauss points has to be enhanced by a factor of 10 as compared to the standard 5-point rule in order to ensure $\mathcal{O}(h^4)$ convergence within the considered range of spatial discretizations (see Figure 4.16(b)). Thus, obviously, the increased integration error resulting from the kink in the penalty force law dominates the spatial discretization error if the standard 5-point Gauss rule is applied. Only an increase in the number of Gauss points, and therefore an increase in the numerical effort, reduces this integration error. An elimination of this kink by means of a smoothed penalty law enables the same accuracy and the optimal convergence order $\mathcal{O}(h^4)$ already with the standard 5-point Gauss rule (see Figure 4.16(c)), which reduces the numerical effort drastically.

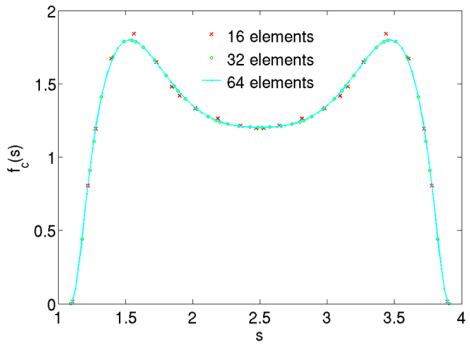

(a) Example 3: Contact force distribution.

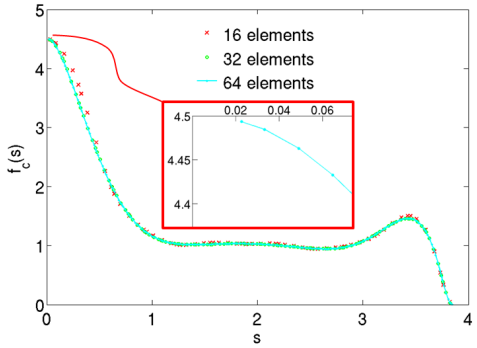

(b) Example 4: Contact force distribution.

Figure 4.17: Comparison of contact force distributions of Example 3 and Example 4.

4.5.1.4 Example 4: Influence of integration segments on convergence

In the first example, it has already been illustrated how the integration error can be reduced via an integration interval segmentation at the beam endpoints. Now, the influence of this method on the spatial convergence behavior will be analyzed. Again, the beam geometry,the material

parameters and the penalty parameter are identical to the last example. In order to enforce an integration across the beam endpoints, the initial geometry of one of the beams is shifted by a value of $r = 2R = 0.02$ along the positive z-axis leading to the representation:

$$\mathbf{r}_{k0}(s) = \begin{pmatrix} (-1)^{k-1} r \\ 0 \\ s + (k-1)r \end{pmatrix}, \quad s \in [0; l], \quad r = 2R, \quad k = 1, 2. \tag{4.101}$$

The following Dirichlet boundary conditions are prescribed at the endpoints of the two beams:

$$\begin{aligned}
&\Delta\hat{d}^r_{1,x} = -0.12, \quad \Delta\hat{d}^r_{2,x} = 0.12, \\
&\Delta\hat{d}^r_{1,y} = \Delta\hat{d}^r_{2,y} = \Delta\hat{d}^r_{1,z} = \Delta\hat{d}^r_{2,z} = 0, \\
&\Delta\hat{d}^l_{1,x} = -r\left[1 - \cos\left(\frac{k2\pi}{N}\right)\right], \quad \Delta\hat{d}^l_{1,y} = r\sin\left(\frac{k2\pi}{N}\right), \\
&\Delta\hat{d}^l_{2,x} = r\left[1 - \cos\left(\frac{k2\pi}{N}\right)\right], \quad \Delta\hat{d}^l_{2,y} = -r\sin\left(\frac{k2\pi}{N}\right), \quad k = 1, ..., N, \\
&\Delta\hat{d}^l_{1,z} = \Delta\hat{d}^l_{2,z} = 0, \\
&\Delta\hat{t}^l_{1,x} = \Delta\hat{t}^l_{2,x} = \Delta\hat{t}^r_{1,x} = \Delta\hat{t}^r_{2,x} = \Delta\hat{t}^l_{1,y} = \Delta\hat{t}^l_{2,y} = \Delta\hat{t}^r_{1,y} = \Delta\hat{t}^r_{2,y} = 0.
\end{aligned} \tag{4.102}$$

The two additional conditions in the first line of (4.102) enforce a negative gap and consequently active contact forces at the (non-matching) right endpoints of the beams. By this means, an integration across a contact force jump at these endpoints is intentionally enforced, which is sensible in order to investigate the effectiveness of the integration interval segmentation. All the remaining Dirichlet conditions appearing in (4.102) are similar to Section 4.5.1.3. The deformed geometry resulting from these boundary conditions is illustrated in Figure 4.18(a).

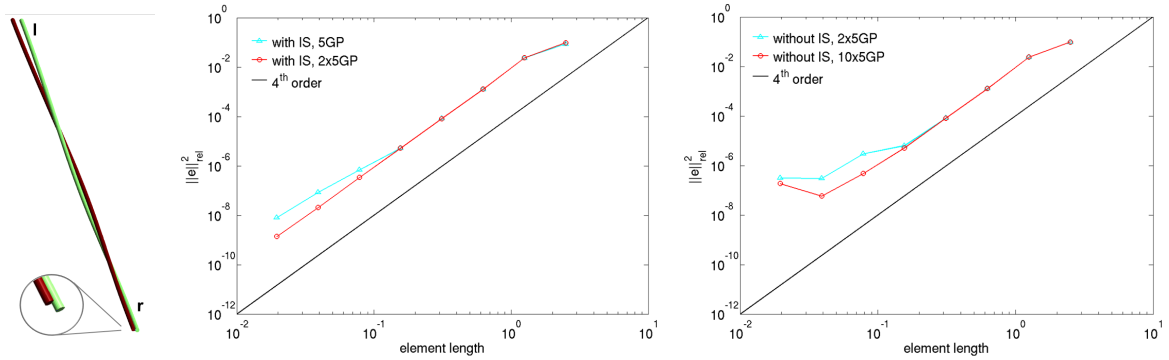

(a) Geometry. (b) Smooth force law with segmentation. (c) Smooth force law without segmentation.

Figure 4.18: Dirichlet-controlled twisting of two parallel beams with non-matching endpoints.

Furthermore, the contact force distributions corresponding to different finite element meshes are presented in Figure 4.17(b). The contact force distributions show the expected jump from a value of $f_c(s = 0.02^-) = 0$ to $f_c(s = 0.02^+) \approx 4.5$ at position $s = 0.02$ (see also the detail view in Figure 4.17(b)). In Figures 4.18(b) and 4.18(c), the relative L^2-error with respect to a numerical

reference solution is plotted for the formulation based on the quadratically regularized force law (regularization parameter $\bar{g} = 0.1R = 0.001$), once with integration interval segmentation (Figure 4.18(b)) and once without a corresponding segmentation (Figure 4.18(c)).

According to Figure 4.18(b), the remaining integration error of the formulation with interval segmentation and a 5-point Gauss rule slightly deteriorates the spatial convergence behavior. However, by applying two instead of one 5-point Gauss integration intervals per element, this influence of the integration error vanishes and the optimal convergence order $\mathcal{O}(h^4)$ can be observed. On the contrary, the convergence behavior of the formulation without integration interval segmentation (see Figure 4.18(c)) is still deteriorated by the integration error for a 5-point Gauss rule even with two intervals per element. Even if the number of intervals is increased to 10, i.e. an increase of the number of Gauss points by a factor of 5, this negative influence is still visible in the range of fine spatial finite element discretizations. Furthermore, it is worth mentioning that this effect is expected to become even more pronounced in practical applications, where the displacements are not Dirichlet-controlled in the direct neighborhood of the strong discontinuity. All in all, it seems that the integration interval segmentation solely applied at the beam endpoints represents a sensible compromise of integration accuracy and computational efficiency. Additionally, in dynamic simulations, this strategy prevents from force and energy jumps in scenarios where active Gauss points of standard integration schemes based on fixed, non-segmented integration intervals would slide across master beam endpoints.

4.5.2 Test cases for *ABC* contact formulation

4.5.2.1 Example 1: Beam rotating on arc

The first example verifying the ABC formulation consists of a completely fixed, rigid arc (beam 1 = slave) lying in the global xz-plane and being discretized by one beam element and a flexible straight beam (beam 2 = master) that initially points into global y-direction and is discretized by three finite elements (see Figure 4.19). The following geometrical and material parameters have been chosen for this example: $E = 1.0 \cdot 10^9$, $R = 0.01$, $l_2 = 2$, $l_1 = \pi r_{arc}$ with $r_{arc} = 1.0$. Furthermore, a quadratically regularized penalty law with $\bar{g} = 0.1R = 0.001$ has been applied. In the following, the model transition between point- and line-contact will be investigated for different choices of the penalty parameters $\varepsilon_\perp$ and $\varepsilon_\parallel$. For the sake of better visualization, the comparatively large shifting interval limited by $\alpha_1 = 10°$ and $\alpha_2 = 30°$ has been chosen. Thereto,

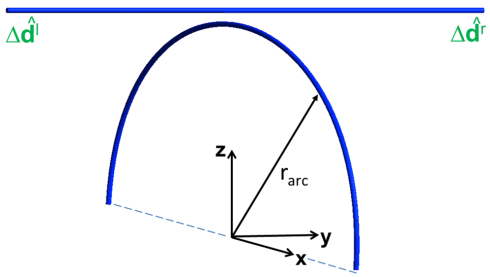

Figure 4.19: Straight flexible beam and rigid arc: $3D$-view of initial configuration.

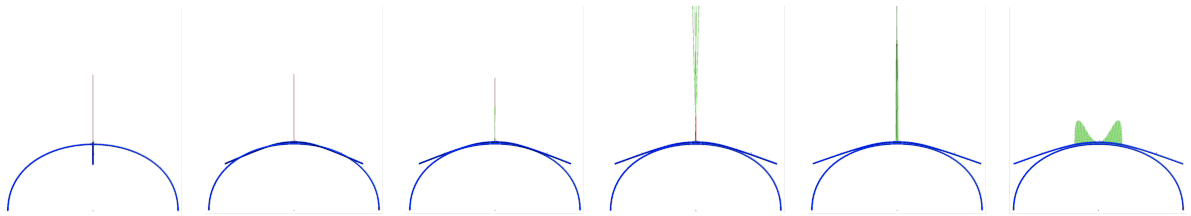

(a) $\theta_k = 0°$. (b) $\theta_k = 0.6 \cdot 90°$. (c) $\theta_k = 0.7 \cdot 90°$. (d) $\theta_k = 0.8 \cdot 90°$. (e) $\theta_k = 0.9 \cdot 90°$. (f) $\theta_k = 1.0 \cdot 90°$.

Figure 4.20: Contact interaction of an initially straight flexible beam rotating on a rigid arc: Top-view (xz-view) of deformed configuration at different rotation angles θ_k.

the endpoints of the master beam are first driven downwards (in negative z-direction) in a displacement controlled manner within 1000 load steps until contact occurs. Then, with contact being active, the two endpoints of the master beam are moved on a circular path within further $N = 4000$ load steps, such that the beam performs a full rotation with respect to the global z-axis, thus covering the whole range of possible contact angles. The only reason for the high number of load steps is a sufficiently high resolution required for the plots presented later on. The following Dirichlet conditions have been applied in the second stage of the deformation process:

$$\begin{aligned} &\Delta\hat{d}^l_{2,x} = \frac{l_2}{2}\sin(\theta_k)\,, \quad \Delta\hat{d}^l_{2,y} = \frac{l_2}{2}\left[1-\cos(\theta_k)\right], \\ &\Delta\hat{d}^r_{2,x} = -\frac{l_2}{2}\sin(\theta_k)\,, \quad \Delta\hat{d}^r_{2,y} = -\frac{l_2}{2}\left[1-\cos(\theta_k)\right], \\ &\Delta\hat{d}^l_{2,z} = \Delta\hat{d}^r_{2,z} = -0.3, \quad \theta_k = \frac{k\cdot 2\pi}{N} \text{ for } k = 1, ..., N. \end{aligned} \tag{4.103}$$

Since an axial displacement of the master beam is precluded by the applied Dirichlet fixation, the value of the beam cross section occurring in the axial stiffness is reduced by a factor of 100, i.e. $A = 0.01R^2\pi$, in order to end up with a deformation that is not completely dominated by the axial stiffness. Different states of deformation during the first quarter of the rotation process are illustrated in Figure 4.20. In the range of large contact angles, a pure point-contact force occurs (see Figures 4.20(a) and 4.20(b)) whose magnitude is illustrated by a red line. Figures 4.20(c) and 4.20(d) represent the realm of model transition: With decreasing contact angle, the magnitude of the point-contact force decreases, while the magnitude of the discrete Gauss point contributions to the line-contact force (illustrated by green lines) increases until a contact angle range of $\alpha < \alpha_1 = 10°$, i.e. a pure line-contact state is reached (see Figure 4.20(e)). Finally, in Figure 4.20(f) both beams lie within one plane ($\alpha = 0°$), thus leading to a state of pure line-contact.

In order to investigate the transition phase between the two contact formulations more closely, the accumulated contact force as well as the accumulated torque of the point and the line contact force with respect to the global z-axis are plotted in Figures 4.21 and 4.22. The three individual plots in each case represent simulations with low ($\varepsilon_\parallel = 5\cdot 10^5$, $\varepsilon_\perp = 2\cdot 10^4$), intermediate ($\varepsilon_\parallel = 5\cdot 10^6$, $\varepsilon_\perp = 2\cdot 10^5$) and high penalty ($\varepsilon_\parallel = 5\cdot 10^7$, $\varepsilon_\perp = 2\cdot 10^6$) parameters. The three point-to-point penalty parameters $\varepsilon_\perp$ assigned to the three given line-to-line penalty parameters $\varepsilon_\parallel$ have been determined according to the approximation (4.74), thus leading to $\varepsilon_\perp/\varepsilon_\parallel \approx 25$. Furthermore, in each plot the following three cases will be compared: a standard force-based *ABC*

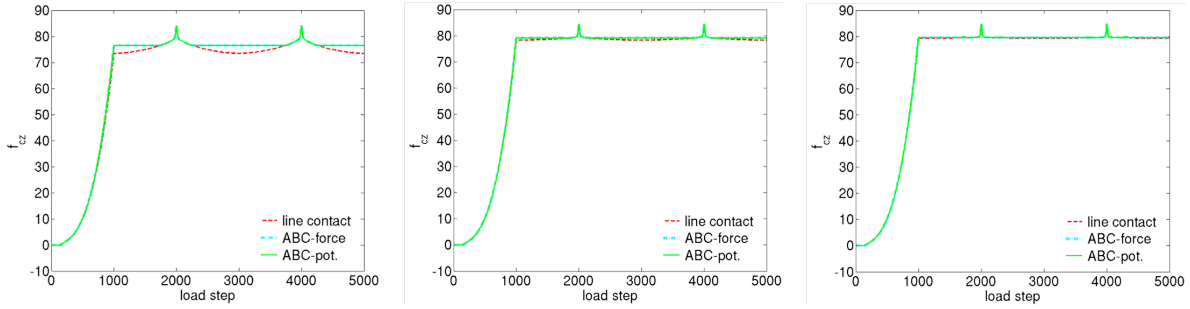

(a) Low ε: $\varepsilon_\perp = 2 \cdot 10^4$, $\varepsilon_\parallel = 5 \cdot 10^5$. (b) Moderate ε: $\varepsilon_\perp = 2 \cdot 10^5$, $\varepsilon_\parallel = 5 \cdot 10^6$. (c) High ε: $\varepsilon_\perp = 2 \cdot 10^6$, $\varepsilon_\parallel = 5 \cdot 10^7$.

Figure 4.21: Evolution of accumulated contact force f_{cz} over the number of load steps.

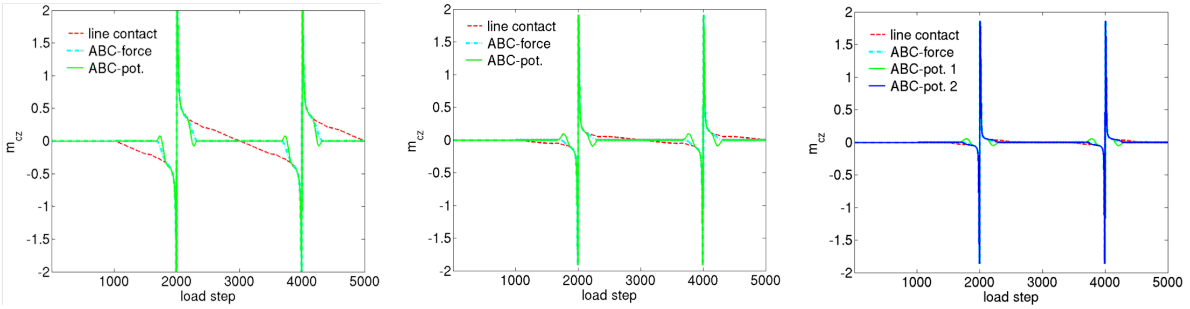

(a) Low ε: $\varepsilon_\perp = 10^4$, $\varepsilon_\parallel = 5 \cdot 10^5$. (b) Moderate ε: $\varepsilon_\perp = 10^5$, $\varepsilon_\parallel = 5 \cdot 10^6$. (c) High ε: $\varepsilon_\perp = 10^6$, $\varepsilon_\parallel = 5 \cdot 10^7$.

Figure 4.22: Evolution of accumulated contact torque m_{cz} over the number of load steps.

formulation, a potential-based *ABC* formulation and finally a pure line-to-line contact formulation. For all cases, $n_{II} = 100$ integration intervals with 5 Gauss points per interval have been chosen. This high number has been chosen such that also the pure line-to-line contact formulation is able to properly resolve the range of large contact angles for the given, very rough spatial discretization. First, the accumulated contact forces resulting from a low penalty parameter (see Figure 4.21(a)) are considered. During the first 1000 load steps, beam 2 is driven downwards. After 200 load steps, the beams come into contact and the contact forces rise. After 1000 load steps the rotation starts. The two peaks occurring in all force plots at load step 2000 and load step 4000 represent configurations where both beams lie within one plane (see Figure 4.20(f)). These force peaks do not represent any numerical artifact or model error, but rather are expected from a mechanical point of view: beam 2 has to be deformed to a higher extent in order to pass this ”parallel“ configuration, which in turn leads to higher overall contact forces in this configuration. The pure line-to-line contact formulation (red dashed line) shows a smooth and steadily increasing contact force evolution in the range $\theta \in [0; 90°]$ (step 1000 until step 2000).

On the contrary, the contact force evolutions of the force-based (blue dashed line) and potential-based (green solid line) *ABC* formulation remain constant in the range of large contact angles. This is the expected evolution of the pure point-contact formulation (for the considered symmetrical problem), which is active in this angle range. After approximately 1700 load steps ($\alpha = 30°$), the transition range begins, characterized by a visible increase of the contact force.

Approximately at load step 1900 ($\alpha = 10°$), the end of the transition interval is reached. From now on, the curves representing the *ABC* formulations and the curve representing the pure line-to-line contact formulation are identical, since the *ABC* formulation reduces to a pure line-to-line contact formulation for angles $\alpha < \alpha_1 = 10°$. As expected, the difference between the pure line-to-line contact formulation and the more efficient *ABC* formulations vanishes with increasing penalty factor (see Figures 4.21(b) and 4.21(c)). Furthermore, no distinctive difference between the contact force evolutions of the force-based and the potential-based *ABC* formulation is visible. In Figure 4.22, the accumulated torque of the contact forces with respect to the global z-axis is plotted. In this example, the resulting contact torque is a consequence of line contact force contributions that do not exactly point into global z-direction at all positions besides the rotation center at position $x = y = 0$. Consequently, the contact torque contribution of the pure point-contact force vanishes. This is visible for the curves representing the *ABC* formulation (see e.g. the blue chain line and the green solid line in Figure 4.22(a)) in the range of large contact angles. The contact torque evolutions show a very steep gradient in the neighborhood of $\alpha = 90°$, which can mechanically be interpreted as a "snap-through" behavior. Exactly at $\alpha = 90°$ (step 2000), the total torque vanishes as a consequence of the geometrical symmetry.

As expected, the difference between the force-based and the potential-based variant due to algorithmic contact moments appearing in the latter formulation is small compared to the model deviation between the pure line-to-line contact and the pure point-to-point contact model (*ABC* formulation in the range $\alpha < 30°$). It is especially small compared to the total magnitude of the mechanically motivated contact torque peaks. Furthermore, this difference decreases with increasing penalty parameter. For the high-penalty case (see Figure 4.22(c)), the variant based on a better penalty approximation $\varepsilon_\perp = 5.4 \cdot 10^5$ (dark-blue solid line) determined via the numerical solution of (4.72) (with $g_{min} = 0.0006$) instead of (4.74) has additionally been plotted. In this case, almost no remaining difference between the force-based and the potential-based variant is visible. All other distinctions of the different formulations, especially the mutual convergence of the three curves with increasing penalty parameter, are similar to the force evolutions above.

4.5.2.2 Example 2: Impact of free flying beams

The next example aims at investigating the conservation properties (linear momentum, angular momentum and total energy) of the proposed *ABC* formulation within a dynamic framework. Thereto, two initially straight beams with $R = 0.01$, $l = 2$, $E = 10^{-6}$ and densities $\rho_1 = 0.1$ and $\rho_2 = 0.05$ are considered. Initially, both beams are arranged in a parallel manner with a distance of $d = 10R = 0.1$ (see Figure 4.23(a)). Within the time interval $t \in [0; 0.06]$, beam 2 (= master) is accelerated by a line load $\tilde{f}_z(\eta, t) = 5 \cdot 10^{-7} \bar{f}_z(t)$ pointing in negative global z-direction and being constant along the beams length. The time scaling factor $\bar{f}_z(t)$ increases linearly from zero to one for $t \in [0; 0.03]$ before it decreases again linearly from one to zero for $t \in [0.03; 0.06]$. The slave beam (beam 1) is loaded by a line load $\tilde{f}_y(\xi, t) = 2.5 \cdot 10^{-6} \cdot \bar{f}_y(t) \cdot \xi$ pointing in global y-direction and increasing linearly with $\xi \in [-1; 1]$, which induces an angular momentum on the beam. The time scaling factor $\bar{f}_y(t)$ increases linearly from zero to one for $t \in [0; 0.02]$ and decreases linearly from one to zero within the interval $t \in [0.02; 0.04]$.

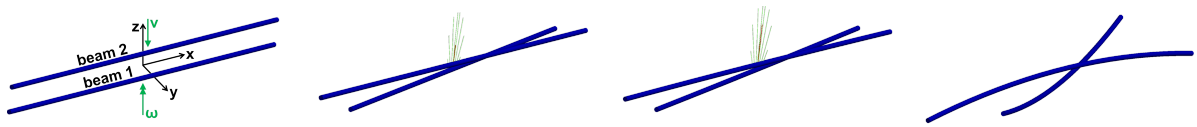

(a) Initial configuration. (b) Time step: 870. (c) Time step: 910. (d) Time step: 2000.

Figure 4.23: Dynamic impact of a rotating and a translationally moving straight beam.

After this acceleration phase, the beams move freely until an impact of the two beams takes place. For time integration, the standard generalized-α scheme according to Section 3.1.1 without numerical dissipation ($\alpha_f = 0.5$, $\alpha_m = 0.5$, $\beta = 0.25$ and $\gamma = 0.5$) and a total simulation time $T = 2.0s$. Since this time integrator cannot guarantee exact energy conservation of the temporally discretized problem for arbitrary time step sizes (see e.g. [207]), the time step size is chosen small enough (standard choice $\Delta t = 0.001s$) such that the impact of the spatial discretization on the conservation properties can be investigated with sufficient accuracy. The system parameters are chosen such that the impact takes place at a contact angle $\alpha \in [\alpha_1; \alpha_2]$ lying within the shifting interval. The configurations at the beginning of the simulation, at the beginning and the end of the impact and the end of the simulation are illustrated in Figures 4.23(a) - 4.23(d).

In Figure 4.24, the system energies are plotted for the force-based and potential-based *ABC* formulation in combination with different penalty laws. Figure 4.24(a) represents the force-based variant in combination with a quadratically regularized penalty law with $\varepsilon_{\parallel} = 3 \cdot 10^{-3}$, $\varepsilon_{\perp} = 3.1 \cdot 10^{-4}$ and $\bar{g} = 10^{-3}$. Here, the point penalty parameter $\varepsilon_{\perp}$ has been determined on the basis of (4.74). Beside the kinetic energy E_{kin} and the internal elastic energy E_{int} of the two beams, the accumulated contact work determined via the following expression (see also (4.80))

$$W_{con}(t) = \sum_{t_i = \Delta t}^{t} \Delta \mathbf{X}(t_i)^T \mathbf{R}_{con}(t_i), \tag{4.104}$$

has been plotted. Here $\mathbf{R}_{con}(t_i)$ denotes the total contact residual contribution and $\Delta \mathbf{X}(t_i)$ the increment of the total displacement vector between time steps t_i and t_{i-1}. The notion of contact work is necessary since no potential is existent for the force-based formulation. Furthermore, the sum of kinetic and internal energy $E_{kin} + E_{int}$ as well as the total work $W_{tot} = W_{con} + E_{kin} + E_{int}$ representing the sum of all three contributions, is illustrated. All mechanical energy and work contributions plotted in Figure 4.24 are normalized with the internal energy $E_0 = EI\pi^2/(8l)$, which corresponds to a beam that has been elastically bent to a quarter-circle. Looking at Figure 4.24(a), one realizes that after the acceleration phase the total work W_{tot} remains constant, which indicates that no relevant energy losses are caused by the applied time integrator.

While the total work basically consists of pure kinetic energy in the first half of the process, the dynamic impact (peak in the contact work) induces a deformation of the beams accompanied by an increase in the internal elastic energy. However, after the contact has re-opened, a remaining contact work in the range of $W_{con} \approx -0.002 \cdot E_0$ can be observed, thus leading to an increase in the energy $E_{kin} + E_{int}$ by the same amount. The fact that the contact work does not decrease to zero after the contact has re-opened again is a direct consequence of the non-conservative nature of the

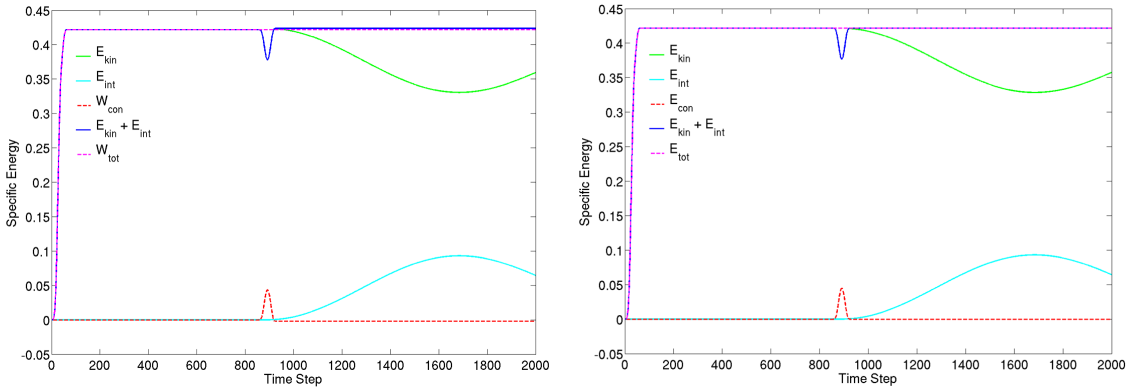

(a) **f**-based: $\varepsilon_{\|} = 3 \cdot 10^{-3}, \varepsilon_{\perp} = 3.1 \cdot 10^{-4}, \bar{g} = 10^{-3}$. (b) Π-based: $\varepsilon_{\|} = 3 \cdot 10^{-3}, \varepsilon_{\perp} = 3.1 \cdot 10^{-4}, \bar{g} = 10^{-3}$.

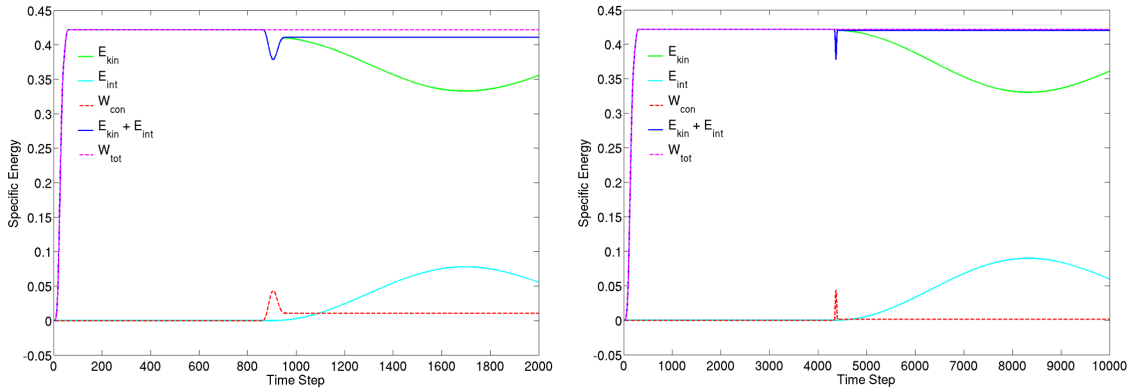

(c) **f**-based: $\varepsilon_{\|} = 3 \cdot 10^{-3}, \varepsilon_{\perp} = 3.1 \cdot 10^{-6}, \bar{g} = 10^{-3}$. (d) **f**-based: $\varepsilon_{\|} = 3 \cdot 10^{-1}, \varepsilon_{\perp} = 7.8 \cdot 10^{-5}, \bar{g} = 10^{-4}$.

Figure 4.24: Conservation of total system energy for dynamic impact scenario.

force-based formulation. On the contrary, the potential-based formulation (see Figure 4.24(b)) is able to represent exact conservation (aside from possible losses caused by a non-conserving time integration scheme) of the total energy $E_{tot} = E_{con} + E_{kin} + E_{int}$, since a contact potential E_{con} is existent that vanishes as soon as the contact re-opens. For comparison reasons, also a variant of the force-based formulation has been plotted, where the penalty parameter $\varepsilon_{\perp} = 3.1 \cdot 10^{-6}$ has been decreased by a factor of 100 as compared to (4.74) (see Figure 4.24(c)). In this case, the amount of accumulated non-conservative contact work that remains after the contact has re-opened increases to $W_{con} \approx 0.011 \cdot E_0$. On the contrary, when applying a better approximation for the optimal penalty parameter $\varepsilon_{\perp} = 2.4 \cdot 10^{-4}$ based on a numerical solution of (4.72) (with $g_{min} = -0.002$), the remaining contact work drops to $W_{con} \approx -0.001 \cdot E_0$ (not illustrated in Figure 4.24). It has already been argued in Section 4.3.1.2 that the non-conservative work contributions of the force-based *ABC* formulation decrease with increasing penalty parameter. Applying a penalty law with increased penalty parameters $\varepsilon_{\|} = 3 \cdot 10^{-1}$, $\varepsilon_{\perp} = 7.8 \cdot 10^{-3}$ ($\varepsilon_{\perp}$ determined with (4.72) and $g_{min} = -0.0002$) and $\bar{g} = 1 \cdot 10^{-4}$ results in a remaining contact work of $W_{con} \approx -0.000003 \cdot E_0$ (not illustrated in Figure 4.24). Even for a decrease of the penalty parameter by a factor of 100 to $\varepsilon_{\perp} = 7.8 \cdot 10^{-5}$, the remaining non-conservative work does not exceed a value of $W_{con} \approx 0.0013 \cdot E_0$ in this case (see Figure 4.24(d)). Finally, in Figure 4.25, the linear and angular momentum normalized with the initial values introduced by the external

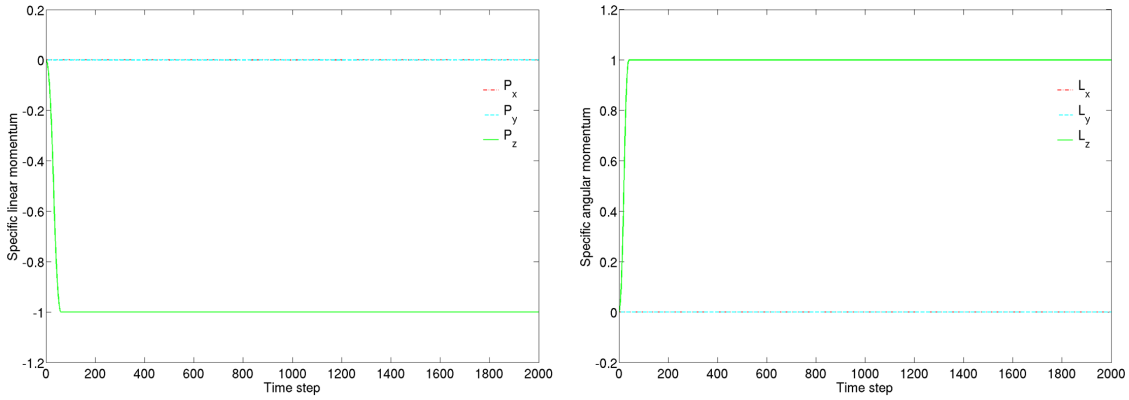

(a) Conservation of linear momentum.

(b) Conservation of angular momentum.

Figure 4.25: Conservation of linear and angular momentum for dynamic impact scenario.

forces are plotted for the force-based *ABC* formulation and the quadratically regularized penalty law with $\varepsilon_{\parallel} = 3{\cdot}10^{-3}$, $\varepsilon_{\perp} = 3.1{\cdot}10^{-4}$ and $\bar{g} = 1{\cdot}10^{-3}$ (corresponding to Figure 4.24(a)). As already expected from analytic investigations (see Section 4.3.4), the linear and angular momentum are exactly conserved. This also holds for the potential-based *ABC* formulation and all penalty laws.

4.5.3 Practical applications

Within the following four sections, the proposed overall *ABC* contact algorithm shall be verified by four practically relevant applications. The employed standard contact algorithm consists of the *ABC* formulation with force-based transition of Section 4.3.1.1 based on properly adapted penalty parameters according to Section 4.3.3 and a quadratically regularized penalty law (4.88), the endpoint contact contributions given in Section 4.4.4, the two-stage search algorithm of Section 4.4.1 as well as the step size control as proposed in Section 4.4.2.

4.5.3.1 Example 1: Simulation of a biopolymer network

In a first practically relevant example, the presented simulation framework is applied in order to investigate the influence of mechanical contact interaction on the three-dimensional Brownian motion of filaments in biopolymer networks. Biopolymer networks are tight meshes of highly slender polymer filaments (e.g. Actin filaments) embedded in a liquid phase, often interconnected by means of a second molecule species (so-called cross-linkers). These networks can for example be found in biological cells. There, they crucially determine the mechanical properties of cells and biologically highly relevant processes such as cell-migration or cell-division. In the recent contribution by Cyron and Wall [61], a finite element model for the Brownian motion of these filaments in the absence of mechanical contact interaction has been proposed. Accordingly, these slender filaments are described by means of a geometrically nonlinear beam theory. The mechanical interaction of the filaments with the surrounding fluid is modeled by means of external distributed line loads consisting of velocity-proportional viscous drag forces and thermal excitation forces. The latter are modeled as stochastic forces characterized by a mean value of zero, a variance determined by the absolute temperature and the properties of the surrounding

fluid and finally by spatial and temporal correlation lengths which are assumed to be zero (see [61] for details). Due to the physical length scales relevant for such systems, inertia forces can often be neglected, thus leading to a system of first-order stochastic partial differential equations (SPDEs). While spatial discretization is performed via the finite element method in combination with the TF beam element formulation (Section 3.7), a Backward Euler scheme is applied in order to discretize the resulting semi-discrete problem in time. In this section, the Brownian dynamics simulation framework presented in [61] is combined with the contact algorithm proposed in the sections before in order to simulate the free diffusion of Actin filaments (without consideration of cross-linker molecules). Thereto, a system of 208 initially straight and randomly distributed Actin filaments with circular cross-section of radius $R = 2.45 \cdot 10^{-3}$, length $l = 4$ and Youngs modulus $E = 1.3 \cdot 10^9$ (all quantities given in the units mg, μm, and s) is considered and illustrated in Figure 4.26(a). All further physical system parameters describing the viscous and stochastic forces are identical to those applied in Müller et al. [160] and can be found therein.

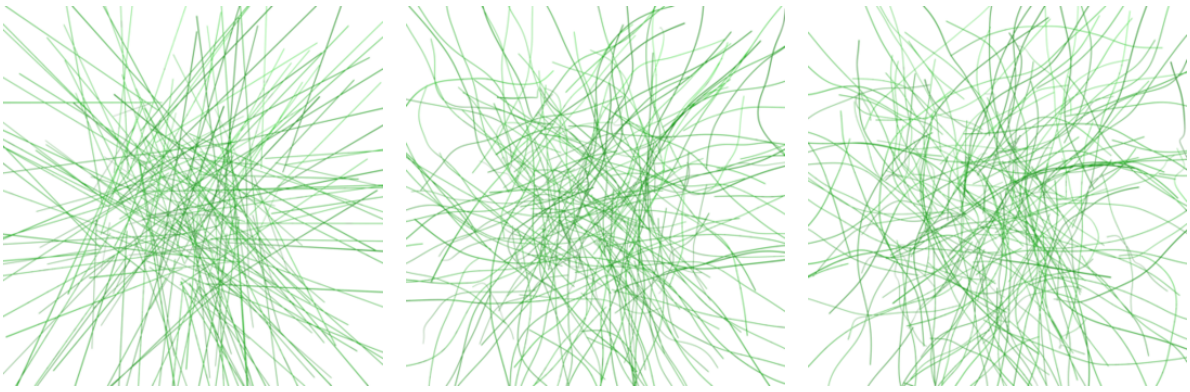

(a) Undeformed initial configuration. (b) Configuration at step 190. (c) Configuration at step 500.

Figure 4.26: Brownian dynamics simulation of the free diffusion of Actin filaments: Initial as well as deformed filament configurations at different time steps.

The simulation has been performed by applying a spatial discretization with 32 beam elements per filament, a time step size of $\Delta t = 1.0 \cdot 10^{-4}$ and a total simulation time of $T = 5.0 \cdot 10^{-1}$. Furthermore, the contact parameters have been chosen as $\varepsilon_\perp = 1.0 \cdot 10^3$, $\varepsilon_\parallel = 5.0 \cdot 10^4$, $\bar{g} = 2.0 \cdot 10^{-3}$, $\alpha_1 = 9°$ and $\alpha_2 = 11°$ in combination with 20 five-point integration intervals per element. The ratio $\varepsilon_\parallel / \varepsilon_\perp \approx 50$ results from (4.74). The applied Gauss point density has been determined on the basis of equation (4.59) with $g_{n,min} = 0.1$ in combination with an adequate safety factor. The spatial configurations at times $t = 0.0, t = 0.19$ and $t = 0.5$ and corresponding detail views are illustrated in Figure 4.26 and 4.27 (where for reasons of better visualization, the cross section radius has been scaled by a factor of 2). As a consequence of the excitatory stochastic forces employed in the considered Brownian dynamics model, the velocity field of these filaments is strongly fluctuating in space and in time, thus leading to drastic and frequent changes in the active contact set. This property in combination with the very high filament slenderness ratio of $\zeta \approx 1600$, comparatively large time step sizes (maximal displacement per time step $\Delta D_{max} := \max\left(||\mathbf{D}(t_i) - \mathbf{D}(t_{i-1})||_\infty\right) \approx 10R$) and complex geometrical contact configurations spanning the whole range of possible contact angles (see e.g. Figure 4.27(b)) make this example

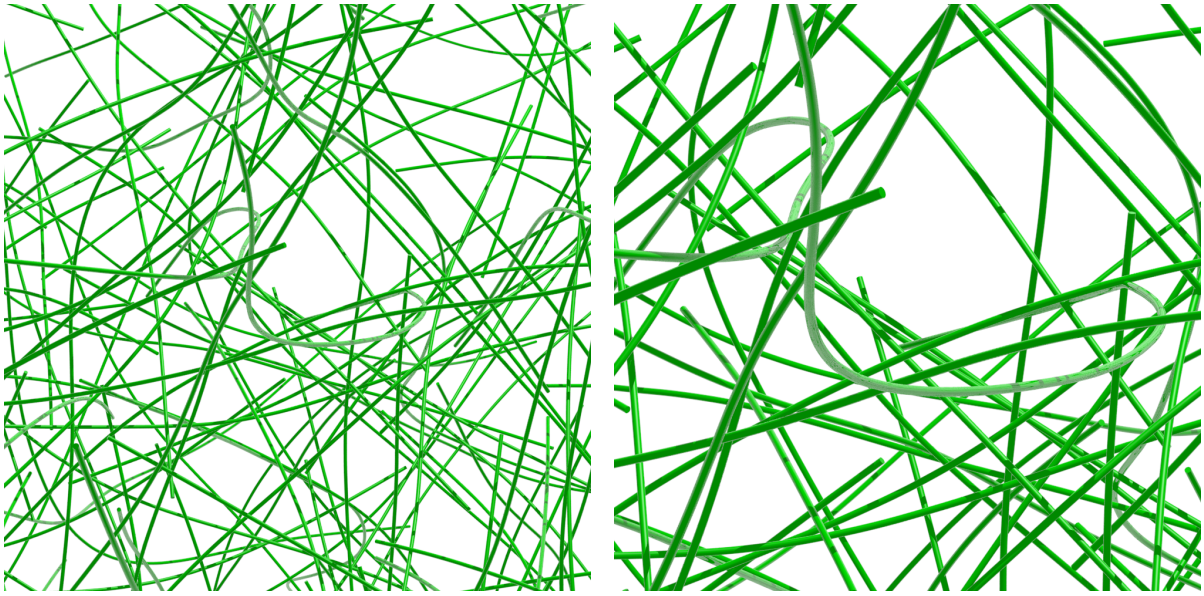

(a) Step 190: magnification factor 4.

(b) Step 190: magnification factor 8.

Figure 4.27: Brownian dynamics simulation of the free diffusion of Actin filaments: Final configuration based on different magnification factors.

very challenging concerning the robustness and efficiency of the proposed contact algorithm. In addition to the step size control of Section 4.4.2, also the load step adaption scheme of Section 3.2.1.3 has been employed. Consequently, in case of non-convergence of the global Newton scheme within 50 iterations, the time step size is halved before it is doubled again after 4 successful Newton loops on the smaller time step level. Considering standard state-of-the-art beam contact algorithms, one would have to apply a line-to-line contact type formulation in order to represent not only intermediate and large contact angles but also the range of small contact angles, which occur with significant frequency in the considered type of application and which cannot be resolved by a beam contact formulation of point-to-point type. A neglect of this small angle range would not only result in a pure physical modeling error, but in impermissibly large penetrations and consequently in non-convergence of the Newton-Raphson scheme for a considerable number of time steps. In the following, the proposed *ABC* formulation will be compared with a pure line-to-line contact formulation. According to (4.59), the number of integration intervals of the line contact formulation has been chosen by a factor of five $(\sin(90°)/\sin(11°) \approx 5)$ higher than for the *ABC* formulation in order to resolve the most critical case $\alpha = 90°$ of the line contact model equivalently to the most critical case $\alpha = 11°$ of the *ABC* formulation.

In Figures 4.28 and 4.29, the total number of active point contacts, active line contact Gauss points, and active beam endpoint contacts of the *ABC* and the pure line-to-line contact formulation have been plotted over the simulation time for the time interval $t \in [0; 0.1]$. While the number of active endpoint contacts is similar for both formulations and the number of active point contacts is, of course, zero for the pure line contact formulation, it becomes obvious that the new *ABC* formulation could reduce the total number of active Gauss points in the line contact regime by approximately a factor of 10. This reduction of computational effort by a factor of 10

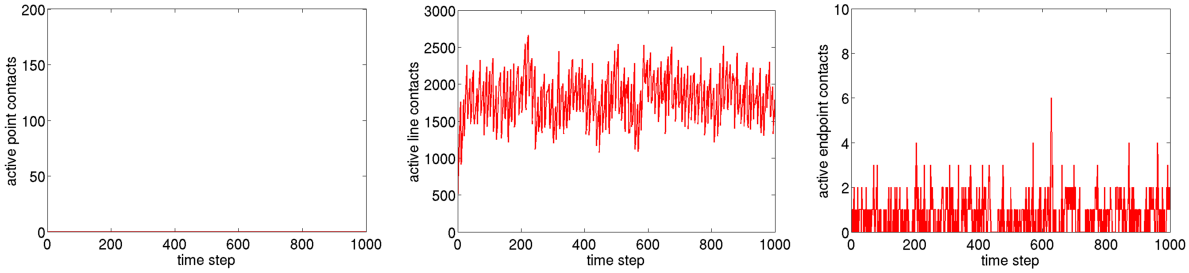

(a) Active point contacts. (b) Active line contact Gauss points. (c) Active endpoint contacts.

Figure 4.28: Number of active contacts for pure line-to-line contact formulation.

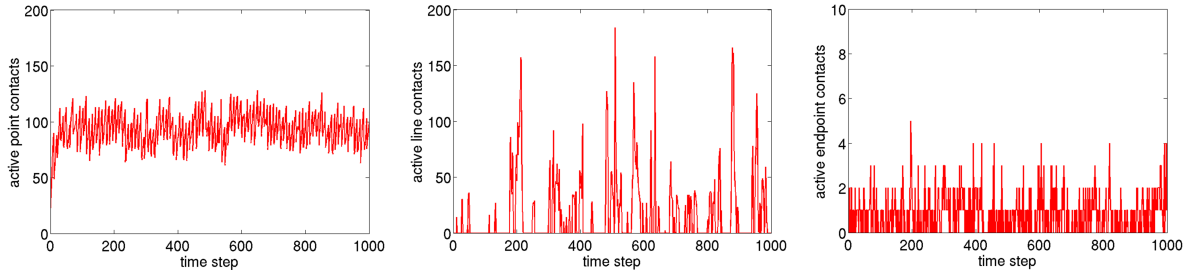

(a) Active point contacts. (b) Active line contact Gauss points. (c) Active endpoint contacts.

Figure 4.29: Number of active contacts for proposed *ABC* contact formulation.

can be split into two individual contributions: First, the required Gauss point density could be reduced by a factor of 5. Secondly, only a small proportion of the total set of active contacts, namely the subset with small contact angles, i.e. $\alpha < 11°$, had to be evaluated by the line-to-line contact formulation. In order to investigate also the influence of the applied two-stage contact search, additional simulations of the *ABC* formulation and the pure line contact formulation have been conducted, where only the first search step has been applied, i.e. a standard octree-search with spherical bounding boxes. The resulting average contact evaluation time $\bar{t}_c$ per Newton step (total CPU time for complete treatment of beam contact including contact search, closest-point projections, contact force and stiffness evaluations etc.) of the resulting four variants are plotted in Table 4.1. Accordingly, as compared to a standard beam contact algorithm consisting of a pure line contact formulation and a one-stage octree search (first line in Table 4.1), approximately a factor of 20 could be saved by the proposed two-stage search.

These savings can be attributed to the tight cylindrical bounding boxes of the second search step yielding a very small set of potential contact segment pairs for which the active Gauss points have to be determined by means of an iterative solution of the unilateral closest point projection. For the *ABC* formulation, the savings due to the second search stage (comparison of the third and fourth line in Table 4.1) are even more emphasized (approximately a factor of 50), which can be explained as follows: The subdivision of the potential contact segment pairs into potential point-to-point and potential line-to-line contact segment pairs that is enabled by the two-stage search algorithm, leads to a considerable reduction of the number of unilateral closest point projections necessary in order to determine the active line contact Gauss points (which is typically

Formulation	Search algorithm	$\max(n_{GP,tot})$	$\bar{t}_c$
Line-to-Line	1-stage	≈ 2700	$1.7 \cdot 10^{1}$ $sec.$
Line-to-Line	2-stage	≈ 2700	$7.7 \cdot 10^{-1} sec.$
ABC	1-stage	≈ 180	$3.6 \cdot 10^{0}$ $sec.$
ABC	2-stage	≈ 180	$7.6 \cdot 10^{-2} sec.$

Table 4.1: Average contact evaluation times for different contact and search schemes.

much higher than the number of bilateral closest point projections in the point contact regime). Obviously, the computational savings resulting from this second search step overcompensate the required numerical effort. However, the efficiency of the second search stage depends on the number of search segments per finite element determined by the maximal segment angle β_{max}, in this example chosen as $\beta_{max} = 1°$. A comparison of the average contact evaluation times of the pure line-to-line and the *ABC* formulation, both in combination with the two-stage contact search (second line and fourth line in Table 4.1) reveals another saving in computation time by a factor of 10 that directly correlates with the reduced number of active Gauss points as already shown in Figures 4.28 and 4.29. Thus, the new *ABC* formulation in combination with the two-stage contact search leads to an overall saving by a factor of 200 as compared to a standard line-to-line beam contact formulation with a one-stage octree search.

In the considered Brownian dynamics example, where dynamic collisions at all possible filament-to-filament orientations can occur, also the significance of the endpoint contact contributions introduced in Section 4.4.4 becomes apparent. In order to underpin this statement, the corresponding total numbers of active beam endpoint contacts in Figure 4.28(c) shall again be considered. Accordingly, the endpoint contact contributions occur with significant frequency. Neglecting these endpoint contact forces would not only allow for nonphysically large penetrations, it would also lead to non-convergence of the Newton-Raphson scheme in many time steps.

Next, the influence of the step size control presented in Section 4.4.2 will be investigated. In order to enable the corresponding investigations in an efficient manner, a second, smaller example of a biopolymer network consisting of only 37 initially straight filaments will be considered as described and illustrated by Meier et al. [158]. The filaments of this second example are characterized by a reduced length $l = 2.0$, are discretized by 8 finite elements per filament and will be observed along a simulation time of $t \in [0.0; 0.1]$. Furthermore, the line-to-line penalty parameter as well as the second shifting angle are slightly changed to $\varepsilon_{\parallel} = 2.0 \cdot 10^{4}$ and $\alpha_2 = 15°$. All other simulation parameters remain unchanged as compared to the first example. In order to investigate the effectiveness of the algorithm proposed in Section 4.4.2, one simulation has been conducted on the basis of this step size control of the iterative displacement increments per Newton step according to (4.84) with a time step size of $\Delta t = 1.0 \cdot 10^{-4}$. A second simulation has been conducted without step size control. The standard procedure, and the simplest variant, of the latter case is based on a constant time step size that is small enough in order to avoid undetected crossing of beams. The choice of this maximal constant time step size has been realized by successively reducing the initial time step size $\Delta t = 1.0 \cdot 10^{-4}$ by factors

$0.5, 0.25, 0.1, 0.05, 0.025, 0.01$ etc. until the restriction of the displacement increment per time step (4.86) holds during the entire simulation, thus leading to a final step size of $\Delta t = 1.0 \cdot 10^{-7}$.

SSC	Time Step Size	# Time Steps	# Total Iterations	# Iterations/Step
No	$1.0 \cdot 10^{-4}$	$1.0 \cdot 10^{3}$	$\approx 2.0 \cdot 10^{4}$	≈ 20
Yes	$1.0 \cdot 10^{-7}$	$1.0 \cdot 10^{6}$	$\approx 2.0 \cdot 10^{6}$	≈ 2

Table 4.2: Comparison of *ABC* formulation with and without Step Size Control (SSC).

Table 4.2 gives a comparison of the two variants "with/without" step size control (SSC). As a consequence of a considerably higher time step size (factor 1000) and limited iterative displacement increments, the average number of Newton iterations per time step is increased by a factor of 10 for the variant with SSC, whereas the total number of Newton iterations during the entire simulation could be reduced approximately by a factor of 100. The remarkable impact of this simple method can be explained by considering the following two aspects: First, similar to a pure time step size reduction, the step size control subdivides a given displacement into small sub-steps with displacement increments of size R. However, in contrast to a pure time step size reduction, the step size control does not require Newton convergence of the intermediate configurations generated by these sub-steps, a fact, that already saves a considerable number of overall Newton iterations. Secondly, the admissible constant time step size in case of a pure time step size reduction might be limited by a small number of individual time steps, whereas for the remaining time steps the displacement per time step might be much smaller than the cross section radius. The step size control on the other hand automatically adapts the number of sub-steps to the amount of total displacement per time step, thus leading to the optimal number of sub-steps.

Of course, there exist applications where the maximal admissible time discretization error is the crucial limiting factor of the time step size. However, in many cases, especially when considering systems of highly slender filaments, the representation of the overall displacements on the length scales of the filament length are of practical interest, and not the resolution of the exact contact dynamics occurring on the length scale of the cross section radius and smaller. This applies in particular to non-deterministic systems such as the considered biopolymer networks, where averaged statistical statements efficiently generated out of a large number of individual stochastic realizations are relevant. There are many questions of interest in this field, e.g. the influence of mechanical contact interaction on filament diffusion or on the development of thermodynamically stable or unstable equilibrium phases [161] in cross-linked biopolymer networks, where a robust contact simulation framework is required. In order to enable simulations along physically relevant time scales, computational efficiency is one of the key requirements.

Finally, this section will be concluded by an exemplary statistical analysis of a physically relevant quantity. Concretely, the influence of the mechanical contact interaction on the filament diffusion measured by the mean square displacement per time step, which is defined as

$$\langle \Delta r^P \rangle := \frac{1}{N} \sum_{i=1}^{N} \Delta r_i^P \quad \text{with} \quad \Delta r_i^P = ||\Delta \mathbf{r}_i^P||, \tag{4.105}$$

will be evaluated. In (4.105), $N = 10^3$ denotes the number of time steps and $\Delta \mathbf{r}_i^P$ the displacement increment of a material filament point P, here chosen as the midpoint of a filament located close to the center of the considered network in the initial configuration, at time step i. In order to enable a statistical analysis, 100 realizations of the underlying Gaussian process have been considered by generating 100 different sets of random numbers for the space-time distribution of the stochastic loads. Having determined the mean square displacement $\langle \Delta r^P \rangle_c^l$ for the case where contact is considered and $\langle \Delta r^P \rangle_{nc}^l$ for the case where contact is neglected, the modeling error m_{rel}^l of the stochastic realization $l = 1, ..., 100$ can be defined as:

$$m_{rel}^l := \frac{\langle \Delta r^P \rangle_{nc}^l - \langle \Delta r^P \rangle_c^l}{\langle \Delta r^P \rangle_c^l}. \tag{4.106}$$

Statistical evaluation of the measured modeling errors finally yield a mean value of 8.5% and a variance of 2.5%. In other words, for the considered example, the mean square displacement per time step is overestimated by 8.5% on average when neglecting mechanical contact interaction. Of course, this analysis only has an exemplary character, since system parameters such as fluid and filament properties, magnitude of stochastic forces, considered simulation time and/or type of chosen (periodic) boundary conditions (not considered here) might drastically change the influence of mechanical contact interaction on the filament diffusion behavior. Nevertheless, this result represents a first indication that mechanical contact may decrease diffusivity noticeably.

4.5.3.2 Example 2: Tube with rod-based microstructure

In this second application, tubes with rod-based microstructure as illustrated in Figure 4.31 shall be investigated. In practically relevant systems such microstructure tubes can e.g. be identified in form of arterial stents employed in medical engineering or in form of carbon nanotubes. Here, the example has been chosen in order to illustrated the flexibility of the WK-ROT elements in the modeling of rigid connections between beam elements (see also the example of Section 3.8.10) embedded in complex microstructures. In the following, quasi-static axial tension tests shall be performed on these microstructure tubes (see Figure 4.32 for the deformed configurations).

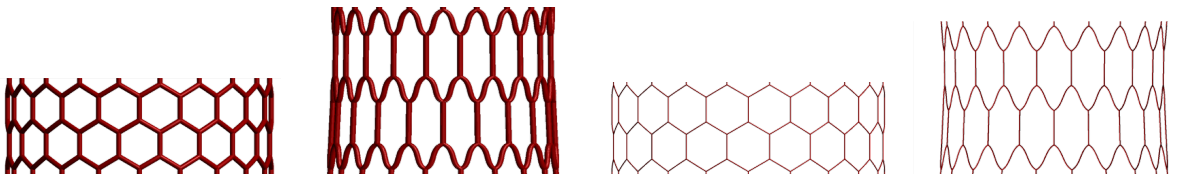

(a) Initial config.: R=0.5. (b) Final config.: R=0.5. (c) Initial config.: R=0.1. (d) Final config.: R=0.1.

Figure 4.30: Axial tension test on microstructure tubes: Detail views for different slendernesses.

Throughout this section, cylinders with three different microstructure resolutions consisting of $n_{hex} = 20$, $n_{hex} = 40$ and $n_{hex} = 100$ hexagonal unit cells along the circumference of the tube will be considered (see Figures 4.31(a), 4.31(b) and 4.31(c)). The cylinder is described by a diameter of 50 and a height of ≈ 70. The material parameters have been chosen as $E = 2G \approx 2 \cdot 10^2$. Each, initially curved hexagon segment is discretized by one WK-TAN element. At the transition

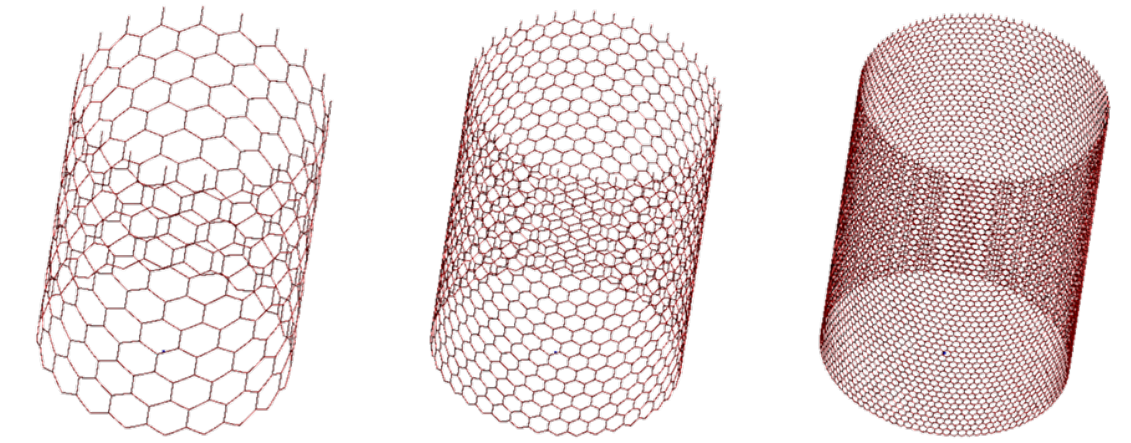

(a) 20 segment on circumference. (b) 40 segment on circumference. (c) 100 segment on circumference.

Figure 4.31: Initial configurations of microstructure tube for three different mesh sizes.

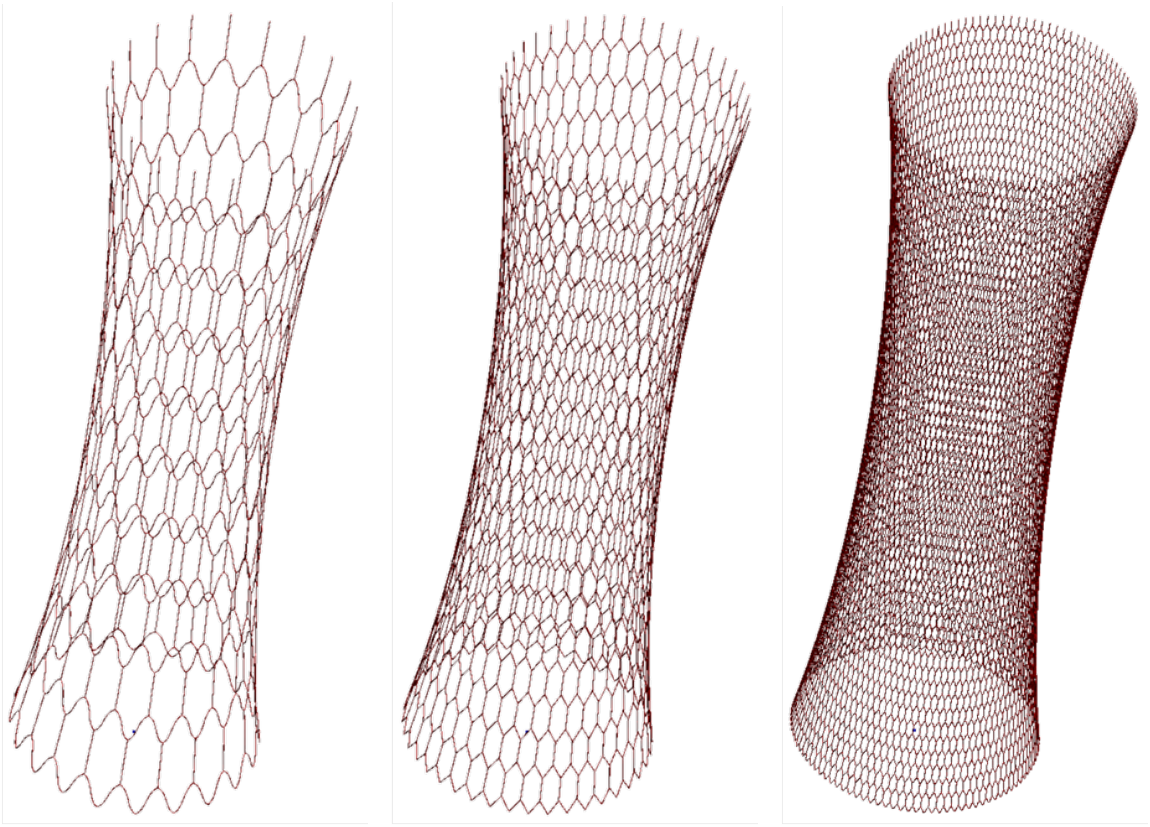

(a) 20 segment on circumference. (b) 40 segment on circumference. (c) 100 segment on circumference.

Figure 4.32: Deformed configurations of microstructure tube for three different mesh sizes.

points, three adjacent segments are rigidly connected. Due to the employed Hermite interpolation and the choice of nodal rotation vectors as primary variables, the resulting ”triple” points between three connected segments are C^1-continuous in the sense that the centerline tangents

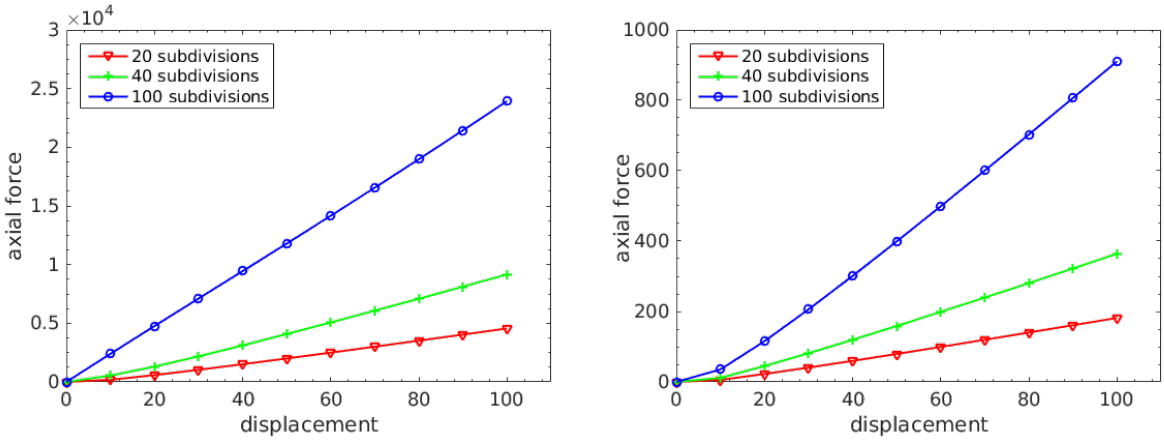

(a) Low slenderness: R=0.5.

(b) High slenderness: R=0.1.

Figure 4.33: Axial tension test on different microstructure tubes: load-displacement curves.

of the corresponding elements at these points all lie within one tangent plane, which is identical to the analytic tangent plane of the cylinder at this point. This smoothness property will be very beneficial for beam-to-beam contact interaction investigated at the end of this section. As consequence of the nodal rotation vector parametrization employed to the WK-ROT elements, no additional constraint equations are required in order to model the rigid connections between the segments. Furthermore, each segment is characterized by a circular cross-section shape. For comparison reasons, the two different cross-section radii $R = 0.5$ and $R = 0.1$ will be investigated. The change of the hexagonal unit cells of the microstructures associated with these two segment slenderness ratios resulting from the global deformation are illustrated in Figures 4.30. The axial tension tests are conducted in a Dirichlet-controlled manner by fully constraining, which means by clamping, all nodes on the top as well as on the bottom of the tubes (see Figures 4.32) and applying an axial displacement with a final magnitude of $\mathbf{u}(T) = 100$.

This test case again underlines the robustness of the applied Kirchhoff beam elements. For example, the deformed configuration of the variant $n_{hex} = 20, R = 0.5$ could be found in one load step and 10 Newton iterations. In Figures 4.33 the resulting load-displacement curves for the six investigated variants have been plotted. Interestingly, the load-displacement curves relating the reaction force $\mathbf{F}(t)$ and the prescribed displacement $\mathbf{u}(t)$ are almost linear and the slope is proportional to the segment cross-section area, i.e. $\mathbf{F}(t) \sim n_{hex} R^2 \mathbf{u}(t)$. Thus, the microstructure tube behaves similarly to an assembly of axis-aligned fibers of cross-section radius R^2. Finally, a first proof-of-principle for the contact interaction between such microstructures is given in Figures 4.34. Again, the ends of the tubes are Dirichlet-controlled such that the two tubes approach each other and finally come into contact. In future research work, it is planned to extend the presented beam-to-beam contact framework also to beam-to-solid contact scenarios. In the context of microstructure tubes as presented in this section, such a beam-to-solid contact interaction between slender and solid bodies could for example occur in the simulation of the placement process of arterial stents which are in tight contact with the surrounding arterial wall.

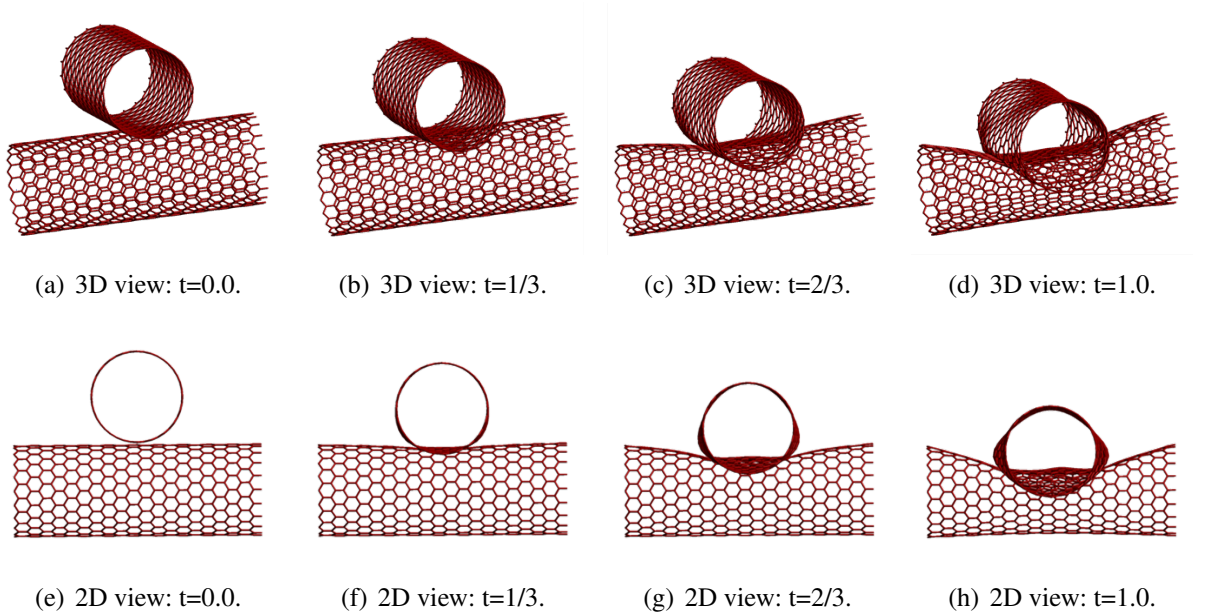

(a) 3D view: t=0.0. (b) 3D view: t=1/3. (c) 3D view: t=2/3. (d) 3D view: t=1.0.

(e) 2D view: t=0.0. (f) 2D view: t=1/3. (g) 2D view: t=2/3. (h) 2D view: t=1.0.

Figure 4.34: Static simulation of contact interaction between two mirco-structure tubes.

4.5.3.3 Example 3: Static load test on a webbing

As third application, a static load test performed on a fibrous webbing shall be analyzed. The webbing consists of $10+20$ ribbons, each of them made out of 10 individual fibers with circular cross-sections. The geometrical and constitutive parameters of an individual fiber are given by $l=500$, $R=1$, $E=2G=1.0\cdot10^7$. Each fiber endpoint is simply supported and the positions of these supports are chosen such that the fibers are initially stress-free in case no beam-to-beam contact interaction is considered. Within a ribbon, two neighboring fibers pointing in global x-direction exhibit a vanishing initial gap $g_0=0$ while the fibers pointing in global y-direction are placed with an initial distance of $g_0=R$. Each fiber is discretized by 20 TF elements yielding a global system that consists of 300 fibers, 6000 finite elements and approximately 38000 DoFs. In this example, the regimes of point and line contact are clearly separated. Thus, the shifting angles have been chosen to $\alpha_1=40^\circ$ and $\alpha_2=45^\circ$. Since no active contacts lying within the transition interval are expected for this example, the line and point penalty parameters do not necessarily have to be harmonized. Concretely, a quadratically regularized penalty law with $\varepsilon_\perp=2.4\cdot10^5$, $\varepsilon_\parallel=2.0\cdot10^4$ and $\bar{g}=0.1R$ in combination with one three-point integration interval per slave element has been chosen. Again, the global Newton-Raphson scheme is supplemented by the step size control of Section 4.4.2 and the load step adaption scheme of Section 3.2.1.3.

In order to determine the pre-stressed initial configuration, the fibers in x-direction are first loaded by a properly chosen sinusoidal line load. However, contact interaction is not considered in this first step. After activating the contact algorithm, the line load is reduced to zero in an incremental manner in order to finally yield the equilibrium configuration of the unloaded system as illustrated in Figure 4.35 (first and second row, left). In a next step, the deformation of the resulting webbing when exposed to a point loading shall be investigated. Thereto, a test piece in form of a rigid sphere (radius 50) is driven into the webbing. This process is performed in an

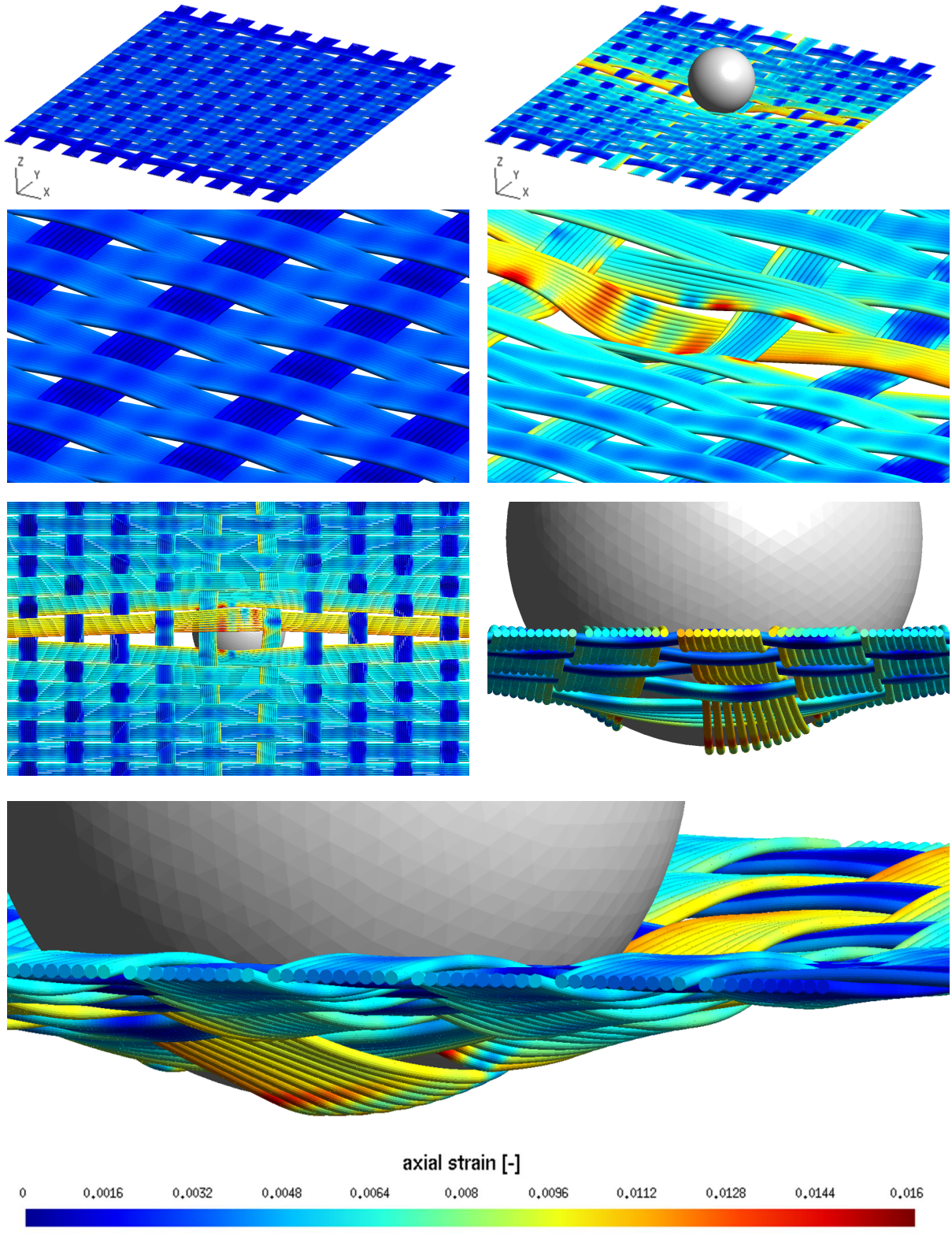

Figure 4.35: Static load test on a webbing: Initial and deformed configurations.

incremental, Dirichlet-controlled manner. The modeling of the contact interaction between the rigid sphere and the individual fibers is similar to the procedure described in Section 4.4.4 in the context of beam endpoint-to-segment contact. Different perspectives of the final deformed configuration are again shown in Figure 4.35. This state is characterized by approximately 15000 active line contact Gauss points, 16000 active point contacts and maximal penetrations in the range of 10% of the cross-section diameter for both regimes. The well-balanced number of active point and line contacts underlines the efficiency potential of the ABC formulation and demonstrates that the computationally expensive line contact contributions have been successfully reduced. In Figure 4.35, also the magnitudes of the resulting axial tension within the individual fibers are illustrated. Often, the mechanical fiber interaction in webbings of the type considered here is strongly determined by friction forces. Thereto, a future extension of the proposed beam-to-beam contact formulation by frictional effects seems to be very promising in order to improve the model quality and the significance of the generated simulation results. Nevertheless, for material pairings exhibiting low friction coefficients, the outcomes visualized in Figures 4.35 already provide a first quantification of the expected fiber stresses and a first hint with respect to possible failure mechanisms within the webbing. Furthermore, the perhaps more important purpose of this example is to demonstrate the robustness and scalability of the presented beam element and beam-to-beam contact formulations when applied to systems of practical relevance and size.

4.5.3.4 Example 4: Twisting process and failure of a rope

In this last example, the static twisting process of a rope will be investigated. The considered rope is built from 7×7 individual fibers with length $l = 5$, circular cross-section of radius $R = 0.01$ and Youngs modulus $E = 10^9$. The arrangement of the initially straight fibers in seven sub-bundles with seven fibers per sub-bundle is illustrated in Figure 4.36(a).

For spatial discretization, 10 TF beam elements per fiber are employed. The contact parameters have been chosen as $\varepsilon = 5.0 \cdot 10^5$ as well as $\bar{g} = 0.1R = 0.001$ in combination with seven 5-point integration intervals per element. In the first stage of the twisting process, each of the seven sub-bundles is twisted by four full rotations within 80 static load steps. The twisting process is performed in a Dirichlet-controlled manner, such that the cross-section center points at one end of the sub-bundles (front side in Figure 4.36) are moving on a circular path (see also Example 2 of Section 4.5.1.2) with respect to the individual sub-bundle center points, while the corresponding points at the other end of the sub-bundles (back side in Figure 4.36) remain fixed. The deformed configurations at characteristic load steps after one, two, three and four full rotations are illustrated in Figures 4.36(b)-4.36(e). In the second stage of the twisting process, all seven sub-bundles together are twisted by one further rotation within 20 additional static load steps. This time, the cross-section center points are moving on a circular path with respect to the center point of the entire 7×7-rope. The deformed configuration at the end of this twisting process is illustrated in Figure 4.36(f). While the cross-section center points of all fiber endpoints at one end of the rope (front side in Figure 4.36) are fixed in axial direction, the cross-section center points of all fiber endpoints at the other end of the rope (back side in Figure 4.36) are free to move in axial direction. Additionally, a constant axial tensile force $\bar{f}_{ax} = 1000$ acting on each of these axially freely movable fiber endpoints provides axial pre-stressing during the entire

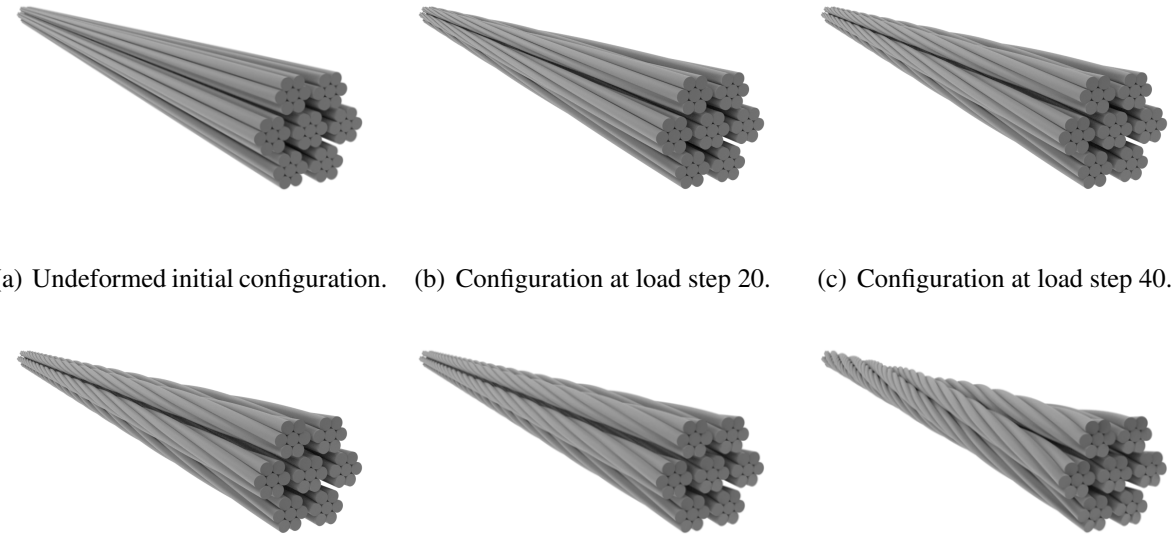

(a) Undeformed initial configuration. (b) Configuration at load step 20. (c) Configuration at load step 40.

(d) Configuration at load step 60. (e) Configuration at load step 80. (f) Configuration at load step 100.

Figure 4.36: Static simulation of the twisting process of a rope consisting of 7×7 fibers.

twisting process. On the contrary to Section 4.5.1.2, the fiber endpoints are simply supported but not clamped. Consequently, Dirichlet conditions are only applied to the positional degrees of freedom $\hat{\mathbf{d}}^i$ at the endpoints but not to the tangential degrees of freedom $\hat{\mathbf{t}}^i$. The initial geometry of the individual fibers as well as the chosen loading and Dirichlet boundary conditions are compatible with the requirements (2.128), (2.136) and (2.137) formulated in Section 2.4. As a result, each individual fiber remains torsion-free and the TF beam elements yield exact results for the considered static example. Given the global twisting state of the rope as illustrated in Figure 4.36(f), this result might contradict first intuition. Nevertheless, of course, an overall external axial torque resulting from the moment contributions of the reaction forces at the beam endpoints with respect to the centerline of the rope is necessary in order to guarantee for static equilibrium of the twisted rope at different load steps. The corresponding evolution of this external axial torque during the deformation process normalized by the maximal torque occurring at load step 100 is plotted in Figure 4.37(a). Interestingly, the evolution of the twisting torque over the twisting angle is almost linear within the two stages of deformation, i.e. the behavior of the rope is similar to the twisting response of a slender continuum. The higher slope in the second twisting stage, where all sub-bundles are twisted uniformly with respect to the centerline of the rope, results from the increased overall elastic stiffness. The external work required in order to perform the considered twisting process in a quasi-static manner is proportional to the area enclosed by the graph of the twisting torque evolution and the horizontal axis of Figure 4.37(a).

From a purely mechanical point of view, it is quite obvious that the presented example, which is dominated by line-to-line contact interaction along the entire length of the rope, should better be modeled by a line-to-line than a point-to-point type contact formulation. However, this choice shall also be motivated from a mathematical point of view. Thereto, the minimal contact angle

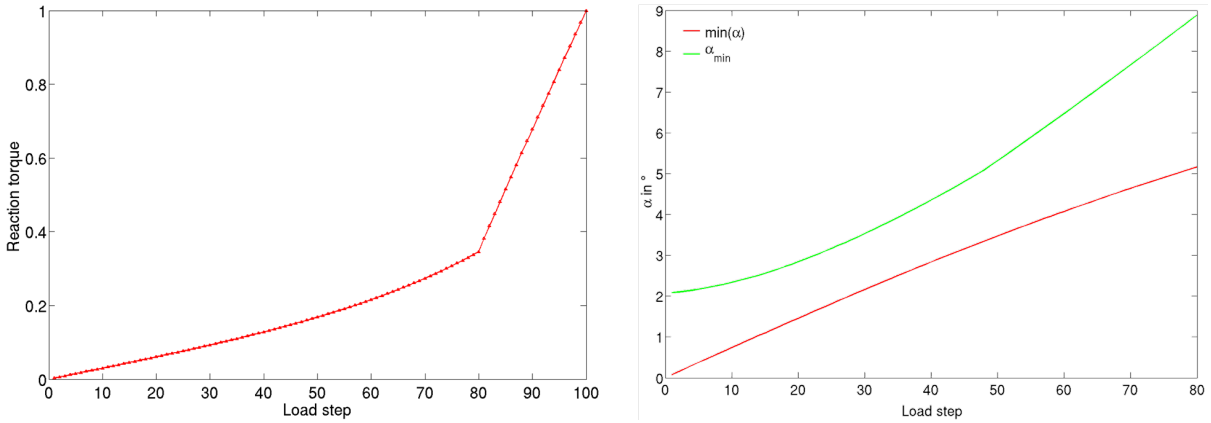

(a) Axial reaction torque during twisting process.

(b) Minimal angle $\min(\alpha)$ / lower bound α_{min}.

Figure 4.37: Reaction torque and contact angle in the numerical simulation of a rope.

$\min(\alpha)$ occurring within the entire rope at a specific load step has been plotted over the first 80 load steps in Figure 4.37(b). As expected, the value of this minimal angle increases with increasing twisting angle/load step. In order to mathematically evaluate the possibility of applying the point-to-point contact formulation to this example, this minimal contact angle will be compared with the lower bound α_{min} according to (4.31), above which a unique bilateral closest point solution can be guaranteed. To be able to do so, the evolution $\alpha_{min} = \arccos(1 - 2R\bar{\kappa}_{max})$ has additionally been plotted over the first 80 loads steps. Here, $R = 0.01$ represents the cross-section radius and $\bar{\kappa}_{max}$ is the maximal curvature value occurring in the entire rope for the considered load step. As can be seen from Figure 4.37(b), the curve representing the minimal angle $\min(\alpha)$ actually occurring in the simulation lies entirely below the curve representing the minimal admissible angle α_{min}. Thus, a unique bilateral closest point solution cannot be guaranteed and hence, as expected, the point-to-point contact formulations is not suitable for this example.

As last and probably most demanding numerical test case, the dynamic failure of two ropes of the type presented above shall be mimicked. In the initial, static equilibrium configuration, the two ropes are oriented in a perpendicular manner and contact each other (such that the imaginary undeformed rope centerlines would exactly cross each other) as illustrated in Figure 4.38(a). Additionally, the penalty parameters have been increased by a factor of ten, i.e. $\varepsilon_{\perp} = 1.5 \cdot 10^5$ and $\varepsilon_{\parallel} = 5.0 \cdot 10^6$, as compared to the static twisting process above. Starting from this configuration, the Dirichlet fixations as well as the axial tensile forces at one of the two ends of each rope (bottom left and bottom right in Figure 4.38(a)) are released, while the Dirichlet conditions at the other ends of the ropes (top left and top right in Figure 4.38(a)) remain fixed. After having consistently calculated the initial accelerations $\ddot{\mathbf{D}}_0$ of this non-equilibrium configuration, a dynamic simulation of the transient system evolution along a total simulation time of $t \in [0.0; 1.5 \cdot 10^{-3}]$ is performed. For time discretization, the standard generalized-α scheme of Section 3.1.1 in combination with a small amount of numerical dissipation provided by a spectral radius of $\rho_\infty = 0.95$ ($\alpha_f \approx 0.49$, $\alpha_m \approx 0.46$, $\beta \approx 0.26$ and $\gamma \approx 0.53$) and a time step size $\Delta t = 1.0 \cdot 10^{-7}$. The deformed configurations at different time steps are illustrated in Figure 4.38. Accordingly, the sudden release of the external (reaction-) forces leads to an initial wave propagation from the free end to

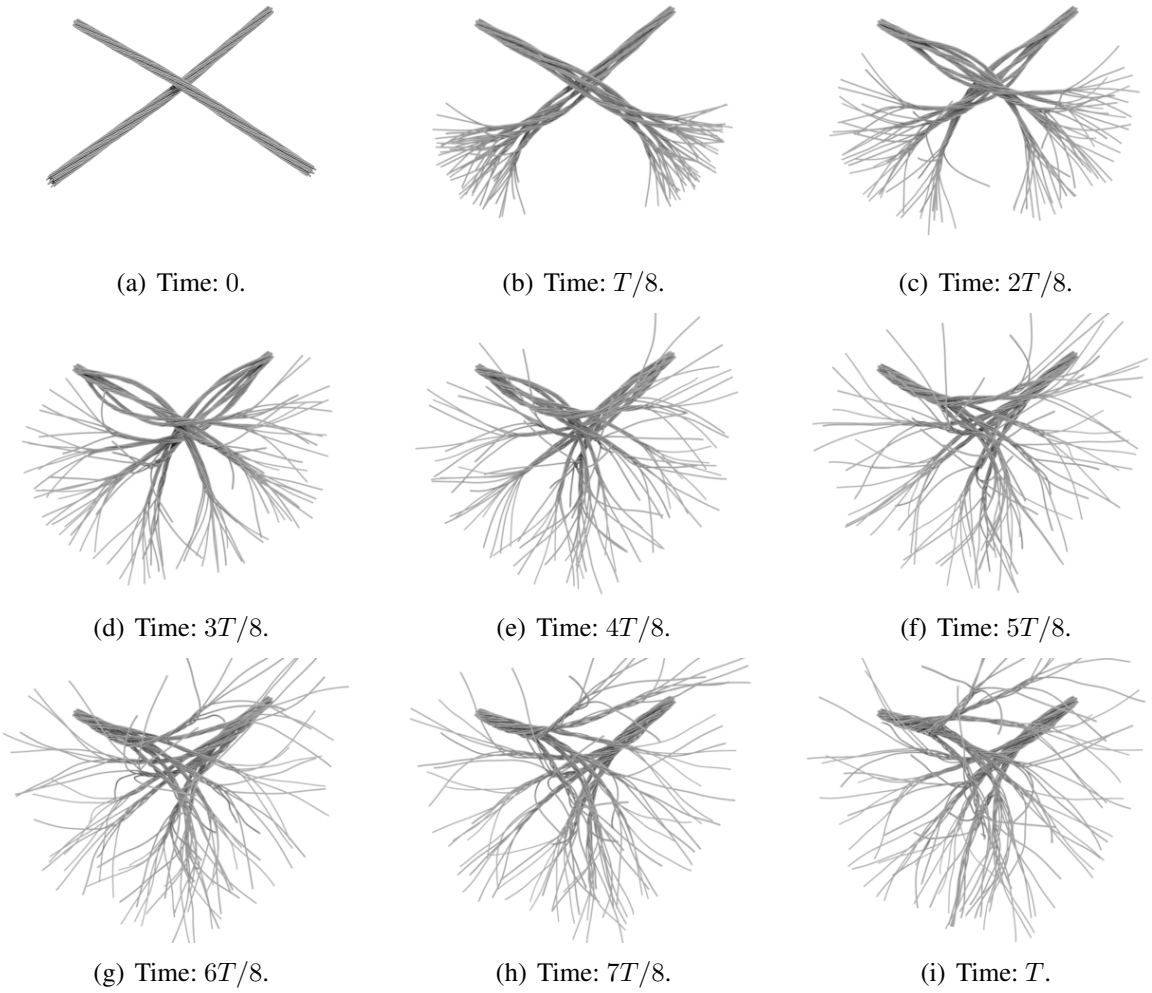

(a) Time: 0. (b) Time: $T/8$. (c) Time: $2T/8$.

(d) Time: $3T/8$. (e) Time: $4T/8$. (f) Time: $5T/8$.

(g) Time: $6T/8$. (h) Time: $7T/8$. (i) Time: T.

Figure 4.38: Simulation of the dynamic failure of two twisted steel cables which are initially in perpendicular contact: Deformed configurations at different time steps.

the clamped end. During the entire process, a highly dynamic contact interaction between the two ropes and between the individual fibers within the ropes can be observed. This contact interaction again includes arbitrary three-dimensional contact configurations spanning the whole range of possible contact angles (see e.g. the detail views in Figures 4.39 and 4.39). This statement is confirmed by Figure 4.42(a), where the minimal and maximal contact angle occurring in each time step is plotted over the simulation time. In Figures 4.41, the total number of active point-to-point contacts, active line-to-line contact Gauss points and active endpoint contacts is displayed. In this rather line-contact-dominated example, a comparatively low number of point contacts can be observed which lies in the range of 5-10 active contacts per time step while the number of active line-to-line contact Gauss points decreases drastically from an initial value of ≈ 60000 to a value of ≈ 3000 in the end of the simulation. The step size control according to Section 4.4.2 allowed for comparatively large time steps, thus leading to maximal displacements per time step in the range of four times the cross section radius, i.e. $\Delta D_{max} = \max\left(||\mathbf{D}(t_i) - \mathbf{D}(t_{i-1})||_\infty\right) \approx 4R$. According to Figure 4.42(b), the total energy consisting of elastic, kinetic and contact contribu-

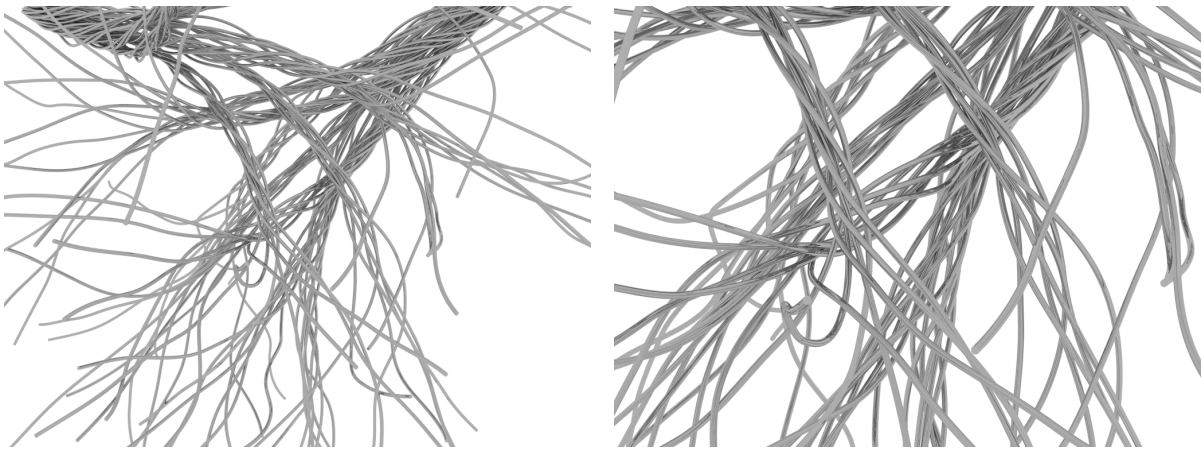

Figure 4.39: Visualization of final configuration based on small / intermediate zoom factors.

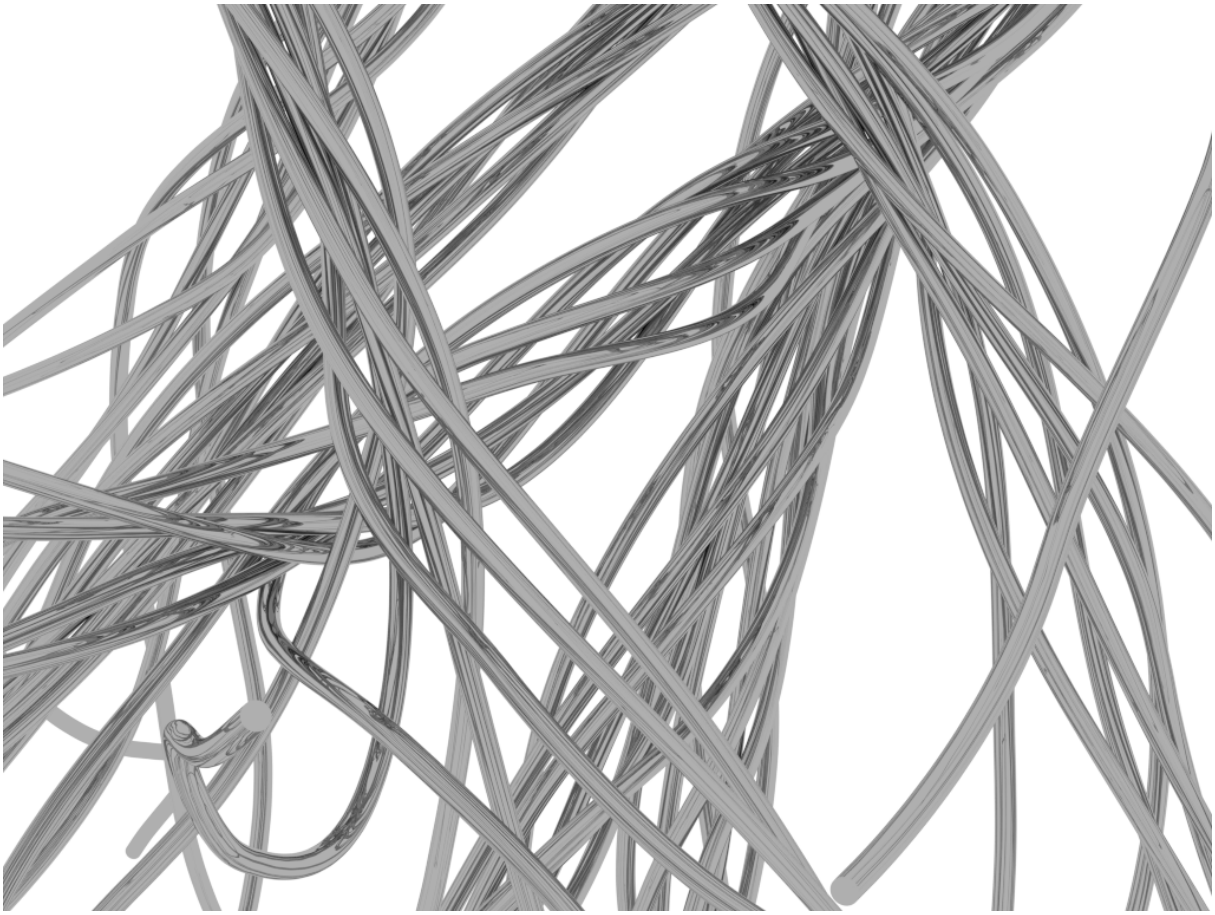

Figure 4.40: Visualization of final configuration based on a high zoom factor.

tions, is conserved very well despite the comparatively large time step size. The decline in total energy as a consequence of the numerical dissipation inherent to the generalized-α scheme with $\rho_\infty = 0.95$ is less than 1% during the total simulation time. Furthermore, due to the adjustment

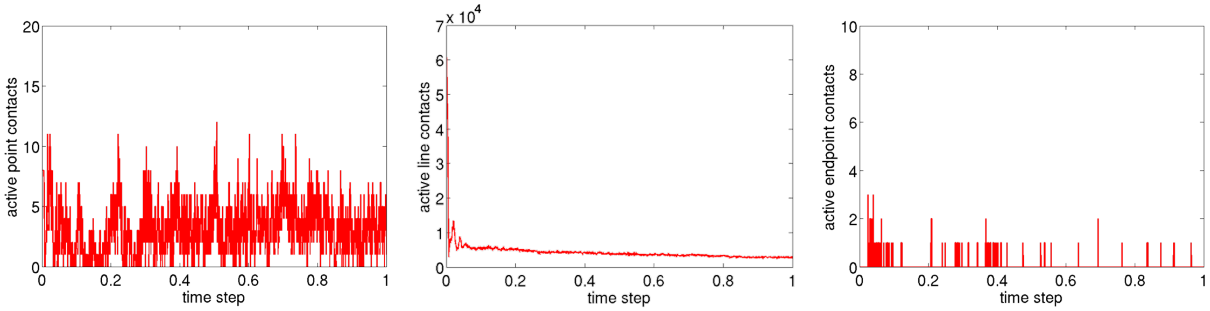

(a) Active point contacts. (b) Active line contact Gauss points. (c) Active endpoint contacts.

Figure 4.41: Simulation of dynamic failure of two steel cables: Active contacts.

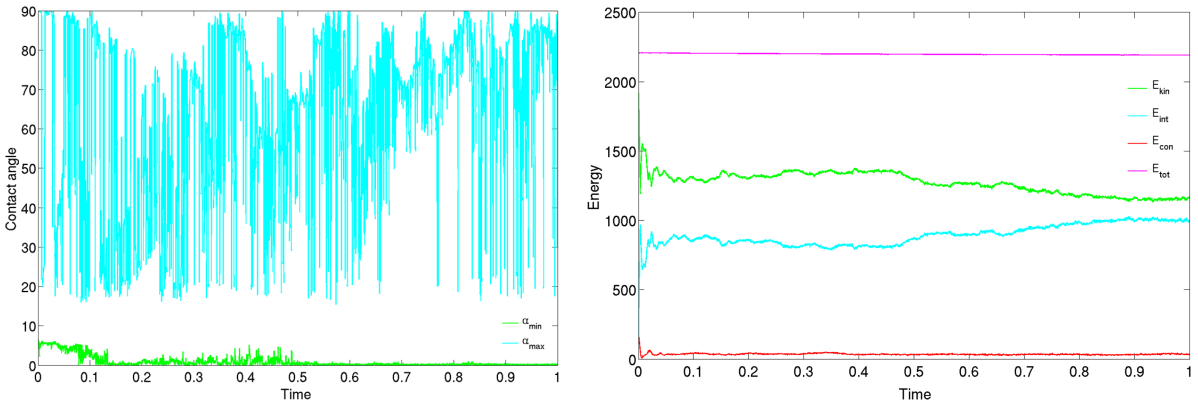

(a) Minimal and maximal contact angle. (b) Evolution of total system energy.

Figure 4.42: Simulation of dynamic failure of two steel cables: Contact angles and gaps.

of point-to-point and line-to-line penalty parameter according to (4.31), no visible energy jumps of the force-based *ABC* formulation could be observed when contact angles in the transition range $\alpha \in [\alpha_1; \alpha_2]$ occurred. On the other hand, a simulation that has been performed without considering endpoint contacts (for comparison reasons) led to considerable jumps in the total energy by several percent - a result that underlines the importance of the endpoint contributions.

All in all, it can be concluded from the practical applications considered in this section that the proposed contact algorithm enables a highly robust treatment of arbitrary contact configurations. The interplay of the individual building blocks such as *ABC* formulation, two-stage contact search and step size control of the nonlinear solver results in considerable computational savings as compared to standard beam-to-beam contact formulations available in the literature.

5 Summary and Outlook

In this thesis, mechanical models for highly slender beams and their contact interaction have been proposed on the basis of the geometrically exact Kirchhoff-Love beam theory. From these models, novel finite element formulations have been derived that allow for an accurate, robust and efficient numerical simulation of physically relevant time scales within complex mechanical systems composed of highly slender fibers with arbitrary orientation. In the following Section 5.1, the accomplishments and most important results of this thesis will be further detailed. Section 5.2, gives a brief outlook on possible future extensions and directions of research.

5.1 Summary

Within this thesis, the first geometrically exact, objective, three-dimensional, large-deformation Kirchhoff-Love beam element formulations representing the modes of axial tension, torsion and bending and accounting for arbitrary initial geometries as well as anisotropic cross-section shapes have been developed. Thereto, two alternative element formulations have been proposed: i) The first formulation is based on a strong enforcement of the Kirchhoff constraint (SK) enabled by a novel orthonormal rotation interpolation scheme. ii) The space-continuous theory of the second variant is based on a weak enforcement of the Kirchhoff constraint (WK). The discrete realization of the Kirchhoff constraint relies on a properly chosen collocation strategy which can entirely abstain from the use of additional Lagrange multipliers. While this second formulation allows for arbitrary rotation interpolations, the investigated numerical realization has employed the well-known orthonormal, geodesic triad interpolation scheme proposed in [58]. Taking advantage of a third-order Hermite interpolation, both element formulations provide a C^1-continuous centerline representation. In this context, detailed theoretical and numerical investigation have been conducted on the optimal choice of the required Hermite constant. In order to avoid possible membrane locking effects in the regime of high beam slenderness ratios, the concept of Minimally Constrained Strains (MCS) has been proposed for re-interpolation of the axial tension field. This concept is especially suited for smooth interpolation schemes with increased continuity, but still of a very general nature and is expected to be easily transferable to other locking phenomena and classes of slender structures. Furthermore, for each of these two element formulations, two different sets of nodal rotation parametrizations are proposed, one based on nodal rotation vectors (ROT) and one on nodal tangent vectors (TAN). While these different choices have been shown to yield identical FEM solutions, they differ in the resulting performance of nonlinear solvers and in the effort required for prescribing essential boundary and transition conditions. The four finite element formulations resulting from a combination of the two interpolation schemes and the two choices of nodal primary variables have been denoted as SK-TAN, SK-ROT, WK-TAN and WK-ROT elements, respectively. Eventually, the proposed beam element formulations are supplemented by an implicit, second-order accurate time inte-

gration scheme recently proposed in the literature for time discretization of large rotations. This integration scheme can be identified as Lie group extension of the well-known generalized-α method with comparable properties. The generality and flexibility of this scheme allow for a straightforward combination with the different element formulations considered in this thesis.

For the two different spatial discretization schemes SK and WK, the fulfillment of essential properties such as objectivity and path-independence, conservation of energy and momentum as well as consistent spatial convergence behavior and the avoidance of locking in the high slenderness regime have been shown theoretically and verified by means of chosen numerical examples. In the context of conservation properties, especially, the influence of applying either Bubnov-Galerkin or Petrov-Galerkin discretizations has been in the focus. Concerning locking behavior, the proposed MCS method has been compared with alternative methods known from the literature such as standard Assumed Natural Strains (ANS) or Reduced Integration (RI). In contrast to these alternative methods, the new MCS method could effectively avoid any evidence of membrane locking for all investigated load cases and slenderness ratios.

On the basis of several numerical examples, detailed and systematic numerical comparisons of the resulting discretization error levels and performance of the nonlinear solver have been performed between the four variants of the proposed geometrically exact Kirchhoff-Love beam elements and two well-established geometrically exact Simo-Reissner beam element formulations known from the literature. Most of the examples have been investigated for the two different slenderness ratios $\zeta = 100$ and $\zeta = 10000$. For the low slenderness ratio $\zeta = 100$, the general model difference between the shear-free Kirchhoff-Love theory and the Simo-Reissner theory of shear-deformable beams, measured in form of the relative L^2-error remaining in the limit of arbitrarily fine spatial discretizations, typically lay below 0.1%. Also the quadratic decrease of this model difference with increasing slenderness ratio could be confirmed numerically. In all investigated examples, the proposed WK elements have shown a lower discretization error level than the investigated Simo-Reissner beam element formulation. These results confirm the theoretical prediction that Kirchhoff type formulations can achieve the same discretization error level as Reissner type formulations with less degrees of freedom, since no shear deformation has to be represented. Compared to the excellent results of the WK elements, the SK elements showed an increased discretization error level, in some examples even higher as for the Simo-Reissner elements. Based on the underlying convergence theory, this phenomenon could be attributed to the polynomial degree $k = 3$ of the employed trial functions and predicted to vanish for higher-order elements with $k > 3$. This prediction has been confirmed by means of a first numerical test case employing Hermite polynomials of order $k = 5$ which resulted in the expected optimal discretization error level lying below the error level of the Simo-Reissner reference formulation. While most of the investigated examples have been conducted in a quasi-static manner, also two dynamic test cases, one of them a well-known benchmark test from the literature, have been conducted. There, the accuracy of the inertia contributions of the proposed elements as well as the energy stability of the employed time integration scheme could be confirmed.

Besides the resulting discretization error level, also the total number of Newton-Raphson iterations required to solve the considered test cases by means of the different element formulations and for different slenderness ratios has been analyzed in a systematic manner. For all investigated

examples and slenderness ratios, the proposed SK-TAN and WK-TAN elements required less Newton iterations to solve the problem as compared to the two well-established Simo-Reissner formulations chosen as reference. In the small slenderness range $\zeta = 100$, the results of the four proposed Kirchhoff-Love variants and the two investigated Simo-Reissner formulations lay at least in the same order of magnitude. While the behavior of the Kirchhoff-Love formulations remained more or less unchanged, the number of Newton iterations required by the two different Simo-Reissner formulations increased considerably with increasing slenderness ratio. In the investigated examples with slenderness ratio $\zeta = 10000$, this number was up to two orders of magnitude higher for the Simo-Reissner elements as compared to the proposed SK-TAN and WK-TAN elements. Also the number of iterations required by the SK-ROT and WK-ROT elements, which are based on nodal rotation vectors for triad parametrization, has been independent from the considered slenderness ratio, higher as for the SK-TAN and WK-TAN elements but still considerably lower as for the Reissner type elements. Recapitulatory, out of the four proposed Kirchhoff variants, the WK-TAN element, based on a weak enforcement of the Kirchhoff constraint and a triad parametrization via nodal tangent vectors, can be recommended in terms of a low discretization error level and an excellent performance of the Newton-Raphson scheme. Of course, further factors could be considered in a comprehensive comparison. For example, the SK-ROT and WK-ROT elements based on nodal rotation vectors simplify the prescription of Dirichlet conditions. The flexibility of the proposed beam element variants allows to combine the advantages of the two different rotation parametrizations by choosing e.g. the WK-TAN element as basic formulation and replace the nodal tangents by nodal rotation vectors at nodes where complex boundary or coupling conditions have to be prescribed. This can be realized by a simple transformation applied to the residual and stiffness contributions of the relevant node.

The abstaining from stiff shear mode contributions underlying the proposed Kirchhoff-Love element formulations does not only yield an improved Newton-Raphson performance. Also the highest eigenfrequency band of slender beams, which is associated with the shear modes, can be avoided by this means. The theoretical considerations made in this thesis give hope for considerably improved stability properties of numerical time integration schemes when combined with the developed shear-free elements. A future numerical investigation of this topic seems to provide a considerable scientific potential. Furthermore, it has also been shown that an additional abstaining from the axial tension modes can considerably improve the condition number of the system matrix, which can in turn improve the performance of iterative linear solvers. For a first proof of concept, the derived elements have been supplemented by an additional inextensibility constraint realized via a constraint enforcement strategy of augmented Lagrange type. In the investigated numerical example, the condition number of the system matrix could be improved by several orders of magnitude without deteriorating the performance of the nonlinear solver as compared to the investigated beam element formulations without inextensibility constraint.

From the general Kirchhoff-Love theory, a reduced torsion-free theory as well as a corresponding beam element realization, which fulfills the same essential properties as the general element formulations, have been consistently derived in this thesis. It has been shown that this torsion-free formulation can be applied to initially straight beams with isotropic cross-section shape as long as no external torsional moments are acting on the beam. These restrictions are valid for many of the applications mentioned in Section 1.1. These applications often represent systems

of straight fibers loaded by pure force loads. Consequently, the developed torsion-free element formulations are of highest practical interest. For the applicant, the torsion-free element formulation is beneficial since it can completely abstain from rotational degrees of freedom. This property considerably simplifies standard procedures such as rotation interpolation, derivation of linearizations, configuration updates, or time integration via finite differences in dynamics. These procedures are typically complicated by the presence of rotational degrees of freedom in common geometrically exact beam element formulations. Furthermore, in contrast to standard geometrically exact beam formulations, the torsion-free element formulation results in a symmetric tangent stiffness matrix (as long as no external moment contributions are considered) and a symmetric and constant mass matrix. For cases where the mentioned limitations with respect to external loads and initial geometries are fulfilled, it has been shown analytically that the torsion-free formulation, as compared to the general Kirchhoff theory, yields i) correct results for static problems as well as ii) good approximations for dynamic problems with a resulting model error that decreases quadratically with increasing slenderness ratio. Thus, it is perfectly compatible with the proposed Kirchhoff formulations, since also the model error of shear-free theories decreases quadratically with the beam slenderness ratio. On the basis of two static and dynamic numerical examples, these theoretical predictions could already be confirmed. All in all, the developed torsion-free element seems to be very beneficial within its extent of validity. Consequently, a further analysis of this type of reduced formulations seems to be very promising.

The second core topic of this thesis was the development of an efficient and robust beam-to-beam contact formulation capable of describing complex contact configurations of slender beams involving arbitrary beam-to-beam orientations. It has been shown by means of a mathematically concise investigation of standard point-to-point beam contact models that these formulations fail to describe a considerable range of practically relevant contact configurations as consequence of a non-unique bilateral closest point projection. On the contrary, a line-to-line contact formulation proposed in this thesis models contact interaction of slender continua by means of distributed line forces. It has been shown analytically that the corresponding unilateral closest point projection relevant for this line contact formulation always possesses a unique solution and thus is applicable for any geometrical contact configuration. By means of theoretical and numerical investigations, different contact discretizations, i.e. Gauss-point-to-segment or mortar type formulations, as well as different constraint enforcement strategies, based on penalty regularization or Lagrange multipliers, have been investigated and compared. On the basis of these comparisons, it has been concluded that a penalty-based Gauss-point-to-segment formulation is most suitable for the considered range of beam-to-beam contact applications. On the one hand, the penalty regularization of the contact constraint, which can be interpreted as mechanical model of the cross-section stiffness, has been shown to be indispensable when employing beam models based on the assumption of rigid cross-sections. On the other hand, as compared to mortar-type approaches, the proposed Gauss-point-to-segment contact discretization is favorable in terms of computational efficiency and implementation effort. The proposed formulation is supplemented by a consistently linearized integration interval segmentation that avoids numerical integration across strong discontinuities at beam endpoints. In combination with a smoothed contact force law and the proposed C^1-continuous beam element formulations, this procedure drastically reduces the numerical integration error. It has been verified numerically that this reduction of the integration error is an essential prerequisite in order to obtain optimal spatial convergence rates.

In this context, a new numerical test case suitable for line-to-line contact scenarios has been designed and a corresponding analytic solution based on the Kirchhoff-Love beam theory has been derived. This test case as well as the associated analytic solution can serve as valuable benchmark for the proposed model but also for future beam contact formulations.

In order to evaluate the numerical effort required for line-based beam contact formulations, a criterion has been derived for the minimally required number of contact evaluation points in dependence on the beam slenderness ratio and the contact angle. Based on this criterion and on the investigations already performed on the point contact model, it has been concluded that, on the one hand, point-to-point contact formulations serve as sensible mechanical models and very efficient numerical algorithms in the range of intermediate and large contact angles while they are not applicable for small contact angles. On the other hand, line-to-line contact formulations provide accurate and robust mechanical models in the small-angle regime whereas the computational efficiency considerably decreases with increasing contact angles. In order to combine the advantages of these basic formulations, a novel all-angle beam contact (*ABC*) formulation has been developed that applies a point contact formulation in the range of large contact angles, the proposed line contact formulation in the range of small contact angles and a smooth model transition within a predefined contact angle interval. Concretely, two types of model transition have been investigated: a variationally consistent one formulated on penalty potential level as well as a simpler force-based model transition. It has been shown analytically that both variants exactly fulfill the essential conservation properties of linear and angular momentum. However, only the potential-based formulation fulfills exact conservation of energy. Nevertheless, for many fields of application, the more efficient force-based model transition could be recommended as method of choice since the non-conservative work contributions of this variant can be minimized by choosing an optimal ratio of the point and line penalty parameters. Furthermore, optimal parameter choices concerning the required Gauss point densities and the model transition shifting angles have been derived. All deformation-dependent quantities have been consistently linearized, thus enabling the application within the framework of implicit time integration. The accuracy and consistency of the *ABC* formulation in terms of conservation properties and contact force distributions has been verified numerically. Eventually, the proposed *ABC* formulation has been supplemented by the contact force contributions arising from the beam endpoints.

It has been shown that endpoint contact contributions as well as small-angle contact configurations without unique bilateral closest point solution are likely to occur in unstructured systems with arbitrarily distributed and oriented fibers. A neglect of these contributions by solely applying a standard point-to-point contact formulation will in general lead to impermissibly large penetrations and an undetected crossing of beams. Even if such undetected large penetrations only occur at individual spatial positions and single points in time and even if the pure modeling error resulting from such a nonphysical behavior might be negligible, the sudden detection of such large penetrations can considerably deteriorate the performance of nonlinear solution schemes or prohibit convergence at all, in dynamic simulations it can induce energy instabilities.

Besides the requirement of highly resolved spatial contact discretizations, the modeling of thin fibers by means of standard beam contact formulations is also limited by small time step sizes. In order to address this limitation, a step size control for the nonlinear solution scheme has been

proposed that enables displacements per time step far above the order of the cross section radius. Additionally, a very efficient two-stage contact search has been developed, which consists of an octree search with spherical bounding boxes in the first step and dynamically adapted search segments enwrapped by tight cylindrical search boxes in the second step. The second search step yields a very tight set of potential contact pairs and allows for subdividing this set into potential point-to-point and potential line-to-line contact pairs. This search strategy allows to fully exploit the efficiency potential of the proposed all-angle beam contact formulation, with regard to two different aspects: On the one hand, a lower number of potential contact pairs has to be evaluated by the computationally more involved line contact formulation, viz. only the ones within the small-angle range. On the other hand, lower Gauss point densities are required within this range.

Eventually, the interplay of the proposed *ABC* formulation and the developed Kirchhoff beam elements has been investigated on the basis of four possible real-life applications: 1) A Brownian dynamics simulation of the free diffusion process of Actin filaments prevalent for example in the cytoskeleton of biological cells; 2) An axial tension test performed on a microstructure tube representing comparable practical systems such as an arterial stent or a segment of a carbon nanotube; 3) A static load test on an industrial webbing; 4) The simulation of the twisting process and the dynamic failure of two high-tensile ropes modeled on the mesoscopic scale of individual fibers. By means of these test cases, it could be verified that the proposed methods yield a beam-to-beam contact algorithm that combines a significant degree of robustness and universality in the implicit(!) numerical treatment of complex contact scenarios and arbitrary beam-to-beam orientations with a considerably increased computational efficiency compared to existing formulations, especially in the range of high slenderness ratios. For the investigated example, both the reduction in the total number of Newton iterations enabled by the step size control as well as the savings in contact evaluation time resulting from a combination of *ABC* formulation and two-stage contact search have been in the range of two orders of magnitude. Thus, the cumulative savings resulting from these two effects can be assumed to lie in the range of four orders of magnitude. When considering examples with strong contact interaction, high slenderness ratios and comparatively rough spatial FEM discretizations enabled by powerful higher-order beam elements, it is precisely the contact evaluation time that may dominate the overall computational costs. Therefore, substantial savings in this scope are of highest practical relevance.

5.2 Outlook

Possible future research work in the field of geometrically exact Kirchhoff beam element formulations concerns for example an extension of the proposed third-order elements to higher polynomial degrees $k > 3$. It has been shown that - at least for the SK-TAN/ROT elements - such an extension might be reasonable in order to fully exploit the approximation power of the underlying trial functions. Furthermore, more detailed evaluations and comparisons of extensible and inextensible Kirchhoff-Love as well as Simo-Reissner beam element formulations considering also the resulting performance of linear solvers and the stability behavior of the applied time integration schemes are desirable. Future research work in this context might for example focus on the development of tailored Lagrange multiplier interpolations that allow for a computationally cheap, global condensation of the Lagrange multipliers in order to avoid the saddle point struc-

ture of the global system of equations. Furthermore, very promising approaches on (first-order) geodesic or helicoidal interpolations on the so-called Special Euclidean group $SE(3)$ have been recently proposed for geometrically exact beam formulations of Simo-Reissner type [212, 213]. The resulting trial spaces for the translational and rotational primary variable fields of such approaches are properly harmonized and no additional means, such as reduced integration, are required in order to avoid locking effects. At least for the 2D case, an extension of this concept to higher-order elements has been proposed recently [66]. Also in the context of geometrically exact Kirchhoff type beam element formulations, an extension of this concept to C^1-continuous, higher-order interpolations in 3D might be very interesting. It is expected that the resulting trial functions associated with the centerline interpolation cannot be stated explicitly but have to be obtained via numerical integration. Thus, a detailed comparison of such element formulations and the Hermite-based elements proposed in this thesis not only in terms of accuracy but also in terms of overall efficiency might be very informative. Finally, the employed Lie-group extension of the well-known generalized-α time integration scheme [40, 41] has been shown to yield energy-stable algorithms for large-deformation beam problems and reasonable time step sizes. Nevertheless, for certain applications an exact conservation of energy and momentum might be crucial, and consequently the development of energy-momentum methods that are suitable for the proposed beam element formulations represents a possible direction of future research.

Possible future extensions of the beam-to-beam contact framework can be subdivided into efforts aiming at an improved computational performance and efforts aiming at an improved model quality. Extensions of the former type might for example consider the development of large-time-step contact algorithms that enable displacements per time step far beyond the beam cross-section dimensions without limiting the size of displacement increments per Newton step. Such formulations can for example be based on history information from the last time step and proper assumptions for the displacement path of material points between two time steps. The main task in the development of such schemes is to derive smooth formulations that are consistent and still highly robust for arbitrary geometrical configurations. Thus, it might still be beneficial to combine such formulations with the step size control proposed in Section 4.4.2, but with iterative displacement increments that may exceed the beam cross-section dimensions. Complex systems of highly slender, contacting fibers as e.g. considered in Section 4.5.3 often exhibit mechanically unstable equilibrium configurations. The prevalence of such instabilities in combination with high beam slenderness ratios and a strong mutual contact interaction between the individual fibers represent a considerable challenge for nonlinear solution schemes, even if inertia contributions are considered. Consequently, a further extension of the employed Newton-Raphson scheme and the development of highly robust but still sufficiently efficient nonlinear solution schemes tailored for this class of mechanical problems seems to be very promising and highly relevant from a practical point of view. For problems involving high-frequency responses or wave-like phenomena, also an application of the presented methods in the framework of explicit dynamics might be interesting. There, the challenging nonlinear solution process could be avoided. Furthermore, such explicit schemes could greatly benefit from the avoidance of high-frequency modes achieved by the proposed extensible and inextensible Kirchhoff type beam element formulations. Eventually, a considerable gain in computational performance seems to be possible by further refining the employed code parallelization strategies. Parallel redistribution strategies can be regarded as highly promising approaches taking into account a possible

change of the optimal parallel distribution of the spatial domain on the applied processors as consequence of continuously changing sets of beam elements interacting via mechanical contact.

Possible future extensions of the employed physical contact model incorporate for example the mechanically consistent modeling of frictional contact interaction in the point contact, the line contact and the transition regime. Already the accurate formulation of friction laws for the basic point contact model as well as for the basic line contact model can be assumed to require significant methodological developments. Most of the friction models and associated finite element discretizations available for beam-to-beam contact formulations are either based on considerably simplifying assumptions, e.g. concerning the friction force direction or the consistent treatment of relative twist rotations, or can not guarantee for objectivity, which is an essential issue not only for geometrically exact beam element formulations but also in the formulation of penalty-regularized friction models. Also an extension of the penalty regularization applied to the normal contact interaction on the basis of suitable physical models (see e.g. [122]) can be considered as reasonable step to improve the overall quality of the contact model. Besides the pure mechanical contact interaction, often denoted as steric interaction, also the potential-based interaction between slender fibers, e.g. induced by electrostatic surface charges or Van-der-Waals effects, might be highly relevant for many applications. An extension of the overall contact algorithm by models capturing such a potential-based beam-to-beam interaction will be simplified by the modular structure of the implemented simulation framework and can be regarded as very promising. Moreover, the contact interaction between slender components, described by beam models, and solid bodies, described by volume-based finite elements, might be important for many applications. As a possible future application of interest, the contact interaction between arterial stents and the walls of surrounding blood vessels, has to be mentioned. A numerical realization resulting from such a beam-to-solid contact model might considerably benefit from the robustness and the smooth surface representation of the proposed Kirchhoff beam elements. In Section 4.5.3.1, the interaction of contacting filaments and a surrounding fluid has been considered in an implicit manner by means of a proper viscous damping model. However, there are many examples for fiber-based systems where an explicit resolution of fluid structure interaction is indispensable. Possible applications comprise the motion of slender viruses in viscous fluid, the dynamics of offshore risers, the resin flow between fibers during the manufacturing process of fiber-reinforced composite materials or the fluid-fiber-interactions in rotational spinning processes employed for example for glass wool production. In this context, an extension of the existing contact framework in order to also account for fluid-to-beam interactions seems to be very promising.

In Section 4.5.3, the developed beam element and beam contact formulations have successfully been applied to four exemplary fields of application. An extension of the existing beam-to-beam contact model by additional physical effects such as anisotropic frictional contact interaction, potential-based interaction involving electrostatic or Van-der-Waals effects or also explicit fluid-structure interaction would considerably broaden the spectrum of potential future applications. Given the variety of practically relevant applications that are crucially based on the prevalence and interaction of highly slender fibers as well as the complexity of accurately analyzing the mesoscopic behavior of such systems, the methods developed in this thesis will contribute to considerably extend the range of accessible length and time scales and eventually to gain further insight into physical phenomena that have not yet been feasible for numerical simulation.

A Supplements to the Geometrically Exact Beam Theory

A.1 Singularities of mappings onto tangent fields

The problem of defining a map $\mathbf{g}_{M2}(\mathbf{g}_1)$ for a given vector $\mathbf{g}_1$ with the orthogonality condition

$$\mathbf{g}_1 \cdot \mathbf{g}_{M2}(\mathbf{g}_1) = 0 \tag{A.1}$$

shall be examined in the following. Mappings of this kind are for example the smallest rotation mapping (2.20) or the mapping defining the Frenet-Serret normal vector (2.113). Since $\mathbf{g}_1$ is a unit vector, it is an element of the unit sphere S^2, a nonlinear manifold defined as

$$S^2 := \{\mathbf{u} \in \Re^3, ||\mathbf{u}|| = 1\}. \tag{A.2}$$

Considering (A.1), the sought-after vector field $\mathbf{g}_{M2}(\mathbf{g}_1)$ can be interpreted as an element of the tangent space of S^2. For a given vector $\mathbf{u} \in S^2$ this tangent field is defined as

$$T_{\mathbf{u}}S^2 := \{\mathbf{v} \in \Re^3, \mathbf{v} \cdot \mathbf{u} = 0\}. \tag{A.3}$$

In this context, the so-called "hairy ball theorem of algebraic topology" (see e.g. [72]) states that there exists no continuous tangent vector field $\mathbf{g}_{M2}(\mathbf{g}_1) \in T_{\mathbf{u}}S^n$ on even-dimensional n-spheres, with $\mathbf{g}_{M2}(\mathbf{g}_1) \neq \mathbf{0} \,\forall\, \mathbf{g}_1 \in S^n$. For the 2-sphere S^2, this means that, if $\mathbf{g}_{M2}(\mathbf{g}_1)$ is a continuous function assigning a vector $\mathbf{g}_{M2} \in T_{\mathbf{u}}S^2$ to every given vector $\mathbf{g}_1 \in S^2$, then there is at least one $\mathbf{g}_1$ such that $\mathbf{g}_{M2}(\mathbf{g}_1) = \mathbf{0}$. Thus, for every function that maps a tangent vector field $\mathbf{g}_1$ onto an orthogonal vector field $\mathbf{g}_{M2}(\mathbf{g}_1)$ fulfilling (A.1), at least one singularity $\mathbf{g}_{M2}(\mathbf{g}_1) = \mathbf{0}$ exists, where no unique direction perpendicular to $\mathbf{g}_1$ is defined.

A.2 Variational problem of Simo-Reissner beam theory

For the case that no external forces act on the beam, i.e. $\mathbf{f}_\sigma = \tilde{\mathbf{f}} = \mathbf{m}_\sigma = \tilde{\mathbf{m}} = \mathbf{0}$, the strong and weak forms (2.49) and (2.52) shall equivalently be formulated via the Hamilton principle:

$$\delta \int_{t=0}^{T} \mathcal{L}\, dt = 0 \quad \text{with} \quad [\delta\mathbf{r} = \delta\boldsymbol{\theta} = \mathbf{0}]_{t=0}^{t=T}\,. \tag{A.4}$$

The Lagrangian $\mathcal{L}$ occurring in (A.4) is defined as the difference of kinetic and potential energy:

$$\mathcal{L} = \int_{s=0}^{l} (\tilde{\Pi}_{kin} - \tilde{\Pi}_{int})\, ds. \tag{A.5}$$

Based on the kinetic energy (2.62) and the hyper-elastic energy (2.58), the variation (A.4) reads:

$$\begin{aligned}\delta\int_{t=0}^{T}\mathcal{L}\,dt &= \int_{t=0}^{T}\int_{s=0}^{l}\left(\delta_o\mathbf{w}^T\mathbf{c}_\rho\mathbf{w}+\delta_o\dot{\mathbf{r}}^T\rho A\dot{\mathbf{r}}-\delta_o\boldsymbol{\omega}^T\mathbf{c}_m\boldsymbol{\omega}-\delta_o\boldsymbol{\gamma}^T\mathbf{c}_f\boldsymbol{\gamma}\right)ds\,dt\\ &= \int_{t=0}^{T}\int_{s=0}^{l}\left(\delta\dot{\boldsymbol{\theta}}^T\tilde{\mathbf{h}}+\delta\dot{\mathbf{r}}^T\tilde{\mathbf{l}}-\delta\boldsymbol{\theta}'^T\mathbf{m}-[\delta\mathbf{r}'-\delta\boldsymbol{\theta}\times\mathbf{r}']^T\mathbf{f}\right)ds\,dt\\ &= -\int_{t=0}^{T}\int_{s=0}^{l}\left(-\delta\boldsymbol{\theta}^T\mathbf{m}_\rho-\delta\mathbf{r}^T\mathbf{f}_\rho+\delta\boldsymbol{\theta}'^T\mathbf{m}+[\delta\mathbf{r}'-\delta\boldsymbol{\theta}\times\mathbf{r}']^T\mathbf{f}\right)ds\,dt=0.\end{aligned}\tag{A.6}$$

From the first to second line, the objective variations $\delta_o\mathbf{w}=\delta\dot{\boldsymbol{\theta}}$, $\delta_o\boldsymbol{\omega}=\delta\boldsymbol{\theta}'$ and $\delta_o\boldsymbol{\gamma}=[\delta\mathbf{r}'-\delta\boldsymbol{\theta}\times\mathbf{r}']$ (see (2.48), (2.53), (2.54)) have been inserted. Furthermore, the additional relation $\delta_o\dot{\mathbf{r}}^T\dot{\mathbf{r}}=(\delta\dot{\mathbf{r}}-\delta\boldsymbol{\theta}\times\dot{\mathbf{r}})^T\dot{\mathbf{r}}=\delta\dot{\mathbf{r}}^T\dot{\mathbf{r}}$ has been applied. From the second to the third line, partial integration of the inertia terms together with the boundary conditions in (A.4) have been applied. Since no external forces and moments are considered, i.e. $\mathbf{f}_\sigma=\mathbf{m}_\sigma=\mathbf{0}$, partial integration of (A.6) yields:

$$\delta\int_{t=0}^{T}\mathcal{L}\,dt=\int_{t=0}^{T}\int_{s=0}^{l}\left(\delta\boldsymbol{\theta}^T\big[\underbrace{\mathbf{m}'+\mathbf{r}'\times\mathbf{f}+\mathbf{m}_\rho}_{\doteq 0}\big]+\delta\mathbf{r}^T\big[\underbrace{\mathbf{f}'+\mathbf{f}_\rho}_{\doteq 0}\big]\right)ds\,dt=0.\tag{A.7}$$

The arbitrariness of $\delta\boldsymbol{\theta}(s,t)$ and $\delta\mathbf{r}(s,t)$ directly yields the strong form (2.49). Inverting the last step from (A.6) to (A.7), by partial integration of the weighted strong form (2.49), this time only along the beam length l, yields the weak form of the balance equations (2.52). The terms occurring in this weak form for an unloaded beam can already be identified in the third line of (A.6). While conservative external forces could also be included into the Lagrangian (A.5), for a consideration of non-conservative external forces and 3D external moments, which are known to be non-conservative (see e.g. [208]), the starting point has to be the strong form (2.49).

A.3 Reformulation of the isotropic weak form

Inserting all simplifications of the isotropic case (Section 2.4.1) in the weak form (2.110) yields:

$$\begin{aligned}0=&\int_0^l\left[\delta\mathbf{r}^T\tilde{\mathbf{f}}_\rho-\delta\mathbf{r}'^T\left(EA\mathbf{h_1}+EI\mathbf{h_2}+2GI\mathbf{h_3}+\frac{\mathbf{S}(\mathbf{r}')\tilde{\mathbf{m}}_{t\rho}}{||\mathbf{r}'||^2}\right)-\delta\mathbf{r}''^TEI\mathbf{h_4}\right]ds\\&+\int_0^l\left[\delta\Theta_1\frac{\mathbf{r}'^T\tilde{\mathbf{m}}_{t\rho}}{||\mathbf{r}'||}-\delta\Theta_1'2GIK_1\right]ds+\left[\delta\mathbf{r}^T\mathbf{f}_\sigma-\delta\mathbf{r}'^T\frac{\mathbf{S}(\mathbf{r}')\mathbf{m}_\sigma}{||\mathbf{r}'||^2}+\delta\Theta_1\frac{\mathbf{r}'^T\mathbf{m}_\sigma}{||\mathbf{r}'||}\right]_{\Gamma_\sigma}.\end{aligned}\tag{A.8}$$

In this weak form, all dependencies on the new primary variables $\mathbf{r}$ and K_1 have already been inserted. Furthermore, the following abbreviations have been introduced:

$$\begin{aligned}\mathbf{h_1} &:= \mathbf{r}'\left(1-\frac{1}{||\mathbf{r}'||}\right), \quad \mathbf{h_2} := \frac{2\mathbf{r}'(\mathbf{r}'^T\mathbf{r}'')^2}{||\mathbf{r}'||^6} - \frac{\mathbf{r}'(\mathbf{r}''^T\mathbf{r}'')+\mathbf{r}''(\mathbf{r}'^T\mathbf{r}'')}{||\mathbf{r}'||^4},\\ \mathbf{h_3} &:= K_1\frac{\mathbf{r}'\times\mathbf{r}''}{||\mathbf{r}'||^3}, \quad \mathbf{h_4} := \frac{\mathbf{r}''}{||\mathbf{r}'||^2} - \frac{\mathbf{r}'(\mathbf{r}'^T\mathbf{r}'')}{||\mathbf{r}'||^4}.\end{aligned} \tag{A.9}$$

The notation $\tilde{\mathbf{m}}_{t\rho}$ indicates that the perpendicular part of the angular momentum is neglected:

$$\tilde{\mathbf{m}}_{t\rho} := \tilde{\mathbf{m}} - \rho I\left(2\dot{W}_1\mathbf{g}_1 + 2W_1\dot{\mathbf{g}}_1\right) \quad \text{and} \quad \tilde{\mathbf{f}}_\rho = \tilde{\mathbf{f}} + \mathbf{f}_\rho = \tilde{\mathbf{f}} - \rho A\ddot{\mathbf{r}}. \tag{A.10}$$

A.4 Analytic solutions for the twist PDE

A.4.1 Boundary conditions of type b)

Here, a solution will be derived for the PDE (2.144) subject to boundary conditions of type b). Again, a homogeneous solution $K_{1h}(s,t)$ based on an approach according to $K_{1h}(s,t) = u(s)v(t)$ is determined such that the boundary condition $K_{1h}(s=0,t)=0$ is fulfilled:

$$K_{1h}(s,t) = \sum_{i=1}^{\infty} \underbrace{\sin\left(\frac{\omega_i s}{c}\right)}_{u_i(s)} \Big(\underbrace{A_i\cos(\omega_i t) + B_i\sin(\omega_i t)}_{v_i(t)} \Big). \tag{A.11}$$

Since a boundary condition has only been formulated at one end of the beam, the frequencies ω_k are not determined so far. Now, it is assumed that the function $F(s,t)$ can be expanded as a Fourier series based on fundamental solutions $u_i(s)$ from (A.11) with unknown frequencies ω_i:

$$F(s,t) = \sum_{i=1}^{\infty}\sum_{j=1}^{\infty} \frac{1}{l}\Omega_j\hat{F}_{ij}\sin\left(\frac{\omega_i s}{c}\right)\sin(\Omega_j t) \quad \text{with} \quad \Omega_j = \frac{j\pi}{T}. \tag{A.12}$$

Differentiation of the Fourier series (A.12) yields the required time derivative $f(s,t) = \dot{F}(s,t)$:

$$f(s,t) = \sum_{i=1}^{\infty}\sum_{j=1}^{\infty} \frac{1}{l}\,\Omega_j^2\,\hat{F}_{ij}\sin\left(\frac{\omega_i s}{c}\right)\cos(\Omega_j t). \tag{A.13}$$

Next, the inhomogeneous solution $K_{1p}(s,t)$ of (2.144) shall be determined based on the ansatz:

$$K_{1p}(s,t) = \sum_{i=1}^{\infty}\sum_{j=1}^{\infty} K_{ij}\sin\left(\frac{\omega_i s}{c}\right)\cos(\Omega_j t). \tag{A.14}$$

Insertion of (A.13) and (A.14) into the PDE (2.144) yields the unknown coefficients K_{ij}:

$$K_{ij} = \frac{\eta_{ij}^2}{1-\eta_{ij}^2}\frac{\hat{F}_{ij}}{l}, \qquad \text{with} \quad \eta_{ij} = \frac{\Omega_j}{\omega_i}. \tag{A.15}$$

The total solution of the torsion $K_1(s,t)$ follows from superposition of $K_{1h}(s,t)$ and $K_{1p}(s,t)$:

$$K_1(s,t) = \sum_{i=1}^{\infty} \sin\left(\frac{\omega_i s}{c}\right) \left(A_i \cos(\omega_i t) + B_i \sin(\omega_i t) + \sum_{j=1}^{\infty} \frac{\eta_{ij}^2}{1-\eta_{ij}^2} \frac{\hat{F}_{ij}}{l} \cos(\Omega_j t) \right). \quad \text{(A.16)}$$

From the initial condition $K_1(s, t=0) = 0$ the first constant A_i can be obtained. It follows:

$$K_1(s,t) = \sum_{i=1}^{\infty} \sin\left(\frac{\omega_i s}{c}\right) \left[B_i \sin(\omega_i t) + \sum_{j=1}^{\infty} \frac{\eta_{ij}^2}{1-\eta_{ij}^2} \frac{\hat{F}_{ij}}{l} \left(\cos(\Omega_j t) - \cos(\omega_i t)\right) \right]. \quad \text{(A.17)}$$

Next, $W_1'(s,t) = \dot{K}_1(s,t) - F(s,t)$ can directly be derived from (A.17) and (A.12):

$$\begin{aligned} W_1'(s,t) = & \sum_{i=1}^{\infty} \sin\left(\frac{\omega_i s}{c}\right) \left(B_i \omega_i \cos(\omega_i t) + \sum_{j=1}^{\infty} \frac{\eta_{ij}^2}{1-\eta_{ij}^2} \frac{\hat{F}_{ij}}{l} \left[\omega_i \sin(\omega_i t) - \Omega_j \sin(\Omega_j t)\right] \right) \\ & - \sum_{i=1}^{\infty} \sin\left(\frac{\omega_i s}{c}\right) \sum_{j=1}^{\infty} \frac{1}{l} \Omega_j \hat{F}_{ij} \sin(\Omega_j t). \end{aligned} \quad \text{(A.18)}$$

From $W_1(s, t=0) \equiv 0$, it follows that also the derivative has to vanish, i.e. $W_1'(s, t=0) \equiv 0$, and consequently $B_i = 0$. Finally, the solutions for $W_1'(s,t)$ and $K_1(s,t)$ read:

$$\begin{aligned} K_1(s,t) = & \sum_{i=1}^{\infty} \sin\left(\frac{\omega_i s}{c}\right) \sum_{j=1}^{\infty} \frac{\eta_{ij}^2}{1-\eta_{ij}^2} \frac{\hat{F}_{ij}}{l} \left(\cos(\Omega_j t) - \cos(\omega_i t)\right), \\ W_1'(s,t) = & \sum_{i=1}^{\infty} \sin\left(\frac{\omega_i s}{c}\right) \left(\sum_{j=1}^{\infty} \frac{1}{1-\eta_{ij}^2} \frac{\hat{F}_{ij}}{l} \left[\eta_{ij}^2 \omega_i \sin(\omega_i t) - \Omega_j \sin(\Omega_j t)\right] \right). \end{aligned} \quad \text{(A.19)}$$

Finally, integration of $W_1'(s,t)$ with respect to the arc-length coordinate s yields $W_1(s,t)$:

$$W_1(s,t) = -\sum_{i=1}^{\infty} c \cos\left(\frac{\omega_i s}{c}\right) \left(\sum_{j=1}^{\infty} \frac{1}{1-\eta_{ij}^2} \frac{\hat{F}_{ij}}{l} \left[\eta_{ij}^2 \sin(\omega_i t) - \eta_{ij} \sin(\Omega_j t)\right] \right). \quad \text{(A.20)}$$

Actually, in (A.20) a time-dependent integration "constant" $c(t)$ is required. However, from the PDE $\dot{W}_1 = c^2 K_1'$ (see (2.141)) and the initial condition $W(s, t=0) = 0$ it follows that this constant has to vanish. With (A.20) and the boundary condition $W_1(s=l, t) = 0$, ω_i can be derived:

$$\cos\left(\frac{\omega_i l}{c}\right) = 0 \quad \rightarrow \quad \omega_i = \frac{2i-1}{2l} \pi c. \quad \text{(A.21)}$$

A.4.2 Boundary conditions of type c)

In this appendix, a solution shall be derived for the PDE (2.145) formulated with respect to $W_1(s,t)$ and subject to boundary conditions of type c). Thus, a homogeneous solution $W_{1h}(s,t)$

based on a separation approach according to $W_{1h}(s,t) = u(s)v(t)$ is determined such that the boundary conditions $W_{1h}(s=0,t)=W_{1h}(s=l,t)=0$ at both ends of the beam are fulfilled:

$$W_{1h}(s,t)=\sum_{i=1}^{\infty}\sin\left(\frac{\omega_i s}{c}\right)\left(A_i\cos\left(\omega_i t\right)+B_i\sin\left(\omega_i t\right)\right) \quad \text{with} \quad \omega_i=\frac{i\pi c}{l}. \tag{A.22}$$

In this case, it is advantageous to employ the cosine-based Fourier series expansion of $F(s,t)$ according to (2.151). Differentiation of (2.151) yields the required derivative $\tilde{f}(s,t)=F'(s,t)$:

$$f(s,t)=-\sum_{i=1}^{\infty}\sum_{j=1}^{\infty}\frac{\omega_i}{lc}\,\Omega_j\,\bar{F}_{ij}\sin\left(\frac{\omega_i s}{c}\right)\sin\left(\Omega_j t\right) \quad \text{with} \quad \omega_i=c\hat{\omega}_i. \tag{A.23}$$

Next, the inhomogeneous solution $K_{1p}(s,t)$ of (2.145) shall be determined based on the ansatz:

$$W_{1p}(s,t)=\sum_{i=1}^{\infty}\sum_{j=1}^{\infty}W_{ij}\sin\left(\frac{\omega_i s}{c}\right)\sin\left(\Omega_j t\right). \tag{A.24}$$

Insertion of (A.23) and (A.24) into the PDE (2.145) yields the unknown coefficients W_{ij}:

$$W_{ij}=-\frac{\eta_{ij}}{1-\eta_{ij}^2}\frac{c}{l}\bar{F}_{ij}, \qquad \text{with} \quad \eta_{ij}=\frac{\Omega_j}{\omega_i}. \tag{A.25}$$

The total solution of $W_1(s,t)$ follows from superposition of $W_{1h}(s,t)$ and $W_{1p}(s,t)$:

$$W_1(s,t)=\sum_{i=1}^{\infty}\sin\left(\frac{\omega_i s}{c}\right)\left(A_i\cos\left(\omega_i t\right)+B_i\sin\left(\omega_i t\right)-\sum_{j=1}^{\infty}\frac{\eta_{ij}}{1-\eta_{ij}^2}\frac{c}{l}\bar{F}_{ij}\sin\left(\Omega_j t\right)\right). \tag{A.26}$$

From the initial condition $W_1(s,t=0)=0$ the first constant $A_i=0$ can be obtained. Next, $\dot{K}_1(s,t)=W_1'(s,t)+F(s,t)$ can directly be derived from (A.26) and (2.151):

$$\begin{aligned}\dot{K}_1(s,t)(s,t)=&\sum_{i=1}^{\infty}\left(\frac{\omega_i}{c}\right)\cos\left(\frac{\omega_i s}{c}\right)\left(B_i\sin\left(\omega_i t\right)-\sum_{j=1}^{\infty}\frac{\eta_{ij}}{1-\eta_{ij}^2}\frac{c}{l}\bar{F}_{ij}\sin\left(\Omega_j t\right)\right)\\&+\sum_{i=0}^{\infty}\sum_{j=1}^{\infty}\frac{\Omega_j}{l}\bar{F}_{ij}\cos\left(\frac{\omega_i s}{c}\right)\sin\left(\Omega_j t\right)\\=&\sum_{i=1}^{\infty}\cos\left(\frac{\omega_i s}{c}\right)\left(\left(\frac{\omega_i}{c}\right)B_i\sin\left(\omega_i t\right)-\sum_{j=1}^{\infty}\frac{\eta_{ij}^2}{1-\eta_{ij}^2}\frac{\Omega_j}{l}\bar{F}_{ij}\sin\left(\Omega_j t\right)\right)\\&+\sum_{j=1}^{\infty}\frac{\Omega_j}{l}\bar{F}_{0j}\sin\left(\Omega_j t\right).\end{aligned} \tag{A.27}$$

Integration of (A.27) with respect to the time t yields the following expression for the torsion:

$$\begin{aligned}K_1(s,t)=&\sum_{i=1}^{\infty}\cos\left(\frac{\omega_i s}{c}\right)\left(-\frac{B_i}{c}\cos\left(\omega_i t\right)+\sum_{j=1}^{\infty}\frac{\eta_{ij}^2}{1-\eta_{ij}^2}\frac{1}{l}\bar{F}_{ij}\cos\left(\Omega_j t\right)\right)\\&-\sum_{j=1}^{\infty}\frac{1}{l}\bar{F}_{0j}\cos\left(\Omega_j t\right)+c(s).\end{aligned} \tag{A.28}$$

Differentiation of (A.28) with respect to s yields the following expression for $K_1'(s,t)$:

$$K_1'(s,t) = \sum_{i=1}^{\infty} \left(\frac{\omega_i}{c}\right) \sin\left(\frac{\omega_i s}{c}\right) \left(\frac{B_i}{c} \cos\left(\omega_i t\right) - \sum_{j=1}^{\infty} \frac{\eta_{ij}^2}{1-\eta_{ij}^2} \frac{1}{l} \bar{F}_{ij} \cos\left(\Omega_j t\right) \right) + c'(s). \quad \text{(A.29)}$$

From the PDE $\dot{W}_1 = c^2 K_1'$ (see (2.141)) the derivative of the integration constant yields $c'(s) = 0$. Consequently, $c(s) = c$ is not a function of s any longer. Furthermore, the constant B_i can be determined from the initial condition $K_1'(s, t=0) = 0$. It follows for the torsion $K_1(s,t)$:

$$\begin{aligned} K_1(s,t) = &\sum_{i=1}^{\infty} \cos\left(\frac{\omega_i s}{c}\right) \sum_{j=1}^{\infty} \frac{\eta_{ij}^2}{1-\eta_{ij}^2} \frac{1}{l} \bar{F}_{ij} \big(\cos\left(\Omega_j t\right) - \cos\left(\omega_i t\right) \big) \\ &- \sum_{j=1}^{\infty} \frac{1}{l} \bar{F}_{0j} \cos\left(\Omega_j t\right) + c. \end{aligned} \quad \text{(A.30)}$$

Finally, the constant c can be determined from the condition $K_1(s, t=0) = 0$, which yields:

$$\begin{aligned} K_1(s,t) = &\sum_{i=1}^{\infty} \cos\left(\frac{\omega_i s}{c}\right) \sum_{j=1}^{\infty} \frac{\eta_{ij}^2}{1-\eta_{ij}^2} \frac{1}{l} \bar{F}_{ij} \big(\cos\left(\Omega_j t\right) - \cos\left(\omega_i t\right) \big) \\ &- \sum_{j=1}^{\infty} \frac{1}{l} \bar{F}_{0j} \big(\cos\left(\Omega_j t\right) - 1 \big). \end{aligned} \quad \text{(A.31)}$$

With the constants B_i being determined, also the final solution of $W_1(s,t)$ can be stated:

$$W_1(s,t) = \sum_{i=1}^{\infty} \sin\left(\frac{\omega_i s}{c}\right) \sum_{j=1}^{\infty} \frac{\eta_{ij}}{1-\eta_{ij}^2} \frac{c}{l} \bar{F}_{ij} \big(\eta_{ij} \sin\left(\omega_i t\right) - \sin\left(\Omega_j t\right) \big). \quad \text{(A.32)}$$

B Supplements to the Temporal and Spatial Discretizations

B.1 Alternative formulation of generalized$-\alpha$ scheme

In the following, the perhaps more common application of the generalized-α method to the spatially discretized problem shall be briefly recapitulated. Thereto, it is assumed that the spatially discretized centerline field, its time derivative and its variation can be expressed as

$$\begin{aligned}
\mathbf{r}_h(s) &= \mathbf{N}_r(s)\mathbf{D}, & \mathbf{r}_h'(s) &= \mathbf{N}_r'(s)\mathbf{D}, & \mathbf{r}_h''(s) &= \mathbf{N}_r''(s)\mathbf{D}, \\
\dot{\mathbf{r}}_h(s) &= \mathbf{N}_r(s)\dot{\mathbf{D}}, & \ddot{\mathbf{r}}_h(s) &= \mathbf{N}_r(s)\ddot{\mathbf{D}}, \\
\delta\mathbf{r}_h(s) &= \mathbf{N}_r(s)\delta\mathbf{D}, & \delta\mathbf{r}_h'(s) &= \mathbf{N}_r'(s)\delta\mathbf{D}, & \delta\mathbf{r}_h''(s) &= \mathbf{N}_r''(s)\delta\mathbf{D},
\end{aligned}$$

where the global matrix $\mathbf{N}_r(s)$ and the global vector $\mathbf{D}$ represent proper assemblies of the shape functions and nodal primary variables associated with the centerline interpolation according to (3.19). The torsion-free element formulation of Section 3.7 is completely described by this interpolation. Inserting this discretization into the weak form (3.160) yields the general form:

$$G = \delta\mathbf{D}^T\mathbf{R} = \delta\mathbf{D}^T(\mathbf{M}\ddot{\mathbf{D}} + \mathbf{R}_{int}(\mathbf{D}) - \mathbf{R}_{ext}(\mathbf{D})) \doteq 0.$$

The Newmark scheme, already solved for the unknown velocities and accelerations, reads:

$$\begin{aligned}
\dot{\mathbf{D}}_{n+1} &= \frac{\gamma}{\beta\Delta t}(\mathbf{D}_{n+1} - \mathbf{D}_n) - \frac{\gamma-\beta}{\beta}\dot{\mathbf{D}}_n - \frac{\gamma-2\beta}{2\beta}\Delta t\ddot{\mathbf{D}}_n, \\
\ddot{\mathbf{D}}_{n+1} &= \frac{1}{\beta\Delta t^2}(\mathbf{D}_{n+1} - \mathbf{D}_n) - \frac{1}{\beta\Delta t}\dot{\mathbf{D}}_n - \frac{1-2\beta}{2\beta}\ddot{\mathbf{D}}_n.
\end{aligned}$$

Again, the discrete nodal displacements, velocities and accelerations as well as the residual contributions $\mathbf{R}_{int}(\mathbf{D})$ and $\mathbf{R}_{ext}(\mathbf{D})$ are evaluated at the generalized midpoints:

$$\begin{aligned}
\mathbf{D}_{n+1-\alpha_f} &= (1-\alpha_f)\mathbf{D}_{n+1} + \alpha_f\mathbf{D}_n, \\
\dot{\mathbf{D}}_{n+1-\alpha_f} &= (1-\alpha_f)\dot{\mathbf{D}}_{n+1} + \alpha_f\dot{\mathbf{D}}_n, \\
\ddot{\mathbf{D}}_{n+1-\alpha_m} &= (1-\alpha_m)\ddot{\mathbf{D}}_{n+1} + \alpha_m\ddot{\mathbf{D}}_n, \\
\mathbf{R}_{ext,n+1-\alpha_f} &= (1-\alpha_f)\mathbf{R}_{ext,n+1} + \alpha_f\mathbf{R}_{ext,n}, \\
\mathbf{R}_{int,n+1-\alpha_f} &= (1-\alpha_f)\mathbf{R}_{int}(\mathbf{D}_{n+1}) + \alpha_f\mathbf{R}_{int}(\mathbf{D}_n).
\end{aligned}$$

The residual contributions $\mathbf{R}_{ext}(\mathbf{D})$ of the external forces are defined similar to (3.5):

$$\begin{aligned}
\mathbf{R}_{ext,n} &= \mathbf{R}_{ext}(\mathbf{D}_n, \tilde{\mathbf{f}}_n, \tilde{\mathbf{m}}_n, \mathbf{f}_{\sigma,n}, \mathbf{m}_{\sigma,n}), \\
\mathbf{R}_{ext,n+1} &= \mathbf{R}_{ext}(\mathbf{D}_{n+1}, \tilde{\mathbf{f}}_{n+1}, \tilde{\mathbf{m}}_{n+1}, \mathbf{f}_{\sigma,n+1}, \mathbf{m}_{\sigma,n+1}).
\end{aligned}$$

Finally, in complete accordance to (3.6), the entire generalized residual vector reads:

$$\mathbf{R}_{int,n+1-\alpha_f} + \mathbf{M}\ddot{\mathbf{D}}_{n+1-\alpha_m} - \mathbf{R}_{ext,n+1-\alpha_f} \doteq 0.$$

The derivation that has just been conducted represents an alternative variant to the derivation made in Section 3.1.1. Since the discrete trial and test functions $\mathbf{r}_h(s)$ and $\delta\mathbf{r}_h(s)$ depend linearly on the nodal primary variables $\mathbf{D}$ and $\delta\mathbf{D}$ and since $\delta\mathbf{D}$ is independent from the considered point in time, it is straightforward to verify that both variants yield an identical result in terms of a set of nonlinear algebraic equations representing the fully discretized beam problem.

B.2 Comparison of four time discretization variants

In the following, the differences between the four different discretization variants resulting from the succession of spatial and temporal discretization as well as from the choice of either the vectors $(\boldsymbol{\psi}, \dot{\boldsymbol{\psi}}, \ddot{\boldsymbol{\psi}})$ or the vectors $(\tilde{\boldsymbol{\Theta}}, \mathbf{W}, \mathbf{A})$ for a time discretization finite difference scheme. For the following comparisons, the four resulting variants are denoted as follows:

1. TS-VS: (Temporal $\rightarrow$ Spatial) discretization; Vector Space integration: $(\boldsymbol{\psi}, \dot{\boldsymbol{\psi}}, \ddot{\boldsymbol{\psi}})$.
2. ST-VS: (Spatial $\rightarrow$ Temporal) discretization; Vector Space integration: $(\boldsymbol{\psi}, \dot{\boldsymbol{\psi}}, \ddot{\boldsymbol{\psi}})$.
3. TS-LG: (Temporal $\rightarrow$ Spatial) discretization; Lie Group integration: $(\tilde{\boldsymbol{\Theta}}, \mathbf{W}, \mathbf{A})$.
4. ST-LG: (Spatial $\rightarrow$ Temporal) discretization; Lie Group integration: $(\tilde{\boldsymbol{\Theta}}, \mathbf{W}, \mathbf{A})$.

Concerning spatial discretization, one two-noded finite element based on the triad interpolation scheme (3.55) with nodal triads $\boldsymbol{\Lambda}^1 = \exp(\mathbf{S}(\boldsymbol{\psi}^1))$ and $\boldsymbol{\Lambda}^2 = \exp(\mathbf{S}(\boldsymbol{\psi}^2))$ will be considered. Concerning time integration, a standard Newmark scheme is applied to the triple $(\boldsymbol{\psi}, \dot{\boldsymbol{\psi}}, \ddot{\boldsymbol{\psi}})$ and its Lie group counterpart to $(\tilde{\boldsymbol{\Theta}}, \mathbf{W}, \mathbf{A})$. For simplicity, only the resulting material angular velocity $\mathbf{W}$, finally expressed via additive rotation vector increments $\Delta\boldsymbol{\psi}^1_{n+1} := \boldsymbol{\psi}^1_{n+1} - \boldsymbol{\psi}^1_n$ and $\Delta\boldsymbol{\psi}^2_{n+1} := \boldsymbol{\psi}^2_{n+1} - \boldsymbol{\psi}^2_n$, will be compared. The two applied time integration rules read:

$$\begin{aligned}
\dot{\boldsymbol{\psi}}_{n+1} &= \frac{\gamma}{\beta\Delta t}\Delta\boldsymbol{\psi}_{n+1} + \left(1 - \frac{\gamma}{\beta}\right)\dot{\boldsymbol{\psi}}_n + \Delta t\left(1 - \frac{\gamma}{2\beta}\right)\ddot{\boldsymbol{\psi}}_n, \\
\mathbf{W}_{n+1} &= \frac{\gamma}{\beta\Delta t}\tilde{\boldsymbol{\Theta}}_{n+1} + \left(1 - \frac{\gamma}{\beta}\right)\mathbf{W}_n + \Delta t\left(1 - \frac{\gamma}{2\beta}\right)\mathbf{A}_n.
\end{aligned} \tag{B.1}$$

The intended investigations shall be simplified by expressing the evolution of $\boldsymbol{\psi}(\xi)$ that results from the triad interpolation scheme (3.55) as function of the nodal rotation vectors $\boldsymbol{\psi}^1$ and $\boldsymbol{\psi}^2$. In a first step, $\boldsymbol{\Lambda}(\xi)$ can be expressed by means of these nodal rotation vectors:

$$\begin{aligned}
\boldsymbol{\Lambda}(\xi) &= \boldsymbol{\Lambda}^1 \exp(\mathbf{S}[\boldsymbol{\Phi}_{lh}(\xi)]) \\
&= \boldsymbol{\Lambda}^1 \exp(\mathbf{S}[L^2(\xi)\boldsymbol{\Phi}^2_l]) \\
&= \boldsymbol{\Lambda}^1 \exp(\mathbf{S}[L^2(\xi)\mathrm{rv}\big(\boldsymbol{\Lambda}^{1T}\boldsymbol{\Lambda}^2\big)]\big) \\
&= \exp(\mathbf{S}[\boldsymbol{\psi}^1]) \exp(\mathbf{S}[L^2(\xi)\mathrm{rv}\big(\exp\{\mathbf{S}[\boldsymbol{\psi}^1]\}^T \exp\{\mathbf{S}(\boldsymbol{\psi}^2)\}\big)]).
\end{aligned} \tag{B.2}$$

Employing the rotation vector extraction operator rv(.) as defined in (2.7), $\boldsymbol{\psi}(\xi)$ yields:

$$\boldsymbol{\psi}(\xi) = \text{rv}\{\exp(\mathbf{S}[\boldsymbol{\psi}^1])\exp(\mathbf{S}[L^2(\xi)\text{rv}\big(\exp\{\mathbf{S}[\boldsymbol{\psi}^1]\}^T\exp\{\mathbf{S}(\boldsymbol{\psi}^2)\}\big)])\} =: \mathbf{f}(\boldsymbol{\psi}^1, \boldsymbol{\psi}^2, \xi). \quad \text{(B.3)}$$

Now, the angular velocities $\mathbf{W}$ resulting for the four different variants shall be derived. The angular velocity $\mathbf{W}$ expressed by means of $\boldsymbol{\psi}^1$ and $\boldsymbol{\psi}^2$ yields for the variant **TS-VS**:

$$\begin{aligned}
\mathbf{W}(s,t) &= \boldsymbol{\Lambda}^T\mathbf{T}^{-1}\dot{\boldsymbol{\psi}},\\
\mathbf{W}_{n+1}(s) &= \boldsymbol{\Lambda}^T\mathbf{T}^{-1}\left(\frac{\gamma}{\beta\Delta t}(\boldsymbol{\psi}_{n+1} - \boldsymbol{\psi}_n) + ...\right),\\
\mathbf{W}_{n+1}(\xi) &= \boldsymbol{\Lambda}^T\mathbf{T}^{-1}\left(\frac{\gamma}{\beta\Delta t}(\mathbf{f}(\boldsymbol{\psi}^1_{n+1}, \boldsymbol{\psi}^2_{n+1}, \xi) - \mathbf{f}(\boldsymbol{\psi}^1_n, \boldsymbol{\psi}^2_n, \xi)) + ...\right).
\end{aligned}$$

The angular velocity $\mathbf{W}$ expressed by means of $\boldsymbol{\psi}^1$ and $\boldsymbol{\psi}^2$ yields for the variant **ST-VS**:

$$\begin{aligned}
\mathbf{W}(s,t) &= \boldsymbol{\Lambda}^T\mathbf{T}^{-1}\dot{\boldsymbol{\psi}},\\
\mathbf{W}(\xi,t) &= \boldsymbol{\Lambda}^T\mathbf{T}^{-1}\dot{\mathbf{f}}(\boldsymbol{\psi}^1(t), \boldsymbol{\psi}^2(t), \xi) = \boldsymbol{\Lambda}^T\mathbf{T}^{-1}\left(\frac{\partial\mathbf{f}}{\partial\boldsymbol{\psi}^1}\dot{\boldsymbol{\psi}}^1 + \frac{\partial\mathbf{f}}{\partial\boldsymbol{\psi}^2}\dot{\boldsymbol{\psi}}^2\right),\\
\mathbf{W}_{n+1}(\xi) &= \boldsymbol{\Lambda}^T\mathbf{T}^{-1}\left(\frac{\partial\mathbf{f}}{\partial\boldsymbol{\psi}^1}\left[\frac{\gamma}{\beta\Delta t}\left(\boldsymbol{\psi}^1_{n+1} - \boldsymbol{\psi}^1_n\right) + ...\right] + \frac{\partial\mathbf{f}}{\partial\boldsymbol{\psi}^2}\left[\frac{\gamma}{\beta\Delta t}\left(\boldsymbol{\psi}^2_{n+1} - \boldsymbol{\psi}^2_n\right) + ...\right]\right).
\end{aligned}$$

The angular velocity $\mathbf{W}$ expressed by means of $\boldsymbol{\psi}^1$ and $\boldsymbol{\psi}^2$ yields for the variant **TS-LG**:

$$\begin{aligned}
\mathbf{W}_{n+1}(s) &= \frac{\gamma}{\beta\Delta t}\tilde{\boldsymbol{\Theta}}_{n+1}(s) + ...\ ,\\
\mathbf{W}_{n+1}(\xi) &= \frac{\gamma}{\beta\Delta t}\left(\text{rv}\left[\exp\{\mathbf{S}[\boldsymbol{\psi}_{n+1}(\xi)]\}^T\exp\{\mathbf{S}[\boldsymbol{\psi}_n(\xi)]\}\right]\right) + ...\\
&= \frac{\gamma}{\beta\Delta t}\left(\text{rv}\left[\exp\{\mathbf{S}[\mathbf{f}(\boldsymbol{\psi}^1_{n+1}, \boldsymbol{\psi}^2_{n+1}, \xi)]\}^T\exp\{\mathbf{S}[\mathbf{f}(\boldsymbol{\psi}^1_n, \boldsymbol{\psi}^2_n, \xi)]\}\right]\right) + ...\ .
\end{aligned}$$

The angular velocity $\mathbf{W}$ expressed by means of $\boldsymbol{\psi}^1$ and $\boldsymbol{\psi}^2$ yields for the variant **ST-LG**:

$$\begin{aligned}
\mathbf{W}(s,t) &= \boldsymbol{\Lambda}^T\mathbf{T}^{-1}\dot{\boldsymbol{\psi}},\\
\mathbf{W}(\xi,t) &= \boldsymbol{\Lambda}^T\mathbf{T}^{-1}\dot{\mathbf{f}}(\boldsymbol{\psi}^1(t), \boldsymbol{\psi}^2(t), \xi) = \boldsymbol{\Lambda}^T\mathbf{T}^{-1}\left(\frac{\partial\mathbf{f}}{\partial\boldsymbol{\psi}^1}\dot{\boldsymbol{\psi}}^1 + \frac{\partial\mathbf{f}}{\partial\boldsymbol{\psi}^2}\dot{\boldsymbol{\psi}}^2\right)\\
&= \boldsymbol{\Lambda}^T\mathbf{T}^{-1}\left(\frac{\partial\mathbf{f}}{\partial\boldsymbol{\psi}^1}\mathbf{T}^1\boldsymbol{\Lambda}^1\mathbf{W}^1 + \frac{\partial\mathbf{f}}{\partial\boldsymbol{\psi}^2}\mathbf{T}^2\boldsymbol{\Lambda}^2\mathbf{W}^2\right),\\
\mathbf{W}_{n+1}(\xi) &= \boldsymbol{\Lambda}^T\mathbf{T}^{-1}\left(\frac{\partial\mathbf{f}}{\partial\boldsymbol{\psi}^1}\mathbf{T}^1\boldsymbol{\Lambda}^1\left(\frac{\gamma}{\beta\Delta t}\tilde{\boldsymbol{\Theta}}^1_{n+1} + ...\right) + \frac{\partial\mathbf{f}}{\partial\boldsymbol{\psi}^2}\mathbf{T}^2\boldsymbol{\Lambda}^2\left(\frac{\gamma}{\beta\Delta t}\tilde{\boldsymbol{\Theta}}^2_{n+1} + ...\right)\right)\\
&= \boldsymbol{\Lambda}^T\mathbf{T}^{-1}\Bigg(\frac{\partial\mathbf{f}}{\partial\boldsymbol{\psi}^1}\mathbf{T}^1\boldsymbol{\Lambda}^1\left(\frac{\gamma}{\beta\Delta t}\text{rv}\left[\exp\{\mathbf{S}[\boldsymbol{\psi}^1_{n+1}]\}^T\exp\{\mathbf{S}[\boldsymbol{\psi}^1_n]\}\right] + ...\right)\\
&\qquad + \frac{\partial\mathbf{f}}{\partial\boldsymbol{\psi}^2}\mathbf{T}^2\boldsymbol{\Lambda}^2\left(\frac{\gamma}{\beta\Delta t}\text{rv}\left[\exp\{\mathbf{S}[\boldsymbol{\psi}^2_{n+1}]\}^T\exp\{\mathbf{S}[\boldsymbol{\psi}^2_n]\}\right] + ...\right)\Bigg).
\end{aligned}$$

By comparing these results it becomes clear, that in general the four variants will yield four different results. It is e.g. quite obvious that the results of the variants TS-VS and ST-VS will differ whenever $\mathbf{f}(\boldsymbol{\psi}_n^1, \boldsymbol{\psi}_n^2))$ is a nonlinear function in $\boldsymbol{\psi}_n^1$ and $\boldsymbol{\psi}_n^2$ since in this case

$$\mathbf{f}(\boldsymbol{\psi}^1, \boldsymbol{\psi}^2)) \neq \frac{\partial \mathbf{f}}{\partial \boldsymbol{\psi}^1}\boldsymbol{\psi}^1 + \frac{\partial \mathbf{f}}{\partial \boldsymbol{\psi}^2}\boldsymbol{\psi}^2.$$

Furthermore, it can already been seen that the numerical effort resulting from these variants might differ considerably. Already for the investigated angular velocity it seems that the third variant TS-LG, the one which has been chosen herein, leads to simpler expressions since the transformation matrix $\mathbf{T}^{-1}$ is not needed. This advantage is even more pronounced, when the angular accelerations have to be determined. While the variants TS-VS, ST-VS and ST-LG additionally require the time derivative of $\mathbf{T}^{-1}$, the expression for the angular acceleration $\mathbf{A}$ given for the variant TS-LG in the second line of (3.15) differs from the corresponding expression for the angular velocity $\mathbf{W}$ given in the first line of (3.15) only by a constant pre-factor. Based on this argumentation, the variant TS-LG has been preferred in this thesis - and in many works on this topic that can be found in the literature. The only additional requirement for such a procedure is that the employed time integration scheme has been extended for the usage on Lie groups.

B.3 Hermite constant for straight beams

In order to find the optimal choice for the constant c, in a first step, the simplest case of initially straight beams shall be considered. In this case, the nodal tangents can be written as

$$\hat{\mathbf{t}}_0 := \hat{\mathbf{t}}_0^1 = \hat{\mathbf{t}}_0^2 = \frac{\hat{\mathbf{d}}_0^2 - \hat{\mathbf{d}}_0^1}{||\hat{\mathbf{d}}_0^2 - \hat{\mathbf{d}}_0^1||} = \frac{\hat{\mathbf{d}}_0^2 - \hat{\mathbf{d}}_0^1}{l_{ele}}. \tag{B.4}$$

where $\hat{\mathbf{d}}_0^1$ and $\hat{\mathbf{d}}_0^2$ are the nodal coordinates and $l_{ele} = ||\hat{\mathbf{d}}_0^2 - \hat{\mathbf{d}}_0^1||$ is the element length. Inserting these nodal position vectors and tangent vectors into (3.43) yields:

$$\mathbf{r}_{0,h,\xi}(\xi) = \frac{1}{4}\left(3l_{ele} - c + 3\xi^2(c - l_{ele})\right)\hat{\mathbf{t}}_0. \tag{B.5}$$

According to (B.5), the choice $c = l_{ele}$ makes the Jacobian $J(\xi) = ||\mathbf{r}_{0h,\xi}(\xi)|| = ||\frac{l_{ele}}{2}\hat{\mathbf{t}}_0|| = \frac{l_{ele}}{2}$ constant, which is desirable for straight beams.

B.4 Hermite constant for curved beams

In Section B.3 it has been shown that the choice $c = l_{ele}$ leads to a constant element Jacobian. This result can not directly be transferred to initially curved beams. However, in the following, it will be shown that at least in the limit of $l_{ele} \to 0$ the element Jacobian becomes constant with an error in the order of $\mathcal{O}({l_{ele}}^4)$ if the constant c is chosen according to $c = l_{ele}$. For this case, it will also be shown that (3.39) enables an exact representation of the Taylor series expansion

$$\mathbf{r}_0(s + \Delta s) = \mathbf{r}_0(s) + \mathbf{r}_0'(s)\Delta s + \mathbf{r}_0''(s)\frac{\Delta s^2}{2} + \mathbf{r}_0'''(s)\frac{\Delta s^3}{6} + \mathcal{O}(\Delta s^4). \tag{B.6}$$

of the initial centerline curve $\mathbf{r}_0(s)$ up to terms of order $\mathcal{O}(\Delta s^4)$. This, in turn, confirms the expected discretization error of order $\mathcal{O}(\xi^4)$ for the employed third-order Hermite polynomials. For the following derivations, the derivatives of (B.6) are required. Differentiation of (B.6) yields:

$$\begin{aligned}\mathbf{r}_0'(s+\Delta s) &= \mathbf{r}_0'(s) + \mathbf{r}_0''(s)\Delta s + \mathbf{r}_0'''(s)\frac{\Delta s^2}{2} + \mathcal{O}(\Delta s^3),\\ \mathbf{r}_0''(s+\Delta s) &= \mathbf{r}_0''(s) + \mathbf{r}_0'''(s)\Delta s + \mathcal{O}(\Delta s^2).\end{aligned} \tag{B.7}$$

Since s has been chosen as an arc-length parameter, the following relations are valid:

$$\mathbf{r}_0'(s)\cdot\mathbf{r}_0'(s) = 1, \quad \mathbf{r}_0'(s)\cdot\mathbf{r}_0''(s) = 0, \quad \mathbf{r}_0''(s)\cdot\mathbf{r}_0''(s) + \mathbf{r}_0'(s)\cdot\mathbf{r}_0'''(s) = 0. \tag{B.8}$$

Making use of these relations allows for the following expansion of the tangent vector norm:

$$||\mathbf{r}_0'(s+\Delta s)|| = 1 + \mathcal{O}(\Delta s^3). \tag{B.9}$$

Now, the arc-length segment $\Delta s \in [-\frac{l_{ele}}{2}; \frac{l_{ele}}{2}]$ shall be discretized by an finite element of length l_{ele}. Thus, also the element length l_{ele} is a small quantity in the order of Δs. It follows from (B.6):

$$\begin{aligned}\hat{\mathbf{d}}_0^1 &= \mathbf{r}_0(s - l_{ele}/2) = \mathbf{r}_0(s) - \mathbf{r}_0'(s)\frac{l_{ele}}{2} + \mathbf{r}_0''(s)\frac{l_{ele}^2}{8} - \mathbf{r}_0'''(s)\frac{l_{ele}^3}{48} + \mathcal{O}({l_{ele}}^4),\\ \hat{\mathbf{d}}_0^2 &= \mathbf{r}_0(s + l_{ele}/2) = \mathbf{r}_0(s) + \mathbf{r}_0'(s)\frac{l_{ele}}{2} + \mathbf{r}_0''(s)\frac{l_{ele}^2}{8} + \mathbf{r}_0'''(s)\frac{l_{ele}^3}{48} + \mathcal{O}({l_{ele}}^4).\end{aligned} \tag{B.10}$$

Since the initial nodal tangents have to be of unit norm, the derivatives $\mathbf{r}_0'(s+l_{ele}/2)$ as well as $\mathbf{r}_0'(s-l_{ele}/2)$ according to (B.7) have to be normalized with the tangent vector norm (B.9):

$$\begin{aligned}\hat{\mathbf{t}}_0^1 &= \frac{\mathbf{r}_0'(s - l_{ele}/2)}{1 + \mathcal{O}({l_{ele}}^3)} = \mathbf{r}_0'(s) - \mathbf{r}_0''(s)\frac{l_{ele}}{2} + \mathbf{r}_0'''(s)\frac{l_{ele}^2}{8} + \mathcal{O}({l_{ele}}^3),\\ \hat{\mathbf{t}}_0^2 &= \frac{\mathbf{r}_0'(s + l_{ele}/2)}{1 + \mathcal{O}({l_{ele}}^3)} = \mathbf{r}_0'(s) + \mathbf{r}_0''(s)\frac{l_{ele}}{2} + \mathbf{r}_0'''(s)\frac{l_{ele}^2}{8} + \mathcal{O}({l_{ele}}^3).\end{aligned} \tag{B.11}$$

Inserting the nodal vectors (B.10) and (B.11) into (3.39) and assuming that the constant c is in the same order of magnitude as the element length, i.e. $c = \mathcal{O}(l_{ele})$, yields the discrete geometry:

$$\begin{aligned}\mathbf{r}_{0h}(\xi) = \mathbf{r}_0(s)&\\ &+ \frac{\mathbf{r}_0'(s)}{8}\left((6l_{ele} - 2c)\,\xi + (-2l_{ele} + 2c)\,\xi^3\right)\\ &+ \frac{\mathbf{r}_0''(s)}{16}\left(\left(2l_{ele}^2 - 2cl_{ele}\right) + 2cl_{ele}\xi^2\right)\\ &+ \frac{\mathbf{r}_0'''(s)}{64}\left(\left(2l_{ele}^3 - 2cl_{ele}^2\right)\xi + \left(-\frac{2}{3}l_{ele}^3 + 2cl_{ele}^2\right)\xi^3\right) + \mathcal{O}({l_{ele}}^4).\end{aligned} \tag{B.12}$$

In the following, a constant map between Δs and ξ is aimed in the limit of small Δs. Having the Taylor series (B.6) in mind, in this case, the discretized geometry has to be of the form

$$\mathbf{r}_{0h}(\xi) = \mathbf{r}_0(s) + \mathbf{r}_0'(s)a_1\xi + \mathbf{r}_0''(s)a_2\xi^2 + \mathbf{r}_0'''(s)a_3\xi^3 + \mathcal{O}(\Delta s^4), \tag{B.13}$$

where the coefficients a_i depend on the constant map between Δs and ξ. From (B.12), it becomes clear that such a form is only possible for the choice $c = l_{ele}$. In this case, (B.12) simplifies to:

$$\mathbf{r}_{0h}(\xi) = \mathbf{r}_0(s) + \mathbf{r}_0'(s)\left(\frac{l_{ele}}{2}\xi\right) + \mathbf{r}_0''(s)\frac{1}{2}\left(\frac{l_{ele}}{2}\xi\right)^2 + \mathbf{r}_0'''(s)\frac{1}{6}\left(\frac{l_{ele}}{2}\xi\right)^3 + \mathcal{O}({l_{ele}}^4). \tag{B.14}$$

By inserting the vectors (B.10) and (B.11) into (3.43) with $c=l_{ele}$, the derivative $\mathbf{r}_{0h,\xi}$ becomes:

$$\mathbf{r}_{0h,\xi}(\xi) = \mathbf{r}_0'(s)\frac{l_{ele}}{2} + \mathbf{r}_0''(s)\frac{l_{ele}^2}{4}\xi + \mathbf{r}_0'''(s)\frac{l_{ele}^3}{16}\xi^2 + \mathcal{O}({l_{ele}}^4). \tag{B.15}$$

With (B.8), also the discrete norm $||\mathbf{r}_{0h,\xi}(\xi)||$ can be expanded as a Taylor series according to

$$||\mathbf{r}_{0h,\xi}(\xi)|| = \frac{l_{ele}}{2}\left(1 + O(l_{ele}^3)\right) = \frac{l_{ele}}{2} + \mathcal{O}(l_{ele}^4). \tag{B.16}$$

As desired, the result is a constant map $d\Delta s = ||\mathbf{r}_{0h,\xi}(\xi)||d\xi = \frac{l_{ele}}{2}d\xi + \mathcal{O}(l_{ele}^4)$ between arc-length and normalized parameter. With $\Delta s(\xi=-1) = -\frac{l_{ele}}{2}$ and $\Delta s(\xi=1) = \frac{l_{ele}}{2}$, one obtains

$$\Delta s = \frac{l_{ele}}{2}\xi + \mathcal{O}(l_{ele}^4). \tag{B.17}$$

Due to this constant map, the parameter choice $c=l_{ele}$ as well as the parameter choice

$$c = l_{ele,h} = \int_{-1}^{1}\left(\frac{l_{ele}}{2} + O(l^4)\right)d\xi = l_{ele} + \mathcal{O}(l^4), \tag{B.18}$$

are equal up to terms of order $\mathcal{O}(l_{ele}^4)$. It can easily be derived from (B.10) that the choice $c = ||\hat{\mathbf{d}}_0^2 - \hat{\mathbf{d}}_0^1|| = l_{ele} + \mathcal{O}(l_{ele}^3)$ equals the choice $c = l_{ele}$ up to terms of order $\mathcal{O}(l_{ele}^3)$. By inserting (B.17) into (B.14), the identity of the discretized geometry with the Taylor series (B.6) up to terms $\mathcal{O}(l_{ele}^4)$ can be shown. It can be concluded that for the choice $c = l_{ele}$ the third-order Taylor expansion of the analytic geometry $\mathbf{r}_0(\Delta s)$ can exactly be represented by the discretized geometry $\mathbf{r}_{0h}(\xi)$. For the deformed geometry $\mathbf{r}(\Delta s)$, it can be shown in a similar manner that the choice $c = l_{ele}$ leads to a constant value of $||\mathbf{r}_{h,\xi}(\xi)||$ up to terms $\mathcal{O}(l_{ele}^4)$, which is equivalent to a constant axial tension ϵ along the element. It should be emphasized that also in the latter case the initial element length l_{ele}, but *not* the current element length, has to be chosen for the sought-after Hermite constant c. Again, a third-order Taylor expansion of the analytic deformed geometry $\mathbf{r}(\Delta s)$ can exactly be represented by the discretized geometry $\mathbf{r}_h(\xi)$. Thus, for the choice $c = l_{ele}$, the discretization error stemming from the pure geometry approximation of $\mathbf{r}(s)$ by $\mathbf{r}_h(\xi)$ can be assumed to be of order $\mathcal{O}(l_{ele}^4)$, which is expected for polynomials of order three. All in all, it can be concluded that the initial element length l_{ele} turned out to be the optimal choice for the constant c appearing in the Hermite interpolation according to (3.39). Whereas the legitimacy of the approximations $c = l_{ele,h}$ has been confirmed, the approximation $c = ||\hat{\mathbf{d}}^2 - \hat{\mathbf{d}}^1||$ might lead to a decrease in the convergence order from $\mathcal{O}(l_{ele}^4)$ to $\mathcal{O}(l_{ele}^3)$.

B.5 Definition of rotational shape function matrices

In this appendix, the shape functions $\tilde{\mathbf{I}}^i(\xi)$ required for the multiplicative rotation increments

$$\Delta\boldsymbol{\theta}(\xi) = \sum_{i=1}^{n_\Lambda} \tilde{\mathbf{I}}^i(\xi)\Delta\hat{\boldsymbol{\theta}}^i, \quad \Delta\boldsymbol{\theta}'(\xi) = \sum_{i=1}^{n_\Lambda} \tilde{\mathbf{I}}^{i\prime}(\xi)\Delta\hat{\boldsymbol{\theta}}^i. \tag{B.19}$$

associated with the triad interpolation 3.55 and originally derived in [116] shall be presented:

$$\begin{aligned}\tilde{\mathbf{I}}^i(\xi) &= L^i(\xi)\boldsymbol{\Lambda}_r\mathbf{T}^{-1}(\boldsymbol{\Phi}_{lh}(\xi))\mathbf{T}(\boldsymbol{\Phi}_l^i)\boldsymbol{\Lambda}_r^T \\ &+ \delta^{iI}\boldsymbol{\Lambda}_r\left[\mathbf{I_3} - \mathbf{T}^{-1}(\boldsymbol{\Phi}_{lh}(\xi))\left\{\sum_{j=1}^{n_\Lambda} L^j(\xi)\mathbf{T}(\boldsymbol{\Phi}_l^j)\right\}\right]\mathbf{v}^I\boldsymbol{\Lambda}_r^T \\ &+ \delta^{iJ}\boldsymbol{\Lambda}_r\left[\mathbf{I_3} - \mathbf{T}^{-1}(\boldsymbol{\Phi}_{lh}(\xi))\left\{\sum_{j=1}^{n_\Lambda} L^j(\xi)\mathbf{T}(\boldsymbol{\Phi}_l^j)\right\}\right]\mathbf{v}^J\boldsymbol{\Lambda}_r^T.\end{aligned} \tag{B.20}$$

In (B.20), no summation over double indices is applied. The vectors $\mathbf{v}^I$ and $\mathbf{v}^J$ are defined as

$$\mathbf{v}^I = \frac{1}{2}\left(\mathbf{I}_3 + \frac{1}{\Phi^{IJ}}\tan\left(\frac{\Phi^{IJ}}{4}\right)\mathbf{S}(\boldsymbol{\Phi}^{IJ})\right), \quad \mathbf{v}^J = \frac{1}{2}\left(\mathbf{I}_3 - \frac{1}{\Phi^{IJ}}\tan\left(\frac{\Phi^{IJ}}{4}\right)\mathbf{S}(\boldsymbol{\Phi}^{IJ})\right), \tag{B.21}$$

with the common abbreviation $\Phi^{IJ} = ||\boldsymbol{\Phi}^{IJ}||$. Moreover, the arc-length derivative $\tilde{\mathbf{I}}^{i\prime}(\xi)$ reads:

$$\begin{aligned}&\tilde{\mathbf{I}}^i(\xi) = L^{i\prime}(\xi)\boldsymbol{\Lambda}_r\mathbf{T}^{-1}(\boldsymbol{\Phi}_{lh}(\xi))\mathbf{T}(\boldsymbol{\Phi}_l^i)\boldsymbol{\Lambda}_r^T + L^i(\xi)\boldsymbol{\Lambda}_r\mathbf{T}_{,s}^{-1}(\boldsymbol{\Phi}_{lh}(\xi))\mathbf{T}(\boldsymbol{\Phi}_l^i)\boldsymbol{\Lambda}_r^T \\ &- \delta^{iI}\boldsymbol{\Lambda}_r\left(\mathbf{T}_{,s}^{-1}(\boldsymbol{\Phi}_{lh}(\xi))\left\{\sum_{j=1}^{n_\Lambda} L^j(\xi)\mathbf{T}(\boldsymbol{\Phi}_l^j)\right\} + \mathbf{T}^{-1}(\boldsymbol{\Phi}_{lh}(\xi))\left\{\sum_{j=1}^{n_\Lambda} L^{j\prime}(\xi)\mathbf{T}(\boldsymbol{\Phi}_l^j)\right\}\right)\mathbf{v}^I\boldsymbol{\Lambda}_r^T \\ &- \delta^{iJ}\boldsymbol{\Lambda}_r\left(\mathbf{T}_{,s}^{-1}(\boldsymbol{\Phi}_{lh}(\xi))\left\{\sum_{j=1}^{n_\Lambda} L^j(\xi)\mathbf{T}(\boldsymbol{\Phi}_l^j)\right\} + \mathbf{T}^{-1}(\boldsymbol{\Phi}_{lh}(\xi))\left\{\sum_{j=1}^{n_\Lambda} L^{j\prime}(\xi)\mathbf{T}(\boldsymbol{\Phi}_l^j)\right\}\right)\mathbf{v}^J\boldsymbol{\Lambda}_r^T.\end{aligned} \tag{B.22}$$

Finally, the required arc-length derivative $\mathbf{T}_{,s}^{-1}(\boldsymbol{\Phi}_{lh}(\xi))$ is given by (see also [56, 115]):

$$\begin{aligned}\mathbf{T}_{,s}^{-1}(\boldsymbol{\Phi}_{lh}(\xi)) &= \boldsymbol{\Phi}_{lh}^T\boldsymbol{\Phi}_{lh}'\frac{\Phi_{lh}\sin\Phi_{lh} - 2(1-\cos\Phi_{lh})}{\Phi_{lh}^4}\mathbf{S}(\boldsymbol{\Phi}_{lh}) + \frac{1-\cos\Phi_{lh}}{\Phi_{lh}^2}\mathbf{S}(\boldsymbol{\Phi}_{lh}') \\ &+ \frac{1}{\Phi_{lh}^2}\left(1 - \frac{\sin\Phi_{lh}}{\Phi_{lh}}\right)(\mathbf{S}(\boldsymbol{\Phi}_{lh})\mathbf{S}(\boldsymbol{\Phi}_{lh}') + \mathbf{S}(\boldsymbol{\Phi}_{lh}')\mathbf{S}(\boldsymbol{\Phi}_{lh})) \\ &+ \boldsymbol{\Phi}_{lh}^T\boldsymbol{\Phi}_{lh}'\frac{3\sin\Phi_{lh} - \Phi_{lh}(2+\cos\Phi_{lh})}{\Phi_{lh}^5}\mathbf{S}(\boldsymbol{\Phi}_{lh})\mathbf{S}(\boldsymbol{\Phi}_{lh}).\end{aligned} \tag{B.23}$$

Here, the abbreviations $\boldsymbol{\Phi}_{lh} = \boldsymbol{\Phi}_{lh}(\xi)$ and $\Phi_{lh} = ||\boldsymbol{\Phi}_{lh}(\xi)||$ have been applied. As mentioned in [116], the limit $\mathbf{T}_{,s}^{-1}(\boldsymbol{\Phi}_{lh}(\xi)) \to 0.5\mathbf{S}(\boldsymbol{\Phi}_{lh}'(\xi))$ can be derived for small angles $\boldsymbol{\Phi}_{lh}(\xi) \to \mathbf{0}$.

B.6 Linearization of SK-TAN element

Before deriving the linearization of the SK-TAN element, some former definitions are repeated:

$$\mathbf{t} := \mathbf{r}', \quad \mathbf{g}_1 := \frac{\mathbf{r}'}{||\mathbf{r}'||}, \quad \tilde{\mathbf{t}} := \frac{\mathbf{r}'}{||\mathbf{r}'||^2}, \quad \mathbf{g}_1' = \frac{\mathbf{r}''}{||\mathbf{r}'||} - \frac{(\mathbf{r}'^T\mathbf{r}'')\mathbf{r}'}{||\mathbf{r}'||^3}, \quad \tilde{\mathbf{t}}' = \frac{\mathbf{r}''}{||\mathbf{r}'||^2} - \frac{2(\mathbf{r}'^T\mathbf{r}'')\mathbf{r}'}{||\mathbf{r}'||^4}. \tag{B.24}$$

These quantities will be required for later derivations. Linearization of (B.24) yields:

$$\begin{aligned}
\Delta\mathbf{g}_1 &= \frac{1}{||\mathbf{r}'||}\left(\mathbf{I}_3 - \mathbf{g}_1\otimes\mathbf{g}_1^T\right)\mathbf{H}'\Delta\hat{\mathbf{d}}, \qquad \Delta\tilde{\mathbf{t}} = \frac{1}{||\mathbf{r}'||^2}\left(\mathbf{I}_3 - 2\mathbf{g}_1\otimes\mathbf{g}_1^T\right)\mathbf{H}'\Delta\hat{\mathbf{d}}, \\
\Delta\mathbf{g}_1' &= -\frac{(\mathbf{r}'^T\mathbf{r}'')}{||\mathbf{r}'||^3}\left(\mathbf{I}_3 - \mathbf{g}_1\otimes\mathbf{g}_1^T\right)\mathbf{H}'\Delta\hat{\mathbf{d}} - \frac{1}{||\mathbf{r}'||}\left(\mathbf{g}_1'\otimes\mathbf{g}_1^T + \mathbf{g}_1\otimes\mathbf{g}_1'^T\right)\mathbf{H}'\Delta\hat{\mathbf{d}} \\
&\quad + \frac{1}{||\mathbf{r}'||}\left(\mathbf{I}_3 - \mathbf{g}_1\otimes\mathbf{g}_1^T\right)\mathbf{H}''\Delta\hat{\mathbf{d}}, \\
\Delta\tilde{\mathbf{t}}' &= -\frac{2(\mathbf{r}'^T\mathbf{r}'')}{||\mathbf{r}'||^4}\left(\mathbf{I}_3 - 2\mathbf{g}_1\otimes\mathbf{g}_1^T\right)\mathbf{H}'\Delta\hat{\mathbf{d}} - \frac{2}{||\mathbf{r}'||^2}\left(\mathbf{g}_1'\otimes\mathbf{g}_1^T + \mathbf{g}_1\otimes\mathbf{g}_1'^T\right)\mathbf{H}'\Delta\hat{\mathbf{d}} \\
&\quad + \frac{1}{||\mathbf{r}'||^2}\left(\mathbf{I}_3 - 2\mathbf{g}_1\otimes\mathbf{g}_1^T\right)\mathbf{H}''\Delta\hat{\mathbf{d}}.
\end{aligned} \tag{B.25}$$

In the following, the linearization of the SK-TAN element will be derived. For completeness, the underlying residual vector (3.123) with inserted strain re-interpolation (3.124) is repeated here:

$$\begin{aligned}
\mathbf{r}_{\hat{\mathbf{d}}} &= \int_{-1}^{1}\left(\mathbf{v}_{\theta_\perp}'\mathbf{m} + \bar{\mathbf{v}}_\epsilon\bar{F}_1 - \mathbf{H}^T\tilde{\mathbf{f}}_\rho - \mathbf{v}_{\theta_\perp}\tilde{\mathbf{m}}_\rho\right)J(\xi)d\xi - \left[\mathbf{H}^T\mathbf{f}_\sigma + \mathbf{v}_{\theta_\perp}\mathbf{m}_\sigma\right]_{\Gamma_\sigma}, \\
\mathbf{r}_{\hat{\Theta}_1} &= \int_{-1}^{1}\left(\mathbf{v}_{\theta_{\|\Theta}}'\mathbf{m} - \mathbf{v}_{\theta_{\|\Theta}}\tilde{\mathbf{m}}_\rho\right)J(\xi)d\xi - \left[\mathbf{v}_{\theta_{\|\Theta}}\mathbf{m}_\sigma\right]_{\Gamma_\sigma}.
\end{aligned} \tag{B.26}$$

The linearization of the element residual vector (B.26) obeys the following general form:

$$\begin{aligned}
\Delta\mathbf{r}_{\hat{\mathbf{d}}} &= \int_{-1}^{1}\left(\Delta\mathbf{v}_{\theta_\perp}'\mathbf{m} + \mathbf{v}_{\theta_\perp}'\Delta\mathbf{m} + \Delta\bar{\mathbf{v}}_\epsilon\bar{F}_1 + \bar{\mathbf{v}}_\epsilon\Delta\bar{F}_1\right)J(\xi)d\xi \\
&\quad - \int_{-1}^{1}\left(\mathbf{H}^T\Delta\mathbf{f}_\rho + \Delta\mathbf{v}_{\theta_\perp}\tilde{\mathbf{m}}_\rho + \mathbf{v}_{\theta_\perp}\Delta\mathbf{m}_\rho\right)J(\xi)d\xi - \left[\Delta\mathbf{v}_{\theta_\perp}\mathbf{m}_\sigma\right]_{\Gamma_\sigma}, \\
\Delta\mathbf{r}_{\hat{\Theta}_1} &= \int_{-1}^{1}\left(\Delta\mathbf{v}_{\theta_{\|\Theta}}'\mathbf{m} + \mathbf{v}_{\theta_{\|\Theta}}'\Delta\mathbf{m} - \Delta\mathbf{v}_{\theta_{\|\Theta}}\tilde{\mathbf{m}}_\rho - \mathbf{v}_{\theta_{\|\Theta}}\Delta\mathbf{m}_\rho\right)J(\xi)d\xi - \left[\Delta\mathbf{v}_{\theta_{\|\Theta}}\mathbf{m}_\sigma\right]_{\Gamma_\sigma}.
\end{aligned} \tag{B.27}$$

In order to identify the element stiffness matrix $\mathbf{k}_{SK-TAN}$, (B.27) has to be brought in the form

$$\Delta\mathbf{r}_{SK-TAN} =: \mathbf{k}_{SK-TAN}\Delta\hat{\mathbf{x}}_{TAN}. \tag{B.28}$$

The vector $\Delta\hat{\mathbf{x}}_{TAN}$ has already been defined in Section 3.4.1. The moment-related terms yield:

$$\begin{aligned}
\Delta\mathbf{v}'_{\theta_\perp}\mathbf{m} &= \mathbf{H}''^T\mathbf{S}(\mathbf{m})\Delta\tilde{\mathbf{t}}+\mathbf{H}'^T\mathbf{S}(\mathbf{m})\Delta\tilde{\mathbf{t}}', \quad \Delta\mathbf{m} = -\mathbf{S}(\mathbf{m})\Delta\boldsymbol{\theta}+\mathbf{c}_m\Delta\boldsymbol{\theta}', \\
\Delta\mathbf{v}_{\theta_\perp}\tilde{\mathbf{m}}_\rho &= \mathbf{H}'^T\mathbf{S}(\tilde{\mathbf{m}}_\rho)\Delta\tilde{\mathbf{t}}, \qquad \Delta\mathbf{v}_{\theta_\perp}\mathbf{m}_\sigma = \mathbf{H}'^T\mathbf{S}(\mathbf{m}_\sigma)\Delta\tilde{\mathbf{t}}, \\
\Delta\mathbf{v}_{\theta_{\parallel\Theta}}\tilde{\mathbf{m}}_\rho &= (\mathbf{L}_\parallel^T\otimes\tilde{\mathbf{m}}_\rho^T)\Delta\mathbf{g}_1, \qquad \Delta\mathbf{v}_{\theta_{\parallel\Theta}}\mathbf{m}_\sigma = (\mathbf{L}_\parallel^T\otimes\mathbf{m}_\sigma^T)\Delta\mathbf{g}_1, \\
\Delta\mathbf{v}'_{\theta_{\parallel\Theta}}\mathbf{m} &= (\mathbf{L}_\parallel'^T\otimes\mathbf{m}^T)\Delta\mathbf{g}_1+(\mathbf{L}_\parallel^T\otimes\mathbf{m}^T)\Delta\mathbf{g}'_1.
\end{aligned} \tag{B.29}$$

Here, many of the relations already derived in Section 3.2.3.4 could be re-used. The field of multiplicative rotation vector increments $\Delta\boldsymbol{\theta}$ follows directly from equation (3.71):

$$\begin{aligned}
\Delta\boldsymbol{\theta} &= \mathbf{v}_{\theta_{\parallel\Theta}}^T\Delta\hat{\boldsymbol{\Theta}}_1+(\mathbf{v}_{\theta_\perp}^T+\mathbf{v}_{\theta_{\parallel d}}^T)\Delta\hat{\mathbf{d}}, \\
\mathbf{v}_{\theta_{\parallel\Theta}} &= \mathbf{L}_\parallel^T\otimes\mathbf{g}_1^T, \quad \mathbf{v}_{\theta_\perp} = -\mathbf{H}'^T\mathbf{S}(\tilde{\mathbf{t}}), \\
\mathbf{v}_{\theta_{\parallel d}} &= \left(\sum_{i=1}^{n_\Lambda} L^i\,\mathbf{v}_{1i}-\mathbf{v}_1\right)\otimes\mathbf{g}_1^T, \quad \mathbf{v}_1 = \frac{\mathbf{H}'^T(\xi)(\mathbf{g}_1^I\times\tilde{\mathbf{t}}) - \mathbf{H}'^T(\xi_I)(\mathbf{g}_1\times\tilde{\mathbf{t}}^I)}{1+\mathbf{g}_1^T\mathbf{g}_1^I}, \\
\mathbf{v}_{1i} &= \mathbf{v}_1(\xi_i) = \frac{\mathbf{H}'^T(\xi_i)(\mathbf{g}_1^I\times\tilde{\mathbf{t}}^i) - \mathbf{H}'^T(\xi_I)(\mathbf{g}_1^i\times\tilde{\mathbf{t}}^I)}{1+\mathbf{g}_1^{iT}\mathbf{g}_1^I}.
\end{aligned} \tag{B.30}$$

In a similar manner, the associated arc-length derivative $\Delta\boldsymbol{\theta}'$ follows from equation (3.72):

$$\begin{aligned}
\Delta\boldsymbol{\theta}' &= \mathbf{v}_{\theta_{\parallel\Theta}}'^T\Delta\hat{\boldsymbol{\Theta}}_1+(\mathbf{v}_{\theta_\perp}'^T+\mathbf{v}_{\theta_{\parallel d}}'^T)\Delta\hat{\mathbf{d}}, \\
\mathbf{v}'_{\theta_{\parallel\Theta}} &= \mathbf{L}_\parallel'^T\otimes\mathbf{g}_1^T+\mathbf{L}_\parallel^T\otimes\mathbf{g}_1'^T, \quad \mathbf{v}'_{\theta_\perp} = -\mathbf{H}''^T\mathbf{S}(\tilde{\mathbf{t}})-\mathbf{H}'^T\mathbf{S}(\tilde{\mathbf{t}}'), \quad \tilde{\mathbf{t}}' = \frac{\mathbf{r}''}{||\mathbf{r}'||^2}-\frac{2(\mathbf{r}'^T\mathbf{r}'')\mathbf{r}'}{||\mathbf{r}'||^4}, \\
\mathbf{v}'_{\theta_{\parallel d}} &= \Big(\sum_{i=1}^{n_\Lambda} L^{i\prime}\,\mathbf{v}_{1i}-\mathbf{v}'_1\Big)\otimes\mathbf{g}_1^T+\Big(\sum_{i=1}^{n_\Lambda} L^i\,\mathbf{v}_{1i}-\mathbf{v}_1\Big)\otimes\mathbf{g}_1'^T, \\
\mathbf{v}'_1 &= \frac{\mathbf{H}'^T(\xi)(\mathbf{g}_1^I\times\tilde{\mathbf{t}}')+\mathbf{H}''^T(\xi)(\mathbf{g}_1^I\times\tilde{\mathbf{t}})-\mathbf{H}'^T(\xi_I)(\mathbf{g}'_1\times\tilde{\mathbf{t}}^I)}{1+\mathbf{g}_1^T\mathbf{g}_1^I}-\frac{(\mathbf{g}_1'^T\mathbf{g}_1^I)\mathbf{v}_1}{1+\mathbf{g}_1^T\mathbf{g}_1^I}.
\end{aligned} \tag{B.31}$$

The remaining linearizations required in equation (B.29) have already been derived in (B.25). In contrast to the spin vector field $\delta\boldsymbol{\theta}$, the increment field $\Delta\boldsymbol{\theta}$ has to be expressed via additive relative angle increments $\Delta\hat{\varphi}^i$. The required relation is given by (3.77) and repeated here:

$$\Delta\hat{\boldsymbol{\Theta}}_1 = (\hat{\Theta}_1^1,\hat{\Theta}_1^2,\hat{\Theta}_1^3)^T, \quad \Delta\hat{\Theta}_1^i = -\frac{\bar{\mathbf{g}}_1^{iT}\mathbf{S}(\mathbf{g}_1^i)}{1+\mathbf{g}_1^{iT}\bar{\mathbf{g}}_1^i}\frac{\mathbf{H}'(\xi^i)\Delta\hat{\mathbf{d}}}{||\mathbf{t}^i||}+\Delta\hat{\varphi}^i. \tag{B.32}$$

The linearization of the element residual terms associated with axial tension results in:

$$\Delta\bar{F}_1 = EA\Delta\bar{\epsilon} = EA\bar{\mathbf{v}}_\epsilon^T\Delta\hat{\mathbf{d}}, \quad \Delta\bar{\mathbf{v}}_\epsilon = \sum_{i=1}^{3} L^i(\xi)\Delta\mathbf{v}_\epsilon(\xi^i), \quad \Delta\mathbf{v}_\epsilon = \frac{\mathbf{H}'^T}{||\mathbf{r}'||}(\mathbf{I}_3+\mathbf{g}_1\otimes\mathbf{g}_1^T)\mathbf{H}'\Delta\hat{\mathbf{d}}. \tag{B.33}$$

Based on equation (3.14), the linearization of the inertia forces can be written as:

$$-\mathbf{H}^T\Delta\mathbf{f}_\rho = \rho A c_{\ddot{\mathbf{r}}1}\mathbf{H}^T\mathbf{H}\Delta\hat{\mathbf{d}}, \quad c_{\ddot{\mathbf{r}}1} = \frac{1-\alpha_m}{(1-\alpha_m)\beta\Delta t^2}. \tag{B.34}$$

The time integration factor $c_{\dot{\mathbf{r}}1}$ of the modified generalized-α scheme according to Section 3.1.2 slightly differs from the corresponding factor of the standard generalized-α scheme according to Section 3.1.1 (see (B.59) for comparison). The linearization of the inertia moments yields:

$$\begin{aligned} -\Delta\mathbf{m}_\rho &= \mathbf{S}(\mathbf{m}_\rho)\Delta\boldsymbol{\theta} + [c_{\mathbf{W}}\{\mathbf{S}(\mathbf{W})\mathbf{C}_\rho - \mathbf{S}(\mathbf{C}_\rho\mathbf{W})\} + c_{\mathbf{A}}\mathbf{C}_\rho]\Delta\tilde{\boldsymbol{\Theta}}_{n+1}, \\ c_{\mathbf{A}} &= \frac{1-\alpha_m}{(1-\alpha_m)\beta\Delta t^2}, \quad c_{\mathbf{W}} = \frac{\gamma}{\beta\Delta t}, \quad \Delta\tilde{\boldsymbol{\Theta}}_{n+1} = \boldsymbol{\Lambda}_n^T\Delta\tilde{\boldsymbol{\theta}}_{n+1} = \boldsymbol{\Lambda}_n^T\mathbf{T}(\tilde{\boldsymbol{\theta}}_{n+1})\Delta\boldsymbol{\theta}. \end{aligned} \tag{B.35}$$

For clarity, the indices $n+1$ and n of the current and previous time step have explicitly been noted for some of the quantities occurring in (B.35). All the other quantities are evaluated at t_{n+1}. As already introduced in Section 3.1.2, the fields $\tilde{\boldsymbol{\Theta}}_{n+1}$ and $\tilde{\boldsymbol{\theta}}_{n+1}$ are the material and spatial multiplicative rotation increments relating the current configuration and the converged configuration of the previous time step t_n. The two vectors are related by the transformation

$$\tilde{\boldsymbol{\Theta}}_{n+1} = \boldsymbol{\Lambda}_{n+1}^T\tilde{\boldsymbol{\theta}}_{n+1} = \boldsymbol{\Lambda}_n^T\tilde{\boldsymbol{\theta}}_{n+1} \rightarrow \Delta\tilde{\boldsymbol{\Theta}}_{n+1} = \boldsymbol{\Lambda}_n^T\Delta\tilde{\boldsymbol{\theta}}_{n+1}. \tag{B.36}$$

The second step in (B.36) is valid since $\tilde{\boldsymbol{\theta}}_{n+1}$ is an eigenvector with eigenvalue one of the rotation tensor $\boldsymbol{\Lambda}_{n+1}\boldsymbol{\Lambda}_n^T$ between the configurations n and $n+1$, thus $\boldsymbol{\Lambda}_{n+1}\boldsymbol{\Lambda}_n^T\tilde{\boldsymbol{\theta}}_{n+1} = \tilde{\boldsymbol{\theta}}_{n+1}$. Furthermore, $\Delta\tilde{\boldsymbol{\Theta}}_{n+1}$ and $\Delta\tilde{\boldsymbol{\theta}}_{n+1}$ represent the fields of additive increments of $\tilde{\boldsymbol{\Theta}}_{n+1}$ and $\tilde{\boldsymbol{\theta}}_{n+1}$ between two successive Newton iterations, whereas $\Delta\boldsymbol{\theta}$ as given by (B.30) represents the field of multiplicative rotation increments between two successive Newton iterations.

B.7 Linearization of WK-TAN element

The residual vector of the WK-TAN element is given in equation (3.155) and repeated here:

$$\begin{aligned} \mathbf{r}_{\hat{\mathbf{d}}} &= \int_{-1}^{1}\left(\bar{\mathbf{v}}'_{\theta_\perp}\mathbf{m} + \bar{\mathbf{v}}_\epsilon\bar{F}_1 - \mathbf{H}^T\tilde{\mathbf{f}}_\rho - \bar{\mathbf{v}}_{\theta_\perp}\tilde{\mathbf{m}}_\rho\right)J(\xi)d\xi - \left[\mathbf{H}^T\mathbf{f}_\sigma + \bar{\mathbf{v}}_{\theta_\perp}\mathbf{m}_\sigma\right]_{\Gamma_\sigma}, \\ \mathbf{r}_{\hat{\boldsymbol{\Theta}}_1} &= \int_{-1}^{1}\left(\bar{\mathbf{v}}'_{\theta_{\parallel\Theta}}\mathbf{m} - \bar{\mathbf{v}}_{\theta_{\parallel\Theta}}\tilde{\mathbf{m}}_\rho\right)J(\xi)d\xi - \left[\bar{\mathbf{v}}_{\theta_{\parallel\Theta}}\mathbf{m}_\sigma\right]_{\Gamma_\sigma}. \end{aligned} \tag{B.37}$$

The linearization of the element residual vector (B.37) obeys the following general form:

$$\begin{aligned} \Delta\mathbf{r}_{\hat{\mathbf{d}}} &= \int_{-1}^{1}\left(\Delta\bar{\mathbf{v}}'_{\theta_\perp}\mathbf{m} + \bar{\mathbf{v}}'_{\theta_\perp}\Delta\mathbf{m} + \Delta\bar{\mathbf{v}}_\epsilon\bar{F}_1 + \bar{\mathbf{v}}_\epsilon\Delta\bar{F}_1\right)J(\xi)d\xi \\ &\quad - \int_{-1}^{1}\left(\mathbf{H}^T\Delta\mathbf{f}_\rho + \Delta\bar{\mathbf{v}}_{\theta_\perp}\tilde{\mathbf{m}}_\rho + \bar{\mathbf{v}}_{\theta_\perp}\Delta\mathbf{m}_\rho\right)J(\xi)d\xi - \left[\Delta\bar{\mathbf{v}}_{\theta_\perp}\mathbf{m}_\sigma\right]_{\Gamma_\sigma}, \\ \Delta\mathbf{r}_{\hat{\boldsymbol{\Theta}}_1} &= \int_{-1}^{1}\left(\Delta\bar{\mathbf{v}}'_{\theta_{\parallel\Theta}}\mathbf{m} + \bar{\mathbf{v}}'_{\theta_{\parallel\Theta}}\Delta\mathbf{m} - \Delta\bar{\mathbf{v}}_{\theta_{\parallel\Theta}}\tilde{\mathbf{m}}_\rho - \bar{\mathbf{v}}_{\theta_{\parallel\Theta}}\Delta\mathbf{m}_\rho\right)J(\xi)d\xi - \left[\Delta\bar{\mathbf{v}}_{\theta_{\parallel\Theta}}\mathbf{m}_\sigma\right]_{\Gamma_\sigma}. \end{aligned} \tag{B.38}$$

In order to identify the element stiffness matrix $\mathbf{k}_{WK-TAN}$, (B.38) has to be brought in the form

$$\Delta \mathbf{r}_{WK-TAN} =: \mathbf{k}_{WK-TAN} \Delta \hat{\mathbf{x}}_{TAN}. \tag{B.39}$$

The linearization of the vectors $\bar{\mathbf{v}}_{...}$ and $\bar{\mathbf{v}}'_{...}$ originally defined in (3.155) follows to:

$$\begin{aligned} \Delta \bar{\mathbf{v}}_{\theta_\perp} &= -\sum_{i=1}^{3} L^i(\xi) \Delta \mathbf{v}_{\theta_\perp}(\xi^i), \quad \Delta \bar{\mathbf{v}}_{\epsilon} = \sum_{i=1}^{3} L^i(\xi) \Delta \mathbf{v}_{\epsilon}(\xi^i), \\ \Delta \bar{\mathbf{v}}_{\theta_{\parallel\Theta}} &= \sum_{i=1}^{3} L^i(\xi) \Delta \mathbf{v}_{\theta_{\parallel\Theta}}(\xi^i) \quad \text{with} \quad \Delta \bar{\mathbf{v}}'_{...} = \sum_{i=1}^{3} \frac{L^i, \xi(\xi)}{J(\xi)} \Delta \mathbf{v}_{...}(\xi^i). \end{aligned} \tag{B.40}$$

The linearization of the vectors $\mathbf{v}_{...}$ and $\mathbf{v}'_{...}$ has already been stated in the last section. Also the linearization of the moment stress resultant has the same form as in the last section:

$$\Delta \mathbf{m} = -\mathbf{S}(\mathbf{m}) \Delta \boldsymbol{\theta} + \mathbf{c}_m \Delta \boldsymbol{\theta}'. \tag{B.41}$$

However, the fields $\Delta\boldsymbol{\theta}$ and $\Delta\boldsymbol{\theta}'$ originally defined in Section 3.2.3.3 are this time given by

$$\Delta \boldsymbol{\theta} = \sum_{i=1}^{3} \tilde{\mathbf{I}}^i(\xi) \Delta \boldsymbol{\theta}(\xi^i), \quad \Delta \boldsymbol{\theta}' = \sum_{i=1}^{3} \frac{1}{J(\xi)} \tilde{\mathbf{I}}^i_{,\xi}(\xi) \Delta \boldsymbol{\theta}(\xi^i). \tag{B.42}$$

Due to the Kirchhoff constraint, the nodal increments $\Delta\boldsymbol{\theta}(\xi^i)$ can be expressed according to:

$$\Delta \boldsymbol{\theta}(\xi^i) = \Delta \hat{\Theta}^i_1 \mathbf{g}_1(\xi^i) + \mathbf{v}^T_{\theta_\perp}(\xi^i) \Delta \hat{\mathbf{d}}, \quad \Delta \hat{\Theta}^i_1 = -\frac{\bar{\mathbf{g}}^{iT}_1 \mathbf{S}(\mathbf{g}^i_1)}{1 + \mathbf{g}^{iT}_1 \bar{\mathbf{g}}^i_1} \frac{\mathbf{H}'(\xi^i) \Delta \hat{\mathbf{d}}}{||\mathbf{t}^i||} + \Delta \hat{\varphi}^i. \tag{B.43}$$

The linearization of the inertia forces is identical to the corresponding results of the last section:

$$-\mathbf{H}^T \Delta \mathbf{f}_\rho = \rho A c_{\ddot{\mathbf{r}}1} \mathbf{H}^T \mathbf{H} \Delta \hat{\mathbf{d}}, \quad c_{\ddot{\mathbf{r}}1} = \frac{1 - \alpha_m}{(1 - \alpha_m) \beta \Delta t^2}. \tag{B.44}$$

This statement also holds for the linearization of the inertia moments, which reads:

$$\begin{aligned} -\Delta \mathbf{m}_\rho &= \mathbf{S}(\mathbf{m}_\rho) \Delta \boldsymbol{\theta} + [c_{\mathbf{W}} \{\mathbf{S}(\mathbf{W}) \mathbf{C}_\rho - \mathbf{S}(\mathbf{C}_\rho \mathbf{W})\} + c_{\mathbf{A}} \mathbf{C}_\rho] \Delta \tilde{\boldsymbol{\Theta}}_{n+1}, \\ c_{\mathbf{A}} &= \frac{1 - \alpha_m}{(1 - \alpha_m) \beta \Delta t^2}, \quad c_{\mathbf{W}} = \frac{\gamma}{\beta \Delta t}, \quad \Delta \tilde{\boldsymbol{\Theta}}_{n+1} = \boldsymbol{\Lambda}^T_n \Delta \tilde{\boldsymbol{\theta}}_{n+1} = \boldsymbol{\Lambda}^T_n \mathbf{T}(\tilde{\boldsymbol{\theta}}_{n+1}) \Delta \boldsymbol{\theta}. \end{aligned} \tag{B.45}$$

However, for the WK-TAN element, the rotation increment field $\Delta\boldsymbol{\theta}$ is given by equation (B.42).

B.8 Linearization of SK-ROT and WK-ROT elements

The nodal primary variable variations of the SK/WK-TAN and the SK/WK-ROT elements read:

$$\begin{aligned} \delta \hat{\mathbf{x}}_{TAN} &:= (\delta \hat{\mathbf{d}}^{1T}, \delta \hat{\mathbf{t}}^{1T}, \delta \hat{\Theta}^1_1, \delta \hat{\mathbf{d}}^{2T}, \delta \hat{\mathbf{t}}^{2T}, \delta \hat{\Theta}^2_1, \delta \hat{\Theta}^3_1)^T, \\ \delta \hat{\mathbf{x}}_{ROT} &:= (\delta \hat{\mathbf{d}}^{1T}, \delta \hat{\boldsymbol{\theta}}^{1T}, \delta \hat{t}^1, \delta \hat{\mathbf{d}}^{2T}, \delta \hat{\boldsymbol{\theta}}^{2T}, \delta \hat{t}_1, \delta \hat{\Theta}^3_1)^T. \end{aligned} \tag{B.46}$$

In a similar manner, the set of iterative nodal primary variable increments have been defined as:

$$\begin{aligned}\Delta\hat{\mathbf{x}}_{TAN} &:= (\Delta\hat{\mathbf{d}}^{1T}, \Delta\hat{\mathbf{t}}^{1T}, \Delta\hat{\varphi}^1, \Delta\hat{\mathbf{d}}^{2T}, \Delta\hat{\mathbf{t}}^{2T}, \Delta\hat{\varphi}^2, \Delta\hat{\varphi}^3)^T, \\ \Delta\hat{\mathbf{x}}_{ROT} &:= (\Delta\hat{\mathbf{d}}^{1T}, \Delta\hat{\boldsymbol{\theta}}^{1T}, \Delta\hat{t}^1, \Delta\hat{\mathbf{d}}^{2T}, \Delta\hat{\boldsymbol{\theta}}^{2T}, \Delta\hat{t}_1, \Delta\hat{\varphi}^3)^T.\end{aligned} \tag{B.47}$$

The transformations between these primary variable variations and increments is given by:

$$\delta\hat{\mathbf{x}}_{TAN} = \tilde{\mathbf{T}}_{\hat{\mathbf{x}}}\delta\hat{\mathbf{x}}_{ROT} \quad \text{and} \quad \Delta\hat{\mathbf{x}}_{TAN} = \mathbf{T}_{M\hat{\mathbf{x}}}\Delta\hat{\mathbf{x}}_{ROT}. \tag{B.48}$$

The transformation matrices $\tilde{\mathbf{T}}_{\hat{\mathbf{x}}}$, originally defined in (3.127), and $\mathbf{T}_{M\hat{\mathbf{x}}}$ have the following form:

$$\tilde{\mathbf{T}}_{\hat{\mathbf{x}}} = \begin{pmatrix} \mathbf{I}_3 & & & & & & \\ & \tilde{\mathbf{T}}^1 & & & & & \\ & & \mathbf{I}_3 & & & & \\ & & & \tilde{\mathbf{T}}^2 & & & \\ & & & & 1 & & \end{pmatrix} \quad \text{and} \quad \mathbf{T}_{M\hat{\mathbf{x}}} = \begin{pmatrix} \mathbf{I}_3 & & & & & & \\ & \mathbf{T}_M^1 & & & & & \\ & & \mathbf{I}_3 & & & & \\ & & & \mathbf{T}_M^2 & & & \\ & & & & 1 & & \end{pmatrix}. \tag{B.49}$$

These two different transformation matrices are required, since the primary variable variations of the SK/WK-TAN elements are based on the multiplicative quantities $\delta\hat{\Theta}_1^i$, whereas the corresponding iterative primary variable increments are based on the additive quantities $\Delta\hat{\varphi}^i$. The submatrices $\tilde{\mathbf{T}}^i$ and $\mathbf{T}_M^i$ (see (2.34) and (2.33)) are evaluated at the two element boundary nodes:

$$\tilde{\mathbf{T}}^i := \tilde{\mathbf{T}}(\xi^i) \quad \text{and} \quad \mathbf{T}_M^i := \mathbf{T}_M(\xi^i) \quad \text{for} \quad i = 1, 2. \tag{B.50}$$

In chapter 3, it has already been shown that the following residual transformation is valid:

$$\mathbf{r}_{ROT} = \tilde{\mathbf{T}}_{\hat{\mathbf{x}}}^T\mathbf{r}_{TAN}. \tag{B.51}$$

In a similar manner, also the linearized element residual vector can be transformed:

$$\Delta\mathbf{r}_{ROT} = \Delta\tilde{\mathbf{T}}_{\hat{\mathbf{x}}}^T\mathbf{r}_{TAN} + \tilde{\mathbf{T}}_{\hat{\mathbf{x}}}^T\underbrace{\Delta\mathbf{r}_{TAN}}_{=\mathbf{k}_{TAN}\Delta\hat{\mathbf{x}}_{TAN}} =: \underbrace{\left(\tilde{\mathbf{H}}_{\hat{\mathbf{x}}}(\mathbf{r}_{TAN}) + \tilde{\mathbf{T}}_{\hat{\mathbf{x}}}^T\mathbf{k}_{TAN}\mathbf{T}_{M\hat{\mathbf{x}}}\right)}_{:=\mathbf{k}_{ROT}}\Delta\hat{\mathbf{x}}_{ROT}. \tag{B.52}$$

Here, the matrix $\tilde{\mathbf{H}}_{\hat{\mathbf{x}}}(\mathbf{r}_{TAN})$ has been introduced, in order to represent the linearization of $\tilde{\mathbf{T}}_{\hat{\mathbf{x}}}$:

$$\tilde{\mathbf{H}}_{\hat{\mathbf{x}}}(\mathbf{r}_{TAN})\Delta\hat{\mathbf{x}}_{ROT} := \Delta\tilde{\mathbf{T}}_{\hat{\mathbf{x}}}^T\mathbf{r}_{TAN} \quad \text{with} \quad \tilde{\mathbf{H}}_{\hat{\mathbf{x}}}(\mathbf{r}_{TAN}) = \begin{pmatrix} \mathbf{0} & & & & & & \\ & \tilde{\mathbf{H}}^1 & & & & & \\ & & \mathbf{0} & & & & \\ & & & \tilde{\mathbf{H}}^2 & & & \\ & & & & 0 & & \end{pmatrix}. \tag{B.53}$$

After calculating the derivative of $\tilde{\mathbf{T}}_{\hat{\mathbf{x}}}$ and re-ordering the result, the submatrices $\tilde{\mathbf{H}}^i$ can be stated:

$$\tilde{\mathbf{H}}^i = \begin{pmatrix} \mathbf{S}(\mathbf{r}_{TAN,\hat{\mathbf{t}}^i})\mathbf{S}(\mathbf{g}_1^i) - r_{TAN,\hat{\Theta}_1^i}\mathbf{S}(\mathbf{g}_1^i) & \mathbf{S}(\mathbf{g}_1^i)\mathbf{r}_{TAN,\hat{\mathbf{t}}^i} \\ -\mathbf{r}_{TAN,\hat{\mathbf{t}}^i}^T\mathbf{S}(\mathbf{g}_1^i) & 0 \end{pmatrix}, \quad i = 1, 2. \tag{B.54}$$

From (B.52), the following transformation rule for the the element stiffness matrix can be stated:

$$\Delta \mathbf{r}_{ROT} = \mathbf{k}_{ROT} \Delta \hat{\mathbf{x}}_{ROT} \quad \text{with} \quad \mathbf{k}_{ROT} = \tilde{\mathbf{H}}_{\hat{\mathbf{x}}}(\mathbf{r}_{TAN}) + \tilde{\mathbf{T}}_{\hat{\mathbf{x}}}^{T} \mathbf{k}_{TAN} \mathbf{T}_{M\hat{\mathbf{x}}}. \tag{B.55}$$

In order to apply this transformation, the components of the element stiffness matrices $\mathbf{k}_{TAN}$ and $\mathbf{k}_{ROT}$ have to be arranged in the same order as the components of the element residual vectors:

$$\begin{aligned} \mathbf{r}_{TAN} &:= (\mathbf{r}_{TAN,\hat{\mathbf{d}}^1}^T, \mathbf{r}_{TAN,\hat{\mathbf{t}}^1}^T, r_{TAN,\hat{\Theta}_1^1}, \mathbf{r}_{TAN,\hat{\mathbf{d}}^2}^T, \mathbf{r}_{TAN,\hat{\mathbf{t}}^2}^T, r_{TAN,\hat{\Theta}_1^2}, r_{TAN,\hat{\Theta}_1^3})^T, \\ \mathbf{r}_{ROT} &:= (\mathbf{r}_{ROT,\hat{\mathbf{d}}^1}^T, \mathbf{r}_{ROT,\hat{\boldsymbol{\theta}}^1}^T, r_{ROT,\hat{t}^1}, \mathbf{r}_{ROT,\hat{\mathbf{d}}^2}^T, \mathbf{r}_{ROT,\hat{\boldsymbol{\theta}}^2}^T, r_{ROT,\hat{t}^2}, r_{ROT,\hat{\Theta}_1^3})^T. \end{aligned} \tag{B.56}$$

B.9 Linearization of TF element

As explained in Section 3.7.1, the term $\mathbf{v}_{\kappa}$ will be replaced with $\mathbf{v}'_{\theta\perp}$ in the element residual vector (3.160) in order to yield a more compact form of the element stiffness matrix.

$$\mathbf{r}_{\hat{\mathbf{d}}} = \int_{-1}^{1} \left[\bar{\mathbf{v}}_{\epsilon} \bar{F}_1 + \mathbf{v}'_{\boldsymbol{\theta}_\perp} \mathbf{m} - \mathbf{H}^T \mathbf{f}_{\rho} \right] \frac{l_{ele}}{2} d\xi - \int_{-1}^{1} \left[\mathbf{H}^T \tilde{\mathbf{f}} + \mathbf{v}_{\boldsymbol{\theta}_\perp} \tilde{\mathbf{m}}_{\perp} \right] \frac{l_{ele}}{2} d\xi - \left[\mathbf{H}^T \mathbf{f}_{\sigma} + \mathbf{v}_{\boldsymbol{\theta}_\perp} \mathbf{m}_{\sigma\perp} \right]_{\Gamma_\sigma} \doteq 0. \tag{B.57}$$

A subsequent linearization of the element residual vector (B.57) yields the following expression:

$$\begin{aligned} \Delta \mathbf{r}_{\hat{\mathbf{d}}} = & \int_{-1}^{1} \left[\Delta \bar{\mathbf{v}}_{\epsilon} \bar{F}_1 + \bar{\mathbf{v}}_{\epsilon} \Delta \bar{F}_1 + \Delta \mathbf{v}'_{\boldsymbol{\theta}_\perp} \mathbf{m} + \mathbf{v}'_{\boldsymbol{\theta}_\perp} \Delta \mathbf{m} - \mathbf{H}^T \Delta \mathbf{f}_{\rho} \right] \frac{l_{ele}}{2} d\xi \\ & - \int_{-1}^{1} \left[\Delta \mathbf{v}_{\boldsymbol{\theta}_\perp} \tilde{\mathbf{m}}_{\perp} \right] \frac{l_{ele}}{2} d\xi - \left[\Delta \mathbf{v}_{\boldsymbol{\theta}_\perp} \mathbf{m}_{\sigma\perp} \right]_{\Gamma_\sigma} \doteq 0. \end{aligned} \tag{B.58}$$

Here, the linearization of the moment stress resultant and the inertia forces results in:

$$\Delta \mathbf{m} = EI \left[-\mathbf{S}(\mathbf{g}'_1) \Delta \mathbf{g}_1 + \mathbf{S}(\mathbf{g}_1) \Delta \mathbf{g}'_1 \right], \quad -\mathbf{H}^T \Delta \mathbf{f}_{\rho} = \rho A c_{\ddot{\mathbf{r}}2} \mathbf{H}^T \mathbf{H} \Delta \hat{\mathbf{d}}, \quad c_{\ddot{\mathbf{r}}2} = \frac{1 - \alpha_m}{\beta \Delta t^2}. \tag{B.59}$$

All the remaining individual linearizations have already been derived in the previous appendices. As expected, the TF element yields a constant and symmetric mass matrix. Also the symmetry of the element stiffness matrix can easily be shown in case $\tilde{\mathbf{m}}_{\perp} = \mathbf{m}_{\sigma\perp} = \mathbf{0}$.

C Supplements to the Beam-to-Beam Contact Formulations

C.1 Linearization of point-to-point and endpoint contact contributions

Since the endpoint contact contributions can be regarded as special case of the point contact, the linearization of this formulation is considered first. The linearization of (4.12) yields:

$$\mathbf{k}_{con,l} = \frac{d\mathbf{r}_{con,l}}{d\hat{\mathbf{d}}_{12}} = \frac{\partial \mathbf{r}_{con,l}}{\partial \hat{\mathbf{d}}_{12}} + \frac{\partial \mathbf{r}_{con,l}}{\partial \xi_c}\frac{d\xi_c}{d\hat{\mathbf{d}}_{12}} + \frac{\partial \mathbf{r}_{con,l}}{\partial \eta_c}\frac{d\eta_c}{d\hat{\mathbf{d}}_{12}} \quad \text{for} \quad l = 1, 2. \tag{C.1}$$

Here, $d\xi_c/d\hat{\mathbf{d}}_{12}$ and $d\eta_c/d\hat{\mathbf{d}}_{12}$ stem from a linearization of the orthogonality conditions (4.5):

$$\begin{aligned}
&\mathbf{A}(\xi_c, \eta_c) \cdot \left(\frac{d\xi_c}{d\hat{\mathbf{d}}_{12}}^T, \frac{d\eta_c}{d\hat{\mathbf{d}}_{12}}^T \right)^T = -\mathbf{B}(\xi_c, \eta_c), \\
\text{with} \quad &\mathbf{A} = \begin{pmatrix} p_{1,\xi} & p_{1,\eta} \\ p_{2,\xi} & p_{2,\eta} \end{pmatrix} = \begin{pmatrix} \mathbf{r}_{1,\xi}^T\mathbf{r}_{1,\xi} + (\mathbf{r}_1 - \mathbf{r}_2)^T\mathbf{r}_{1,\xi\xi} & -\mathbf{r}_{1,\xi}^T\mathbf{r}_{2,\eta} \\ \mathbf{r}_{1,\xi}^T\mathbf{r}_{2,\eta} & -\mathbf{r}_{2,\eta}^T\mathbf{r}_{2,\eta} + (\mathbf{r}_1 - \mathbf{r}_2)^T\mathbf{r}_{2,\eta\eta} \end{pmatrix}, \\
\text{and} \quad &\mathbf{B} = \begin{pmatrix} p_{1,\mathbf{d}_{12}} \\ p_{2,\mathbf{d}_{12}} \end{pmatrix} = \begin{pmatrix} (\mathbf{r}_1 - \mathbf{r}_2)^T\mathbf{H}_{1,\xi} + \mathbf{r}_{1,\xi}^T\mathbf{H}_1 & -\mathbf{r}_{1,\xi}^T\mathbf{H}_2 \\ \mathbf{r}_{2,\eta}^T\mathbf{H}_1 & (\mathbf{r}_1 - \mathbf{r}_2)^T\mathbf{H}_{2,\eta} - \mathbf{r}_{2,\eta}^T\mathbf{H}_2 \end{pmatrix}.
\end{aligned} \tag{C.2}$$

Here, the terms $p_{1,\xi}, p_{1,\eta}, p_{2,\xi}$ and $p_{2,\eta}$, which are collected in matrix $\mathbf{A}$, can be used for an iterative solution of the orthogonality conditions (4.5) for the unknown closest point coordinates ξ_c and η_c by means of a local Newton-Raphson scheme. The partial derivatives of the residual vectors with respect to $\mathbf{d}_{12}$ as occurring in (C.1) are given by:

$$\begin{aligned}
&\frac{\partial \mathbf{r}_{con,1}}{\partial \hat{\mathbf{d}}_{12}} = \varepsilon \left(\mathbf{H}_1^T\mathbf{n}\frac{\partial g}{\partial \hat{\mathbf{d}}_{12}} + g\mathbf{H}_1^T\frac{\partial \mathbf{n}}{\partial \hat{\mathbf{d}}_{12}} \right), \quad \frac{\partial \mathbf{r}_{con,2}}{\partial \hat{\mathbf{d}}_{12}} = \varepsilon \left(\mathbf{H}_2^T\mathbf{n}\frac{\partial g}{\partial \hat{\mathbf{d}}_{12}} + g\mathbf{H}_2^T\frac{\partial \mathbf{n}}{\partial \hat{\mathbf{d}}_{12}} \right), \\
&\frac{\partial g}{\partial \hat{\mathbf{d}}_{12}} = \mathbf{n}^T \left[\mathbf{H}_1, -\mathbf{H}_2 \right], \quad \frac{\partial \mathbf{n}}{\partial \hat{\mathbf{d}}_{12}} = \frac{\mathbf{I}_3 - \mathbf{n} \otimes \mathbf{n}^T}{||\mathbf{r}_1 - \mathbf{r}_2||} \left[\mathbf{H}_1, -\mathbf{H}_2 \right].
\end{aligned} \tag{C.3}$$

The partial derivatives with respect to the closest point coordinates ξ_c and η_c yield:

$$\begin{aligned}
&\frac{\partial \mathbf{r}_{con,1}}{\partial \xi_c} = \varepsilon \left(\mathbf{H}_1^T\mathbf{n}g_{,\xi} + g\mathbf{H}_{1,\xi}^T\mathbf{n} + g\mathbf{H}_1^T\mathbf{n}_{,\xi} \right) \big|_{(\xi_c,\eta_c)}, \quad \frac{\partial \mathbf{r}_{con,2}}{\partial \xi_c} = \varepsilon \left(\mathbf{H}_2^T\mathbf{n}g_{,\xi} + g\mathbf{H}_2^T\mathbf{n}_{,\xi} \right) \big|_{(\xi_c,\eta_c)}, \\
&\frac{\partial \mathbf{r}_{con,1}}{\partial \eta_c} = \varepsilon \left(\mathbf{H}_1^T\mathbf{n}g_{,\eta} + g\mathbf{H}_1^T\mathbf{n}_{,\eta} \right) \big|_{(\xi_c,\eta_c)}, \quad \frac{\partial \mathbf{r}_{con,2}}{\partial \eta_c} = \varepsilon \left(\mathbf{H}_2^T\mathbf{n}g_{,\eta} + g\mathbf{H}_{2,\eta}^T\mathbf{n} + g\mathbf{H}_2^T\mathbf{n}_{,\eta} \right) \big|_{(\xi_c,\eta_c)}, \\
&g_{,\xi} = \mathbf{n}^T\mathbf{r}_{1,\xi}, \quad g_{,\eta} = -\mathbf{n}^T\mathbf{r}_{2,\eta}, \quad \mathbf{n}_{,\xi} = \frac{\mathbf{I}_3 - \mathbf{n}\otimes\mathbf{n}^T}{||\mathbf{r}_1 - \mathbf{r}_2||}\mathbf{r}_{1,\xi}, \quad \mathbf{n}_{,\eta} = -\frac{\mathbf{I}_3 - \mathbf{n}\otimes\mathbf{n}^T}{||\mathbf{r}_1 - \mathbf{r}_2||}\mathbf{r}_{2,\eta}.
\end{aligned} \tag{C.4}$$

Depending on the considered case (point-, line-, endpoint-contact), (C.4) can be simplified due to $\mathbf{n}^T\mathbf{r}_{1,\xi}=0$ and/or $\mathbf{n}^T\mathbf{r}_{2,\eta}=0$. In case of endpoint contact, only the partial derivatives $d\xi_c/d\hat{\mathbf{d}}_{12}$ and $d\eta_c/d\hat{\mathbf{d}}_{12}$ have to be adapted, while all other terms remain unchanged. In case of contact between an endpoint of beam 1, i.e. $\xi_c=-1$ or $\xi_c=1$, with a segment $\eta_c\in[-1;1]$ on beam 2, the second line of (C.2) is considered in order to determine $d\eta_c/d\hat{\mathbf{d}}_{12}$, while $d\xi_c/d\hat{\mathbf{d}}_{12}$ vanishes:

$$\frac{d\xi_c}{d\hat{\mathbf{d}}_{12}}=\mathbf{0} \quad \text{and} \quad \frac{d\eta_c}{d\hat{\mathbf{d}}_{12}}=-\frac{p_{2,\hat{\mathbf{d}}_{12}}}{p_{2,\eta}}. \tag{C.5}$$

Correspondingly, the condition $p_2(\eta_c)=0$ and the derivative $p_{2,\eta}$ can be used for an iterative determination of η_c. In case of contact between an endpoint of beam 2, i.e. $\eta_c=-1$ or $\eta_c=1$, with a curve segment $\xi_c\in[-1;1]$ on beam 1, the first line of equation (C.2) has to be considered in order to determine $d\xi_c/d\hat{\mathbf{d}}_{12}$, while $d\eta_c/d\hat{\mathbf{d}}_{12}$ vanishes:

$$\frac{d\xi_c}{d\hat{\mathbf{d}}_{12}}=-\frac{p_{1,\mathbf{d}_{12}}}{p_{1,\xi}} \quad \text{and} \quad \frac{d\eta_c}{d\hat{\mathbf{d}}_{12}}=\mathbf{0}. \tag{C.6}$$

In this case, $p_1(\xi_c)=0$ and $p_{1,\xi}$ can be used for an iterative determination of ξ_c. Considering the contact between two endpoints, $\xi_c=-1$ or $\xi_c=1$ and $\eta_c=-1$ or $\eta_c=1$, yields:

$$\frac{d\xi_c}{d\hat{\mathbf{d}}_{12}}=\frac{d\eta_c}{d\hat{\mathbf{d}}_{12}}=\mathbf{0}. \tag{C.7}$$

C.2 Linearization of the line-to-line contact formulation

This linearization is based on the general form (4.47). It is focused on the most general case with an integration interval segmentation being applied on both sides of the slave element. In the line contact case, the orthogonality condition p_2 on beam 2 is relevant. Its linearization reads:

$$p_{2,\xi}\frac{d\xi}{d\hat{\mathbf{d}}_{12}}+p_{2,\eta_c}\frac{d\eta_c}{d\hat{\mathbf{d}}_{12}}=-p_{2,\hat{\mathbf{d}}_{12}}\rightarrow\frac{d\eta_c}{d\hat{\mathbf{d}}_{12}}=\left(\underbrace{\frac{-p_{2,\xi_{ij}}}{p_{2,\eta}}}_{=\frac{\partial\eta_c}{\partial\xi_{ij}}}\cdot\frac{d\xi_{ij}}{d\hat{\mathbf{d}}_{12}}+\underbrace{\frac{-1}{p_{2,\eta}}p_{2,\hat{\mathbf{d}}_{12}}}_{=\frac{\partial\eta_c}{\partial\hat{\mathbf{d}}_{12}}}\right)\Bigg|_{(\xi_{ij},\eta_c(\xi_{ij}))}. \tag{C.8}$$

With the help of (4.44), the linearization $d\xi_{ij}/d\hat{\mathbf{d}}_{12}$ of the slave evaluation points yields

$$\frac{d\xi_{ij}}{d\hat{\mathbf{d}}_{12}}=\frac{\partial\xi_{ij}}{\partial\xi_{1,i}}\frac{d\xi_{1,i}}{d\hat{\mathbf{d}}_{12}}+\frac{\partial\xi_{ij}}{\partial\xi_{2,i}}\frac{d\xi_{2,i}}{d\hat{\mathbf{d}}_{12}} \quad \text{with} \quad \frac{\partial\xi_{ij}}{\partial\xi_{1,i}}=\frac{1.0-\bar{\xi}_j}{2} \quad \text{and} \quad \frac{\partial\xi_{ij}}{\partial\xi_{2,i}}=\frac{1.0+\bar{\xi}_j}{2}, \tag{C.9}$$

where $\bar{\xi}_j$ are constant Gauss point coordinates. Here, η is fixed at the master beam endpoints:

$$\frac{d\xi_{1,i}}{d\hat{\mathbf{d}}_{12}}=\left(\underbrace{\frac{-1}{p_{2,\xi}}p_{2,\hat{\mathbf{d}}_{12}}}_{=\frac{\partial\xi_{B1}}{\partial\hat{\mathbf{d}}_{12}}}\right)\Bigg|_{(\xi_{B1}(\eta_{EP}),\eta_{EP})} \quad \text{and} \quad \frac{d\xi_{2,i}}{d\hat{\mathbf{d}}_{12}}=\left(\underbrace{\frac{-1}{p_{2,\xi}}p_{2,\hat{\mathbf{d}}_{12}}}_{=\frac{\partial\xi_{B2}}{\partial\hat{\mathbf{d}}_{12}}}\right)\Bigg|_{(\xi_{B2}(\eta_{EP}),\eta_{EP})}. \tag{C.10}$$

Since $\partial \mathbf{r}_{con,l}^{ij} / \partial \xi_{1,i}$ and $\partial \mathbf{r}_{con,l}^{ij} / \partial \xi_{2,i}$ solely stem from the explicit dependence of the total Jacobian $J_{c1}(\xi_{ij}, \xi_{1,i}, \xi_{2,i})$ on the boundary coordinates $\xi_{1,i}$ and $\xi_{2,i}$, these terms can be rewritten:

$$\begin{aligned} \frac{\partial \mathbf{r}_{con,l}^{ij}}{\partial \xi_{1,i}} &= \frac{\mathbf{r}_{con,l}^{ij}}{J_{c1}(\xi_{ij}, \xi_{1,i}, \xi_{2,i})} \cdot J_{c1,\xi_{1,i}}(\xi_{ij}, \xi_{1,i}, \xi_{2,i}), \\ \frac{\partial \mathbf{r}_{con,l}^{ij}}{\partial \xi_{2,i}} &= \frac{\mathbf{r}_{con,l}^{ij}}{J_{c1}(\xi_{ij}, \xi_{1,i}, \xi_{2,i})} \cdot J_{c1,\xi_{2,i}}(\xi_{ij}, \xi_{1,i}, \xi_{2,i}) \quad \text{with} \quad l = 1, 2. \end{aligned} \tag{C.11}$$

The linearizations of the Jacobian occurring in (C.11) follow directly from the definition (4.42):

$$J_{c1,\xi_{1,i}}(\xi_{ij}, \xi_{1,i}, \xi_{2,i}) = -\frac{J(\xi(\bar{\xi}_i))}{2}, \quad J_{v1,\xi_{2,i}}(\xi_{ij}, \xi_{1,i}, \xi_{2,i}) = \frac{J(\xi(\bar{\xi}_i))}{2}. \tag{C.12}$$

The derivative $\partial \mathbf{r}_{con,l}^{ij} / \partial \hat{\mathbf{d}}_{12}$ with respect to $\hat{\mathbf{d}}_{12}$ shows strong similarities to the terms in (C.1):

$$\begin{aligned} \frac{\partial \mathbf{r}_{con,1}^{ij}}{\partial \hat{\mathbf{d}}_{12}} =& w_j J_{c1}(\xi_{ij}, \xi_{1,i}, \xi_{2,i}) \varepsilon \frac{\partial g(\xi_{ij})}{\partial \hat{\mathbf{d}}_{12}} \mathbf{H}_1^T(\xi_{ij}) \mathbf{n}(\xi_{ij}) \\ &+ w_j J_{c1}(\xi_{ij}, \xi_{1,i}, \xi_{2,i}) \varepsilon g(\xi_{ij}) \mathbf{H}_1^T(\xi_{ij}) \frac{\partial \mathbf{n}(\xi_{ij})}{\partial \hat{\mathbf{d}}_{12}}, \\ \frac{\partial \mathbf{r}_{con,2}^{ij}}{\partial \hat{\mathbf{d}}_{12}} =& -w_j J_{c1}(\xi_{ij}, \xi_{1,i}, \xi_{2,i}) \varepsilon \varepsilon \frac{\partial g(\xi_{ij})}{\partial \hat{\mathbf{d}}_{12}} \mathbf{H}_2^T(\eta_c(\xi_{ij})) \mathbf{n}(\xi_{ij}) \\ &- w_j J_{c1}(\xi_{ij}, \xi_{1,i}, \xi_{2,i}) \varepsilon g(\xi_{ij}) \mathbf{H}_2^T(\eta_c(\xi_{ij})) \frac{\partial \mathbf{n}(\xi_{ij})}{\partial \hat{\mathbf{d}}_{12}}. \end{aligned} \tag{C.13}$$

The terms $\partial g / \partial \hat{\mathbf{d}}_{12}$ and $\partial \mathbf{n} / \partial \hat{\mathbf{d}}_{12}$ are identical to the ones in (C.3). The derivatives of the residual contributions $\mathbf{r}_{con,1}^{ij}$ and $\mathbf{r}_{con,2}^{ij}$ with respect to the evaluation points ξ_{ij} result in:

$$\begin{aligned} \frac{\partial \mathbf{r}_{con,1}^{ij}}{\partial \xi_{ij}} =& w_j J_{c1,\xi_{ij}}(\xi_{ij}, \xi_{1,i}, \xi_{2,i}) \varepsilon g(\xi_{ij}) \mathbf{H}_1^T(\xi_{ij}) \mathbf{n}(\xi_{ij}) \\ &+ w_j J_{c1}(\xi_{ij}, \xi_{1,i}, \xi_{2,i}) \varepsilon g_{,\xi_{ij}}(\xi_{ij}) \mathbf{H}_1^T(\xi_{ij}) \mathbf{n}(\xi_{ij}) \\ &+ w_j J_{c1}(\xi_{ij}, \xi_{1,i}, \xi_{2,i}) \varepsilon g(\xi_{ij}) \mathbf{H}_{1,\xi_{ij}}^T(\xi_{ij}) \mathbf{n}(\xi_{ij}) \\ &+ w_j J_{c1}(\xi_{ij}, \xi_{1,i}, \xi_{2,i}) \varepsilon g(\xi_{ij}) \mathbf{H}_1^T(\xi_{ij}) \mathbf{n}_{,\xi_{ij}}(\xi_{ij}), \\ \frac{\partial \mathbf{r}_{con,2}^{ij}}{\partial \xi_{ij}} =& -w_j J_{c1,\xi_{ij}}(\xi_{ij}, \xi_{1,i}, \xi_{2,i}) \varepsilon g(\xi_{ij}) \mathbf{H}_2^T(\xi_{ij}) \mathbf{n}(\xi_{ij}) \\ &- w_j J_{c1}(\xi_{ij}, \xi_{1,i}, \xi_{2,i}) \varepsilon g_{,\xi_{ij}}(\xi_{ij}) \mathbf{H}_2^T(\xi_{ij}) \mathbf{n}(\xi_{ij}) \\ &- w_j J_{c1}(\xi_{ij}, \xi_{1,i}, \xi_{2,i}) \varepsilon g(\xi_{ij}) \mathbf{H}_2^T(\xi_{ij}) \mathbf{n}_{,\xi_{ij}}(\xi_{ij}). \end{aligned} \tag{C.14}$$

Similarly, The derivatives of $\mathbf{r}_{con,1}^{ij}$ and $\mathbf{r}_{con,2}^{ij}$ with respect to the evaluation points η_c yield:

$$\begin{aligned}
\frac{\partial \mathbf{r}_{con,1}^{ij}}{\partial \eta_c} &= w_j J_{c1}(\xi_{ij}, \xi_{1,i}, \xi_{2,i}) \varepsilon g_{,\eta_c}(\xi_{ij}) \mathbf{H}_1^T(\xi_{ij}) \mathbf{n}(\xi_{ij}) \\
&\quad + w_j J_{c1}(\xi_{ij}, \xi_{1,i}, \xi_{2,i}) \varepsilon g(\xi_{ij}) \mathbf{H}_1^T(\xi_{ij}) \mathbf{n}_{,\eta_c}(\xi_{ij}), \\
\frac{\partial \mathbf{r}_{con,2}^{ij}}{\partial \eta_c} &= -w_j J_{c1}(\xi_{ij}, \xi_{1,i}, \xi_{2,i}) \varepsilon g_{,\eta_c}(\xi_{ij}) \mathbf{H}_2^T(\xi_{ij}) \mathbf{n}(\xi_{ij}) \\
&\quad - w_j J_{c1}(\xi_{ij}, \xi_{1,i}, \xi_{2,i}) \varepsilon g(\xi_{ij}) \mathbf{H}_{2,\eta_c}^T(\xi_{ij}) \mathbf{n}(\xi_{ij}) \\
&\quad - w_j J_{c1}(\xi_{ij}, \xi_{1,i}, \xi_{2,i}) \varepsilon g(\xi_{ij}) \mathbf{H}_2^T(\xi_{ij}) \mathbf{n}_{,\eta_c}(\xi_{ij}).
\end{aligned} \tag{C.15}$$

The partial derivatives of g and $\mathbf{n}$ are again identical to the ones presented in (C.4). The partial derivative $J_{c1,\xi_{ij}} = J_{\xi_{ij}}(\xi_{2,i} - \xi_{1,i})/2$ of the total Jacobian is only relevant in case of a non-constant element Jacobian J. It should again be emphasized that this most general linearization in (4.47) is only necessary for slave elements with valid master beam endpoint projections according to (4.45). In practical simulations, for the vast majority of contact element pairs this is not the case, i.e. $d\xi_{1,i}/d\hat{\mathbf{d}}_{12} = \mathbf{0}$ and $d\xi_{2,i}/d\hat{\mathbf{d}}_{12} = \mathbf{0}$, and the linearization in (4.48) is sufficient.

C.3 Residual and linearization of the *ABC* formulation

In a first step, the residual and linearization terms of the *ABC* formulation with force-based model transition will be considered. The residual contributions directly follow from inserting the discretized weak forms (4.12) and (4.43) into (4.61). Following the chain rule, the corresponding linearization consists of the basic linearizations of the point-to-point and line-to-line formulations according to (C.1) and (C.2) scaled by the transition factor occurring in (4.61) and supplemented by additional terms containing the linearization of the transition factor itself. The linearization of the transition factor follows directly from (4.67) and (4.68) by replacing the variation $\delta\hat{\mathbf{d}}_{12}$ with the increment $\Delta\hat{\mathbf{d}}_{12}$. According to (4.65), the residual of the *ABC* formulation with potential-based model transition basically consists of the residual terms of the variant with force-based model transition (with squared transition factor $k(z)^2$ instead of $k(z)$; terms on the left-hand side) and additional contact moment contributions composed of energy-like scalar terms of the form εg^2 multiplied with the transition factor and the variation of the transition factor according to (4.67) and (4.68). The linearization of the potential-based variant is straight-forward, but more involved than for the force-based variant, since the linearization of the transition factor variation (4.67) and (4.68) is required. For that reason, a convenient automatic differentiation tool has been employed instead of deriving this linearization analytically.

C.4 Derivation of an analytical solution for the twisting of two beams

The following derivations are based on the PDEs (2.118) and (2.119). Concretely, the possibility of finding a parameter choice for the example "Twisting of two beams" that leads to a solution in form of a helix with constant slope according to (4.91) for both considered beams shall be

investigated. Per definition, such a helix with radius r and slope h exhibits the following constant expressions for the mathematical curvature $\bar{\kappa}$ and torsion $\bar{\tau}$ along the beams length:

$$\bar{\kappa} = \frac{r}{h^2 + r^2} = \text{const.} \quad \text{and} \quad \bar{\tau} = \frac{h}{h^2 + r^2} = \text{const.} \tag{C.16}$$

Since the mathematical curvature $\bar{\kappa}$ and torsion $\bar{\tau}$ are defined as angle increments per (current) arc-length increment, and the mechanically relevant quantities $\kappa = (1+\epsilon)\bar{\kappa}$ and $\tau = (1+\epsilon)\bar{\tau}$ are defined as angle increments per initial/undeformed arc-length, the following expressions can be derived between the individual kinematic quantities occurring in (2.119):

$$\kappa = \frac{r(1+\epsilon)}{h^2 + r^2} = \text{const.} \quad \rightarrow \quad m_b' = 0 \quad \text{and} \quad \tau = \frac{h(1+\epsilon)}{h^2 + r^2} = \text{const.} \tag{C.17}$$

The external load for a beam in static equilibrium according to Figure 4.15(a) consists of discrete point forces and moments at the left and right endpoints of the beams due to the applied Dirichlet conditions and a line load $\tilde{f}_n$ in n_{FS}-direction from the contact interaction. In case of a prescribed constant gap $g_0 < 0$ in the equilibrium configuration, this contact line load obeys the relation:

$$\tilde{f}_n = \varepsilon g_0. \tag{C.18}$$

All remaining distributed external loads vanish. Concretely, this means that:

$$\tilde{f}_{g_1} = \tilde{f}_b = \tilde{m}_{g_1} = \tilde{m}_n = \tilde{m}_b = 0. \tag{C.19}$$

Now, the most simple solution of this kind shall be found with a prescribed constant axial tension $\epsilon = 0.01$ and a constant torsion $\tau + \varphi' = \text{const}$. With (2.119) and (C.17), this requirement yields:

$$f_{g_1}' = m_{g_1}' = 0. \tag{C.20}$$

Inserting equations (2.119) and (C.20) into equations (2.118) leads to one remaining relation

$$-\frac{\tau}{1+\epsilon}\left(\kappa m_{g_1} - \tau m_b\right) + \kappa f_{g_1} + \tilde{f}_n = 0, \tag{C.21}$$

that has to be satisfied by the system parameters, while the other three equilibrium equations of (2.118) are satisfied automatically. From the family of solutions provided by equation (C.21), in the following the one with vanishing mechanical torsion will be considered:

$$m_{g_1} = GI_T\left(\tau + \varphi'\right) = 0 \quad \rightarrow \quad \varphi' = -\tau = -\frac{h}{h^2 + r^2}. \tag{C.22}$$

Altogether, equations (C.21) and (C.22) postulate a requirement for the penalty parameter:

$$\begin{aligned} &\frac{h^2(1+\epsilon)^2}{(h^2+r^2)^2} \cdot \frac{EIr}{h^2+r^2} + \frac{r(1+\epsilon)EA\epsilon}{h^2+r^2} + \varepsilon g_0 = 0 \\ &\rightarrow \varepsilon = -\frac{(1+\epsilon)r}{(r^2+h^2)g_0}\left(EA\epsilon + \frac{EI(1+\epsilon)h^2}{(r^2+h^2)^2}\right). \end{aligned} \tag{C.23}$$

In a next step, the Dirichlet boundary conditions have to be determined. The additional relation $r = R - |g_0|/2$ for the helix radius appearing in (4.91) stems from the simple observation that the

distance between the two helix centerlines has to satisfy $2r = 2R - |g_0|$ in order to generate the required gap g_0. With r being defined this way, the derivation of the conditions (4.93) and (4.94) is trivial in order to end up with a helix with radius r. However, the condition (4.92) for the axial displacement requires some further calculations. Thereto, the required constant distribution of the axial tension $\epsilon = 0.01$ of the helix has to be expressed as a function of the total length $\tilde{l}$ of the deformed helix in order to determine the helix slope h:

$$\epsilon = \frac{\tilde{l} - l}{l} = \frac{1}{l} \int_{\varphi=0}^{2\pi} \left|\left| \frac{d\mathbf{r}_k(\varphi)}{d\varphi} \right|\right| d\varphi - 1 = \frac{2\pi\sqrt{r^2 + h^2}}{l} - 1 \tag{C.24}$$

$$\rightarrow \quad h = \sqrt{\left(\left(\frac{(1.0 + \epsilon) l}{2\pi} \right)^2 - r^2 \right)}. \tag{C.25}$$

Equation (C.24) yields the required helix slope in case of a given helix radius r and a prescribed axial tension ϵ. The required axial displacement u of the right endpoint follows from (4.91) as:

$$\Delta d^l_{1,z} = \Delta d^l_{2,z} = u = 2\pi h - l. \tag{C.26}$$

Finally, the Dirichlet-conditions for the tangential degrees of freedom have to be determined. The constant bending moment m_b has to be considered via proper moment boundary conditions at the beam endpoints. According to (2.1), the virtual work contribution of an external moment vector $m^j_b \mathbf{b}^j_{FS}$ in b-direction at the left/right boundary node $j = l, r$ leads to a residual entry

$$\begin{aligned} & m^j_b \mathbf{b}^{jT}_{FS} \left(\delta\alpha^j \mathbf{g}^j_1 + \frac{\mathbf{g}^j_1 \times \delta\mathbf{t}^j}{||\mathbf{t}^j||} \right) = \frac{m^j_b}{||\mathbf{t}^j||} \delta\mathbf{t}^{jT} \mathbf{n}^j_{FS} = \frac{m^j_b}{||\mathbf{t}^j||} \delta t^j_n \\ & \text{with} \quad \mathbf{g}^j_1 = \frac{\mathbf{t}^j}{||\mathbf{t}^j||}, \ \mathbf{b}^{jT}_{FS} \mathbf{g}^j_1 = 0, \ \mathbf{b}^j_{FS} \times \mathbf{g}^j_1 = \mathbf{n}^j_{FS} \end{aligned} \tag{C.27}$$

into the n-component of the corresponding nodal tangential degrees of freedom. Since the local n-directions coincide with the global x-directions at the beam endpoints here, it is sufficient to prescribe the x-components of the nodal tangents via Dirichlet constraints in order to enable proper reaction moments. According to (4.91), these x-components have to vanish:

$$\Delta t^l_{1,x} = \Delta t^l_{2,x} = \Delta t^r_{1,x} = \Delta t^r_{2,x} = 0. \tag{C.28}$$

Since the system parameters have been chosen in a way that leads to vanishing torsion, *no* additional torsional external moments have to be applied at the beam endpoints, i.e. $\mathbf{g}^{lT}_1 \mathbf{m}^l_\sigma = \mathbf{g}^{rT}_1 \mathbf{m}^r_\sigma = 0$. For this reason, the application of the torsion-free Kirchhoff beam element presented in Section 3.7.1 is justified for this example and leads to the correct mechanical solution.

Bibliography

[1] L. X. Ademir, Static Kirchhoff rods under the action of external forces: Integration via Runge-Kutta method, *Journal of Computational Methods in Physics* **2014**, 650365, 2014.

[2] S. S. Antman, Kirchhoff's problem for nonlinearly elastic rods, *Quarterly of Applied Mathematics* **32**, 221–240, 1974.

[3] S. S. Antman, *Nonlinear problems of elasticity*, Springer, 1995.

[4] J. Argyris, An excursion into large rotations, *Computer Methods in Applied Mechanics and Engineering* **32**, 85–155, 1982.

[5] J. H. Argyris, H. Balmer, J. S. Doltsinis, P. C. Dunne, M. Haase, M. Kleiber, G. A. Malejannakis, H.-P. Mlejnek, M. Müller, and D. W. Scharpf, Finite element method–the natural approach, *Computer Methods in Applied Mechanics and Engineering* **17-18**, 1–106, 1979.

[6] F. Armero and J. Valverde, Invariant Hermitian finite elements for thin Kirchhoff rods. I: The linear plane case, *Computer Methods in Applied Mechanics and Engineering* **213-216**, 427–457, 2012.

[7] F. Armero and J. Valverde, Invariant Hermitian finite elements for thin Kirchhoff rods. II: The linear three-dimensional case, *Computer Methods in Applied Mechanics and Engineering* **213-216**, 458–485, 2012.

[8] M. Arnold and O. Brüls, Convergence of the generalized-α scheme for constrained mechanical systems, *Multibody System Dynamics* **18**, 185–202, 2007.

[9] M. Arnold and B. Simeon, Pantograph and catenary dynamics: A benchmark problem and its numerical solution, *Applied Numerical Mathematics* **34**, 345–362, 2000.

[10] D. G. Ashwell and A. B. Sabir, Limitations of certain curved finite elements when applied to arches, *International Journal of Mechanical Sciences* **13**, 133–139, 1971.

[11] D. G. Ashwell, A. B. Sabir, and T. M. Roberts, Further studies in the application of curved finite elements to circular arches, *International Journal of Mechanical Sciences* **13**, 507–517, 1971.

[12] A. Avello, J. G. de Jaln, and E. Bayo, Dynamics of flexible multibody systems using cartesian co-ordinates and large displacement theory, *International Journal for Numerical Methods in Engineering* **32**, 1543–1563, 1991.

[13] K.-J. Bathe, *Finite element procedures*, Prentice Hall, 1996.

[14] K.-J. Bathe and S. Bolourchi, Large displacement analysis of three-dimensional beam structures, *International Journal for Numerical Methods in Engineering* **14**, 961–986, 1979.

[15] K.-J. Bathe, A. Iosilevich, and D. Chapelle, An inf-sup test for shell finite elements, *Computers & Structures* **75**, 439–456, 2000.

[16] J.-M. Battini and C. Pacoste, Co-rotational beam elements with warping effects in instability problems, *Computer Methods in Applied Mechanics and Engineering* **191**, 1755–1789, 2002.

[17] O. A. Bauchau and C. L. Bottasso, On the design of energy preserving and decaying schemes for flexible, nonlinear multi-body systems, *Computer Methods in Applied Mechanics and Engineering* **169**, 61–79, 1999.

[18] O. A. Bauchau, S. Han, A. Mikkola, and M. K. Matikainen, Comparison of the absolute nodal coordinate and geometrically exact formulations for beams, *Multibody System Dynamics* **32**, 67–85, 2014.

[19] A. M. Bauer, M. Breitenberger, B. Philipp, R. Wüchner, and K.-U. Bletzinger, Nonlinear isogeometric spatial Bernoulli beam, *Computer Methods in Applied Mechanics and Engineering* **303**, 101–127, 2016.

[20] T. Belytschko and B. J. Hseih, Nonlinear transient finite element analysis with convected coordinates, *International Journal for Numerical Methods in Engineering* **7**, 255–271, 1973.

[21] T. Belytschko and W. G. Lawrence, Applications of higher order corotational stretch theories to nonlinear finite element analysis, *Computers & Structures* **10**, 175–182, 1979.

[22] T. Belytschko, W. K. Liu, and B. Moran, *Nonlinear finite elements for continua and structures*, Wiley, 2000.

[23] M. Berger and B. Gostiaux, *Differential geometry: Manifolds, curves, and surfaces*, Volume 115 of *Graduate texts in mathematics*, Springer, 2012.

[24] M. Bergou, M. Wardetzky, S. Robinson, B. Audoly, and E. Grinspun, Discrete elastic rods, *ACM Transactions on Graphics* **27**, 63:1–63:12, 2008.

[25] F. Bertails, B. Audoly, M.-P. Cani, B. Querleux, F. Leroy, and J.-L. Lévêque, Super-helices for predicting the dynamics of natural hair, *ACM Transactions on Graphics* **25**, 1180–1187, 2006.

[26] P. Betsch and P. Steinmann, Constrained integration of rigid body dynamics, *Computer Methods in Applied Mechanics and Engineering* **191**, 467–488, 2001.

[27] P. Betsch and P. Steinmann, Frame-indifferent beam finite elements based upon the geometrically exact beam theory, *International Journal for Numerical Methods in Engineering* **54**, 1775–1788, 2002.

[28] R. L. Bishop, There is more than one way to frame a curve, *The American Mathematical Monthly* **82**, 246–251, 1975.

[29] J. Bonet and R. D. Wood, *Nonlinear continuum mechanics for finite element analysis*, Cambridge University Press, 1997.

[30] W. Boothby, *An introduction to differentiable manifolds and Riemannian geometry*, Academic, 2003.

[31] M. Borri and C. Bottasso, An intrinsic beam model based on a helicoidal approximation - Part I: Formulation, *International Journal for Numerical Methods in Engineering* **37**, 2267–2289, 1994.

[32] M. Borri and C. Bottasso, An intrinsic beam model based on a helicoidal approximation - Part II: Linearization and finite element implementation, *International Journal for Numerical Methods in Engineering* **37**, 2291–2309, 1994.

[33] D. P. Boso, P. Litewka, B. A. Schrefler, and P. Wriggers, *Analysis and simulation of contact problems*, Springer, 2006.

[34] D. P. Boso, P. Litewka, and B. A. Schrefler, *Recent developments and innovative applications in computational mechanics*, Springer, 2011.

[35] C. L. Bottasso and M. Borri, Integrating finite rotations, *Computer Methods in Applied Mechanics and Engineering* **164**, 307–331, 1998.

[36] F. Boyer and D. Primault, Finite element of slender beams in finite transformations: A geometrically exact approach, *International Journal for Numerical Methods in Engineering* **59**, 669–702, 2004.

[37] F. Boyer, G. De Nayer, A. Leroyer, and M. Visonneau, Geometrically exact Kirchhoff beam theory: Application to cable dynamics, *Journal of Computational and Nonlinear Dynamics* **6**, 1–14, 2011.

[38] F. Brezzi, On the existence, uniqueness and approximation of saddle-point problems arising from lagrangian multipliers, *ESAIM: Mathematical Modelling and Numerical Analysis - Modélisation Mathématique et Analyse Numérique* **8**, 129–151, 1974.

[39] F. Brezzi and M. Fortin, *Mixed and hybrid finite elements*, Springer, 1991.

[40] O. Brüls and A. Cardona, On the use of Lie group time integrators in multibody dynamics, *Journal of Computational and Nonlinear Dynamics* **5**, 031002, 2010.

[41] O. Brüls, A. Cardona, and M. Arnold, Lie group generalized-α time integration of constrained flexible multibody systems, *Mechanism and Machine Theory* **48**, 121–137, 2012.

[42] M. Cannarozzi and L. Molari, A mixed stress model for linear elastodynamics of arbitrarily curved beams, *International Journal for Numerical Methods in Engineering* **74**, 116–137, 2008.

[43] A. Cardona and M. Géradin, A beam finite element non-linear theory with finite rotations, *International Journal for Numerical Methods in Engineering* **26**, 2403–2438, 1988.

[44] A. Cardona, M. Géradin, and D. B. Doan, Rigid and flexible joint modelling in multibody dynamics using finite elements, *Computer Methods in Applied Mechanics and Engineering* **89**, 395–418, 1991.

[45] M. Ceze and K. J. Fidkowski, Constrained pseudo-transient continuation, *International Journal for Numerical Methods in Engineering* **102**, 1683–1703, 2015.

[46] M. Chamekh, S. Mani-Aouadi, and M. Moakher, Modeling and numerical treatment of elastic rods with frictionless self-contact, *Computer Methods in Applied Mechanics and Engineering* **198**, 3751–3764, 2009.

[47] M. Chamekh, S. Mani-Aouadi, and M. Moakher, Stability of elastic rods with self-contact, *Computer Methods in Applied Mechanics and Engineering* **279**, 227–246, 2014.

[48] Q.-Z. Chen, V. Acary, G. Virlez, and O. Brüls, A nonsmooth generalized-α scheme for flexible multibody systems with unilateral constraints, *International Journal for Numerical Methods in Engineering* **96**, 487–511, 2013.

[49] J. K. Choit and J. K. Lim, General curved beam elements based on the assumed strain fields, *Computers & Structures* **55**, 379–386, 1995.

[50] J. Chung and G. M. Hulbert, A time integration algorithm for structural dynamics with improved numerical dissipation: The generalized-α method, *Journal of Applied Mechanics* **60**, 371–375, 1993.

[51] E. Cosserat and F. Cosserat, *Théorie des Corps Déformables*, Traité de Physique, Paris, second ed. Edition, 1909.

[52] M. A. Crisfield, A fast incremental/iterative solution procedure that handles snap-through, *Computers & Structures* **13**, 55–62, 1981.

[53] M. A. Crisfield, *Variable step-lengths for non-linear structural analysis*, TRRL laboratory report, Bridges Division, Structures Department, Transport and Road Research Laboratory, 1982.

[54] M. A. Crisfield, An arc-length method including line searches and accelerations, *International Journal for Numerical Methods in Engineering* **19**, 1269–1289, 1983.

[55] M. A. Crisfield, A consistent co-rotational formulation for non-linear, three-dimensional, beam-elements, *Computer Methods in Applied Mechanics and Engineering* **81**, 131–150, 1990.

[56] M. A. Crisfield, *Non-linear finite element analysis of solids and structures, Volume 2: Advanced topics*, Wiley & Sons, 1997.

[57] M. A. Crisfield, *Non-linear finite element analysis of solids and structures, Volume 1: Essentials*, Wiley & Sons, 2003.

[58] M. A. Crisfield and G. Jelenić, Objectivity of strain measures in the geometrically exact three-dimensional beam theory and its finite-element implementation, *Proceedings of the Royal Society of London. Series A: Mathematical, Physical and Engineering Sciences* **455**, 1125–1147, 1999.

[59] M. A. Crisfield, U. Galvanetto, and G. Jelenić, Dynamics of 3-D co-rotational beams, *Computational Mechanics* **20**, 507–519, 1997.

[60] L. A. Crivelli and C. A. Felippa, A three-dimensional non-linear Timoshenko beam based on the core-congruential formulation, *International Journal for Numerical Methods in Engineering* **36**, 3647–3673, 1993.

[61] C. J. Cyron and W. A. Wall, Numerical method for the simulation of the Brownian dynamics of rod-like microstructures with three-dimensional nonlinear beam elements, *International Journal for Numerical Methods in Engineering* **90**, 955–987, 2012.

[62] F. Demoures, F. Gay-Balmaz, S. Leyendecker, S. Ober-Blöbaum, T. S. Ratiu, and Y. Weinand, Discrete variational Lie group formulation of geometrically exact beam dynamics, *Numerische Mathematik* **130**, 73–123, 2015.

[63] P. Deuflhard, *Newton methods for nonlinear problems*, Volume 35 of *Springer Series in Computational Mathematics*, Springer, 2004.

[64] E. H. Dill, Kirchhoff's theory of rods, *Archive for History of Exact Sciences* **44**, 1–23, 1992.

[65] A. D. Drozdov and Y. Rabin, Elasticity of thin rods with spontaneous curvature and torsion - beyond geometrical lines, *arXiv preprint, arXiv:cond-mat/0002004*, 2000.

[66] E. P. Dukić, G. Jelenić, and M. Gaćeša, Configuration-dependent interpolation in higher-order 2D beam finite elements, *Finite Elements in Analysis and Design* **78**, 47–61, 2014.

[67] D. Durville, Modelling of contact-friction interactions in entangled fibrous materials, In *VI World Wide Congress on Computational Mechanics, Beijing*, 2004.

[68] D. Durville, Finite element simulation of textile materials at mesoscopic scale, In *Finite element modelling of textiles and textile composites, Saint-Petersbourg : Russian Federation*, 2007.

[69] D. Durville, Simulation of the mechanical behaviour of woven fabrics at the scale of fibers, *International Journal of Material Forming* **3**, 1241–1251, 2010.

[70] D. Durville, Contact-friction modeling within elastic beam assemblies: An application to knot tightening, *Computational Mechanics* **49**, 687–707, 2012.

[71] E. N. Dvorkin, E. Oñate, and J. Oliver, On a non-linear formulation for curved Timoshenko beam elements considering large displacement/rotation increments, *International Journal for Numerical Methods in Engineering* **26**, 1597–1613, 1988.

[72] M. Eisenberg and R. Guy, A proof of the hairy ball theorem, *The American Mathematical Monthly* **86**, 571–574, 1979.

[73] T. Elguedj, A. Gravouil, and H. Maigre, An explicit dynamics extended finite element method. Part 1: Mass lumping for arbitrary enrichment functions, *Computer Methods in Applied Mechanics and Engineering* **198**, 2297–2317, 2009.

[74] S. R. Eugster, C. Hesch, P. Betsch, and C. Glocker, Director-based beam finite elements relying on the geometrically exact beam theory formulated in skew coordinates, *International Journal for Numerical Methods in Engineering* **97**, 111–129, 2014.

[75] W. W. Fan and W. D. Zhu, An accurate singularity-free formulation of a three-dimensional curved EulerBernoulli beam for flexible multibody dynamic analysis, *Journal of Vibration and Acoustics* **138**, 051001, 2016.

[76] C. A. Felippa and B. Haugen, A unified formulation of small-strain corotational finite elements: I. Theory, *Computer Methods in Applied Mechanics and Engineering* **194**, 2285–2335, 2005.

[77] I. Fried, Shape functions and the accuracy of arch finite elements, *American Institute of Aeronautics and Astronautics Journal* **11**, 287–291, 1973.

[78] I. Fried and D. S. Malkus, Finite element mass matrix lumping by numerical integration with no convergence rate loss, *International Journal of Solids and Structures* **11**, 461–466, 1975.

[79] J. Frischkorn and S. Reese, A solid-beam finite element and non-linear constitutive modelling, *Computer Methods in Applied Mechanics and Engineering* **265**, 195–212, 2013.

[80] M. W. Gee, C. T. Kelley, and R. B. Lehoucq, Pseudo-transient continuation for nonlinear transient elasticity, *International Journal for Numerical Methods in Engineering* **78**, 1209–1219, 2009.

[81] M. Géradin and A. Cardona, Kinematics and dynamics of rigid and flexible mechanisms using finite elements and quaternion algebra, *Computational Mechanics* **4**, 115–135, 1989.

[82] M. Géradin and A. Cardona, *Flexible multibody dynamics - a finite element approach*, Wiley, 2001.

[83] S. Ghosh and D. Roy, Consistent quaternion interpolation for objective finite element approximation of geometrically exact beam, *Computer Methods in Applied Mechanics and Engineering* **198**, 555–571, 2008.

[84] S. Ghosh and D. Roy, A frame-invariant scheme for the geometrically exact beam using rotation vector parametrization, *Computational Mechanics* **44**, 103–118, 2009.

[85] P. E. Gill and W. Murray, *Safeguard steplength algorithms for optimization using descent method*, National Physics Laboratory report NAC 37, National Physical Laboratory, 1974.

[86] O. Gonzalez, Time integration and discrete Hamiltonian systems, *Journal of Nonlinear Science* **6**, 449–467, 1996.

[87] O. Gonzalez, Exact energy and momentum conserving algorithms for general models in nonlinear elasticity, *Computer Methods in Applied Mechanics and Engineering* **190**, 1763–1783, 2000.

[88] S. Goyal, N. C. Perkins, and C. L. Lee, Nonlinear dynamics and loop formation in Kirchhoff rods with implications to the mechanics of DNA and cables, *Journal of Computational Physics* **209**, 371–389, 2005.

[89] G. M. Grason, Geometry and optimal packing of twisted columns and filaments, *Reviews of Modern Physics* **87**, 401–419, 2015.

[90] L. Greco and M. Cuomo, B-Spline interpolation of Kirchhoff-Love space rods, *Computer Methods in Applied Mechanics and Engineering* **256**, 251–269, 2013.

[91] L. Greco and M. Cuomo, An isogeometric implicit mixed finite element for Kirchhoff space rods, *Computer Methods in Applied Mechanics and Engineering* **298**, 325–349, 2016.

[92] F. Gruttmann, R. Sauer, and W. Wagner, A geometrical nonlinear eccentric 3D-beam element with arbitrary cross-sections, *Computer Methods in Applied Mechanics and Engineering* **160**, 383–400, 1998.

[93] M. E. Gurtin, *An introduction to continuum mechanics*, Academic Press, 1981.

[94] G. J. Hall and E. P. Kasper, Comparison of element technologies for modeling stent expansion, *Journal of Biomechanical Engineering* **128**, 751–756, 2006.

[95] M. R. Hestenes and E. Stiefel, Methods of conjugate gradients for solving linear systems, *Journal of Research of the National Bureau of Standards* **49**, 409–436, 1952.

[96] H. M. Hilber, T. J. R. Hughes, and R. L. Taylor, Improved numerical dissipation for time integration algorithms in structural dynamics, *Earthquake Engineering & Structural Dynamics* **5**, 283–292, 1977.

[97] E. Hinton, T. Rock, and O. C. Zienkiewicz, A note on mass lumping and related processes in the finite element method, *Earthquake Engineering & Structural Dynamics* **4**, 245–249, 1976.

[98] G. A. Holzapfel, *Nonlinear solid mechanics: A continuum approach for engineering*, Wiley, 2000.

[99] J. Howard, *Mechanics of motor proteins and the cytoskeleton*, Sinauer Associates, 2001.

[100] K. M. Hsiao and R. T. Yang, A co-rotational formulation for nonlinear dynamic analysis of curved Euler beam, *Computers & Structures* **54**, 1091–1097, 1995.

[101] K. M. Hsiao, R. T. Yang, and A. C. Lee, A consistent finite element formulation for nonlinear dynamic analysis of planar beam, *International Journal for Numerical Methods in Engineering* **37**, 75–89, 1994.

[102] K. M. Hsiao, J. Y. Lin, and W. Y. Lin, A consistent co-rotational finite element formulation for geometrically nonlinear dynamic analysis of 3-D beams, *Computer Methods in Applied Mechanics and Engineering* **169**, 1–18, 1999.

[103] T. J. R. Hughes, *The finite element method - linear static and dynamic finite element analysis*, Dover, 2000.

[104] T. J. R. Hughes, R. L. Taylor, and W. Kanoknukulchai, A simple and efficient finite element for plate bending, *International Journal for Numerical Methods in Engineering* **11**, 1529–1543, 1977.

[105] T. J. R. Hughes, T. K. Caughey, and W. K. Liu, Finite-element methods for nonlinear elastodynamics which conserve energy, *Journal of Applied Mechanics* **45**, 366–370, 1978.

[106] A. Ibrahimbegović, On finite element implementation of geometrically nonlinear Reissner's beam theory: Three-dimensional curved beam elements, *Computer Methods in Applied Mechanics and Engineering* **122**, 11–26, 1995.

[107] A. Ibrahimbegović, On the choice of finite rotation parameters, *Computer Methods in Applied Mechanics and Engineering* **149**, 49–71, 1997.

[108] A. Ibrahimbegović and F. Frey, Finite element analysis of linear and non-linear planar deformations of elastic initially curved beams, *International Journal for Numerical Methods in Engineering* **36**, 3239–3258, 1993.

[109] A. Ibrahimbegović and S. Mamouri, Energy conserving/decaying implicit time-stepping scheme for nonlinear dynamics of three-dimensional beams undergoing finite rotations, *Computer Methods in Applied Mechanics and Engineering* **191**, 4241–4258, 2002.

[110] A. Ibrahimbegović and R. L. Taylor, On the role of frame-invariance in structural mechanics models at finite rotations, *Computer Methods in Applied Mechanics and Engineering* **191**, 5159–5176, 2002.

[111] A. Ibrahimbegović, F. Frey, and I. Kozar, Computational aspects of vector-like parametrization of three-dimensional finite rotations, *International Journal for Numerical Methods in Engineering* **38**, 3653–3673, 1995.

[112] A. Iosilevich, K.-J. Bathe, and F. Brezzi, On evaluating the infsup condition for plate bending elements, *International Journal for Numerical Methods in Engineering* **40**, 3639–3663, 1997.

[113] M. Iura and S. N. Atluri, Dynamic analysis of finitely stretched and rotated three-dimensional space-curved beams, *Computers and Structures* **29**, 875–889, 1988.

[114] M. K. Jawed, P. Dieleman, B. Audoly, and P. M. Reis, Untangling the mechanics and topology in the frictional response of long overhand elastic knots, *Physical Review Letter* **115**, 118302, 2015.

[115] G. Jelenić and M. A. Crisfield, Interpolation of rotational variables in nonlinear dynamics of 3D beams, *International Journal for Numerical Methods in Engineering* **43**, 1193–1222, 1998.

[116] G. Jelenić and M. A. Crisfield, Geometrically exact 3D beam theory: Implementation of a strain-invariant finite element for statics and dynamics, *Computer Methods in Applied Mechanics and Engineering* **171**, 141–171, 1999.

[117] G. Jelenić and M. Saje, A kinematically exact space finite strain beam model - finite element formulation by generalized virtual work principle, *Computer Methods in Applied Mechanics and Engineering* **120**, 131–161, 1995.

[118] P. Jung, S. Leyendecker, J. Linn, and M. Ortiz, A discrete mechanics approach to the Cosserat rod theory - Part 1: Static equilibria, *International Journal for Numerical Methods in Engineering* **85**, 31–60, 2011.

[119] C. Kane, J. E. Marsden, M. Ortiz, and M. West, Variational integrators and the Newmark algorithm for conservative and dissipative mechanical systems, *International Journal for Numerical Methods in Engineering* **49**, 1295–1325, 2000.

[120] R. K. Kapania and J. Li, A formulation and implementation of geometrically exact curved beam elements incorporating finite strains and finite rotations, *Computational Mechanics* **30**, 444–459, 2003.

[121] D. Karamanlidis and R. Jasti, Curved mixed beam elements for the analysis of thin-walled free-form arches, *Ingenieur-Archiv* **57**, 361–367, 1987.

[122] O. Kawa and P. Litewka, Contact with friction between 3D beams with deformable circular cross-sections, *Engineering Transactions* **63**, 439–462, 2015.

[123] C. T. Kelley, *Solving nonlinear equations with Newton's method*, Volume 1 of *Fundamentals of algorithms*, SIAM, 2003.

[124] C. T. Kelley and D. E. Keyes, Convergence analysis of pseudo-transient continuation, *SIAM Journal on Numerical Analysis* **35**, 508–523, 1998.

[125] G. Kirchhoff, Ueber das Gleichgewicht und die Bewegung eines unendlich dünnen elastischen Stabes, *Journal für die reine und angewandte Mathematik* **56**, 285–313, 1859.

[126] W. T. Koiter, On the nonlinear theory of thin elastic shells, In *Proceedings of the Koninklijke Nederlandse Akademie van Wetenschappen*, Volume 69, 1966.

[127] K. Kondoh, K. Tanaka, and S. N. Atluri, An explicit expression for the tangent-stiffness of a finitely deformed 3-D beam and its use in the analysis of space frames, *Computers & Structures* **24**, 253–271, 1986.

[128] A. Konyukhov and K. Schweizerhof, On the solvability of closest point projection procedures in contact analysis: Analysis and solution strategy for surfaces of arbitrary geometry, *Computer Methods in Applied Mechanics and Engineering* **197**, 3045–3056, 2008.

[129] A. Konyukhov and K. Schweizerhof, Geometrically exact covariant approach for contact between curves, *Computer Methods in Applied Mechanics and Engineering* **199**, 2510–2531, 2010.

[130] F. Koschnick, *Geometrische Locking-Effekte bei Finiten Elementen und ein allgemeines Konzept zu ihrer Vermeidung*, PhD thesis, Lehrstuhl für Statik, Technische Universität München, 2004.

[131] D. Kuhl and M. A. Crisfield, Energy-conserving and decaying algorithms in non-linear structural dynamics, *International Journal for Numerical Methods in Engineering* **45**, 569–599, 1999.

[132] D. Kuhl and E. Ramm, Constraint energy momentum algorithm and its application to non-linear dynamics of shells, *Computer Methods in Applied Mechanics and Engineering* **136**, 293–315, 1996.

[133] D. Kuhl and E. Ramm, Generalized energy-momentum method for non-linear adaptive shell dynamics, *Computer Methods in Applied Mechanics and Engineering* **178**, 343–366, 1999.

[134] J. B. Kuipers, *Quaternions and rotation sequences*, Princeton University Press, 1999.

[135] A. Kulachenko and T. Uesaka, Direct simulations of fiber network deformation and failure, *Mechanics of Materials* **51**, 1–14, 2012.

[136] H. Lang and M. Arnold, Numerical aspects in the dynamic simulation of geometrically exact rods, *Applied Numerical Mathematics* **62**, 1411–1427, 2012.

[137] H. Lang, J. Linn, and M. Arnold, Multi-body dynamics simulation of geometrically exact Cosserat rods, *Multibody System Dynamics* **25**, 285–312, 2010.

[138] J. Langer and D. A. Singer, Lagrangian aspects of the Kirchhoff elastic rod, *SIAM Review* **38**, 605–618, 1996.

[139] T. A. Laursen, *Computational contact and impact mechanics*, Springer, 2002.

[140] A. Lazarus, J. J. T. Miller, and P. M. Reis, Continuation of equilibria and stability of slender elastic rods using an asymptotic numerical method, *Journal of the Mechanics and Physics of Solids* **61**, 1712–1736, 2013.

[141] T.-N. Le, J.-M. Battini, and M. Hjiaj, A consistent 3D corotational beam element for nonlinear dynamic analysis of flexible structures, *Computer Methods in Applied Mechanics and Engineering* **269**, 538–565, 2014.

[142] P. G. Lee and H. C. Sin, Locking-free straight beam element based on curvature, *Communications in Numerical Methods in Engineering* **9**, 1005–1011, 1993.

[143] S. H. Lee, Rudimentary considerations for effective line search method in nonlinear finite element analysis, *Computers & Structures* **32**, 1287–1301, 1989.

[144] E. V. Lens and A. Cardona, A nonlinear beam element formulation in the framework of an energy preserving time integration scheme for constrained multibody systems dynamics, *Computers & Structures* **86**, 47–63, 2008.

[145] J. Linn, H. Lang, and A. Tuganov, Geometrically exact Cosserat rods with Kelvin-Voigt type viscous damping, *Mechanical Sciences* **4**, 79–96, 2013.

[146] P. Litewka, The penalty and Lagrange multiplier methods in the frictional 3D beam-to-beam contact problem, *Civil and Environmental Engineering Reports* **1**, 189–207, 2005.

[147] P. Litewka, Hermite polynomial smoothing in beam-to-beam frictional contact, *Computational Mechanics* **40**, 815–826, 2007.

[148] P. Litewka, *Finite element analysis of beam-to-beam contact*, Springer, 2010.

[149] P. Litewka, Enhanced multiple-point beam-to-beam frictionless contact finite element, *Computational Mechanics* **52**, 1365–1380, 2013.

[150] P. Litewka, Frictional beam-to-beam multiple-point contact finite element, *Computational Mechanics* **56**, 243–264, 2015.

[151] P. Litewka and P. Wriggers, Contact between 3D beams with rectangular cross-sections, *International Journal for Numerical Methods in Engineering* **53**, 2019–2041, 2002.

[152] P. Litewka and P. Wriggers, Frictional contact between 3D beams, *Computational Mechanics* **28**, 26–39, 2002.

[153] A. E. H. Love, *A treatise on the mathematical theory of elasticity*, Dover, 1944.

[154] M. Lyly, R. Stenberg, and T. Vihinen, A stable bilinear element for the Reissner-Mindlin plate model, *Computer Methods in Applied Mechanics and Engineering* **110**, 343–357, 1993.

[155] J. E. Marsden and T. J. R. Hughes, *Mathematical foundations of elasticity*, Dover, 1994.

[156] C. Meier, A. Popp, and W. A. Wall, An objective 3D large deformation finite element formulation for geometrically exact curved Kirchhoff rods, *Computer Methods in Applied Mechanics and Engineering* **278**, 445–478, 2014.

[157] C. Meier, A. Popp, and W. A. Wall, A locking-free finite element formulation and reduced models for geometrically exact Kirchhoff rods, *Computer Methods in Applied Mechanics and Engineering* **290**, 314–341, 2015.

[158] C. Meier, A. Popp, and W. A. Wall, A finite element approach for the line-to-line contact interaction of thin beams with arbitrary orientation, *Computer Methods in Applied Mechanics and Engineering*, accepted for publication.

[159] C. Meier, A. Popp, and W. A. Wall, A unified approach for beam-to-beam contact, *Computer Methods in Applied Mechanics and Engineering*, submitted for publication.

[160] K. W. Müller, R. F. Bruinsma, O. Lieleg, A. R. Bausch, W. A. Wall, and A. J. Levine, Rheology of semiflexible bundle networks with transient linkers, *Physical Review Letters* **112**, 238102, 2014.

[161] K. W. Müller, C. Meier, and W. A. Wall, Resolution of sub-element length scales in Brownian dynamics simulations of biopolymer networks with geometrically exact beam finite elements, *Journal of Computational Physics* **303**, 185–202, 2015.

[162] A. G. Neto, P. M. Pimenta, and P. Wriggers, Self-contact modeling on beams experiencing loop formation, *Computational Mechanics* **55**, 193–208, 2015.

[163] A. G. Neto, P. M. Pimenta, and P. Wriggers, A master-surface to master-surface formulation for beam to beam contact. Part I: frictionless interaction, *Computer Methods in Applied Mechanics and Engineering* **303**, 400–429, 2016.

[164] A. Neto, C. Martins, and P. Pimenta, Static analysis of offshore risers with a geometrically-exact 3D beam model subjected to unilateral contact, *Computational Mechanics* **53**, 125–145, 2014.

[165] A. Neto, P. Pimenta, and P. Wriggers, Contact between rolling beams and flat surfaces, *International Journal for Numerical Methods in Engineering* **97**, 683–706, 2014.

[166] N. M. Newmark, A method of computation for structural dynamics, *Journal of the Engineering Mechanics Division ASCE* **85**, 67–94, 1959.

[167] J. Nocedal and S. Wright, *Numerical optimization*, Springer, 2006.

[168] A. K. Noor and J. M. Peters, Mixed models and reduced/selective integration displacement models for nonlinear analysis of curved beams, *International Journal for Numerical Methods in Engineering* **17**, 615–631, 1981.

[169] R. W. Odgen, *Non-linear elastic deformation*, Dover Publications, 1997.

[170] J. M. Ortega and W. C. Rheinboldt, *Iterative solution of nonlinear equations in several variables*, Volume 30 of *Classics in applied Mathematics*, SIAM, 1970.

[171] P. F. Pai and A. N. Palazotto, Large-deformation analysis of flexible beams, *International Journal of Solids and Structures* **33**, 1335–1353, 1996.

[172] E. Petrov and M. Géradin, Finite element theory for curved and twisted beams based on exact solutions for three-dimensional solids Part 1: Beam concept and geometrically exact nonlinear formulation, *Computer Methods in Applied Mechanics and Engineering* **165**, 43–92, 1998.

[173] A. Popp and W. A. Wall, Dual mortar methods for computational contact mechanics – overview and recent developments, *GAMM-Mitteilungen* **37**, 66–84, 2014.

[174] A. Popp, M. W. Gee, and W. A. Wall, A finite deformation mortar contact formulation using a primal-dual active set strategy, *International Journal for Numerical Methods in Engineering* **79**, 1354–1391, 2009.

[175] A. Popp, M. Gitterle, M. W. Gee, and W. A. Wall, A dual mortar approach for 3D finite deformation contact with consistent linearization, *International Journal for Numerical Methods in Engineering* **83**, 1428–1465, 2010.

[176] G. Prathap, The curved beam/deep arch/finite ring element revisited, *International Journal for Numerical Methods in Engineering* **21**, 389–407, 1985.

[177] G. Prathap and B. P. Naganarayana, Analysis of locking and stress oscillations in a general curved beam element, *International Journal for Numerical Methods in Engineering* **30**, 177–200, 1990.

[178] A. Quarteroni, R. Sacco, and S. Fausto, *Numerical mathematics*, Springer, 2000.

[179] S. B. Raknes, X. Deng, Y. Bazilevs, D. J. Benson, K. M. Mathisen, and T. Kvamsdal, Isogeometric rotation-free bending-stabilized cables: Statics, dynamics, bending strips and coupling with shells, *Computer Methods in Applied Mechanics and Engineering* **263**, 127–143, 2013.

[180] E. Ramm, Nonlinear finite element analysis in structural mechanics, In *Proceedings of the Europe-U.S. workshop Ruhr-Universität Bochum, Germany*, 1981.

[181] B. D. Reddy, *Functional analysis: An introductory treatment*, Longman, London and Wiley, 1986.

[182] J. N. Reddy, *An introduction to nonlinear finite element analysis*, Oxford University Press, 2004.

[183] E. Reissner, On one-dimensional finite-strain beam theory: The plane problem, *Zeitschrift für Angewandte Mathematik und Physik (ZAMP)* **23**, 795–804, 1972.

[184] E. Reissner, On finite deformations of space-curved beams, *Zeitschrift für Angewandte Mathematik und Physik (ZAMP)* **32**, 734–744, 1981.

[185] M. Repupilli, *A robust method for beam-to-beam contact problems based on a novel tunneling constraint*, PhD thesis, University of California, Los Angeles, 2012.

[186] D. Rodney, B. Gadot, O. R. Martinez, S. R. Roscoat, and L. Orgéas, Reversible dilatancy in entangled single-wire materials, *Nature Materials* **15**, 72–77, 2016.

[187] I. Romero, The interpolation of rotations and its application to finite element models of geometrically exact rods, *Computational Mechanics* **34**, 121–133, 2004.

[188] I. Romero, A comparison of finite elements for nonlinear beams: The absolute nodal coordinate and geometrically exact formulations, *Multibody System Dynamics* **20**, 51–68, 2008.

[189] I. Romero, Formulation and performance of variational integrators for rotating bodies, *Computational Mechanics* **42**, 825–836, 2008.

[190] I. Romero and F. Armero, An objective finite element approximation of the kinematics of geometrically exact rods and its use in the formulation of an energymomentum conserving scheme in dynamics, *International Journal for Numerical Methods in Engineering* **54**, 1683–1716, 2002.

[191] I. Romero, M. Urrecha, and C. J. Cyron, A torsion-free non-linear beam model, *International Journal of Non-Linear Mechanics* **58**, 1–10, 2014.

[192] B. Roy, S. Lerouge, K. Inaekyan, C. Kauffmann, R. Mongrain, and G. Soulez, Experimental validation of more realistic computer models for stent-graft repair of abdominal aortic aneurysms, including pre-load assessment, *International Journal for Numerical Methods in Biomedical Engineering*, e02769. doi: 10.1002/cnm.2769.

[193] Y. Saad, *Iterative methods for sparse linear systems*, SIAM, 2003.

[194] O. Sander, Geodesic finite elements for Cosserat rods, *International Journal for Numerical Methods in Engineering* **82**, 1645–1670, 2010.

[195] C. Sansour and W. Wagner, Multiplicative updating of the rotation tensor in the finite element analysis of rods and shells - a path independent approach, *Computational Mechanics* **31**, 153–162, 2003.

[196] C. Sansour, T. L. Nguyen, and M. Hjiaj, An energy-momentum method for in-plane geometrically exact Euler-Bernoulli beam dynamics, *International Journal for Numerical Methods in Engineering* **102**, 99–134, 2015.

[197] H. A. F. A. Santos, P. M. Pimenta, and J. P. M. Almeida, A hybrid-mixed finite element formulation for the geometrically exact analysis of three-dimensional framed structures, *Computational Mechanics* **48**, 591–613, 2011.

[198] M. G. Schmidt, A. E. Ismail, and R. A. Sauer, A continuum mechanical surrogate model for atomic beam structures, *International Journal for Multiscale Computational Engineering* **13**, 413–442, 2015.

[199] M. Schulz and F. C. Filippou, Non-linear spatial Timoshenko beam element with curvature interpolation, *International Journal for Numerical Methods in Engineering* **50**, 761–785, 2001.

[200] A. A. Shabana and R. Y. Yakoub, Three dimensional absolute nodal coordinate formulation for beam elements: Theory, *Journal of Mechanical Design* **123**, 606–613, 2001.

[201] A. A. Shabana, H. A. Hussien, and J. L. Escalona, Application of the absolute nodal coordinate formulation to large rotation and large deformation problems, *Journal of Mechanical Design* **120**, 188–195, 1998.

[202] Y. Shi and J. E. Hearst, The Kirchhoff elastic rod, the nonlinear Schrödinger equation, and DNA supercoiling, *The Journal of Chemical Physics* **101**, 5186–5200, 1994.

[203] K. Shoemake, Animating rotation with quaternion curves, *ACM SIGGRAPH Computer Graphics* **19**, 245–254, 1985.

[204] J. C. Simo, A finite strain beam formulation. The three-dimensional dynamic problem. Part I, *Computer Methods in Applied Mechanics and Engineering* **49**, 55–70, 1985.

[205] J. C. Simo and T. J. R. Hughes, On the variational foundations of assumed strain methods, *Journal of Applied Mechanics* **53**, 51–54, 1986.

[206] J. C. Simo and T. J. R. Hughes, *Computational inelasticity*, Springer, 1998.

[207] J. C. Simo and N. Tarnow, The discrete energy-momentum method. Conserving algorithms for nonlinear elastodynamics, *Zeitschrift für angewandte Mathematik und Physik (ZAMP)* **43**, 757–792, 1992.

[208] J. C. Simo and L. Vu-Quoc, A three-dimensional finite strain rod model. Part II: Computational aspects, *Computer Methods in Applied Mechanics and Engineering* **58**, 79–116, 1986.

[209] J. C. Simo and L. Vu-Quoc, On the dynamics in space of rods undergoing large motions - a geometrically exact approach, *Computer Methods in Applied Mechanics and Engineering* **66**, 125–161, 1988.

[210] J. C. Simo and K. K. Wong, Unconditionally stable algorithms for rigid body dynamics that exactly preserve energy and momentum, *International Journal for Numerical Methods in Engineering* **31**, 19–52, 1991.

[211] W. M. Smolenski, Statically and kinematically exact nonlinear theory of rods and its numerical verification, *Computer Methods in Applied Mechanics and Engineering* **178**, 89–113, 1998.

[212] V. Sonneville, A. Cardona, and O. Brüls, Geometrically exact beam finite element formulated on the special Euclidean group, *Computer Methods in Applied Mechanics and Engineering* **268**, 451–474, 2014.

[213] V. Sonneville, A. Cardona, and O. Brüls, Geometric interpretation of a non-linear beam finite element on the Lie group SE(3), *Archive of Mechanical Engineering* **61**, 305–329, 2014.

[214] R. A. Spurrier, Comment on "singularity-free extraction of a quaternion from a direction-cosine matrix", *Journal of Spacecraft and Rockets* **15**, 255–255, 1978.

[215] H. Stolarski and T. Belytschko, Membrane locking and reduced integration for curved elements, *Journal of Applied Mechanics* **49**, 172–176, 1982.

[216] G. Strang and G. Fix, *An analysis of the finite elment method*, Wellesley-Cambrigde Press, 2008.

[217] J. Stuelpnagel, On the parametrization of the three-dimensional rotation group, *SIAM Review* **6**, 422–430, 1964.

[218] A. Tessler and L. Spiridigliozzi, Curved beam elements with penalty relaxation, *International Journal for Numerical Methods in Engineering* **23**, 2245–2262, 1986.

[219] S. P. Timoshenko, On the correction for shear of the differential equation for transverse vibrations of prismatic bars, *Philosophical Magazine Series 6* **41**, 744–746, 1921.

[220] P. Češarek, M. Saje, and D. Zupan, Kinematically exact curved and twisted strain-based beam, *International Journal of Solids and Structures* **49**, 1802–1817, 2012.

[221] T. D. Vu, D. Durville, and P. Davies, Finite element simulation of the mechanical behavior of synthetic braided ropes and validation on a tensile test, *International Journal of Solids and Structures* **58**, 106–116, 2015.

[222] W. A. Wall and M. W. Gee, BACI: A multiphysics simulation environment, Technical report, Technical University of Munich, 2016.

[223] Q. Wang and C. M. Wang, The constitutive relation and small scale parameter of nonlocal continuum mechanics for modelling carbon nanotubes, *Nanotechnology* **18**, 075702, 2007.

[224] Q. Wang, Q. Tian, and H. Hu, Dynamic simulation of frictional contacts of thin beams during large overall motions via absolute nodal coordinate formulation, *Nonlinear Dynamics* **77**, 1411–1425, 2014.

[225] Q. Wang, Q. Tian, and H. Hu, Dynamic simulation of frictional multi-zone contacts of thin beams, *Nonlinear Dynamics* **83**, 1919–1937, 2016.

[226] O. Weeger, S.-K. Yeung, and M. L. Dunn, Isogeometric collocation methods for Cosserat rods and rod structures, *Computer Methods in Applied Mechanics and Engineering*, http://dx.doi.org/10.1016/j.cma.2016.05.009, 2016.

[227] H. Weiss, Dynamics of geometrically nonlinear rods: I. Mechanical models and equations of motion, *Nonlinear Dynamics* **30**, 357–381, 2002.

[228] H. Weiss, Dynamics of geometrically nonlinear rods: II. Numerical methods and computational examples, *Nonlinear Dynamics* **30**, 383–415, 2002.

[229] G. Wempner, Finite elements, finite rotations and small strains of flexible shells, *International Journal of Solids and Structures* **5**, 117–153, 1969.

[230] B. I. Wohlmuth, *Discretization methods and iterative solvers based on domain decomposition*, Springer, 2001.

[231] B. I. Wohlmuth, Variationally consistent discretization schemes and numerical algorithms for contact problems, *Acta Numerica* **20**, 569–734, 2011.

[232] W. L. Wood, M. Bossak, and O. C. Zienkiewicz, An alpha modification of Newmark's method, *International Journal for Numerical Methods in Engineering* **15**, 1562–1566, 1980.

[233] P. Wriggers, *Computational contact mechanics*, Springer, 2006.

[234] P. Wriggers and G. Zavarise, On contact between three-dimensional beams undergoing large deflections, *Communications in Numerical Methods in Engineering* **13**, 429–438, 1997.

[235] L. Xiang, H. Y. Wang, Y. Chen, Y. J. Guan, Y. L. Wang, and L. H. Dai, Modeling of multi-strand wire ropes subjected to axial tension and torsion loads, *International Journal of Solids and Structures* **58**, 233–246, 2015.

[236] Y. Yang, I. Tobias, and W. K. Olson, Finite element analysis of DNA supercoiling, *The Journal of Chemical Physics* **98**, 1673–1686, 1993.

[237] G. Zavarise and P. Wriggers, Contact with friction between beams in 3-D space, *International Journal for Numerical Methods in Engineering* **49**, 977–1006, 2000.

[238] Z. Zhang, Z. Qi, Z. Wu, and H. Fang, A spatial Euler-Bernoulli beam element for rigid-flexible coupling dynamic analysis of flexible structures, *Shock and Vibration* **2015**, 208127, 2015.

[239] Z. Zhao and G. Ren, A quaternion-based formulation of Euler–Bernoulli beam without singularity, *Nonlinear Dynamics* **67**, 1825–1835, 2012.

[240] X.-Y. Zhou, F. Zheng, H.-G. Li, and C.-L. Lu, An environment-friendly thermal insulation material from cotton stalk fibers, *Energy and Buildings* **42**, 1070–1074, 2010.

[241] H. Ziegler, *Principles of structural stability*, Birkhauser, 1977.

[242] O. C. Zienkiewicz and R. L. Taylor, *The finite element method for solid and structural mechanics*, Elsevier Butterworth-Heinemann, 2005.

[243] O. C. Zienkiewicz, R. L. Taylor, and J. Z. Zhu, *The finite element method: Its basis & fundamentals*, Elsevier Butterworth-Heinemann, 2005.

[244] D. Zupan and M. Saje, Finite-element formulation of geometrically exact three-dimensional beam theories based on interpolation of strain measures, *Computer Methods in Applied Mechanics and Engineering* **192**, 5209–5248, 2003.

[245] D. Zupan and M. Saje, The linearized three-dimensional beam theory of naturally curved and twisted beams: The strain vectors formulation, *Computer Methods in Applied Mechanics and Engineering* **195**, 4557–4578, 2006.

[246] E. Zupan, M. Saje, and D. Zupan, On a virtual work consistent three-dimensional Reissner–Simo beam formulation using the quaternion algebra, *Acta Mechanica* **224**, 1709–1729, 2013.